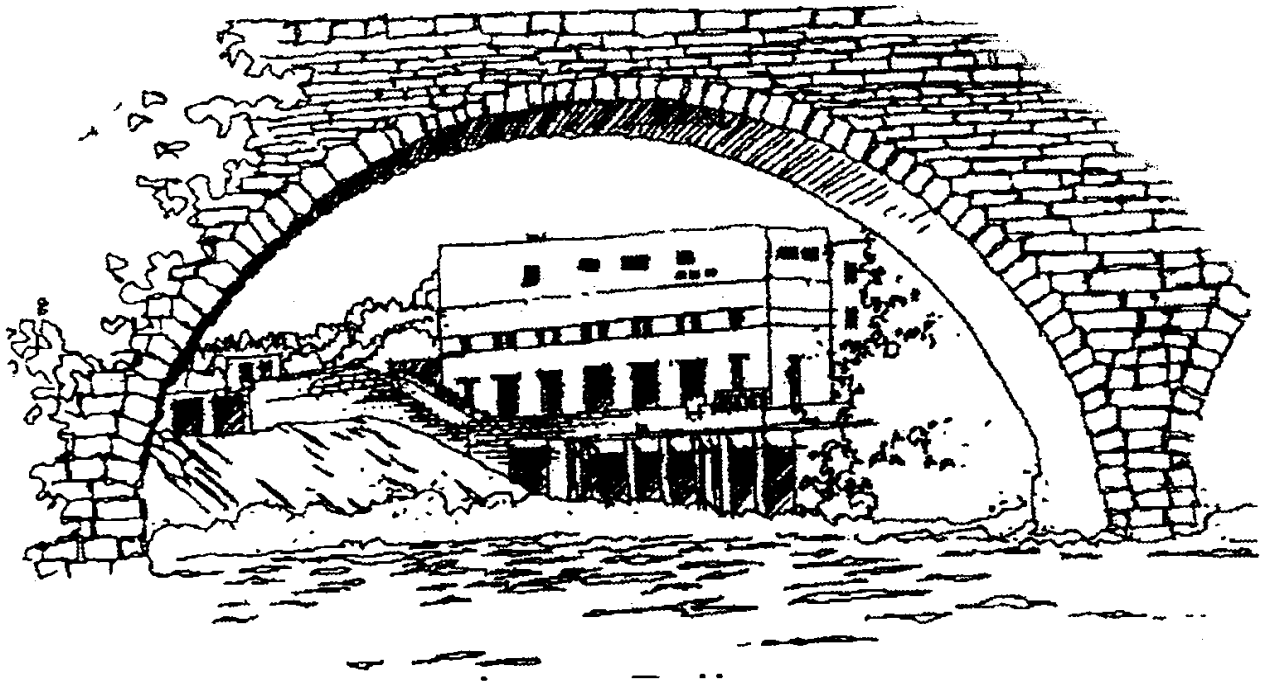*A collection of papers on*

"LANDSCAPE ORGANIZATION, SIGNATURE OF PROCESS ON FORM, AND THE ROLE OF FLUCTUATIONS ON GEOMORPHIC TRANSPORT"

by:

The hydro-geomorphology group at the University of Minnesota, Department of Civil Engineering (see inside for full list of contributors)

2006 -2010

SAFL

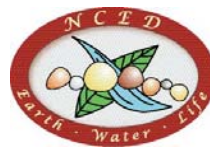**St. Anthony Falls Laboratory**
University of Minnesota
Minneapolis, MN

National Center for Earth Dynamics

CONTRIBUTORS

University of Minnesota

Efi Foufoula-Georgiou
Elizabeth Barnes
Kurt Fienberg
Chandana Gangodagamage
Vamsi Ganti
Miki Hondzo
Bruno Lashermes
Jeff Marr
Chris Paola
Paola Passalacqua
Fernando Porté-Agel
Guillermo Sapiro
Arvind Singh
Vaughan Voller

External Collaborators

William Dietrich (University of California – Berkeley)
Michael Ghil (University of California – Los Angeles)
Douglas J. Jerolmack (University of Pennsylvania)
Stefano Lanzoni (Università di Padova, Italy)
Mark Meerschaert (Michigan State University)
David Mohrig (Massachusetts Institute of Technology)
Gary Parker (University of Illinois)
Mary E. Power (University of California – Berkeley)
Ignacio Rodriguez-Iturbe (Princeton University)
Leonard Sklar (San Francisco State University)
Colin Stark (Columbia University)
Tien Do Trung (Ecole Normale Superieure de Cachan, Paris)
Enrica Viparelli (University of Illinois)
Peter Wilcock (Johns Hopkins University)
Ilya Zaliapin (University of Nevada – Reno)

TABLE OF CONTENTS

1. Foufoula-Georgiou, E., and C. Stark, Rethinking geomorphic transport: stochastic theories, broad scales of motion and non-locality, *J. Geophys. Res. - Earth Surface*, in press, 2010

2. Singh, A., F. Porté-Agel, and E. Foufoula-Georgiou, On the influence of gravel bed dynamics on velocity power spectra, *Water Resour. Res.*, in press, 2010.

3. Zaliapin, I., E. Foufoula-Georgiou, and M. Ghil, Transport on river networks: a dynamical approach, *J. Geophys. Res. - Earth Surface*, in press, 2010.

4. Foufoula-Georgiou, E., V. Ganti, and W. E., Dietrich, A non-local theory for sediment transport on hillslopes, *J. Geophys. Res. - Earth Surface*, under review, 2009.

5. Ganti, V., M. Meerschaert, E. Foufoula-Georgiou, E. Viparelli, and G. Parker, Normal and anomalous dispersion of gravel tracer particles in rivers, *J. Geophys. Res. - Earth Surface*, in press, 2010.

6. Passalacqua, P., T. Do Trung, E. Foufoula-Georgiou, G. Sapiro, and W. E. Dietrich, A geometric framework for channel network extraction from LiDAR: nonlinear diffusion and geodesic paths, *J. Geophys. Res.*, 115, F01002, doi:10.1029/2009JF001254, 2010.

7. Ganti, V. A. Singh, P. Passalacqua, and E. Foufoula-Georgiou, A subordinated Brownian motion model for sediment transport, *Phys. Rev. E*, 80, 011111, 2009.

8. Singh, A., K. Fienberg, D. J. Jerolmack, J. Marr, and E. Foufoula-Georgiou, Experimental evidence for statistical scaling and intermittency in sediment transport rates, *Journal of Geophysical Research*, 114, F01025, doi:10.1029/2007JF000963, 2009.

9. Singh, A., S. Lanzoni, and E. Foufoula-Georgiou, Nonlinearity and complexity in gravel bed dynamics, in Stochastic Environmental Research and Risk Assessment, Springer Velrag, N.Y, doi: 10.1007/S00477-008-0269-8, 2008

10. Stark, C.P., E. Foufoula-Georgiou, and V. Ganti, A nonlocal theory of sediment buffering and bedrock channel evolution, *Journal of Geophysical Research*, doi:10.1029/2008JF000981, 2008.

11. Fienberg, K., A. Singh, E. Foufoula-Georgiou, D. Jerolmack, and J. Marr, A theoretical framework for interpreting and quantifying the sampling time dependence of gravel bedload transport rates, under review, 2008.

12. Barnes E. A., M. E. Power, E. Foufoula-Georgiou, M. Hondzo, W. E. Dietrich, Upscaling river biomass using dimensional analysis and hydrogeomorphic scaling, *Geophys. Res. Lett.*, 34, L24S26, doi:10.1029/2007GL031931, 2007.

13. Lashermes, B., E. Foufoula-Georgiou, and W. E. Dietrich, Channel network extraction from high resolution topography using wavelets, *Geophys. Res. Lett.*, 34, L23S04, doi:10.1029/2007GL031140, 2007

14. Lashermes, B. and E. Foufoula-Georgiou, Area and width functions of river networks: New results on multifractal properties, *Water Resour. Res.*, 43, W09405, doi:10.1029/2006WR005329, 2007

15. Gangodagamage, C., E. Barnes, and E. Foufoula-Georgiou, Scaling in river corridor widths depicts organization in valley morphology, *Geomorphology*, 91(3-4), 198-215, doi:10.1016/j.geomorph.2007.04.014, 2007

16. Passalacqua P., F. Porté-Agel, E. Foufoula-Georgiou, C. Paola, Application of dynamic subgrid-scale concepts from large-eddy simulation to modeling landscape evolution, *Water Resources Research*, 42, W06D11, doi:10.1029/2006WR004879, 2006.

17. Sklar L. S., W. E. Dietrich, E. Foufoula-Georgiou, B. Lashermes, D. Bellugi, Do gravel bed river size distributions record channel network structure?, *Water Resources Research*, 42, W06D18, doi:10.1029/2006WR005035, 2006.

18. Paola C., E. Foufoula-Georgiou, W. E. Dietrich, M. Hondzo, D. Mohrig, G. Parker, M. E. Power, I. Rodriguez-Iturbe, V. Voller, P. Wilcock, Toward a unified science of the Earth's surface: Opportunities for synthesis among hydrology, geomorphology, geochemistry, and ecology, *Water Resources Research*, 42, W03S10, doi:10.1029/2005WR004336, 2006.

RETHINKING GEOMORPHIC TRANSPORT:
STOCHASTIC THEORIES, BROAD SCALES OF MOTION AND NON-LOCALITY

By

Efi Foufoula-Georgiou[1] and Colin Stark[2]

[1] Department of Civil Engineering, National Center for Earth-surface Dynamics, and St. Anthony Falls Laboratory, University of Minnesota, Minneapolis, MN

[2] Lamont-Doherty Earth Observatory, Columbia University, Palisades, NY 10964

ABSTRACT

In many geomorphic transport systems, the time and length scales of motion vary widely: particles can be trapped for both short and long periods of time and they can travel large or small distances in very short intervals of time. To model such systems we need fresh conceptual and mathematical formalisms. The goal of this collection of papers is to challenge existing thinking in geomorphic transport by putting forward new ideas and theories for environmental fluxes, from particle transport in a single stream, to landslide debris mobilization, sediment and water transport on hillslopes, dynamic transport on river networks, and interpretation of sedimentary deposits over geologic time. Advanced stochastic theories of transport are proposed, the notion of non-local flux is introduced, and fractional advection-diffusion equations are explored as possible models of geomorphic transport.

1. INTRODUCTION

In November, 2007 a working group meeting entitled *Stochastic Transport and Emergent Scaling on the Earth's Surface (STRESS)* was convened in Lake Tahoe, Nevada. Its scope was to bring together geomorphologists, hydrologists, mathematicians, and physicists with the goal of rethinking the mathematical treatment of transport processes on the Earth's surface. The specific questions asked were: (1) How can we reconcile observed patterns and organization (from sand dunes, to landslides, sedimentary deposits, hillslope profiles, and sediment transport in rivers) with theories and dynamical models that can reproduce these patterns? (2) Are geomorphic transport laws based on the notion of a locally derived flux limited in some fundamental sense, and is the notion of a non-local flux (flux determined by conditions at some distance from the point of interest) a physically viable alternative? (3) How can we relate micro- and macro-scale dynamics in stochastic transport theories and in predictive models?

The papers in this special issue provide some insight into these questions. They stretch the envelope of geomorphic modeling by introducing new mathematical theories and models of transport, providing new explanations of old data, and posing alternative hypotheses to explain process from form. They also open new questions for future research.

2. CHALLENGING OLD THEORIES: THE NOTION OF NON-LOCALITY

Current geomorphic transport laws for landscape evolution are formulated as partial differential equations framed around approximations of the physics of advection and diffusion/dispersion: in particular, assumptions are made that facilitate the integration of processes from micro-scales in time and space to geomorphic model scales. Such assumptions are inconsistent with transport processes in which significant contributions to the total flux come from events across a broad span of magnitude and frequency.

For example, the advection-dispersion equation (ADE) is based on the classical definition of divergence of a vector field. The classical notion of divergence maintains that as an arbitrary control volume shrinks, the ratio of total surface flux to volume must converge to a single value. However, if a considerable fraction of the total sediment flux during the period of observation arises from a flux of particles from far upstream, then the classical divergence theorem fails. Instead, a divergence associated with a finite volume, and defined as the ratio of total flux to volume, is more appropriate. However, by increasing the arbitrary volume a greater heterogeneity in the medium properties and in the physical processes contributing to transport is sampled, and the degree of resulting variability is bound to depend on scale. Thus, the ratio of total flux to volume does not remain constant but varies with the size of the volume. As a result, the classical diffusion equation is no longer self-contained with a closed-form solution at all scales. Within the limits of classical theory, the best that can be done is to assume that the total flux to volume ratio is constant within small ranges of scales, allowing one to talk about an ``effective'' scale-dependent dispersion coefficient. Another approach is to depart altogether from the classical theory.

Recently, the physics of advection and dispersion has evolved beyond describing classical phenomena to include materials that exhibit variability from large to very small scales, power-law velocity distributions, chaotic dynamics, and slow reactive transport (e.g., see the review paper of *Schumer et al*. [2009], this issue). Fractional calculus treatments of advection and diffusion/dispersion capture non-classical behavior in a simple and elegant form. For example, changing the second derivative in the diffusion equation to a fractional derivative of order less than two yields a model for superdiffusion, in which particles spread faster than the classical diffusion equation predicts. Changing the first order time derivative in that same equation to a fractional derivative of order less than one models subdiffusion. Superdiffusive models are connected with power-law particle jump lengths; subdiffusive models emerge from power-law waiting times between jumps.

Several techniques have been proposed in the subsurface transport literature to tackle the problem of scale-dependent dispersivity which arises for similar reasons, namely, the presence of inhomogeneities at all scales and the wide range of length and time scales of motion [see discussion and references in *Schumer et al, 2009*, this issue] . The treatment of surface transport faces similar challenges, i.e., time and scale-dependent flux statistics, presence of heterogeneities at all scales, scale-invariance and power-law spectra of landscapes (in analogy with fractal porous media in the subsurface), and yet geomorphic flux laws that can accommodate such behavior are not available. The contributions in this issue are a step in this direction.

3. NEW THEORIES AND NEW PERSPECTIVES

The contributions in this volume can be broadly classified as addressing the following three geomorphic transport problems: (a) bedload transport in rivers (*Ganti et al*., *Bradley et al*., *Ancey*, *McElroy et al.*, and *Hill et al*.); (b) transport on hillslopes (*Foufoula-Georgiou et al., Tucker and Bradley*, *Furbish et al, a,b, Harman et al*., and *Stark & Guzzetti*); and (c) transport in erosional-depositional systems and river networks (*Voller and Paola*, *Zaliapin et al*., and *Schumer and Jerolmack*). A summary of these developments is presented below.

3.1. Bedload transport in rivers

Despite considerable research over the past several decades, the problem of accurate estimation of bedload sediment transport in rivers remains unsolved. One of the main challenges lies in the fact that the motions of individual particles happen at random, rendering the process of transport a stochastic process. Along these lines, contributions in this issue relate to the development of new stochastic discrete or continuous formulations of transport that can explicitly account for stochastic behaviors such as large variations in particle displacement and long times spent in immobile phase.

Ganti et al. reconsider the problem of tracer dispersal in rivers and argue that long leading tails in tracer concentration are to be expected in certain cases where the step length distribution of particle movements is heavy tailed [see also *Stark et al, 2009*]. Starting with an active layer formulation of the probabilistic Exner equation they show that the continuum equation describing the tracer concentration in this case takes the form of a fractional advection-dispersion equation. By identifying the probabilistic Exner equation as a forward Kolmogorov equation, they also propose a stochastic model describing the evolution of tracer concentration and show that the classical (normal) and fractional (anomalous) advection-diffusion equations arise as long-time asymptotic solutions of this stochastic model. More data are needed to fully verify such a model based on particle-scale and macro-scale statistics.

Bradley et al. revisit a 50-year old tracer experiment in which the tracer plume exhibits behavior not possible to be explained with classical transport models, namely, anomalously high fraction of tracers in the downstream tail of the distribution, a decrease of detected tracer mass over time and enhanced particle retention near the source. They propose a fractional advection-dispersion equation and a two-phase transport model (which partitions mass into detectable mobile and undetectable immobile phases) and show an impressive agreement with observations.

McElroy et al. note that the movement of bed material associated with bed deformation is not accounted for in standard methods of calculating sediment flux and propose a framework for calculating that portion of the flux in sandy bed rivers (which they term deformation flux). They note differences between laboratory and real river systems in the statistics of the bed deformation rates and define normalized metrics for comparing systems of different size. They also note the time-dependence (power-law scaling) of the deformation flux in sand-bed rivers, not explainable by classical theories of advection-dispersion, motivating the exploration of fractional dispersion models that can explain such scaling behavior.

Ancey examines the influence of randomness in bed sediment flux on the initial genesis of bedforms, and shows how strong fluctuations in flux can arise even in the absence of heavy-tailed probability distributions of stream-bed sediment exchange. A Markovian, birth-death process model of sediment entrainment is developed and cast into a stochastic form of the Exner equation. In the large number limit, he shows that the model admits a Fokker-Planck representation, simplifying subsequent analysis. Derivations of the stochastically varying number of particles in motion and of the coupled bed height are provided, allowing prediction of the scaling of the variance of model bed topography with time.

Hill et al. consider the problem of modeling bedload transport in gravel bed rivers which exhibit a broad range of particle sizes. Based on a series of carefully controlled flume experiments, they document an exponential distribution of the travel time of entrained particles of a given size, with the parameter of the distribution (mean travel distance) depending on both particle size and shear stress. In real settings, the convolution of the distributions of travel distances and particle sizes is shown to yield a power law distribution, which requires re-consideration of standard diffusion models and introduction of superdiffusive models of transport.

3.2. Transport on hillslopes

Sediment transport on hillslopes forms an area of active research both theoretical and experimental. Typical models available to date include standard diffusive models which consider a linear or nonlinear formulation of flux based on local slope or other local attributes such as soil depth. The contributions in this issue address some important elements of hillslope transport related to stochasticity in the diffusion coefficient to incorporate rain splash effects or dependence on soil thickness, extension to a non-local flux formulation (in a discrete or continuous framework) to incorporate large scales of particle motion, reformulation of the kinematic wave equation for hillslope subsurface transport, and a stochastic theory for landslide-driven erosion.

Stark and Guzetti present a physically-based stochastic theory for landslide-driven erosion. The proposed model describes a simplified process of rupture propagation, slope failure and debris mobilization, and it reproduces the probability distributions observed for landslide source areas and volumes, including their power-law tail scaling. The peak (rollover) and tail scaling of the distributions are explained in terms of the relative importance of cohesion over friction in setting slope stability, allowing thus for a physical interpretation. Numerical experiments validate the analytical results and document the sensitivity of the model to parameterization. The interplay of river incision and hillslope steepening in adjusting the landslide magnitude-frequency is interpreted in physical and statistical terms.

Furbish et al. [2009a] revisit the problem of soil grain transport by rain splash and formulate it as a stochastic advection-dispersion process. One of their innovations rests on the explicit separation of the grain activity probability (determined by the rain storm intensity and soil properties at weather time scales) from the physics of the grain motions. They perform rain-splash experiments to confirm that gradients in raindrop intensity are as important as gradients in grain concentration and surface slope in affecting overall transport. Their result points to the importance of the ecological behavior of desert shrubs as "resource islands" (temporary storage zones of soil derived from areas surrounding the shrubs) and the implication that this behavior can have for land-surface evolution modeling. The proposed formulation provides a general framework for transport and dispersal of any soil material moveable by rainsplash, including nutrients, seeds and soil-borne pathogens.

Furbish et al [2009b] probe the physical justification of the linear slope-dependent transport formulation. Balancing the particle fluxes that tend to loft a soil with the gravitationally driven particle settling, they show how a slope-dependent transport relation emerges with, however, a statistical description of the diffusion-like coefficient. This coefficient involves the active soil thickness as a fundamental length scale that provides the minimum length scale over which measurement of the surface slope is meaningful. This in turn implies that the diffusion-like linear slope-dependent model

(soil flux proportional to the depth-slope product) is applicable at scales larger than the disturbance scales producing the transport. The formulation is consistent with observations of topographic profiles of hillslopes evolving by soil creep and by transport associated with biomechanical mixing. However, the theory does not explain the nonlinear flux-slope relations observed in many systems.

Tucker and Bradley are concerned with transport on hillslopes exhibiting a broad distribution of grain-motion length scales. They examine, in a simple discrete particle-based model, relations between grain-motion dynamics, bulk transport rates, and hillslope morphology, and they illustrate conditions under which standard local-gradient theory is not appropriate. They show that a nonlinear relationship between flux and local gradient emerges from their discrete model formulation at steep slopes and make a preliminary exploration of continuum generalizations based on a probabilistic form of the Exner equation. They provide insightful discussion on the notion of non-local flux computation and how high-probability, long-distance particle motions violate the assumption embedded in many commonly used local gradient-based geomorphic transport laws, calling for extensions.

Foufoula-Georgiou et al. propose a non-local formulation of sediment flux on hillslopes to account for the wide range of particle displacement lengths related to disturbance processes. This formulation computes flux at a point not only as a function of local topographic attributes, such as slope, but also as a function of topography upslope of the point of interest. They show that such a formulation leads to a continuum constitutive law that takes the form of fractional diffusion. The model predicts a hillslope equilibrium profile that is parabolic in shape very close to the ridge top and becomes power law downslope, with an exponent equal to the non-locality model parameter. Furthermore, they show that a nonlinear relationship between sediment flux and local gradient emerges from this linear non-local model and that the model reproduces, with a single parameter, the natural variability of sediment flux found in real landscapes.

Harman et al. revisit the problem of subsurface transport in hillslopes with heterogeneous conductivity fields. They argue that, in such cases, variations in the down-slope velocity of impulses induce a non-piston type flow response (piston response would arise from impulses starting at different locations but moving at a constant speed). Assuming heavy tails in the velocity distribution of those impulses, they invoke the notion of subordination (replacing real time with a random time representing the time that impulses spend in motion). As a result they recast the standard kinematic wave equation into a subordinated kinematic wave equation appropriate for modeling flow response in heterogeneous hillslopes. They evaluate their model under different degrees of heterogeneity and link the statistical parameters of the heterogeneous random fields and the parameters of the subordinator, implying that the subordinator can eventually be parameterized by physical measurements of hillslope properties.

3.3. Transport in erosional-depositional systems and river networks

Zaliapin et al. aim to develop simple theories of dynamic transport on river networks. They introduce the concept of a "dynamic tree" to describe transport of fluxes on a topological static tree representing the river network. They show that the corresponding dynamic trees exhibit self-similarity, albeit with different parameters than the underlying static trees, providing thus the possibility of developing process-specific dynamic scaling frameworks. They also report a "phase transition" in the dynamics of river networks indicating a time (or equivalently length) scale at which the connectivity of the system reaches a critical point, i.e., the system acts as a single cluster. Analysis of three real river networks indicates a possible universality and points to the need for further analysis to understand how this framework can be used for stochastic flux propagation and for scaling of dynamic processes operating on river networks.

Schumer and Jerolmack, provide a novel interpretation of the field-documented observation that sediment deposition rate decreases as a power law function of the measurement interval. They argue that this phenomenon is the result of the heavy tailed

distribution of non-deposition periods and use limit theory and Continuous Time Random Walk (CTRW) models to estimate the actual average deposition rate from observations of the surface location over time. Their analysis highlights that caution has to be exercised in attributing observed changes in accumulation rates through time to real changes in the rates of erosion and deposition. The consequences of these finding for interpreting the stratigraphic record in terms of climate variability are important.

Voller and Paola, put forth the observation that laboratory experiments of aggrading rivers, driven by subsidence or base-level rise, display profiles that deviate from those expected from standard diffusion models. They propose a fractional diffusion model which accounts for non-Fickian sediment transport in systems where the length scale of significant sediment extraction is comparable to the scale range of the channel-pattern behavior. They point out that these length scales seem well separated in natural systems but not in laboratory systems. This distinction may explain discrepancies between laboratory and natural system profiles and has implications for modeling.

4.   CLOSING REMARKS AND OPEN PROBLEMS

The 15 papers in this volume present new ideas for modeling transport on the Earth's surface from tracer and bedload transport in rivers, to hillslope transport, to the complexities of mixed erosional/depositional systems, and to transport along the whole river network. They explore stochastic formulations that account for the deformation of bedforms as they contribute to sediment flux, the erosional impact of spatially and temporally variable raindrops as they contribute to the ecology and geomorphology of hillslopes, theories for explaining the power law distributions of landslide areas and volumes, and theories that take into account the broad range of scales participating in transport. Several papers revisit old data sets and show that predictions from generalized transport laws agree with observations more closely than predictions based on classical theories. A few papers attempt to make connections between micro-scale (particle-scale) dynamics and macro-scale statistics and note that parameters of the macro-scale models

can be resolved from physical observables as opposed to empirical fitting. Emphasis is placed on parsimonious parameterizations, that is, on models that can explain the observed structure and variability with few parameters. The idea of non-locality in flux computation is discussed in several papers and fractional advection-dispersion formulations or discrete space-time models are proposed.

Several open problems have emerged from the research presented in these papers. First, the physical motivation of non-local transport laws and the data needed to more directly estimate model parameters and discriminate between local and non-local hypotheses are areas of future study. Also, stochastic formulations that invoke particle-scale statistics explicitly or implicitly require new kinds of data, such as statistics of particle movement, to be tested and validated. The same applies to models that consider bedform deformation as a diffusion problem. The idea of extending well known transport models via time-subordination is compelling and awaits more exploration: such an approach will have application in the modeling of environmental fluxes in which "time in motion" rather than "clock time" is relevant and where time can therefore be treated as a random variable. The exploration of Continuum Time Random Walk (CTRW) models as discrete counterparts of continuum formulations has to be further studied, and extensions of those models to two dimensions awaits development.

A problem with all local geomorphic transport laws is that they yield scale-dependent sediment flux since the local slope and curvature are scale (resolution)-dependent. As such, closures are needed to incorporate the effect of sub-grid scale variability and render the model coefficients scale-independent [e.g., see *Passalacqua et al.*, 2007]. An open problem for future research is to examine whether non-local transport models naturally overcome the problem of scale-dependence, as this becomes an issue of increasing concern with the availability of high resolution topographic data.

Theories for the transport of fluxes on river networks where the heterogeneity of the input (e.g., spatially variable precipitation which dynamically changes over time, or discrete fluxes that are injected at only a portion of the nodes of the network) await further

development such that scaling relations incorporating both the topology of the network and the dynamics of the driving process are considered. Finally, models for transport in erosional/depositional systems that capture the large range of scales of motion, and the use of these models for the interpretation of the stratigraphic record (e.g., apparent scale-dependent erosion rate), require new data to be rigorously tested and validated. The outcomes could have important implications for deciphering climate variability from stratigraphy.

Acknowledgments

REFERENCES

Ancey, C., Stochastic approximation of the Exner equation under lower-regime conditions, *Journal of Geophysical Research, THIS ISSUE,* 2009.

Bradley, D., G. Tucker, and D. A. Benson, Anomalous dispersion in a sand-bed river, *Journal of Geophysical Research, THIS ISSUE,* 2009.

Ganti, V., M. M. Meerschaert, E. Foufoula-Georgiou, E. Viparelli, and G. Parker, Normal and Anomalous diffusion of gravel tracer particles in rivers, *Journal of Geophysical Research, THIS ISSUE,*2009.

Hill, K. M., L. DellAngelo, and M. M. Meerschaert, Particle size dependence of the probability distribution functions of travel distances of gravel particles in bedload transport, *Journal of Geophysical Research, THIS ISSUE,* 2009.

Harman, C. J., D. M. Reeves, B. Baeumer, and M. Sivapalan, A subordinated kinematic wave equation for heavy-tailed flow responses from heterogeneous hillslopes, *Journal of Geophysical Research, THIS ISSUE,* 2009.

Foufoula-Georgiou, E., V. Ganti, and W. E. Dietrich, A non-local theory of sediment transport on hillslopes, *Journal of Geophysical Research, THIS ISSUE,* 2009.

Furbish, D. J., P. K. Haff, W. E. Dietrich, and A. M. Heimsath, Statistical description of slope-dependent soil transport and the diffusion-like coefficient, *Journal of Geophysical Research, THIS ISSUE,* 2009.

Furbish, D. J., E. M. Childs, P. K. Haff, and M. W. Schmeeckle, Rain splash of soil grains as a stochastic advection-dispersion process, with implications for desert plant-soil interactions and land-surface evolution, *Journal of Geophysical Research, THIS ISSUE,* 2009.

McElroy, B., and D. Mohrig, The nature of deformation of sandy bedforms, *Journal of Geophysical Research, THIS ISSUE,* 2009.

Passalacqua, P., F. Porte-Agel, E. Foufoula-Georgiou, and C. Paola, Application of dynamic subgrid-scale concepts from large-eddy simulation to modeling landscape evolution, *Water Resour. Res*., 42, W06D11, doi:10.1029/2006WR004879, 2006.

Podlubny, I., Geometric and physical interpretation of fractional integration and fractional differentiation, *Fractional Calculus and Applied Analysis*, 5 (4), 2002.

Tucker, G. E., and D. N. Bradley, Locality and non-locality in Geomorphic transport systems: Implications of a particle-based model of hillslope evolution, *Journal of Geophysical Research, THIS ISSUE,* 2009.

Stark, C. P., and F. Guzzetti, Landslide rupture and the probability distribution of mobilized debris volumes, *Journal of Geophysical Research, THIS ISSUE,* 2009.

Stark, C. P., E. Foufoula-Georgiou, and V. Ganti. A nonlocal theory of sediment buffering and bedrock channel evolution. *Journal of Geophysical Research*, 114:F01029, 2009.

Schumer, R., and D. J. Jerolmack, Real and apparent changes in sediment deposition rates over time, *Journal of Geophysical Research, THIS ISSUE,* 2009.

Schumer, R., M. M. Meerschaert, and B. Baeumer, Fractional advection-dispersion equations for modeling transport at the Earth surface, *Journal of Geophysical Research, THIS ISSUE,* 2009.

Voller, V. R., and C. Paola, Can anomalous diffusion describe depositional fluvial profiles?, *Journal of Geophysical Research, THIS ISSUE,* 2009.

Zaliapin, I., E. Foufoula-Georgiou, and M. Ghil, Transport on river networks: A dynamic tree approach, *Journal of Geophysical Research, THIS ISSUE,* 2009.

On the influence of gravel bed dynamics on velocity power spectra

Arvind Singh, Fernando Porté-Agel, and Efi Foufoula-Georgiou

Department of Civil Engineering, St. Anthony Falls Laboratory and National Center for Earth-Surface Dynamics, University of Minnesota, Minnesota, USA.

Abstract. A series of flume experiments were conducted to study the effect of bedform dynamics on the flow over a gravel bed comprised of a wide distribution of grain sizes. Instantaneous high-frequency streamwise flow velocities were sampled using ADV at a frequency of 200 Hz, while the simultaneous bed elevations were sampled using sonar transducers at a frequency of 0.2 Hz for a duration of 20 hours. Spectral analysis of the measured velocity fluctuations reveals the existence of two distinct power-law scaling regimes. At high frequencies, an inertial subrange of turbulence with $\sim -5/3$ Kolmogorov scaling is observed. At low frequencies, another scaling regime with spectral slope of about -1.1 is found. We interpret this range as the signature of the evolving multi-scale bed topography on the near-bed velocity fluctuations. The two scaling ranges are separated by a spectral gap, i.e., a range of intermediate scales with no additional energy contribution. The high-frequency limit of the spectral gap corresponds to the integral scale of turbulence. The low-frequency end of the gap corresponds to the scale of the smallest bedforms identified by the velocity sensor, which depends on the position of the sensor. Our results also show that the temporal scales of the largest bedforms can be potentially identified from spectral analysis of low resolution velocity measurements collected near the channel bed.

1. Introduction

Measurement of turbulent flow structures in a gravel-bedded environment has received considerable attention in the past few decades; yet, there is still debate about the origin and development of these flow structures and, in turn, their influence on the bed surface itself [*Wiberg and Smith*, 1991; *Dinehart*, 1992; *Robert et al.*, 1992; *Buffin-Bélanger and Roy*, 1998; *Lacey and Roy*, 2007; *Hardy et al.*, 2009]. It has been suggested that the initiation of gravel movement is strongly influenced by large transient coherent flow structures with time scales of about 1-10 seconds which are superimposed on the more random small-scale turbulence [*Drake et al.*, 1988; *Kirkbride*, 1993; *Kirkbride and McLelland*, 1994; *Kirkbride and Fergusson*, 1995; *Lamarre and Roy*, 2005]. Over a rough boundary, such as in a gravel-bedded channel, friction created by individual gravel particles or clusters of particles (i.e., microtopography as well as bedforms) retards the flow velocity, but the effect diminishes with increasing height above the bed [*Lacey and Roy*, 2007, 2008]. This surface roughness creates near-bed turbulence which is responsible for entrainment of particles predominately linked to sweeps, bursts and larger coherent structures [*Robert et al.*, 1992; *Best*, 1993; *Robert et al.*, 1993; *Lamarre and Roy*, 2005; *Schmeeckle et al.*, 2007; *Hardy et al.*, 2009]. These large-scale coherent flow structures are a key component of turbulent boundary layers and scale with the flow depth, h [*Roy et al.*, 2004]. In a mobile gravel bed the size of these macro-turbulent flow structures is found to scale with h in the vertical direction and 2 to 12 times h in the horizontal direction [*Shvidchenko and Pender*, 2001; *Roy et al.*, 2004]. The downstream motion of these flow structures may cause quasiperiodic fluctuations of the local flow velocity components and could lead to the development of troughs and ridges on the mobile bed, inducing bed particle destabilization (sediment transport). *Imamoto and Ishigaki* [1986a, b] investigated the turbulent flow structure over smooth and rough immobile beds and detected the existence of upwelling and downwelling circular fluid motion over the entire flow depth. They found that both the lateral and the longitudinal integral scale of fluid motion was about $2h$. *Yalin* [1992] hypothesized that the macro-turbulent structures are closely linked to the bursting phenomena in boundary layers and do not originate in their full size ($\sim h$). According to *Yalin* [1992] turbulent eddies are generated near the bed surface as a result of bursts with sizes much smaller than h, then grow until their size becomes approximately equal to h; they are then destroyed, prompting the generation of new smaller eddies, and so on. The complete cycle of the eddies' formation, evolution, and destruction occurs over a distance of $\sim 6h$.

In spite of the important role that these macro-turbulent structures could play in the dynamics of rivers, there is no model that relates the interaction of turbulent flow structures to bed topography and sediment transport. This is partly due to the unavailability of long reliable records of turbulent data sampled at high-resolution and partly due to the presence of complex bed topography varying spatially and temporally in a gravel-bedded channel [*Paiement-Paradis et al.*, 2003; *Marquis and Roy*, 2006]. In particular, little is known about how the relatively slow evolution of moving multi-scale topography can affect the scaling properties (e.g., spectral density) of the velocity field at different positions in the flow. For instance, *Dinehart* [1999] associated the presence of large-scale/low-frequency fluctuations of velocity, obtained from long velocity records, to migrating bedforms in gravel bed rivers. In a previous study [*Dinehart*, 1989] documented the passage of bedforms at periods ranging from 2 to 5 min that corresponds with velocity fluctuations. In a recent study *Nikora* [2008] suggested that the currently used three-range spectral model (production range, inertial subrange and dissipation range) for gravel

bed rivers should be further refined by adding an additional range, leading to a model that consists of four ranges of scales with different spectral behavior and should be tested with field and experimental observations. However, to resolve the potential differences in velocity spectra, for example, between fixed and weakly mobile gravel beds, much longer velocity records would be required [*Nikora and Goring*, 2000].

Unlike the situation in river flows, a considerable amount of work has been performed in atmospheric boundary layer flows towards characterizing and isolating the signature of relatively slow (synoptic scale, mesoscale) variability from that of the turbulence (for examples, see *Van Der Hoven* [1957]; *Fiedler and Panofsky* [1970]; *Smedman-Högström and Högström* [1975]). In a classical work *Van Der Hoven* [1957] showed a marked spectral gap between mesoscale (synoptic) and microscale (turbulent) flow variability in the analysis of large-range spectrum of horizontal wind velocity. Since then, several investigators have confirmed the existence of a spectral gap in the spectra of horizontal wind velocity over land. *Hess and Clarke* [1973] also showed a tendency for a gap in the spectra of wind velocity measured at different heights between the surface layer and free atmosphere.

In this paper we use simultaneous high resolution long time series of bed elevations and velocity fluctuations along with longitudinal transects of bed profile measured over a gravel-bedded experimental channel to quantify the multi-scale variability of both flow structures and bed structures. Our results show the signature of bed structures on the near-bed velocity fluctuations and point to the potential of using relatively low frequency measurements of velocity in the field to detect time scale of bed topography in real rivers.

2. Experimental setup and data analyzed

Experiments were conducted in the Main Channel facility at St. Anthony Falls Laboratory, University of Minnesota. These experiments were the follow-up of previous experiments conducted in spring of 2006 known as Stream-Lab06 [*Wilcock et al.*, 2008]. StreamLab06 was an 11 month multidisciplinary laboratory channel study focused on various aspects of ecogeomorphology in gravel bed streams. Five separate projects were conducted as part of Stream-Lab06, while all the studies shared the same sediment and general experimental configuration. The extensive data set collected in these experiments includes hydraulic conditions (discharge, water slope, bed slope, depth average velocity, and flow field), morphological conditions (bed topography, bar locations and shapes, photo images of the bed), sediment transport characterization (continuous sediment flux, recirculation grain size information), water chemistry (temperature, dissolved oxygen, nutrient concentrations) and biological conditions (heterotrophic respiration, biomass accumulation, nutrient processing rates). For the experiments presented here (which we call Streamlab08), we focus on flow field and spatio-temporal bed topography for the discharges of 2000 l/s and 2800 l/s.

The Main Channel is a 55 m long, 2.74 m wide channel with a maximum depth of 1.8 m and maximum discharge capacity of 8000 l/s (Figure 1). It is a partially sediment recirculating channel while the water flows through the channel without recirculation. The sediment recirculation system is capable of entraining and recirculating particles up to 76 mm in size. The recirculation system's intake is in the bed trap below the weigh-pan system, where a horizontal auger, driven by a variable-speed motor, spans the full width of the channel. The rotating auger conveys sediments accumulated from weigh-pan dumps toward an outlet recessed in

the right side of the flume and into the recirculation-pump (dredging-pump) intake. The recirculation auger speed was adjusted manually every 30 mins to maintain a constant elevation of sediment in the auger hopper and to continuously transport sediment through the recirculation pipe. This procedure avoided sending large pulses of sediment through the pipe each time a weigh-pan dumped. Intake of the water in the channel was directly from the Mississippi River.

The bed of the channel was composed of a mixture of gravel (median particle size diameter, $d_{50} = 11.3$ mm) and sand (median particle size diameter, $d_{50} = 1$ mm). It is fluvial in nature. A total of 15% sand was added to the gravel. The final grain size distribution obtained after mixing the sediments had a $d_{50} = 7.7$ mm, $d_{16} = 2.2$ mm and $d_{84} = 21.2$ mm. The mean specific density of sediment of all size fractions was ~ 2.65. The thickness of the bed at the start of the run was approximately 0.45 m. Figure 2 shows the patches of bed surface obtained at the end of the run for a discharge of 2000 l/s (Figure 2, left) and for 2800 l/s (Figure 2, right).

Prior to data collection a constant water discharge, Q, was fed into the channel to achieve quasi-dynamic equilibrium in transport and slope adjustment for both water surface and bed. Sediment transport rates were measured simultaneously during the entire course of the run. Determination of the dynamic equilibrium state was evaluated by checking the stability of the 60 min average total sediment flux at the downstream end of the test section. Using the pan accumulation data, the acquisition software computed a 60 min mean of sediment flux in all five pans. Dynamic equilibrium was reached when variation in this value became negligible. In other words, when the average of the previous 60 min of instantaneous flux values computed from the pan data stabilized, we determined the channel to be in dynamic equilibrium and proceeded with formal data collection and sampling. After attaining equilibrium, experiments ran for approximately 20 hrs. (More details about the experimental setup can be found in *Singh et al.* [2008, 2009]).

The data presented here are the velocity fluctuations (in the flow direction), simultaneous temporal bed elevation collected at the downstream end, and the longitudinal transects of bed profile, measured along the centerline of the channel. The continuous velocity fluctuations were measured using Acoustic Doppler Velocitimeter (ADV) at an approximate distance of 15 cm above the mean bed level. Relative heights, the ratio between D_p (distance of velocity probe from mean bed level) and D (average depth of flow), were computed to be 0.23 and 0.29 for the discharge of 2000 l/s and 2800 l/s respectively (see Table 1). $NortekVectrino^+$ ADV was used for this study. The ADV was mounted 20 cm upstream of the centrally located bed sonar (sonar 3, see Figure 3) and could measure 3D water velocity with a sampling frequency of 200 Hz, and a precision of +/- 1 mm/s.

For the bed elevation measurements, submersible sonar transducers of 2.5 cm diameter were deployed 0.3 m (on an average) below the water surface. These sonar transducers were mounted to the end of rigid 1.5-cm steel tubes and directed perpendicular to the bed. The transducers collected continuous temporal bed elevation information upstream of each weigh-pan. The sampling interval of bed elevation measurements was 5 sec with a vertical precision of 1 mm. Figure 1 and Figure 3 (schematic) show the setup of ADV and the sonar placed at the downstream end of the channel. Measurements were taken over a range of discharges corresponding to different bed shear stresses. Bed shear stress is often characterized in terms of the dimensionless Shields stress, τ_b^*. For steady, uniform flow it may be approximated as

$$\tau_b^* = \frac{h_R S}{R d_{50}}, \tag{1}$$

where h_R and S are the hydraulic radius and channel slope, respectively, and $R = 1.65$ is the relative submerged density of silica. Here we report the data collected at discharges of 2000 l/s and 2800 l/s corresponding to Shields stress of 0.058 and 0.099 respectively (for details about the hydraulic conditions see Table 1). (Note that for computing Reynolds number and Froude number, kinematic viscosity of water (ν), and acceleration due to gravity (g), were taken as $1 \times 10^{-6} m^2/s$, and 9.81 m/s^2 respectively). Critical Shields stress (τ_c^*) was assumed to be 0.03 as suggested by *Buffington and Montgomery* [1997] and references therein. Figures 4a and 4c show the time series of velocity fluctuations (top) and the corresponding bed elevations (bottom) for discharges of 2000 l/s and 2800 l/s, respectively, collected for the duration of 20 hrs.

For the longitudinal bed profiles a three-axis positionable data acquisition (DAQ) carriage was used. This DAQ was designed, fabricated, and installed at St. Anthony Falls Laboratory. The DAQ carriage was capable of traversing the entire 55 x 2.74 meter test section and could position probes to within 1 mm in all three axes. Streamwise travel speeds of DAQ could be set up to 2 m/s. The DAQ carriage was controlled by a backbone computer that also served as the master time clock for all data collection in the study.

Because the data were collected in the fall, there were some leaves floating in the channel which might have resulted in spikes in the velocity and bed elevation data. Even though the amount of spurious spikes in the data (0.81 percent for 2000 l/s and 0.79 percent for 2800 l/s) was found to be very small, these were removed as part of the data treatment for erroneous measurements using the methodology described in *Parsheh et al.* [2009]. *Parsheh et al.* [2009] used modified version of the Universal Phase-Space-Thresholding technique proposed by [*Goring and Nikora*, 2002] for detecting the spikes and subsequently replacing them by the last valid data points with Sample-and-Hold technique [*Adrian and Yao*, 1987].

3. Spectral analysis results

Power spectral density (hereafter PSD) is a commonly used tool to measure the distribution of energy (variance) in the signal across frequencies (or scales). In other words, it shows at which scales the contribution to the signal variance are strong and at which scales contribution to the signal variance are weak. For a signal $X(t)$, the power spectral density is given by

$$\Phi(\omega) = \frac{1}{2\pi} \int_{-\infty}^{\infty} R(\tau)e^{-i\omega\tau}d\tau \qquad (2)$$

where $R(\tau)$ is the autocorrelation function defined as

$$R(\tau) = \frac{E[(X(t) - \mu)(X(t + \tau) - \mu)]}{\sigma^2}, \qquad (3)$$

τ is the time lag, μ and σ are the mean and standard deviation of the signal respectively, and ω is the frequency. A simple way to estimate PSD is by taking the fast Fourier transform (FFT) of the signal [*Stoica and Moses*, 1997; *Lacey and Roy*, 2007]. In our case, the signal $X(t)$ is the flow velocity or the bed elevation in the streamwise direction. Special emphasis is placed here on identifying spectral scaling regimes, i.e., ranges of scales over which log-log linearity is observed in the power spectral density. (Note that the units for the velocity spectrum is $quantity^2/frequency$, i.e., m^2/s).

The power spectrum of the velocity fluctuations (measured at 200 Hz) at a discharge of 2000 l/s is shown in Figure 5a. Two clear scaling ranges can be observed, separated by a spectral gap. For relatively small scales (high frequencies) in the range of 0.1 sec to 0.5 sec, the slope of the PSD

(power spectral density) is $\sim -5/3$, which corresponds to the inertial subrange of turbulence. A second scaling range is observed for scales between 2 min and 55 min, for which the slope of PSD is ~ -1.05. The range of observed spectral gap is from 10 sec to 2 min (see Table 2). The scales from high frequency end of the spectral gap which also coincides with the integral scale of the turbulence (see the following section for discussion about ~ -1 spectral slope) to the low frequency end of the inertial subrange shows a spectral slope ~ -1. Figure 5b shows the PSD of the bed elevation (measured at sampling intervals of 5 sec). A clear scaling is also found in the elevation field, with a PSD slope of ~ -1.94 for the scales of 15 sec to 42 min (Table 2). Figures 6a and 6b show the power spectral density of the velocity fluctuations (measured at 200 Hz) and the bed elevations (measured at 0.2 Hz), respectively, for the discharge of 2800 l/s. The second scaling range (low frequency regime) in the PSD of velocity fluctuations at the discharge of 2800 l/s is shifted towards higher frequencies and is from 35 sec to 28 min with a spectral slope ~ -1.15 (Figure 6a). Temporal bed elevations for the same discharge show a scaling range of 15 sec to 28 min with a spectral slope of -2.1 (Figure 6b). Figures 7a and 8a show the spatial bed transects for the discharge of 2000 l/s and 2800 l/s respectively, measured along the centerline of the channel. The spectral slopes of spatial bed elevations are similar to those of temporal bed elevations as can be seen by comparison of Figures 5b, 7b, and Figures 6b, 8b.

4. Interpretation of the results and discussion

Power spectral densities of streamwise velocity have been studied extensively in the case of wall-bounded turbulent flows over flat homogeneous surfaces (e.g., *Perry et al.* [1986]; *Katul et al.* [1995]; *Porté-Agel et al.* [2000]). In those flows, three scaling subranges have been identified. At low frequencies, a scaling subrange often referred to as the production subrange is found at scales larger than approximately $2\pi z$ (where z is the distance to the surface) and smaller than the integral scale of the turbulence (on the order of the depth of the flow in a channel). This range is characterized by a -1 spectral slope [*Kader and Yaglom*, 1991; *Katul et al.*, 1995]. At intermediate frequencies, an inertial subrange with a $-5/3$ spectral slope [*Kolmogorov*, 1961] is observed. It is associated with eddy scales smaller than approximately $2\pi z$. The third scaling subrange is the viscous subrange observed at smaller scales than the surface roughness size where spectra decays much faster than in the inertial subrange [*Nezu and Nakagawa*, 1993; *Nikora and Goring*, 2000].

In the case of flow over bedforms, it is expected that the turbulence will lead to similar scaling regimes as those found in the velocity spectra calculated over flat surfaces. More specifically, one would expect to find both an inertial subrange and a production subrange, even though the transition scale between these two ranges and the slope of the production subrange are likely to be affected by the presence of the topography, which may cause eddy shedding effects [*Lapointe*, 1992; *Buffin-Bélanger and Roy*, 1998; *Hardy et al.*, 2007].

In the hypothetical case of stationary bedforms, turbulence is the only source of velocity fluctuations and, consequently, no additional energy is introduced at scales larger than the integral scale of the turbulence (on the order of the flow depth in the channel). However, in the case of a moving bed, the evolution of the bedforms introduces additional variability in the velocity field at the range of temporal scales associated with that evolution. We set forth the hypothesis

that this effect explains the existence of the second scaling range (between 2 min and 55 min for the case of 2000 l/s, and 0.5 min to 28 min for the case of 2800 l/s) in the power spectrum of velocity, as shown in Figures 5a and 6a. Notice that the largest scale in that range ($\sim$ 55 min for 2000 l/s and 28 min for 2800 l/s) corresponds to the integral scale of the measured bed elevation field presented in Figures 5b and 6b. This largest scale is the characteristic time scale at which the largest bedforms move. Also notice that the second scaling range in the velocity spectra (scaling range due to bedform migration) shifts towards the higher frequencies, right in PSD, (compare Figure 5a to Figure 6a) with an increase in discharge, suggesting that the bedforms at higher flow (2800 l/s) are moving faster than the bedforms in the lower flow (2000 l/s). The clear signature of the large-scale bedforms on the multi-scale variability of the velocity time series as captured in its PSD suggests the potential of using relatively low frequency velocity measurements near the bed to detect the characteristic time scales associated with the evolution of bed topography. The spectral analysis of our velocity measurements also shows that this scaling range is separated from the turbulence range by a spectral gap, i.e., a range of scales with virtually no additional contribution to the velocity variance.

We hypothesize that the presence of a spectral gap is due to the lack of physical processes which could support the velocity fluctuations in this frequency range. A similar spectral gap was reported in the seminal work of *Van Der Hoven* [1957], who analyzed velocity time series collected in the atmospheric boundary layer.(Note that in that study the spectral density is plotted as $\omega S(\omega)$, while in our work it is $S(\omega)$). In that flow, the gap separates the energy contributions associated with turbulence at the high frequencies from those corresponding to relatively slower frequency mesoscale and diurnal-cycle variability. The presence of this gap has important practical implications since it allows to separate the contribution of the turbulence from that of mesoscale motions to the total kinetic energy and fluxes. Similarly, the presence of the spectral gap in channel flows with moving bedforms should be considered when using velocity time series to study turbulent transport in these flows.

The high frequency end of the spectral gap coincides with the integral scale of the turbulence, i.e., the scale of the largest turbulent eddies present in the flow. (Note that integral sale of turbulence is computed via visual inspection from the figure of velocity spectra.) In Figures 5a and 6a, that integral scale is found at a frequency of approximately 0.1 Hz for both flow discharges under consideration. The low frequency end of the spectral gap is associated with the characteristic time scale of the smallest bedform structures that can be identified by the velocity sensor. From Figures 5a and 6a, that limit corresponds to frequencies of approximately 0.01 Hz and 0.02 Hz, for the 2000 l/s and 2800 l/s cases, respectively. This contrasts with the approximately 0.1 Hz associated with the relatively fast evolution of the smallest bedform structures, as shown in the spectral density of bed elevation (Figures 5b and 6b).

It is important to note that the size of the smallest features detected by the velocity sensor and, as a result, the width of the spectral gap, should depend on the distance from the sensor to the bed. This is consistent with results from a previous study of the multiscale wavelet correlation between surface shear stress and velocity in a flat turbulent boundary layer [*Venugopal et al.*, 2003]. That study showed that turbulent eddies of vertical size smaller than the distance to the surface z (and horizontal size smaller than $2\pi z$) that affect the surface shear stress do not produce a signature on the velocity measured at height z. With that in mind, here we speculate that the larger the distance between the velocity sensor and the surface, the larger the spectral gap. In general, the width of the spectral gap Δ_{gap} could be expressed as:

$$\triangle_{gap} = f(k, \tau_b^*), \qquad (4)$$

where, $k = \frac{D_p}{\sigma_b}$, D_p is the distance from the probe to the mean bed level, and σ_b is the standard deviation of the temporal bed elevation (note that in our case, for both discharges, the ratio k is constant and close to 5). In the limiting case of a deep flow (flow depth much larger than bedform variability), if the velocity sensor is placed far enough from the bed surface, above the blending height (level above which the effect of the bed surface heterogeneity cannot be detected), the spectral gap would not exist. Future research will investigate this issue through comparison of spectra from measurements collected at different distances from the bed surface and, consequently, different k ratios.

Bed elevation fields and their evolution are found to share important similarities with other natural surfaces such as landscapes. Landscapes present multiscale self-similar properties through a wide range of scales (see *Vening Meinesz* [1951]; *Newman and Turcotte* [1990]; *Pelletier* [1999]; *Passalacqua et al.* [2006] and references therein). In fact, *Passalacqua et al.* [2006] documented that landscapes also share important similarities with turbulence since both systems exhibit scale invariance (self-similarity) over a wide range of scales and their behavior can be described using comparable dynamic equations. This similarity can be seen, for example, in the behavior of power spectra of the landscapes which exhibit a log-log scaling range with a slope of approximately -2. Here also, we observe a slope of ~ -2 in power spectra of bed elevations for both the discharges of 2000 l/s and 2800 l/s (Figure 5b and 6b). Furthermore, *Singh et al.* [2009] have shown the multi-scale behavior of bed elevations (bed topography) for different flow conditions in a gravel-bedded environment. In that study, they quantified the slope of the second order structure function $2H$ (which is related to slope of the PSD with a relation $\beta = 2H + 1$, where β is the slope of PSD, and H is the Hurst exponent), and found that it is similar to the slope obtained here in the PSD of bed elevation fluctuations (Figure 5b and Figure 6b). In the case of bedforms in gravel-bedded channels little is known about the scaling properties of bed surfaces [*Nikora et al.*, 1998; *Marion et al.*, 2003; *Nikora and Walsh*, 2004]. For instance *Nikora et al.* [1998] characterized gravel bed roughness using second order structure functions. They found that the bed elevation distribution in laboratory flumes (unworked beds) and in natural gravel-bed streams (water-worked beds) was close to Gaussian although the latter was skewed positively. They also observed that the scaling exponent (Hurst exponent) $H = 0.79$ for natural beds was significantly higher than that of unworked beds, $H = 0.5$. A similar analysis was performed in [*Aberle and Nikora*, 2006].

Spectral densities of the time series (Figures 5b and 6b) and of spatial transects (Figures 7b and 8b) of bed elevations are not independent of each other. Both have a clear scaling range with slope of approximately -2, expanding over a similar range of scales (about two decades). The spatial spectra of bed elevation saturate at the same scale for both flow conditions (see Figures 7b and 8b, and Table 2). That scale is about 10 m and it can be interpreted as the integral scale, i.e., the characteristic scale of the largest bed forms. The temporal scales associated with these bed forms are approximately 55 min and 28 min for the 2000 l/s and 2800 l/s flows, respectively (Figures 5 and 6). Considering these integral spatial and temporal scales, it is possible to determine a characteristic travel speed of the largest bedforms. This advection velocity is approximately 14 m/hour and 22 m/hour for the 2000 l/s and 2800 l/s discharges, respectively.

Comparison of spectral densities of flow velocity and bed elevation measurements shows that relatively low-resolution velocity measurements collected near the channel bed can be used to estimate the travel time of the largest bedforms. This application can potentially be used in the field; though it would require a long time series of river flow velocities [*Soulsby*, 1980; *Nikora and Goring*, 2000].

Two major priorities for further research are suggested by this work. First, a better understanding is needed of what controls the slope of low frequency velocity fluctuations in the PSD, and how it is related to the slope of PSD of temporal bed elevations and flow conditions. Second, the quantification of the dependence of length scale of the spectral gap on the Shields stress, depth-wise position of velocity measurements, and grain size distribution of the bed material should be undertaken. In order to meet these objectives, future work will be focused on the behavior of spectral density of velocity measured at different positions along the depth of the flow as a function of varying Shields stress and grain size distribution.

5. Conclusions

This paper investigates the behavior of power spectral density of flow velocity and bed elevation time series measured in a large-scale experimental channel under two flow conditions. The power spectral density of the velocity shows two distinct power-law scaling regimes. At high frequencies, an inertial subrange with $\sim -5/3$ Kolmogorov scaling is observed. It is associated with turbulent eddy motions of sizes smaller than the distance from the velocity sensor to the gravel bed. For slightly larger eddy scales, up to the integral scale of the flow, the effect of the bed leads to a reduction in the slope of the velocity spectrum. At lower frequencies, another scaling range with spectral slope of approximately -1.1 is found. This range is associated with the relatively slow evolution of the multiscale bed topography. At intermediate scales, a clear spectral gap, i.e., a range of scales with no additional energy contribution, separates the turbulence and bed evolution spectral ranges. The high frequency limit of the spectral gap corresponds to the integral scale of the turbulence. The low-frequency end of the gap corresponds to the scale of the smallest bedforms identified by the velocity sensor, and it is expected to depend on measurement location and bed variability. Our results also show that the temporal scales of the largest bedforms can be potentially identified from spectral analysis of low resolution velocity measurements collected near the channel bed.

References

Aberle, J., and V. Nikora (2006), Statistical properties of armored gravel bed surfaces, *Water Resour. Res.*, *42*, W11414, doi:10.1029/2005WR004674.

Adrian, R. J., and C.S. Yao (1987), Power spectra of fluid velocities measured by laser Doppler velocimetries, *Exp. Fluids*, 5, 117-128.

Best, J. L. (1993), On the interactions between turbulent flow structure, sediment transport and bedform development: some considerations from recent experimental research. In: Clifford, N.J., French, J.R., Hardisty, J. (Eds.), *Turbulence: Perspectives on Flow and Sediment Transport*, Wiley, Chichester, pp. 61-92.

Buffin-Bélanger, T., and A. G. Roy (1998), Effects of a pebble cluster on the turbulent structure of a depth-limited flow in a gravel-bed river, Geomorphology, 25, 249267, doi:10.1016/S0169-555X(98)00062-2.

Buffington, J. M., and D. R. Montgomery (1997), A systematic study of eight decades of incipient motion studies, with special reference to gravel-bedded rivers, *Water Resour. Res.*, *33(8)*, 1993-2029.

Dinehart, R. L. (1989), Dune migration in a steep, coarse-beddeds tream, *Water Resour. Res.*, *25(5)*, 911-923.

Dinehart, R.L. (1992), Evolution of coarse gravel bedforms: field measurements at flood stage. *Water Resour. Res.*,*28(10)*, 2667-2689.

Dinehart, R. L. (1999), Correlative Velocity Fluctuations Over a Gravel River Bed, *Water Resour. Res.*, *35(2)*, 569582.

Drake, T., R. Shreve, W. Dietrich, P. Whiting, and L. Leopold (1988), Bedload transport of fine gravel observed by motion-picture photography, *J. Fluid Mech.*, *192*, 193-217.

Fiedler, F., and H. A. Panofsky (1970), Atmospheric scales and spectral gaps, *Bullet. Amer. Meteor. Soc.*, 51, 1114-1119.

Goring, D. G., and V. I. Nikora (2002), Despiking Acoustic Doppler Velocimeter Data, *J. Hydraul. Eng.*, *128(1)*, 117-126.

Hardy, R. J., S. N. Lane, R. I. Ferguson, and D. R. Parsons (2007), Emergence of coherent flow structures over a gravel surface: A numerical experiment, *Water Resour. Res.*, *43*, W03422, doi:10.1029/2006WR004936.

Hardy, R. J., J. L. Best, S. N. Lane, and P. E. Carbonneau (2009), Coherent flow structures in a depth-limited flow over a gravel surface: The role of near-bed turbulence and influence of Reynolds number, J. Geophys. Res., 114, F01003, doi:10.1029/2007JF000970.

Hess, G.D., and R.H. Clarke (1973), Time spectra and cross-spectra of kinetic energy in the planetary boundary layer, *Quart. J. Roy. Meteor. Soc.*, *99*, 130-153.

Imamoto, H., and T. Ishigaki (1986a), The three dimensional structure of turbulent shear flow in an open channel, paper presented at the *Fifth Congress of the Asian and Pacific Regional Division of the International Association for Hydraulic Research*, Seoul, Korea.

Imamoto, H., and T. Ishigaki (1986b), Visualization of longitudinal eddies in an open channel flow, in *Flow Visualization IV: Proceedings of the Fourth International Symposium on Flow Visualization*, edited by C. Veret, pp. 333-337, Hemisphere, Washington, D. C.

Kader, B. A., and A. M. Yaglom (1991), Spectra and correlation functions of surface layer atmospheric turbulence in unstable thermal stratification, *In Turbulence and Coherent Structures* (ed. O. Métais and M. Lesieur), Kluwer.

Katul, G. G., C. R. Chu, M. B. Parlange, J. D. Albertson, and T. A. Ortenburger (1995), Low wavenumber spectral characteristics of velocity and temperature in the atmospheric boundary layer, *J. Geophys. Res.*, *100*, 14243-14255.

Kirkbride, A. D. (1993), Observations of the influence of bed roughness on turbulence structure in depth-limited flows over gravel beds, in *Turbulence: Perspectives on Flow and Sediment Transport*, edited by N. J. Clifford, J. R. French, and J. Hardisty, pp. 185196, John Wiley, Chichester, U. K.

Kirkbride, A.D., and M.J. McLelland (1994), Visualization of the turbulent flow structures in a gravel bed river, *Earth surface processes and landforms*, *19*, 819-825.

Kirkbride, A.D., and R.I. Ferguson (1995), Turbulent flow structure in a gravel-bed river: Markov chain analysis of the fluctuating velocity profile, *Earth Surf. Processes Landforms*, *20*, 721-733.

Kolmogorov, A. (1961), Dissipation of energy in the locally isotropic turbulence, in *Turbulence: Classic Papers on Statistical Theory*, edited by S. K. Friedlander and L. Topper, pp. 151-155, Wiley-Interscience, Hoboken, New Jersey.

Lacey, R. W. J., and A. G. Roy (2007), A comparative study of the turbulent flow field with and without a pebble cluster in a gravel bed river, *Water Resour. Res.*, *43*, W05502, doi:10.1029/2006WR005027.

Lacey, R. W. J., A. G. Roy (2008), Fine-Scale Characterization of the Turbulent Shear Layer of an Instream Pebble Cluster, *J. Hydr. Engrg.*, *134*, 7, 925-936.

Lamarre, H., and A. G. Roy (2005), Reach scale variability of turbulent flow characteristics in a gravel-bed river, *Geomorpholgy*, *60*, 95-113.

Lapointe, M. F. (1992), Burst-like sediment suspension events in a sand bed river, *Earth Surf. Processes Landforms*, *17*, 253-270.

Marion, A., S. J. Tait, and I. K. McEwan (2003), Analysis of small-scale gravel bed topography during armoring, *Water Resour. Res.*, *39(12)*, 1334, doi:10.1029/2003WR002367

Marquis, G. A., and A. G. Roy (2006), Effect of flow depth and velocity on the scales of macroturbulent structures in gravel-bed rivers, *Geophys. Res. Lett.*,*33*, L24406, doi:10.1029/2006GL028420.

Newman, W. I., and D. L. Turcotte (1990), Cascade model for fluvial geomorphology, *Geophys. J. Int.*, *100*, 433-439.

Nezu, I., and H. Nakagawa (1993), Turbulence in open-channel flows, Balkema, Rotterdam, The Netherlands.

Nikora, V. I., D. G. Goring, and B. J. F. Biggs (1998), On gravel-bed roughness characterization, *Water Resour. Res.*,*34(3)*, 517527.

Nikora, V. I., and D. G. Goring (2000), Flow turbulence over fixed and weakly mobile gravel beds, *J. Hydraul. Eng.*, *126(9)*, 679-690.

Nikora, V., and J. Walsh (2004), Water-worked gravel surfaces: High-order structure functions at the particle scale, *Water Resour. Res.*,*40*, W12601, doi:10.1029/2004WR003346.

Nikora, V (2008), Hydrodynamics of gravel-bed rivers: scale issues, in *Gravel-bed rivers VI: From Process Understanding to River Restoration*, Habersack H, Piegay H and Rinaldi M (Eds), Elsevier B. V., 61-81.

Paiement-Paradis, G., T. Buffin-Blanger, and A. G. Roy (2003), Scalings for large turbulent flow structures in gravel-bed rivers, *Geophys. Res. Lett.*, *30(14)*, 1773, doi:10.1029/2003GL017553.

Parsheh, M., F. Sotiropoulos, and F. Porté-Agel (2009), Estimation of Power Spectra of Acoustic-Doppler Velocimetry Data Contaminated with Intermittent Spikes, *J. Hydraul. Engg.*. (In Review)

Passalacqua P., F. Porté-Agel, E. Foufoula-Georgiou, C. Paola (2006), Application of dynamic subgrid-scale concepts from large-eddy simulation to modeling landscape evolution, *Water Resour. Res.*, *42*, W06D11, doi:10.1029/2006WR004879.

Perry, A. E., S. Henbest, and M. S. Chong (1986), A theoretical and experimental study of wall turbulence, *J. Fluid Mech.*, *165*, 163-199.

Porté-Agel, F., C. Meneveau, M. B. Parlange (2000), A scale-dependent dynamic model for large-eddy simulation: application to a neutral atmospheric boundary layer, *J. Fluid Mech.*, *415*, 216-284.

Pelletier, J.D. (1999), The self-organization and scaling relationships of evolving river networks, *J. Geophys. Res.*, *104*, 7359-7375.

Robert, A., A.G. Roy, and B. De Serres (1992), Changes in velocity profiles at roughness transitions in coarse-grained channels, *Sedimentology*, *39*, 725-735.

Robert, A., A.G. Roy, and B. De Serres (1993), Spacetime correlations of velocity measurements at a roughness transition in a gravel-bed river, In: N.J. Clifford, J.R. French and J. Hardisty, Editors, *Turbulence: perspectives on flow and sediments transport*, Wiley, Chichester, pp. 167-183.

Roy, A.G., T. Buffin-Belanger, H. Lamarre, and A.D. Kirkbride (2004), Size, shape and dynamics of large-scale turbulent flow structures in a gravel-bed river, *J. Fluid Mech.*, *500*, 1-27.

Schmeeckle, M. W., J. M. Nelson, and R. L. Shreve (2007), Forces on stationary particles in near-bed turbulent flows, *J. Geophys. Res.*, *112*, F02003, doi:10.1029/2006JF000536.

Shvidchenko, A. B., and G. Pender (2001), Macroturbulent structure of open-channel flow over gravel beds, *Water Resour. Res.*, *37(3)*, 709719.

Singh, A., K. Fienberg, D. J. Jerolmack, J. Marr, and E. Foufoula-Georgiou (2009), Experimental evidence for statistical scaling and intermittency in sediment transport rates, *J. Geophys. Res.*, *114*, F01025, doi:10.1029/2007JF000963.

Singh, A., S. Lanzoni, and E. Foufoula-Georgiou (2008), Nonlinearity and complexity in gravel-bed dynamics, *SERRA, Special issue on Modeling and Prediction of Complex Environmental System*, Springer Velrag, N.Y, doi: 10.1007/S00477-008-0269-8.

Smedman-Högström, A.S., and U. Högström (1975), Spectral Gap in Surface-Layer Measurements, *J. Atmos. Sci.*,*32*, 340-350.

Soulsby, R.L. (1980), Selecting record length and digitization rate for near-bed turbulence measurements, *J. Phys. Oceanogr.*, *10*, 208-219.

Stoica, P., R. L. Moses (1997), Introduction to spectral analysis, Upper Saddle River, New Jersey, Prentice Hall, 07458.

Van Der Hoven, I. (1957), Power spectrum of horizontal wind speed in the frequency range from 0.0007 to 900 cycles per hour, *J. Meteor.*, *14*, 160-194.

Vening Meinesz, F. A. (1951), A remarkable feature of the Earths topography, *Proc. K. Ned. Akad. Wet. Ser. B. Palaeontol. Geol Phys. Chem. Anthropol.*, *54*, 212-228.

Venugopal V., F. Porté-Agel, E. Foufoula-Georgiou, and M. Carper (2003), Multiscale interactions between surface shear stress and velocity in turbulent boundary layers, *J. Geophys. Res.*, *108*, doi:10.1029/2002JD003025.

Wiberg, P. L., and J. D. Smith (1991), Velocity Distribution and Bed Roughness in High-Gradient Streams, *Water Resour. Res.*, *27(5)*, 825838.

Wilcock, P. R., C. H. Orr, and J. D. G. Marr (2008), The need for full-scale experiments in river science, *Eos Trans. AGU*, *89(1)*, doi:10.1029/2008EO010003.

Yalin, M. S. (1992), *River Mechanics*, 219 pp., Elsevier, New York.

Department of Civil Engineering, St. Anthony Falls Laboratory and National Center for Earth-Surface Dynamics, University of Minnesota, Minnesota, USA. (fporte@umn.edu)

Table 1: Hydraulic conditions and characteristics of temporal series of bed elevation

Q_w (l/s)	D(m)	v (m/sec)	S_w	h_R (m)	Shields stress ($\tau*_b$)	R_e	F_r	T_{mean} (°C)	D_p (cm)	σ_b (mm)	k
2000	0.55	1.18	0.0019	0.39	0.058	646640	0.51	23.5	12.59	23.95	5.3
2800	0.64	1.55	0.0029	0.44	0.099	992000	0.62	16.23	19.17	38.65	5.0

where,

Q_w = water discharge for the run

D = average depth of flow in test section

v = average flow velocity

h_R = hydraulic radius

S_w = water surface slope

$\tau*_b$ = dimensionless Shields stress (computed using hydraulic radius)

R_e = Reynolds number (kinematic viscosity of water, $v = 1 \times 10^{-6}$ m^2/sec)

F_r = Froude number

T_{mean} = mean water temperature.

D_p = distance of the velocity probe from mean bed level

σ_b = standard deviation of temporal bed elevation series

 k = ratio between D_p and σ_b

Table 2: Characteristics of power spectrum for velocity, temporal bed elevations and spatial bed elevations.

| Q_w (l/s)	Velocity v(t)			Temporal-bed elevation h(t)		Spatial-bed elevation h(x)	
	dynamic slope	scaling regime	spectral gap	spectral slope	scaling regime	spectral slope	scaling regime
2000	-1.05	2 min - 55 min	10 sec - 2 min	-1.94	15 sec - 42 min	-1.87	10 cm – 10 m
2800	-1.15	35 sec - 28 min	6 sec – 35 sec	-2.1	15 sec - 28 min	-2.06	15 cm - 10 m

Figure 1. Experimental channel facility at St. Anthony Falls Laboratory, University of Minnesota showing the locations of ADV and the sonar at the downstream end of the channel. A total of seven submersible sonars were deployed. In this study the data collected from the ADV and the sonar (located 15 cm downstream of ADV) along the centerline of the channel (see also schematic in Figure 3) are used. The direction of the flow is from bottom to the top of the figure.

Figure 2. Photograph of bed surface at the end of the flow for the discharges of 2000 l/s (left), and 2800 l/s (right). The direction of flow in both cases is from the top to the bottom of the figures.
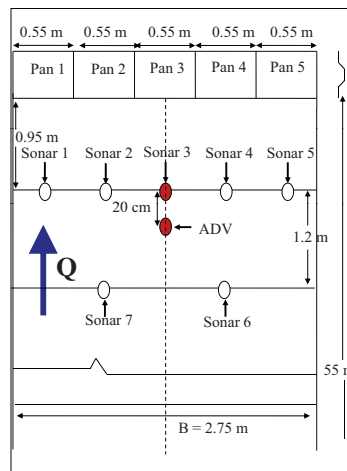
Figure 3. Schematic of experimental setup showing the locations of sonars (used for measuring temporal bed elevation) and the ADV (used for measuring velocity fluctuations) at the downstream end of the channel. Note that the solid dots represent the measurement locations of temporal bed elevations (h(t)) and velocity (v(t)) used in this study. The dash line represents the centerline of the channel.
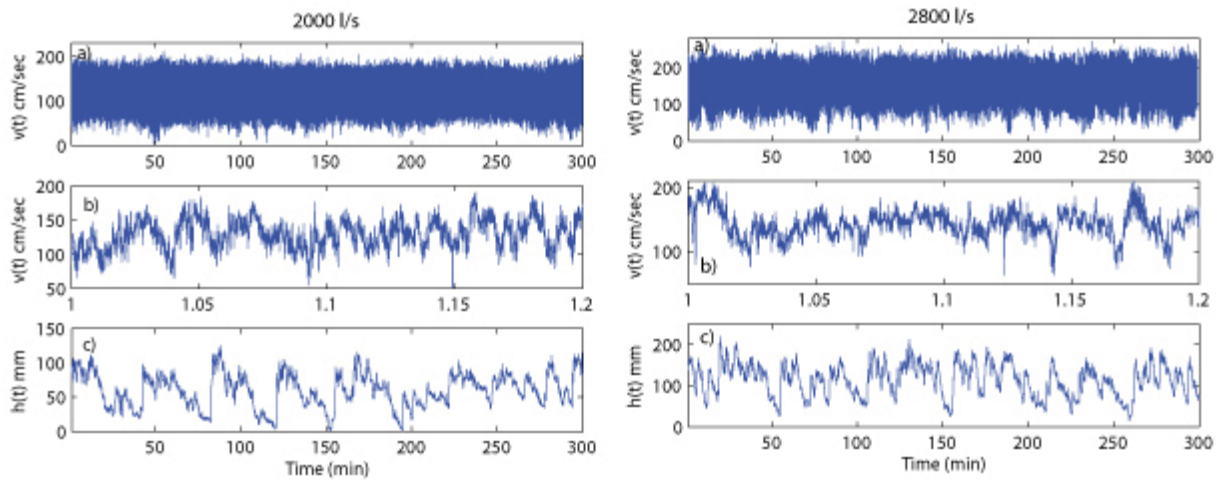
Figure 4. Time series of velocity (top) and bed elevation (bottom) measured at the downstream end of the channel for flow discharges of 2000 l/s (left) and 2800 l/s (right) over a duration 300 mins. The middle panels show a blown-up image of the velocity series shown in the top panels for a duration 0.2 mins. The flow velocity was measured at a frequency of 200 Hz (sampling interval, $\Delta t = 0.005$ sec) and the bed elevations were sampled at a frequency 0.2 Hz (sampling interval, $\Delta t = 5$ sec). In the case of bed elevation (bottom panel), it can be seen that short fluctuations are superimposed on larger ones. This suggests that small bedforms (small dunes, ripples or bedload sheets) are propagated over larger dunes.
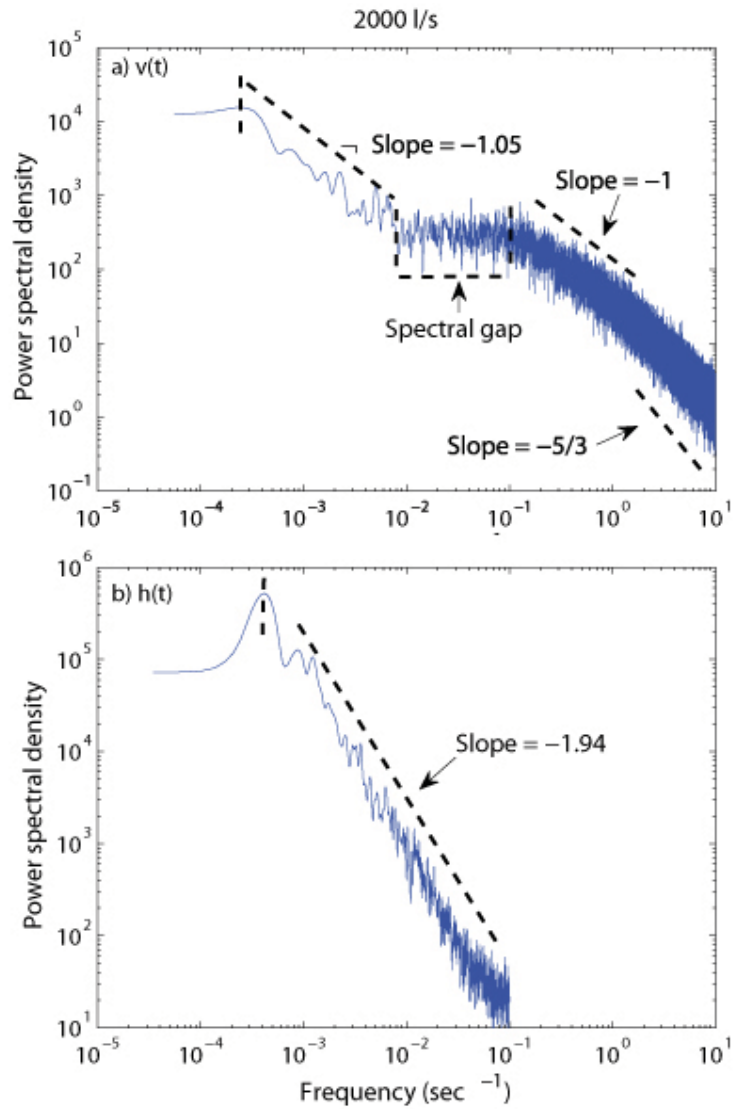
Figure 5. Power spectral density of a) velocity fluctuations and, b) corresponding bed elevations for a discharge of 2000 l/s. In the velocity spectrum, scaling at small scales is due to turbulence while at larger scales it is modulated by bed topography.
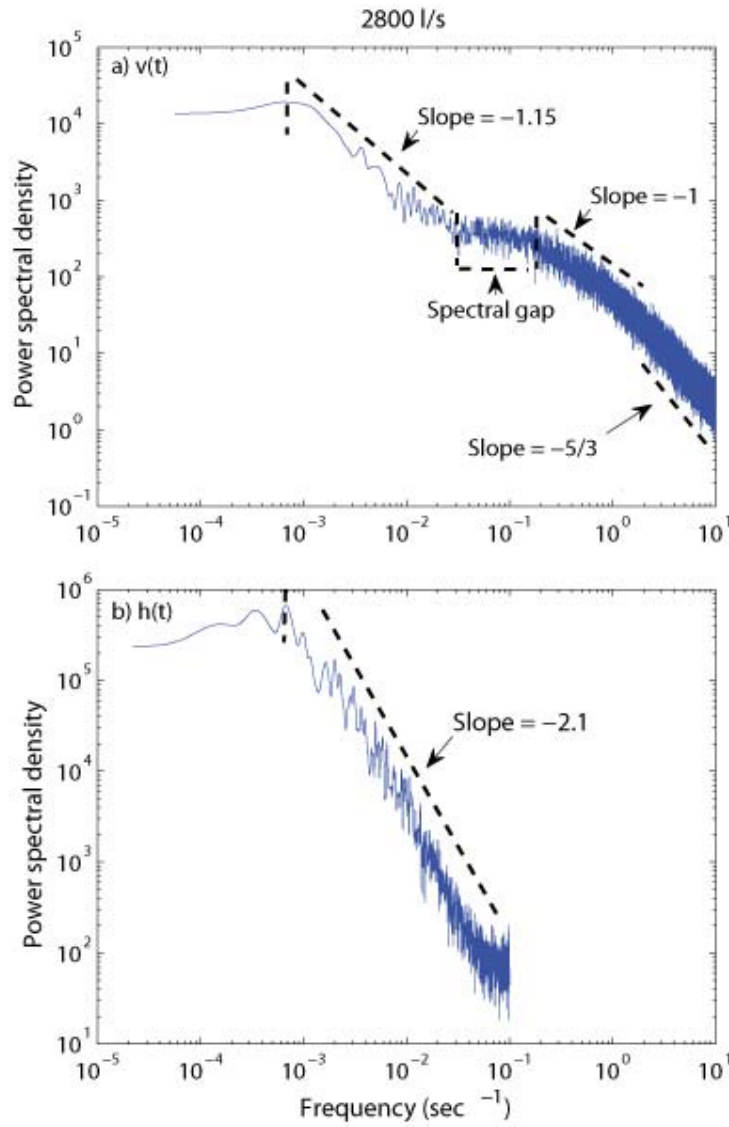
Figure 6. Power spectral density of a) velocity fluctuations and, b) corresponding bed elevation for a discharge of 2800 l/s. In the velocity spectrum, scaling at small scales is due to turbulence while at larger scales it is modulated by bed topography.
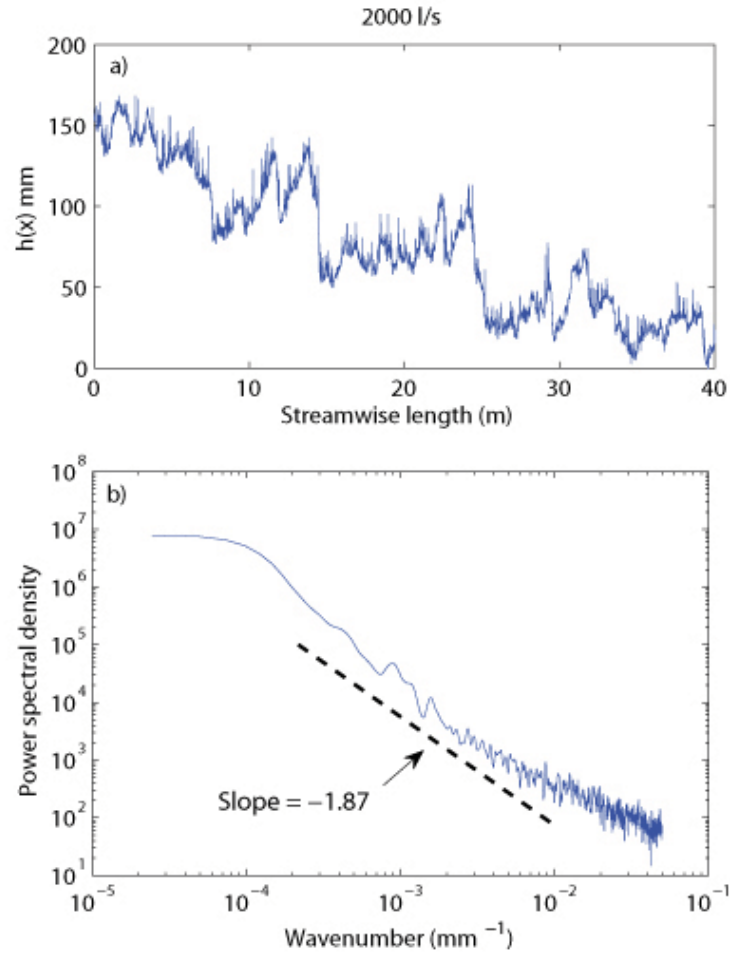
Figure 7. a) Longitudinal transect of bed profile elevations at a resolution of 10mm and, b)its power spectral density for a discharge of 2000 l/s. Note that similar spectral slopes are observed in both temporal bed elevation and spatial bed elevation series (compare with Fig. 5b).
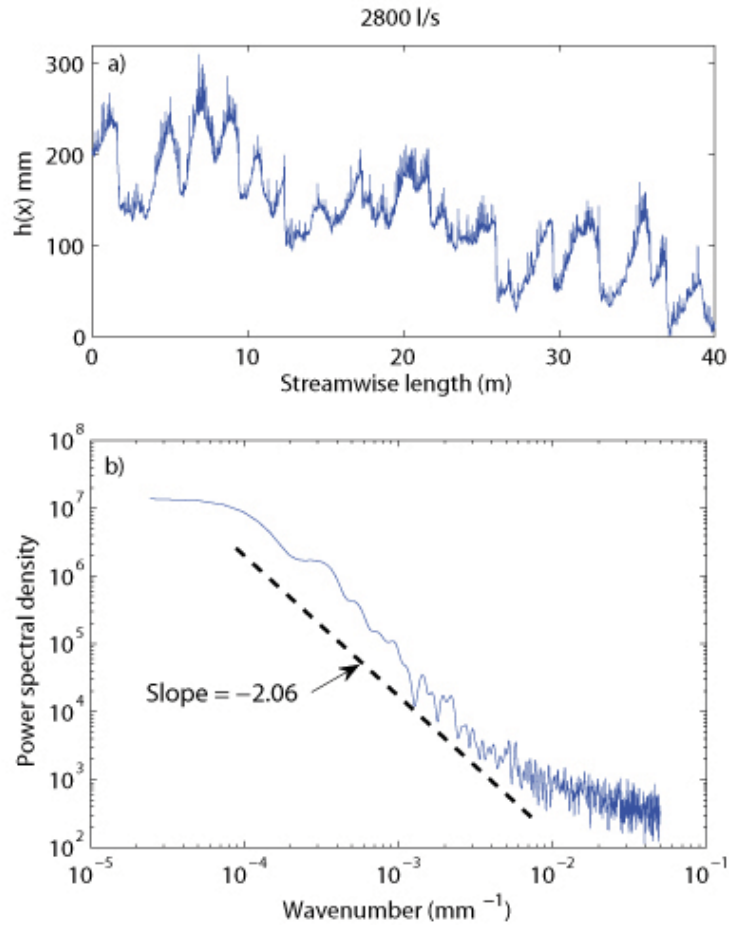
Figure 8. a) Longitudinal transect of bed elevations sampled at a resolution of 10mm and, b)its power spectral density for a discharge of 2800 l/s. Note that similar spectral slopes are observed in both temporal bed elevation and spatial bed elevation series (compare with Fig. 6b).

Transport on river networks: A dynamic-tree approach

Ilya Zaliapin

Department of Mathematics and Statistics, University of Nevada, Reno

Efi Foufoula-Georgiou

St. Anthony Falls Laboratory and National Center for Earth-surface Dynamics, Department of Civil
Engineering, University of Minnesota, Minneapolis

Michael Ghil

Geosciences Department and Laboratoire de Météorologie Dynamique (CNRS and IPSL), Ecole Normale
Supérieure, Paris, FRANCE, and Department of Atmospheric and Oceanic Sciences and Institute of Geophysics
and Planetary Physics, University of California, Los Angeles

Abstract. This study is motivated by problems related to environmental transport on
river networks. We establish statistical properties of a flow along a directed branching
network and suggest its compact parameterization. The downstream network transport
is treated as a particular case of nearest-neighbor hierarchical aggregation with respect
to the metric induced by the branching structure of the river network. We describe the
static geometric structure of a drainage network by a tree, referred to as the *static tree*,
and introduce an associated *dynamic tree* that describes the transport along the static
tree. It is well known that the static branching structure of river networks can be de-
scribed by *self-similar trees*; we demonstrate that the corresponding dynamic trees are
also self-similar, albeit with different self-similarity parameters. We report an unexpected
phase transition in the dynamics of three river networks, one from California and two
from Italy, demonstrate the universal features of this transition, and seek to interpret
it in hydrological terms.

1. Introduction and motivation

The topology of river networks has been extensively stud-
ied over the past decades using the suite of quantitative
methods developed in the pioneering works of *Horton* [1945],
Strahler [1957], *Shreve* [1966], and *Tokunaga* [1978]. These
authors found that the geometry of real river networks
can be closely approximated by so-called *self-similar trees*
(SSTs). Such trees can be completely specified by a small
number of parameters; this specification facilitates the de-
velopment of similarity metrics and scaling theories within
and across river networks. As a result, stream-ordering
schemes and statistical self-similarity concepts have been
explored to a considerable extent [see *Jarvis and Wolden-
berg*, 1984; *Rodriguez-Iturbe et al.*, 1992; *Peckham*, 1995;
Rodriguez-Iturbe and Rinaldo, 1997; *Sposito*, 1998; *Peckham
and Gupta*, 1999; *Veitzer and Gupta*, 2000; *Dodds and Roth-
man*, 2000; and references therein].

The connection between river network topology and the
hydrologic response of a basin has also been extensively
studied; see, for instance, the early work of *Surkan* [1969],
Kirkby [1976], and *Rodriguez-Iturbe and Valdes* [1979], while
Gupta and Mesa [1988], and *Rodriguez-Iturbe and Rinaldo*
[1997] review the later developments. Apart from stream-
flow, the river network is also known to structure other
processes operating on it, such as sediment bedload, grain
size, nutrients, riparian vegetation, and the food web struc-
ture of aquatic organisms [*e.g.*, *Sklar et al.*, 2006; *Benda
et al.*, 2004a,b; *Kiffney et al.*, 2006; *Lowe et al.*, 2006;
Muneepeerakut et al., 2006; *Power and Dietrich*, 2002; *Rice
and Church*, 1998; *Rice et al.*, 2006; *Stewart-Koster et al.*,

2007; *Wohl et al.*, 2007]. The impact of such processes is
of great interest from environmental, economic, and societal
points of view.

The development of a systematic framework within which
to study dynamical processes on river networks remains of
considerable theoretical and practical interest in hydrology,
geomorphology, and river ecology. In this paper, we propose
a new way of studying dynamical processes that operate on
directed trees, which are commonly used to model river net-
works. Specifically, we introduce the concept of a "dynamic
tree," which describes the directed transport along the links
of a "static tree" that has a given topology and link-length
distribution, as well as other space- and time-dependent at-
tributes.

This dynamic tree is likely to have a different hierarchy
and topology than the static one. For instance, some of the
static-tree branches might be completely cut off, either due
to a blockage that prevents transport along these branches
or due to the absence of conditions that favor sediment or
nutrient generation for downstream transport. In this and
other cases, the structure of the dynamic tree will differ from
that of the static one, and this difference might affect the
scaling of fluxes that participate in defining the envirody-
namics on the network of interest. In general, a static tree of
a given Horton-Strahler order [*Horton*, 1945; *Strahler*, 1957]
could become a dynamic tree of a lesser or higher order,
depending on the dynamics acting on the tree.

The purpose of this paper is to study the dynamic topol-
ogy of directed trees, starting with several simple cases, first
synthetic and then realistic. We work here with downstream
fluxes, oriented from the sources to the outlet, and with
time-continuous transport. The possibility of reverse (up-
stream) motion, as in tidal systems or in association with
the movements of biota, and discontinuous transport is left
for future work. We focus on a dynamic hierarchy built on
the concept of "connectivity": once two streams are con-
nected, they both influence the downstream dynamics. In

other words, a dynamic node of order 2 is created only when the fluxes from both order-1 streams do reach the connecting node. Such considerations will result in a different ordering of the dynamic tree than of the static one. Moreover, the newly created dynamic tree will be *time-oriented*, a property that is absent in conventional static trees. Alternatively, one might keep track of traveled distance, rather than time: the two are equivalent if the flow velocity is constant along all the branches, which we will assume in the present paper, for simplicity's sake.

The static branching structure of river networks can be described by self-similar trees, following *Tokunaga* [1978], *Peckham* [1995], and *Peckham and Gupta* [1999], among others. It is shown here, using three actual river networks, that the corresponding dynamic trees are also self-similar, although their properties differ systematically from those of the corresponding static trees. We also demonstrate an unexpected *phase transition* in the dynamics on river networks, from a pattern of numerous disconnected fluxes initiated at the network sources to a single connected flux. Finally, we place our findings within the general framework of *hierarchical aggregation* and *cluster dynamics*. This framework helps describe and understand such diverse phenomena as population genetics, interacting particle systems in statistical mechanics, phylogeny, percolation, and extreme natural hazards.

The paper is structured as follows. We review in Section 2 the relevant concepts and main results in river network topology, including the branching taxonomies of *Horton* [1945] and *Strahler* [1957] and of *Tokunaga* [1978]. Section 3 introduces the concept of a *dynamic tree* that is associated with a given *static tree*, by using two examples from river transport. Hierarchical aggregation, including aggregation in an abstract metric space, is introduced in Section 4. Section 5 describes the three river basins from California and Italy that we study here, as well as the static trees that represent the stream networks of these basins. The results of the study are presented in Section 6. A summary and discussion, as well as an outline of further work follow in Section 7. Examples of hierarchical aggregation from several fields of inquiry appear in Appendix A.

2. Network topology: Overview of concepts and results

This section summarizes the main concepts used in the topological analysis of river networks, as well as the key results of this analysis.

2.1. Branching-order taxonomies

In our study of river transport, a drainage network is represented by a tree $\mathbb{T}$ (see Fig. 1). In this representation, the stream *junctions* correspond to tree nodes, the stream segments between junctions – to *links* or edges, the network's *sources* – to tree leaves, and the basin *outlet* – to the root of the tree. A *source link* is a link attached to a stream head; while an *outlet link* is the link attached to the basin outflow node.

In many applications, there is a need to order the network links or tree edges according to their importance in forming the entire network. *Horton* [1945] developed a convenient way to order hierarchically organized river tributaries; this method was later refined by *Strahler* [1957] and further expanded by *Tokunaga* [1978]. Currently, the so-called Horton-Strahler (HS) and Tokunaga ordering schemes are standard tools of branching analysis, well beyond purely hydrological applications.

Horton-Strahler ordering is performed in a hierarchical fashion, from the sources to the outlet. Each source link in a *binary rooted tree* is assigned an HS *order* $r(\text{source}) = 1$;

see Fig. 2(a). When two links with the same order r meet, the link immediately downstream is assigned order $r + 1$; when two links with different orders meet, the link immediately downstream is assigned the larger one of the two orders [*e.g.*, *Horton*, 1945; *Strahler*, 1957; *Newman et al.*, 1997]. A *branch* is defined as a union of connected links with the same order. We will denote by N_r the total number of branches of order r. Notice that each branch has *linear* structure: each of its links can be connected to only one upstream and/or one downstream link from the same branch. The order Ω of a tree is the maximal order of its branches. An HS order can also be assigned to the stream junctions (tree nodes); in this case the order is the same as that of the immediate downstream link.

Tokunaga indexing [*Tokunaga*, 1978; *Peckham*, 1995; *Newman et al.*, 1997] expands upon the Horton-Strahler orders; it is illustrated in Fig. 2(b). This indexing catalogues the merging points between branches of different order. A first-order branch that merges with a second-order branch is indexed by "12" and the total number of such branches is denoted by N_{12}. A first-order branch that merges with a third-order branch is indexed by "13" and the total number of such branches is N_{13}, and so on. In general, N_{ij} for $j > i$ denotes the total number of order-i branches that join an order-j branch.

The Tokunaga index T_{ij} is the number of branches of order i that merge with a branch of order j, normalized by the total number of branches of order j; in other words, T_{ij} is the average number of branches of order $i < j$ per branch of order j:

$$T_{ij} = \frac{N_{ij}}{N_j}. \tag{1}$$

Merging of branches of different orders is referred to as *side branching*. A *complete tree* is one where side branching is absent. For incomplete trees, the side-branching indices become increasingly important as they help define a tree's structure and may help specify distinct classes of trees.

For consistency, we denote the total number of order-i branches that merge with other order-i branches by N_{ii} and notice that in a complete binary tree $N_{ii} = 2 N_{i+1}$. The "diagonal" Tokunaga indices T_{ii} thus satisfy:

$$T_{ii} = \frac{N_{ii}}{N_{i+1}} \equiv 2.$$

The set $\{T_{ij} : 1 \leq i \leq \Omega - 1, 1 \leq j \leq \Omega\}$ of Tokunaga indices provides therewith a complete statistical description of the branching structure of an order-Ω tree.

We also use in this study the following two link statistics: the number of links within a given branch and the number m_i of sources upstream from a link i. The latter statistic is also called a link's *magnitude* [*Shreve*, 1966]; a branch's magnitude is the magnitude of its furthest downstream link. The branch magnitude is coarsely proportional to the branch drainage area, with the coefficient of proportionality equal to the average drainage area for the stream sources. The average number of nodes and average magnitude of an order-r branch are denoted by C_r and M_r respectively.

2.2. Self-similar trees and Horton laws

The concept of *self-similarity* provides a powerful tool for describing and studying trees. A self-similar tree (SST) is defined by the constraint that the value of each Tokunaga index T_{ij} depends only on the difference $(j - i)$ between the orders of respective branches. Accordingly, we define, for all i,

$$T_k := T_{i(i+k)} \quad \text{for } k = 1, 2, \ldots. \tag{2}$$

Tokunaga [1978] was probably the first to study SSTs; he assumed also that the ratio of two consecutive branching indices is constant:

$$\frac{T_{k+1}}{T_k} = c, \quad \text{or} \quad T_k = a \, c^{k-1} \quad \text{for } a, c > 0. \tag{3}$$

The SSTs that satisfy (3) are called *Tokunaga trees*.

Empirically, the average values of branching statistics for observed river networks depend exponentially on the order r, for large r and Ω. In particular, for the total number N_r of branches of order r, the average magnitude M_r, and the average number C_r of links within an order-r branch we have:

$$N_r = N_0\, R_B^{\Omega-r}, \quad M_r = M_0\, R_M^{r-1}, \quad C_r = C_0\, R_C^r \qquad (4)$$

for some positive constants N_0, M_0 and C_0. Such relationships are called *Horton laws*; the bases R_B, R_M, and R_C of the exponential relatonships are called *stream ratios*.

McConnell and Gupta [2008] showed that the first two of the Horton laws (4) hold asymptotically, *i.e.* for $r \to \infty$, in a self-similar Tokunaga tree; they also proved that $R_B = R_M$. *Zaliapin* [2009] demonstrated asymptotic validity of all the laws in (4) and established the stream ratio inequality

$$R_C < R_B = R_M, \qquad (5)$$

that had been conjectured by *Peckham* [1995]. In addition, *Zaliapin* [2009] showed that the Horton laws may or may not hold, under some additional assumptions on the Tokunaga indices T_k, for self-similar trees that do not necessarily satisfy condition (3).

3. Dynamic *vs.* static trees

The topological structure of a river network is well described by a directed tree, which we denote by $\mathbb{T}_S$ and call the *static tree*. To describe the downstream transport on $\mathbb{T}_S$ we introduce the notion of a *dynamic tree* $\mathbb{T}_D$, which combines the topological structure of $\mathbb{T}_S$ with the corresponding link-length values. The dynamic tree is introduced as follows. Imagine that we inject a dye simultaneously into all the sources of our river network $\mathbb{T}_S$, and the dye starts propagating down the river, from the sources to the outlet, with the same constant velocity along all the streams. The influx of the dye is continuous and happens at a constant rate. The tree $\mathbb{T}_D$ describes the time-dependent history of the mergings of the colored streams.

We consider below two detailed examples to further clarify this concept, while restricting ourselves to the simplest case of constant velocity along all the streams. Taking this velocity to be unity allows one to interchange time and length scales. We shall see that the dynamic tree $\mathbb{T}_D$ is completely determined by the static tree $\mathbb{T}_S$ and the set of time *delays* τ_i necessary for the dye to propagate from a junction i to the nearest downstream junction. These delays can be proportional to the link lengths, as is the case in the present study, or be determined by spatially or temporally variable velocities. The latter extension is left for a future study.

3.1. Synthetic example

Figure 3 shows how to construct the dynamic tree for a basin with four sources **a, b, c,** and **d**. The static tree for this basin is a complete binary tree shown in the top rightmost panel. The same tree with the link lengths explicitly displayed is shown in the top row of the panels; the top leftmost panel indicates the values of these lengths.

The consecutive phases of construction of the dynamic tree are shown in the bottom row of panels. At step 0 (the leftmost top and bottom panels), all the links in the tree are "empty" (dashed lines) and the dye is injected into the sources **a, b, c,** and **d**. Accordingly, we have four disconnected clusters of colored flux; they correspond to four disconnected nodes in the lower left panel. We assume that the dye is being continuously injected at all later times at a constant rate. Each step in the figure is a snapshot of this

process after a unit time interval; recall that we use only constant velocity in this paper and, without loss of generality, this velocity equals unity.

At step 1 the dye has propagated a unit length along each stream, which is depicted by solid lines in the top panel. Since all four streams are disconnected so far, the dynamic tree still consists of four disconnected branches, each of which corresponds to a colored stream of unit length. At step 2 the streams **a** and **b** merge, and so the nodes **a** and **b** are now connected into a single cluster in the dynamic tree. Notice that the sources **a** and **b** are not directly connected in the static tree; this connection reflects a property of the dye's downstream propagation.

At step 3 stream **c** reaches stream **a**. Since stream **a** by that time is already merged with stream **b**, we say that the stream **c** merges with the cluster of **a** and **b**; this is reflected in the dynamic tree in the corresponding lower panel. Hence, at step 3 there exist two connected clusters of the colored flux: one cluster is formed by streams **a, b,** and **c**, while stream **d** alone forms the second cluster. Finally, at step 4, all the colored fluxes have merged. The conventional representation of both static and dynamic trees, which does not show the link lengths, is given in the two rightmost panels.

This example shows that the dynamic tree $\mathbb{T}_D$ can be very different from the corresponding static tree $\mathbb{T}_S$. We notice in particular that in this example the static tree is a tree with no side branching; it has the largest possible Horton-Strahler order, $\Omega = 3$, for a tree with four sources. At the same time, the dynamic tree exhibits exhaustive side-branching; accordingly, it has the smallest possible order, $\Omega = 2$, for a tree with four sources.

3.2. Data-based hydrologic example

We illustrate here the dynamic tree for an order-3 subbasin of the Upper Noyo basin. This basin is located in Mendocino County, California, USA; it is described by *Sklar et al.* [2006] and appears in Fig. 7(a) of Section 5, along with an outline of the subbasin discussed in the present example. The stream network for this subbasin is shown in Fig. 4; its fifteen sources are marked by numbers 1 to 15 and fourteen stream junctions by letters **a** to **n**. The static tree $\mathbb{T}_S$ for this stream network is shown in Fig. 5(a); it has the Horton-Strahler order $\Omega = 3$.

The time-oriented dynamic tree $\mathbb{T}_D$ is shown in Fig. 5(b) against the distance traveled by the dye from each source (on the ordinate). Notice that distance in Fig. 5(b) can also be interpreted as time. The order of the dynamic tree is $\Omega = 4$. In this example (unlike the synthetic example of Fig. 3), the dynamic tree shows a smaller degree of side-branching compared to the static tree; this smaller degree yields a larger HS order. We shall see in other realistic examples, further below, that this seems to be the case for most actual river networks. Three snapshots of the simulated dye propagation, at distances $d = 20, 200$ and 600 are shown in Fig. 6 to further illustrate the dynamic tree concept.

4. The dynamics of hierarchical aggregation

The consecutive merging of river streams discussed in the previous section gives rise to a time-oriented dynamic tree. Study of such trees calls for the development of a new mathematical framework: *hierarchical aggregation* is a promising candidate for such a framework.

4.1. Hierarchical aggregation

Hierarchical aggregation studies how multiple individual particles (molecules, species, individuals, *etc.*) merge (aggregate, collide) with each other to form clusters in different

physical, chemical, biological, or sociological settings [*Albert and Barabasi*, 2002; *Leyvraz*, 2003; *Wakeley*, 2009]. In the river transport setting, particles represent individual channel links, merging refers to the situation of two channels joining downstream, and a cluster represents all the upstream channels that jointly contribute to the flow at a given junction.

Formally, consider a process that starts at time $t = 0$ with N individual *particles* (say the sources of a river network), which can be considered as *clusters* of unit mass. As time evolves (and as a substance propagates down the river network) the clusters start to merge with one another, according to a set of rules imposed by the dynamics of propagation, thus forming consecutively larger clusters. If we assume that only two clusters can merge at the same time, then the number of clusters decreases by one after each merging. The process continues until all particles have merged into a single cluster of mass N; in our case, this would be when all the nodes of the river network are parts of the same cluster, *i.e.* when the whole system is connected.

The evolution of the above process can be described by a time-oriented binary tree, whose leaves correspond to the initial particles, the root to the final cluster of N particles, and each internal node to an intermediate cluster. Among the many instances of the above general aggregation scheme, we mention population genetics [*Wakeley*, 2009], phylogenetic trees [*Maher*, 2002], percolation [*Albert and Barabasi*, 2002; *Zaliapin et al.*, 2005], and billiards [*Gabrielov et al.*, 2008]; see Appendix A for details. *Bertoin* [2006] gives a modern review of mathematical results related to aggregation.

An important role in aggregation studies is played by the notion of *cluster dynamics* [*Bogolyubov*, 1960; *Sinai*, 1973]. This concept refers to a system that contains an infinite number of interacting particles, which can be decomposed into *finite* clusters that move independently of each other for some random interval of time. After this time, the particle interactions give rise to infinite-range correlations (meaning that the mean cluster size becomes infinite, or an infinite number of particles affects each other's dynamics), although the system can be decomposed into yet another set of finite independent clusters, and so on.

Sinai [1973, 1974] developed a self-consistent mathematical formalism and proved the existence of cluster dynamics for some particle systems in statistical mechanics. The ideas of cluster dynamics have been applied to plasma physics, economics, and the study of precursory patterns for extreme events in geophysics [*Rotwain et al.*, 1997; *Molchan et al.*, 1990; *Keilis-Borok and Soloviev*, 2003]. Recently, *Gabrielov et al.* [2008] evaluated numerically the cluster dynamics of elastic billiards, leading to the detection of what appear to be the first genuine *phase transitions* and *scaling phenomena* with time, rather than usual temperature T or density, being the order parameter. Thus, a transition occurs and scaling develops as time t approaches a critical value t^*, rather than as the parameter T crosses a critical value T^*. As will be shown in Section 6.2, we report here a remarkably similar and equally unexpected phase transition, with time being the order parameter, in the cluster dynamics of a river network.

4.2. Nearest-neighbor clustering

Hierarchical aggregation can be described in great generality by using the framework of nearest-neighbor clustering in a metric space. Specifically, consider a finite set $\mathbb{S}$ with distance $d(a, b)$ for $a, b \in \mathbb{S}$; the elements of the set will be called *points*. The distance $d(A, B)$ between two subsets of points $A = \{a_i\}_{i=1,...,N_A}$ and $B = \{b_i\}_{i=1,...,N_B}$ from $\mathbb{S}$ is defined as the shortest distance between the elements of the sets:

$$d(A, B) = \min_{1 \le i \le N_A, 1 \le j \le N_B} d(a_i, b_j).$$

Nearest-neighbor clustering is a process that combines points from $\mathbb{S}$ into consecutively larger subsets, called *clusters*, by connecting at each step the two nearest clusters; this process can be described by the *nearest-neighbor spanning tree* $\mathbb{T}$. Specifically, consider N points $c_i^0 \in \mathbb{S}$, $i = 1, \ldots, N$ with pairwise distances $d_{ij}^0 \equiv d(c_i^0, c_j^0)$. These points, considered as clusters of unit mass ($m_i = 1$), form N leaves of the tree $\mathbb{T}$. Each node in this tree is assigned a time mark, thus producing a time-oriented tree; the leaves are assigned the time mark $t = 0$. Recall that in this work we focus on the constant-velocity transport and thus use the time and distance interchangeably. Accordingly, one can talk about a distance-oriented tree $\mathbb{T}$ with distance marks being equal to the time marks. The first internal tree node is formed at the time $t_1 = \min_{ij} d_{ij}^0$ by merging two closest points c_{i*}^0 and c_{j*}^0 with $(i^*, j^*) = \text{argmin}_{ij} d_{ij}^0$, where $\text{argmin}_{ij} f(i, j)$ is defined as a pair (i^*, j^*) such that $f(i^*, j^*) = \min_{ij} f(i, j)$. This merging creates a new cluster of two points, with a mass of $m_i + m_j = 2$. Hence, at time t_1, there exist $N - 1$ clusters: $N - 2$ clusters with unit mass and one cluster of mass $m = 2$.

We can now reindex so as to work with clusters c_i^1, $i = 1, \ldots, N - 1$; their total mass is $\sum_{i=1}^{N-1} m_i = N$ and pairwise distances are $d_{ij}^1 \equiv d(c_i^1, c_j^1)$. The second internal node of tree $\mathbb{T}$ is formed at time $t_2 = \min_{ij} d_{ij}^1 > t_1$ by merging the two closest clusters from the set $\{c_i^1\}_{i=1,...,N-1}$. Thus, at time t_2 we have $N-2$ clusters c_i^2 such that their total mass is N and pairwise distances are $d_{ij}^2 \equiv d(c_i^2, c_j^2)$. We continue in the same fashion, so the k-th internal cluster, for $1 \le k \le N - 2$, is formed at time $t_k = \min_{ij} d_{ij}^k > t_{k-1}$, and at that time we have $(N - k)$ clusters c_i^k, $i = 1, \ldots, N - k$ with masses m_i such that $\sum_{i=1}^{N-k} m_i = N$. Finally, at time t_{N-1} we create a single cluster of mass N that combines all points c_i^0; this cluster forms the root of the tree $\mathbb{T}$.

Consider two nodes a and b from the nearest-neighbor tree and let t_a and t_b be their time marks; recall that the tree is time-oriented by the definition of the successive times $t_k = \min_{ij} d_{ij}^k > t_{k-1}$ at which the cluster mergers occur. The *ancestors* of a node are its parent, the parent of its parent, and so on, all the way to the root. Clearly, the time mark for an ancestor is larger than that of a descendant. The *nearest common ancestor* p of nodes a and b is their common ancestor with the minimal time mark t_p.

The distance $u(a, b)$ along the nearest-neighbor tree is defined as the maximum of the values $u(a, p) \equiv t_p - t_a$ and $u(b, p) \equiv t_p - t_b$. This distance satisfies two of the usual distance axioms, symmetry and strict positivity, but the triangle inequality can be replaced by a more stringent one, namely

$$u(a, b) \le \max [u(a, c), u(c, b)],$$

which holds for any three nodes a, b and c. Such a distance function is called an *ultrametric* [*Rammal et al.*, 1986; *Schikhof*, 2007]. Ultrametric spaces have many peculiar properties; for instance, one can rename *any* triplet a, b, c of nodes in such a way that

$$u(a, c) = u(b, c).$$

These unusual properties give ultrametric spaces considerable flexibility in applications, and point sets connected via nearest-neighbor clustering are a representative example of such spaces.

In our river transport problem, the space $\mathbb{S}$ is the set of all river sources. The distance $d(a, b)$ between two sources is defined as the time necessary for the corresponding fluxes injected into these two sources to meet down the river path. If the static river geometry is described by the tree $\mathbb{T}_S$ (and we assume, as previously stated, that fluxes move downstream

continuously with unit speed) the distance $d(a, b)$ between two sources equals the maximal length along the tree to their nearest common parent in $\mathbb{T}_S$. The nearest-neighbor spanning tree of hierarchical-aggregation theory thus becomes what we called so far, in the context of river transport, the dynamic tree $\mathbb{T}_D$.

As previously stated, this dynamic tree differs, in general, from the static tree $\mathbb{T}_S$ and depends not only on the topology of the latter, but also on the actual length of the links. The ultrametric distance $u(a, b)$ equals the time necessary for the above-mentioned fluxes to belong to the same cluster or, equivalently, the time to establish a connected colored path between sources a and b. If the velocities vary in time or space, then the spanning tree $\mathbb{T}_D$ will depend on the specific dynamics of the processes operating on the static tree.

To better understand transport on river networks, we elucidate in the next sections the connection between the statistical properties of $\mathbb{T}_S$ and those of $\mathbb{T}_D$ by using three real river networks.

5. River basin data

We have analyzed three river basins: Upper Noyo, Mendocino County, California, USA (called here Noyo); Tirso, Sardinia, Italy; and a part of the Brenta basin at the confluence with the Grigno river, Trento, Italy (called here Grigno). Information about the physiographic and geologic characteristics of these basins can be found in *Sklar et al.* [2006], *Pinna et al.* [2004], and *Guzzetti et al.* [2005], respectively. In our analysis we used Digital Elevation Models (DEMs) with regularly gridded pixel resolutions of 10 m for the Noyo basin, 30 m for the Grigno basin, and 100 m for the Tirso basin.

In an actual landscape, channels are initiated when the area upstream suffices to create a sustainable source of streamflow and this source imprints a permanent channel on the terrain. Although these channels are typically detectable by field observations, the extraction of the channel initiation points, or "channel heads," from DEMs has been a subject of sustained effort [*e.g., Montgomery and Dietrich,* 1989; *Tarboton et al.,* 1991; *Montgomery and Foufoula-Georgiou,* 1993; *Costa-Cabral and Burges,* 1994; *Giannoni et al.,* 2005; *Hancock and Evans,* 2006].

In typical DEM analysis, channel heads are mapped where the upstream area, or (area)×(typical slope), exceed a given threshold; the parameters of such relationships are field-calibrated. More recently, the availability of high-resolution, 1-m elevation data from LIght Detection and Ranging (LIDAR) has initiated a new generation of methodologies for the automatic detection of channels as terrain "features" [*e.g., Lashermes et al.,* 2007; *Passalacqua et al,* 2009]. Given the available DEM resolution, and the fact that the focus of this study is not the extraction of the most accurate river network from the available DEMs, we adopted a simple criterion for channel initiation as $A_c = 100$ pixels for all three basins. This criterion is certain to miss the smallest first order basins in the Tirso basin but the extracted network, although clipped in its uppermost branches, still has the right topology.

The extracted stream networks for the three river basins (using the steepest gradient D8 algorithm) are shown in Fig. 7. The corresponding dynamic stream networks were then constructed for each basin, assuming a constant unit speed of downstream propagation for the fluxes. We thus analyzed two different kinds of trees, static and dynamic, for each basin.

6. Branching characteristics of river networks

In this section we quantify similarities and differences between the branching topology of static and dynamic trees and demonstrate a phase transition phenomenon in the dynamics of river networks.

6.1. Self-similarity indices

Figure 8 shows the distributions of the number N_r, average magnitude M_r, and the average number C_r of links for branches of order r for the static trees (panels (a,b)) and dynamic trees (panels (c,d)) of the three basins.

Despite the usual small-sample fluctuations, the figures demonstrate a large degree of consistency among the branching indices. All branching statistics considered are closely approximated by the Horton laws. Moreover, these results suggest that the relationship (5) holds in all the cases considered herein.

We observe that the values of the stream ratios for static trees are higher than the corresponding values for dynamic trees. This means that the degree of side-branching (i.e., the proportion of network branches that merge with branches of a higher Horton-Strahler order) is larger for static trees than for dynamic trees.

The only indices that deviate considerably from the Horton laws at higher orders are C_r (the average number of nodes within an order-r branch) for the Noyo basin's static and dynamic trees; this discrepancy warrants further investigation. Apart from this point, we conclude that both types of trees, dynamic and static, can be closely approximated by Tokunaga SSTs; the characteristic indices, however, differ from one type to the other.

6.2. Phase transition in dynamic trees

Does river network connectivity, in terms of elements of the network participating in transport, exhibit a *phase transition*, with time being the order parameter, akin to those found in other systems? Figure 9 shows the fractional magnitudes m_i/N of the branches in the dynamic trees as a function of the distance d traveled by the dye. Recall that this distance can also be interpreted as the time t when the node was created by merging of upstream branches.

In all three panels we observe the following scenario: We start at distance $d = 0$ (or time $t = 0$) with N branches (clusters) of unit magnitude corresponding to the network sources. As distance increases (time evolves), the number of clusters decreases while their magnitudes become larger and exhibit substantial variability. In particular, at small distances the maximal magnitude increases exponentially with distance; this growth is reflected by an approximately linear form of an upper envelope of the points in the figures (envelope not shown). Furthermore, we notice that at short distances (small times) the magnitude distribution is "continuous," *i.e.* it does not have significant gaps. At some critical distance d^* (time t^*), however, the distribution undergoes a marked qualitative change: a prominent maximal cluster appears, such that its magnitude becomes significantly larger than that of the second-largest cluster. Moreover, while the magnitude of the largest cluster keeps growing, the rest of the distribution is fading off and so, after some time, all clusters present at $d = 0$ merge with the largest cluster. Still, at the critical distance d^*, the magnitude of the largest cluster is just about 10% of the total magnitude N of the system, and this is the case for all six panels.

The magnitude distribution of the clusters was analyzed for d varying from 0 to about $2\,d^*$, in both log-log and semilogarithmic scales (not shown). Our analysis strongly suggests that the magnitude distribution at smaller distances has an exponential tail, while at the critical distance d^* it becomes a power law. This observation is illustrated in

Fig. 9, panels (b,d,f), which show the magnitude distribution, in log-log coordinates, at the critical distance d^* and at a shorter distance $d \approx d^*/2$; those distances are indicated by vertical lines in panels (a,c,e). Recall that, in a log-log plot, power-law behavior shows up as a straight line, while exponential behavior becomes a convex curve. This change indicates that a phase transition occurs at the distance d^*.

This phase transition is further illustrated in Fig. 10, which shows three snapshots of the dye propagating down the Noyo basin. The distances traveled by the dye at these snapshots are marked by vertical lines in Fig. 11; the largest distance is chosen to be equal to the critical distance d^* for this basin. The figure shows the number of clusters (dotted line) and the magnitude of the largest cluster for the Noyo dynamic tree (solid line), as a function of downstream propagation distance. One can easily see how unconnected clusters suddenly merge together at the critical distance $d^* \approx 1000$m. Importantly, the value of critical distance is independent of the basin order; hence such a merging happens simultaneously at all the scales (basin orders), constituting a phase transition.

7. Concluding remarks

7.1. Summary and discussion

In this study we have focused on the statistical description of environmental transport on river networks. We have approached the problem by considering downstream transport on such a network as a particular case of nearest-neighbor *hierarchical aggregation*. The so-called *ultrametric* induced by the branching structure of the river network provides the distance function with respect to which the downstream flow gives rise to clusters that decrease in number and increase in size with time (see Figs. 10 and 11).

We have described the static topological structure of a river network by the type of tree structure that goes back to the pioneering studies of *Horton* [1945], *Strahler* [1957], and *Shreve* [1966]; this structure has been referred to as a *static tree*, to distinguish it from the associated *dynamic tree* (Section 3, Figs. 3 and 5). The latter concept helps describe downstream transport along the static tree.

We have studied the statistical properties of both static and dynamic trees using the Horton-Strahler and Tokunaga branching taxonomies. Using the DEM-extracted river networks in three river basins (Noyo, Grigno and Tirso) we have shown that both static and dynamic trees can be well approximated by Tokunaga *self-similar trees (SSTs)*. The Horton-Strahler and Tokunaga parameters of these two types of trees differ significantly, though, for each of the three basins (Section 6.1, Fig. 8). This difference supports the relevance of the dynamic tree concept; its parameter values depict important properties of the envirodynamics on a given river network that are not captured by the conventional, static tree.

An important new result of this study is the phase transition we have found in river network dynamics in Section 6.2: as one fills an empty river network through its sources, or injects a dye at the sources of a water-filled one, the number of clusters of connected nodes decreases and the size of the largest cluster of connected streams forms. During this process, the time-dependent size distribution of the connected clusters changes from an exponential to a power-law function as the critical time approaches (Fig. 9).

This phenomenon, which may seem rather unexpected in the present hydrological setting, can be better understood within the framework of complex networks. This framework has been explored in many natural and socio-economic settings, ranging from the functioning of a cell to the organization of the Internet [*Albert and Barabasi*, 2002; *Dorogovtsev and Mendes*, 2002; *Newman*, 2003].

The mathematical theory of complex networks considers a group of nodes that can be connected with each other according to some problem-specific rules, thus forming a graph. In the simplest case, the node connections are independent of each other and can be specified by the probability p that two randomly chosen nodes are connected. There exists a critical value p_c such that, for $p < p_c$, the network consists of isolated clusters, while a single giant cluster appears as p crosses p_c, and spans the entire network. The same phenomenon is observed under more realistic rules of node connectivity as well. The appearance of the giant cluster is remarkably reminiscent of infinite-cluster formation in percolation theory [*Stauffer and Aharony*, 1994].

Albert and Barabasi [2002] review parallels and differences between complex-network theory and percolation theory. The book by *Newman et al.* [2006] collects the major papers in complex network theory, while *Barrat et al.* [2008] provide an introduction for a readership of physicists, and *Durrett* [2007] gives a rigorous mathematical treatment of the topic.

It readily follows from the analysis of Section 3 that transport on river networks fits rather naturally the complex-network paradigm. Formally, each stream source is represented by a node and two streams are considered to be connected when their respective fluxes join downstream. This is exactly the scheme we used to define a dynamic tree, with the only difference that we have ignored the connections between nodes within already formed clusters. This difference does not affect the process of cluster formation, so the results of the complex-network theory do apply to enviro-dynamics on river networks. From this point of view, the rather sudden formation of the giant cluster and the corresponding transition of the cluster magnitude distribution from exponential to power-law seems rather natural.

There is an important difference, though, between complex networks in general and the dynamic trees considered in this study. Our dynamic trees, unlike general networks, are time-oriented, *i.e.*, their nodes can be ordered in "time" or with respect to a "downstream distance" parameter. The ultrametric distance along such trees satisfies a stronger triangle inequality than ordinary distance (see Section 4.2), and thus induces interesting properties [*e.g.*, *Schikhof*, 2007]. In fact, a set of points in a metric space with a traditional distance d naturally forms an ultrametric tree according to the nearest-neighbor clustering procedure described in Section 4. As shown there, hierarchical aggregation via nearest-neighbor clustering provides a common framework for many apparently different processes (such as billiards, river transport, and percolation) in the setting of ultrametric trees, and thus may provide novel insights into these processes.

In percolation models, the cluster-size distribution at phase transition is given by a power law whose index is a function of the system's dimension alone. In our three river networks, this index differs from one network to another (see Fig. 9, panels (b,d,f)). We notice that in the hierarchical aggregation on dynamic trees, different clustering rules may correspond to different effective "dimensions" of the system. At the same time, it is known that the critical percolation indices are universal for systems in high dimensions [*Hara and Slade*, 1990] and trees are a simple model for infinite-dimensional systems [*Albert and Barabasi*, 2002]. Thus, one expects to see the same values of the critical indices when working with percolation on a tree. From this perspective, the fact that our critical exponents vary from basin to basin still needs to be understood.

7.2. Further work

In this study we have considered only the simplest clustering rules for river streams: two streams belong to the

same cluster if there is a connected path from one stream to another along the river network. This approach is patterned after percolation studies and allows for a straightforward treatment. It may result, however, in a situation when two streams belong to the same cluster despite the fact that the respective fluxes are not mixed yet: think of two short streams that merge with a spatially extended cluster at about the same time. Formulating a physically more appropriate set of clustering rules might yield more realistic results for a wealth of transport problems related to river networks.

So far, we have investigated only dynamic trees that have the same set of sources as the corresponding static tree; doing so is equivalent to injecting a flux through the sources alone. We emphasize at this point that the present study formulates merely a conceptual model, rather than attempting to mimic the realistic dynamics of fluxes in river networks. Indeed, actual precipitation or seepage from groundwater corresponds to activating multiple internal nodes within the network, not only its sources. Moreover, it might happen that a flux of interest is injected exclusively into an internal node, *e.g.*, an industrial pollutant from a plant or nutrient production from a local biotic activity. Such situations can be modeled by considering a dynamic tree whose sources sample the entire river network. More elaborate models along these lines are also left to further study.

The flux-propagation model used in this paper is highly idealized (constant speed) and it only allows for continuous downstream transport, while real fluxes can violate both of these assumptions. For instance, sediments can be routed intermittently, undergoing several periods of intervening storage before arrival at points downstream. In addition, there exist upstream extensions of surface flow into headwater valleys of zero-order. We notice also that the flux velocity may depend on slope or other factors, thus violating our assumption of constant transport velocity. These as well as other extensions of the simple model considered herein can be incorporated, in principle, into our general framework. Doing so certainly constitutes an interesting avenue for future work. It remains, of course, to be seen whether or not any of these potential extensions affect the main conceptual and qualitative conclusions of this study.

To construct a richer theoretical framework for envirodynamics on river networks one may also model the transport along real and synthetic networks by using Boolean delay equations (BDEs) [*Dee and Ghil*, 1984; *Ghil and Mullhaupt*, 1985]. In BDEs, the discrete state variables describe the flux through the river branches; naturally, the rules for updating these variables inherit the child-parent relationship of the stream's static tree. The parent variables are updated based on the values of the children variables, after delays that correspond to the time it takes the flux to propagate from a child to its parent. *Ghil et al.* [2008] recently reviewed BDEs and their applications to climate and earthquake modeling. We expect such models to shed further light on the complex and important problems of transport on river networks.

8. Acknowledgments

Appendix A: Hierarchical aggregation and cluster dynamics: Examples

Among the many instances of the general aggregation scheme of Section 4, we mention here the following three.

Percolation: In the *site percolation* process on an $L \times L$ lattice, the initial $N = L^2$ particles correspond to the sites of the lattice, while clusters correspond to connected patches of occupied sites that are formed during the percolation process [*Albert and Barabasi*, 2002; *Zaliapin et al.*, 2005]. The same scheme can be applied to bond percolation, as well as to percolation on grids in higher dimensions.

Billiards: *Elastic billiard* on a rectangular table can be used to model *gas dynamics* in two dimensions (2-D). Here the initial particles are the N billiard balls (gas molecules) at time $t = 0$. Each of the balls is assigned an initial position and velocity. The clusters at time Δ are formed by balls that have collided during the time interval $[0, \Delta]$ [*Gabrielov et al.*, 2008]. Formally, two balls are called Δ-*neighbors* if they collided during the time interval $[0, \Delta]$. Each connected component of this neighbor relation is called a Δ-*cluster*. Notice that within an arbitrary Δ-cluster each ball has collided with at least one other ball during the time interval $[0, \Delta]$. In other words, a Δ-cluster is a group of balls that have affected each other's dynamics during the time interval of duration Δ. The mass of each cluster is simply the total number of balls within that cluster. Upon many collisions of the balls, the whole system will be composed of clusters of different sizes. As time evolves, the number of clusters will decrease and their mass increase.

The same scheme can be applied to a system of particles that interact according to some potential $U(\mathbf{x})$. *Bogolyubov* [1960] suggested that when the interaction of particles is restricted to the near field, the system can be decomposed into finite clusters so that during some random interval of time, each cluster moves independently of other clusters as a finite-dimensional dynamical system. After this time interval, the system can be decomposed again into other dynamically independent clusters and so on. This type of dynamics is called *cluster dynamics* and *Sinai* [1974] showed analytically that it exists in a one-dimensional (1-D) system of statistical mechanics. Numerical results of *Gabrielov et al.* [2008] describe the presence and various properties of cluster dynamics in a 2-D system of hard balls.

In the metric setup of Section 4.2 for the billiard dynamics, the space $\mathbb{S}$ is the set of N billiard balls and the distance function $d(a, b)$ equals the time before the first collision of the balls a and b. Naturally, this distance depends on the initial positions and velocities of the two balls a and b, but it is also affected by the global billiard dynamics: our two balls may be set to collide at a given time t^* in the absence of other balls, but may be hit by some other ball at time $t < t^*$, thus postponing the collision. The ultrametric distance $u(a, b)$ equals the time before both a and b belong to the same dynamic cluster. It is readily seen that $u(a, b) \leq d(a, b)$ since two balls do not have to collide to be within the same cluster; yet a collision necessarily puts them into the same cluster.

Phylogenetic trees: Probably the best-known application of hierarchical aggregation is in constructing phylogenetic trees that describe the evolutionary relationships

among biological species [*Maher*, 2002]. Here, a node corresponds to a set of species. Two species are connected if they have a direct common ancestor; the link length from a species to its direct ancestor equals the time it took to develop the descendant species from that ancestor.

References

Albert, R. and A.-L. Barabasi (2002), Statistical mechanics of complex networks, *Rev. Mod. Phys., 74*, 47–97.

Barrat, A., M. Barthélemy, and A. Vespignani (2008), *Dynamical Processes on Complex Networks*, Cambridge University Press.

La Barbera, P. and R. Rosso (1987), Fractal geometry of river networks, *EOS Trans. AGU, 68(44)*, 1276.

Benda, L., N. Leroy, D. Miller, T. Dunne, G. Reeves, G. Pess, and M. Pollock (2004a), The network dynamics hypothesis: How channel networks structure river habitat, *Bioscience, 54(5)*, 413.

Benda L., K. Andras, D. Miller, and P. Bigelow (2004b), Confluence effects in rivers: Interactions of basin scale, network geometry, and disturbance regimes, *Water Resour. Res., 40*, W05402, doi:10.1029/2003WR002583.

Bertoin, J. (2006), *Random Fragmentation and Coagulation Processes*, Cambridge University Press.

Bogolyubov, N. N. (1960), *Problems of Dynamic Theory in Statistical Physics,* Oak Ridge, Tenn., Technical Information Service.

Costa-Gabral, M. C. and S. J. Burges (1994), Digital elevation model neworks (DEMON): A model flow over hillslopes for computation of contributing and dispersal areas, *Water Resour. Res., 30*, 1681–1692.

Dee D., and M. Ghil (1984), Boolean difference equations, I: Formulation and dynamic behavior. *SIAM J. Appl. Math, 44*, 111–126.

Dodds, P.S. and D.H. Rothman (2000), Scaling, Universality, and Geomorphology, *Annual Review of Earth and Planetary Sciences*, 28, 571–610, doi:10.1146/annurev.earth.28.1.571.

Dorogovtsev, S. N. and J. F. F. Mendes (2002), Evolution of Networks, *Adv. Phys., 51*, 1079–1187.

Durrett, R. (2007), *Random Graph Dynamics*, Cambridge University Press.

Gabrielov, A., V. Keilis-Borok, Y. Sinai, and I. Zaliapin (2008), Statistical properties of the cluster dynamics of the systems of statistical mechanics, in G. Gallavotti, W. Reiter and J. Yngvason (eds.), *ESI Lecture Notes in Mathematics and Physics: Boltzmann's Legacy*, European Mathematical Society, 203–216.

Ghil, M. and A. P. Mullhaupt (1985), Boolean delay equations. II: Periodic and aperiodic solutions. *J. Stat. Phys., 41,* 125–173.

Ghil, M., I. Zaliapin, and B. Coluzzi (2008), Boolean Delay Equations: A Simple Way of Looking at Complex Systems. *Physica D, 237,* 2967–2986.

Giannoni, F., G. Roth and R. Rudari (2005), A procedure for drainage network identification from geomorphology and its application to the prediction of the hydrologic response, *Adv. Wat. Resource, 28*, 567–581.

Gupta, V. K. and O. Mesa (1988), Runoff generation and hydrologic response via channel network geomorphology — Recent progress and open problems, *J. Hydrol., 102*, 3-28.

Guzzetti, F., C. P. Stark, and P. Salvati (2005), Evaluation of flood and landslide risk to the population of Italy, *Environmental Management, 36(1)*, 15-36.

Hancock, G. R. and K. G. Evans (2006), Channel head location and characteristics using digital elevation models, *Earth Surf. Land. Process, 31*, 809–826.

Hara, T. and G. Slade (1990), Mean-field critical behaviour for percolation in high dimensions. *Commun. Math. Phys., 128*, 333–391.

Horton, R. E. (1945), Erosional development of streams and their drainage basins: Hydrophysical approach to quantitative morphology, *Geol. Soc. Am. Bull., 56*, 275–370.

Jarvis, R. S. and M. J. Woldenberg (eds.) (1984), *River Networks*, Benchmark Papers in Geology, **80**, Hutchinson Ross. Stroudsburg, PA.

Keilis-Borok, V. I. and A. A. Soloviev (eds.) (2003), *Nonlinear Dynamics of the Lithosphere and Earthquake Prediction*, Springer-Verlag, Heidelberg, 337 pp.

Kiffney, P.M., C.M. Greene, J.E. Hall, and J.R. Davies (2006), Tributary streams create spatial discontinuities in habitat, biological productivity, and diversity in mainstream rivers, *Can. J. Fish. Aquat. Sci., 63*, 2518–2530, doi:10.1139/F06-138.

Kirkby, M. J. (1976), Tests of the random network model, and its application to basin hydrology, *Earth Surf. Processes, 1*, 197–212.

Lashermes, B., E. Foufoula-Georgiou, and W. E. Dietrich (2007), Channel network extraction from high resolution topography using wavelets, *Geophys. Res. Lett., 34*, L23S04, doi:10.1029/2007GL031140.

Leyvraz, F. (2003), Scaling theory and exactly solved models in the kinetics of irreversible aggregation, *Phys. Rep., 383(2-3)*, 95–212.

Lowe, W.H., G.E. Likens, and B.J. Cosentino (2006), Self-organization in streams: the relationship between movement behavior and body condition in a headwater salamander, *Freshwater Biology, 51*, 2052-2062, doi:10.1111/j.1365-2427.2006.01635.x.

Maher, B. A. (2002), Uprooting the Tree of Life, *The Scientist, 16*: 18.

McConnell, M., and V. Gupta (2008), A proof of the Horton law of stream numbers for the Tokunaga model of river networks. *Fractals, 16(3)*, 227–233.

Montgomery D. R. and W. E. Dietrich (1989), Source areas, drainage density, and channel initiation, *Water Resour. Res., 25*, 1907–1918.

Montgomery D. R. and E. Foufoula-Georgiou (1993), Channel network source representation using digital elevation models, *Water Resour. Res., 29*, 3925–3934.

Molchan, G., O. Dmitrieva, I. Rotwain and J. Dewey (1990), Statistical analysis of the results of earthquake prediction, based on bursts of aftershocks, *Phys. Earth Planet. Inter., 61*, 128–139.

Newman, M. E. J. (2003), The structure and function of complex networks. *SIAM Rev., 45*, 167–256.

Newman, M. E. J., A.-L. Barabasi, and D. J. Watts (2006), *The Structure and Dynamics of Networks*, Princeton University Press.

Newman, W. I., D. L. Turcotte, and A. M. Gabrielov (1997), Fractal trees with side branching, *Fractals, 5*, 603–614.

Passalacqua, P., T. Tang, E. Foufoula-Georgiou, G. Sapiro, and W. E. Dietrich (2009) River network extraction from high-resolution topography: Nonlinear diffusion and geodesic paths, *Water Resour. Res.*, in review.

Peckham, S. (1995), New results for self-similar trees with applications to river networks, *Water Resour. Res., 31(4)*, 1023–1029.

Peckham, S. and V. Gupta (1999), A reformulation of Horton's laws for large river networks in terms of statistical self-similarity, *Water Resour. Res., 35(9)*, 2763–2777.

Pinna, M., A. Fonnesu, F. Sangiorgio, and A. Basset (2004), Influence of summer drought on spatial patterns of resource availability and detritus processing in Mediterranean stream sub-basins (Sardinia, Italy), *Internat. Rev. Hydrobiol., 89(5-6)*, 484–499.

Power, M. E. and W. E. Dietrich (2002), Food webs in river networks, *Ecological Research, 17*, 451–471.

Rammal, R., G. Toulouse, and M. A. Virasoro (1986) Ultrametricity for physicists, *Rev. Mod. Phys., 58*, 765–788.

Rice, S. and M. Church (1998), Grain size along two gravel-bed rivers: Statistical variation, spatial pattern and sediment links, *Earth Surf. Processes Landforms, 23*, 345–363.

Rice, S.P., R.I. Ferguson, and T.B. Hoey (2006), Tributary control of physical heterogeneity and biological diversity at river confluences, *Can. J. Fish. Aquat. Sci., 63*, 2553-2556, doi:10.1139/F06-145.

Rodriguez-Iturbe, I. and A. Rinaldo (1997), *Fractal River Networks: Chance and Self-Organization*, Cambridge University Press, New York.

Rodriguez-Iturbe, I., E. Ijjasz-Vasquez, R. L. Bras, and D. G. Tarboton (1992), Power law distributions of mass and energy in river basins, *Water Resour. Res., 28(4)*, 1089–1093.

Rotwain, I., V. Keilis-Borok, and L. Botvina (1997), Premonitory transformation of steel fracturing and seismicity, *Phys. Earth Planet. Inter., 101*, 61–71.

Schikhof, W. H. (2007), *Ultrametric Calculus: An Introduction to P-Adic Analysis*, Cambridge University Press, New York, 318 pp.

Shreve, R. L. (1966), Statistical law of stream numbers. *J. Geol.*, *74*, 17–37.

Sklar L. S., W. E. Dietrich, E. Foufoula-Georgiou, B. Lashermes, D. Bellugi (2006), Do gravel bed river size distributions record channel network structure?, *Water Resour. Res., 42*, W06D18, doi:10.1029/2006WR005035.

Sinai, Ya. G. (1973), Construction of dynamics in infinite systems of particles, *Theor. Math. Phys.*, *12*, 487.

Sinai, Ya. G. (1974), Construction of cluster dynamics for dynamical systems of statistical mechanics, *Proc. Moscow State Univ.*, *1*, 152–158 (In Russian); English transl. *Moscow Univ. Math. Bull.* (1974), *29*, 124-129.

Sposito, G. (ed.) (1998), *Scale Dependence and Scale Invariance in Hydrology*, Cambridge Univ. Press, New York.

Stauffer, D. and A. Aharony (1994), *Introduction to Percolation Theory,* 2-nd ed., Taylor & Francis.

Strahler, A. N. (1957), Quantitative analysis of watershed geomorphology, *Trans. Am. Geophys. Un.*, *38*, 913–920.

Stewart-Koster, B., M.J. Kennard, B.D. Harch, F. Sheldon, A.H. Arthington, and B.J. Pusey (2007), Partitioning the variation in stream fish assemblages within a spatio-temporal hierarchy, *Marine and Freshwater Res., 58*, 675–686.

Surkan, A. J. (1969), Synthetic Hydrographs: Effects of Network Geometry, *Water Resour. Res., 5*, 112–128.

Tarboton D. R., R. L. Bras, and I. Rodriguez-Iturbe (1991), On the extraction of channel networks from digital elevation data, *Hydrologic Processes, 5*, 81–100.

Tokunaga, E. (1978), Consideration on the composition of drainage networks and their evolution, *Geographical Rep. Tokyo Metro. Univ.*, *13*, 1–27.

Veitzer, S. and V. K. Gupta (2000), Random self-similar river networks and derivations of generalized Horton laws in terms of statistical simple scaling, *Water Resour. Res., 36*, 1033–1048.

Wakeley, J. (2009), *Coalescent Theory*, Roberts and Company Publishers.

Wohl, E., D. Cooper, L. Poff, F. Rahel, D. Staley, and D. Winters (2007), Assessment of stream ecosystem function and sensitivity in the Bighorn National Forest, *Environ. Manage., 40*, 282–302, doi:10.1007/s00267-006-0168-z.

Zaliapin, I. (2009), Horton laws in self-similar trees. Manuscript.

Zaliapin, I., H. Wong, and A. Gabrielov (2005), Inverse cascade in percolation model: Hierarchical description of time-dependent scaling, *Phys. Rev. E, 71*, No. 066118.

I. Zaliapin, Department of Mathematics and Statistics, University of Nevada, Reno, USA. (zal@unr.edu)

E. Foufoula-Georgiou, St. Anthony Falls Laboratory and National Center for Earth-surface Dynamics, Department of Civil Engineering, University of Minnesota, Minneapolis 55414, USA. (efi@umn.edu)

M. Ghil, Geosciences Department and Laboratoire de Météorologie Dynamique (CNRS and IPSL), Ecole Normale Supérieure, Paris, FRANCE, and Department of Atmospheric and Oceanic Sciences and Institute of Geophysics and Planetary Physics, University of California, Los Angeles, USA. (ghil@atmos.ucla.edu)

(a) River network   (b) Corresponding tree
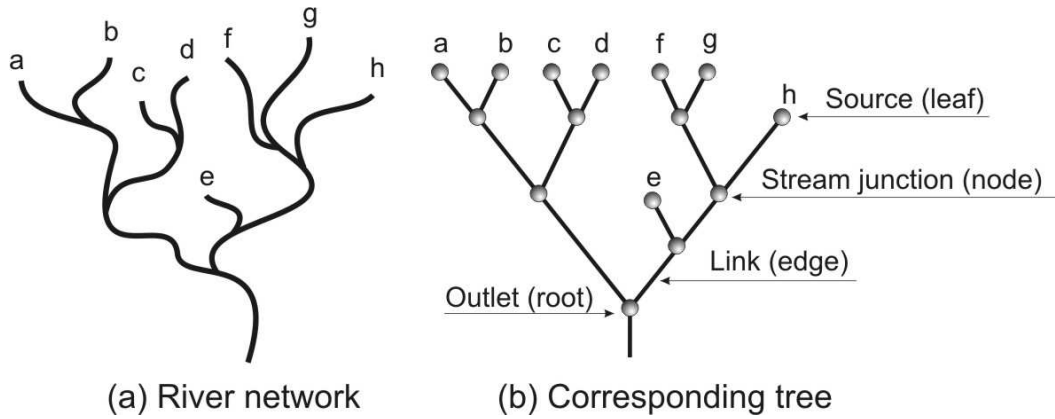
Figure 1. Tree representation of a river network: (a) hypothetical river network; and (b) its representation by a binary tree. The network sources and the respective tree leaves are marked by the same letters in both panels. The figure also illustrates the terminology used in our river transport study.


(a) Horton-Strahler orders   (b)Tokunaga indices
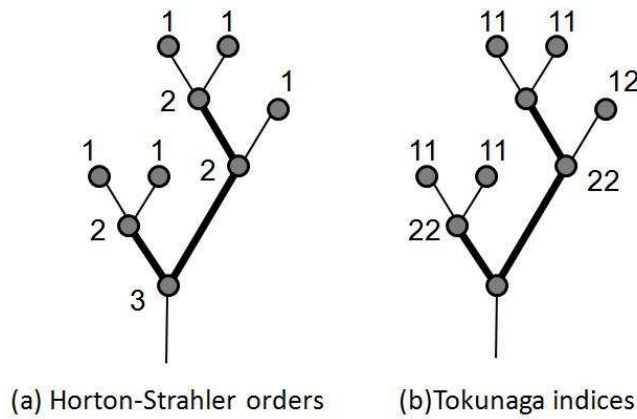
Figure 2. Example of (a) Horton-Strahler ordering, and of (b) Tokunaga indexing of a *static* tree $\mathbb{T}_S$. Two order-2 branches are depicted by heavy lines in both panels. The Horton-Strahler orders refer, interchangeably, to the stream junctions or to the immediate downstream links. The Tokunaga indices refer to entire branches, and not to individual links; these indices are shown next to the last downstream junction on each branch.
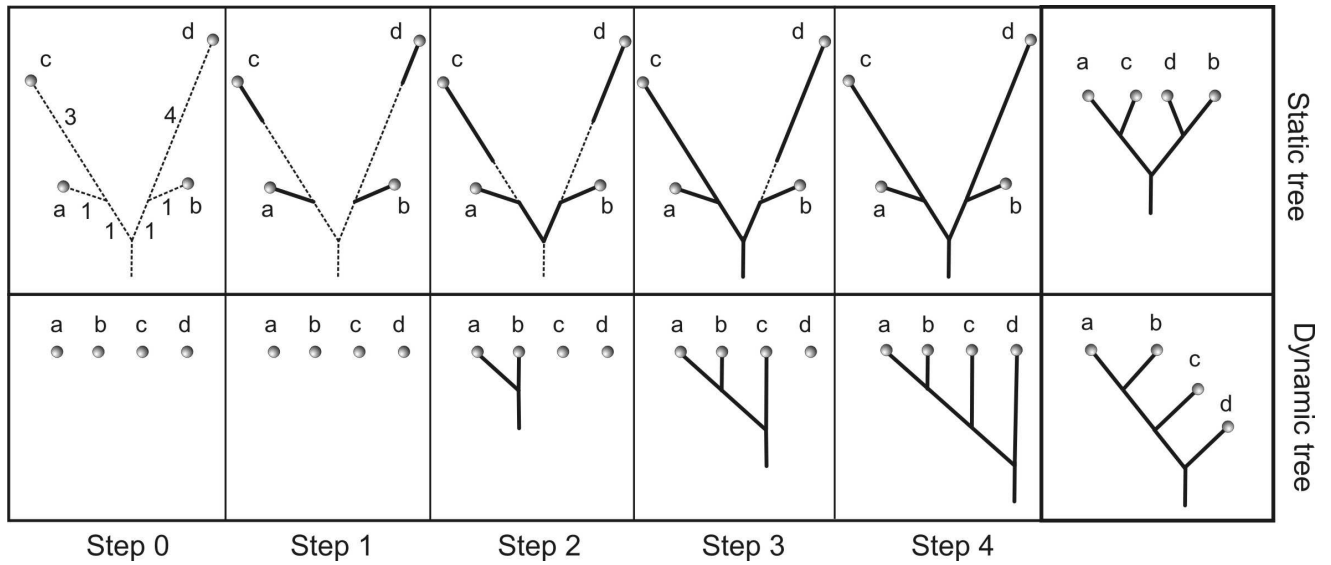
Figure 3. Constructing a *dynamic* tree $\mathbb{T}_D$. The initial static tree $\mathbb{T}_S$ and the final dynamic tree $\mathbb{T}_D$ are shown in the rightmost pair of panels. The dynamic tree reflects the propagation of a flux from the sources to the outlet of the static tree, at a constant velocity. The top row of panels shows the static tree at different steps of this process; for visual convenience we explicitly show the static tree's link lengths. The bottom row shows the corresponding phases of the dynamic tree. The top leftmost panel indicates the lengths of the links in the static tree; each step in the figure takes one time unit, that is the flux propagates one unit of length downstream. See Section 3.1 for details.
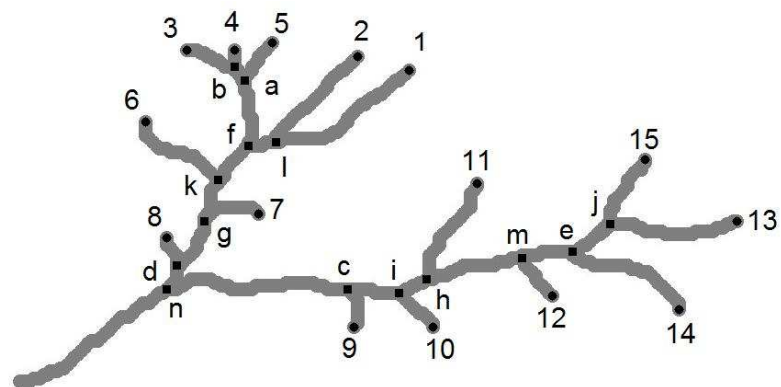
Figure 4. Stream network for an order-3 subbasin of the Noyo river, Mendocino County, California. The location of this subbasin is shown in Fig. 7(a); sources are marked by numbers (1 to 15), and stream merging points by letters (*a* to *n*). The same marks are used in Fig. 5 below, which shows both the static and the dynamic tree for this subbasin.
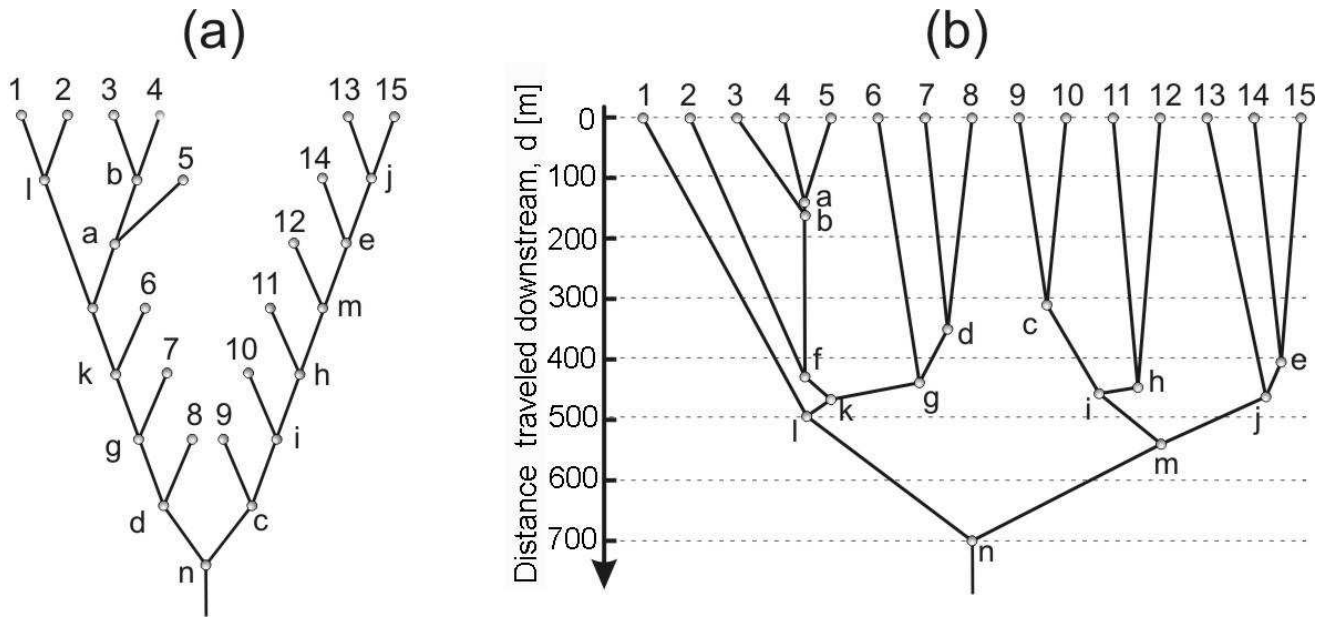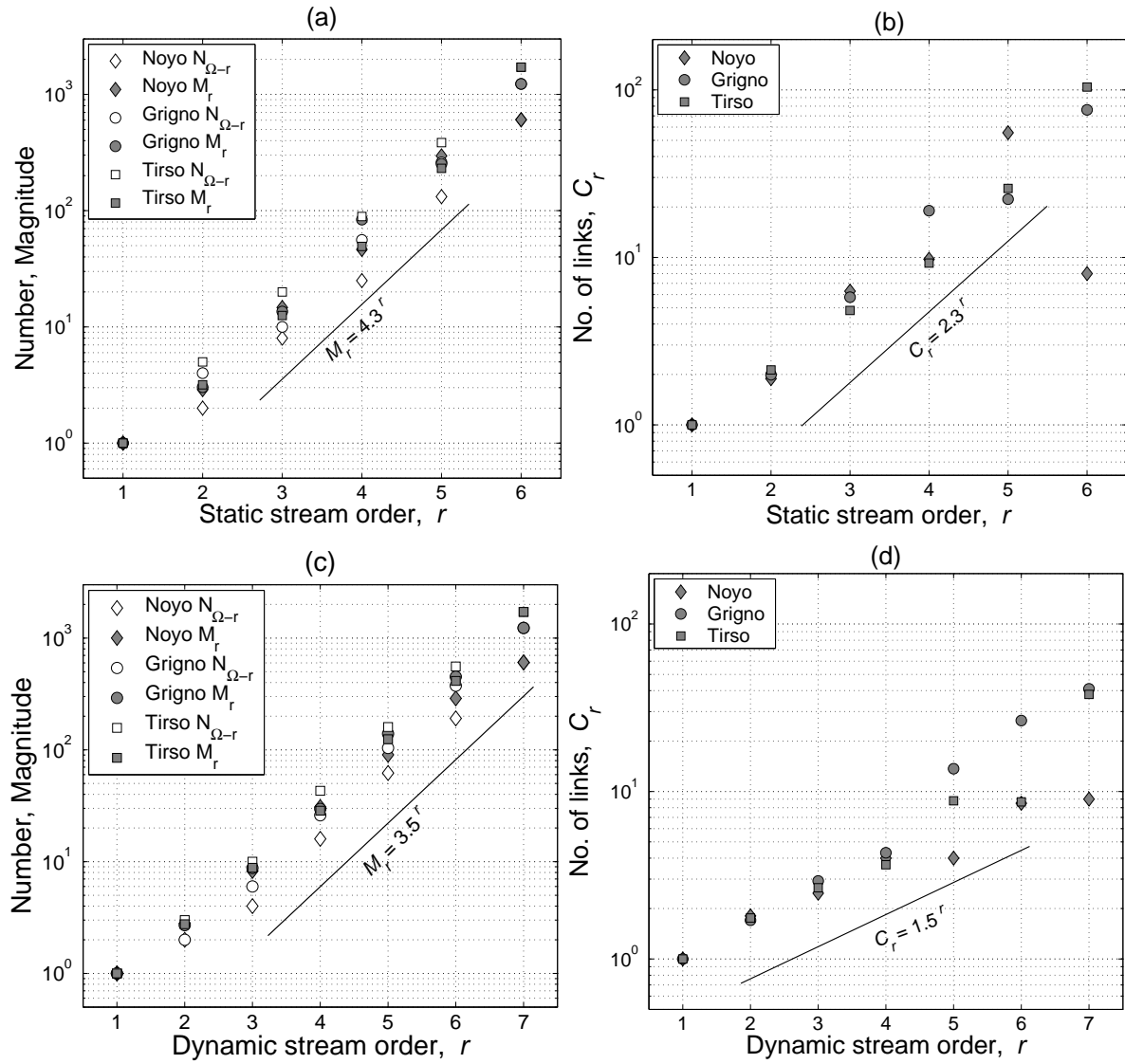
Figure 5. The static and the dynamic tree for the Noyo subbasin of Fig. 4. (a) Static tree $\mathbb{T}_S$, and (b) dynamic tree $\mathbb{T}_D$. Letter and number markings are the same as in Fig. 4.
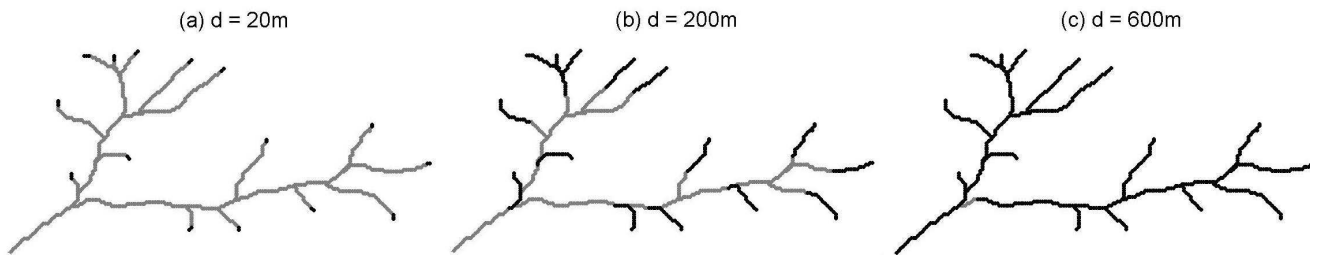
Figure 6. Three snapshots of the evolution of the dynamic tree (heavy solid lines) on the static tree (light solid lines) for the stream network of Fig. 4.

(a) Noyo

(b) Grigno

(c) Tirso
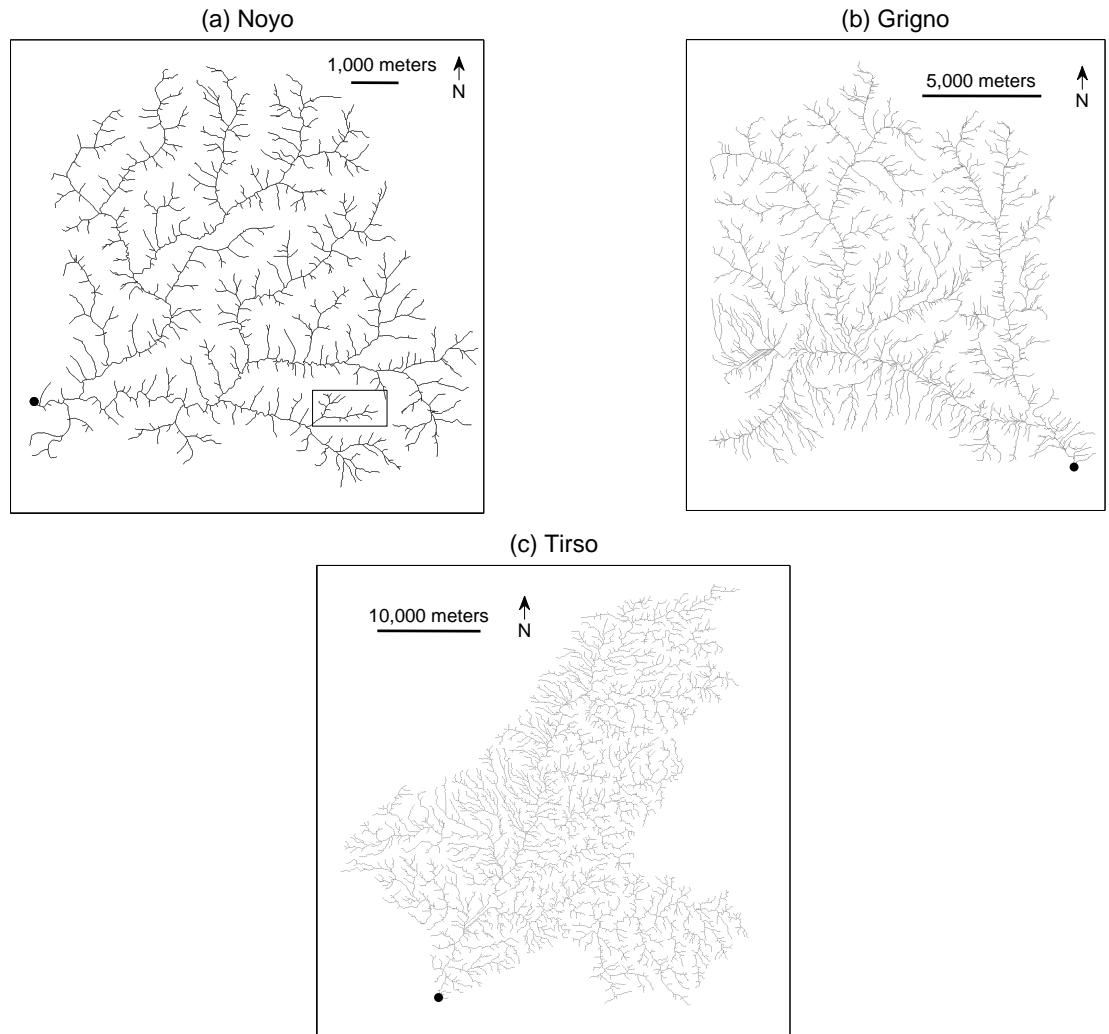
Figure 7. Stream networks of the three basins analyzed in this study, shown as static trees; outlets are marked by black dots. (a) Upper Noyo basin, Mendocino County, California, USA; the outlet is located at $39°26'$ N, $123°45'$ W, and the order-3 subbasin of Figs. 4–6 is outlined by a small, light rectangle in the panel's lower-right (*i.e.*, southeastern) corner. (b) A part of the Brenta basin, at the confluence with the Grigno river (called here Grigno basin), Trento, Italy; the outlet is located at $40°00'04.96''$ N, $8°49'59.26''$ E. (c) Tirso, Sardinia, Italy; the outlet is located at $46°00'28.40''$ N, $11°38'21.55''$ E. See Section 5 for details of channel initiation.

Figure 8. Branching statistics for the stream trees of the Noyo, Grigno, and Tirso basins, shown in Fig. 7. (a,c) Number N_r and average magnitude M_r for (a) the three static, and (c) the three dynamic trees; and (b,d) average number C_r of links within a branch for (b) static and (d) dynamic trees.
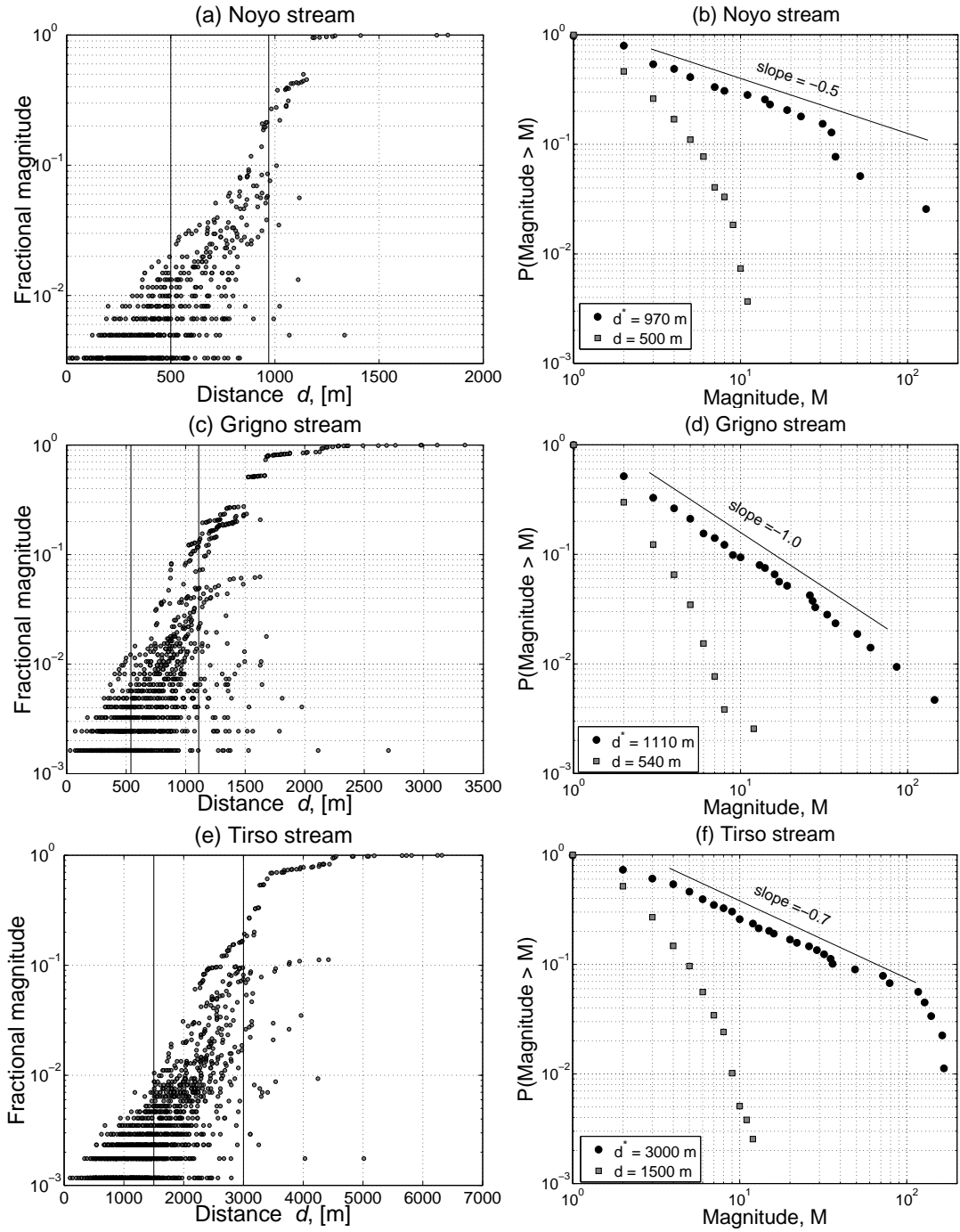
Figure 9. Phase transition in river network dynamics. (a,c,e) Fractional branch magnitudes m_i/N as a function of the distance d_i traveled by the dye at the instant of branch creation. (b,d,f) Distribution of branch magnitudes m_i at the critical distance d^* (circles) and at an earlier time, given by d (squares), for the dynamic trees of the three basins. Each of these panels shows two distributions, at distances d^* and $d < d^*$, respectively; the corresponding distances are depicted by vertical lines in panels (a,c,e). The downward deviations from pure power laws are due to the finite-size effect. (a,b) Noyo stream; (c,d) Grigno stream; (e,f) Tirso stream.
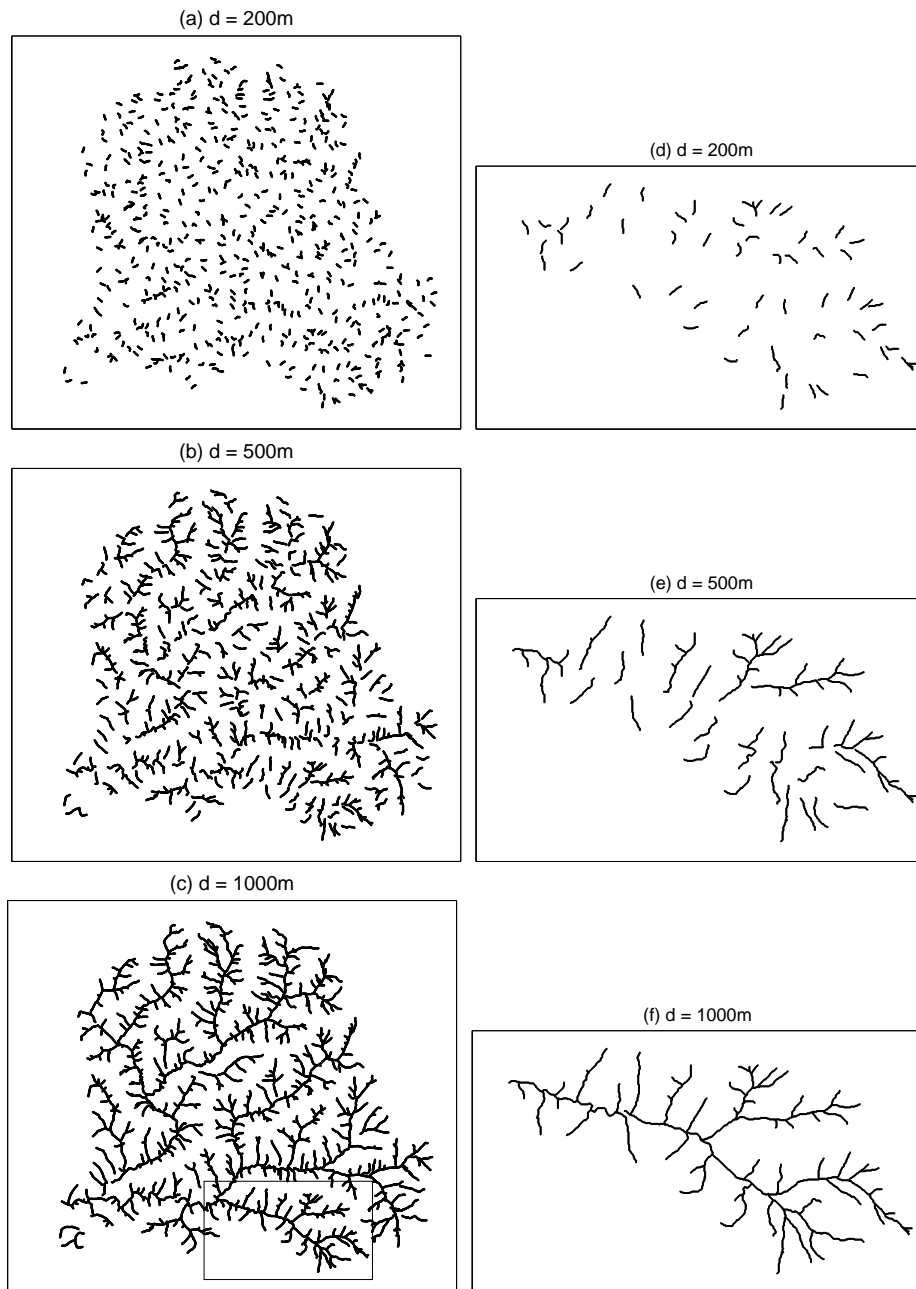
Figure 10. Transport down the Noyo stream network. Three snapshots of flux propagation from the stream sources to the outlet, at (a,d) $d = 200$ m; (b,e) $d = 500$ m; and (c,f) $d = 1000$ m. Panels (a)–(c) show the entire Noyo basin, while panels (d)–(f) zoom onto an order-4 subbasin located in the basin's southeastern part. This order-4 subbasin encompasses the order-3 subbasin shown in Figs. 4–6; its location is depicted by a light rectangle in panel (c). See also Fig. 11.
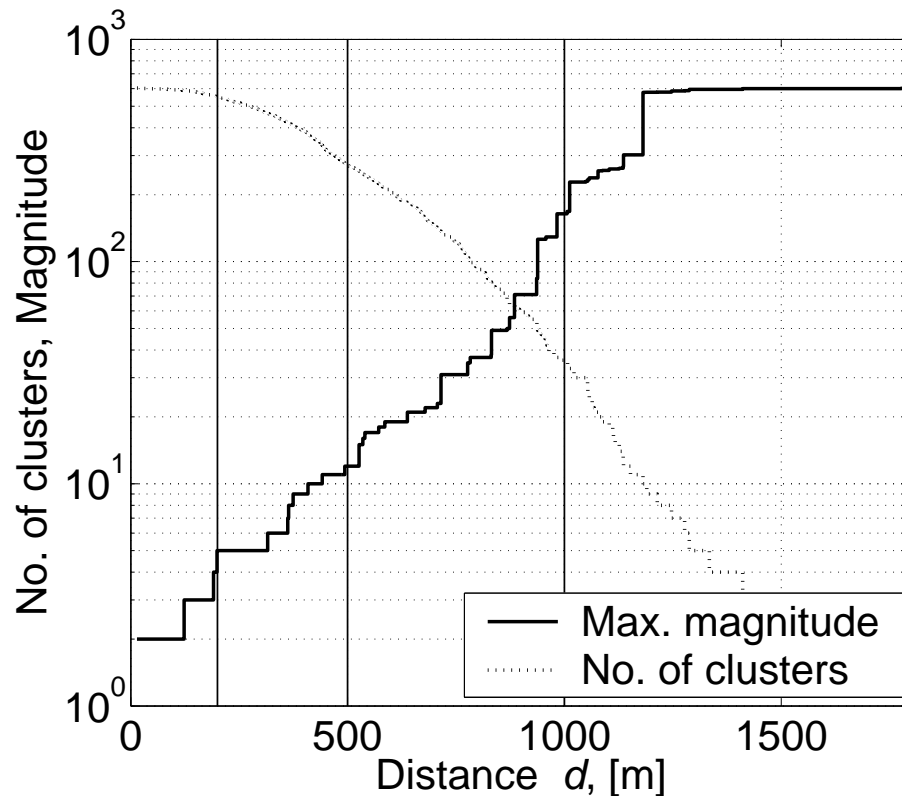
Figure 11. Cluster evolution for the Noyo basin downstream flux transport: number of clusters (dotted line) and largest-cluster size (heavy solid line). Light vertical lines correspond to the three snapshots in Fig. 10.

A non-local theory of sediment transport on hillslopes

E. Foufoula-Georgiou[1], V. Ganti[1], and W.E. Dietrich[2]

[1] St. Anthony Falls Laboratory and National Center for Earth-surface Dynamics, Department of Civil Engineering, University of Minnesota, 2 Third avenue SE, Minneapolis 55414, USA.
[2] Department of Earth and Planetary Science, University of California, Berkeley, CA 94720, USA.

ABSTRACT

Hillslopes are typically shaped by varied processes which have a wide range of event-based downslope transport distances, some of the order of the hillslope length itself. We hypothesize that this can lead to a heavy-tailed distribution of displacement lengths for sediment particles. Here, we propose that such a behavior calls for a non-local computation of the sediment flux, where the sediment flux at a point is not strictly a function (linear or nonlinear) of the gradient at that point only but is an integral flux taking into account the upslope topography (convolution Fickian flux). We encapsulate this non-local behavior in a simple fractional diffusive model which involves fractional derivatives, with the order of differentiation ($1 < \alpha \leq 2$) dictating the degree of non-locality ($\alpha = 2$ corresponds to linear diffusion and strictly local dependence on slope). The model predicts an equilibrium hillslope profile which is parabolic close to the ridgetop and transits, at a short downslope distance, to a power law with an exponent equal to the parameter α of the fractional transport model. Hillslope profiles reported in previously studied locations support this prediction. Furthermore, we show that the non-local transport model gives rise to a nonlinear dependency on local slope, and that variable upslope topography leads to widely varying rates of sediment flux for a given local hillslope gradient. Both of these results are consistent with available field data and suggest that non-linearity in hillslope flux relationships may arise in part from non-local transport effects in which displacement lengths increase with hillslope gradient. The proposed hypothesis of non-local transport implies that field studies and models of sediment fluxes should consider the size and displacement lengths of disturbance events that mobilize hillslope colluvium.

1. Introduction

In absence of overland flow-driven or wind-driven transport, the movement of soil on landscapes requires some kind of disturbance (Figure 1). This disturbance arises in many ways—leading to a wide range of length scales of displacement. In clay-rich soils mantling sloping landscapes, periodic wetting of the ground may cause swelling and downslope flow, but even as the soils remain wet, progressively increasing grain resistance may halt motion. Drying and cracking then resets the contacts and allows another period of flow in the next wet season [*Fleming and Johnson*, 1975]. This cycle operates over some length scale of displacement. Simple wetting expansion and drying collapse through a season can incrementally shift near surface soils short distances downslope [e.g., *Kirkby*, 1967]. Seasonal cycles of movement by ice-driven processes shift soils and during spring melt can give way as continuously moving solifluction lobes which may carry soil a considerable distance even on gentle slopes [e.g., *Washburn*, 1973]. Biota work the soil at a wide range of scales, leading to dilation and displacement downslope. Insects and worms may cause minor local displacement but through their persistent and pervasive activity cause significant movement [e.g., *Darwin*, 1881]. Burrowing animals can make an extensive network of tunnels and push piles of dirt meters downslope. The collapse of large trees may rotate and expose their root system and displace clumps of soil meters downslope [e.g. *Norman et al.*, 1995; *Gabet et al.*, 2003]. The exposed, locally-steep, tree throw mound and the smaller annual burrow mounds are sites of accelerated rain splash, raveling and fine scale biotic disturbance. In effect, the biotic roughening of the ground surface by the local mound formation leads to accelerated soil movement. On sufficiently steep granular soils, fire may suddenly remove particles stored behind fallen woody debris and unleash particles to ravel downslope [e.g., *Roering and Gerber*, 2005], sometimes tens of meters. Shallow landslides may also initiate, mobilize, and redeposit on hillslopes. Soil movement, then, arises through the sum of stochastic processes, influenced by seasonal and biotic cycles, the integral of which is a net flux of soil which tends to increase with increasing hillslope gradient. The individual particle step lengths resulting from disturbances will vary greatly.

On gentle hillslopes there is field evidence [e.g., *McKean et al.*, 1993] that the mean soil transport varies linearly with local gradient. On steeper slopes, however, theory and limited observations suggest that transport increases non-linearly with slope [e.g., *Roering et al.*, 1999]. Increasing field and theoretical evidence indicates that flux also depends on active transport depth [*Heimsath, et al.*, 1999; *Roering*, 2008, *Furbish et al.*, in this volume]. In particular, *Furbish et al.* [in this volume] show that a diffusivity-like coefficient which takes into account the local slope-depth product produces a sediment flux which varies linearly with local gradient. Both linear and non-linear flux laws assume that transport depends on some

"local" slope, although we lack theory for what sets the length scale over which that slope should be determined. The disturbance by biota creates an irregular ground surface, with locally steep piles of loose soil that diffuse downslope across the mean slope (Figure 1). Hence, the slope at any point may not represent the actively contributing slope-driving processes, and cannot account for travel distances resulting from disturbances. If we could monitor every particle on a hillslope where these disturbance-driven processes (often placed together under the term "creep") occur, it is possible that long transport events occur with a finite, non-vanishing, non-exponentially decaying probability such that the pdf of transport distances is heavy-tailed [e.g., *Tucker and Bradley,* 2009 this issue]. This conception of soil transport may not be well represented by a transport expression that relates flux to a "local" slope. Moreover, the possibility of heavy-tailed particle travel histories makes selecting a meaningful mean slope for the application of such local laws problematic. To date, empirical fitting procedures (reducing variance by increasing the length scale of averaging while trying to maintain local profile curvature) have been used for the estimation of the mean slope; common methods include polynomial fitting and Gaussian filtering (e.g., *Roering et al*., 1999; *Lashermes et al*., 2007)

Here we propose an alternative formulation of sediment transport on hillslopes which relies on the notion of non-local computation of sediment flux, reflecting the fact that mass flux at a point on the hillslope is being influenced by disturbances well upslope and not simply linked to local slope (and soil depth). Our analysis may also explain the variance in flux rate for a given local slope observed in some studies. Our theory, although not derived from physical considerations (e.g. involving balances of forces and resistances), presents a general mathematical framework within which the upslope influences to the sediment flux at a given point can be cast into a continuum constitutive law for sediment transport. Specifically, we propose a non-local formulation of transport laws which relies on an integral (non-Fickian) flux computation which explicitly takes into account the upslope topography from any point of interest. The proposed non-local transport model includes linear-diffusive transport as a special case.

The paper is structured as follows. In section 2, we formulate the non-local constitutive law for sediment transport on hillslopes and in section 3 we derive its steady-state equilibrium profile under appropriate boundary conditions. In Section 4 we interpret observed hillslope profiles in the Oregon Coast Range, in the Appalachians of Maryland and Virginia, and east of San Francisco (California) within the non-local transport formulation. In section 5 we compare the linear, non-linear and non-local transport models in several ways. The most important result is that the linear non-local model gives rise to a non-linear relationship between sediment flux and local slope, akin to that observed on steep slopes. In section 6 we

demonstrate that applying the non-local flux model to an ensemble of hillslope profiles produces significant variability of sediment flux for a given value of local slope as a result of variations in upslope topography. In section 7, we discuss the relationship between the shape of the probability density function of the sediment displacement lengths (which dictate the microscopic behavior of the transport process but which are typically not measured) and the parameter α of the non-local transport model (which describes the macroscopic properties of the transport). In section 8 we present some preliminary thoughts as to the ability of the non-local transport formulations to circumvent the scale-dependence of sediment flux computed using local, non-linear models. We conclude that our model shows the possibility that non-local sediment transport processes may be important on hillslopes and warrant more consideration both in field studies and theoretically. Our model anticipates more process-based considerations that would account mechanistically for biotic disturbance and it suggests that models for transport and weathering of colluvial soils and geochronological analysis of particles on steep hillslopes should consider the possible effects of non-local transport.

2. A non-local constitutive law for hillslope sediment transport: Convolution Fickian flux

The simplest sediment flux law, proposed by *Culling* [1960] in analogy to Fick's law of diffusion, expresses sediment flux as proportional to the topographic gradient:

$$q_s(x) = -K\nabla h(x) \tag{1}$$

where $q_s(x)$ is sediment flux (volume per unit time per unit width: $L^3/L/T$) at location x (where x is distance from the ridgetop), K is the diffusivity coefficient (L^2/T) and $h(x)$ is the surface elevation with respect to a datum. It is easy to show (e.g. *Howard*, 1994) that substituting (1) in the continuity (Exner) equation:

$$\rho_r \frac{\partial h}{\partial t} = \rho_r U - \rho_s \nabla \cdot q_s \tag{2}$$

where ρ_s and ρ_r are the bulk densities of sediment and rock respectively and U is the rock uplift rate, results in the linear diffusion equation:

$$\frac{\partial h}{\partial t} = U + K\nabla^2 h \tag{3}$$

where we have assumed for simplicity that the bulk densities of rock and sediment are the same (which is almost never the case) and have ignored chemical erosion. (Note that equation (3) can also be derived using a moving coordinate system of erosion driven by diffusive transport in which the uplift term enters as a lower boundary condition.) If the rate of surface erosion is approximately balanced by the rock uplift, i.e., dynamic equilibrium [*Gilbert*, 1909; *Hack*, 1960], then $\partial h / \partial t \approx 0$ and the

2

steady-state 1D case can be written as:

$$\frac{\partial h}{\partial t} = 0 \Leftrightarrow \frac{d^2 h}{dx^2} = -\frac{U}{K} \qquad (4)$$

Integrating twice and imposing the boundary conditions:

$$h(0) = H_{top} = \frac{U}{2K}L^2$$

$$\left.\frac{dh}{dx}\right|_{x=0} = 0 \qquad (5)$$

such that $h(L) = 0$ (river edge), the solution is given by:

$$h(x) = H_{top} - \frac{U}{2K}x^2 \qquad (6)$$

for $0 \leq x \leq L$ [e.g. *Koons*, 1989]. Furthermore, the properties of the equilibrium hillslope profiles predicted by linear diffusion are: (a) linear increase of local slope with downslope distance, and (b) constant curvature along the hillslope profile.

The underlying assumption of a classical diffusion equation is that the step lengths of sediment particles, defined as the distances traveled by the particles once entrained until they are deposited again on the surface, have a thin-tailed (e.g., exponential or Gaussian) distribution [e.g., *Ganti et al., Schumer et al.,* in this volume]. However, for the reasons discussed in the introduction, the distribution of step lengths of sediment particles may be heavy-tailed, i.e., they have a small but significant chance of traveling a large distance downslope. In such cases, the sediment flux at a point x has a significant contribution from a large upslope distance and thus a local computation of flux, such as that of equ (1), is no longer appropriate. Recently, a particle-based model for sediment transport on hillslopes was developed based on a plausible set of rules capturing disturbance-driven transport processes and it was shown that a heavy-tailed step length distribution can emerge due to the interactions between these disturbances and microtopography [*Tucker and Bradley,* in this volume]. Here, we develop a continuum constitutive model for such a behavior. Specifically, we propose a notion of non-local sediment flux which takes into account the heavy-tails in step lengths of sediment particles by expressing the sediment flux at a given point as a weighted average of the upslope topographic attributes:

$$q_s^*(x) = -K^* \int_0^x g(l)\nabla h(x-l)dl \qquad (7)$$

where $q_s^*(x)$ is sediment flux (volume per unit time per unit width: $L^3/L/T$) at location x (where x is distance from the ridgetop), K^* is the diffusivity coefficient, $h(x)$ is the topographic elevation at location x, and $g(l)$ is a kernel performing a weighted average of local gradients upslope of the point of interest x as they contribute to the sediment flux at the point x (Figure 1) . This is a special case of the more general convolution Fickian flux laws [*Cushman*, 1991, 1997]. It has been shown [*Cushman and Ginn*, 2000] that when the weighting function $g(l)$ has no characteristic length scale, i.e., when $g(l)$ decays as a power law with the lag l, $g(l) \sim l^{2-\alpha}$, (5) takes the form of a fractional derivative:

$$q_s^*(x) = -K^* \nabla^{\alpha-1}h(x) \qquad (8)$$

where $\alpha \in (1,2]$. Substituting (8) in the continuity equation (2) and making the assumption that bulk densities of rock and sediment are equal, leads to a fractional diffusion equation:

$$\frac{\partial h}{\partial t} = U + K^* \nabla^\alpha h \qquad (9)$$

The order of differentiation, α, directly relates to the heaviness of the distribution of step lengths [*Meerschaert et al.*, 1999, 2001; *Schumer et al.,* 2001, *Schumer et al.,* in this volume] and $1 < \alpha < 2$ implies a distribution of step lengths with a finite population mean but infinite population variance (sample variance that diverges unstably as the number of samples increases) [*Lamperti,* 1962], resulting in an accelerated diffusion (super-diffusion). It is noted that for $\alpha = 2$, (8) becomes the standard Fickian flux (1), and (9) collapses to the linear diffusion equation (3).

The concept of non-local transport, implemented via fractional derivatives or Continuous Time Randon Walk (CTRW) models, has been extensively used in other fields of study, such as subsurface transport [e.g., *Benson et al.*, 2000a; *Berkowitz et al.*, 2002], transport of pollutants in rivers [*Deng et al.*, 2005, 2006], hydrodynamics [e.g., *Metzler and Compte*, 2002], statistical mechanics [e.g., *Bouchaud and Georges*, 1990; *Pekalski and Sznajd-Weron*, 1999; *Sclesinger et al.*, 1995], molecular biology [e.g., *Campos et al.*, 2005] and turbulence [e.g., *Biler et al.*, 1998; *Woyczynski*, 1998]. Recently, it has been used in geomorphology to encapsulate the non-locality of bed sediment transport along bedrock channels [*Stark et al.*, 2009] and to model the anomalous diffusion of tracer particles in gravel streams and sand- bed rivers [*Ganti et al.* 2009; *Bradley et al.,* 2009; in this volume]. A review of the application of partial fractional differential equations to the transport of solutes and sediment can be found in *Schumer et al.* [in this volume].

3. Equilibrium hillslope profiles for non-local transport

In order to derive the equilibrium hillslope profile for the fractional diffusion equation (9) we note that under dynamic equilibrium, the steady state 1D equation can be written as:

$$\frac{\partial h}{\partial t} = 0 \Leftrightarrow \frac{d^\alpha h}{dx^\alpha} = -\frac{U}{K^*} \qquad (10)$$

The two most commonly used definitions of a fractional derivative are the Riemann-Liouville and the Caputo forms [*Miller and Ross*, 1993]. These differ from each

3

other in that the Riemann-Liouville definition expresses the fractional derivative as an integer order differential of a fractional integral (equation 11a), whereas the Caputo definition expresses the fractional derivative as a fractional integral of an integer order derivative (equation 11b):

$$\frac{d^\alpha h}{dx^\alpha} = \frac{d^n}{dx^n}\left(I_x^{n-\alpha} h(x)\right) \tag{11a}$$

$$\frac{d^\alpha h}{dx^\alpha} = I_x^{n-\alpha}\left(\frac{d^n h(x)}{dx^n}\right) \tag{11b}$$

where n is an integer such that $n-1 < \alpha < n$ and $I_x^{n-\alpha}(\cdot)$ is a fractional integration operator of order $n-\alpha$. This distinction is important in the case of boundary-valued and initial-valued problems as the Riemann-Liouville definition requires the calculation of the derivatives of the fractional integrals of the function at the initial value, whereas the Caputo definition only requires the calculation of initial values of the function and its integer derivatives [see *Voller and Paola,* in this issue for a detailed discussion]. It is further worth noting that the Caputo-fractional derivative (equ 11b) of a constant is zero, and in this form a fractional integral and a fractional derivative are commutative, whereas the Riemann-Liouville fractional derivative (equ 11a) of a constant is a power law. Specifically, the α-order fractional integral of a constant c is a power function:

$$I_x^\alpha\{c\} = \frac{c}{\Gamma(1+\alpha)} x^\alpha \tag{12}$$

where $I_x^\alpha\{\cdot\}$ is the fractional integral operator of order α, c is a constant and $\Gamma(\cdot)$ is the gamma function. Implementation of the fractional derivative on a finite domain $0 \le x \le L$ with boundary conditions, requires defining the functional value $h(x)$ beyond the left boundary, that is for $x < 0$. In a boundary-valued problem, the Caputo-form of the fractional derivative assigns the values of the function (in this case $h(x)$) beyond the boundary to be equal to the value of the function at the boundary, i.e., it inherently assumes that $h(-\infty)$ up to $h(0)$ are assigned the value of $h(0) = H_{top}$. This, however, is physically unreasonable as no sediment is supplied at the ridge from any point beyond the ridge. In order to circumvent this issue we numerically evaluate the steady-state equilibrium hillslope profiles predicted by equation (10).

A fractional derivative can be discretized using the one-shift Grünwald expansion [*Meerschaert and Tadjeran,* 2004]:

$$\frac{d^\alpha h(x)}{dx^\alpha} \approx \frac{1}{\Delta x^\alpha}\sum_{k=0}^{N} g_k h(x - k\Delta x + \Delta x) \tag{13}$$

where g_k are the one-shift Grünwald weights, Δx is the spatial step-size in the numerical implementation, N is the number of node points upslope of the given point and

$1 < \alpha \le 2$ is the order of differentiation. The Grünwald weights are given by the following expression [*Grünwald,* 1967; *Meerschaert and Tadjeran,* 2004]:

$$g_k = \frac{\Gamma(k-\alpha)}{\Gamma(-\alpha)\Gamma(k+1)} \tag{14}$$

Imposing the boundary conditions:

$$h(0) = H_{top} = \frac{U}{\Gamma(1+\alpha)K^*} L^\alpha$$

$$\left.\frac{dh}{dx}\right|_{x=0} = 0 \tag{15}$$

such that $h(L) = 0$ at the river edge, and imposing an additional condition that
$h(x) = 0$ for $x < 0$
(since there is no sediment supply to the domain from any point beyond the ridge), one can solve numerically for the steady-state equilibrium hillslope profiles predicted by equation (10). Figure 2a shows the hillslope equilibrium profile for fractional transport with degree of non-locality $\alpha = 1.5$. It is noted that the hillslope profile is parabolic close to the ridge and transitions to a power law with an exponent of α.

It is worth noting that under the Caputo form of the fractional derivative (which assumes that the values of $h(x) = H_{top}$ for $x < 0$), equ (10) can be solved analytically. The analytical solution of equation (10) with the boundary conditions (15) and $h(x) = H_{top}$ for $x < 0$ is given as:

$$h(x) = H_{top} - \frac{U}{\Gamma(1+\alpha)K^*} x^\alpha \tag{16}$$

where x is the horizontal distance from the ridgetop, and H_{top} is the elevation of the ridgetop. As shown in Figure 2(b), this solution is reached in the numerically evaluated profile (which assumes $h(x) = 0$ for $x < 0$) only at a finite distance downslope of the ridge when enough upslope topographic distance exists for the non-local contribution to substantially contribute to the sediment flux at a given point. Hence overall, the steady-state hillslope equilibrium profile is parabolic near the ridgetop and becomes, shortly after, a power law profile with an exponent α (given by equation (16)). Further, we note that the steady-state solution to the fractional diffusion equation predicts power law relationships of local gradient and curvature with downslope distance given by:

$$-\nabla h \sim x^{\alpha-1} \tag{17}$$

$$\nabla^2 h \sim x^{\alpha-2} \tag{18}$$

That is, the fractional flux law predicts that curvature downslope of the ridge is not constant but decreases with downslope distance in a manner dictated by the exponent

α (such a decrease has been documented, for example, in field observations in *Roering et al.* [1999]). For $\alpha = 2$ the non-local transport model reproduces the linear profile in gradient and constant curvature with downslope distance, as expected for linear diffusive transport, while values of α between 1 and 2 give the flexibility of reproducing a suite of observed hillslope profiles. In the next section, we analyze field data from several real hillslopes and show that they are consistent with the non-local hypothesis of sediment flux.

4. Observed hillslope profiles interpeted within the non-local transport theory

The one-dimensional non-local theory presented here applies to hillslope profiles in which transport is assumed to be only along that profile, i.e., a one-dimensional approximation. Hillslopes, however, typically have significant contour (planform) curvature (i.e. ridges and hollows) and at steady state such curvature can accommodate the increasing soil production that must be carried downslope such that a single profile along the hillslope can be straight even in the case of linear flux-dependent transport and spatially constant erosion rates. Only a few detailed studies of hillslope form and process have been reported on hillslopes without significant planform curvature. Here we re-examine three well-known study sites (one clearly lacking planform curvature) and interpret them within the proposed non-local flux theory.

Roering et al. [1999] motivate their work on non-linear flux laws by reporting hillslope profiles in the Oregon Coast Range that clearly deviate from parabolic shape or constant curvature. Their study site experiences large scale disturbances due to massive tree throw mounds (*Heimsath et al*, 1999), mammal burrowing and periodic fire (*Roering and Gerber*, 2005) and there is evidence for approximate steady state with considerable local variation over timescales of hillslope soil adjustment and develoment (*Roering, et al.*, 1999; *Heimsath et al.*, 2001; *Reneau and Dietrich*, 1991). One of their profiles is shown in Figure 3(a) and the log-log plot of elevation fall versus horizontal distance (Fig. 3b) suggests a slope of 1.3 for distances beyond 10 m downslope of the ridgetop and a slope of 2 close to the ridge (only 3 points are shown in Fig 3b at distance 0 to 10 m, but the slope of 2 is supported by more points obtained from the interpolated profile shown by the dashed line in Fig 3a). This profile is consistent with the non-local flux hypothesis and suggests that the non-local transport model proposed herein might be an alternative to the non-linear model of *Roering et al.* [1999]. The conceptual bases of these two models are fundamentally different as they hypothesize different mechanisms of erosion and transport. This profile will be further analyzed in the next section.

In their seminal paper on the geomorphology and forest ecology of the Shenandoah River area of Virginia, *Hack and Goodlett* [1960] report the result of plotting fall against distance for both their intensely surveyed study site and for a broad survey of 27 hillslopes in the Appalchians in Maryland and Virginia. They propose that the many regularities of the landforms and soils in the studied regions suggest steady-state landscape adjustment. Ignoring the data points close to the divide, they report log-log linear profiles with a slope of 1.23 for the survey site and values ranging from close to 1 up to 1.7 for Maryland and Virginia. It is not clear how the broad survey data were collected (in the field versus from available topographic maps), nor whether they avoided slopes with planform curvature, but it is worth noting that the profiles do not include data points near the divide. They conclude that steeper hillslopes are generally straight (α values close to 1) and gentle ones more curved (α values closer to 2). Within our theory, this would suggest non-local transport on steeper hillslopes and local transport (linear diffusion) on gentle slopes. *Hack and Goodlett's* [1960] describe soil transport as being driven by "growing roots, burrowing animals, falling raindrops, frost, tree blowdowns and the like" (p. 58). These processes would create a wide range of transport distances for a given slope. Specific localities and erosion rates for the hillslope profiles are not reported, so we must consider this suggestion as only a possibility, not an established condition.

McKean et al. [1993] selected a hillslope transect with minimal planform curvature in the grasslands east of San Francisco, CA underlain by marine shales and documented soil transport rates using [10]Be concentrations in the clay-rich soils (Figure 4). From analysis of three soil pits within the first 35 m of hillslope length (from the ridge) they found evidence for a linear flux law and quantified the diffusive rate constant K (i.e. equation 1). The soil transport occurs by seasonal creep of the high-plastic clay with biogenic transport being of some importance near the divide. Soil thickness varies inversely with curvature, consistent with a balance between soil production and linear transport [*Yoo et al.*, 2005; 2006]. The thickness is about 40 cm near the ridge and then increases downslope. Boundary conditions (channel incision rate and history) strongly influence hillslope profiles and at this study site the hillslope terminates in a broad, aggraded valley, which has led to a break in slope at the base of the hillslope and progressive thickening of soil towards the valley axis [*Yoo et al.*, 2005]. Both *Yoo et al.*, 2005 and *McKean et al.* 1993 suggest that the upper smoothly convex hillslope could be at approximate steady state erosion, that is, the effect of stabilization of the lower boundary has not reached to the divide.

We used the survey data collected by *McKean et al.* [1993] to construct the longitudinal profile reported in Figure 4a. By plotting on a log-log scale the elevation fall versus horizontal distance from the ridge (Figure 4b) we observe a slope of ≈ 1.8 from a distance of 8 m from the ridgetop up to approximately 25 m downslope; in the first 8 m from the ridgetop one would expect a parabolic profile

(slope of 2). The hillslope rapidly flattens upslope from 8 m and the available survey data do not provide adequate constraint on the profile shape. The gentle hillslope gradient and high clay content (which favors creep) and the dry, grassy, relatively low biota mantle on the convex hilltop all would favor an almost local transport, and the slope value of 1.8 extending for the first 25 m is consistent with this expectation. Downslope of 50 m to the lowest portion of the hillslope surveyed the slope of the power law plot of elevation against distance is ≈ 1.2. This transition is not consistent with the non-local flux law of $\alpha = 1.8$ discussed above; rather the bottom part of the hillslope is interpreted as experiencing a change from net erosion to progressive soil accumulation (due to lower boundary conditions) and field observations support this interpretation. This example illustrates that the non-local flux theory can also be used as a diagnostic tool for inferring process from form and further motivate data collection to test alternative hypotheses.

5. Nonlocal versus nonlinear flux: Same behavior for different reasons
5.1. Nonlinear transport model as an emulator of super-diffusivity

Deviation from purely diffusive behavior in many hillslopes has prompted the development of more complex transport laws which have a nonlinear dependence on topographic gradient. A review of several of these laws can be found in *Dietrich et al.* [2003]. For example, for soil mantled hillslopes, *Roering et al.* [1999] proposed the following flux equation [see also *Andrews and Buckman*, 1987; *Howard*, 1994]:

$$q'_s = \frac{K \nabla h}{1 - \left(\left|\nabla h\right|/S_c\right)^2} \quad (19)$$

where q'_s is the sediment flux calculated at a point via the non-linear flux law, K is the diffusivity coefficient and S_c is called the "critical gradient". It is noted that the above equation imitates a super-diffusive behavior, that is, close to linear diffusion at low slopes and accelerated diffusion at high slopes. Although this can be directly seen from (19), it is interesting to see it from a different perspective. By substituting (19) in (2) and performing a Taylor series expansion we obtain:

$$\frac{\partial h}{\partial t} = K \nabla^2 h + K \frac{\nabla^2 h}{S_c^2} (|\nabla h|)^2 + \dots \quad (20)$$

The second term in the RHS of (20) shows that the nonlinear transport law of (19) captures the super-diffusive behavior at high slopes by enhancing the regular diffusion with the addition of a term that has an explicit non-linear dependence on gradient. The gradient in the above equation is "local". We propose that such super-diffusive behavior in steep hillslopes can be addressed using non-local transport laws, which are linear (i.e., they involve only linear combinations of local gradients) but take into account that disturbances contributing to sediment flux at a point of interest have an origin far upslope of that point. It is interesting to note that the proposed non-local flux law gives rise to a non-linear dependence of sediment flux on the local gradient at any point (this will be presented in the next section) but for reasons different than the explicit quadratic dependence of flux on local gradient as in equation (20).

5.2. Nonlocality gives rise to a nonlinear dependence of flux on local gradient

We use the *Roering et al.* [1999] hillslope profile from the Oregon Coast Range to illustrate the computation of the sediment flux from the nonlocal transport model of (8) and compare it to those of the linear (1) and nonlinear (19) models. In order to have a continuous set of elevation data points over the domain of interest, the observations were interpolated using a spline as shown in Figure 3a with dashed lines.

The computation of the fractional flux was performed on a discrete grid of size Δx by the Grünwald-Letnikov discrete approximation of the fractional integral operator given as [*Grünwald*, 1967; *Podlubny*, 1999]:

$$\nabla^{\alpha-1} h(x) = I_x^{2-\alpha}\{\nabla h(x)\} = \lim_{\Delta x \to 0} (\Delta x)^{2-\alpha} \sum_{k=0}^{x/\Delta x} \frac{\Gamma(2-\alpha+k)}{k!\Gamma(2-\alpha)} \nabla h(x-k\Delta x) \quad (21)$$

It is noted that writing the fractional flux as a fractional integral of the local slopes (first equality in the above equation) is enabled by use of the Caputo definition of the fractional derivative (equation 11b).

The parameters chosen for the three flux laws (linear, non-linear and non-local) are $K = 0.0015 m^2 / yr$, $S_c = 1.4$, $\alpha = 1.5$ and $K^* = 0.0007 m^\alpha / yr$. The model parameters for the non-linear flux law are chosen from the ones calibrated for Oregon Coast Range in *Roering et al.*, [1999]. For the non-local flux law, α is set to 1.5 and K^* is chosen such that all the three flux laws show a similar increase in sediment flux with slope at lower gradients. This is done in order to study the effect of the three flux laws at the higher gradients. Figure 5 shows the sediment flux computed using the three different flux laws. The sediment flux computed from the non-local transport law (8) shows a similar behavior as the non-linear, local transport law (equ. 19), with enhanced diffusion at higher gradients. Hence, a non-linear relationship between sediment flux and local gradient can also arise from a non-local, linear flux model. It is emphasized that in a real hillslope, the parameters K for the non-linear model and K^* for the non-local model are obtained via calibration; the unfamiliar units of K^* (L^α / T) are not an issue and simply reflect that the quantity $(K^* t)^{1/\alpha}$ maintains the units of length (length scale of diffusion) in analogy to the quantity $(Kt)^{1/2}$ for

standard diffusion [e.g., see *Benson,* 1998].

5.3. Non-locality and upslope "region of influence"

The non-local transport law differs from any local transport law (linear or nonlinear) in that in the former, the sediment flux contribution to a given point on the hillslope is computed from a weighted average of the topographic gradients upslope of that point. Therefore, unlike the local transport laws, the non-local transport law has a "memory" of the upslope topography. Although the power law kernel $g(l)$ of the non-local integral flux (equation 7) implies lack of characteristic scale over which the averaged gradient is computed, we take the liberty below to introduce a cut-off scale in order to illustrate this upslope influence effect. Specifically, we introduce a physically tangible measure of non-locality for the computation of sediment flux by defining an *influence length*, L_α, as the distance upslope from a given point, beyond which the contribution of the sediment flux is less than 10% of the total, i.e., L_α is defined by the equation:

$$K^* \int_0^{L_\bullet} g(l) \nabla h(x-l)dl \approx 0.9 q_s^*(x),$$
$$1 < \alpha < 2 \tag{22}$$

where $g(l) \sim l^{2-\alpha}$ are the weights given to the gradients upslope and q_s^* is the non-local flux calculated by (8). The cutoff of 10% is chosen here arbitrarily to illustrate the behavior of non-local flux and it can be chosen to be lower or higher depending on the problem at hand.

The influence length was calculated for the *Roering et al.* [1999] profile from equation (22) for three different values of α and is shown in Figure 6. The degree of non-locality increases with a decrease in α, i.e., the closer the value of α is to 1.0 the more non-local the transport is compared to a value of α closer to 2. As expected, a higher degree of non-locality results in a larger value of L_α as seen in Fig. 6. For $\alpha = 2$, equation (25) is not applicable for computation of the influence length. In this case, the step lengths have a thin-tailed distribution whose characteristic scale (standard deviation) can be used to define the influence length.

6. Non-locality naturally reproduces spatial variability of sediment flux

In the previous sections, all the flux laws were discussed in the context of a single hillslope profile. However, even in a small hillslope, there exists considerable variability in the form of hillslope profiles which results in a considerable variability in the observed sediment flux. This flux variability was documented in *Roering et al.* [1999] for the MR1 basin of Oregon Coast Range. They computed the sediment flux using:

$$q_s = U \frac{\rho_r}{\rho_s} \frac{a}{b} \tag{23}$$

where U is the constant rock uplift rate, ρ_r and ρ_s are bulk densities of rock and sediment respectively, and a/b is the drainage area per unit contour length, and compared it against the flux computed from their non-linear transport model. Figure 7 (reproduced from *Roering et al.* [1999]) shows the spread of the computed sediment flux as a function of gradient. Notice that for a given gradient, say for a gradient of 0.8 there is an order of magnitude variability in the computed flux. To describe this variability with the non-linear law, equation (19), the calibrated parameters of the model had to vary considerably: $K = 0.0015 m^2/yr$ to $0.0045 m^2/yr$ and $S_c = 1.0$ to 1.4 as reported in *Roering et al.* [1999]. We note that S_c is a calibration parameter which was attached a physical meaning of a critical slope and was related to the angle of repose in *Roering et al.*, [1999]; later in *Roering and Gerber* [2005] it was proposed that K increased and S$_c$ decreased in response to forest fire.

Here we pose the hypothesis that a non-local transport model can capture the observed variability of sediment flux within a given hillslope by a single or very narrow range of parameters, unlike any local transport law. To test the hypothesis, we generated a set of hillslope profiles using different cubic polynomials (see Figure 8) to imitate the natural variability of hillslope profiles within a small basin. Along those profiles the sediment flux was computed using the non-local, linear flux model (equation 8) and local, non-linear flux model (equation 19). Figure 9 shows the computed sediment flux as a function of the local gradient. The non-local transport law with a single set of parameters K^* and α produces a variability of sediment flux for a given gradient comparable to that observed in real hillslopes (Fig. 8). However, the local transport law cannot reproduce this variability with a single set of parameters K and S_c but requires a considerable range of parameters as indicated by the envelope curves in Fig. 9. This is simply because two points with the same local slope would result in the same flux from any local transport law but different fluxes from a non-local law, due to different upslope topography. Having the need for such a wide range of parameters to reproduce the sediment flux variabilty in a small hillslope makes physical interpretation of those parameters difficult. Apart from the upslope hillslope profile variability considered here, there are other factors contributing to the sediment flux/ local gradient variability, such as, for example, the dependence of K on soil depth [e.g., *Roering*, 2008].

7. Probability distribution of particle displacement and fractional transport

Sediment transport on hillslopes can be thought of as disturbance driven, in which soil is mobilized en masse or as individual particles. A single disturbance event may move the mobilized sediment a considerable distance (e.g. raveling after a fire). Disturbed piles of sediment (e.g. tree throw mounds) will create sustained local areas of elevated flux—and increased downslope delivery. For simplicity we can think of event-based transport as a kind of "hopping" process, where the sediment moves downslope in a series of steps resulting from local disturbances. Here a single hop can be thought of as the distance covered by a grain of sediment from where disturbance has displaced it into an active flux state to where it comes to transient rest (until next disturbance). It can also be thought of as a package of sediment made significantly more active due to local mounding and exposure, say during a tree throw, which results in rapid flux compared to what would happen under mean slope conditions. As discussed in the introduction, many processes generate slope-dependent transport and operate over a wide range of distances. These processes may result in a heavy-tailed PDF of the sediment "hops" or displacement distance (see also *Tucker and Bradley*, in this volume), which means that there is a relatively small but significant possibility that sediment grains will move a great distance downslope in a single hop. In other words, these distances do not have a characteristic length scale and may assume values comparable to the size of the hillslope itself.

If the PDF of hopping distances were thin tailed, e.g., Gaussian or exponential with an e-folding distance small relative to the size of the hillslope, then the continuum equation describing the evolution of the hillslope would be the diffusion equation [*Feller*, 1971; see also Schumer et al., 2009 this issue]. However, if the probability distribution of hopping distances is broad-tailed as argued above, then a faster than linear diffusion is expected. It turns out that, since a sum of broad-tailed PDFs results in an α-stable distribution for the hopping process [*Feller*, 1971], then the governing equation of elevation change consistent with this distribution is the fractional diffusion equation (9) [*Meerschaert et al.*, 1999; 2001; Schumer et al, this issue]. That is, the corresponding macroscopic process of sediment transport can be described using a modified diffusion equation where the ∇^2 operator is replaced with a non-local operator ∇^α. The degree of non-locality is governed by the order of differentiation, α. The lower the value of α, the greater is the degree of non-locality. This is a manifestation of the fact that an α-stable PDF has a heavier tail for lower values of α.

8. Locality and scale-dependence of computed flux

In this section we discuss some preliminary ideas related to the potential of non-local transport laws to circumvent the problem of scale dependence of sediment flux computations. We start with the classical divergence theorem and elementary control volume which is of little use when there is no characteristic scale in particle displacement distances. Then, we allude to the fact that local transport laws suffer from scale dependencies which would require closures [e.g., see *Passalacqua et al.*, 2006] and which can be naturally taken care of by the nonlocal transport laws.

The advection-dispersion equation (ADE) is based on the classical definition of divergence of a vector field. The divergence is defined as the ratio of total flux through a closed surface to the volume enclosed by the surface when the volume shrinks to zero [e.g., *Schey*, 1992; see also *Benson*, 1998, for an exposition relevant to subsurface transport]:

$$\nabla \cdot q_s = \lim_{V \to 0} \frac{1}{V} \iint_S q_s \cdot \eta dS \qquad (24)$$

where q_s is a vector field, V is an arbitrary volume enclosed by surface S, and η is a unit normal vector. Implicit in this equation is that the limit of the integral exists, i.e., the vector q_s exists and is smooth as $V \to 0$.

The classical notion of divergence maintains that, as an arbitrary control volume V shrinks to zero, the ratio of total surface flux to volume must converge to a single value. However, when a heavy-tailed distribution of displacement lengths exists, this notion of convergence is challenged. In fact, due to the lack of a characteristic scale of the displacement distances, no convergence is guaranteed when the size of the control volume changes. As a result, the classical diffusion equation is no longer self-contained with a closed-form solution at all scales. To adopt the classical theory, the best approximation that can be done is to assume that the total flux to volume ratio can be assumed piece-wise constant within small ranges of scales, allowing one to talk about an "effective" scale-dependent dispersion coefficient [e.g., see Benson, 1998]. Several techniques have been proposed in the subsurface transport literature to tackle the problem of scale-dependent dispersivity. These vary from small perturbation approaches and effective parameterizations [e.g., *Gelhar and Axness*, 1983; *Dagan*, 1997], to power law dependence of D on scale [e.g., *Su*, 1995], to volume statistical averaging [e.g., *Cushman*, 1991, 1997] and to fractional advection dispersion equations (fADE) [e.g., *Benson*, 1998; *Benson et al.*, 2000b; *Bauemer et al.*, 2001; *Schumer et al.*, 2001; 2009 this issue].

Any sediment transport law that directly involves a "local" gradient or curvature in the computation of flux, will be scale-dependent as gradients and curvatures depend on the scale at which they are computed [e.g., see *Lashermes et al.*, 2007]. For example, this was demonstrated in *Passalacqua et al.* [2006] using a local non-linear flux law (a Langevin model which has square

dependence on local slope). In that study, the development of a closure term, akin to the Large Eddy Simulation (LES) turbulence closures, was proposed to handle this scale-dependence and the closure term was shown to have a power-law dependence on scale (grid size). The proposed non-local fractional diffusive model has in principle the ability to remove this scale-dependency as it is free of any "representative" or "control volume" concept and the power-law integration of local gradients (see equation (21)) eliminates the need for the aforementioned power-law closure [e.g., see discussion in *Foufoula-Georgiou et al, 2008*]. This issue requires further study.

9. Discussion and Conclusions

Most geomorphic transport laws proposed to date are local in character, i.e., they express the sediment flux or erosion at a point as a function of the elevation gradient, contributing drainage area, or other geomorphic quantities at that point only. For the case of soil-mantled landscapes, it is reasonable to propose that disturbance processes inducing transport have widely varying transport distances and this gives rise to a non-locality of sediment transport, as proposed here. As summarized below, we see several advantages to the non-local transport law.

(1) The proposed non-local transport model with boundary conditions of zero-slope at the ridgetop and constant elevation at the ridge bottom predicts a steady-state profile which is parabolic very close to the ridgetop and changes, after a short distance downslope to a power law with exponent equal to the parameter α (order of differentiation) in the fractional transport law. This prediction is supported by data in three study sites and provides useful insight for one of the sites which may still experience transition from net erosion to soil accumulation.

(2) The non-local linear model gives rise to a non-linear relationship between the sediment flux at a point and the local slope. Hence, non-locality of sediment flux is an alternative hypothesis that can explain the observed hillslope profiles and the non-linear flux dependence on slope.

(3) In a practical implementation of a local sediment flux law (linear or nonlinear), the "local" slope is always assigned a "scale" over which some smoothing or averaging is done, without however a theory as to how to select this scale. The non-local flux law is scale-free (it lacks a characteristic scale of upstream particle displacement distance); rather it uses a "power-law weighted average slope" stating that upslope hillslope gradients matter to local flux, but with diminishing influence as a function of upslope distance.

(4) The proposed non-local model produces significant variability of sediment flux for a given local slope, as it explicitly takes into account variations in upslope topography. In this case, transport parameters, such as K^*, can remain constant, and retain, perhaps, a stronger physical meaning while reproducing the variability observed in real hillslopes.

(5) The non-local model has the potential to eliminate scale-dependency. The usefulness of non-local fractional models to address issues of scale-dependence in subsurface transport (e.g., scale-dependent dispersivity in porous media with multiple scales of heterogeneity) has been amply demonstrated and needs to be explored for similar problems on the Earth's surface.

We consider this paper as the beginning of a dialogue on concepts of non-locality and collective behavior as they relate to transport on the earth's surface. Important questions arise as to how these concepts can most concisely be expressed in or incorporated into new classes of geomorphic transport laws and also how non-locality can be directly verified from observations. Together with several other papers in this issue, a new direction of thinking emerges which shows promise for better understanding of cause and effect in landscape processes and landscape evolution models.

References
Andrews, D. J., and R. C. Buckman, Fitting degradation of shoreline scarps by a nonlinear diffusion model, *Journal of Geophysical Research*, *92*(12), 857--867, 1987.

Baeumer, B., D. Benson, M. Meerschaert, and S. Wheatcraft , Subordinated advection-dispersion equation for contaminant transport, *Water Resour.*

Res., 37(6), 1543-1550, 2001.

Benson, D. , The Fractional Advection-Dispersion Equation: Development and Applications, Ph.D Thesis, University of Nevada, Reno, 1998.

Benson, D. A., S. W. Wheatcraft, and M. M. Meerschaert, Application of a fractional advection-dispersion equation, *Water Resour. Res.*, *36*(6), 1403--1412, 2000 a .

Benson, D. A., S. W. Wheatcraft, and M. M. Meerschaert, The fractional-order governing equation of Lévy motion, *Water Resour. Res.*, *36*(6), 1413--1423, 2000 b .

Berkowitz, B., J. Klafter, R. Metzler, and H. Scher, Physical pictures of transport in heterogeneous media: Advection-dispersion, random-walk, and fractional derivative formulations, *Water Resour. Res.*, *38*(10), 1191--, doi:10.1029/2001WR001030, 2002.

Biler, P., T. Funaki, and W. Woyczynski, Fractal Burgers Equations, *J. Diff. Equations*, *148*, 9--46, 1998.

Bouchaud, J.-P. and A. Georges, Anomalous diffusion in disordered media: Statistical mechanisms, models and physical applications, *Physics Reports*, *195*(4), 127--293, 1990.

Bradley, D. N., G. E. Tucker, and D. A. Benson, Fractional dispersion in a sand-bed river, *J. Geophys. Res.*, *under review*, in this volume, 2009.

Campos, D., J. Fort and V. Mendez , Transport on fractal river networks: Application to migration fronts, *Theoretical Population Biology*, *69*, 88--93, 2005.

Culling W. E. H., Analytical theory of erosion, *J. Geology*, *68*, 336-344, 1960.

Cushman, J. H., On diffusion in fractal porous media, *Water Resources Res.*, Vol. *27*(4), 643--644, 1991.

Cushman, J. H., *The Physics of Fluids in Hierarchical Porous Media: Angstroms to Miles*, 467 pp., *Kluwer Acad., Norwell, Mass*, 1997.

Cushman, J. H., and T. Ginn, Fractional advection-dispersion equation: A classical mass balance with convolution-Fickian flux, *Water Resour. Res.*, Vol. *36*(12), 3763--3766, 2000.

Dagan G. , *Subsurface flow and transport: A stochastic approach*, Cambridge Univ. Press, Cambrdge, Mass, 1997.

Deng, Z. Q., J. L. M. P. de Lima, and V. P. Singh, Fractional Kinetic Model for First Flush of Stormwater Pollutants, *J. Environ. Engineering*, *131*(2), 232--241, DOI:10.1061/(ASCE)0733-9372(2005)131:2, 2005.

Deng, Z. Q., J. L. M. P. de Lima, M. I. P. de Lima, and V. P. Singh, A fractional dispersion model for overland solute transport, *Water Resour. Res.*, *42*, W03416, doi:10.1029/2005WR004146, 2006.

Dietrich, W. E., D. G. Bellugi, L. S. Sklar, J. D. Stock, A.

M. Heimsath, and J. J. Roering, Geomorphic transport laws for predicting landscape form and dynamics, in *Prediction in geomorphology*, *Geophysical Monograph Series*, vol. 135, edited by P. Wilcock and R. Iverson, pp. 103--132, AGU, Washington, D.C., doi:10.1029/135GM09, 2003.

Feller, W., *An Introduction to Probability Theory and Its Applications*, vol. 2, second ed., Wiley, New York, [1st edn. 1966], 1971.

Fleming, R. W., and A.M. Johnson, Rates of seasonal creep of silty clay soil, *Q. J. Eng. Geol.*, 8, 1-29, 1975.

Foufoula-Georgiou, E., V. Ganti and P. Passalacqua, Geomorphic Transport Laws: Non-local flux with classical mass balance, *University of Minnesota Supercomputing Institute Report UMSI 2008/27,* May 2008.

Furbish, D. J., P. K. Haff, W. E. Dietrich, and A. M. Heimsath, Statistical description of slope-dependent soil transport and the diffusion-like coefficient, *J. Geophys. Res.,* in this volume, 2009.

Gabet, E. J., D. J. Reichman, and E. W. Seabloom, The effects of bioturbation on soil processes and sediment transport, *Ann. Rev. of Earth and Planetary Sciences*, *31*, 249-273, 2003.

Ganti, V., M. Meerchaert, E. Foufoula-Georgiou, E. Viparelli, and G. Parker, Normal and anomalous diffusion of gravel tracer particles in rivers, *J. Geophys. Res.*, in review, this issue.

Gelhar, L.W. and C.L. Axness , Three-dimensional stochastic analysis of macrodispersion in aquifers, *Water Resour. Res.*, 19(1), 161–180, 1983.

Gilbert, G. K., The convexity of hilltops, *J. Geology*, *17*, 344-350, 1909.

Grünwald, A. K., Uber "begrenzt" derivation und deren anwendung, *Z.angew. Math. und Phys.*, *12*, 441--480, 1867.

Hack, J. T., Interpretation of erosional topography in humid temperate regions, *Am. J. Sci.*, *258A*, 80-97, 1960.

Hack, J. T., and J. C. Goodlett, Geomorphology and forest ecology of a mountain region in the central Appalachians, *U.S. Geol. Surv. Prof. Paper*, *347*, 66 pp., 1960.

Heimsath, A. M., W. E. Dietrich, K. Nishilzumi, and R. C. Finkel, Cosmogenics nuclides, topography, and spatial variation of soil depth, *Geomorphology*, *27*, 151--172, 1999.

Heimsath, A. M., W. E. Dietrich, K. Nishiizumi, R. C. Finkel, 2001, Stochastic processes of soil production and transport: erosion rates, topographic variation, and cosmogenic nuclides in the Oregon Coast Range, *Earth Surface Processes and Landforms*, v26, p.531-552.

Howard, A. D., A detachment-limited model of drainage basin evolution, *Water Resour. Res.*, *30* (7), 2261--2285, 1994.

Kirkby, M. J, Measurement and theory of Soil Creep, *J. Geology*, *75*, 359–78, 1967.

Koons, P. O., The topographic evolution of collisional mountain belts: a numerical look at the Southern Alps, New Zealand, *American Journal of Science*, 288, 1041-1069.

Lamperti, J., Semi-stable stochastic processes, *Trans. Am. Math. Soc.*, *104*, 62–78, 1962.

Lashermes, B., E. Foufoula-Georgiou and W. E. Dietrich, Channel network extraction from high resolution topography using wavelets, *Geophys. Res. Letters*, 34, L23S04, doi::10.1029/2007GL031140, 2007.

McKean, J. A., W. E. Dietrich, R. C. Finkel, J. R. Southon, and M. W. Caffee, Quantification of soil production and downslope creep rates from cosmogenic 10Be accumulations on a hillslope profile, *Geology*, 21,343-346, 1993.

Meerschaert, M. M., D. A. Benson, and B. Baeumer, Multidimensional advection and fractional dispersion, *Phys. Rev. E*, 59, 5026– 5028, 1999.

Meerschaert, M. M., D. A. Benson, and B. Baeumer, Operator Le´vy motion and multiscaling anomalous diffusion, *Phys. Rev. E*, 63, 021112–021117, 2001.

Meerschaert, M. M., and C. Tadjeran, Finite difference approximations of fractional advection-dispersion flow equations, *J. Comput. Appl. Math., 172, 65–77, 2004.*

Metzler, R. and A. Compte , Generalized diffusion-advection schemes and dispersive sedimentation: A fractional approach, *J. Phys. Chem. B*, *104*(16), 3858--3865, 2002.

Miller K. S. and B. Ross, *An Introduction to the Fractional Calculus and Fractional Differential Equations*, J. Wiley and Sons, New York, 1993.

Norman SA, Schaetzl RJ, Small TW., Effects of slope angle on mass movements by tree uprooting. *Geomorphology* **14**: 19–27, 1995.

Oldham, K. B., and J. Spanier, *The Fractional Calculus*, Academic Press, New York, 1974.

Passalacqua, P., F. Porté-Agel, E. Foufoula-Georgiou, and C. Paola, Application of dynamic subgrid-scale concepts from large-eddy simulation to modeling landscape evolution, *Water Resour. Res.*, 42, W06D11, doi:10.1029/2006WR004879, 2006.

Pekalski, A., and K. Sznajd-Weron (Eds.), *Anomalous Diffusion. From Basics to Applications*, Lecture notes in Physics *519*, Springer-Verlag, Berlin, 1999.

Podlubny, I., *Fractional Differential Equations*, vol. 198, Academic Press, San Diego, 1999.

Reneau, S. L. and W. E. Dietrich, 1991, Erosion rates in the southern Oregon Coast Range: evidence for an equilibrium between hillslope erosion and sediment yield, *Earth Surface Processes and Landforms*, vol. 16, p.307-322.

Roering, J., J. Kirchner, and W. E. Dietrich, Evidence for nonlinear, diffusive sediment transport on hillslopes and implications for landscape morphology, *Water Resour. Res.*, Vol. *36*, 853--870, 1999.

Roering, J.J., Gerber, M.. Fire and the evolution of steep, soilmantled landscapes, *Geology*, 33 (5), 349–352, 2005.

Roering, J.J.,, How well can hillslope evolution models 'explain' topography? Simulating soil production and transport using high-resolution topographic data**, *Geological Society of America Bulletin,* v. 120, p. 1248-1262, 2008.

Schey, H. , *Div Grad Curl and All That*, 2nd ed., W. W. Norton & Company, New York, 1992.

Schumer, R., D. Benson, M. Meerschaert, and S. Wheatcraft, Eulerian derivation of the fractional advection-dispersion equation, *J. Contaminant Hydrology*, 38, 69-88, 2001.

Schumer, R., M. M. Meerschaert, and B. Baeumer, What are fractional advection-dispersion equations?, *J. Geophys. Res.,* in this volume, 2009.

Shlesinger, M. F., G. M. Zaslavsky, and U. Frisch (Eds.), *Lévy Flights and Related Topics in Physics*, Lecture notes in Physics *450*, Springer-Verlag, Berlin, 1995.

Stark, C. P., E. Foufoula-Georgiou, and V. Ganti, A nonlocal theory of sediment buffering and bedrock channel evolution, *J. Geophys. Res.*, *114,* F01029, doi:10.1029/2008JF000981, 2009.

Su, N. , Development of the Fokker--Planck equation and its solutions for modeling transport of conservative and reactive solutes in physically heterogeneous media, *Water Resour. Res.*, 31(12), 1995.

Tucker, G. E., and D. N. Bradley, Locality and non-locality in geomorphic systems: Implications of a particle-based model of hillslope evolution, *J. Geophys. Res.,* in this volume, 2009.

Voller, V., and C. Paola, Can anomalous diffusion describe depositional fluvial profiles, *J. Geophys. Res.,* in this volume, 2009.

Washburn, A. L., *Periglacial processes and environments*, Edward Arnold, London, 320pp.,1973.

Woyczynski, W., *Burgers-KPZ Turbulence: Gottingen Lectures*, Lecture notes in Mathematics, Springer, Germany, 1998.

Yoo, K., Amundson, R., Heimsath, A.M., Dietrich,W.E., Process-based model linking pocket gopher (Thomomys bottae) activity to sediment transport and soil thickness. *Geology*, 33 (11), 917–920, 2005.

Yoo, K., R. Amundson, A. M. Heimsath, and W. E. Dietrich, Spatial patterns of soil organic carbon on hillslopes: Integrating geomorphic processes and the biological C cycle, *Geoderma*, 130, 47– 65, 2006.
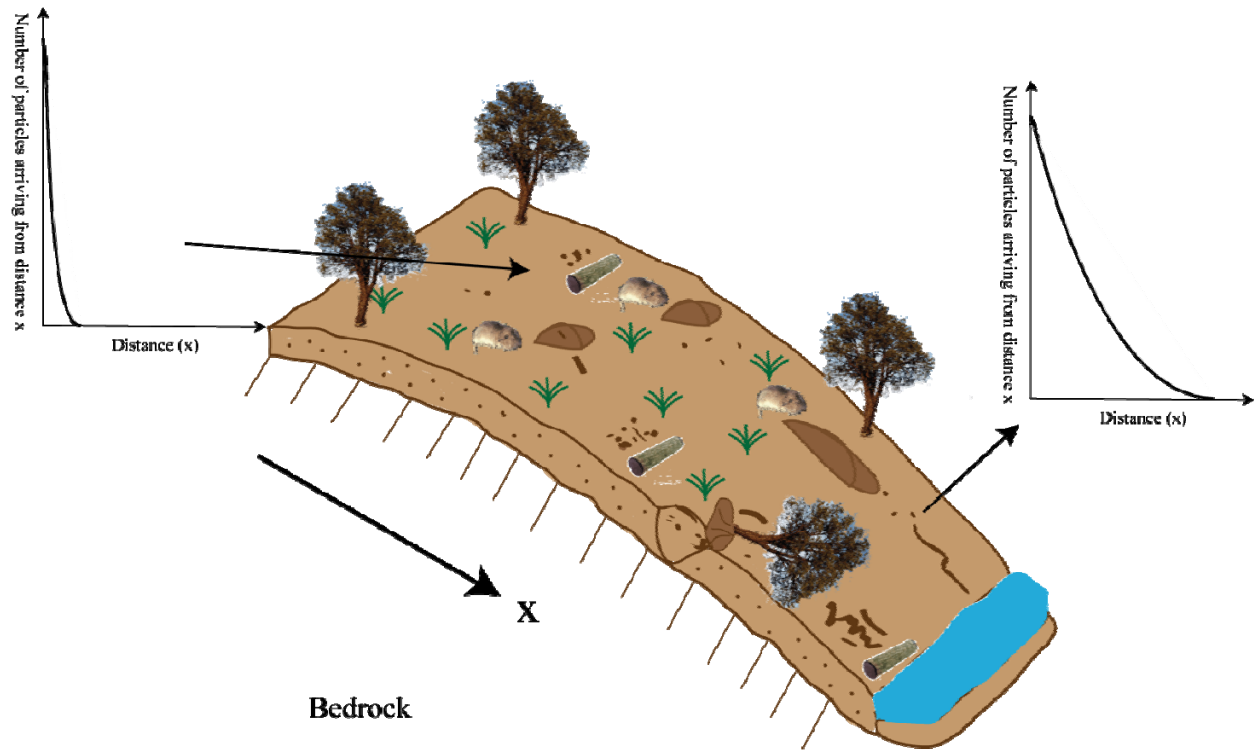
Figure 1: Cartoon illustrating processes such as gopher mounds, tree throws and wood blockage which contribute to sediment transport on a hillslope. Owing to the varied range of length scales of transport of these processes, the number of sediment particles arriving at a given location downslope is influenced by a region of upslope topography. This can be treated using the notion of a non-local flux (equation 8) which is computed by a weighted average of upslope contributions.
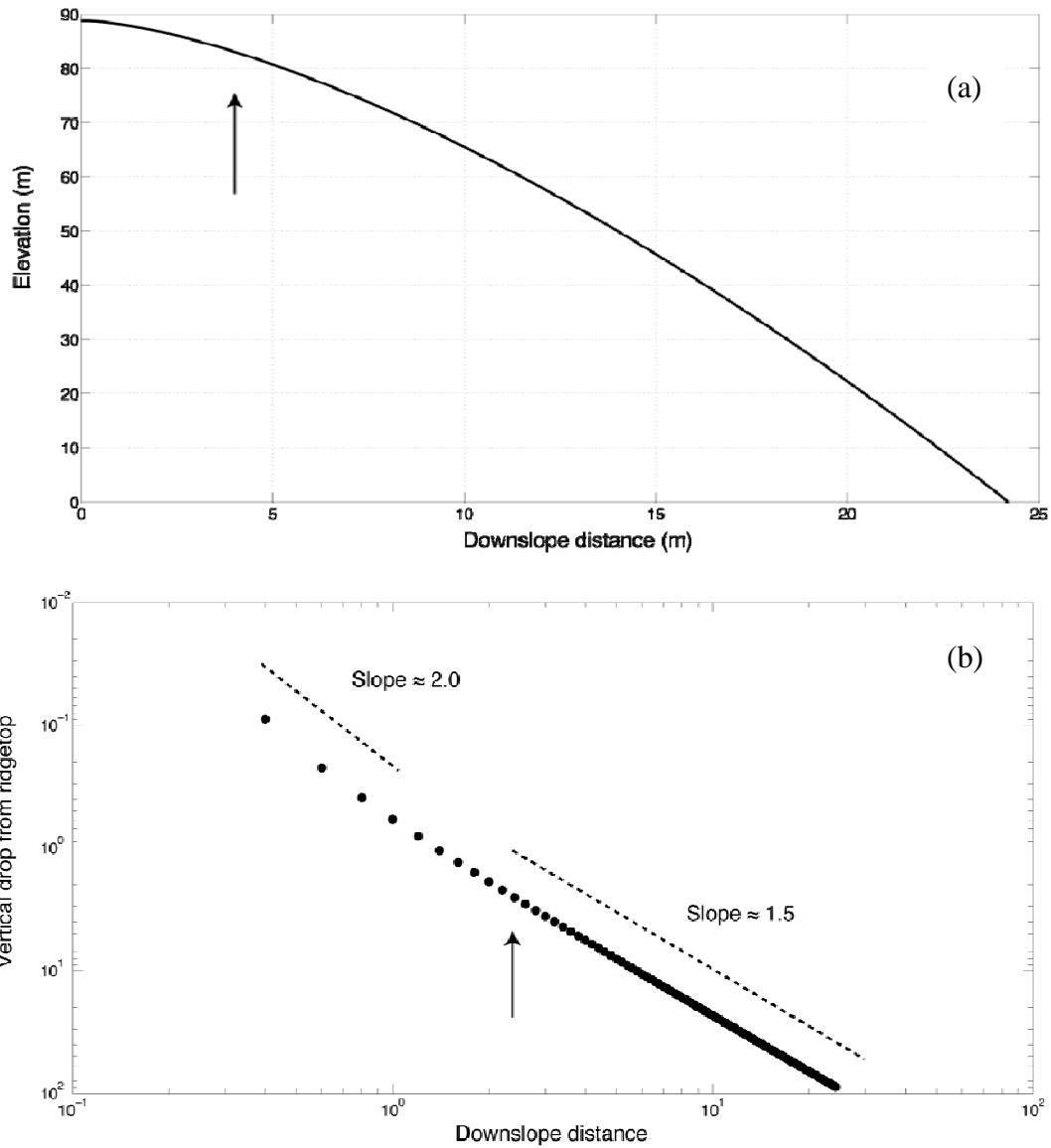
Figure 2: Steady-state hillslope equilibrium profile predicted from fractional diffusive transport (equation 8) with $\alpha = 1.5$ and boundary conditions of zero slope at the ridge and zero elevation at the most downslope point. The parameter of the model K^* was chosen to be 1.0 $m^{1.5}/yr$ and the rock uplift rate was set to unity [m/yr] (Note that a different value of rock uplift rate would not change the shape of the profile but only its absolute elevation would differ). (a) Profile shape; and (b) log-log plot of vertical drop from the ridge top versus downslope distance. Notice the transition to a power law profile with exponent $\alpha = 1.5$ at a distance of approximately 3 m from the ridgetop (arrow).

13
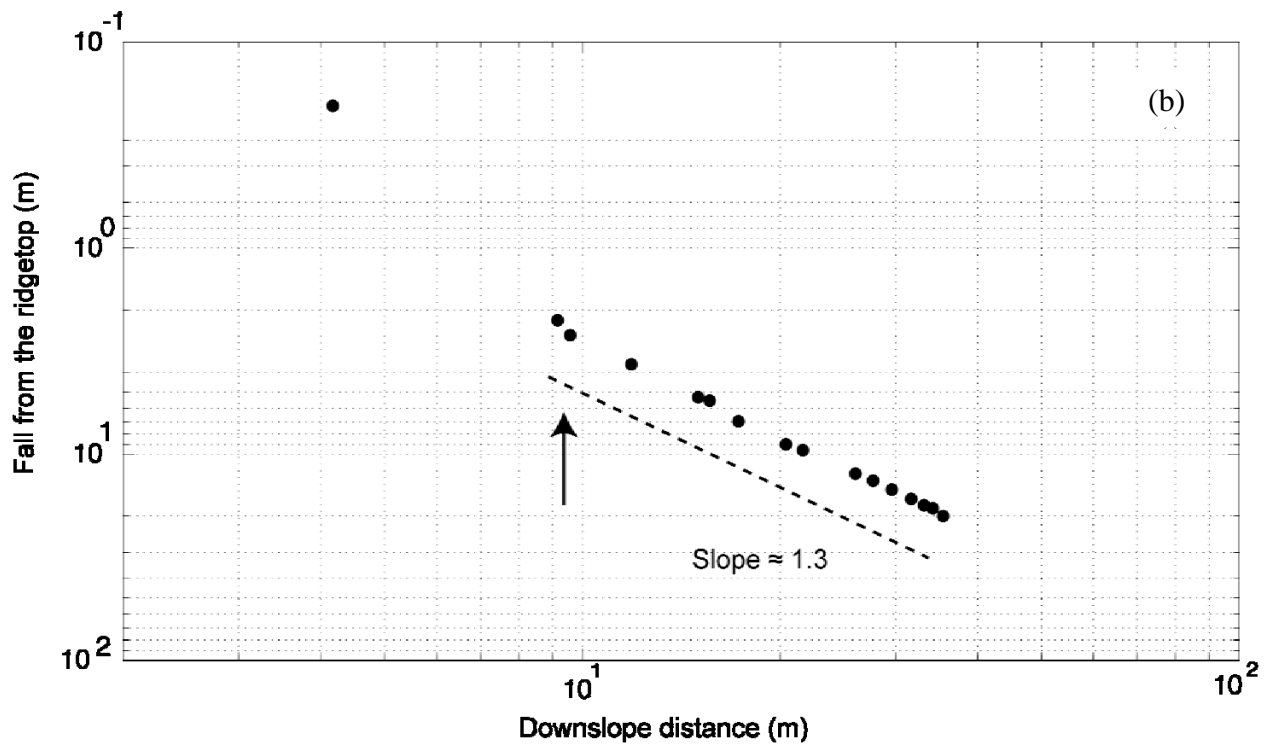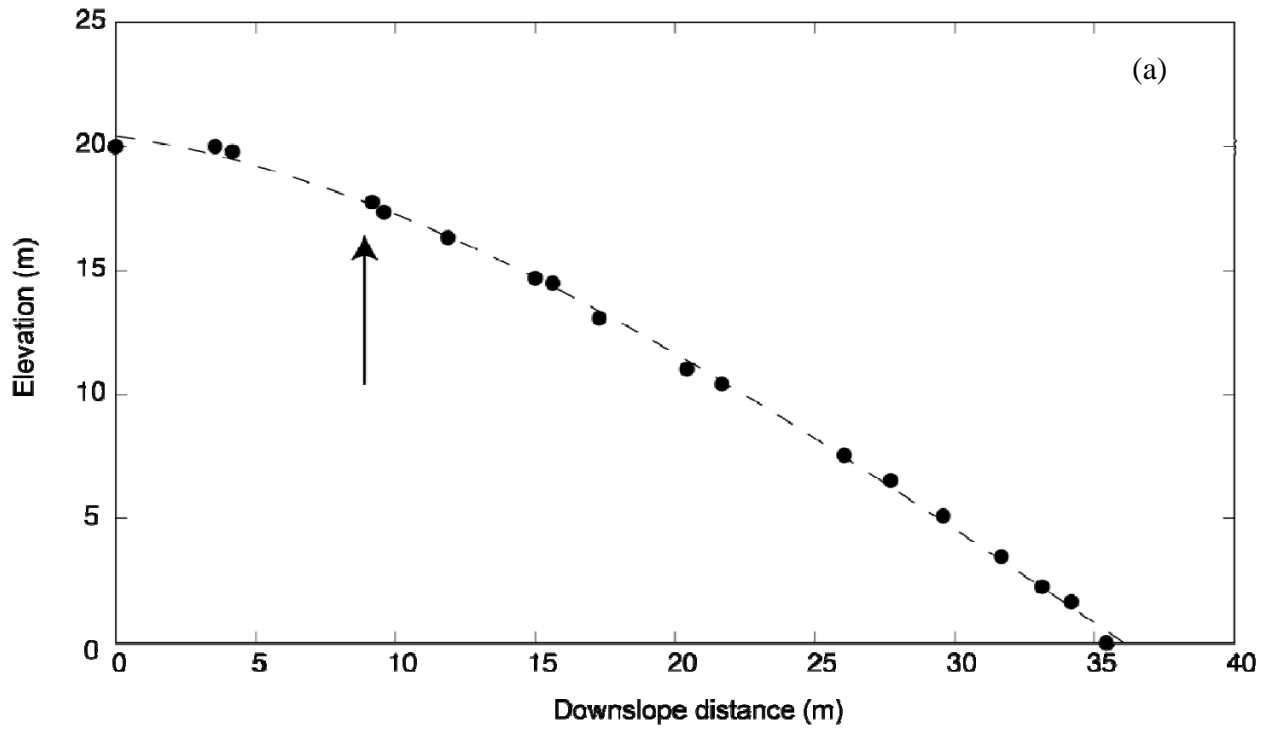
Figure 3: (a) A hillslope profile in the Oregon Coast Range. Solid circles represent the observed data points (reproduced from *Roering et al.*, 1999) and the dashed line indicates a spline fit to the observations; (b) log-log plot of the fall from the hilltop versus horizontal distance for the above profile. Notice the power law profile with exponent 1.3 starting at a distance of 9 m from the ridgetop (arrow) consistent with a non-local transport law with parameter $\alpha = 1.3$.
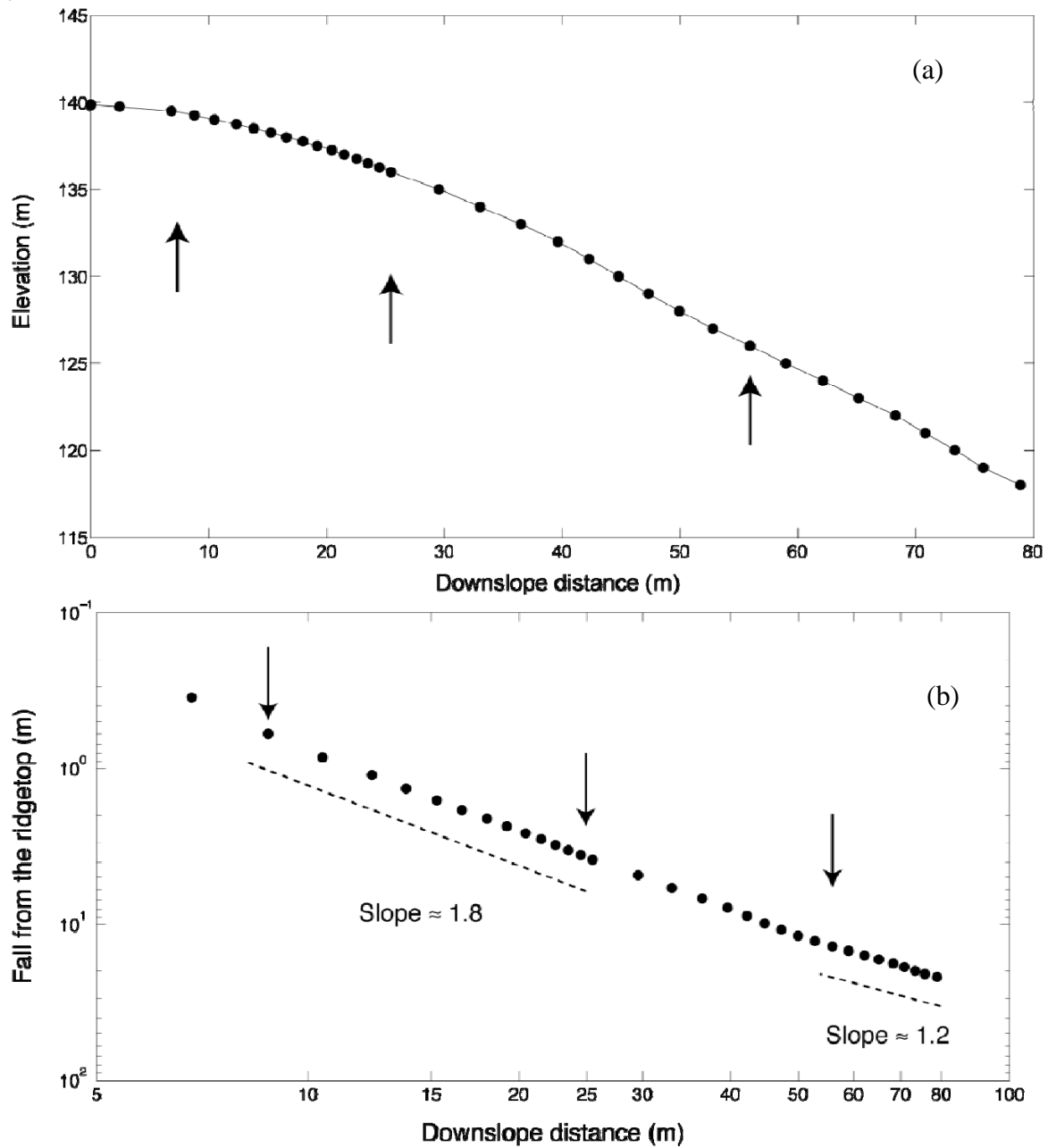
Figure 4. (a) Longitudinal profile of a hillslope reproduced from the survey data collected by *McKean et al.* [1993]. (b) Log-log plot of the fall from the hilltop versus horizontal distance. Notice the power law regime with exponent 1.8 starting at approximately 8 m from the ridgetop until 25 m downslope. This profile is consistent with a non-local flux hypothesis with exponent $\alpha = 1.8$. The abrupt transition to a slope of 1.2 on the lower portion of the hillslope is indicative that this part is still experiencing changes from net erosion to progressive soil accumulation.

15
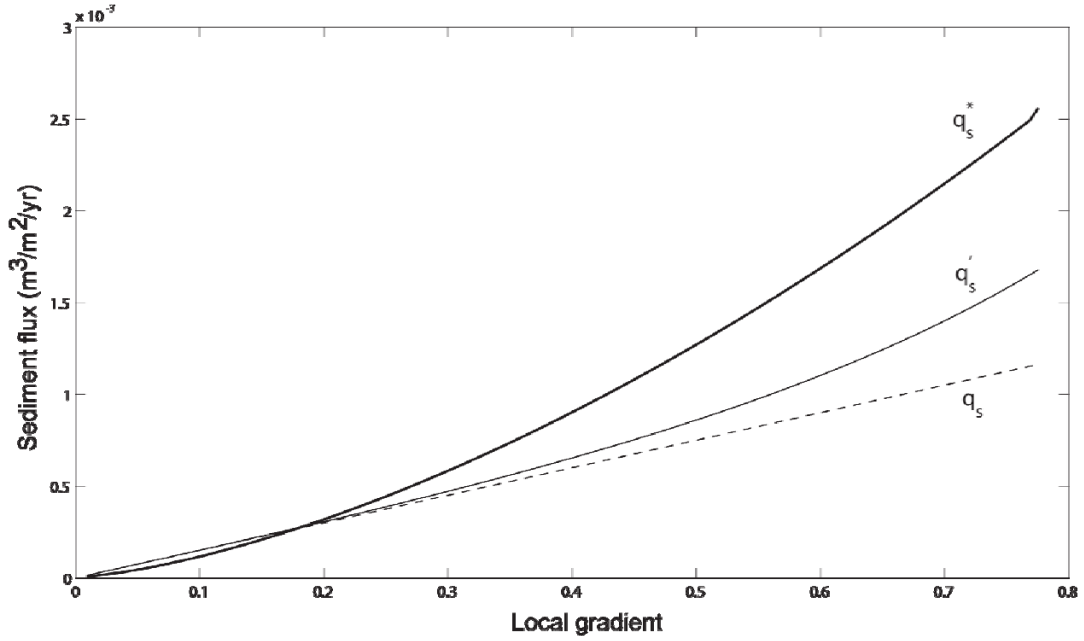
Figure 5: Comparison of the three flux laws. The dashed line shows the sediment flux predicted by linear, local flux law (equation (1)). The thick line shows the sediment flux predicted by the linear, non-local law (equation (8)) and the thin line shows the sediment flux predicted by local, non-linear (equation (19)). The parameters for $q_s^{'}$ are chosen to be $K = 0.0015 \, m^2 / yr$ and $S_c = 1.4$ (from *Roering et al.* [1999]). The parameters for the calculation of q_s^{*} are chosen to be $\alpha = 1.5$ and $K^{*} = 0.0007 \, m^{1.5} / yr$.
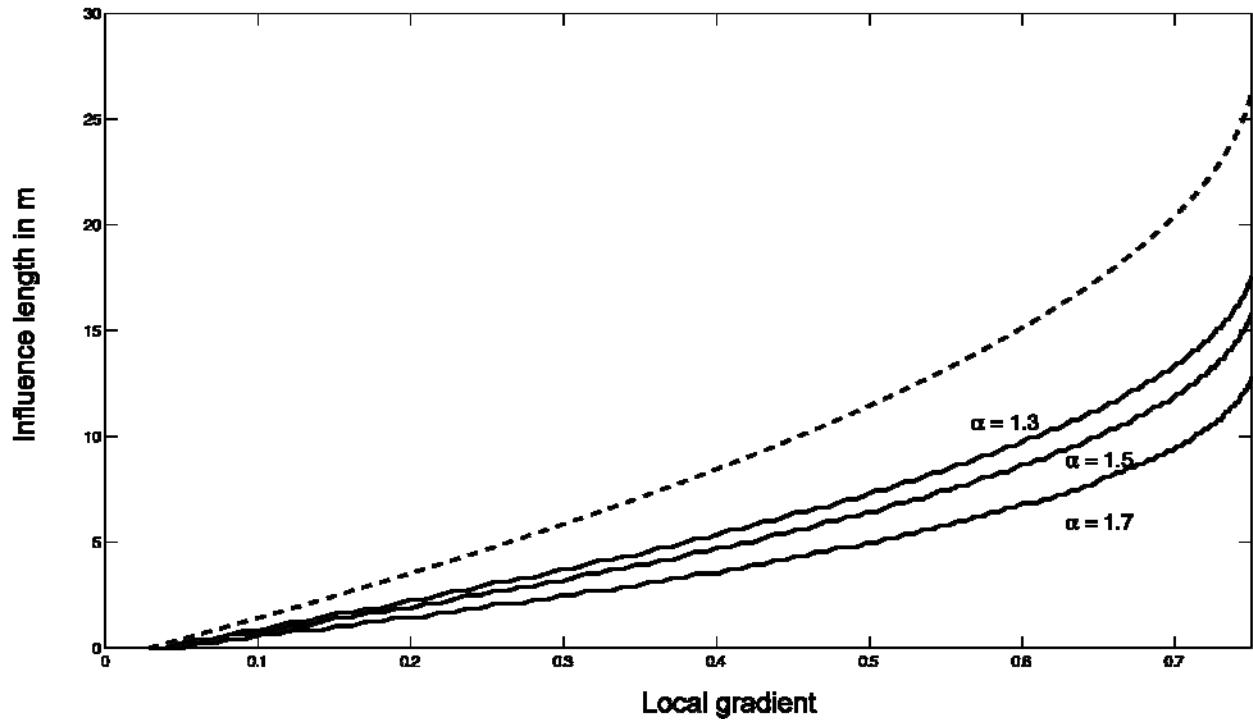
Figure 6: Plot showing the upslope influence length L_α (see text for definition) as a function of local gradient and degree of non-locality for the hillslope of *Roering et al*. [1999]. The dashed line indicates the distance to the ridgetop, in other words, the maximum available distance to take part in the transport.
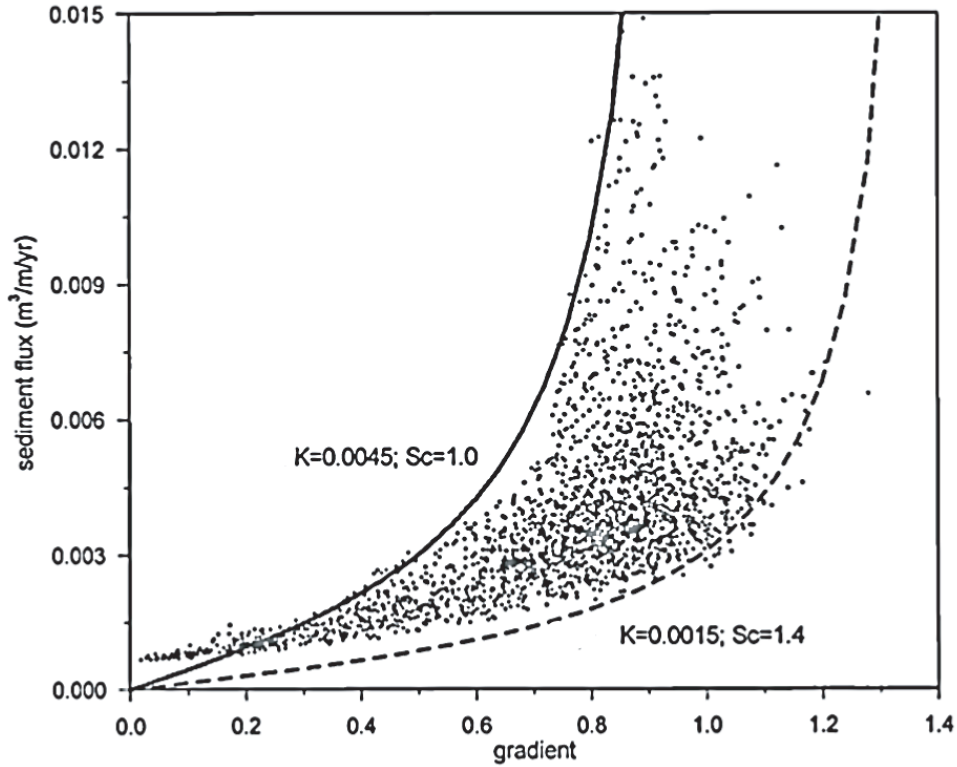
Figure 7: Figure reproduced from *Roering et al.* [1999] to illustrate the large natural variability of calculated sediment flux (dots) even in a small hillslope (MR1 basin in Oregon Coast Range; sediment flux calculated using equation (23)), and the wide range of fitted parameters K (m^2/yr) and S_c that would be needed to reproduce the observed variability under the assumption of a non-linear local transport law.
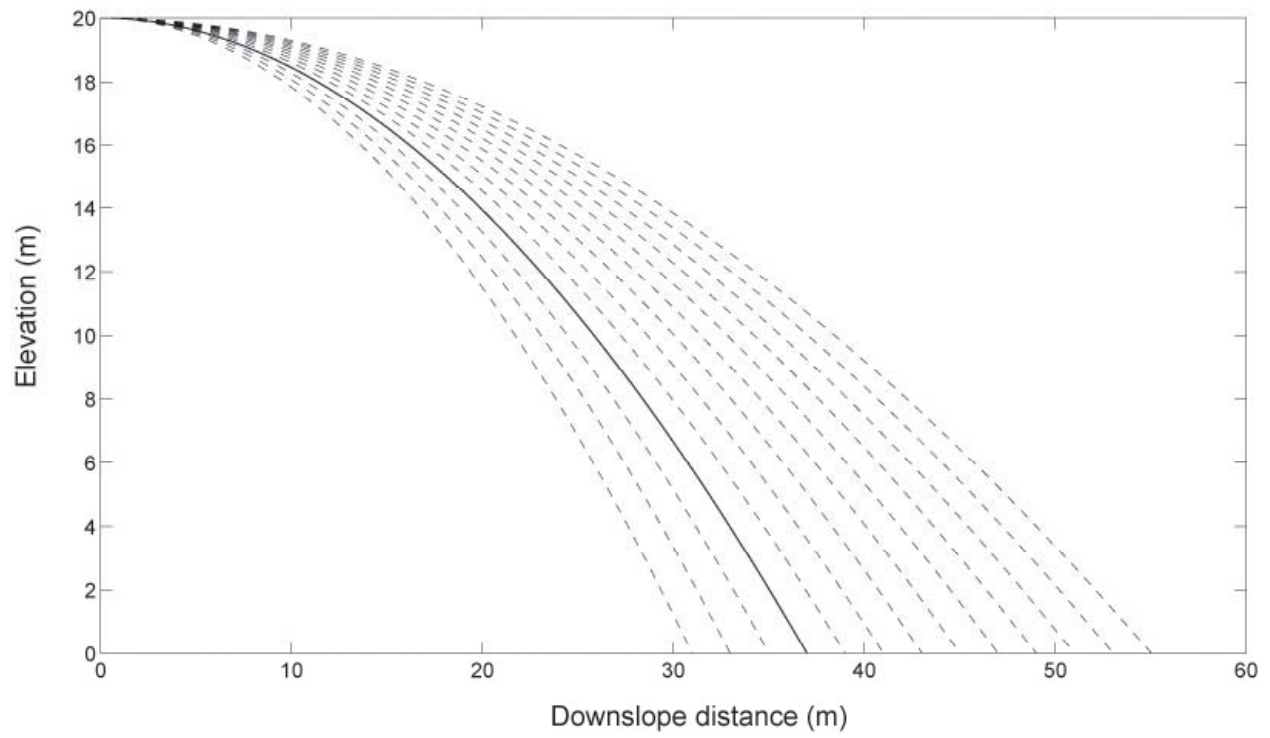
Figure 8: Plot showing the suite of generated hillslope profiles to imitate the natural variability of profiles (flowpaths perpendicular to contour lines) in a zero-order basin. The thick line indicates the profile reproduced from *Roering et al.* [1999].
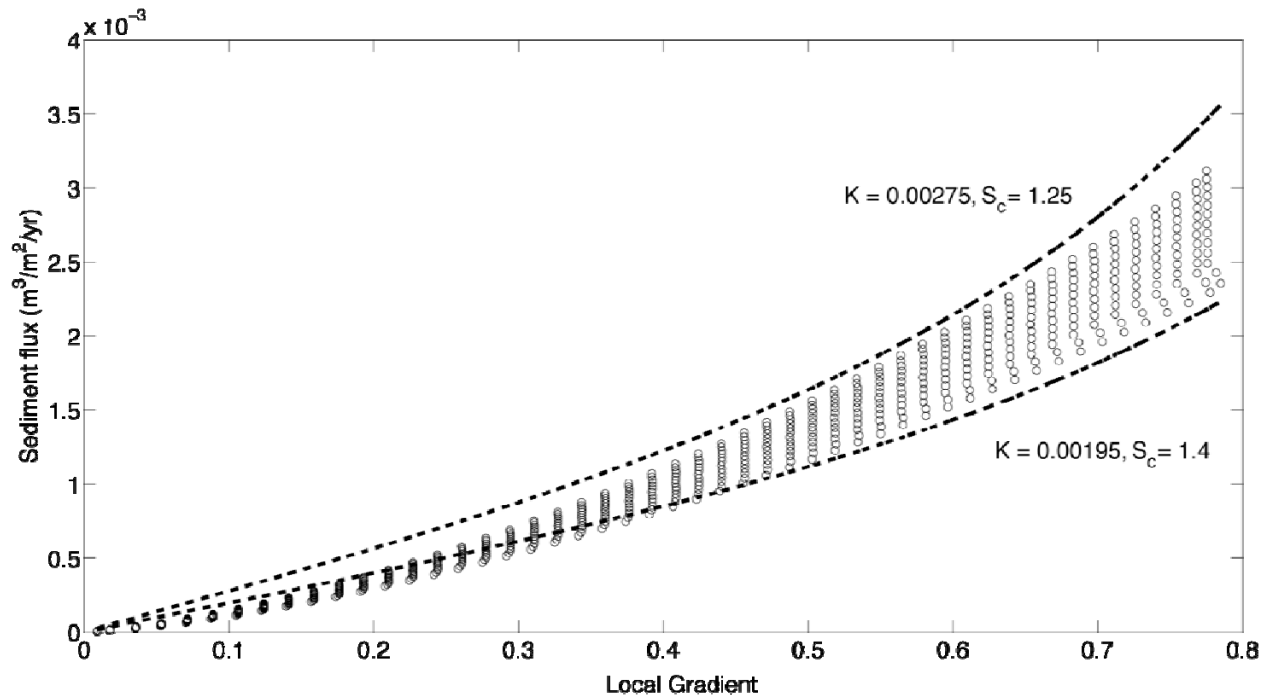
Figure 9: Sediment flux computed on the suite of hillslope profiles (shown in Figure 8) using the linear, non-local transport law (equation 8) with parameters α = 1.5 and K^{*} = 0.0007 m^{α} / yr (open circles). Note that while these parameters are kept constant, a large variability of the sediment flux is produced due to the variability in the ensemble of profiles. In order to reproduce this variability with the non-linear transport law (equation 19), the range of fitted parameters required (concentrating on the higher gradients where the non-linear transport law is more pertinent – see also Fig. 8) is: K = 0.00195 m^{2} / yr and S_{c} = 1.4, and K = 0.00275 m^{2} / yr and S_{c} = 1.25 (broken lines).

Normal and Anomalous Diffusion of Gravel Tracer Particles in Rivers

Vamsi Ganti,[1] Mark M. Meerschaert,[2] Efi Foufoula-Georgiou,[1] Enrica Viparelli,[3]and Gary Parker[3]

Abstract. One way to study the mechanism of gravel bedload transport is to seed the bed with marked gravel tracer particles within a chosen patch, and to follow the pattern of migration and dispersal of particles from this patch. In this study, we invoke the probabilistic Exner equation for sediment conservation of bed gravel, formulated in terms of the difference between the rate of entrainment of gravel into motion and the rate of deposition from motion. Assuming an active layer formulation, stochasticity in particle motion is introduced by considering the step length (distance traveled by a particle once entrained until it is deposited) as a random variable. For step lengths with a relatively thin (e.g., exponential) tail, the above formulation leads to the standard advection-diffusion equation for tracer dispersal. However, the complexity of rivers, characterized by a broad distribution of particle sizes, and extreme flood events transporting bed material, can give rise to a heavy tailed distribution of step lengths. This consideration leads to an anomalous advection-diffusion equation involving fractional derivatives. By identifying the probabilistic Exner equation as a forward Kolmogorov equation for the location of a randomly selected tracer particle, a stochastic model describing the temporal evolution of the relative concentrations is developed. The normal and anomalous advection-diffusion equations are revealed as its long-time asymptotic solution. Sample numerical results illustrate the large differences that can arise in predicted tracer concentrations under the normal and anomalous diffusion models. They highlight the need for intensive data collection efforts to aid the selection of the appropriate model in real rivers.

1. Introduction

The stones that make up the bed of gravel-bed rivers are transported as bedload during floods. During periods of overall transport, each particle undergoes alternating periods of movement and rest. Movement consists of rolling, sliding or saltation, which continues until a single step length of motion is completed. The particle is at rest when it is deposited, either on the bed or deeper within the deposit. One way to study the mechanism of bedload transport in gravel bed rivers is to seed the bed with marked tracer particles within some small area of the bed (patch), and to follow the pattern of migration and dispersal of particles from that patch [e.g., *Hassan and Church*, 1991; *Church and Hassan*, 1992; *Wilcock*, 1997; *Ferguson and Wathen*, 1998; *Ferguson and Hoey*, 2002; *Pyrce and Ashmore*, 2003]. Tracers provide a way of characterizing not only mean parameters pertaining to transport, but also the stochasticity of particle motion itself.

This stochasticity was first elaborated by *Einstein* [1937]. Einstein based his analysis on experimental observations of painted tracer particles. He noted that: "The results demonstrated clearly that even under the same experimental conditions stones having essentially identical characteristics were transported to widely varying distances · · · Consequently, it seemed reasonable to approach the subject of particle movement as a probability problem." Einstein considered a particle that moves in discrete steps punctuated by periods of inactivity. He quantified the problem in terms of the statistics of step length and resting period (waiting time). *Einstein* [1942] went on to explain how these quantities enter into the delineation of macroscopic relations of bedload transport

(i.e., relations that represent averages over the stochasticity of sediment motion). More specifically, *Einstein* [1942] showed that the bedload transport rate is proportional to the step length and inversely proportional to the resting period. Following the seminal work of *Einstein* [1942], many stochastic theories for sediment transport have been proposed which account for the aforementioned stochasticity (see for example, *Einstein and El-Sammi* [1949]; *Paintal* [1971]; *Nelson et al.* [1995]; *Cheng and Chiew* [1998]; *Lopez and Garcia* [2001]; *Kleinhans and van Rijn* [2002]; *Cheng* [2004]; *Cheng et al.* [2004]; *Charru et al.* [2004], *Ancey et al.* [2006, 2008]; *Ancey* [2009]; *Furbish et al.* [2009],*Ganti et al.* [2009] and references therein).

Two macroscopic quantities that can be captured by means of statistical analyses of tracer motion are the overall tendencies of ensembles of tracers to be advected downstream, and to disperse, or diffuse. (Various authors use the terms "dispersion" or "diffusion" of tracers to describe the same process: here we rather arbitrarily use the term "diffusion".) Both advection and diffusion are governed by a wide range of factors.

Bedload particles may roll, slide or saltate over the bed. In the case of grains of uniform size, mean saltation length may be on the order of ten diameters [e.g., *Niño and Garcia*, 1998]; whereas mean step length may be on the order of 100 grain diameters [*Einstein*, 1950; *Tsujimoto*, 1978; *Wong et al.*, 2007]. *Einstein* [1950] suggested that mean step length can be approximated as a constant multiple of grain diameters, whereas *Wong et al.* [2007] indicate a weak variation with Shields number, which is a proxy for flow strength. Step length is known, however, to vary stochastically [e.g., *Tsujimoto*, 1978]. As illustrated below, this stochasticity is one source of diffusion.

When a particle comes to rest, it may deposit so as to be exposed at the bed surface, or it may become buried at depth [e.g., *Hassan and Church*, 1994]. From a statistical

point of view, deeper burial in general implies a longer resting time before exhumation and re-entrainment. This effect can influence both diffusion and advection [*Ferguson and Hoey*, 2002]. Most natural gravels consist of a mixture of grain sizes, each of which undergoes steps and resting periods according to size-specific probabilities. For example, *Tsujimoto* [1978] has shown that larger grains in a mixture have longer step lengths, but also longer resting times. As these different sizes move downstream, their motion is affected by the presence of bedforms such as dunes [e.g., *Blom et al.*, 2006], bars and bends associated with channel meandering/braiding [e.g., *Pyrce and Ashmore*, 2003], and large-scale variations in channel width. In addition, the bed may be undergoing aggradation, which enhances the capture of bedload particles, or degradation, which causes the exhumation of grains that have undergone long-term storage [e.g., *Ferguson and Hoey*, 2002]. Grains can also enter floodplain storage for long periods of time, and then be exhumed as the channel migrates into the relevant deposit [e.g., *Bradley*, 1970; *Lauer and Parker*, 2008a, b]. Again, all these effects can influence the advection/diffusion of tracer particles.

The macroscopic transport of grains undergoing steps and rest periods governed by statistical laws can be most simply characterized in terms of the classical advection-diffusion model, according to which the particles spread downstream with a constant diffusivity. When step lengths and rest periods are governed by a multiplicity of mechanisms over a very wide range of spatial and temporal scales, however, the advection/diffusion of tracer particles may no longer be characterizable in terms of the classical model. It is widely known in the groundwater literature that a multiplicity of scales over which transport takes place can lead to "anomalous diffusion", for which the advection/diffusion equation can be characterized by fractional derivatives [e.g., *Benson*, 1998; *Berkowitz et al.*, 2002; *Cushman and Ginn*, 2000; *Schumer et al.*, 2003].

Nikora et al. [2002] have studied the diffusion of bedload particles using the measured motion of individual particles in a canal as the basis for ensemble averaging. They extracted from their data various moments characterizing particle location as a function of time. They delineated three ranges of temporal and spatial scales, each with different regimes of diffusion: ballistic diffusion (at the scale of saltation length), normal/anomalous diffusion (at a scale of step length) and sub-diffusion (at global scale). Their study thus represents a pioneering effort in the identification of anomalous diffusion of bedload particles.

We develop here a theoretical model for the study of anomalous diffusion of tracer particles moving as bedload. The present model is not intended to be comprehensive, in that it covers only a restricted set of phenomena that might lead to anomalous diffusion. It is our desire, however, that this first model should serve as an example illustrating the pathway to more general models of anomalous diffusion.

The paper is structured as follows. In Section 2, a straightforward formulation of the Exner equation for sediment conservation is presented which incorporates the probability density function (pdf) for step lengths, i.e., the distances traveled by particles once they are entrained to when they are deposited again on the river bed. In Section 3 we show that the assumption of step lengths having a distribution with thin tails (e.g., exponential, normal, log-normal distributions) leads to a classical advection-diffusion equation for tracer dispersal. However, in real rivers the complexity resulting from broad distributions of particle sizes and flood events can lead to a heavy tail in the pdf of step lengths (arising, for example, from the combination of an exponential distribution for step length conditional on a particle size and a gamma distribution of particle sizes). In Section 4, we show that this consideration leads to an anomalous advection-diffusion formulation which includes fractional derivatives. That model was introduced earlier in the context of other problems, such as groundwater dispersion. Section 5 shows how a heavy-tail step length distribution can arise from a thin-tailed (exponential) pdf of step length for particles of a given size, together with a thin-tailed grain size distribution. In Section 6, we build a stochastic model to describe the time evolution of the relative concentration of the tracers in the active layer, and show that the approximate solutions obtained in Sections 3 and 4 are long-time asymptotic solutions of the derived model. Finally, in section 7, numerical results are presented showing the difference between normal and anomalous advection-diffusion of gravel tracer particles.

2. Formulation

The starting point for our analysis is the entrainment-based one-dimensional Exner equation for sediment balance [*Tsujimoto*, 1978; *Parker et al.*, 2000; *Garcia*, 2008];

$$(1 - \lambda_p) \frac{\partial \eta(x,t)}{\partial t} = D_b(x,t) - E_b(x,t) \qquad (1)$$

where η denotes local mean bed elevation, t denotes time, x denotes the downstream co-ordinate, D_b denotes the volume rate per unit area of deposition of bedload particles onto the bed, E_b denotes the volume rate per unit area of entrainment of bed particles into bedload, and λ_p is the porosity of bed sediment. We assume that, once entrained, a particle undergoes a step with length r before depositing. We further assume that this step length is probabilistic, with a probability density $f_s(r)$ (pdf of step length). The deposition rate of tracers $D_b(x,t)$ is then given as:

$$D_b(x,t) = \int_0^\infty E_b(x - r, t) f_s(r) dr \qquad (2)$$

In the above formulation E_b is a macroscopically determined parameter, which can be shown to vary inversely with the mean resting time of a particle. The formulation thus includes the effect of stochasticity in step length, but not in resting time.

A model formulation for tracers that simplifies the above-mentioned model of entrainment and deposition is the active layer formulation. According to this formulation, grains in an active bed layer of thickness L_a below the local mean bed surface exchange directly with bedload grains. Grains below the active layer, i.e., grains in the substrate, exchange with the active layer only by means of bed aggradation (when active layer grains are transferred to the substrate) and degradation (when substrate grains are transferred to the active layer). In such a model, substrate grains do not directly exchange with the bedload grains.

Let $f_a(x,t)$ denote the fraction of tracer particles in the active layer at any location x and time t. In addition, let $f_I(x,t)$ denote the fraction of tracer particles in the sediment that is exchanged across the interface between the active layer and the substrate as the bed aggrades or degrades. The equation of mass conservation of tracers can then be written as:

$$(1 - \lambda_p) \left(f_I(x,t) \frac{\partial \eta(x,t)}{\partial t} + L_a \frac{\partial f_a(x,t)}{\partial t} \right) = D_{bT}(x,t) - E_{bT}(x,t) \qquad (3)$$

where E_{bT} denotes the volume entrainment rate of tracers and D_{bT} denotes the corresponding deposition rate, which are given as [*Parker et al.*, 2000]:

$$E_{bT}(x,t) = E_b(x,t) f_a(x,t) \qquad (4)$$

and

$$D_{bT}(x,t) = \int_0^\infty E_b\,(x-r,t)\,f_a\,(x-r,t)\,f_s(r)dr \qquad (5)$$

Here we exclude the complication induced by bedforms such as dunes [e.g., *Blom et al.*, 2006] by considering conditions of lower regime plane-bed transport, such as those investigated by *Wong et al.* [2007].

The fraction f_I of tracers exchanged at the interface as the mean bed elevation fluctuates can be expected to differ depending upon whether or not the bed is aggrading or degrading. *Hoey and Ferguson* [1994] and *Toro-Escobar et al.* [1996] have suggested forms for interfacial exchange fractions which can be adapted to the problem of tracers. Here we restrict consideration to the case for which the bed elevation is at equilibrium, so that L_a, E_b, η and the pdf $f_s(r)$ are all constant in x and t. Under this condition, equations (3), (4) and (5) reduce to:

$$(1 - \lambda_p)\,\frac{L_a}{E_b}\,\frac{\partial f_a(x,t)}{\partial t} = \int_0^\infty f_a\,(x-r,t)\,f_s(r)dr - f_a(x,t) \tag{6}$$

The nature of the pattern of tracer diffusion predicted by equation (6) depends on the nature of the pdf $f_s(r)$ of step lengths. As shown in the next sections, a thin-tailed pdf, i.e., one for which all moments of $f_s(r)$ exist, leads to a classical Fickian advection-diffusion equation, while a heavy-tailed pdf, i.e., one for which moments larger than a given order do not exist, can lead to an anomalous advection-diffusion equation.

3. Tracer transport with thin-tailed step length distribution

In this section, we show that a thin-tailed pdf for the step length distribution, $f_s(r)$, in equation (6) leads to a classical Fickian (normal) advection-diffusion equation. For simplicity, we assume the porosity to be zero, i.e., $\lambda_p = 0$. The simplest way to solve the integral equation (6) is to use Fourier transforms, since the convolution becomes a product in Fourier space. The Fourier transform of a function $f_a(x,t)$ is given by:

$$\hat{f}_a(k,t) = \int_{-\infty}^\infty e^{-ikx} f_a(x,t)\,\mathrm{d}x \tag{7}$$

Taking the Fourier transforms in equation (6) and manipulating yields:

$$\frac{L_a}{E_b}\,\frac{\partial \hat{f}_a(k,t)}{\partial t} = \left(\hat{f}_s(k) - 1\right)\hat{f}_a(k,t) \tag{8}$$

Expanding the Fourier transform of $f_s(r)$ as Taylor series gives:

$$\hat{f}_s(k) = 1 - ik\mu_1 + \frac{1}{2}\,(ik)^2\,\mu_2 + \cdots \tag{9}$$

where $\mu_n = \int r^n f_s(r)dr$ denotes the nth order moment of the step length distribution. The above expansion is valid provided that the moments μ_n exist and are finite, and the series converges uniformly in a neighborhood of $k = 0$ [*Papoulis and Pillai*, 2002]. Substituting equation (9) into (8) we obtain:

$$\frac{L_a}{E_b}\,\frac{\partial \hat{f}_a(k,t)}{\partial t} = \left(-ik\mu_1 + \frac{1}{2}\,(ik)^2\,\mu_2 + \cdots\right)\hat{f}_a(k,t) \quad (10)$$

Recall that $(ik)\hat{f}_a(k,t)$ is the Fourier transform of $\partial f_a(x,t)/\partial x$. By making the approximation that higher order terms can be neglected (which will be shown equivalent, in Section 6, to considering a long-time asymptotic solution), and by setting $v = \mu_1$ and $2D_d = \mu_2$, it follows by

an inverse Fourier transform that the function $f_a(x,t)$ is the approximate solution to the advection-diffusion equation:

$$\frac{L_a}{E_b}\,\frac{\partial f_a}{\partial t} = -v\frac{\partial f_a}{\partial x} + D_d\frac{\partial^2 f_a}{\partial x^2} \tag{11}$$

This is the standard form of the advection-diffusion equation for tracer dispersal, and applies under equilibrium bedload conditions where v and D_d can be considered constant. The associated Green's function, i.e., the solution to the above equation with a pulse as the initial condition at $t = 0$, is the Gaussian distribution, which describes the tracer concentration at any given time $t > 0$. If the source is distributed in space and/or time, the solution to equation (11) is the convolution of the Green's function with the source.

4. Tracer transport with heavy-tailed step length distribution

As detailed in the next section, a heavy-tailed, power-law distribution for step lengths in gravel bed rivers can result from a thin-tailed pdf of step length for particles of a given size, together with a thin-tailed pdf of grain sizes. In this section, we develop a formalism that incorporates heavy tails for the step length distribution in the probabilistic Exner equation. In equation (6), consider $f_s(r)$ to be a step length distribution with power-law decaying tail, i.e., $f_s(r) \approx C\alpha r^{-\alpha-1}$ for $r > 0$ sufficiently large, some constant $C > 0$, and some power law index $1 < \alpha < 2$. In this case, the Fourier transform expansion (9) in terms of statistical moments of $f_s(r)$ is not valid, as the integrals $\mu_n = \int r^n f_s(r)dr$ do not converge for $n > 1$ [e.g., *Lamperti*, 1962]. Instead, we may use a fractional Taylor expansion to write [*Odibat and Shawagfeh*, 2007; *Wheatcraft and Meerschaert*, 2008]:

$$\hat{f}_s(k) = 1 - ik\mu_1 + c_\alpha\,(ik)^\alpha + \cdots \tag{12}$$

where c_α is a constant that depends only on C and α. Substituting back in equation (8) we obtain:

$$\frac{L_a}{E_b}\,\frac{\partial \hat{f}_a(k,t)}{\partial t} = (-ik\mu_1 + c_\alpha\,(ik)^\alpha + \cdots)\,\hat{f}_a(k,t) \tag{13}$$

This equation (13) can be understood in terms of fractional derivatives. Fractional derivatives are close cousins of their integer order counterparts. The fractional derivative $\partial^\alpha f_a(x,t)/\partial x^\alpha$ can be defined simply as the function whose Fourier transform is $(ik)^\alpha\,\hat{f}_a(k,t)$. As in the normal advection-diffusion case, we make an approximation by including the first two terms in the expansion and neglecting the higher order terms (shown equivalent in Appendix A to a long-time asymptotic solution). Then by setting $v = \mu_1$ and $D_d = c_\alpha$, it follows from (13) that the function $f_a(x,t)$ is approximately the solution of the fractional advection-diffusion equation:

$$\frac{L_a}{E_b}\,\frac{\partial f_a}{\partial t} = -v\frac{\partial f_a}{\partial x} + D_d\frac{\partial^\alpha f_a}{\partial x^\alpha} \tag{14}$$

Fractional advection-diffusion has been extensively used in modeling the dispersal of tracers or pollutants in porous media which exhibit multiple scales of variability, as in subsurface transport [e.g., *Benson et al.*, 2000a, b; *Berkowitz et al.*, 2002] and pollutant transport in rivers [e.g., *Deng et al.*, 2005, 2006]. However, to the best of our knowledge, its application has not yet been explored in the context

of river transport, apart from a recent study which uses fractional advection for transporting sediment in buffered bedrock rivers [*Stark et al.*, 2009].

In most natural rivers, the distribution of step lengths holds in the near field, but eventually transport steps become limited by river features (e.g., bars) that change the intermediate and far field distributions. The application of the governing equations (11) and (14) depends on the natural truncation of the step length distributions. If the truncation occurs at a very small threshold, then the Central Limit Theorem applies and a standard advection-diffusion equation will be the governing equation for the fraction of tracers in the active layer. However, if the truncation occurs at a large threshold, then the distribution can still be approximated by a power-law in the intermediate field and the governing equation for the fraction of tracers in the active layer is the fractional advection-diffusion equation. It is worth noting that equation (14) is the governing equation on scales where the power-law approximation of the step length distribution is accurate. In the next section, we explain how a power-law distribution for step lengths could emerge by combining a thin-tailed pdf of step length for particles of a given size with a thin-tailed pdf of grain sizes. Then in Section 6 we describe the stochastic model underlying the probabilistic Exner equation (6), and we show how equations (11) and (14) represent long-time asymptotic solutions.

5. Transport of sediment mixtures

A generalization of equation (6) for a range of grain sizes D can be expressed as follows. Let $f_{ad}(x, t, D)$ denote the fraction of tracers in the active layer with grain size D, so that,

$$f_a(x,t) = \int_0^\infty f_{ad}(x,t,D)dD \qquad (15)$$

In addition, let $E_{bu}(D)$ denote the entrainment rate per unit bed content of size D. The generalization of equation (6) is then [e.g., *Parker*, 2008],

$$(1 - \lambda_p) L_a \frac{\partial f_a(x,t,D)}{\partial t} = E_{bu}(D) \left(\int_0^\infty f_{ad}(x-r,t,D) f_s(r|D) dr - f_{ad}(x,t,D) \right) \qquad (16)$$

In the above formulation, the conditional pdf of step length f_s is specified as a function of grain size, but the thickness of the active layer L_a is taken to be a constant for all grain sizes. The form corresponding to equation (6) is obtained by integrating over all grain sizes,

$$(1 - \lambda_p) L_a \frac{\partial f_a(x,t)}{\partial t} = \int_0^\infty E_{bu}(D) \left(\int_0^\infty f_{ad}(x-r,t,D) f_s(r|D) dr \right) dD \qquad (17)$$

In general, E_{bu} and f_{ad} can both be expected to vary significantly in D. Closure of equation (17) requires specification of forms for E_{bu} and f_{ad} as functions of, among other parameters, grain size D. Such forms are available in the literature [e.g., *Tsujimoto*, 1978].

The goal of the present analysis is, however, to study the role of heavy-tailed pdfs for step lengths in driving the diffusion of tracer particles. With this in mind, the problem is simplified for the purposes of illustration to one in which f_{ad} varies in D but E_{bu} does not. More specifically, by assuming independence of grain size D on space-time location (x, t), one can write $f_{ad}(x, t, D) = f_a(x, t)f(D)$. Then unconditioning $f_s(r|D)$ with the grain size pdf $f(D)$ in equation (17) is used to develop the Exner equation for a grain size mixture. In the next subsection, we show that a heavy-tailed pdf for step lengths in a mixture of particles can emerge, under certain conditions, from two thin-tailed pdfs.

5.1. Power laws emerging from thin tails

A typical finding in sediment transport is that step lengths r are exponentially distributed for a given grain size D [e.g., *Nakagawa and Tsujimoto*, 1976, 1980], i. e.,

$$\mathbb{P}(R > r \,|\, D) = e^{-r/\mu_r(D)} \qquad (18)$$

where $\mu_r(D)$ is the mean step length as a function of grain size D. If we let f denote the pdf of grain sizes, then the unconditional distribution of step length can be derived from:

$$\mathbb{P}(R > r) = \int_0^\infty e^{-r/\mu_r(D)} f(D) \, dD. \qquad (19)$$

The resulting pdf for step length, relating to a mixture of particle sizes, depends on both the mean step length $\mu_r(D)$ for grains of size D, and the pdf of grain sizes.

In this study we explore two distinct cases, one in which $\mu_r(D)$ increases with grain size, and another for which $\mu_r(D)$ decreases with grain size. The true dependence of mean step length on grain size in sediment mixtures remains somewhat ambiguous. In the case of uniform sediment, *Niño and Garcia* [1998] found that grain saltation length decreases with increasing grain size. One step length, however, typically consists of around 10 saltation lengths. *Hassan and Church* [1992] have studied the travel distance of size mixtures of stones in gravel-bed rivers, and have found a marked tendency for travel distance to decrease with increasing grain size. This result must be qualified in light of the fact that the distance traveled by a grain during a flood can be expected to be associated with multiple step lengths. This qualification notwithstanding, the data suggest a range of conditions under which the dependence between grain size and mean travel distance can be approximated by the simplified model:

$$\mu_r(D) = \kappa/D \qquad (20)$$

where κ is a constant. A lognormal pdf of grain sizes

$$f(D) = \frac{1}{D\sigma\sqrt{2\pi}} e^{-\frac{1}{2}\frac{(\ln D - \mu)^2}{\sigma^2}} \qquad (21)$$

was invoked by *Wilcock and Southard* [1989]; *Garcia* [2008]; *Lanzoni and Tubino* [1999]; *Parker* [2008], where μ, σ are the mean and standard deviation of the sedimentological scale $\psi = \ln D$. The overall (unconditional) step length distribution can then be obtained, in principle, by substituting equations (20) and (21) into equation (19) and computing the integral. However, this integral is difficult to compute analytically with a log-normal form for $f(D)$. Figure 1 shows the grain size data from *Wilcock and Southard* [1989] along with a lognormal fit, as well as an alternative gamma distribution fit to the same data. The gamma pdf

$$f(D) = \frac{\nu^\nu}{\Gamma(\nu)D_m{}^\nu} D^{\nu-1} \exp\left(-\nu \frac{D}{D_m}\right) \qquad (22)$$

with mean D_m and shape parameter ν provides a convenient alternative to the lognormal distribution that makes it possible to analytically evaluate the integral (19). Following the argument of *Stark et al.* [2009], we substitute equations (20) and (22) into equation (19) and evaluate the integral to obtain the unconditional probability distribution of step length:

$$\mathbb{P}(R > r) = \left(1 + \left(\frac{D_m}{\nu\kappa}\right) r\right)^{-\nu} \qquad (23)$$

The above equation (23) represents a heavy-tailed power-law pdf for the step length distribution arising from a thin-tailed pdf of step length combined with a thin-tailed pdf of

grain sizes. The distribution in equation (23) is known as the Generalized Pareto, and its variance exists only when the shape parameter $\nu > 2$ [*Feller*, 1971]. The Generalized Pareto distribution also arises from exceedances over a fixed high threshold, and has consequently been used in modeling extreme floods and other hydrological phenomena [e.g., *Hosking and Wallace*, 1987].

The relationship (20) between mean step length and grain size may not be applicable in all situations. Depending upon the grain size distribution and the flow conditions, large particles may roll over holes that trap smaller particles, so that step length increases with grain size. Such a tendency has been reported in the experiments of *Tsujimoto* [1978]. Also *Wong et al.* [2007] observed that, in the case of uniform sediment subject to the same bed shear stress, step length increases with grain size. Such an increase in step length does not directly translate into a higher bedload transport rate for coarser grains, because the entrainment rate $E_{bu}(D)$ in equation (17) may decline with increasing grain sizes. In the present simplified analysis, where E_{bu} is assumed to be independent of grain size, the tendency for step length to increase with grain size can be captured in terms of the following simple form:

$$\mu_r(D) = \kappa D \quad (24)$$

where κ is a constant.

If D has an inverse gamma pdf with mean D_m and shape parameter ν, also similar in shape to the lognormal,

$$f(D) = \frac{(\nu - 1)^\nu D_\mathrm{m}{}^\nu}{\Gamma(\nu)} D^{-\nu - 1} \exp\left(-\frac{(\nu - 1)D_\mathrm{m}}{D}\right) \quad (25)$$

then a change of variables $y = 1/D$ in (19) leads to another generalized Pareto:

$$\mathbb{P}(R > r) = \left(1 + \left(\frac{1}{(\nu - 1)D_\mathrm{m}\kappa}\right) r\right)^{-\nu} \quad (26)$$

as shown in *Hill et al.* [2009], so that again the step length distribution averaged over all particle sizes has a heavy tail.

Note that in both cases considered above, whether mean step length increases or decreases with grain size, a heavy-tailed distribution for step lengths can emerge from a combination of two thin-tailed distributions. The gamma and inverse gamma distributions are used for particle sizes, as opposed to the more typical log-normal distribution, in order to derive analytically the heavy-tail pdf of the resulting step length distribution for a mixture of grain sizes. The alternative pdf assumption should be considered reasonable if the reader accepts that the fitted log-normal and gamma distributions for the grain size data from *Wilcock and Southard* [1989] in Figure 1 are practically indistinguishable. We hasten to emphasize, however, that the finding of a possible heavy-tailed pdf for step length is by no means universal. Many different choices of the grain size pdf $f(D)$ would certainly lead to a thin-tailed pdf of step length. Our point is simply that both thin-tail and heavy-tail models are reasonable, and hence it becomes very important to investigate the grain size distributions more exhaustively, to determine which type of overall step length pdf applies in a given situation.

6. Stochastic model for gravel transport in rivers

In this section, we develop a stochastic model to describe the time evolution of the relative concentration of gravel tracer particles in rivers. We derive an exact solution for $f_a(x,t)$ and show that, in the long-time asymptotic limit,

a thin tail for the step length distribution leads to classical advection-diffusion, whereas heavy tails for the step length distribution leads to anomalous advection-diffusion. We start by rewriting (6) in the equivalent form:

$$\frac{\partial f_a(x,t)}{\partial t} = -\lambda f_a(x,t) + \lambda \int_0^\infty f_a(x - r, t) f_s(r) \, \mathrm{d}r \quad (27)$$

where $\lambda = E_b/L_a$ is the rate at which particles are entrained. The Fourier transform of the above equation is given by:

$$\frac{\partial \hat{f}_a(k,t)}{\partial t} = -\lambda \hat{f}_a(k,t) \left(1 - \hat{f}_s(k)\right) \quad (28)$$

Equation (27) describes the time evolution of the pdf $f_a(x,t)$ and can be regarded as a Kolmogorov forward equation for some Markov process $X(t)$, where $X(t)$ represents the location of a randomly selected gravel particle at time $t > 0$ [see *Feller*, 1971]. In this context, $f_a(x,t)$ is the pdf of the random variable $X(t)$. In this Markov process, the waiting time between entrainments has an exponential distribution with a rate parameter λ, and the number of entrainment events, $N(t)$, by any time $t > 0$ has a Poisson distribution with mean λt [*Feller*, 1971], i.e.,

$$P[N(t) = n] = e^{-\lambda t} \frac{(\lambda t)^n}{n!} \quad (29)$$

Let Y_n denote the travel distance during the nth entrainment period. Since there are $N(t)$ entrainment periods by time $t > 0$, the particle location at some time $t > 0$ is given by the random sum:

$$X(t) = Y_1 + \cdots + Y_{N(t)} = \sum_{i=1}^{N(t)} Y_i \quad (30)$$

This random sum is a compound Poisson process [e.g., *Feller*, 1971]. Its pdf can be derived directly from equation (28) whose point source solution is:

$$\hat{f}_a(k,t) = \exp\left(-\lambda t \left(1 - \hat{f}_s(k)\right)\right) \quad (31)$$

As a result, the fraction of tracers in the active layer, $f_a(x,t)$, can be obtained by taking the inverse Fourier transform of (31) and is given by:

$$f_a(x,t) = e^{-\lambda t} \sum_{n=0}^\infty \frac{(\lambda n)^n}{n!} f_s^{n^*}(x) \quad (32)$$

where $f_s^{n^*}(x)$ is the n-fold convolution of the density function $f_s(x)$ (recall that $f_s^{n^*}(x)$ is the inverse Fourier transform of $\hat{f}_s(k)^n$), which is also the pdf of $Y_1 + \cdots + Y_n$. One way to understand this formula for $f_a(x,t)$ is that it randomizes the density of the sum of the particle movements according to the pdf of the number of jumps $N(t)$. The random sum, equation (30), is a special case of a continuous time random walk (CTRW) [*Montroll and Weiss*, 1965; *Scher and Lax*, 1973; *Meerschaert and Scheffler*, 2004]. It is important to note that the connection of the probabilistic Exner equation with CTRWs allows one to obtain the exact solution of equation (27) via simulation of the tracer particle motion. For example, a forward Kolmogorov equation of a Markov process can be solved by simulating a CTRW with an exponential waiting time distribution and step length distribution $f_s(r)$ [e.g., *Scalas et al.*, 2004; *Fulger et al.*, 2008]. Even if the complete shape of the pdf of step lengths is not known, the behavior of the stochastic process $X(t)$ is well defined in the long-time limit as shown below.

Consider the standardized particle location:

$$Z(t) = \frac{X(t) - \lambda\mu_1 t}{\sqrt{\lambda\mu_2 t}} \qquad (33)$$

This random process has a mean 0 and variance 1 at every time $t > 0$. An easy calculation shows that the pdf of $Z(t)$ has Fourier transform:

$$\hat{f}_a\left(\frac{k}{\sqrt{\lambda\mu_2 t}}, t\right) \exp\left(\frac{ik\lambda\mu_1 t}{\sqrt{\lambda\mu_2 t}}\right) \qquad (34)$$

Combining this equation with:

$$\hat{f}_a(k,t) = \exp\left(-\lambda t\left(ik\mu_1 - \frac{1}{2}(ik)^2\mu_2 + \cdots\right)\right) \qquad (35)$$

which is obtained by substituting equation (9) into equation (31) results in the Fourier transform of the pdf of $Z(t)$ taking the form:

$$\exp\left(-\lambda t\left(-\frac{1}{2}\frac{(ik)^2}{\lambda\mu_2 t}\mu_2 + \frac{1}{3!}\frac{(ik)^3}{(\lambda\mu_3 t)^{\frac{3}{2}}}\mu_3 + \cdots\right)\right) \qquad (36)$$

As $t \to \infty$, (36) tends to $\exp\left(-\frac{1}{2}k^2\right)$ which is the Fourier transform of a standard normal density. This shows that $Z(t)$ tends to a standard normal deviate, Z, for all large $t > 0$. Substituting into equation (33) and solving, we see that the long-time asymptotic solution for the particle location is:

$$X(t) \approx \lambda\mu_1 t + \sqrt{\lambda\mu_2 t}Z \qquad (37)$$

By taking the Fourier transforms of the corresponding pdfs we obtain:

$$\hat{f}_a(k,t) = \exp\left(-\lambda\mu_1 t(ik) + \frac{1}{2}\lambda\mu_2 t(ik)^2\right) \qquad (38)$$

which is the point source solution to the differential equation:

$$\frac{\partial \hat{f}_a(x,t)}{\partial t} \approx \left(-\lambda\mu_1(ik) + \frac{1}{2}\lambda\mu_2(ik)^2\right)\hat{f}_a(k,t) \qquad (39)$$

Inverting this Fourier transform yields the advection-diffusion equation (11) with $v = \lambda\mu_1$ and $2D_d = \lambda\mu_2$, as in Section 3. In summary, equation (11) governs the asymptotic particle density in the long-time limit.

Now consider the case of a particle jump length density with a heavy tail. A similar argument shows that equation (14) governs the asymptotic particle density in the long-time limit, when the particle jump length density $f_s(r)$ has a heavy tail with a power-law decay, i.e., $f_s(r) \approx C\alpha r^{-\alpha-1}$ for $r > 0$ sufficiently large, some constant $C > 0$, and some power law index $1 < \alpha < 2$ (see Appendix A for a detailed proof). In this case, we note that the governing equation in the long-time asymptotic limit for $\hat{f}_a(k,t)$ is given by:

$$\frac{\partial \hat{f}_a(k,t)}{\partial t} \approx \left(-\lambda\mu_1(ik) + \lambda c_\alpha(ik)^\alpha\right)\hat{f}_a(k,t) \qquad (40)$$

Inverting the Fourier transform yields the fractional advection-diffusion equation (14) with $v = \lambda\mu_1$ and $D_d = \lambda c_\alpha$, as in Section 4. We remark that, while the derivation in this section is new in the context of stone tracer dispersion, a similar approach was taken to derive the fractional advection-diffusion equation for tracers in ground water, under a different set of assumptions [Schumer et al., 2001]. The next section provides a numerical demonstration to illustrate how a source of tracers will disperse over time under normal or anomalous diffusion.

7. Tracer dispersal under normal and anomalous diffusion

Consider a patch of tracers entrained instantaneously in the flow at a location x_0 and initial time t_0. This patch will advect and diffuse on the gravel bed over time. It is useful to track the time evolution of the fraction of tracers $f_a(x,t)$ in the active layer at any location x and time t. As was shown in the previous sections, the probabilistic Exner equation can be approximated at late time by a normal or anomalous diffusion, equations (11) and (14) respectively, depending on the pdf of step length. In this section we illustrate the time evolution of a patch of tracers under normal and anomalous advection-diffusion. We know from theory that the Green's function solution to the normal advection-diffusion equation is the Gaussian distribution, and the Green's function solution to the fractional advection-diffusion is the α-stable distribution [Benson et al., 2000b]. The α-stable distributions are also known as Lévy distributions. Specifically, in our case, the Green's function solution to the fractional advection-diffusion equation is an α-stable distribution with a skewness parameter $\beta = 1$, owing to the fact that step lengths are positive, so that the stable pdf has a heavy leading tail (see Appendix B for a description of stable distributions). Figure ?? shows the evolution of $f_a(x,t)$ under normal advection-diffusion from a pulse at $t = 0$ and $x = 0$, i.e., $f_a(0,0) = 1$. Figure ?? shows the evolution of $f_a(x,t)$ under anomalous advection-diffusion with $\alpha = 1.5$ from a pulse at $x = 0$. The α-stable densities in Figures ?? and ?? were simulated using the method of Nolan [1997]. In this hypothetical experiment, we chose the parameter values of the normal and anomalous diffusion equations to be unity, i.e., $v = 1$ m/day and $D_d = 1$ m$^\alpha$/day. Note that the units of the diffusion coefficient, D_d, is $[L^\alpha/T]$. As can be seen by comparing Figures ?? and ??, anomalous advection-diffusion predicts a faster spreading of tracers downstream (heavy leading tails). For example, the leading tails of the fraction of tracers at $t = 100$ reaches a near-zero value at ~ 50 m downstream of its mean in normal advection-diffusion, whereas it reaches this value at ~ 200 m downstream of its mean in fractional advection-diffusion with $\alpha = 1.5$. Note that the mean of $f_a(x,t)$ in both cases is the same. It is worth noting that both the Gaussian pdf, and the skewed stable pdf, assign some extremely small but mathematically nonzero probability to the interval left of the particle source, while the probabilistic Exner equation assigns zero probability to that interval. This illustrates the fact that both the Gaussian and skewed stable pdfs are only approximations to the relative concentration of tracer particles. However, the probability assigned to to the interval left of the particle source is exceedingly small, since both the Gaussian and skewed stable pdfs fall off at a super-exponential rate on the left tail [Zolotarev, 1986], and this approximation is perfectly reasonable in practice.

As seen in the previous section, under equilibrium bedload transport conditions, the long-time asymptotic solutions of the probabilistic Exner equation converge to the normal and anomalous advection-diffusion equation depending on the pdf of the step length. Therefore, long-time asymptotic solutions of the probabilistic Exner equation are the Gaussian and α-stable distributions in the respective cases of thin or heavy tailed pdfs for step length. In Figure 3 we compare the long-time asymptotic solutions for several values of α, starting from $\alpha = 2$ (Gaussian corresponding to the solution of normal advection-diffusion equation) to $\alpha = 1.1$. One can easily see the marked difference in the dispersal of tracers downstream in normal and anomalous advection-diffusion. For example, after 500 days, only $\sim 5\%$ of the tracers have been recovered at ~ 550 m in standard

advection-diffusion, whereas $\sim 8\%$ and $\sim 18\%$ of tracers are recovered at the same distance in fractional advection-diffusion for $\alpha = 1.5$ and $\alpha = 1.1$, respectively. Note that in the case of $\alpha = 1.1$ the gravel tracer particles are transported very long distances downstream when compared with the normal advection-diffusion case ($\alpha = 2$). Note that the parameter α of the fractional advection-diffusion relates to the heaviness of the tail of the pdf of particle step lengths, in effect determining how far downstream the tracers disperse from the source. In practice, the parameter α will have to be estimated from observations which typically will not be in the form of step lengths but in the form of "breakthrough curves" or pdfs of particle concentration at a given location downstream of the source. Tracer experiments in a large experimental flume are currently under development to document the possibility of faster-than-normal diffusion of tracers and the estimation of the parameter α.

8. Conclusions

In this work, a mathematical framework for the continuum treatment of tracer particle dispersal in rivers has been proposed, based on the probabilistic Exner equation. We have shown that when the step length distribution is thin-tailed, the governing equation for the tracer dispersal in the long-time limit is given by the standard advection-diffusion equation. However, the step length distributions can be heavy-tailed with power-law decay arising from heterogeneity in grain sizes and other complexities in real gravel bed rivers. It was shown that these heavy tails can be modeled using fractional derivatives, akin to contaminant transport in subsurface hydrology [e.g., *Benson*, 1998; *Benson et al.*, 2000a, b; *Berkowitz et al.*, 2002]. For a simplified active layer formulation, the probabilistic Exner equation was shown to be governed by a Markov process that describes the tracer dispersal problem. Further, it was shown that the classical (normal) advection-diffusion and fractional (anomalous) advection-diffusion equations arise as long-time asymptotic solutions of that stochastic model. A numerical example was then provided to illustrate the profound effect of fractional diffusion on the leading edge of the particle distribution.

The material presented here is intended to serve as an introduction to the problem of anomalous diffusion in the context of transport in gravel-bed rivers. The full power of the techniques introduced here remains to be realized through future research. For example, the innate variability of rivers is such that the entrainment rate E_b and bed elevation η are unlikely to be constant in x and t. This variability can lead to long-term sequestration, and subsequent long-delayed exhumation of tracers. *Parker et al.* [2000] and *Blom et al.* [2006] have shown how the fractional Exner equation (1) can be generalized to a formulation that assigns a probabilistic structure not only to step length, but also to the probabilities of entrainment and deposition as continuously varying functions of vertical position within the bed deposit. These complications can lead to anomalous sub-diffusion, if particle resting times have a heavy, power-law tail. A model that can explain the deposition and exhumation of particles at arbitrary depth, including variability in entrainment rate and bed elevation as well as grain size, has the potential to explain at least part of the tendency for a decrease in advection velocity over time described by *Ferguson and Hoey* [2002]. One possible approach to modeling anomalous sub-diffusion caused by power law waiting times between particle movements is by using fractional time derivatives, as discussed in the paper of *Schumer and Jerolmack* [2009] in this volume in the context of interpreting geological deposition records. The anomalous advection-diffusion model proposed herein, as well as further extensions to accommodate additional stochastic elements of transport as discussed above, will require extensive experiments and data collection to directly verify the nature of the distribution of step lenghts, waiting times and entrainment rates of particles in order to select the most appropriate model for transport.

Appendix A: Long-time asymptotics for heavy-tailed distributions

The standardized particle location cannot be expressed using equation (33) when the step length distribution has a heavy tail, because the second moment μ_2 of the distribution $f_s(r)$ does not exist, i.e., the population variance is infinite while the sample variance diverges unstably as the number of samples increases [*Lamperti*, 1962]. Instead, we consider the normalized process:

$$S(t) = \frac{X(t) - \lambda\mu_1 t}{(\lambda c_\alpha t)^{\frac{1}{\alpha}}} \tag{A1}$$

The pdf of $S(t)$ has the Fourier transform:

$$\hat{f}_a\left(\frac{k}{(\lambda c_\alpha t)^{\frac{1}{\alpha}}}, t\right) \exp\left(\frac{ik\lambda\mu_1 t}{(\lambda c_\alpha t)^{\frac{1}{\alpha}}}\right) \tag{A2}$$

Substitution of equation (12) into equation (31) results in:

$$\hat{f}_a(k, t) = \exp\left(-\lambda t\left(ik\mu_1 - c_\alpha(ik)^\alpha - d_\alpha(ik)^{2\alpha} + \cdots\right)\right) \tag{A3}$$

which combined with (A2) gives the left-hand side of the equation (A4) for the Fourier transform of the PDF of $S(t)$. In the long-time limit, i.e., as $t \to \infty$ this tends to the limit in the right-hand side below, i.e.,

$$\exp\left(\lambda t\left(c_\alpha\frac{(ik)^\alpha}{\lambda c_\alpha t} + d_\alpha\frac{(ik)^{2\alpha}}{(\lambda c_\alpha t)^2} + \cdots\right)\right) \to \exp\left((ik)^\alpha\right) \tag{A4}$$

since the higher order terms tend to zero as $t \to \infty$. This limit is the Fourier transform of a standard stable density, and the limit argument is closely related to the convergence criterion for compound Poisson random variables (see Chapter 3 in *Meerschaert and Scheffler* [2001] for more details and extensions). Hence, $S(t) \approx S$ is standard stable for all large $t > 0$. Substituting into equation (A1) and solving, we see that the long-time asymptotic approximation for the particle location is:

$$X(t) \approx \lambda\mu_1 t + (\lambda c_\alpha t)^{\frac{1}{\alpha}} S \tag{A5}$$

Taking the Fourier transforms of the corresponding pdfs, we obtain:

$$\hat{f}_a(k, t) \approx \exp\left(-\lambda\mu_1 t(ik) + \lambda c_\alpha t(ik)^\alpha\right) \tag{A6}$$

This is the Fourier transform of $f_a(x, t)$ with the higher order terms removed, as well as the point source solution to the differential equation:

$$\frac{\partial f_a(\hat{k}, t)}{\partial t} \approx \left(-\lambda\mu_1(ik) + \lambda c_\alpha(ik)^\alpha\right)\hat{f}_a(k, t) \tag{A7}$$

Inverting this Fourier transform results in the fractional advection-diffusion equation (14).

Appendix B: Stable distributions

If $X, X_1, X_2, \ldots$ are mutually independent random variables with a common distribution F_s, then the distribution F_s is

said to be stable if for each $n \in \mathbb{Z}$, there exists constants C_n and r_n such that [e.g., *Lamperti*, 1962; *Feller*, 1971]:

$$S_n \overset{d}{=} C_n X + r_n \qquad \text{(B1)}$$

where $S_n = X_1 + X_2 + \cdots + X_n$ and $\overset{d}{=}$ means identical in distribution. In other words, stable distributions are aggregation invariant up to a scale parameter, C_n, and location parameter, r_n. The norming constant C_n is of the form $n^{\frac{1}{\alpha}}$ for $0 < \alpha \leq 2$, where α is called the characteristic exponent of the distribution F_s. The distribution F_s is said to be strictly stable when $r_n = 0$. Closed-form expressions of the density functions of stable distributions exist for values of α equal to $2, 1$ and 0.5. In general, the stable pdf is defined by its Fourier transform [see *Stuart and Ord*, 1987]:

$$\hat{\rho}(k) = \left\{ -i\delta k - |\gamma k|^{\alpha} \left(1 + i\beta \mathrm{sgn}(k) \tan\left(\frac{\pi\alpha}{2}\right) \right) \right\} \quad \text{(B2)}$$

for $0 < \alpha \leq 2$ and $\alpha \neq 1$. In the above equation $\mathrm{sgn}(\cdot)$ denotes the signum function. The remaining parameters of the distribution are the location parameter $(-\infty < \delta < \infty)$, scale parameter $(\gamma > 0)$ and the skewness parameter $(-1 \leq \beta \leq 1)$. The distribution is symmetric for $\beta = 0$ and is said to be completely skewed for $\beta = -1$ and $\beta = 1$. For $\alpha = 2$, $\hat{\rho}(k)$ gives the Fourier transform of a Gaussian density with mean δ and variance $2\gamma^2$. For the special case $\alpha = 1$, the Fourier transform is expressed in a slightly different way. When $\alpha = 1$ and $\beta = 0$, the stable distribution is also called a Cauchy distribution.

If a random variable X has an α-stable distribution, then its theoretical statistical moments exist only up to order α. The mean of the distribution exists when $1 < \alpha \leq 2$, but when $0 < \alpha < 1$ both the mean and variance of the distribution are undefined. Thus, the Gaussian distribution is the only stable distribution with finite mean and variance. Stable distributions provide good approximations for spatial rainfall fluctuations in convective storms [e.g., *Kumar and Foufoula-Georgiou*, 1993], daily discharges in river flows [e.g., *Dodov and Foufoula-Georgiou*, 2004], spatial snapshots of tracer plumes in underground aquifers [e.g., *Benson et al.*, 2000a] and river flows [e.g., *Deng et al.*, 2004].

Notation

x	streamwise co-ordinate.
t	time.
η	local mean bed elevation.
t	time.
ν	shape parameter of the gamma distribution.
λ_p	porosity.
D_b	volume rate per unit area of deposition of bedload particles.
E_b	volume rate per unit area of entrainment of bedload particles.
$f_s(r)$	pdf of step lengths.
$f_s(r|D)$	pdf of step lengths conditioned on grain size.
$f_a(x,t)$	fraction of tracer particles in the active layer.
$f_I(x,t)$	fraction of the tracer particles in the sediment that is exchanged across the interface between active layer and substrate.
L_a	thickness of the active layer.
E_{bT}	volume entrainment rate of tracers.
D_{bT}	volume deposition rate of tracers.
v	advection velocity of tracers.
D_d	diffusivity of tracers.
D	grain-size.
D_m	arithmetic-mean of the grain-size distribution.
D_g	geometric mean of the grain-size distribution.
α	tail index of the stable distribution and the order of fractional differentiation.
$\mu_r(D)$	mean step length for grain-size D.
$f_{ad}(x,t,D)$	fraction of tracers in the active layer with grain-size D.
$E_{bu}(D)$	entrainment rate per unit bed content of grain-size D.

References

Ancey, C., T. Böhm, M. Jodeau, and P. Frey, Statistical description of sediment transport experiments, *Phys. Rev. E*, (74), 011302, 2006.

Ancey, C., A. C. Davidson, T. Böhm, M. Jodeau, and P. Frey, Entrainment and motion of coarse particles in a shallow water stream down a steep slope, *J. Fluid Mech.*, (595), 83–114, 2008.

Ancey C., Stochastic approximation of the Exner equation under lower-regime conditions, *J. Geophys. Res.*, under review, 2009 (in this issue).

Benson, D. A., The fractional advection-dispersion equation: Development and application, Ph.D. thesis, University of Nevada, Reno, 1998.

Benson, D. A., S. W. Wheatcraft, and M. M. Meerschaert, Application of a fractional advection-dispersion equation, *Water Resour. Res.*, *36*(6), 1403–1412, 2000a.

Benson, D. A., S. W. Wheatcraft, and M. M. Meerschaert, The fractional-order governing equation of Lévy motion, *Water Resour. Res.*, *36*(6), 1413–1423, 2000b.

Berkowitz, B., J. Klafter, R. Metzler, and H. Scher, Physical pictures of transport in heterogeneous media: Advection-dispersion, random-walk, and fractional derivative formulations, *Water Resour. Res.*, *38*(10), 1191–, doi:10.1029/2001WR001030, 2002.

Blom, A., G. Parker, J. S. Ribberink, and H. J. de Vriend, Vertical sorting and the morphodynamics of bed-form-dominated rivers: An equilibrium sorting model, *J. Geophys. Res.*, 111, 16 p., 2006.

Bradley, W. C., Effect of weathering on abrasion of granitic gravel, Colorado River, Texas., *Geological Soc. of Am. Bull.*, *81*, 61 – 80, 1970.

Charru, F., H. Mouilleron, and O. Eiff, Erosion and deposition of particles on a bed sheared by viscous flow, *J. Fluid Mech.*, *519*, 55 – 80, 2004.

Cheng, N., and Y. Chiew, Pickup probability for sediment entrainment, *J. Hydraul. Eng.*, *124*(2), 232 – 235, 1998.

Cheng, N., Analysis of bedload transport in laminar flows, *Adv. Water Resour.*, *27*, 937 – 942, 2004.

Cheng, N. S., T. Tang, and L. Zhu, Evaluation of bedload transport subject to high sheer stress fluctuations, *Water Resour. Res.*, *40*, W05601, doi:10.1029/2003WR003001, 2004.

Church, M., and M. A. Hassan, Size and distance of travel of unconstrained clasts on a streambed, *Water Resour. Res.*, *28*, 299 – 303, 1992.

Cushman, J. H., and T. R. Ginn, Fractional advection-dispersion equation: a classical mass balance with convolution-Fickian flux, *Water Resour. Res.*, *36*, 3763 – 3766, 2000.

Deng, Z.-Q., V. P. Singh, and L. Bengtsson, Numerical solution of fractional advection-dispersion equation, *J. Hydraul. Eng.*, *130*(5), 422–431, 2004.

Deng, Z. Q., J. L. M. P. de Lima, and V. P. Singh, Fractional Kinetic Model for First Flush of Stormwater Pollutants, *J. Environ. Engineering*, *131*(2), 232–241, DOI:10.1061/(ASCE)0733-9372(2005)131:2, 2005.

Deng, Z. Q., J. L. M. P. de Lima, M. I. P. de Lima, and V. P. Singh, A fractional dispersion model for overland solute transport, *Water Resour. Res.*, *42*, W03416, doi:10.1029/2005WR004146, 2006.

Dodov, B., and E. Foufoula-Georgiou, Generalized hydraulic geometry: Derivations based on multiscaling formalism, *Water Resour. Res.*, *40*, W06302, doi:10:10.1029/2003WR002082, 2004.

Einstein, H. A., Der Geschiebetrieb als Wahrscheinlichkeitsproblem, in *Mitteilung der Versuchsanstalt für Wasserbau an der Eidgenössische Technische Hochschule Zürich*, Verlag Rascher, Zurich, Switzerland. (English translation, *Sedimentation*, edited by H. W. Shen, pp. C1 – C105, Colo. State Univ., Fort Collins)

Einstein, H. A., Formulas for the transportation of bed load, *Transactions*, ASCE Paper No. 2140, 1942.

Einstein, H., and E. A. El-Sammi, Hydrodynamic forces on a rough wall, *Rev. Mod. Phys.*, *21*, 520–524, 1949.

Einstein, H. A., The bed-load function for sediment transportation in open channel flows, *Tech. Bull.*, 1026., Soil Conserv. Serv., U. S. Dept. of Agric., Washington, D. C. 78 p., 1950.

Feller, W., *An Introduction to Probability Theory and Its Applications*, vol. 2, second ed., Wiley, New York, [1st edn. 1966], 1971.

Ferguson, R. I., and S. J. Wathen, Tracer-pebble movement along a concave river profile: Virtual velocity in relation to grain size and shear stress, *Water Resour. Res.*, *34*, 2031–2038, 1998.

Ferguson, R. I., and T. B. Hoey, Long-term slowdown of river tracer pebbles: Generic models and implications for interpreting short-term tracer studies, *Water Resour. Res.*, *38*(8), 1142, 2002.

Fulger, D., E. Scalas, and G. Germano, Monte Carlo simulation of uncoupled continuous-time random walks yielding a stochastic solution of the space-time fractional diffusion equation, *Phys. Rev. E*, *77*, 021122, 2008.

Furbish, D. J., P. K. Haff, W. E. Dietrich, and A. M. Heimsath, Statistical description of slope-dependent soil transport and diffusion-like coefficient, *J. Geophys. Res.*, *114*, F00A05, doi:10.1029/2009JF001267, 2009.

Ganti, V., A. Singh, P. Passalacqua, and E. Foufoula-Georgiou, Subordinated Brownian motion model for sediment transport, *Phys. Rev. E*, *80*(1), 2009.

Garcia, M. H., *Sedimentation Engineering Processes, Measurements, Modeling and Practice*, ASCE Manual No. 110, 1050 p., 2008.

Hassan, M. A., and M. Church, Distance of movement of coarse particles in gravel bed streams, *Water Resour. Res.*, *27*(4), 503–511, 1991.

Hassan, M. A., and M. Church, Size and distance of travel of unconstrained clasts on a streambed, *Water Resour. Res.*, *28*(1), 299–303, 1992.

Hassan, M. A., and M. Church, Vertical mixing of coarse particles in gravel bed rivers: A kinematic model, *Water Resour. Res.*, *30*, 1173–1186, 1994.

Hill, K. M., L. DellAngelo, and M. M. Meerschaert, Particle size dependence of the probability density distributions of travel distances of gravel particles in bedload transport, *J. Geophys. Res.*, under review, 2009.

Hoey, T. B., and R. I. Ferguson, Numerical simulation of downstream fining by selective transport in gravel bed rivers: Model development and illustration, *Water Resour. Res.*, *30*, 2251–2260, 1994.

Hosking, J. R. M., and J. R. Wallace, Parameter and quantile estimation for the generalized Pareto distribution, *Technometrics*, *29*(3), 339–349, 1987.

Kleinhans, M. G., and L. C. van Rijn, Stochastic prediction of sediment transport in sand-gravel bed rivers, *J. Hydraul. Res.*, *128*(4), 412–425, 2002.

Kumar, P., and E. Foufoula-Georgiou, A multicomponent decomposition of spatial rainfall fields, 2. Self-similarity in fluctuations, *Water Resour. Res.*, *29*(8), 2533–2544, 1993.

Lamperti, J., Semi-stable stochastic processes, *Trans. Am. Math. Soc. 104*, 62–78, 1962.

Lanzoni, S., and M. Tubino, Grain sorting and bar instability, *J. Flu. Mech. 393*, 149–174, 1999.

Lauer, J. W., and G. Parker, Modeling framework for sediment deposition, storage, and evacuation in the floodplain of a meandering river: Theory, *Water Resour. Res. 44*, W04425, 2008a.

Lauer, J. W., and G. Parker, Modeling framework for sediment deposition, storage, and evacuation in the floodplain of a meandering river: Application to the Clark Fork River, Montana, *Water Resour. Res. 44*, W08404, 2008b.

Lopez, F., and M. H. Garcia, Risk of sediment erosion and suspension in turbulent flows, *J. Hydraul. Res. 127*(3), 231–235, 2001.

Meerschaert, M. M., and H. P. Scheffler, *Limit Distributions for Sums of Independent Random Vectors: Heavy Tails in Theory and Practice*, Wiley, New York, 2001.

Meerschaert, M. M., and H.P. Scheffler, Limit theorems for continuous time random walks with infinite mean waiting times. *J. Applied Probab.*, *41*, No. 3, 623–638, 2004.

Montroll, E. W., and G.H. Weiss, Random walks on lattices. II. *J. Mathematical Phys.* **6**, 167–181, 1965.

Nakagawa, H., and T. Tsujimoto, On probabilistic characteristics of motion of individual sediment particles on stream beds, in Proceedings of the 2nd IAHR International Symposium on Stochastic Hydraulics, pp. 293-316, Int. Assoc. of Hydraul. Eng. and Res., Madrid, 1976.

Nakagawa, H., and T. Tsujimoto, Sand bed instability due to bed load motion, *J. Hydraul. Div. Am. Soc. Civ. Eng.*, *106*(HY12), 2029-2051, 1980.

Nelson, J., R. L. Shreve, S. R. McLean, and T. G. Drake, Role of near-bed turbulence structure in bed load transport and bed form mechanics, *Water Resour. Res.*, *31*(8), 2071–2086, 1995.

Nikora, V., H. Habersack, T. Huber, and I. McEwan, On bed particle diffusion in gravel bed flows under weak bed load transport, *Water Resour. Res.*, *38*(6), 1081, 2002.

Niño, Y., and M. Garcia, Experiments on saltation of sand in water, *J. Hydraulic Engg.*, *124*(10), 1014-1025, 1998.

Nolan, J. P., Numerical calculation of stable densities and distribution functions. *Commun. Statist.-Stochastic Models, 13*(4), 759–774, 1997.

Odibat, Z. M., and N. T. Shawagfeh, Generalized Taylor's formula, *Appl. Math. Comput.*, *186*, 286–293, 2007.

Paintal, A. S., A stochastic model for bed load transport, *J. Hydraulic Res.*, *9*(4), 527–554, 1971.

Papoulis, A., and S. Pillai, *P*robability, random variables and stochastic processes, McGraw Hill, 2002.

Parker, G., C. Paola, and S. Leclair , Probabilistic Exner sediment continuity equation for mixtures with no active layer, *Journal of Hydrualic Engg.*, *126*(11), 818–826, 2000.

Parker, G., Transport of gravel and sediment mixtures, Chapter 3, *Sedimentation Engineering Processes, Measurements, Modeling and Practice*, ASCE Manual and Reports on Engineering Practice 110, M. Garcia, ed., 2008.

Podlubny, I., *Fractional Differential Equations*, vol. 198, Academic Press, San Diego, 1999.

Pyrce, R. S., and P. E. Ashmore, Particle path length distributions in meandering gravel-bed streams: Results from physical models, *Earth Surf. Processes Landforms*, *28*, 951–966, 2003.

Scalas, E., R. Gorenflo, and F. Mainardi, Uncoupled continuous-time random walks: Solution and limiting behavior of the master equation, *Phys. Rev. E*, *69*, 011107(1-8), 2004.

Scher, H. and M. Lax, Stochastic transport in a disordered solid. I. Theory. *Phys. Rev. B* **7**, 4491–4502, 1973.

Schumer R., D. A. Benson, M. M. Meerschaert and S. W. Wheatcraft, Eulerian derivation of the fractional advection-dispersion equation. *J. Contaminant Hydrol.*, *48*, 69–88, 2001.

Schumer R., D. A. Benson, M. M. Meerschaert and B. Baeumer, Fractal mobile/immobile solute transport, *Water Resour. Res., 39*(10), 1296-1307, 2003.

R. Schumer and D.J. Jerolmack, Real and apparent changes in sediment deposition rates through time. *Journal of Geophysical Research*, in press, 2009.

Stark, C. P., E. Foufoula-Georgiou, and V. Ganti, A nonlocal theory of sediment buffering and bedrock channel evolution, *J. Geophys. Res., 114*, F01029, doi:10.1029/2008JF000981, 2009.

Stuart, A., and J. K. Ord, *Kendall's Advanced Theory of Statistics*, Vol. 1, Oxford University Press, New York, 1987.

Toro-Escobar, C. M., G. Parker and C. Paola, Transfer function for the deposition of poorly sorted gravel in response to streambed aggradation, *J. Hydraulic Res., 34*(1), 35–53, 1996.

Tsujimoto, T., Probabilistic model of the process of bedload transport and its application to mobile-bed problems, Ph.D. Thesis, Kyoto University, 174pp., 1978.

Wheatcraft, S. W., and M. M. Meerschaert, Fractional conservation of mass, *Adv. Water Resour., 31*, 1377–1381, 2008.

Wilcock, P. R., and J. B. Southard, Bed-load transport of a mixed-size sediment: Fractional transport rates, bed forms, and the development of a coarse bed-surface layer, *Water Resour. Res., 25*(7), 1629–1641, 1989.

Wilcock, P. R., Entrainment, displacement and transport of tracer gravels, *Earth Surf. Processes Landforms, 22*, 1125–1138, 1997.

Wong, M., G. Parker, P. DeVries, T. M. Brown, and S. J. Burges, Experiments on dispersion of tracer stones under lower-regime plane-bed equilibrium bed load transport, *Water Resour. Res., 43*, W03440, doi:10.1029/2006WR005172, 2007.

Zolotarev, V. M., One-dimensional stable distributions, *Translations of Mathematical Monographs, 65*, American Mathematical Society, Providence, RI, 1986. Translated from Russian by H. H. McFaden, Translation edited by Ben Silver.

E. Foufoula-Georgiou, and V. Ganti, St. Anthony Falls Laboratory and National Center for Earth-surface Dynamics, Department of Civil Engineering, University of Minnesota, 2 Third avenue SE, Minneapolis 55414, USA.

M. M. Meerschaert, Department of Statistics and Probability, Michigan State University, East Lansing,MI, USA.

E. Viparelli, and G. Parker, Ven Te Chow Hydrosystems Laboratory, Departments of Civil and Environmental Engineering and Geology, University of Illinois, Urbana, Illinois, USA.
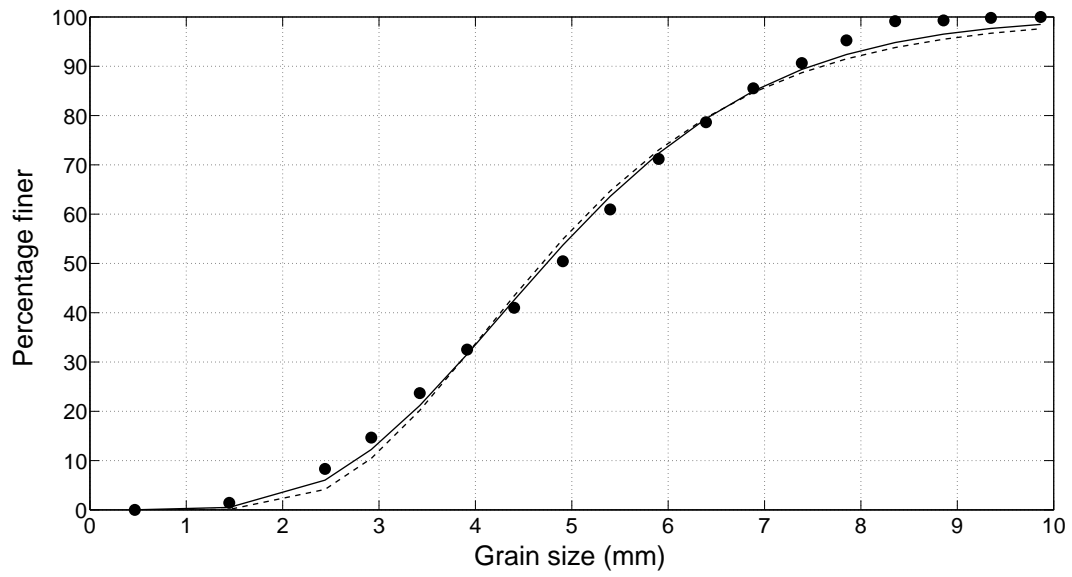
Figure 1. Plot showing fitted log-normal (dashed line) and gamma (solid line) distributions, to a grain-size distribution (solid points) reproduced from *Wilcock and Southard* [1989].
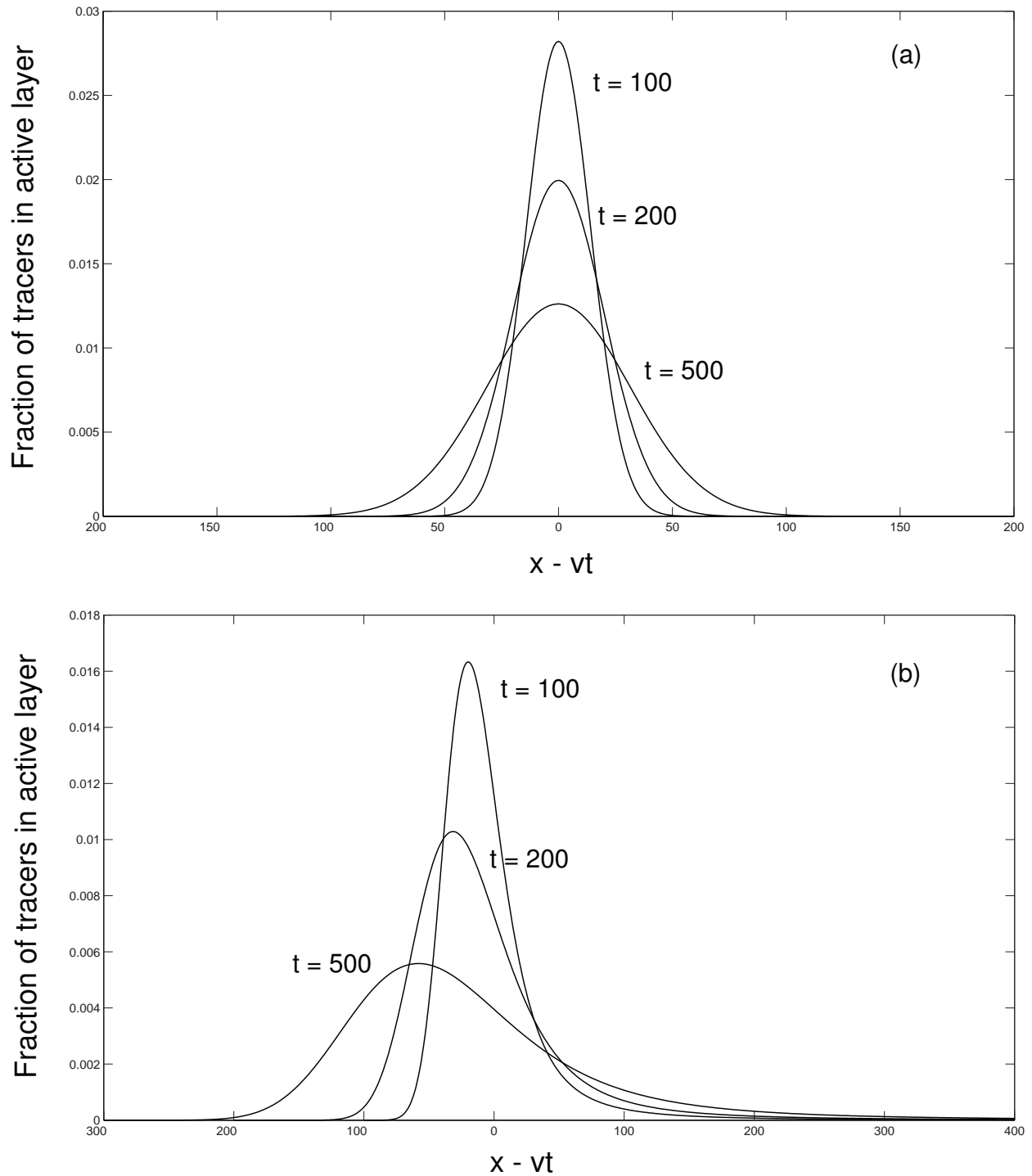
Figure 2. Time evolution of the fraction of tracers in the active layer, $f_a(x,t)$, by (a) normal advection-diffusion ($\alpha = 2$), and (b) anomalous advection-diffusion with $\alpha = 1.5$. Note that the advection term has been removed to facilitate comparison of the dispersion of the tracers at different times. The initial condition is a pulse at $x = 0$. The solutions are obtained with parameters $v = 1$ m/day and $D_d = 1$ m$^\alpha$/day. The times (in days) at which the solutions are obtained are labeled in the figure.
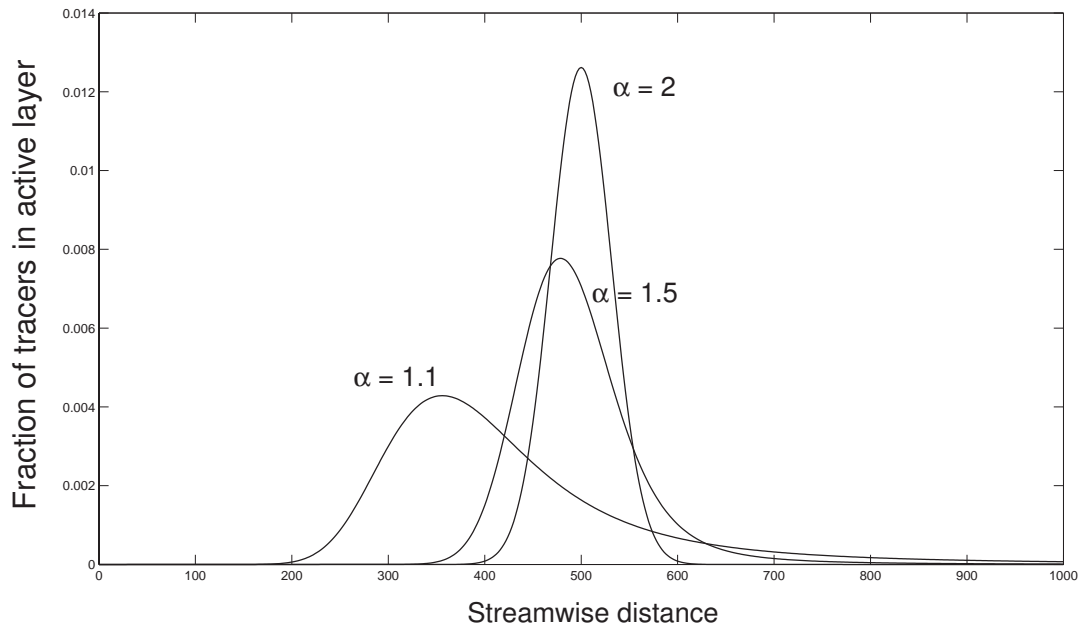
Figure 3. Long-time asymptotic solutions of the anomalous advection-diffusion equation for three different values of α. The solutions shown above are for 500 days after a patch of tracers is entrained into the flow. Normal advection-diffusion corresponds to $\alpha = 2$.

A geometric framework for channel network extraction from lidar: Nonlinear diffusion and geodesic paths

Paola Passalacqua,[1] Tien Do Trung,[2] Efi Foufoula-Georgiou,[1] Guillermo Sapiro,[3] and William E. Dietrich[4]

[1] A geometric framework for the automatic extraction of channels and channel networks from high-resolution digital elevation data is introduced in this paper. The proposed approach incorporates nonlinear diffusion for the preprocessing of the data, both to remove noise and to enhance features that are critical to the network extraction. Following this preprocessing, channels are defined as curves of minimal effort, or geodesics, where the effort is measured on the basis of fundamental geomorphological characteristics such as flow accumulation area and isoheight contours curvature. The merits of the proposed methodology, and especially the computational efficiency and accurate localization of the extracted channels, are demonstrated using light detection and ranging (lidar) data of the Skunk Creek, a tributary of the South Fork Eel River basin in northern California.

1. Introduction

[2] The detection of channel networks and the localization of channel heads from digital elevation (DEM) data are fundamental to the accurate modeling of water, sediment, and other environmental fluxes in a watershed. Several methodologies to delineate channel heads and channel networks from DEMs have been proposed [e.g., *Montgomery and Dietrich*, 1988; *Tarboton et al.*, 1988, 1991; *Montgomery and Foufoula-Georgiou*, 1993; *Costa-Cabral and Burges*, 1994; *Giannoni et al.*, 2005; *Hancock and Evans*, 2006]. Channel heads typically are found in unchanneled valleys and appear to occur where some erosion threshold has been crossed (e.g., landsliding, overland flow incision through a vegetated surface, seepage erosion, etc.) [e.g., *Montgomery and Dietrich*, 1988; *Dietrich et al.*, 1993]. Field data also show that channel head location varies with a topographic threshold that depends on drainage area and local valley slope [e.g., *Montgomery and Dietrich*, 1988, 1989, 1992, 1994]. More recently, for example, *McNamara et al.* [2006]

located channel heads in a small watershed in Thailand and suggested that different channel initiation processes produced different slope-area relationships. Several studies employ, instead, an assumption of constant critical support area for determining the location of channel heads [e.g., *O'Callaghan and Mark*, 1984; *Band*, 1986; *Mark*, 1988; *Tarboton et al.*, 1989, 1991; *McMaster*, 2002], although empirical support from field observations was not reported. Other work has explored the localization of channel heads by identifying valley heads as concave areas in DEMs [*Tribe*, 1991, 1992].

[3] With the availability of high-resolution topographic data obtained by airborne laser mapping, new methodologies have been proposed for the determination of the locations and distribution of landslide activity [e.g., *McKean and Roering*, 2004; *Glenn et al.*, 2006; *Ardizzone et al.*, 2007; C. Gangodagamage et al., Statistical signature of deep-seated landslides, submitted to *Journal of Geophysical Research*, 2009], the geomorphological mapping of glacial landforms [*Smith et al.*, 2006], numerical modeling of shallow landslides [e.g., *Dietrich et al.*, 2001; *Tarolli and Tarboton*, 2006], computation of channel slope [*Vianello et al.*, 2009], identification of depositional features of alluvial fans [*Staley et al.*, 2006; *Frankel and Dolan*, 2007; *Cavalli and Marchi*, 2008] and of channel bed morphology [*Cavalli et al.*, 2008], and the detection of hillslope-to-valley transition [*Tarolli and Dalla Fontana*, 2009].

[4] Light detection and ranging (lidar) data now permits direct detection of channels, rather than estimation of likely channel location based on topographic features (slope, drainage area, or topographic curvature). Recently, *Lashermes et al.* [2007] proposed a wavelet-based filtering

[1]Saint Anthony Falls Laboratory, National Center for Earth Surface Dynamics, Department of Civil Engineering, University of Minnesota, Minneapolis, Minnesota, USA.
[2]Département de Mathématiques, Ecole Normale Supérieure de Cachan, Paris, France.
[3]Department of Electrical and Computer Engineering, University of Minnesota, Minneapolis, Minnesota, USA.
[4]Department of Earth and Planetary Science, University of California, Berkeley, California, USA.

methodology to extract channels and channel networks from high-resolution topography that can be obtained from airborne lidar data. In the methodology of *Lashermes et al.* [2007], multiscale analysis, i.e., going from fine to coarser scales, was achieved via a convolution of the original image with a Gaussian kernel at different scales. This is equivalent to applying the heat equation on the image going forward in time (e.g., see *Braunmandl et al.* [2003] and later in this paper). Gaussian linear filtering, however, smoothes small-scale structures at the same rate as it smoothes larger-scale structures (actually some of the most critical scales are smoothed even faster, which can be shown following the theory of robust estimation). This might not be desirable in DEM feature extraction as small-scale structures, such as the crest of a ridge or channel bank, should remain sharp during coarsening until the whole ridge disappears. This problem of edge preservation has prompted in image processing the introduction of adaptive geometric filters which reduce smoothing at the edges of features while applying Gaussian filtering to the rest of the image.

[5] In this paper, a geometric framework which significantly advances the accurate and automatic extraction of channel networks from lidar data is developed using such scale-adaptive filtering. The first component of the framework is the use of nonlinear geometric filtering (via partial differential equations), instead of linear filtering via wavelets, which naturally adapts to a given landscape and facilitates the enhancement of features for further processing. Early uses of nonlinear partial differential equations for digital elevation maps appear in the work of *Braunmandl et al.* [2003], *Almansa et al.* [2002], and *Solé et al.* [2004]. The form of this filtering is such that it behaves as linear diffusion at low-elevation gradients, while it arrests diffusion as the gradients become large (other features could be used to control the nonstationary diffusion as well). It is noted that the nonlinear diffusion term here employed refers to the filtering methodology in image processing and not to the nonlinear erosion laws [e.g., *Kirkby*, 1984, 1985; *Andrews and Buckman*, 1987; *Anderson and Humphrey*, 1989; *Anderson*, 1994; *Howard*, 1994a, 1994b, 1997; *Roering et al.*, 1999]. The second key component of the proposed framework is the novel formulation of the channel network extraction problem as a geodesic energy minimization problem with a cost function which is geomorphologically informed; that is, it is defined in terms of local attributes of the landscape such as upstream drainage area and isoheight contours curvature. In other words, channels are defined as curves of minimal effort. Such curves are derived from global integration of local quantities and computed in optimal linear complexity. This global integration methodology makes the channel network extraction robust to noise and data interruptions, contrary to what obtained with more common forward marching approaches (e.g., following steepest descent directions).

[6] This paper is organized as follows. Section 2 gives a brief mathematical background on nonlinear diffusion, geometric filtering, geodesics, and energy minimization principles. In section 3 these techniques are applied to the problem of channel network extraction and demonstrated in a real basin. Finally, section 4 presents concluding remarks and challenges for future research.

2. Mathematical Background on the Proposed Methodology

[7] This section presents the basic mathematical background that provides the foundation for the channel network extraction geometric framework introduced in this paper. First, the notion of nonlinear anisotropic filtering is introduced. Next, the framework of geodesic computations is presented. The channel extraction methodology presented here has been released to the community as a toolbox called GeoNet. The code is available for download at http://software.nced.umn.edu/geonet/.

2.1. Nonlinear Diffusion and Geometric Filtering

[8] Let us denote by $h_0(x, y): \mathbb{R}^2 \to \mathbb{R}$ the provided DEM image, i.e., high-resolution digital elevation data. Typical of any feature extraction methodology is the application of a *smoothing* filter on the original data $h_0(x, y)$ to remove "noise" (observational noise or irregularities at scales smaller than the scales of interest) and identify features as entities that persist over a range of scales. This operation of smoothing is also very important to make computations such as derivatives mathematically well posed. A popular smoothing filter is the Gaussian kernel, which, when applied to $h_0(x, y)$, results in landscapes at coarser resolutions:

$$h(x, y, t) = h_0(x, y) \star G(x, y; t) \qquad (1)$$

where $\star$ denotes the convolution operation and $G(x, y; t)$ is a Gaussian kernel of standard deviation t (larger values of t result in coarser resolution landscapes), centered at location (x, y):

$$G_{x,y,t}(u, v) = \frac{1}{2\pi t} \exp\left[-\frac{(u - x)^2 + (v - y)^2}{2t} \right] \qquad (2)$$

As it was shown and exploited in the work of *Lashermes et al.* [2007], the use of the classical Gaussian smoothing kernel naturally leads to a multiscale (scale-space in the computer vision terminology) efficient computation of local slopes and Laplacian curvatures via wavelets, where wavelets were selected as the first and second derivatives of a Gaussian kernel (see *Burt and Adelson* [1983], *Koenderink* [1984], and *Witkin* [1983] for early developments and the introduction of Gaussian filtering for multiscale image analysis).

[9] The family of coarsened landscapes resulting from (1) may be seen as solutions of the linear heat or diffusion equation, e.g., see *Koenderink* [1984], with the initial condition $h(x, y; 0) = h_0(x, y)$:

$$\partial_t h(x, y, t) = \nabla \cdot (c \nabla h) = c \nabla^2 h \qquad (3)$$

where c is the diffusion coefficient and ∇ is the gradient operator. Thus, processing the landscape with Gaussian

filters of increasing spatial scale, as done by *Lashermes et al.* [2007], is equivalent to applying an isotropic diffusion equation over time on the landscape with the spatial scale of the filter (variance) and the time of diffusion being related to each other (since derivatives are linear operations, filtering and then differentiating is equivalent to filtering with the corresponding derivatives of the original filter; see also *Lashermes et al.* [2007] for a formal exposition). Once the time of diffusion is fixed, the spatial scale over which the Gaussian smoothing is applied on the original landscape is spatially uniform; that is, the landscape is uniformly diffused at all points and in all directions.

[10] The choice of the Gaussian kernel as smoothing filter is motivated in part by two criteria defined by *Koenderink* [1984] as (1) *causality* and (2) *homogeneity/isotropy*. The *causality* guarantees that no spurious feature should be generated at coarser resolutions, since any feature at a coarse level of resolution must have a cause at a finer level of resolution. This guarantees noise reduction in the original data as the resolution is coarsened. The *homogeneity/isotropy* criterion requires the blurring to be space invariant. The Gaussian kernel thus satisfies the standard "scale-space paradigm" as stated by *Koenderink* [1984]. It is noted, however, that the Gaussian filtering is isotropic and does not respect the natural boundaries of the features and diffuses across boundaries throughout the landscape. This obviously degrades the spatial localization of these boundaries, especially at larger scales of smoothing. These boundaries represent, in the case of landscapes, important discontinuities such as crests and valleys. *Perona and Malik* [1990] reformulated the space-scale paradigm to address this issue. The new paradigm was reformulated to satisfy three criteria: (1) *causality*, as previously stated by *Koenderink* [1984], (2) *immediate localization*, which searches, at each resolution, sharp and meaningful region boundaries, and (3) *piecewise smoothing*, which indicates preferential smoothing (intraregion rather than interregion).

[11] In the standard linear diffusion equation (3), the diffusion coefficient c is constant, that is, independent of the space location. An extension to the Gaussian filtering is obtained by choosing the diffusion coefficient c to be a suitable function of spatial location, such that the new space-scale paradigm criteria are satisfied. The modified diffusion equation can be written as

$$\partial_t h(x,y,t) = \nabla \cdot [c(x,y,t)\nabla h] \qquad (4)$$

where ∇ indicates as before the gradient operator. Note that (4) reduces to the linear diffusion equation (3) if $c(x, y, t)$ is constant.

[12] If the location of a channel were known, then, in order to achieve noise reduction and edge enhancement, smoothing should preferentially happen in the region outside and within the channel, rather than across its boundary. This could be achieved by setting $c = 0$ at the channel boundaries and $c = 1$ everywhere else. However the channel location is not known in advance, and what can be computed instead is an estimate of it, or some geometric characteristic that defines it, thereby stopping, or at least reducing, diffusion across the channel boundary.

[13] Let $\vec{E}(x, y, t)$ denote the vector-valued function representing an estimate of the channel's location. The diffusion coefficient can be chosen as a function of the magnitude of $\vec{E}(x, y, t)$:

$$c = p(|\vec{E}|) \qquad (5)$$

where $p(\cdot)$ has to be designed such that it ideally does not allow diffusion across boundaries. *Perona and Malik* [1990] have proposed a simple first estimate of the channel's location (or image edges in their original application), given by the gradient of the elevation $h(x, y; t)$ at the location (x, y) and time t:

$$\vec{E}(x,y,t) = \nabla h(x,y,t) \qquad (6)$$

This provides a local estimator of the edges/discontinuities within the nonlinear space-scale paradigm. Note that we could also use curvature, area in combination with slope, or other higher-order features to localize channels and thus define the diffusion coefficient c, while the use of gradients is the most standard formulation in image processing and found to be sufficient for our application (see also discussion of *Perona and Malik* [1990] for advantages of such a simple formulation). The diffusion equation thus takes the following form:

$$\partial_t h(x,y,t) = \nabla \cdot [p(|\nabla h|)\nabla h] \qquad (7)$$

Perona and Malik suggested the following as possible edge-stopping functions:

$$p(|\nabla h|) = \frac{1}{1 + (|\nabla h|/\lambda)^2} \qquad (8)$$

or

$$p(|\nabla h|) = e^{-(|\nabla h|/\lambda)^2} \qquad (9)$$

where λ is a constant. Such expressions (when properly regularized, e.g., via Gaussian smoothing) of the edge-stopping function guarantee basic properties of the scale-space paradigm, while at the same time enhancing the discontinuities, thereby allowing their easier extraction (see *Alvarez et al.* [1992], *Perona and Malik* [1990], and the Appendix for details). From a numerical point of view, we employ the version of the Perona-Malik filter proposed by *Catté et al.* [1992]. The diffusion coefficient c is computed in the four directions (north, south, east, and west) with the gradients in (8) or (9) computed through standard finite differences on Gaussian filtered data (with a very small standard deviation of the kernel $\sigma = 0.05$ m), to avoid the stability issues related to the Perona-Malik original formulation [*Catté et al.*, 1992]. Then, the gradients in (7) are computed on the nonsmoothed data through standard finite differences, multiplied by the diffusion coefficient in each direction and then summed to advance in time.

[14] The just introduced nonlinear diffusion equation (7) will be used as a preprocessing step on the elevation data, to remove unwanted details and enhance the features that are relevant for channel network extraction. While many alternatives exist in the literature for nonlinear diffusion, we
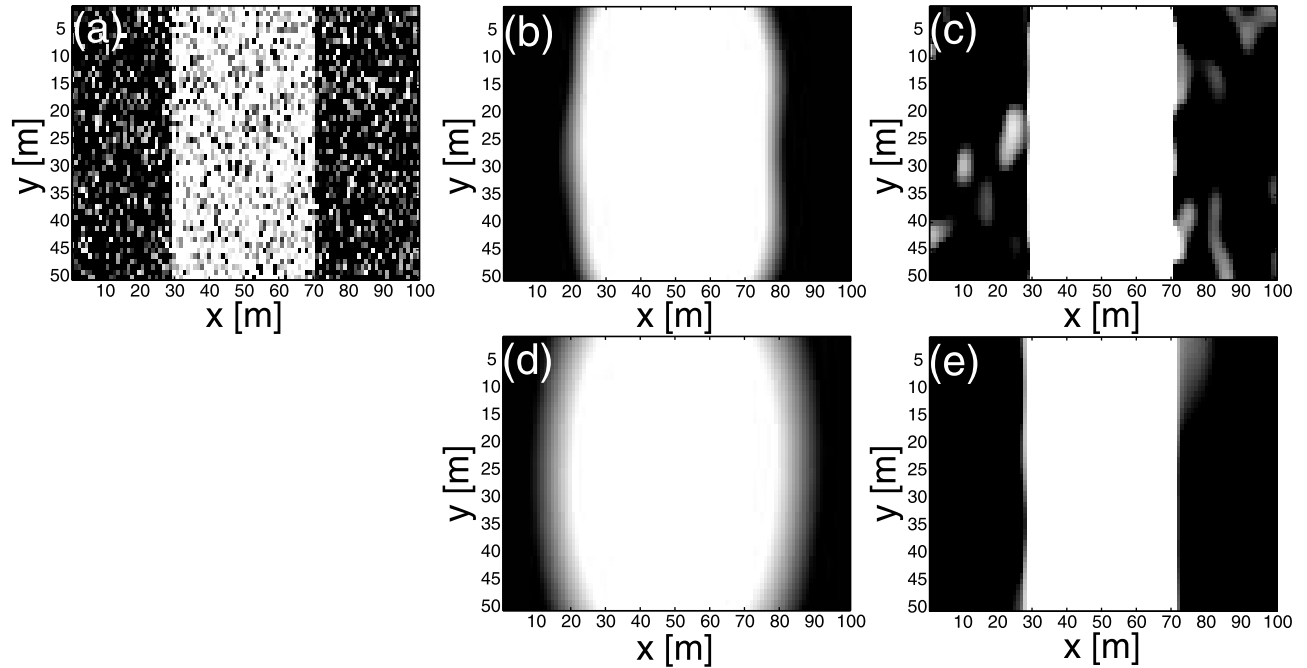
Figure 1. Comparison of the effect of Gaussian (linear) versus Perona-Malik (nonlinear) filtering on an idealized landscape. The white area represents an idealized ridge, with an elevation higher than the surrounding landscape. (a) Noise has been added on the original data. (b) Gaussian filtering achieves noise reduction at the expense of the boundaries localization (standard deviation of the kernel $\sigma = 7$ m), while (c) Perona-Malik filtering achieves noise reduction while preserving the right localization, avoiding diffusion across its boundaries (number of iterations $t = 50$). (d) Note how further processing with Gaussian filtering results in a completely blurred ridge ($\sigma = 14$ m), while (e) the Perona-Malik filtering operation only reduces the noise further, without affecting the feature and its localization ($t = 200$).

found this basic and most classical one to be sufficient to introduce the ideas and to obtain state-of-the-art results for the tested lidar elevation data.

[15] We have constructed an example to show the effect of Gaussian (linear) versus Perona-Malik (nonlinear) filtering on an idealized landscape (Figure 1a) with noise added on the surface. The white band represents an idealized ridge at a higher elevation compared to the surrounding landscape. As shown in Figure 1b Gaussian filtering (standard deviation of the kernel $\sigma = 7$ m which corresponds to $t = \sigma^2 = 49$) achieves noise reduction at the expense of the localization of the ridge, as it appears diffused in the neighboring landscape. The Perona-Malik filter (Figure 1c after $t = 50$ iterations) achieves noise reduction without affecting the boundaries localization. Note how after further processing the idealized landscape through Gaussian filtering (Figure 1d with $\sigma = 14$ m which corresponds to $t = 196$) the ridge and its location are not identifiable anymore, while the Perona-Malik filtering (Figure 1e with $t = 200$) only improves noise reduction, without affecting the feature. In addition Figure 2 shows the profiles extracted from the idealized landscape shown in Figure 1. Figure 2a shows the case of an idealized landscape with no noise added on the surface. Note how the profile extracted from the Perona-Malik filtered data after $t = 50$ iterations resembles the original one, while the idealized ridge has almost disappeared from the Gaussian filtered landscape. The profiles shown in Figures 2b and 2c refer to the same idealized landscape with noise added on the surface shown in

Figure 1. Note how well defined and enhanced appear the ridge after further Perona-Malik filtering of the data. This is due to the fact that at the boundary between the ridge and the surrounding landscape the gradients are large, thus diffusion is stopped.

2.2. Geodesics and Energy Minimization Principles for Network Extraction

[16] Having applied the Perona-Malik filter to the initial DEM image, unwanted details have been eliminated, or reduced, and the features enhanced. The question then arises as to how to best (optimally) extract the whole channel network.

[17] If we have two fixed points a and b on the surface, we know there are infinite possible curves passing through them. If a and b now represent the outlet and a channel head of a tributary river network, then we know that among all the possible curves, only one will be a channel. (The detection of the outlet and of the channel sources will be explained later in section 3.2. For now, let us assume their locations are known). Topographic attributes that distinguish channels from the rest of the landscape are the surface curvature and the flow accumulation. Channelized areas are, in fact, commonly characterized by positive curvature (or curvature above a threshold value which indicates convergent topography, while negative curvature indicates divergent topography correspondent to hillslopes) and by large values of flow accumulation (as channelized paths collect water in the downstream direction). If we were able to
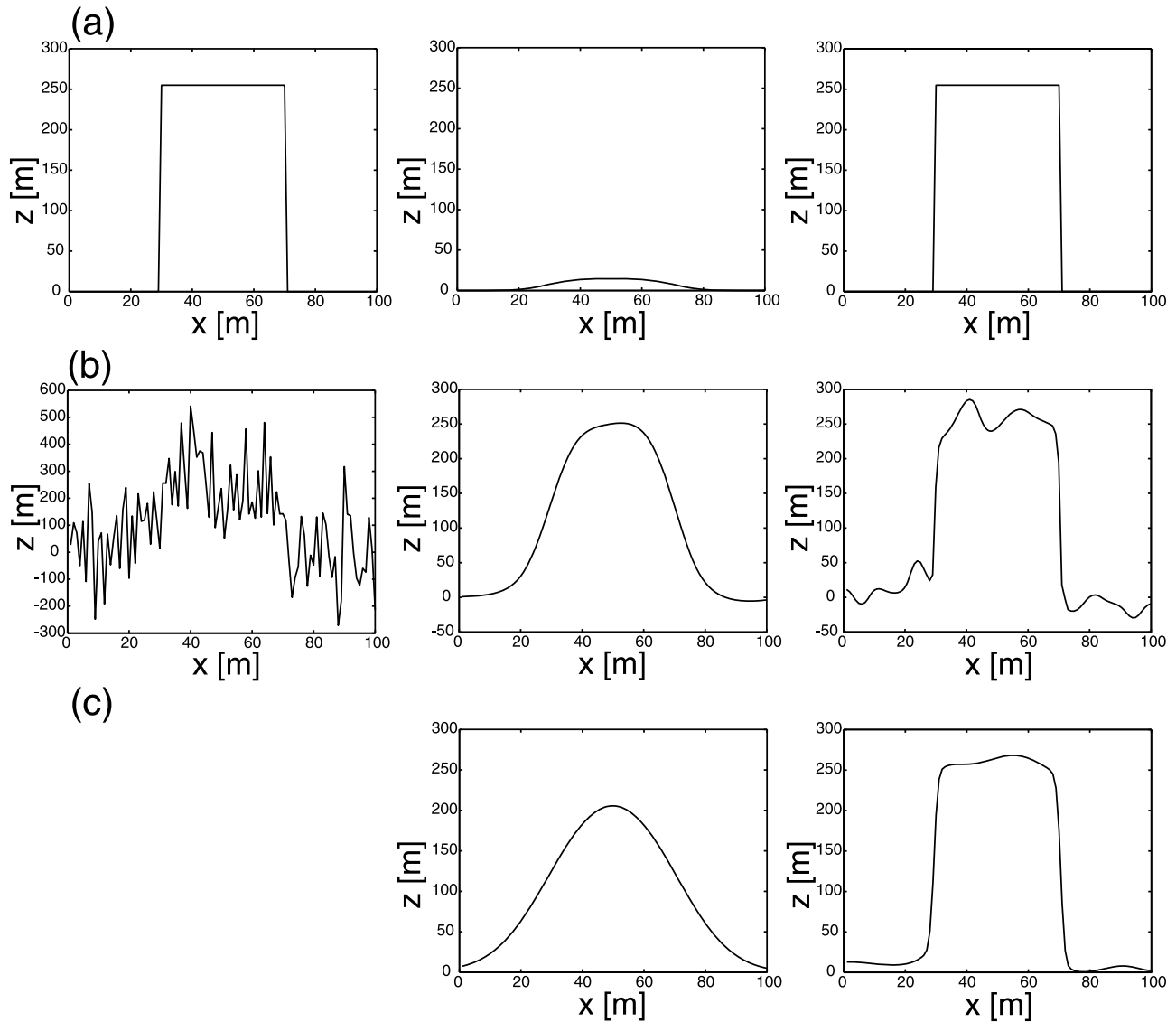
Figure 2. The 1-D representation of the example shown in Figure 1. (a) Idealized landscape with no noise added on the surface. Profiles extracted from the original idealized landscape (left), the Gaussian filtered landscape ($\sigma = 7$ m) (middle), and the Perona-Malik filtered landscape ($t = 50$) (right). (b) Idealized landscape with noise added on the surface as shown in Figure 1. Profiles extracted from the original idealized landscape (left), the Gaussian filtered landscape ($\sigma = 7$ m) (middle), and the Perona-Malik filtered landscape ($t = 50$) (right). (c) Effect of further smoothing on the data shown in Figure 2b. Profiles extracted from the Gaussian filtered landscape ($\sigma = 14$ m) (middle) and Perona-Malik filtered landscape ($t = 200$) (right).

choose among all the possible curves connecting point a and point b (the outlet and a channel head of our river network) the one with the largest overall positive curvature and flow accumulation, then we would have identified the channel. This concept can be mathematically expressed through a function, called the "cost function" and indicated by ψ, which represents the cost of traveling between point a and point b, in this case in terms of surface curvature and flow accumulation. This means that while the channel itself will be the curve with minimum cost (as will meet the requirements of positive curvature and large flow accumulation), the other curves will be penalized with a higher cost. The curve with the minimal cost corresponds to a mathemati-

cally defined quantity called the *geodesic curve* and formally defined as follows:

$$g(a, b) := \arg\left(\min_{C \in \Omega} \int_a^b \psi(s)ds\right) \qquad (10)$$

where s is the standard Euclidean arc length [*Do Carmo*, 1976]. The minimum is taken over all the possible curves C that start at point a and end at point b.

[18]   Before we give more details on how the computation of the geodesic curve is performed, let us make two important observations related to the just introduced concepts. First,

having said that for the detection of channels we define the cost function in terms of positive surface curvature and large flow accumulation, implies that different feature selections of the cost function will lead to different curves on the surface. This means that this approach could be used for the detection of other features of interest, such as roads or landslides for example, with the only challenge of being able to identify the most appropriate topographic attributes needed. Also, as it can be seen from equation (10) the integral sign indicates that the minimum is achieved in a global sense, not locally. If, for example, channels were to be traced following steepest descent directions, then the presence of noise in a pixel would deviate the channel in an erroneous way, while the global approach guarantees robustness. The same happens in the case of missing data: while forward marching techniques would stop, global approaches such as the geodesic framework would naturally "jump" over them, as they always connect the selected extreme points.

[19] The computation of the geodesic curve involves another well defined mathematical quantity called *geodesic distance*:

$$d(a, x) := \min_{C \in \Omega} \int_a^x \psi(s) ds \qquad (11)$$

This is the quantity which gives us the minimum distance from any point x to location a, computed by minimizing the cost function. Intuitively we can now see how, if we want to travel from point a to point b along the geodesic curve (which in our case it means that we want to identify the channel that connects the outlet and a channel head), we need to use the information given by the geodesic distances. Formally, the actual geodesic curve is computed by gradient descent on the distance function $d(a, \cdot)$, backtracking from the "downstream" point b. The geodesic is thus the integral curve of ∇d starting at point b, and the gradient is intrinsically computed on the surface. Clearly, the efficiency of the computation of the geodesic curves depends on the computation of the geodesic distances. Several algorithms are available in the literature for the efficient computation of the geodesic distances [e.g., *Yatziv et al.*, 2006; *Dial*, 1969; *Dijkstra*, 1959]. These algorithms are applicable to all diverse types of surface representations, from triangulated surfaces [*Kimmel*, 2003] to point cloud data as in lidar [*Memoli and Sapiro*, 2005]. These extensions are based on the fact that the geodesic distance function satisfies a Hamilton-Jacobi geometric partial differential equation, $|\nabla d| = \psi$, where the gradient is intrinsic to the surface in the most general case. Additional information on these efficient computations can be found in the work of *Helmsen et al.* [1996], *Sethian* [1999], *Tsitsiklis* [1995], *Tsai et al.* [2003], and *Zhao* [2004]. Note that these algorithms are of complexity linear on the number of grid points, and thereby computationally optimal.

3. Channel Network Extraction

[20] The objective of this section is to illustrate the concepts described above through their application on lidar data of the South Fork Eel River basin in northern California. We use the ALSM (Airborne Laser Swath Mapping) data

(2.6 m average bare earth data spacing, gridded to 1 m) acquired by NCALM (National Center for Airborne Laser Mapping) (the data are available online at the data distribution archive http://www.ncalm.org/). We focus in particular on the Skunk Creek, a 0.54 km^2 landslide complex tributary located just upstream of the Elder Creek. The subbasin and the location map are shown in Figure 3. For the Skunk Creek we had available a hand-drawn channel network map (field survey done by Joel Scheingross and Eric Winchell, University of California, Berkeley). The digitized version of the hand-drawn map is shown in Figure 3 as well. As can be seen, the part of the network close to the outlet is composed by *active* channels (channels with well defined banks and presence of bed material), while the part close to the divide consists of inactive (poorly formed channels with limited bed material but with definable channel banks) and *transient* channels (which present characteristics in between the inactive and active channels). Because the channel network of Skunk Creek is disrupted by deep-seated landsliding (see also analysis of C. Gangodagamage et al. (submitted manuscript, 2009)) and is discontinuous in its upper reaches, several channel heads occur along individual valley paths (see Figure 3). We preserve this discontinuity to explore how well we can detect not only channel initiation points but also channel disruptions through our proposed techniques. The channel network of the Skunk Creek is a very challenging basin for testing a channel extraction methodology. Nevertheless, the capability of our methodology in capturing channel disruptions, as shown in this section, makes it a very interesting application.

3.1. Preprocessing: Regularization of High-Resolution Digital Elevation Data Through Nonlinear Filtering

[21] We focus our analysis on a 200 m × 200 m portion of the Skunk Creek, referred to as portion A (see Figure 4). The landscape A has been processed with a Gaussian filter (isotropic linear diffusion) and the Perona-Malik filter (anisotropic nonlinear diffusion). To allow comparison of the two filtered landscapes, the time of forward diffusion (iteration steps) has been set to 50 iterations in both (in general, there is no exact mathematical correspondence between the corresponding diffusion times). This corresponds to a Gaussian spatial filter of approximate $\sigma = 7$ m (scale of smoothing of the landscape of approximately $4\sigma = 28$ m) [see *Lashermes et al.*, 2007, Table 1]. As is apparent from the theory, no such unique and uniform equivalent spatial scale of smoothing can be assigned to the nonlinearly filtered landscape as the effective smoothing scale varies locally at every point depending on the local gradient. Specifically, the effective spatial scale of smoothing is smaller in the vicinity of feature boundaries (e.g., the channel boundaries, where the gradient is large and the edge stopping function of equation (8) assigns a small diffusivity coefficient), and larger in areas of spatially homogeneous and small gradients (recall also the example shown in Figures 1 and 2). The Perona-Malik filter used in this analysis is that of equation (8) with parameter λ estimated from the 90% quantile of the probability distribution function (pdf) of the gradients, as also suggested by *Perona and Malik* [1990] (the selection of such a parameter can be made fully automatic also following the robust statistics approach
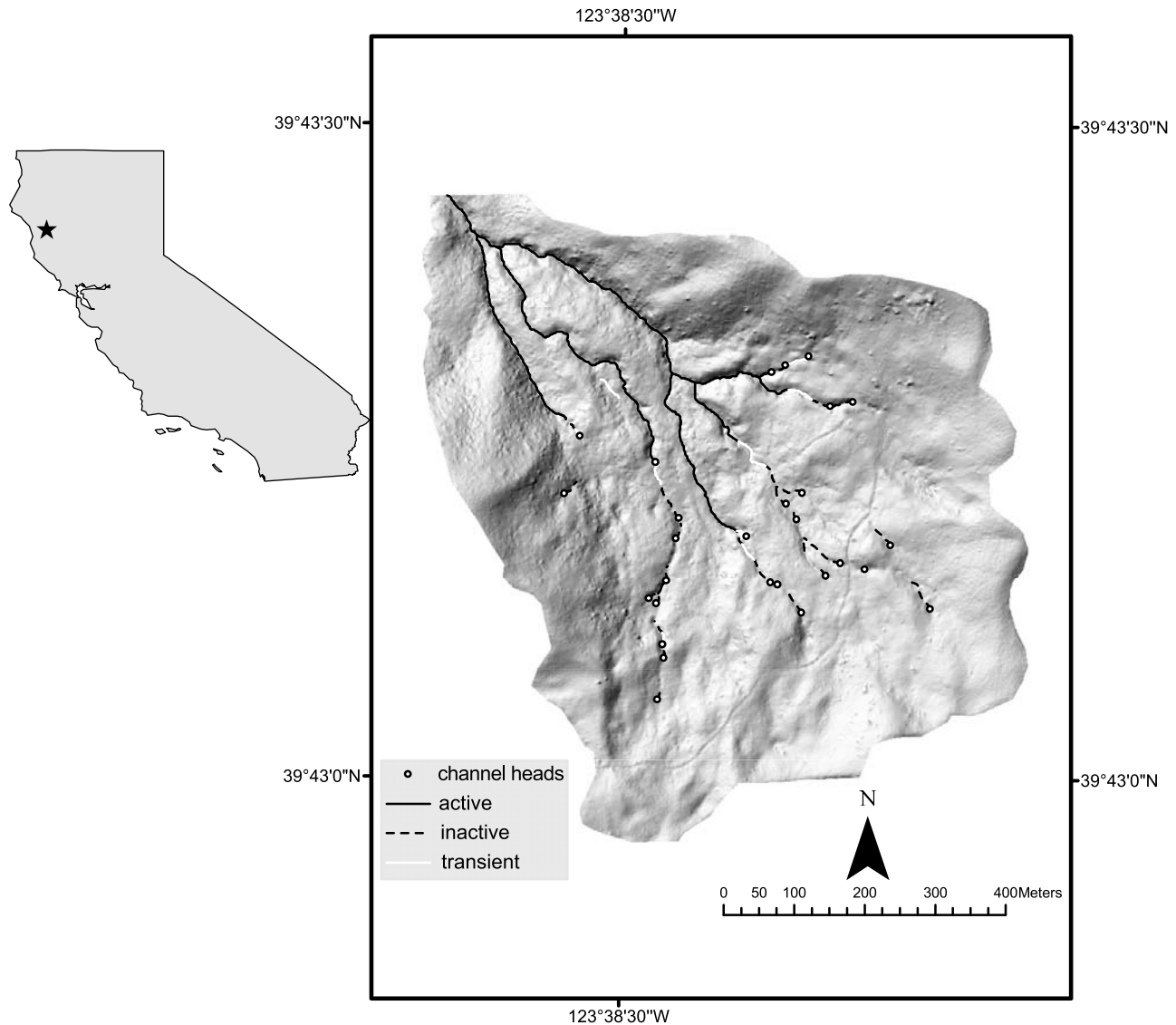
Figure 3. Skunk Creek, a 0.54 km^2 tributary located just upstream of Elder Creek, part of the South Fork Eel River in northern California. The upper half of the basin consists of active channels (well defined banks and presence of bed material), while the bottom half consists of inactive (poorly formed channels with limited bed material) and transient channels (with characteristics in between active and inactive).

by *Black et al.* [1998]). Note that the standard deviation of the Gaussian kernel and the number of iterations of the Perona-Malik filter have to be defined based on the scale of the objects we want to remove from the data. In particular the notion of 50 iterations has to be interpreted as a parameter of the algorithm. It represents the number of steps needed to achieve noise reduction and discontinuities enhancement before proceeding with the channel extraction.

[22] Figure 5a shows the original landscape at the resolution of 1 m with 3 m contours superimposed on it, as well as the computed gradients and curvatures (using simple first- and second-order numerical differentiation). Figures 5b and 5c show the filtered landscapes with the Gaussian filter and Perona-Malik filter, respectively, using for both 50 iterations as the stopping time of the forward diffusion as explained

above. The curvature reported here in all cases is the (geometric) curvature of the isoheight contours:

$$\kappa = \nabla \cdot (\nabla h / |\nabla h|) \tag{12}$$

computed by standard finite differences. The advantages in using the geometric curvature instead of the Laplacian will be addressed later in this section.

[23] Several observations can be made from Figure 5. First, it is easily seen from Figure 5b that the Gaussian filter smoothes the contours along the channels much more than the Perona-Malik filter. This is expected from the theoretical properties of the Perona-Malik filter which deforms the landscape much less along the discontinuities. In fact, the Perona-Malik filter achieves a limited deformation of con-
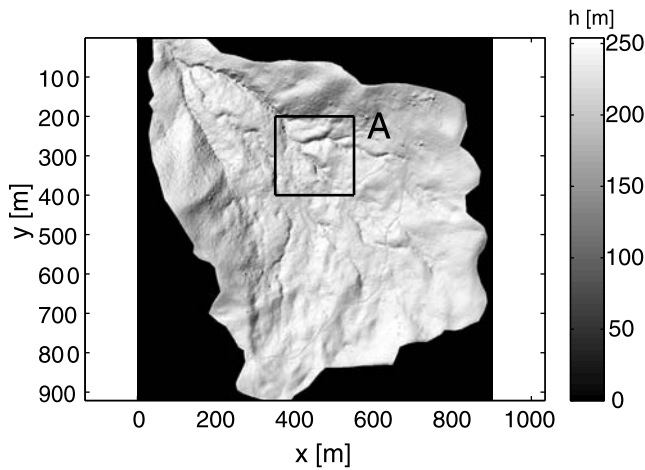
Figure 4. Location of the 200 m × 200 m square, named portion A, in Skunk Creek.

tours along the discontinuities such that it encourages the localization of these features. It is also observed that the areas of the landscape over which the curvature is positive (along the channelized areas) are much broader, and thereby deformed, in the Gaussian filtered landscape than in the Perona-Malik landscape. This is also expected from the basic properties of the two filters. One can argue that the Gaussian filtering (isotropic diffusion) could be stopped earlier, i.e, smaller spatial scale of filtering, to result in better localization of the channelized valleys. However, as it will be seen later, such a smaller-scale filtering would not adequately eliminate the isolated high curvature areas that are not pertinent to channel extraction. Furthermore, nonlinear diffusion is enhancing the discontinuities (acting in those regions as backward diffusion as shown by *Perona and Malik* [1990]; see also Appendix), which is critical for facilitating the automatic channel network extraction.

[24] Figure 6 shows the pdfs of the geometric curvatures of the original data and the filtered landscapes as well as the
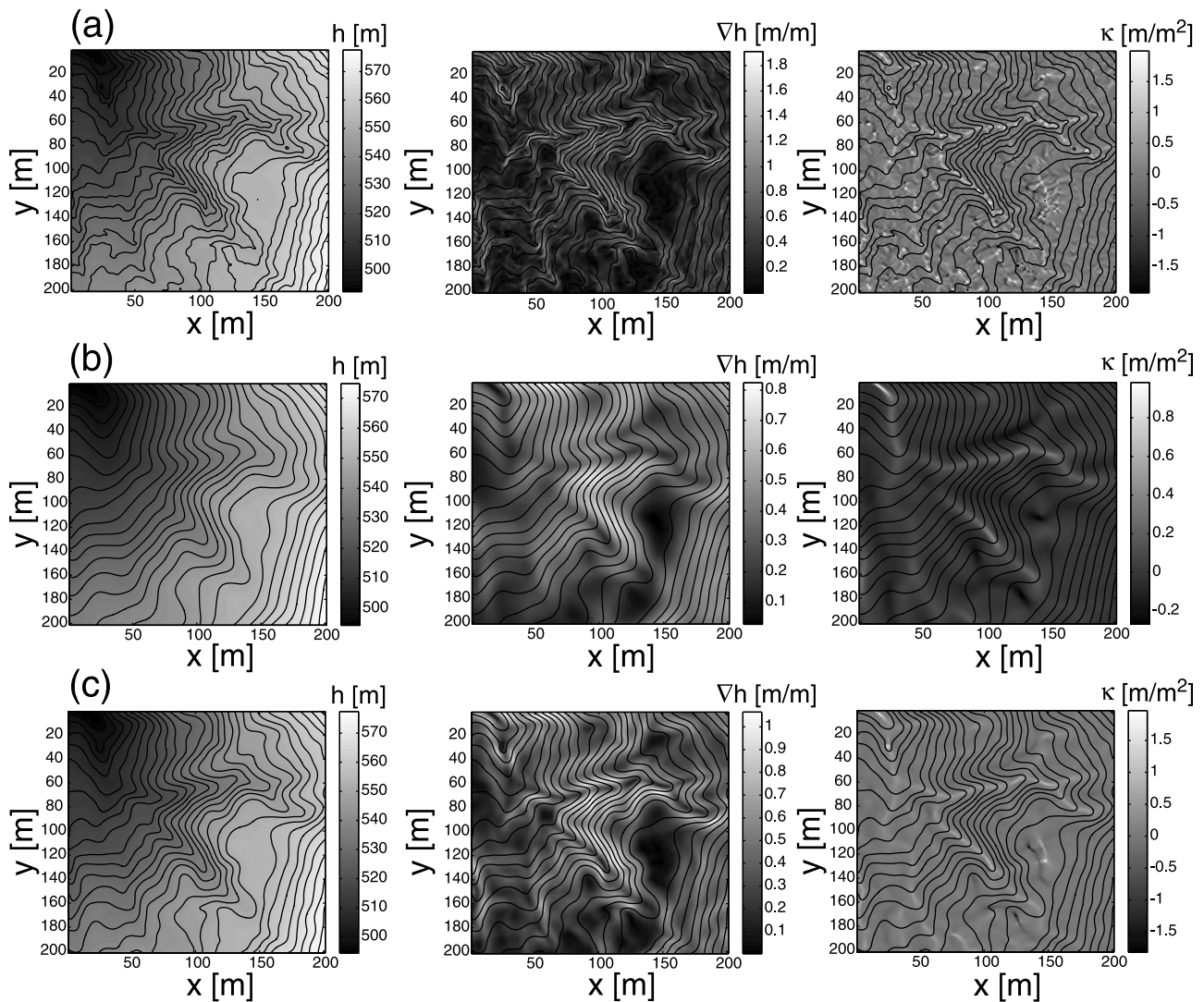
Figure 5. Comparison of the (left) elevation, (middle) gradient, and (right) curvature between the (a) original data, (b) Gaussian filtered data (scale $\sigma = 7$ m), and (c) Perona-Malik filtered data (50 iterations) computed in portion A of Skunk Creek shown in Figure 4. In all plots, elevation contours at 3 m spacing are superimposed. Notice the sharper localization of the channels in the Perona-Malik filtered lidar data.
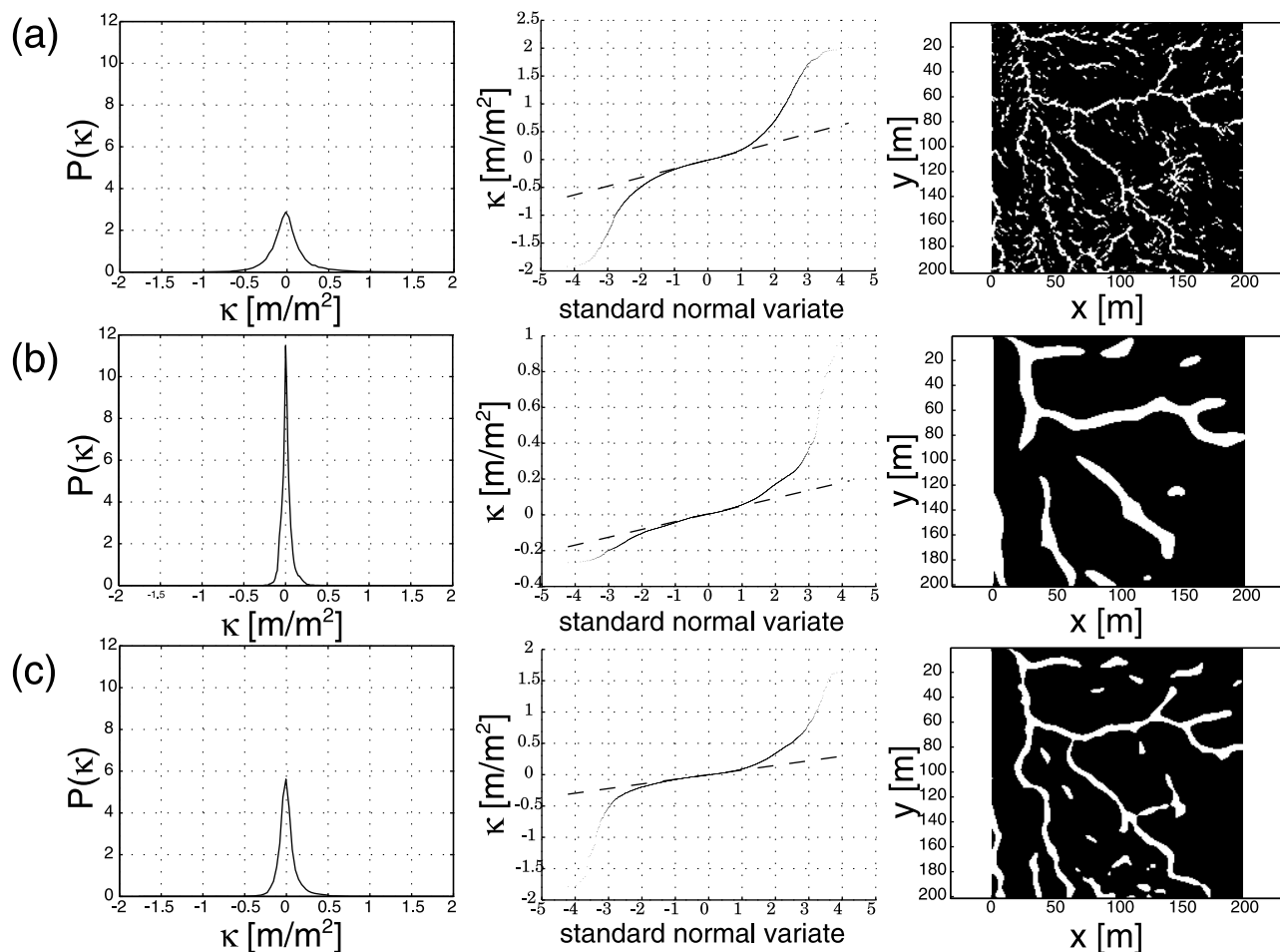
Figure 6. Comparison of the pdfs of (left) curvature, (middle) q-q plots of curvature from which the threshold value is determined, and (right) skeleton of pixels with above-threshold curvature for the (a) original data, (b) Gaussian filtered data (scale $\sigma = 7$ m), and (c) Perona-Malik filtered data (50 iterations) computed in portion A of Skunk Creek shown in Figure 4. The Perona-Malik filter does the best in terms of accurately localizing the channelized valleys while reducing background noise (see text for more discussion).

quantile-quantile plots of those curvatures. As discussed in the work of *Lashermes et al.* [2007] for the Laplacian, the sudden change in the statistical signature of the landscape, depicted by the (positive) curvature at which the pdf deviates from a Gaussian pdf, marks the transition from hillslopes to valleys. It is interesting to observe that although the actual value of the threshold curvature is different for the original image and the two filtered images, as expected, the quantile at which this transition occurs is scale- and filter-independent and as reported in the work of *Lashermes et al.* [2007] for the Laplacian, corresponds to the standard normal deviate of $z = 1$ (approximately the 84th quantile of the pdf of curvatures). Figure 6 (right) depicts the pixels at which the curvature was greater than the threshold curvature identified from the corresponding pdfs; white pixels correspond to pixels with curvature greater than the threshold value while black pixels correspond to pixels with curvature smaller than the threshold value. Several observations can be made. First, the above-threshold curvature pixels in the original high-resolution data depict the channelized part of the landscape but at the same time one sees several isolated small areas which are strongly convergent due to the high frequency variability present on the landscape (e.g., bumpy ground, vegetation, etc.). The operation of smoothing is thus performed in order to focus the channel identification on the scale of interest. Second, the above-threshold curvature pixels on the Gaussian filtered landscape eliminate the noise and nicely depict the valleys or channelized areas only; however, the corridors of the convergent areas are too wide due to the smoothing of the landscape which has been done at the scale of approximately 28 m throughout the landscape.

[25] The above-threshold curvature pixels in the Perona-Malik filtered landscape (shown in Figure 6c), depict in a much sharper way the channelized valleys. Of course, a smaller-scale Gaussian filter would also result in a sharper delineation of the channelized valleys. While this is true, however, the smaller scale of smoothing would not eliminate the isolated small convergent areas which are not part of the channel network. This is demonstrated in Figure 7, which displays the above-threshold curvature pixels for three standard deviations of the Gaussian filter: $\sigma = 2$ m
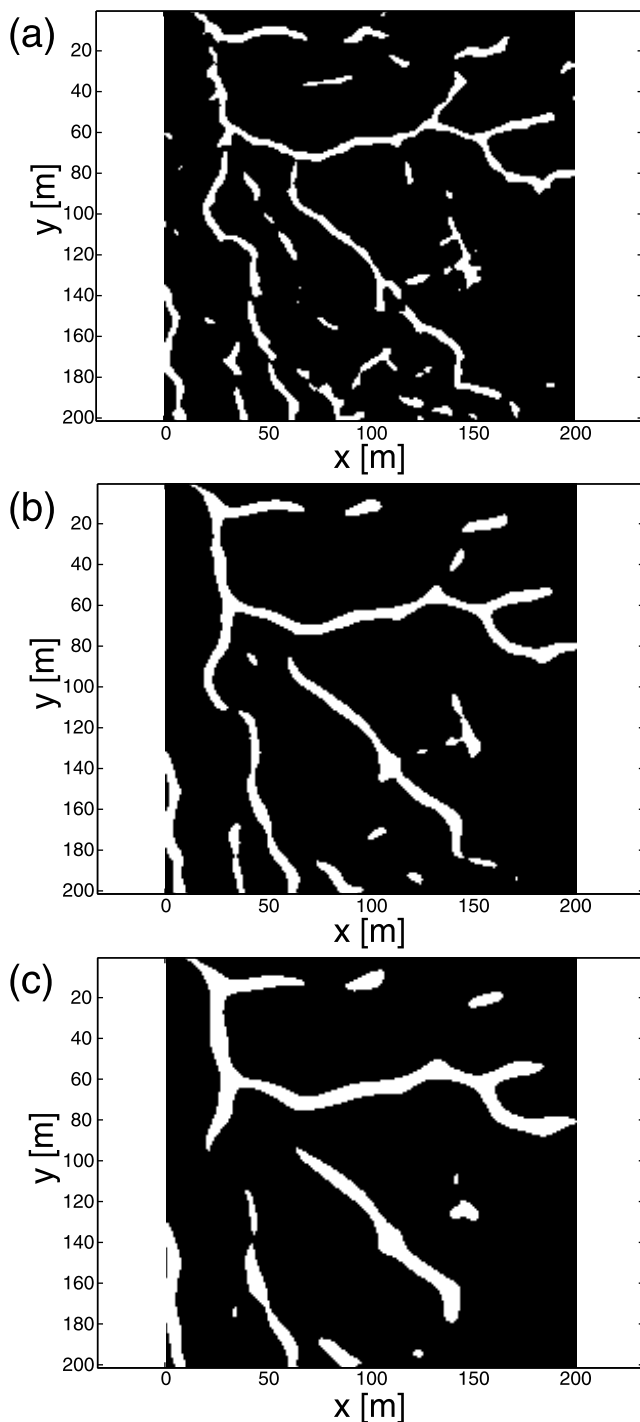
Figure 7. Comparison of the images obtained thresholding the curvature computed on the Gaussian filtered data with $\sigma = 2$ m, 4 m, 6 m (landscape smoothing scales of 8.9 m, 17.8 m, and 26.7 m, respectively). White pixels indicate pixels with above-threshold curvature. The plots refer to portion A of Skunk Creek shown in Figure 4.

(landscape smoothing scale $a = 8.9$ m); $\sigma = 4$ m (landscape smoothing scale $a = 17.8$ m); $\sigma = 6$ m (landscape smoothing scale $a = 26.7$ m). It is noted by comparing Figures 6c and 7 that the Perona-Malik localization of the channelized valleys (measured by the width of the white corridors) is

comparable to the localization provided by the Gaussian filter at scale of approximately 9 m ($\sigma = 2$ m). However, at this small scale of smoothing, the Gaussian filtering results in many more isolated high curvature areas as can be seen in Figure 7a compared to Figure 6c. Thus we conclude overall, that the Perona-Malik filter is a more efficient filter to use for preprocessing of the raw data (to produce what is called "regularized data") on which further operations for automatic channel extraction can be performed.

[26] It is also worth pointing out the advantage of using the (geometric) curvature κ instead of the Laplacian. This can be seen by comparing Figure 6b to Figure 8. The figures show the skeletons of pixels above-threshold curvature obtained on the Gaussian filtered data (scale $\sigma = 7$ m) using geometric curvature (Figure 6b) and Laplacian (Figure 8). Note how sharper and well defined is the skeleton obtained using the geometric curvature.

[27] Before demonstrating in the next section the geodesic energy minimization approach for the automatic extraction of the whole channel network of the Skunk Creek, we note that one can further process the regularized data to eliminate even more the occasional isolated convergent pixels seen in Figure 6c. This is a further operation which can be easily done via a contributing area threshold, where the threshold used has to be small enough not to interfere with channel initiation. For example, Figure 9 shows the skeleton of Figure 6c after applying the additional contributing area threshold of $A = 3000$ m^2, meaning that only the pixels with contributing area equal to or above this threshold were selected. The contributing area was computed using the Dinf algorithm [*Tarboton*, 1997]. We have then compared this value to the minimum contributing area at the channel heads, obtained using the same algorithm at the 11 farthest surveyed channel heads in Skunk Creek. As it can be seen from the histogram of the contributing area shown in Figure 10, the minimum value is equal to 3329 m^2, thus the chosen contributing area threshold of 3000 m^2 does not interfere with channel initiation. It is noted that, while the curvature threshold is easily identifiable from the
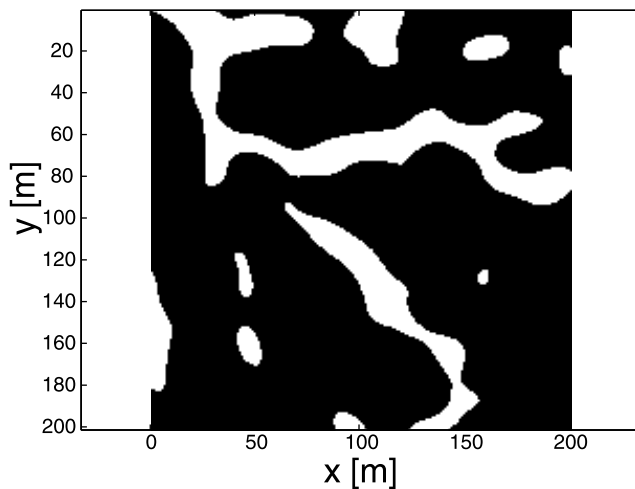
Figure 8. Skeleton of pixels above threshold curvature for the Gaussian filtered data using the Laplacian with $\sigma = 7$ m (landscape smoothing scale of 31.1 m). The plot refers to portion A of Skunk Creek shown in Figure 4.
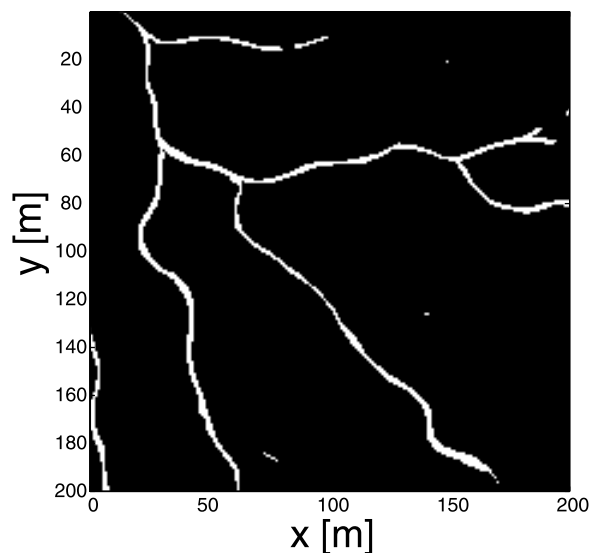
Figure 9. Skeleton obtained by thresholding curvature and contributing area for the portion A of Skunk Creek shown in Figure 4. Introducing the contributing area criterion eliminates all the isolated pixels which have a positive curvature above threshold but are not part of the channel network.

quantile-quantile plot, as explained earlier, the contributing area threshold is an arbitrarily chosen value, the smallest able to reduce the noise further in the skeleton of likely channelized pixels. It is observed that this further operation not only removes isolated convergent areas, but also further narrows the width of the likely channelized valleys providing a better preprocessed data on which channel heads are identified for the geodesic optimization to be performed (see discussion later in the application to the Skunk Creek basin).

3.2. Automatic Extraction of Channel Paths From the Regularized Data

[28] In this section we focus on the regularized data set of Skunk Creek obtained through nonlinear filtering and illustrate how the concepts of geodesics and energy minimization described earlier allow a fast and efficient extraction of the channel network. The first step of the extraction procedure is the creation of the skeleton obtained by nonlinear filtering and thresholding the curvature and the contributing area, as discussed in the previous section. The threshold curvature was easily identified by a clear change in the statistical behavior of the curvature, while the threshold area was set to a value of 3000 m^2. The extracted skeleton for the Skunk Creek river basin is shown in Figure 11.

[29] Several observations can be made by comparing Figure 11 with the surveyed network shown in Figure 3. First, in Figure 3 one observes that most of the channels in the part of the network close to the divide are labeled as "transient" or "inactive" and indeed the extracted skeleton depicts this topography by a series of interrupted areas of high curvature (and large contributing area). Second, at the points where the surveyed channel heads are located, our algorithm depicts a substantial interruption in the channel-

ized valley. It is observed therefore, that the preprocessing already allows one to investigate more closely the richness of the landscape form, something not possible with other current algorithms.

[30] From the skeleton of Figure 11, we can detect the river network outlet, as the point with the maximum flow accumulation area, computed, for example, using the Dinf algorithm [Tarboton, 1997]. After the outlet of the network has been identified, we can proceed with the detection of the end points. First the algorithm uses the skeleton of Figure 11 to compute how many continuous elements compose the skeleton and how many pixels belong to each of them. With this we mean that we label with a sequential number all the parts of the skeleton which are completely connected and do not present disruptions (i.e., the skeleton is continuously equal to 1, while the disruption is represented by one or more pixels equal to zero). We call the variable representing the number of pixels in each connected element N and plot in Figure 12a its histogram. As it can be seen, the Skunk Creek skeleton is composed by 56 connected elements, one of which is composed by 4508 pixels and 55 much smaller elements. This is something we could have expected having already observed that Skunk Creek is an extremely disrupted basin, and we can deduce that the element composed by 4508 pixels is the one which includes the part of the basin close to the outlet (the most continuous one), while the 55 smallest elements compose the skeleton of the part of the basin close to the divide (which, as we already pointed out, appears extremely disrupted in agreement with the fact that the channels here are either inactive or transient). Note that some of these elements may also represent small isolated noisy areas still present in the data.

[31] Now that the connected elements of the skeleton are identified, the algorithm looks for the end points. These are identified as the points at which the branches end. Since the branches are wider than one pixel, the actual point taken as end point is the one which belongs to the minimum geodesic distance path. Thus we need to define the cost
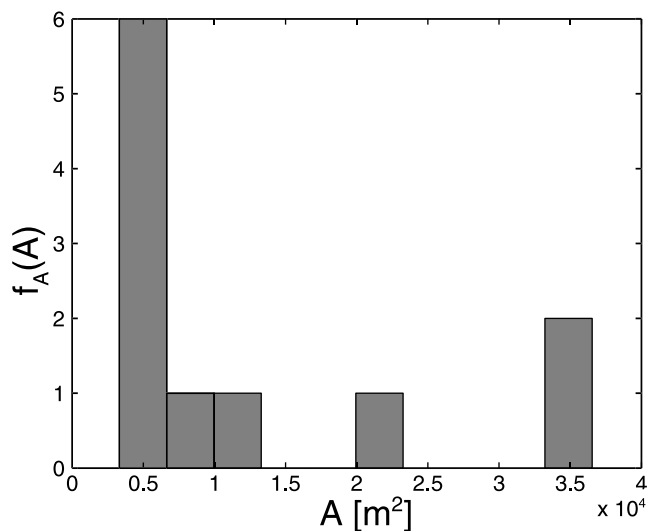
Figure 10. Histogram of the contributing area computed with the Dinf algorithm at the 11 farthest channel heads surveyed in Skunk Creek.
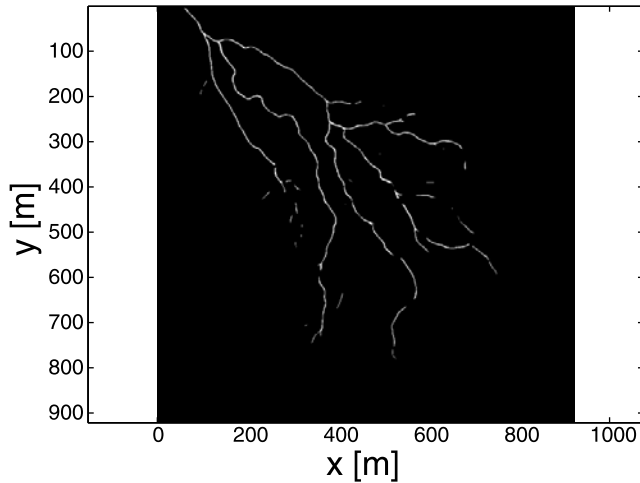
**Figure 11.** Skeleton obtained by thresholding curvature and contributing area for Skunk Creek.

function which will be used to identify the end points and connect them to the outlet through geodesic curves. This *cost function* was chosen to give penalty for selecting paths along which the drainage area does not have large flow accumulation and along which the curvature is not large compared to the surrounding points. The chosen form of the cost function ψ used in (10) is the following:

$$\psi = \frac{1}{(\alpha \cdot A + \delta \cdot \kappa)} \tag{13}$$

where A is the contributing area, κ is the curvature (of isoheight contours for our examples), and α and δ are constants which have to be chosen appropriately for the application at hand. The purpose of these constants is to take care of the dimensionality of ψ (as A is measured in m^2, while κ in 1/m) and of the difference in the order of magnitude between the quantities employed (A varies between 1 and 5×10^5 m^2, while κ has been normalized and thus varies between 0 and 1).

[32] We will discuss later in this section how the choice of the constants α and δ can be made. For now, to illustrate how the end points are detected, let us assume we have identified the optimal parameters of the cost function (13) for our application, namely $\alpha = 1$ m^{-2} and $\delta = 10^3$ m (see discussion later in this section on how these parameters can be determined). We focus on the 200 m × 200 m portion A of the Skunk Creek used in section 3.1. Figure 13a shows the skeleton of Skunk Creek (the same previously shown in Figure 9) and Figure 13b shows the end points as detected by the algorithm and indicated by a white circle. We can notice that the locations marked as A, B, and C do not appear to belong to a channel, but rather to be small convergent areas still present in the skeleton after preprocessing. It is clear that we need to identify these elements and ignore them, such that they will not be erroneously considered as channels. If we plot again the histogram of N, the number of pixels belonging to each connected element of the skeleton, ignoring the largest element, as shown in Figure 12b, we notice that there is a large number of

small connected elements located below and around a value of $N = 10$ pixels. We can interpret these elements as small isolated convergent areas and detect the end points only on the elements of the skeleton with $N > 10$ pixels. Note that we expect the identification of this threshold of N to be much simpler in the case of a basin more homogeneous than Skunk Creek. Due to the nature of the basin here in analysis, the choice of this value of N is extremely challenging, while a more homogeneous basin would probably present the skeleton as a unique connected element, with a few smaller ones, which could be easily interpreted as isolated areas. The result of adding a threshold $N > 10$ pixels in the end points detection can be seen in Figure 13c. Locations A, B, and C are now ignored and the end points (indicated by white circles) are identified only on the branches that appear to be channels. Following this procedure we have identified
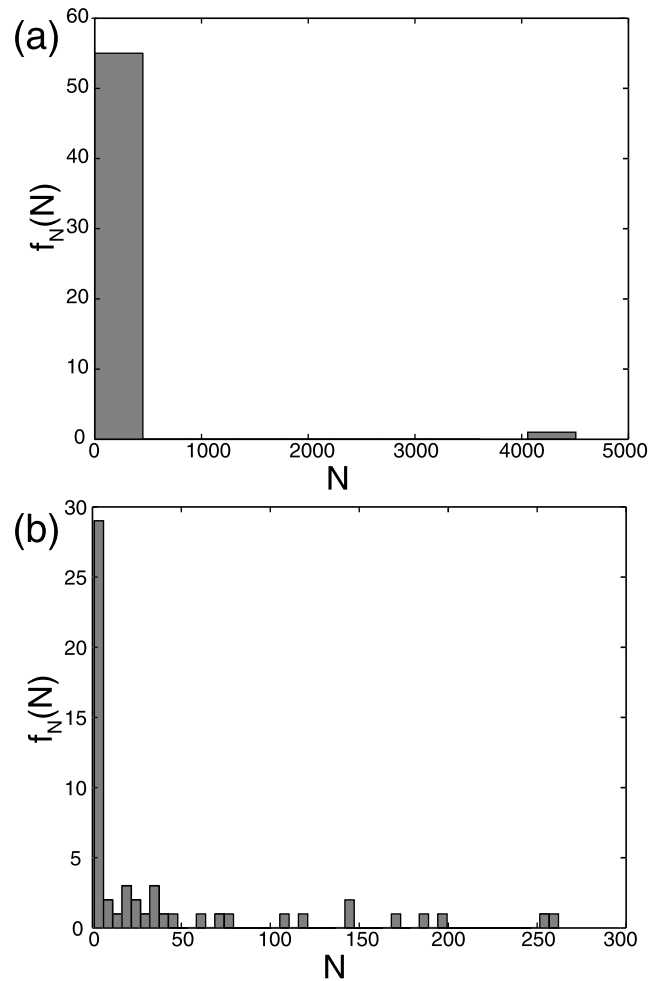
Figure 12. (a) Histogram of the number of pixels belonging to each connected element of the skeleton of Skunk Creek. The skeleton is composed by 56 elements of which one includes the majority of the pixels. (b) Excluding the most connected element, the histogram highlights a large number of small connected elements below and around $N = 10$ pixels. This value can be interpreted as the size of small isolated convergent areas which do not belong to channels.

(a)
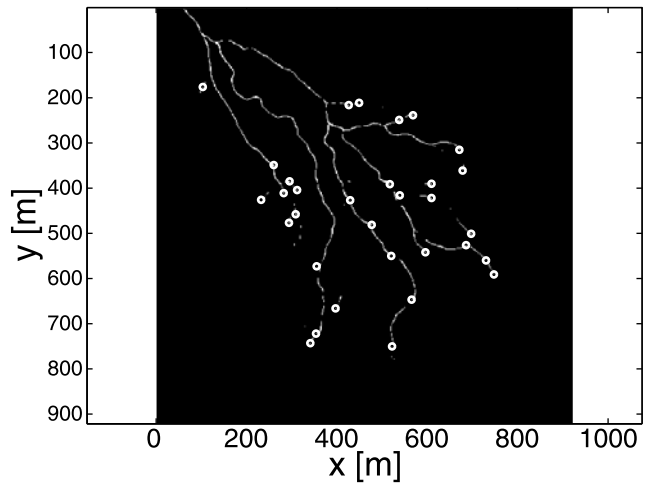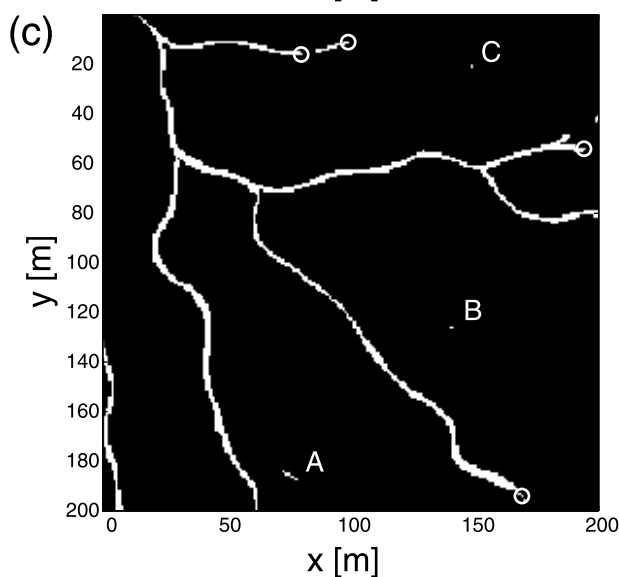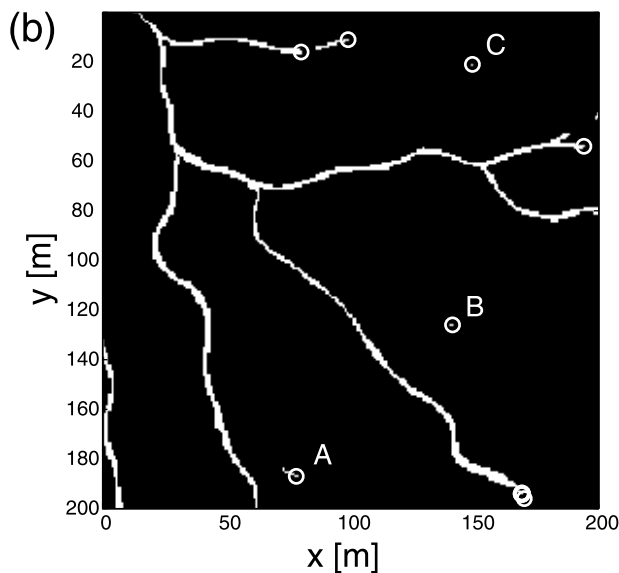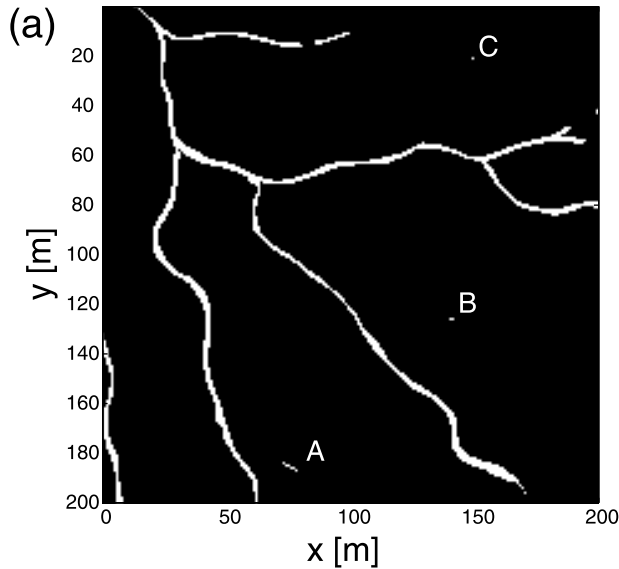
Figure 14. End points automatically detected in Skunk Creek.

all the end points in the Skunk Creek skeleton, as shown in Figure 14.

[33] After all the end points have been detected, we connect them with geodesic curves through the above defined cost function (13). Let us now discuss the selection of the constants α and δ. A helpful quantity in the definition of the constants α and δ is the geodesic distance d (11). Since the geodesic curves (10) are computed by gradient descent on d, then d can be used to understand how optimal is the choice of the constants. This is illustrated in Figure 15. Figures 15a–15j show the geodesic distances d and the extracted network correspondent to different choices of α and δ in the cost function ψ (13). Figures 15a and 15c show the geodesic distances d corresponding to $\alpha = 1$ m^{-2} and $\delta = 0$ m and $\alpha = 0$ m^{-2} and $\delta = 1$ m respectively, and Figures 15b and 15d the corresponding extracted networks. It is clear that using only one of the two quantities does not give good results. Figures 15e through 15j show the geodesic distances and the extracted networks for $\alpha = 1$ m^{-2} and $\delta = 1$, 10^3, 10^5 m. It can be seen how the choice of $\alpha = 1$ m^{-2} and $\delta = 1000$ m gives the smallest values of the geodesic distance along the skeleton of the network. This can be used as guidance to ensure an optimal computation of the geodesic curves. Note that the value of $\delta = 1000$ m corresponds to the order of magnitude of the mean contributing area computed on the whole surface $\overline{A} \simeq 550$ m^2.

[34] Figure 16 shows the extracted channel network obtained for the Skunk Creek with $\alpha = 1$ m^{-2} and $\delta = 1000$ m and compared to the surveyed data. As discussed before, this is a challenging basin for the automatic channel network extraction due to many interruptions due to land-

(b)

(c)

Figure 13. Detection of the end points. (a) Skeleton-obtained thresholding curvature and contributing area in portion A of Skunk Creek. (b) Without a threshold in N, the number of pixels composing each connected element, locations A and B are identified as channels. (c) The threshold $N > 10$ pixels allows to exclude locations A and B from the end points detection. End points are here indicated by a white circle.
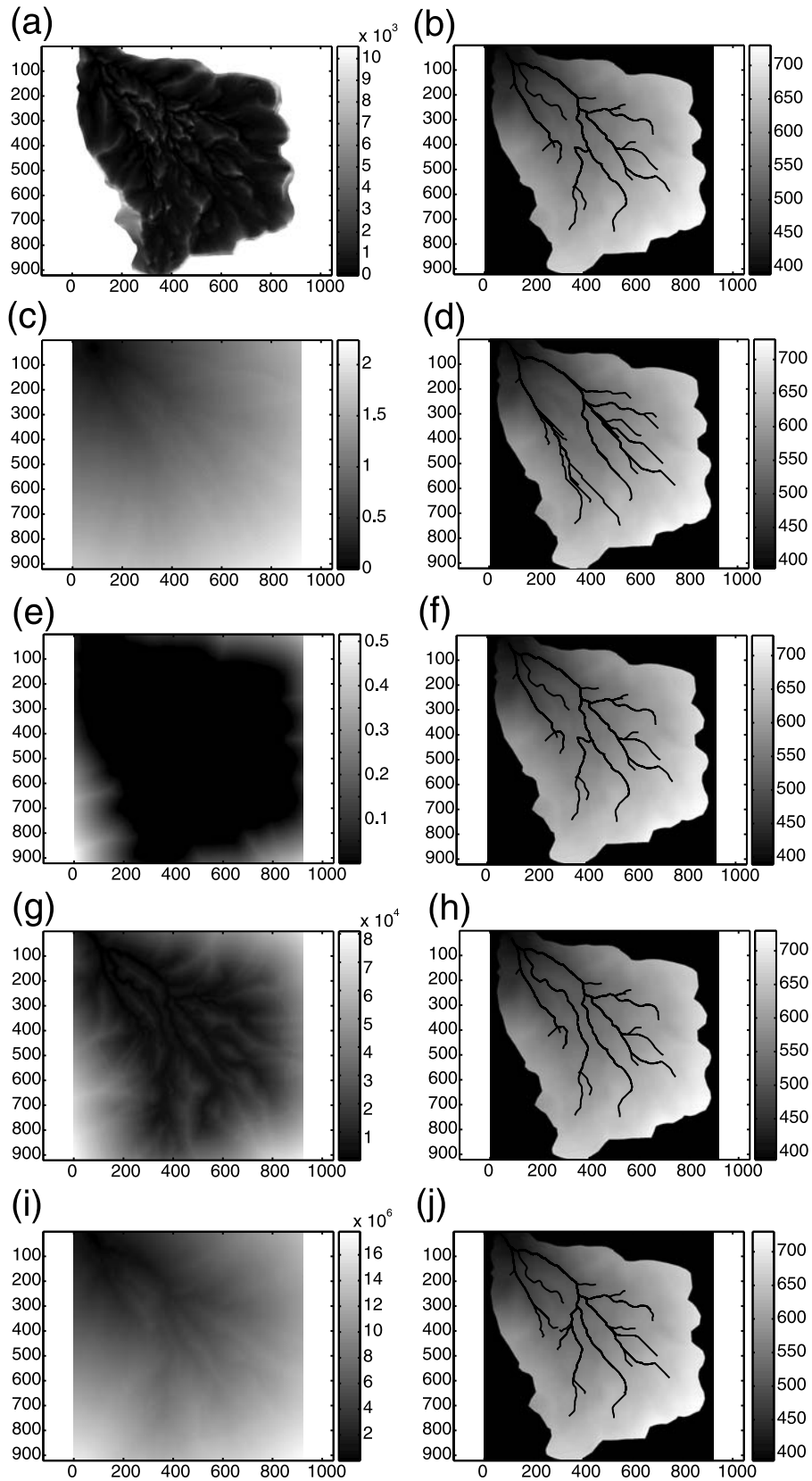
Figure 15. The geodesic distances d and the extracted networks for different choices of the parameters of the cost function ψ. The geodesic distances are useful in understanding if the choice of the cost function guarantees the optimal tracing of geodesic curves. (a and b) $\psi = \frac{1}{A}$; (c and d) $\psi = \frac{1}{\kappa}$; (e and f) $\psi = \frac{1}{A+\kappa}$; (g and h) $\psi = \frac{1}{A+10^3 \cdot \kappa}$; (i and j) $\psi = \frac{1}{A+10^5 \cdot \kappa}$.
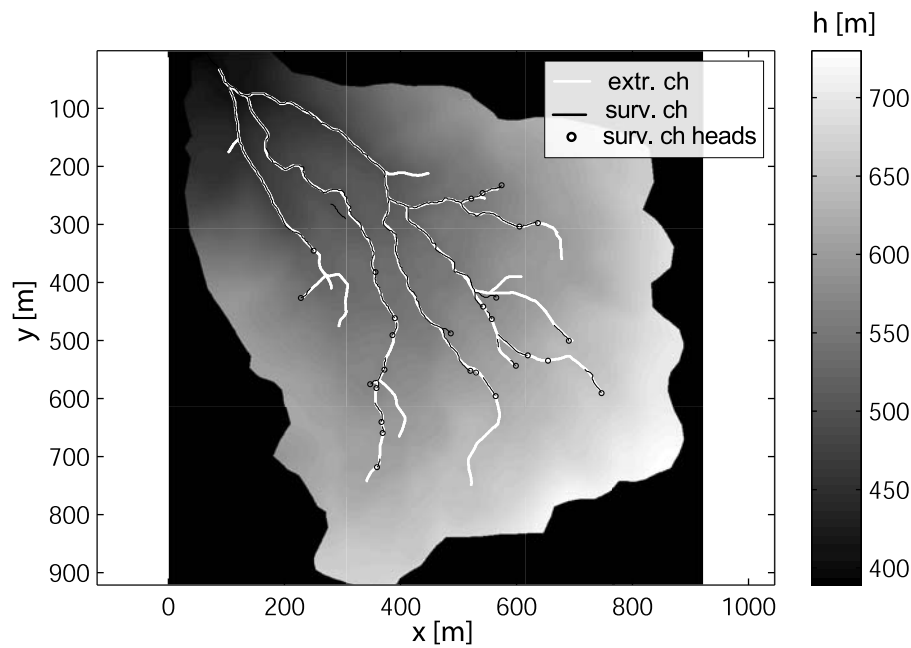
Figure 16. Automatically extracted river network for Skunk Creek using the geodesic optimization on the Perona-Malik filtered landscape compared to the digitized surveyed data.

slides and debris flows. Nevertheless, the automatically extracted channel network compares well with the field-surveyed river network. Recall that the only information that was externally provided was the threshold area of 3000 m^2 and the values of the parameters α and δ, though guidelines for the possible automatic selection of these parameters were provided as well.

[35] As discussed earlier, our algorithm allows the detection of channel disruptions (see Figure 11) which are depicted in the skeleton and can be kept before the geodesic optimization is performed. The channels are traced continuously to the farthest end points detected, but the user knows the location and the extent of the disruptions from the skeleton. Figures 17a and 17b show the histogram of the length of the channel disruptions measured on the surveyed data of Figure 3 and on the extracted skeleton of Figure 11. As it can be seen the extracted network of Skunk Creek shows, statistically, the same level of disruptiveness characteristic of the area.

4. Concluding Remarks

[36] High-resolution DEMs offer new opportunities for extracting detailed features from landscapes (e.g., channels, disruptions, channel heads), but also challenges in developing extraction methodologies that are objective and computationally efficient. The problem really becomes one of image processing relying on scale-space representation, i.e., coarsening the landscape without smoothing out features of interest and detecting features efficiently. In this paper we introduced a geometric framework for the extraction of channel networks from lidar data. The proposed approach includes two main components: the preprocessing of the data via nonlinear diffusion, to reduce noise and enhance features that are relevant to the network extraction,

and the computation of channel networks in the filtered data via geodesic curves that incorporate geomorphological knowledge such as contributing area and (geometric) curvature. The methodology presented in this paper has been applied to Skunk Creek, a tributary of the South Fork Eel River basin in northern California. Despite the challenges presented by the basin analyzed, which is a complex landslide-disrupted basin, the proposed methodology has demonstrated to be computationally efficient and able to detect, not only channels, but also the presence of channel disruptions.

[37] This work, which introduces the idea of approaching geomorphological analysis as a geometric task, opens the door to many problems in the automatic extraction of information from lidar data. For the particular case of channel networks, it is important to study the possible benefits of using other nonlinear equations for preprocessing and the introduction of additional features in the geodesic penalty function. Similarly, the exploitation for geomorphological analysis of other models which are popular in the partial differential equations and variational formulations in image processing community, such as the Mumford-Shah functional [*Mumford and Shah*, 1989], is of great interest. For example, the channel networks can be considered as discontinuity fields and outliers, and as such be automatically computed by such an approach [*Sapiro*, 2001]. Beyond this, the methodology is being presented here for the case of a tributary system, but with an appropriate modification of the cost function, could be applied to a distributary or mixed systems. Moreover channel networks are just one of the many important features in landscapes, and the exploration of the geometric approach here initiated for the extraction of other geomorphic features, such as landslides, debris flow regions,
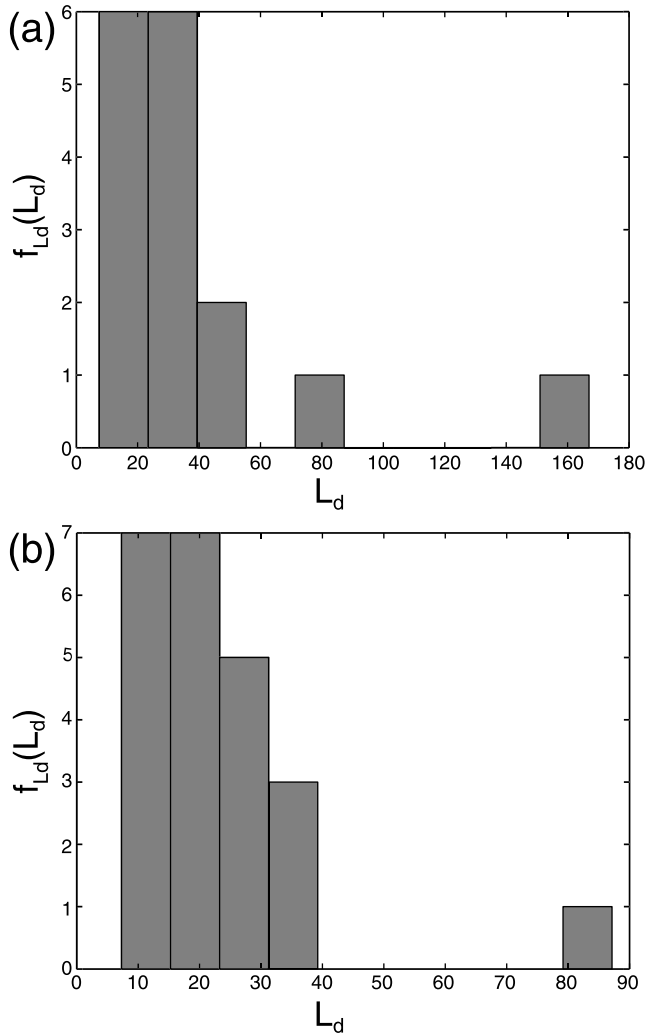
Figure 17. (a) Histogram of the length of the channel disruptions L_d measured on the surveyed data. (b) Histogram of the length of the channel disruptions L_d measured on the extracted data.

ravines, channel morphology, etc., is a subject of future research.

Appendix A

[38] In this Appendix we illustrate the property of the Perona-Malik filtering. In particular we include part of the formulation in the original *Perona and Malik* [1990] paper to show that this filter acts as a backward diffusion in regions of high gradients such that it results in enhancing these edges for easy extraction. We illustrate this via a simple 1-D example of an *edge* modeled as a step function convolved with a Gaussian, assumed to be aligned with the *y* axis (see Figure A1). The divergence operator in this case simplifies as follows:

$$\nabla \cdot [c(x, y, t)\nabla h] = \partial_x[c(x, y, t)\partial_x h] \qquad (A1)$$

Choose c to be a function of the gradient of h: $c(x, y, t) = p[\partial_x h(x, y, t)]$ and define the flux: $\phi(\partial_x h) \equiv c \cdot \partial_x h \equiv p(h_x) \cdot h_x$.

Then, the 1-D version of the nonlinear diffusion equation (7) becomes:

$$\partial_t h = \partial_x \phi(h_x) = \phi'(h_x) \cdot h_{xx} \qquad (A2)$$

We are interested in the variation in time of the slope of the edge, which is given by $\partial_t(h_x)$. If $c(\cdot) > 0$ and the function h is smooth, the order of differentiation may be inverted:

$$\partial_t(h_x) = \partial_x(h_t) = \partial_x[\partial_x \phi(h_x)] = \phi'' \cdot h_{xx}^2 + \phi' \cdot h_{xxx} \qquad (A3)$$

Assuming the edge to be oriented such that $h_x > 0$, then, at the point of inflection, being the point with maximum slope, $h_{xx} = 0$, and $h_{xxx} \gg 0$. Then as can be seen from (A3) if $\phi'(h_x) > 0$ the slope of the edge decreases with time, while if $\phi'(h_x) < 0$ the slope increases with time (the edge becomes sharper with time). Several possible choices
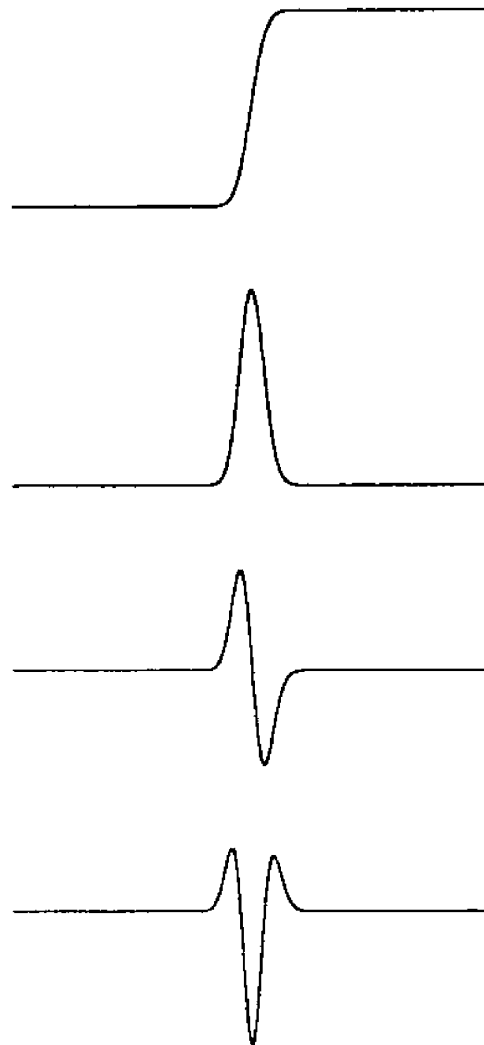
Figure A1. The 1-D edge modeled as a step function convolved with a Gaussian kernel and its first, second, and third derivatives. Figure adapted from *Perona and Malik* [1990] (copyright 1990 with permission from IEEE).
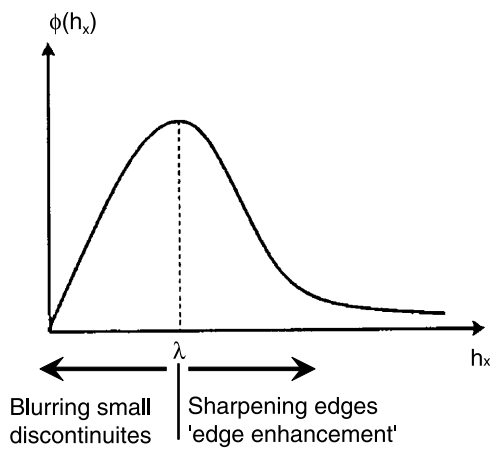
Figure A2. One form of the flux ϕ. There is a certain threshold value below which $\phi(\cdot)$ is monotonically increasing and beyond which $\phi(\cdot)$ is monotonically decreasing, achieving noise reduction and edge enhancement. Figure adapted from *Perona and Malik* [1990] (copyright 1990 with permission from IEEE).

of the function $\phi(\cdot)$ exist, one being the following (see Figure A2):

$$\phi(h_x) = C / \left(1 + (h_x/\lambda)^{1+\alpha} \right) \qquad (A4)$$

with $\alpha > 0$. This means that there is a certain threshold value related to λ and α, below which $\phi(\cdot)$ is monotonically increasing, and beyond which $\phi(\cdot)$ is monotonically decreasing, achieving noise reduction and edge enhancement. In a neighborhood of the steepest region of an edge, $\phi'(h_x)$ is negative, which means that the nonlinear diffusion acts as backward in time, thus achieving edge enhancement, while preserving the advantages of the stability given by the maximum principle satisfied by this type of elliptic equation. For more details the reader is referred to the original publication of *Perona and Malik* [1990].

References

Almansa, A., F. Cao, and B. Rouge (2002), Interpolation of digital elevation models via partial differential equations, *IEEE Trans. Geosci. Remote Sens.*, 40(2), 314–325.
Alvarez, L., P. L. Lions, and J. M. Morel (1992), Image selective smoothing and edge detection by nonlinear diffusion, *SIAM J. Numer. Anal.*, 29(3), 845–866.

Anderson, R. S. (1994), Evolution of the Santa Cruz Mountains, California, through tectonic growth and geomorphic decay, *J. Geophys. Res.*, 99(20), 161–179.
Anderson, R. S., and N. F. Humphrey (1989), Interaction of weathering and transport processes in the evolution of arid landscapes, in *Quantitative Dynamic Stratigraphy*, edited by T. A. Cross, pp. 349–361, Prentice-Hall, Englewood Cliffs, N. J.
Andrews, D. J., and R. C. Buckman (1987), Fitting degradation of shoreline scarps by a nonlinear diffusion model, *J. Geophys. Res.*, 92(12), 857–867.
Ardizzone, F., M. Cardinali, M. Galli, F. Guzzetti, and P. Reichenbach (2007), Identification and mapping of recent rainfall-induced landslides using elevation data collected by airborne lidar, *Nat. Hazards Earth Syst. Sci.*, 7(6), 637–650.
Band, L. E. (1986), Topographic partition of watersheds with digital elevation models, *Water Resour. Res.*, 22(1), 15–24.
Black, M., G. Sapiro, D. Marimont, and D. Heeger (1998), Robust anisotropic diffusion, *IEEE Trans. Image Process.*, 7(3), 421–432.
Braunmandl, A., T. Canarius, and H. P. Helfrich (2003), Diffusion methods for form generalisation, in *Dynamics of Multiscale Earth Systems*, Lect. Notes Earth Sci., vol. 97, edited by H. J. Neugebauer and C. Simmer, pp. 89–101, Springer, Berlin.
Burt, P., and E. Adelson (1983), The Laplacian pyramid as a compact image code, *IEEE Trans. Commun.*, COM-31, 532–540.
Catté, F., P.-L. Lions, J.-M. Morel, and T. Coll (1992), Image selective smoothing and edge detection by nonlinear diffusion, *SIAM J. Numer. Anal.*, 29(1), 182–193.
Cavalli, M., and L. Marchi (2008), Characterisation of the surface morphology of an alpine alluvial fan using airborne lidar, *Nat. Hazards Earth Syst. Sci.*, 8(2), 323–333.
Cavalli, M., P. Tarolli, L. Marchi, and G. Dalla Fontana (2008), The effectiveness of airborne lidar data in the recognition of channel bed morphology, *Catena*, 73, 249–260, doi:10.1016/j.catena.2007.11.001.
Costa-Cabral, M. C., and S. J. Burges (1994), Digital elevation model networks (DEMON): A model of flow over hillslopes for computation of contributing and dispersal areas, *Water Resour. Res.*, 30(6), 1681–1692.
Dial, R. B. (1969), Algorithm 360: Shortest-path forest with topological ordering, *Commun. ACM*, 12(11), 632–633.
Dietrich, W. E., C. J. Wilson, D. R. Montgomery, and J. McKean (1993), Analysis of erosion thresholds, channel networks and landscape morphology using a digital terrain model, *J. Geol.*, 101(2), 259–278.
Dietrich, W. E., D. Bellugi, and R. Real de Asua (2001), Validation of the shallow landslide model, SHALSTAB, for forest management, in *Land Use and Watersheds: Human Influence on Hydrology and Geomorphology in Urban and Forest Areas*, Water Sci. Appl. Ser., vol. 2, edited by M. S. Wigmosta and S. J. Burges, pp. 195–227, AGU, Washington, D. C.
Dijkstra, E. (1959), A note on two problems in connection with graphs, *Numer. Math.*, 1(1), 269–271.
Do Carmo, M. P. (1976), *Differential Geometry of Curves and Surfaces*, Prentice-Hall, Englewood Cliffs, N. J.
Frankel, K. L., and J. F. Dolan (2007), Characterizing arid region alluvial fan surface roughness with airborne laser swath mapping digital topographic data, *J. Geophys. Res.*, 112, F02025, doi:10.1029/2006JF000644.
Giannoni, F., G. Roth, and R. Rudari (2005), A procedure for drainage network identification from geomorphology and its application to the prediction of the hydrologic response, *Adv. Water Resour.*, 28(6), 567–581.
Glenn, N. F., D. R. Streutker, D. J. Chadwick, G. D. Tahckray, and S. J. Dorsch (2006), Analysis of lidar-derived topography information for characterizing and differentiating landslide morphology and activity, *Geomorphology*, 73, 131–148.
Hancock, G. R., and K. G. Evans (2006), Channel head location and characteristics using digital elevation models, *Earth Surf. Processes Landforms*, 31(7), 809–824.
Helmsen, J., E. G. Puckett, P. Collela, and M. Dorr (1996), Two new methods for simulating photolithography development in 3-D, *Proc. SPIE Int. Soc. Opt. Eng.*, 2726, 253–261.
Howard, A. D. (1994a), A detachment-limited model of drainage basin evolution, *Water Resour. Res.*, 30(7), 2261–2285.
Howard, A. D. (1994b), Badlands, in *Geomorphology of Desert Environments*, edited by A. D. Abrahams and A. J. Parsons, pp. 213–242, Chapman and Hall, New York.
Howard, A. D. (1997), Badland morphology and evolution: Interpretation using a simulation model, *Earth Surf. Processes Landforms*, 22, 211–227.
Kimmel, R. (2003), *Numerical Geometry of Images: Theory, Algorithms, and Applications*, 209 pp., Springer, New York.
Kirkby, M. J. (1984), Modeling cliff development in South Wales: Savigear re-reviewed, *Z. Geomorphol.*, 28, 405–426.
Kirkby, M. J. (1985), A model for the evolution of regolith-mantled slopes, in *Models in Geomorphology*, edited by M. J. Woldenberg, pp. 213–237, Allen and Unwin, Winchester, Mass.

Koenderink, J. (1984), The structure of images, *Biol. Cybern.*, *50*(5), 363–370.

Lashermes, B., E. Foufoula-Georgiou, and W. E. Dietrich (2007), Channel network extraction from high-resolution topography using wavelets, *Geophys. Res. Lett.*, *34*, L23S04, doi:10.1029/2007GL031140.

Mark, D. M. (1988), Network models in geomorphology, in *Modeling Geomorphological Systems*, edited by M. G. Anderson, pp. 73–97, John Wiley, New York.

McKean, J., and J. J. Roering (2004), Objective landslide detection and surface morphology mapping using high-resolution airborne laser altimetry, *Geomorphology*, *57*, 331–351, doi:10.1016/S0169-555X(03)00164-8.

McMaster, K. J. (2002), Effects of digital elevation model resolution on derived stream network positions, *Water Resour. Res.*, *38*(4), 1042, doi:10.1029/2000WR000150.

McNamara, J. P., A. D. Ziegler, S. H. Wood, and J. B. Vogler (2006), Channel head locations with respect to geomorphologic thresholds derived from a digital elevation model: A case study in northern Thailand, *For. Ecol. Manage.*, *224*, 147–156.

Memoli, F., and G. Sapiro (2005), Distance functions and geodesics on submanifolds of R^d and point clouds, *SIAM J. Appl. Math.*, *65*(4), 1227–1260.

Montgomery, D., and W. E. Dietrich (1988), Where do channels begin?, *Nature*, *336*, 232–234, doi:10.1038/336232a0.

Montgomery, D. R., and W. E. Dietrich (1989), Source areas, drainage density, and channel initiation, *Water Resour. Res.*, *25*(8), 1907–1918.

Montgomery, D. R., and W. E. Dietrich (1992), Channel initiation and the problem of landscape scale, *Science*, *255*, 826–830.

Montgomery, D. R., and W. E. Dietrich (1994), Landscape dissection and drainage area-slope thresholds, in *Process Models and Theoretical Geomorphology*, edited by M. J. Kirkby, pp. 221–246, John Wiley, New York.

Montgomery, D., and E. Foufoula-Georgiou (1993), Channel network source representation for digital elevation models, *Water Resour. Res.*, *29*(12), 3925–3934.

Mumford, D., and J. Shah (1989), Optimal approximation by piecewise smooth functions and associated variational problems, *Commun. Pure Appl. Math.*, *42*, 577–685.

O'Callaghan, J., and D. Mark (1984), The extraction of drainage networks from digital elevation data, *J. Comput. Vis. Graph. Image Process.*, *28*(3), 323–344.

Perona, P., and J. Malik (1990), Scale-space and edge detection using anisotropic diffusion, *IEEE Trans. Pattern Anal. Mach. Intel.*, *12*(7), 629–639.

Roering, J. J., J. Kirchner, and W. E. Dietrich (1999), Evidence for nonlinear, diffusive sediment transport on hillslopes and implications for landscape morphology, *Water Resour. Res.*, *35*(3), 853–870.

Sapiro, G. (2001), *Geometric Partial Differential Equations and Image Analysis*, 412 pp., Cambridge Univ. Press, New York.

Sethian, J. A. (1999), *Level Set Methods and Fast Marching Methods*, 400 pp., Cambridge Univ. Press, Cambridge, U. K.

Smith, M. J., J. Rose, and S. Booth (2006), Geomorphological mapping of glacial landforms from remotely sensed data: An evaluation of the principal data sources and an assessment of their quality, *Geomorphology*, *76*, 148–165, doi:10.1016/j.geomorph.2005.11.001.

Solé, A., V. Caselles, G. Sapiro, and F. Arándiga (2004), Morse description and geometric encoding of digital elevation maps, *IEEE Trans. Image Process.*, *13*(9), 1245–1262.

Staley, D. M., T. A. Wasklewicz, and J. S. Blaszczynski (2006), Surficial patterns of debris flow deposition on alluvial fans in Death Valley, CA using airborne laser swath mapping, *Geomorphology*, *74*, 152–163.

Tarboton, D. G. (1997), A new method for the determination of flow directions and contributing areas in grid digital elevation models, *Water Resour. Res.*, *33*(2), 309–319.

Tarboton, D. G., R. L. Bras, and I. Rodriguez-Iturbe (1988), The fractal nature of river networks, *Water Resour. Res.*, *24*(8), 1317–1322.

Tarboton, D. G., R. L. Bras, and I. Rodriguez-Iturbe (1989), The analysis of river basins and channel networks using digital terrain data, *Rep. 326*, Ralph M. Parson Lab., Dep. of Civ. Eng., Mass. Inst. of Technol., Cambridge, Mass.

Tarboton, D. G., R. L. Bras, and I. Rodriguez-Iturbe (1991), On the extraction of channel networks from digital elevation data, *Hydrol. Processes*, *5*(1), 81–100.

Tarolli, P., and G. Dalla Fontana (2009), Hillslope to valley transition morphology: New opportunities from high resolution DTMs, *Geomorphology*, *113*, 47–56.

Tarolli, P., and D. G. Tarboton (2006), A new method for determination of most likely landslide initiation points and the evaluation of digital terrain model scale in terrain stability mapping, *Hydrol. Earth Syst. Sci.*, *10*(5), 663–677.

Tribe, A. (1991), Automated recognition of valley heads from digital elevation models, *Earth Surf. Processes Landforms*, *16*(1), 33–49.

Tribe, A. (1992), Automated recognition of valley lines and drainage networks from grid digital elevation models: A review and a new method, *J. Hydrol.*, *139*, 263–293.

Tsai, Y. R., L. T. Cheng, S. Osher, and H. K. Zhao (2003), Fast sweeping algorithms for a class of Hamilton-Jacobi equations, *SIAM J. Numer. Anal.*, *41*(2), 673–694.

Tsitsiklis, J. N. (1995), Efficient algorithms for globally optimal trajectories, *IEEE Trans. Autom. Control*, *40*(9), 1528–1538.

Vianello, A., M. Cavalli, and P. Tarolli (2009), Lidar-derived slopes for headwater channel network analysis, *Catena*, *76*, 97–106.

Witkin, A. P. (1983), Scale-space filtering, paper presented at 10th International Joint Conference on Artificial Intelligence, ACM Inc., New York.

Yatziv, L., A. Bartesaghi, and G. Sapiro (2006), O(N) implementation of the fast marching algorithm, *J. Comput. Phys.*, *212*, 393–399.

Zhao, H. K. (2004), A fast sweeping method for Eikonal equations, *Math. Comput.*, *74*(250), 603–627.

_____

W. E. Dietrich, Department of Earth and Planetary Science, University of California, Berkeley, CA 94720, USA.

T. Do Trung, Département de Mathématiques, École Normale Supérieure de Cachan, Bâtiment Laplace 1er étage, 61 Ave. du Président Wilson, F-94235 Paris, Cachan CEDEX, France.

E. Foufoula-Georgiou and P. Passalacqua, Saint Anthony Falls Laboratory, National Center for Earth Surface Dynamics, Department of Civil Engineering, University of Minnesota, 2 3rd Ave. SE, Minneapolis, MN 55414, USA. (efi@umn.edu)

G. Sapiro, Department of Electrical and Computer Engineering, University of Minnesota, 200 Union St. SE, Minneapolis, MN 55455, USA.

Subordinated Brownian motion model for sediment transport

Vamsi Ganti, Arvind Singh, Paola Passalacqua, and Efi Foufoula-Georgiou

Department of Civil Engineering, St. Anthony Falls Laboratory and National Center for Earth-Surface Dynamics,
University of Minnesota, Minnesota, USA

Following the introduction of the Brownian motion model for sediment transport by Einstein, several stochastic models have been explored in the literature motivated by the need to reproduce the observed non-Gaussian probability density functions (PDFs) of the sediment transport rates observed in laboratory experiments. Recent studies have presented evidence that PDFs of bed elevation and sediment transport rates depend on time scale (sampling time), but this dependence is not accounted for in any previous stochastic models. Here we propose an extension of Brownian motion, called fractional Laplace motion, as a model for sediment transport which acknowledges the fact that the time over which the gravel particles are in motion is in itself a random variable. We show that this model reproduces the multiscale statistics of sediment transport rates as quantified via a large-scale laboratory experiment.

I. INTRODUCTION

Stochastic theories of sediment transport were initiated with the seminal work of Einstein [1], who introduced a Brownian motion model for particle motion. Since then, these theories were advanced by the need to reproduce the observed statistics of sediment transport rates or particle movement. In [2], a birth-death process was proposed for sediment transport, which was later shown, in [3], to be inadequate as it failed to predict the heavy tails found in the probability density functions (PDFs) of the number of moving particles in a given observation window. In [4], the birth-death model was extended to a birth-death-immigration-emigration model to reproduce the experimentally observed negative binomial distributions for the number of moving sediment particles. The stochastic nature of sediment particle entrainment has been widely recognized and considerable efforts have been invested in modeling this behavior [5–8]. The underlying assumption of these models is that the shear stress, which is the initiator for sediment entrainment, follows a Gaussian distribution. However, many experimental studies have shown that the shear stress fluctuations do not follow a Gaussian distribution, and in particular it has been shown that they follow a Gamma distribution (e.g., [9,10]). The role of near-bed turbulence in sediment transport has also been recognized to play an important role [11,12]. However, turbulence is well known to exhibit variability over a range of scales, and it is reasonable to ask whether this multiscale variability shows its effect on sediment transport series and bed elevation fluctuations.

In a recent study [13], the dependence of the statistics of sediment transport on time scale (sampling time) akin to the scale-dependent statistics of fully developed turbulence [14] was documented. Specifically, it was shown that the PDF of sediment transport rates at small sampling times exhibits a heavy-tailed distribution which however approaches a Gaussian distribution as the sampling time increases. To the best of our knowledge, no stochastic model of sediment transport exists which reproduces this observed multiscale statistical structure of sediment transport series. It is the scope of this paper to present such a model and discuss its mathematical properties and its physical relevance to modeling sediment transport.

The paper is structured as follows. In the following section a brief review of multiscale statistics of sediment transport series observed in a large-scale laboratory experiment is given. In Sec. III the application of a stochastic model, called the fractional Laplace motion, is proposed to characterize the sediment transport series and is shown that it is able to reproduce the observed statistics. In Sec. IV the proposed model is validated against the sediment transport series obtained from a large-scale laboratory experiment. Finally, discussion and conclusions are given in Secs. V and VI.

II. MULTISCALE STATISTICS OF SEDIMENT TRANSPORT SERIES

A large-scale laboratory experiment was recently conducted in the Main Channel facility at the St. Anthony Falls Laboratory, University of Minnesota, in order to study sediment transport dynamics in gravel and sand-bed rivers. The details of the experimental facility can be found in [13,15,16]. Here we briefly describe one of the experiments from which data were used in this study. The flume is 2.74 m wide and 55 m long, with a maximum depth of 1.8 m (see Fig. 1). Gravel with a median particle size (D50) of 11.3 mm was placed in a 20-m-long mobile-bed section of the 55-m-long channel. A constant discharge of water at 4300 liters per second was released into the flume. At the downstream end

FIG. 1. Experimental flume facility at the St. Anthony Falls Laboratory, University of Minnesota.

of the test section was located a bedload trap, consisting of five weighing pans of equal size that spanned the width of the channel. Any bedload sediment transported to the end of the test section of the channel would fall into the pans, which automatically recorded the weight of the accumulated sediment every 1.1 s. Data were collected over a period of 30 h once a state of statistical equilibrium was reached (see [13,16]). The original series of 1.1 s sampling interval were converted to 2 min sediment accumulations via moving averaging in order to remove mechanical (due to vibration) noise present in the raw data (see [13,16]). Let us denote by $S(t)$ the 2 min sediment accumulation series which is shown in Fig. 2. In this section, we present the multiscale analysis performed on this sediment transport series.

The goal of a multiscale analysis is to quantify the manner in which the statistics of the local fluctuations, or variability in a series, changes with scale. In order to investigate the multiscale structure of $S(t)$ over a range of scales, differences (or increments) were computed at different scales (lags) r, denoted by $\delta S(t, r)$, as

$$\delta S(t, r) = S(t + r\Delta t) - S(t), \tag{1}$$

i.e., $\delta S(t, r)$ is the incremental sediment accumulation within a time interval $r\Delta t$, where $\Delta t = 2$ mins. In [13], "generalized fluctuations" were used defined via wavelet transforms (acting as a differencing filter). Notice that while $S(t)$ can only be positive, the fluctuation series $\delta S(t, r)$ will have zero mean and can be both positive and negative. The estimates of the qth-order statistical moments of the absolute values of sediment transport increments at scale r, also called the partition functions or structure functions, $M(q, r)$ are defined as

$$M(q, r) = \frac{1}{N_r} \sum_{t=1}^{N_r} |\delta S(t, r)|^q, \tag{2}$$

where N_r is the number of data points of sediment transport increments at a scale r. The statistical moments $M(q, r)$ for all q completely describe the shape of the PDFs as the scale r changes. Statistical scaling, or scale invariance, requires that $M(q, r)$ is a power-law function of the scale, that is,

$$M(q, r) \sim r^{\tau(q)}, \tag{3}$$

where $\tau(q)$ is the so-called scaling exponent function. For a scale-invariant series, it has been shown that the function $\tau(q)$ completely determines how the PDF of the variable changes with scale (e.g., [17,18]). The simplest form of scaling, known as simple scaling or monoscaling, is when the scaling exponents are a linear function of the moment order, i.e., when $\tau(q) = Hq$. In this case, the shape of the PDF remains the same over scales apart from a rescaling by a deterministic function which depends on the single parameter H. If $\tau(q)$ is nonlinear, the shape of the PDF changes over scales and more than one parameter is required to describe this change (e.g., [17,18]). In this case, the series is called a multifractal. For most processes the nonlinear relationship of $\tau(q)$ with q can be parameterized as a polynomial, and the simplest form is a quadratic approximation,
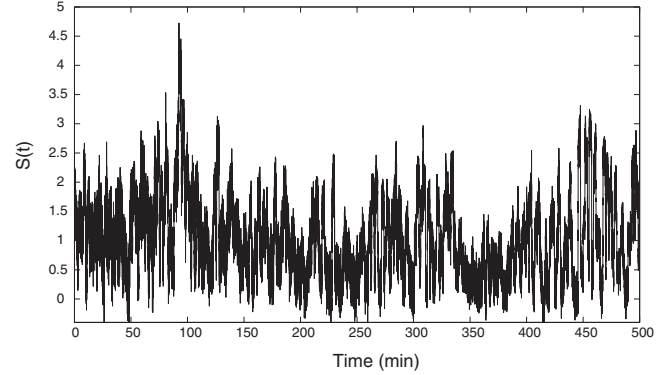

FIG. 2. Sediment transport series $S(t)$ (in kgs) at a sampling interval of 2 min, i.e., series of 2 min sediment accumulation.

$$\tau(q) = c_1 q - \frac{c_2}{2} q^2. \tag{4}$$

The multiscale analysis in this framework provides a compact way, using two parameters c_1 and c_2, of parametrizing the change of the PDF over a range of scales. In parallel to the statistical interpretation of these parameters, there is also a geometrical interpretation. Specifically, the parameter c_1 is a measure of the average "roughness" of the series and c_2, the so-called intermittency coefficient, is a measure of the temporal heterogeneity of the abrupt local fluctuations in the series [in fact, it relates to the variance of the so-called local Hölder exponent which measures the local degree of nondifferentiability of the series (e.g., [18])]. It is noted that using a higher than second degree polynomial approximation of $\tau(q)$, say a third degree polynomial, introduces a third parameter c_3, which is a measure of the third moment of the local differentiability of the series and it might be hard to accurately estimate from a limited sample size of data. Thus, in most practical applications the approximation of $\tau(q)$ curve is restricted to a quadratic function which is parameterized by c_1 and c_2. Estimation of the multifractal parameters, c_1 and c_2, can be performed in various ways. For example, one can use a quadratic fit to the whole $\tau(q)$ curve [estimated for several values of q from the slopes of $M(q, r)$ vs r in log-log space] or use the first two scaling exponents only, $\tau(1)$ and $\tau(2)$, or use the cumulant analysis method (e.g., [18] and references therein). In this study, we use the quadratic fit to the $\tau(q)$ curve for the estimation of the parameters c_1 and c_2.

The multiscale analysis described above was performed on the sediment transport series shown in Fig. 2. Figure 3(a) shows the scaling of the moments of the sediment transport increment series $\delta S(t, r)$ with scale r. It is to note that the structure functions follow a power-law relation in r over a range of scales from $r = 4$ to 64 (8 to 128 min). The scaling exponents of the structure functions $M(q, r)$ are plotted as a function of the order of moments q in Fig. 3(b) for $q = 0.5, 1, 1.5, \ldots, 3$. We observe that $\tau(q)$ has a nonlinear dependence on q, which is an indication of the presence of multifractality and the fact that the shape of the PDF changes with scale. Figure 3(c) displays the PDFs of sediment transport increments at two scales, $r = 10$ and $r = 60$ (i.e., 20 and
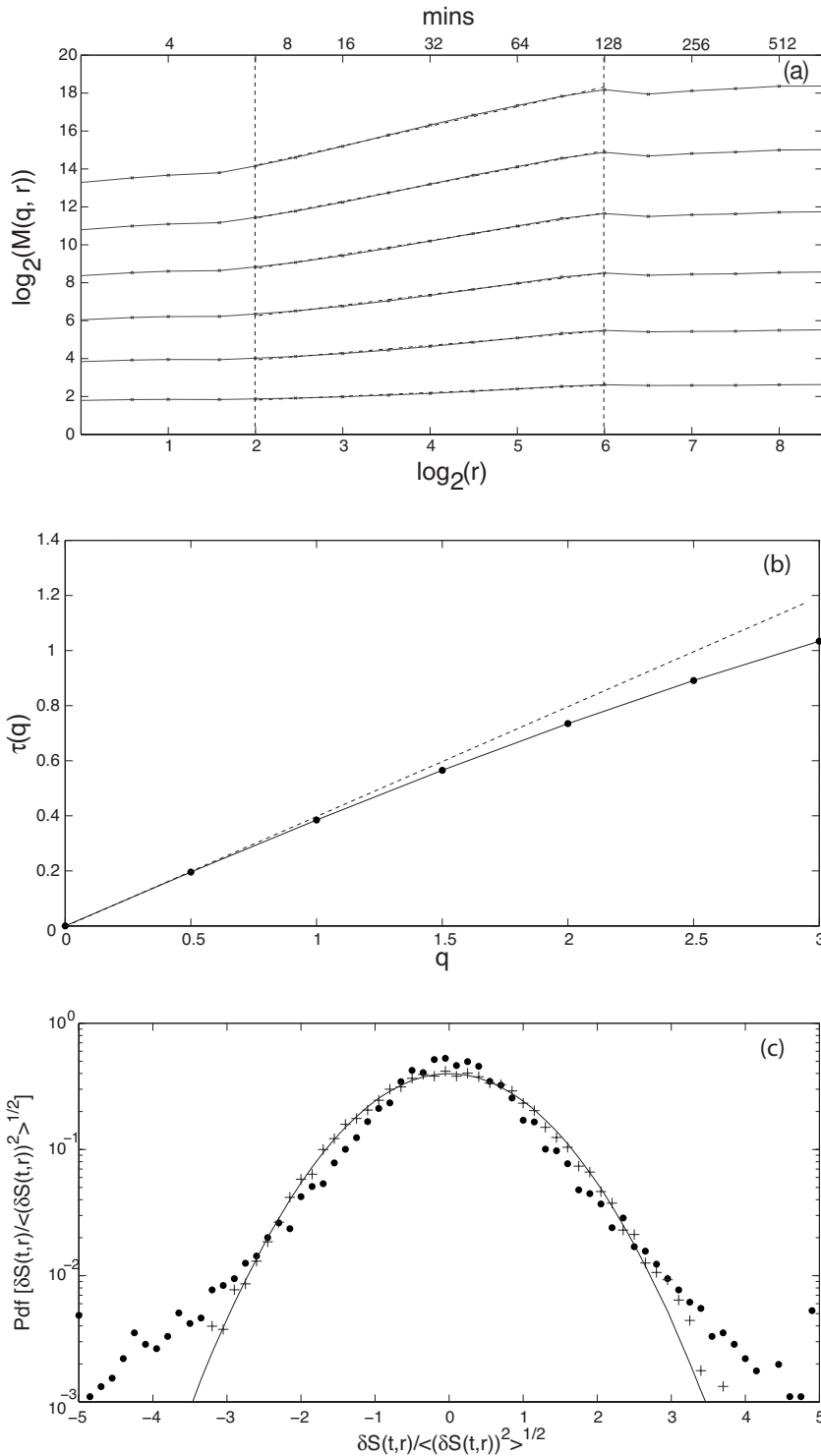
FIG. 3. (a) Structure functions of sediment transport series. Vertical lines delineate the scaling regime which is between 8 and 128 min (see top horizontal axis). (b) Estimated $\tau(q)$ curve (solid points) from the slopes of structure functions and a quadratic fit (solid line). Deviation from the straight line establishes the presence of multifractality (see text for parameter values). (c) Change in PDF of sediment transport increments with scale. The solid dots correspond to PDF at increments of $r=10$ (20 min) and $+$ correspond to increments at $r=60$ (120 min). The solid line indicates a Gaussian PDF.

120 min sediment accumulations, respectively). It is noted that at smaller scales the PDF of the sediment increments deviates from a Gaussian distribution and is close to a double exponential. The PDF, eventually, becomes Gaussian at larger scales. The PDFs reported in Fig. 3(c) are for scales that fall within the scaling regime of the sediment data series [see Fig. 3(a)]. The dependence of the statistics of the sediment transport rates on scale has also been documented in field observations (see [19] and a discussion in [13]). As discussed above, we estimated the parameters of multifrac-

tality by approximating the $\tau(q)$ curve in Fig. 3(b) as a quadratic function in q and the estimates obtained together with their 95% standard errors were $c_1=0.41\pm0.005$ and $c_2=0.04\pm0.004$. It is noted for comparison that the c_2 estimate of velocity fluctuations in fully developed turbulence is of the order of 0.03 [14]. We emphasize that no existing stochastic model for sediment transport addresses the issue of statistical scale dependence documented in experimental and field observations. In the following section, we propose a stochastic model for sediment transport which exhibits the

observed change in PDFs of sediment transport increments over scales, reproduces the multifractal behavior of the experimental data series, and provides the potential for relating the observed macroscale statistics to the microscale dynamics of sediment particle movement.

III. PROPOSED MODEL: FRACTIONAL LAPLACE MOTION

A. Brownian motion

Brownian motion is widely recognized to be a special case of a continuous time random walk (CTRW). In general, CTRWs specify the particle location x_i at a time t_i by the iterative discrete equations (e.g., [20,21]),

$$x_{i+1} = x_i + \eta_i, \tag{5a}$$

$$t_{i+1} = t_i + \tau_i, \tag{5b}$$

where (η_i, τ_i) is a set of random numbers drawn from a PDF $\Psi(\eta, \tau)$. One can recast the above equations in the following form:

$$t_n = \sum_{i=1}^{n} \tau_i, \tag{6a}$$

$$x(t) = \sum_{i=1}^{n} \eta_i, \tag{6b}$$

where $t \in [t_n, t_{n+1})$. The CTRW is said to be decoupled when the random variables η_i and τ_i are mutually independent. Brownian motion is a special case of a decoupled CTRW where η_i are independent identically distributed (i. i. d) random variables drawn from a Gaussian distribution and τ_i are i. i. d random variables sampled from an exponential distribution. It is to note that the increments of Brownian motion follow a Gaussian distribution. However, the increments of most natural phenomena often show deviation from Gaussian PDFs and this has prompted the introduction of other stochastic processes such as Lévy walks and continuous-time Lévy flights, where the random variables η_i and/or τ_i are sampled from heavy-tailed PDFs. However, such processes do not have all of their statistical moments convergent. For example, Lévy walks and Lévy flights do not have convergent second moments [22]. It is also noted that modeling real data with such processes typically requires an exponential truncation of the algebraic decays [23] or sometimes even milder than algebraic decay [24]. Correlation and long-range dependence in the observed data can be modeled by relaxing the independence assumption in sampling η_i and/or τ_i or by relaxing the independence assumption of a decoupled CTRW. Fractional Brownian motion, denoted by $B_H(t)$, is a decoupled CTRW starting at zero and has the following correlation function:

$$E[B_H(t)B_H(s)] = \frac{1}{2}(|t|^{2H} + |s|^{2H} - |t-s|^{2H}), \tag{7}$$

where $E(.)$ denotes the expectation operator and H is a parameter of fractional Brownian motion called the Hurst exponent. For $H = 0.5$, the fractional Brownian motion reduces to the standard Brownian motion with independent increments. For other values of $0 < H < 1$, $B_H(t)$ is called the fractional Brownian motion and its increments are positively correlated for $H > 0.5$ and negatively correlated for $H < 0.5$.

An extension of Brownian motion, or fractional Brownian motion, can be obtained via subordination. The notion of subordination was originated by Bochner [25]. One can obtain a subordinated stochastic process $Y(t) = X[T(t)]$ by randomizing the clock time of a stochastic process $X(t)$ using a new time $t_* = T(t)$. The resulting process $Y(t)$ is said to be subordinated to the so-called *parent process* $X(t_*)$, and t_* is commonly referred to as the *operational time* [26]. We propose the application of subordination of fractional Brownian motion (called fractional Laplace motion) as an extension to the Brownian motion model proposed by Einstein for sediment transport [2]. In the following subsection, we describe the properties of subordinated fractional Brownian motion.

B. Fractional Laplace motion

Fractional Laplace motion is a subordinated stochastic process, whose *parent process* is fractional Brownian motion and the *operational time* is a Gamma process [27],

$$L(t) = B_H(\Gamma_t), \tag{8}$$

where $B_H(t)$ is fractional Brownian motion with Hurst exponent $0 < H < 1$ and Γ_t represents a Gamma process for any $t \geq 0$. The increments of the Gamma process $(\Gamma_{t+s} - \Gamma_t)$ have a gamma distribution with shape parameter $\nu = s$ and scale parameter $\beta = 1$, i.e.,

$$f(x) = \frac{1}{\beta^\nu \Gamma(\nu)} x^{\nu-1} e^{-x}. \tag{9}$$

For $H = 0.5$ the subordinated process $L(t) = B_H(\Gamma_t)$ is called the Laplace motion.

Increments of the fractional Laplace motion defined by $Y(t, r) = L(t+r) - L(t)$, called the fractional Laplace noise, form a stationary process. Fractional Laplace noise has three parameters, namely, the Hurst exponent of the parent process H, the variance of the parent process $B_H(t)$ at the smallest scale $t = 1$, i.e., $\sigma^2 = \text{Var}[B_H(1)]$, and the shape parameter of the Gamma process (Γ_t), ν. The variance of the fractional Laplace noise can be expressed as a function of the scale r and its parameters as [27]

$$\text{Var}[Y(t,r)] = \sigma^2 \frac{\Gamma(2H + r/\nu)}{\Gamma(r/\nu)}. \tag{10}$$

The covariance function of the fractional Laplace noise at a given scale r, defined as $\rho(n) = E[Y(t,r)Y(t+n,r)]$, can be expressed in terms of its parameters for any $n \geq 1$ as

$$\rho(n) = \frac{\sigma^2}{2} \left\{ \frac{\Gamma[2H + (n+1)r/\nu]}{\Gamma[(n+1)r/\nu]} + \frac{\Gamma[2H + (n-1)r/\nu]}{\Gamma[(n-1)r/\nu]} - 2\frac{\Gamma(2H + nr/\nu)}{[\Gamma(nr/\nu)]} \right\}. \tag{11}$$

Fractional Laplace noise is positively correlated for $H > 0.5$

and is negatively correlated for $H < 0.5$. In particular, fractional Laplace noise exhibits long-range dependence for $H > 0.5$.

The fundamental difference between fractional Laplace motion and other similar stochastic processes such as fractional Brownian motion and Lévy motion is that in the latter two cases the PDFs of the increments remain Gaussian and Lévy stable, respectively, at all scales. In fractional Laplace motion, the PDFs of the increments are variable with scale with Laplace PDFs at small scales and as the scale increases the PDFs approach Gaussian. In particular, fractional Laplace motion deviates from the classical self-similarity and shows stochastic self-similarity [27]. The Laplace PDF emerges from a different and less well-known central limit theorem called the geometric central limit theorem, which states that the sum of a random number of independent identically distributed variates with finite variance is asymptotically Laplace if the random count is geometrically distributed [28]. In fact, the Laplace PDF can be considered as a Gaussian PDF with a random variance or spread [29]. Given the stochastic self-similarity extensively documented in sediment transport series (in [13] and also in Sec. II of this paper), the subordination of the fractional Brownian motion model proposed herein offers an attractive and simple extension to Brownian motion for particle movement, as demonstrated in more detail in the next section.

IV. FRACTIONAL LAPLACE MOTION MODEL FOR SEDIMENT TRANSPORT

The physical relevance of the fractional Laplace motion to model sediment transport is argued on the basis that the notion of operational time acknowledges the randomness in the entrainment time experienced by sediment particles which are subject to a varied range of velocities in turbulent flows. It is known that turbulent velocity fluctuations themselves exhibit intermittency and possess a multifractal behavior (e.g., [14]). Turbulent velocity "sweeps" and "bursts" are expected to influence particle motion and introduce a multiscale variability in the fluctuations of the resulting sediment transport series. In groundwater hydrology, the notion of operational time has been used to acknowledge the fact that time passes faster for particles in higher velocity zones [30,31]. Along these lines, a subordinated Brownian motion model has been proposed to model hydraulic conductivity [28] and connections between turbulent velocities and heterogeneous sediment properties have been proposed [32].

In the following subsections we study the multiscale properties of fractional Laplace motion and show that fractional Laplace motion reproduces the intricate stochastic structure shown by the sediment transport series. Further, we elaborate on the model parameter fitting to the sediment transport series.

A. Multifractal properties of fractional Laplace motion

In order to study the self-similar behavior of fractional Laplace motion, we first study the analytical behavior of the structure functions of fractional Laplace motion. The struc-
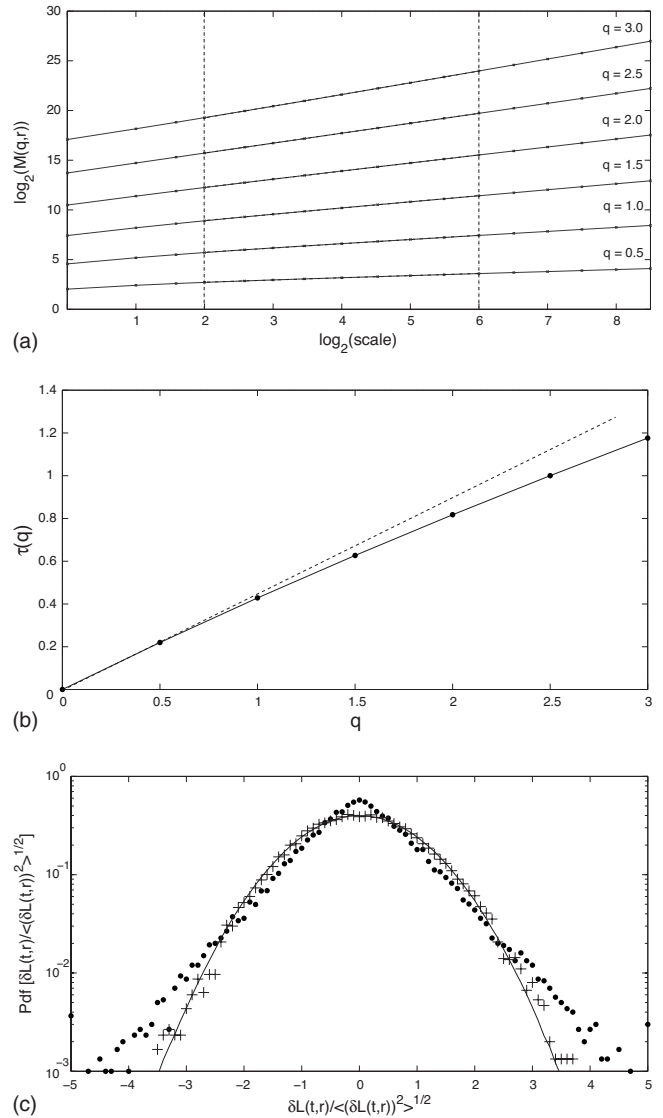

FIG. 4. (a) Structure functions of fractional Laplace motion for a set of chosen parameters $H=0.4$, $\nu=3.0$, and $\sigma=1$ computed from Eq. (12). The vertical lines correspond to the scaling regime of the sediment transport series which is from scales of $r=4$ to $r=64$. (b) Estimated $\tau(q)$ curve (solid points) from the fitted slopes of the structure functions. The solid line indicates a quadratic fit and the nonlinear dependence of $\tau(q)$ on q establishes that fractional Laplace motion shows a multifractal behavior in the scales under consideration. (c) Change of PDF of increments of simulated fractional Laplace motion series. Solid dots correspond to PDF of increments at $r=10$ and $+$ to $r=60$. Solid line indicates a Gaussian PDF.

ture functions of fractional Laplace motion for $\sigma=1$ can be written in terms of its parameters H and ν as [27]

$$M(q,r) = \sqrt{\frac{2^q}{\pi}} \Gamma\left(\frac{1+q}{2}\right) \frac{\Gamma(Hq + r/\nu)}{\Gamma(r/\nu)}. \quad (12)$$

Statistical scaling or self-similar behavior requires that the structure functions follow a power-law relationship in scales. Figure 4(a) shows the structure-function dependence on

scales in log-log space for an arbitrary choice of the parameter values, $H=0.4$ and $\nu=3.0$. (These values of H and ν are used for illustration of the model properties and the estimation of these parameters is discussed more thoroughly in the next subsection). It is to note that from Fig. 4(a) that although Eq. (12) does not analytically accept a power-law expression on r, for all practical purposes, fractional Laplace motion can be approximated by a self-similar process, i.e., the structure functions show a power-law relationship in scales at least for the range of scales which coincide with the scaling regime of sediment transport series (scales or lags of $r=4$ to $r=64$). Plotting the $\tau(q)$ curve [estimated from the slopes of $M(q,r)$ vs r in log-log space within the above scaling regime] one can see that the scaling exponents, $\tau(q)$, show a nonlinear dependence on the order of moments q [see Fig. 4(b)]. It is to note that the scaling exponents $\tau(q)$ are independent of the variance of the parent process σ^2. The change in PDF of the increments of fractional Laplace motion with scale is shown in Fig. 4(c), where the PDF at small scales [$r=10$ in Fig. 4(a)] shows a double-exponential behavior and it eventually tends to a Gaussian distribution for large scales [$r=60$ in Fig. 4(a)]. The above results document that fractional Laplace motion can be approximated by a stochastic self-similar process in an intermediate range of scales and within those scales it exhibits a multifractal behavior. At the limit of very large time scales, i.e., as $r \to \infty$, fractional Laplace motion tends to a fractional Brownian motion with $\tau(q)$ a linear function of q (i.e., monofractal behavior).

It is interesting to note from Eq. (12) that the second-order structure function of Laplace motion ($H=0.5$ and $q=2$) obeys a power-law relationship in scales and in particular it shows a linear dependence on scales

$$M(2,r) = \left[\frac{2}{\nu\sqrt{\pi}} \Gamma(1.5) \right] r, \tag{13}$$

yielding an exponent of $\tau(2)=1$. This implies that Laplace motion has self-similar second-order moments, i.e., it shows a log-log linear power spectrum (although higher order moments are not exact power laws). In the next subsection we elaborate on the parameter estimation of the fractional Laplace motion from the sediment transport series.

B. Model fitting

As seen in the previous section, fractional Laplace motion has three parameters H, ν and σ. The scale parameter of the operational time PDF, β, is 1 by the definition of fractional Laplace motion [27]. Estimation of the parameters H and ν from the sediment transport series is performed by minimizing the mean squared error between the empirical and theoretical $\tau(q)$ curves. The mean squared error, denoted by MSE, is a function of H and ν and is independent of σ,

$$\text{MSE}(H,\nu) = \sum_q \left[\tau_m(q) - \hat{\tau}(q) \right]^2, \tag{14}$$

where $\hat{\tau}(q)$ are the estimated scaling exponents of the sediment transport series [see Fig. 3(b)] and $\tau_m(q)$ are the scaling exponents of the fractional Laplace motion model which are computed from the slopes of the theoretical $M(q,r)$ versus r

within the scaling regime of the sediment transport series ($4 < r < 64$) in the log-log space [see Fig. 4(b)]. Minimization of the mean squared error for the sediment transport series yields a Hurst exponent of $H=0.39$ and a shape parameter of $\nu=6.8$. It is to note that the multiscale structure of fractional Laplace motion model is determined by the parameters H and ν. Further, we estimate the parameter σ by minimizing the mean squared error between the variance of the increments of sediment transport series and the fractional Laplace noise for $H=0.39$ and $\nu=6.8$ over the scaling regime ($4 < r < 64$),

$$\sigma = \text{Min} \sum_{r=4}^{r=64} \{ \text{Var}[\delta S(t,r)] - \text{Var}[Y(t,r)] \}^2, \tag{15}$$

where $\text{Var}[\delta S(t,r)]$ is the variance of the increments of sediment transport series and $\text{Var}[Y(t,r)]$ is the variance of fractional Laplace noise at the scale r, given by Eq. (10). The value of σ estimated using Eq. (15) was $\sigma=0.296$. The multifractal parameters of the fractional Laplace motion model computed with the estimated parameters of $H=0.39$ and $\nu=6.8$ were $c_1=0.41$ and $c_2=0.041$, which compare very well to the values estimated from the sediment transport data of $c_1=0.41$ and $c_2=0.04$. [Note that c_1 and c_2 were not used directly in the model fitting which was done via Eq. (14) on the whole $\tau(q)$ curve]. As a result the model and the data-estimated $\tau(q)$ curves are indistinguishable. Figure 5(a) shows the increments of sediment transport series at a scale of $r=20$ or 40 min (note that this scale lies within the scaling regime of the sediment transport series). For visual comparison, the fractional Laplace noise simulated series with the estimated parameters $H=0.39$, $\nu=6.8$, and $\sigma=0.296$ at the same scale is shown in Fig. 5(b).

As noted in the previous section, fractional Laplace noise is negatively correlated for $H<0.5$. Figure 6(a) shows the autocorrelation function of the increments of sediment transport series at the scale $r=20$ (40 min). The data show a negative correlation in the scaling regime of the sediment transport series for small lags. This is qualitatively consistent with the fractional Laplace noise model which shows a negative correlation for the estimated parameter values [see Fig. 6(b)]. The increments of fractional Laplace motion at small scales follow a Laplace PDF which eventually becomes Gaussian at larger scales. Figure 7(a) shows the PDF of sediment transport increments at a scale of $r=4$ which is the beginning of the scaling regime of the sediment transport series. A Laplace PDF provides a good fit to the increments at that scale. As noted in Fig. 7(b), the PDF of sediment transport increments at a scale of $r=64$ (128 min) tends to a Gaussian PDF. Thus, one can see that the sediment transport series are consistent with the properties of fractional Laplace motion within the scaling regime.

V. DISCUSSION

In the previous section we established the fact that the fractional Laplace motion model is able to reproduce the intricate stochastic structure of the observed sediment transport series over a range of scales and also reproduce the
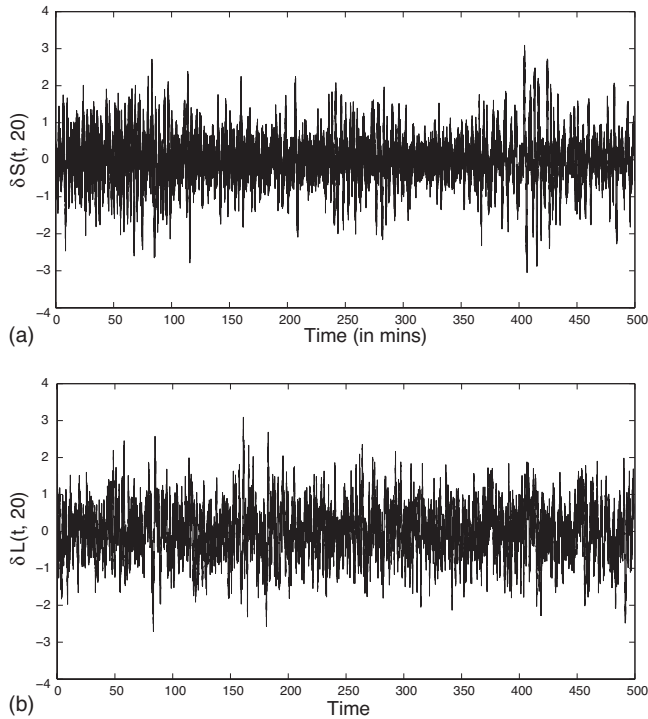
FIG. 5. (a) Comparison of the increments of the sediment transport series in kgs at scale $r=20$ (40 min) and (b) the same scale increments of simulated fractional Laplace motion series with $H=0.39$, $\nu=6.8$, and $\sigma=0.3$. The values of H and ν were obtained by minimizing the mean squared error defined in Eq. (14). The value of σ was obtained using Eq. (15). The scale of $r=20$ was chosen for comparison as it lies within the scaling regime of the sediment transport series.
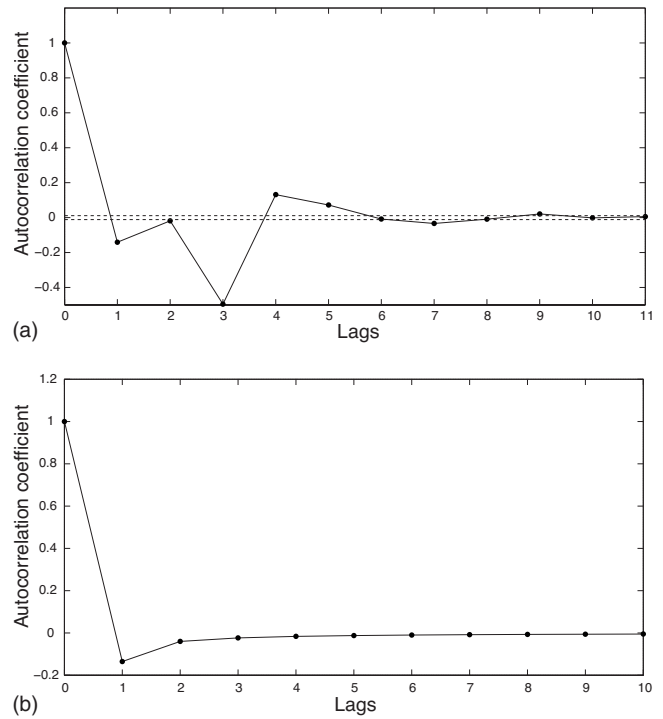

FIG. 6. (a) The autocorrelation function of the increments of sediment transport series at a scale of $r=20$ (40 min). The dashed lines indicate the 95% confidence intervals (approximated as $\pm 1.96/\sqrt{N}$, $N=30\,293$ points) on the autocorrelation coefficients. (b) The autocorrelation function of generated fractional Laplace noise series at the same scale with parameters $H=0.39$ and $\nu=6.8$ fitted to the data. The autocorrelation of the fractional Laplace noise is computed from Eqs. (10) and (11).

change of the PDFs of increments of sediment transport series in the scaling regime. In this section, we discuss the physical significance of the notion of operational time in sediment transport series. Near-bed turbulence is known to play an important role in sediment transport [12]. Turbulent velocity fluctuations pick up sediment particles and transport them over long distances. However, since the turbulent velocities themselves are known to exhibit variability over a large range of scales, the entrainment time experienced by the sediment particles is also expected to carry some of this variability. This consideration leads to a randomization of time over which a sediment particle is operated upon, as sediment particles in different velocity zones experience time to move faster or slower depending on whether they are in a high- or low-velocity zone, respectively. Thus, the notion of operational time can arise due to the stochastic nature of sediment particle entrainment. It is interesting to note that the turbulent velocity fluctuations themselves exhibit Laplace and stretched Laplace distributions at small scales and their PDFs become Gaussian at larger scales [33]. It is also interesting to note that the rate of sediment particle entrainments, which are proportional to the shear stress fluctuations at the bed, have been reported to follow a Gamma distribution [9]. Both these observations are qualitatively consistent with the fractional Laplace motion model for sediment transport proposed in this paper.

The observed multiscaling and intermittency in sediment transport series (macroscale behavior) was shown to arise by the introduction of the notion of operational time in Brownian-type particle movement (microscale behavior). Thus, while the model parameters H and ν relate to the (unobserved) particle movement statistics, they are estimated from the (observed) sediment transport statistics, and specifically from their multiscale behavior concisely parameterized via the parameters c_1 and c_2. It is of interest to study how the parameter space of (H, ν) relates to that of (c_1, c_2) in order to gain insight on model sensitivity and the physical meaning of the parameter ν which characterizes the variability of the particle motion. We compute the multifractal parameters c_1 and c_2 for different values of the model parameters H and ν by evaluating $M(q,r)$ from Eq. (12), estimating $\tau(q)$ in the range $4 \leq r \leq 64$, and approximating the $\tau(q)$ curve as a quadratic function in q [Eq. (4)]. Figure 8 shows the contour plots of c_1 and c_2 for different values of H and ν. It is to note that the average "roughness" of the sediment series, quantified by the parameter c_1, is strongly dependent on the Hurst exponent of the fractional Brownian motion H [see Fig. 8(a)] and not as much on the parameter ν of the operational time. On the other hand, from Fig. 8(b), one can see that the intermittency coefficient c_2 is strongly dependent on the shape parameter ν of the distribution of operational time for a given value of H. In particular, for a given value of H, the value of c_2 is higher for a higher value of ν. One way to understand this is to note that for higher values of ν the Gamma distribution has a higher variance. Thus, for higher
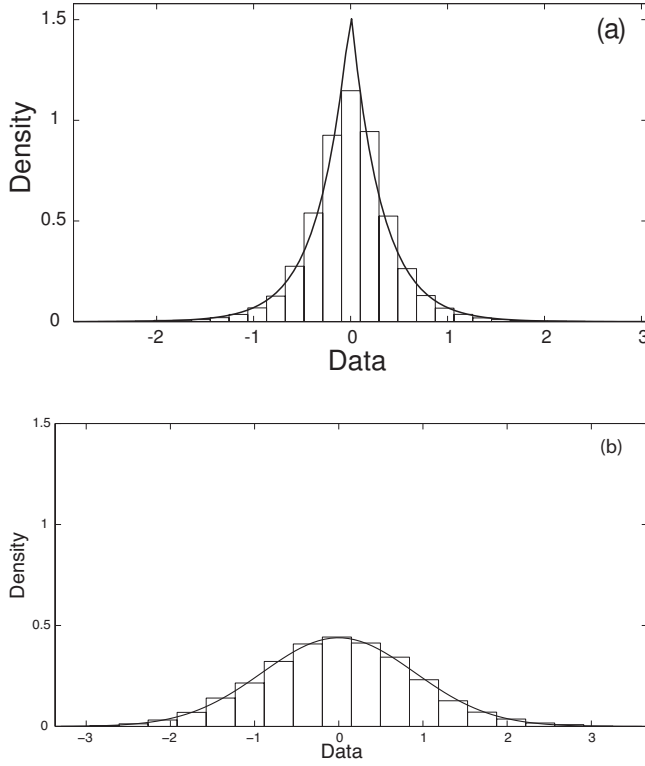
FIG. 7. Change in PDF of sediment transport increments in the scaling regime. (a) Laplace PDF (solid line) provides a good fit to the PDF of sediment transport increments at $r=4$ (8 min; beginning of the scaling regime) and (b) the PDF of sediment transport increments becomes Gaussian (solid line) at $r=64$ (128 min; ending of the scaling regime).

FIG. 8. Contour plots of the multifractal parameters, (a) c_1 and (b) c_2, for different values of the fractional Laplace motion model parameters H and ν.

values of ν the operational time is sampled from a distribution with higher variance and this variability in the operational time shows up as a higher intermittency coefficient in the sediment transport series (larger degree of temporal heterogeneity in bursts of sediment transport increments). It is emphasized that estimation of the parameter values of the fractional Laplace motion, H and ν, was performed through the scaling exponents of the structure functions of the sediment transport series [Eq. (14)]. Direct estimation of the parameters H and ν, or for that matter direct assessment of the whole statistical structure of operational time from observations, would require access to series of particle entrainment which are difficult to make and are not available in the experimental setting studied here. Rather, the present study attempted a physical insight via relating the macroscale statistics of the sediment series to the microscale dynamics of particle movement.

VI. CONCLUDING REMARKS

In this work we proposed the adaptation of fractional Laplace motion as a stochastic model for sediment transport. Fractional Laplace motion arises from randomization of the clock time in fractional Brownian motion, and introduces the notion of operational time. The physical significance of op-erational time in the context of sediment transport was reasoned on the basis that the stochastic nature of turbulent velocity fluctuations near the bed induces stochasticity in particle entrainment and, therefore, the time over which particles are in motion. The proposed model was shown able to reproduce the multiscale statistics of sediment transport series and was validated against a data set from a large-scale laboratory experiment. The effect of the model parameters on the multifractal parameters of sediment transport series was also discussed. Although direct estimation of the model parameters would require particle-scale observations, it was shown here that an indirect estimation based on the statistics of sediment transport series is possible. We see this work as a step toward relating the microscale dynamics of particle movement to the macroscale statistics of sediment transport via minimum complexity stochastic models.

[1] A. Einstein, *Investigations of the Theory of Brownian Movement* (Dover, New York, 1956).

[2] H. A. Einstein, *Sedimentation, Symposium to honor H. A. Einstein*, Fort Collins, Colorado, 1972, edited by H. W. Shen (unpublished).

[3] C. Ancey, T. Böhm, M. Jodeau, and P. Frey, Phys. Rev. E **74**, 011302 (2006).

[4] C. Ancey, A. C. Davidson, T. Böhm, M. Jodeau, and P. Frey, J. Fluid Mech. **595**, 83 (2008).

[5] A. Papanicolaou, P. Diplas, N. Evangelopoulos, and S. Fotopoulos, J. Hydraul. Eng. **128**, 369 (2002).

[6] H. A. Einstein, U.S. Department of Agriculture Technical Bulletin (1950).

[7] J. Gessler, Ph.D. thesis, Swiss Federal Institute of Technology, 1967.

[8] H. Nakagawa and T. Tsujimoto, J. Hydraul. Eng. **106**, 2029 (1980).

[9] C. Paola, S. M. Weile, and M. A. Reinhart, Sedimentology **36**, 47 (1989).

[10] X. Zhang and B. Xie, J. Hydraul. Eng. **10**, 53 (1995).

[11] A. Papanicolaou, P. Diplas, C. Dancey, and M. Balakrishnan, J. Eng. Mech. **127**, 211 (2001).

[12] A. Papanicolaou, Ph.D. thesis, Virginia Institute of Technology, 1997.

[13] A. Singh, K. Fienberg, D. J. Jerolmack, J. G. Marr, and E. Foufoula-Georgiou, J. Geophys. Res., [Earth Surface] **114**, F01025 (2009).

[14] G. Parisi and U. Frisch, in *Turbulence and Predictability in Geophysical Fluid Dynamics*, edited by M. Ghil (North-Holland, Amsterdam, 1985), Vol. 84.

[15] A. Singh, S. Lanzoni, and E. Foufoula-Georgiou, *SERRA, Special Issue on Modeling and Prediction of Complex Environmental System* (Springer Verlag, New York, 2008).

[16] K. Fienberg, A. Singh, D. J. Jerolmack, J. G. Marr, and E. Foufoula-Georgiou, Bedload Research International Cooperative (BRIC): Proceedings of the International Bedload–Surrogate Monitoring Workshop, April 11—14, 2007, Minneapolis, Minnesota, 2007.

[17] B. Castaing, Y. Gagne, and E. J. Hopfinger, Physica D **46**, 177 (1990).

[18] V. Venugopal, S. G. Roux, E. Foufoula-Georgiou, and A. Arneodo, Water Resour. Res. **42**, W06D14 (2006).

[19] K. Bunte and S. R. Abt, Water Resour. Res. **41**, W11405 (2005).

[20] D. Fulger, E. Scalas, and G. Germano, Phys. Rev. E **77**, 021122 (2008).

[21] V. V. Novikov, in *Fractals, Diffusion and Relaxation in Disordered Complex Systems*, edited by W. Cofey and Y. P. Kalmykov (Wiley, New York, 2006).

[22] J. Lamperti, Trans. Am. Math. Soc. **104**, 62 (1962).

[23] M. Dentz, A. Cortis, H. Scher, and B. Berkowitz, Adv. Water Resour. **27**, 155 (2004).

[24] A. Cortis, Y. Chen, H. Scher, and B. Berkowitz, Phys. Rev. E **70**, 041108 (2004).

[25] S. Bochner, Proc. Natl. Acad. Sci. U.S.A. **48**, 2039 (1962).

[26] R. Gorenflo, F. Mainardi, and A. Vivoli, Chaos, Solitons Fractals **34**, 87 (2007).

[27] T. J. Kozubowski, M. M. Meerschaert, and K. Podgórski, Adv. Appl. Probab. **38**, 451 (2006).

[28] M. M. Meerschaert, T. J. Kozubowski, F. J. Molz, and S. Lu, Geophys. Res. Lett. **31**, L08501 (2004).

[29] S. Kotz, T. J. Kozubowski, and K. Podgórski, *The Laplace Distribution and Generalizations* (Birkhauser Boston, Cambridge, Massachusetts, 2001).

[30] B. Baeumer, D. A. Benson, M. M. Meerschaert, and S. W. Wheatcraft, Water Resour. Res. **37**, 1543 (2001).

[31] B. Berkowitz and H. Scher, Phys. Rev. Lett. **79**, 4038 (1997).

[32] F. J. Molz, M. M. Meerschaert, T. J. Kuzobowski, and P. D. Hyden, *Dynamics of Fluids and Transport in Fractured Rock*, edited by B. Faybishenko, P. A. Witherspoon, and J. GaleGeophysical Monograph No. 162 (American Geophysical Union, Washington, DC, 2005), pp. 13—22.

[33] E. S. C. Ching and Y. Tu, Phys. Rev. E **49**, 1278 (1994).

Click Here for Full Article

Experimental evidence for statistical scaling and intermittency in sediment transport rates

Arvind Singh,[1] Kurt Fienberg,[1] Douglas J. Jerolmack,[2] Jeffrey Marr,[1] and Efi Foufoula-Georgiou[1]

[1] Understanding bed load transport fluctuations in rivers is crucial for development of a transport theory and for choosing a sampling interval for "mean" transport rates. Field-scale studies lack sufficient resolution to statistically characterize these fluctuations, while laboratory experiments are limited in scale and hence cannot be directly compared to field cases. Here we use a natural-scale laboratory channel to examine bed load transport fluctuations in a heterogeneous gravel substrate under normal flow conditions. The novelty of our approach is the application of a geometrical/statistical formalism (called the multifractal formalism), which allows characterization of the "roughness" of the series (depicting the average strength of local abrupt fluctuations in the signal) and the "intermittency" (depicting the temporal heterogeneity of fluctuations of different strength). We document a rougher and more intermittent behavior in bed load sediment transport series at low-discharge conditions, transitioning to a smoother and less intermittent behavior at high-discharge conditions. We derive an expression for the dependence of the probability distribution of bed load sediment transport rates on sampling interval. Our findings are consistent with field observations demonstrating that mean bed load sediment transport rate decreases with sampling time at low-transport conditions and increases with sampling time at high-transport conditions. Simultaneous measurement of bed elevation suggests that the statistics of sediment transport fluctuations are related to the statistics of bed topography.

1. Introduction

[2] Measurements of bed load transport rates are fundamental to estimating material transport in a river, yet even defining a representative time period over which to sample is difficult due to the inherent variability and stochastic character of sediment transport. This variability is present over a wide range of scales, from the movement of individual grains [*Iseya and Ikeda*, 1987; *Drake et al.*, 1988; *Nikora et al.*, 2002; *Schmeeckle and Nelson*, 2003; *Sumer et al.*, 2003; *Ancey et al.*, 2008] up to the propagation of dunes and bars [*Kuhnle and Southard*, 1988; *Gomez et al.*, 1989; *Cudden and Hoey*, 2003; *Jerolmack and Mohrig*, 2005], even under steady flow conditions. Computed statistics of instantaneous bed load transport rates (flux) have shown that probability distributions are often skewed toward larger values [e.g., *Gomez et al.*, 1989], implying a high likelihood of extreme fluctuations, the prediction of which is essential

for protecting hydraulic structures and assessing the stability of riverine habitat [*Yarnell et al.*, 2006]. It has also been observed that the mean sediment flux depends on the time interval (sampling time) over which the mean is computed, and previous work has suggested that this time dependence is the result of large, infrequent transport events [see *Bunte and Abt*, 2005, and references therein].

[3] An analogous time dependence that has been more thoroughly studied is that of the sedimentary record, where apparent deposition rate (measured from two dated surfaces) diminishes rapidly with measurement duration in virtually all depositional environments [*Sadler*, 1981, 1999]. Models show that this scale dependence is a direct result of the statistics of transport fluctuations [e.g., *Jerolmack and Sadler*, 2007]. In the case of geologic rates the data have been assumed to obey simple scaling over a wide range of time scales; that is, the statistical moments can be fitted as power law functions of scale, with the exponents linear in moment order. This power law relationship provides a value for the Hurst exponent, H, which may be used to compare rates at one scale to rates at a different scale via a simple statistical transformation (see also section 5). However, many geophysical processes exhibit multiscaling (or multifractal behavior), which implies that a range of exponents (and not a single exponent) is required to describe the

---

[1]St. Anthony Falls Laboratory and National Center for Earth-surface Dynamics, Department of Civil Engineering, University of Minnesota-Twin Cities, Minneapolis, Minnesota, USA.
[2]Department of Earth and Environmental Science, University of Pennsylvania, Philadelphia, Pennsylvania, USA.

changes in the probability density function (pdf) with scale. Examples include rainfall intensities [e.g., *Lovejoy and Schertzer*, 1985; *Venugopal et al.*, 2006b], cloud structures [e.g., *Lovejoy et al.*, 1993; *Arneodo et al.*, 1999a], river flows [e.g., *Gupta and Waymire*, 1996], river network branching topologies [e.g., *Rinaldo et al.*, 1993; *Marani et al.*, 1994; *Lashermes and Foufoula-Georgiou*, 2007], braided river systems [e.g., *Foufoula-Georgiou and Sapozhnikov*, 1998], and valley morphology [e.g., *Gangodagamage et al.*, 2007]. This rich multiscale statistical structure includes extreme but rare fluctuations ("bursts") that occur inhomogeneously over time, giving rise to the so-called "intermittency" and leading to a nontrivial scaling of the statistical moments. A prime example of this is the velocity fluctuations in fully developed isotropic turbulence [e.g., *Parisi and Frisch*, 1985; *Frisch*, 1995; *Arneodo et al.*, 1999b].

[4] To the best of our knowledge, bed load sediment transport series have not been analyzed before from the perspective of quantifying how the statistical moments of the series change with scale. In an early study, *Gomez et al.* [1989] acknowledged that the probability distribution of sediment transport rates depends on sampling time (scale) and extended the Einstein and Hamamori distributions to a scale-dependent form, without, however, attempting any scale renormalization. Knowledge of the variability inherent in bed load transport rates at all scales is essential for quantifying material flux, for designing appropriate measurement programs, and for comparison among different data sets and model predictions at different temporal and spatial scales. Also, quantifying the statistical structure of these fluctuations across scales may yield insight into the fundamental physics of sediment transport and provide a set of diagnostics against which to rigorously test competing theories and bed load transport models [see also *Ancey et al.*, 2006, 2008].

[5] One would expect that the statistics of bed load sediment transport would relate in some way to the statistics of the fluctuations in bed elevation. Although river bed elevations have been analyzed much more than sediment fluxes and have been found to exhibit fluctuations across a wide range of scales, in both sandy [e.g., *Nikora et al.*, 1997; *Nikora and Hicks*, 1997; *Jerolmack and Mohrig*, 2005] and gravelly [*Dinehart*, 1992; *Nikora and Walsh*, 2004; *Aberle and Nikora*, 2006] systems, the link between bed topography and sediment flux remains largely unexplored due to the difficulty in simultaneous data acquisition. Establishing a relationship between the statistics of bed elevations and sediment transport rates is important for effective modeling of river bed morphodynamics and also for understanding the physics of sediment transport. More practically, since bed elevation data are far easier to collect than sediment flux measurements, an understanding of how the statistics of the one variable relate to those of the other, at least over a range of temporal scales, could greatly facilitate estimating sediment transport rate in the field.

[6] To address these issues we present here an analysis of data from a unique experimental laboratory setup capable of mimicking transport conditions in the field (see section 3). High-resolution, long-duration time series of sediment transport rates and bed elevation were simultaneously collected in a suite of experiments with a heterogeneous gravel bed. We use the multifractal formalism, originally developed for fluid turbulence [*Parisi and Frisch*, 1985; *Frisch*, 1995; *Muzy et al.*, 1994], to quantify the "roughness" (the average strength of local burstiness in the signal) and the "intermittency" (the temporal variability or heterogeneity of bursts of different strengths) and relate those geometrical quantities to the statistics of sediment flux and bed topography over a range of time scales. (Note that throughout the paper the term "roughness," as defined mathematically via the strength of local singularities, refers to the signal roughness being that sediment transport rates or bed elevation fluctuations and it is not to be confused with other uses of the term roughness such as bed roughness or hydraulic roughness.) We substantiate the findings of *Bunte and Abt* [2005] that mean sediment transport rate diminishes with increasing sampling time at low bed stress (slightly above critical) but does the opposite for high-transport conditions, and we relate this reversal in trend to the influence of large-scale bed forms. Our analysis also allows characterization of the sampling time dependence of all of the statistical moments, allowing thus the prediction of extremes at small scales from the statistics at larger scales.

2. Description of Experiments

2.1. Experimental Setup

[7] The experiments reported here were conducted in the Main Channel facility at the St. Anthony Falls Laboratory, University of Minnesota, as part of the StreamLab06 project undertaken by the National Center of Earth-surface Dynamics (NCED) [*Wilcock et al.*, 2008]. StreamLab06 was an 11 month multidisciplinary laboratory channel study focused on various aspects of ecogeomorphology in gravel bed streams. Five separate projects were conducted as part of StreamLab06 and an extensive data set was collected including hydraulic conditions (discharge, water slope, bed slope, depth average velocity, and flow field), morphological conditions (bed topography, bar locations and shapes, photo images of the bed), sediment transport characterization (continuous sediment flux, recirculation grain size information), water chemistry (temperature, dissolved oxygen, nutrient concentrations) and biological conditions (heterotrophic respiration, biomass accumulation, nutrient processing rates). For the work presented here, we focus on bed topography and sediment flux data collected in the first of the five StreamLab06 projects, which focused on ground truth testing of various conventional and surrogate bed load monitoring technologies.

[8] The Main Channel is 2.74 m wide and has a maximum depth of 1.8 m. It is a partial-recirculating channel with the ability to recirculate gravel while the water flows through the channel without recirculation. Water for the channel was drawn directly from the Mississippi River, with a maximum discharge capacity of 8000 L/s. Water discharge was controlled by a sluice gate situated at the head end of the facility while flow depth was regulated by a sharp-crested weir located at the downstream end of the channel. The channel has a 55-m-long test section and in the experiments reported here a poorly sorted gravel bed extended over the last 20 m of this test section. Short, 0.4-m-high bulkhead walls were located upstream and downstream of the test section and served to contain the gravel bed material. The gravel used in these experiments had a broad

Figure 1. Weighing pans located at the downstream end of the experimental Main Channel.

particle size distribution characterized by d_{50} = 11.3 mm, d_{16} = 4.3 mm and d_{84} = 23.1 mm [see also *Fienberg et al.*, 2008]. The thickness of the gravel bed at the start of run was approximately 0.45 m.

[9] The Main Channel was equipped with a sediment flux monitoring system that provided the ability to collect high-resolution, long-duration data sets of sediment transport dynamics using field-scale gravel particle sizes and transport rates. The sediment flux and recirculation systems were colocated in the channel at the downstream end of the 20-m test section. The flux monitoring system was composed of five adjacent, identical aluminum weighing pans (positioned 0.54 m apart) that spanned the width of the channel and independently measured the submerged weight of the gravel intercepted by the bed load trap (see Figure 1). Each pan could accommodate up to 76-mm-diameter particles and hanged from an aluminum frame that extended from its sides to a load cell connected to the ceiling above the Main Channel (see Figure 2). The system used load cells manufactured by Interface Advanced Force Measurement (SM-250) that had a capacity of 113 kg and were accurate to ±45 gram force. As a safety margin to avoid exceeding the capacity of the weighing pan system, the pan rotation that voided each bin's contents was triggered at a user-specified net weight, which in our case was set to 20 kg force (kg f).

[10] Removable stainless steel cover plates with 45-cm by 15-cm slots served to funnel the intercepted bed load downward into the pans. The pans (also referred as drums) were constructed of aluminum and had three radial baffles welded to a common 3.8-cm diameter hub and to two 81.3-cm-diameter end plates. They were oriented horizontally and transverse to the channel under the sediment trap. The three radial baffles formed two adjacent 120° "V"-shaped bins, each of which had a capacity of 62 L. The submerged weight of sediment in a bin at maximum capacity was 62 kg f. Each pan operated independently using a tipping bucket arrangement with "tips" consisting of alternating clockwise and counterclockwise 120° rotations. When the sediment mass in a pan reached a specified threshold, an air cylinder either extended or retracted, causing the pan to rotate 120 degrees. This action resulted in dumping the contents of one bin and repositioning the adjacent empty bin under the funnel to continue collecting bed load. In this manner, all bed load was continuously captured and weighed in the five independently operating pans.

[11] Bed load material that was transported out of the test section fell by gravity into the pans and incrementally added to the weight of the pan which was recorded every 1.1 s. Material dumped out of the pans was collected in a large hopper located underneath the pans, which also served as the material source for the recirculation system. The rate of gravel removal out of this hopper, and delivery to the upstream end of the channel via a large pump, was manually set by adjusting the rotation speed of a large helix, which served to push gravel laterally out of the hopper and into the recirculation line. In this way, the collection hopper and helix served to buffer small fluctuations in sediment flux out of the test section, providing a more steady "feed-type" delivery of sediment to the upstream end. Because the physical size of the collection hopper was finite, the auger speed (and hence upstream input sediment feed rate to the test section) was manually adjusted periodically to maintain storage in the hopper. In other words, an auger rate set too high could potentially remove material faster than the test section would deliver resulting in emptying of the hopper. Conversely, an auger rate set too low would result in overfilling of the hopper. We used periodic visual observations of the fill level in the collection hopper to inform our manual adjustments of the auger speed. Slight adjustments to auger speed were necessary every 30–60 min and very rarely did the system collection hopper empty or overfill meaning that the feed rate out of the collection hopper was in balance with the long-term flux of bed load out of the test section.

[12] The experimental setup also included five stationary 2.5-cm-diameter, submersible sonar transducers deployed 0.95 m below the water surface and 0.95 m upstream of each pan. The sonar transducers, mounted to the end of rigid 1.5-cm steel tubes and directed perpendicular to the bed, were used to collect continuous temporal bed elevation information upstream of the each pan. Sonar data was sampled at every 10 sec with a vertical precision of ∼1 mm. The acquisition times for the bed elevation and sediment accumulation data were based on precisely synchronized clocks allowing the two data sets to be analyzed together. Water temperature was also measured using YSI thermistor capable of measuring up to ±0.1°C. Water temperature for the two runs studied in this research averaged 3.0°C.

[13] Measurements of bed elevation and sediment transport were taken over a range of discharges corresponding to
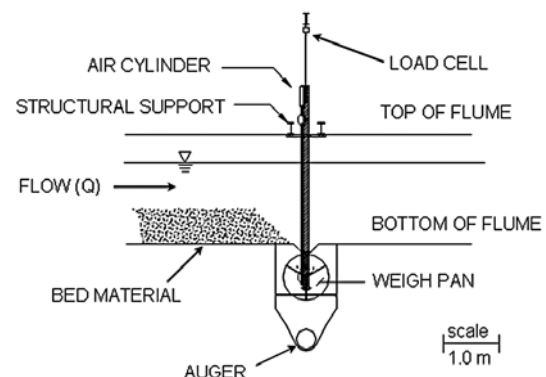
Figure 2. Side view schematic of a pan and sediment recirculation system in the Main Channel.

Table 1. Hydraulic Conditions for the Two Studied Discharges[a]

| Q_w (L/s)	Depth (m)	V (m/s)	h_R (m)	S_w (%)	τ^*_b	T_{mean} (°C)
	1.3	1.20	0.67	0.23	0.085	3.5
4300						
5500	1.3	1.54	0.67	0.53	0.196	2.7

[a]Q_w is design water discharge for the run; depth is average depth of flow in test section; v is velocity of flow; h_R is hydraulic radius; S_w is water surface slope; τ^*_b is dimensionless Shields stress (computed using hydraulic radius); and T_{mean} is mean water temperature.

different bed shear stresses. Bed shear stress is often characterized in terms of the dimensionless Shields stress, τ^*_b. For steady, uniform flow it may be approximated as $\tau^*_b = h_R S/Rd_{50}$, where h_R and S are the hydraulic radius and channel slope, respectively, and $R = 1.65$ is the relative submerged density of silica. In the analysis presented here, we report on two different discharges: a low-discharge case, with a discharge of 4300 L/s, corresponding to a dimensionless bed stress of about twice the critical value (Shields stress, $\tau^*_b = 0.085$ using median diameter) and a high discharge, 5500 L/s, corresponding to a bed stress about five times the critical value (Shields stress, $\tau^*_b = 0.196$); see Table 1 for relevant hydraulic parameters. (Note that the critical Shields stress (also known as Shields number) was estimated to be 0.047 [*Meyer-Peter and Müller*, 1948].)

[14] For both bed stress conditions, the channel was allowed to run prior to data collection such that a dynamic equilibrium was achieved in transport and slope adjustment of the water surface and bed. Determination of the dynamic equilibrium state was evaluated by checking the stability of the 60 min average total sediment flux at the downstream end of the test section. Using the pan accumulation data, the acquisition software computed a 60 min mean of sediment flux in all five pans. Dynamic equilibrium was reached when variation in this value became negligible. In other words, when the average of the previous 60 min of instantaneous flux values computed from the pan data stabilized, we determined the channel to be in dynamic equilibrium and proceeded with formal data collection and sampling.

[15] The bed load sediment accumulation series and the corresponding bed elevation series were then recorded over a span of approximately 20 h for each experiment. Figures 3a and 3b display the time series of sediment accumulation over 2 min and 10 min intervals, respectively, for pan 4, and Figure 3c the corresponding bed elevation series (recorded by the sonar transducer immediately upstream of pan 4) for the low-discharge conditions over a period of 10 h. Figure 4 shows the same series for the high-discharge conditions. Considering the bed elevation series, it can be observed that the low bed stress run (Figure 3c) produced a channel bed with only limited topographic variation, i.e., without obvious large-scale structures in the bed (the standard deviation in the bed is 10.1 mm, compared to a d_{50} grain size of 11.3 mm). However, the higher stress run (Figure 4c) generated substantial bed variability at large scale in the form of dunes, with intermediate to particle-scale fluctuations superimposed on these larger-scale features. In this study we focus on
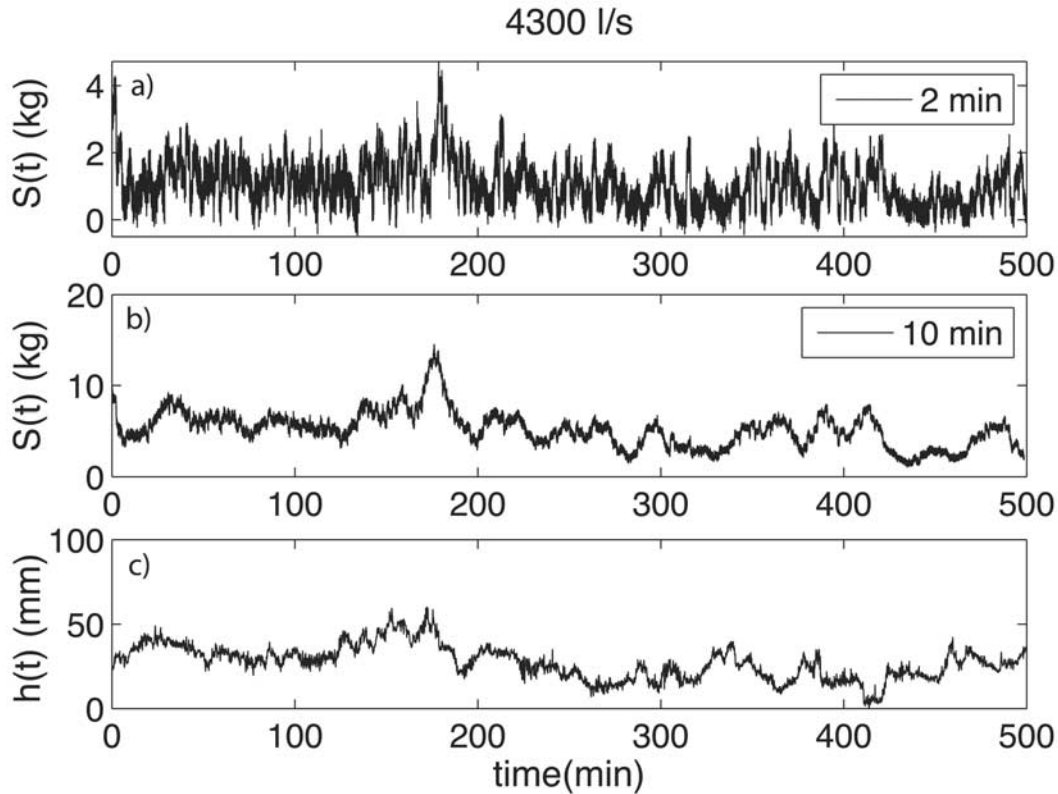
Figure 3. Low-transport conditions (flow rate 4300 L/s). Bed load sediment transport series accumulated every (a) 2 min and (b) 10 min and (c) the corresponding series of gravel bed elevations.
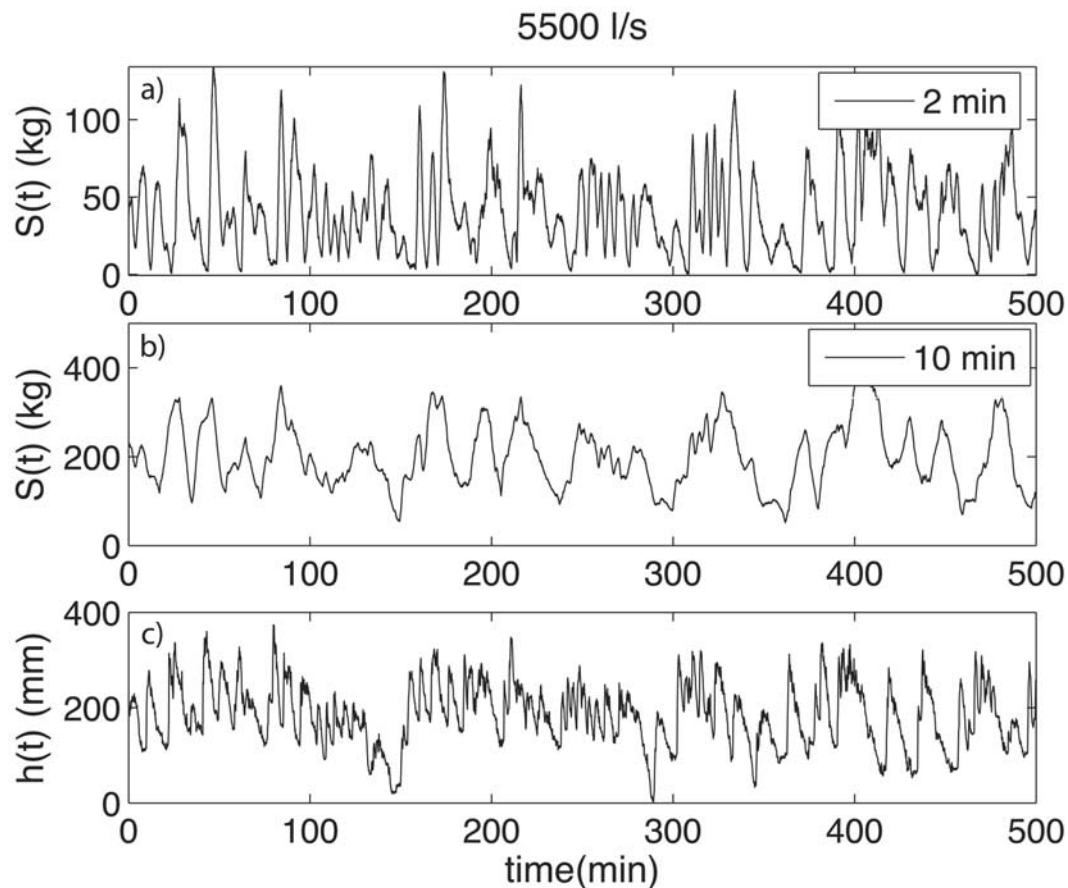
Figure 4. High-transport conditions (flow rate 5500 L/s). Bed load sediment transport series accumulated every (a) 2 min and (b) 10 min and (c) the corresponding series of gravel bed elevations.

comparing these two runs using the multiscale analysis techniques described in section 3.

2.2. Sources of Error in the Data

[16] One source of error in the accumulated sediment series was the tipping events of the pans. To account for this, the raw sediment accumulation data were preprocessed prior to the analysis presented here. The preprocessing involved removal of pan dumping events from the data and translating the data set into a continuous accumulation of sediment time series for each pan over the duration of the experiment. A single tipping event required the removal of no more than eight data points (∼8.8 s) from the record. To get the final time series of accumulated sediment transport, the time series prior to the tipping event was left unchanged, the tipping event was removed from the series, and all subsequent points were shifted backward in time to create a continuous time series as though the tipping event never occurred. Overall, the data affected by the pan tipping constituted less than 0.15% of the total data record and is, thus, negligible.

[17] There were other sources of error, however. Sediment accumulation data in the pans should increase monotonically, when corrected for tipping of the scales as discussed above. At the resolution of our measurements (approximately 1 s), however, sediment accumulation showed negative excursions which would imply negative bed load flux, which is not physically possible given the

experimental setup [see *Fienberg et al.*, 2008, Figure 3]. These errors have been attributed to (1) the fluctuating water surface over the pan, (2) the natural oscillation of the pans after being hit by the falling gravel, and (3) to the vibration caused by the large gravel recirculation pump which was placed near to the pans. This error makes the raw sediment data at small time scales (from 1 s up to approximately 1–2 min accumulations) unusable. As a check, we computed distributions of sediment flux values averaged over different time scales and found that data averaged over less than 2 min showed negative values, supporting the contention that scales smaller than 2 min are error prone. Also, although there were five pans, pans 1 and 5 (Figure 1) were not used in order to avoid data potentially impacted by wall effects.

[18] Bed elevation data were substantially less error prone, due to the acoustic (rather than mechanical) nature of the measurements. Our multiscale analysis showed a small noise regime which was only a small factor larger than the sampling interval of 10 s.

3. Roughness, Intermittency, and Statistical Scaling

3.1. Characterizing Signal Roughness and Intermittency

[19] Previous authors [e.g., *Gomez et al.*, 1989; *Ancey et al.*, 2006] have observed and documented high fluctuations in bed load sediment transport rates or particle counts at

short time scales and have described these series as "intermittent." In these and other studies it has also been noted that as flow rate increased, the sediment transport was seen to be "smoother" or more continuous, whereas at low flow rates it was "rougher" or more "bursty." These terms have been used in a qualitative way to describe the presence (or absence) of sudden bursts of sediment or high fluctuations at short time scales that arise from the stochastic nature of the transport and the collective behavior of particle dynamics.

[20] In this paper the "roughness" and "intermittency" of the sediment transport series are mathematically defined, allowing a more precise quantification of the nature of the fluctuations in bed load sediment at small time scales. A mathematical characterization of the strength of local fluctuations in a function $X(t)$ is given by the Hölder or singularity exponent $h(t_0)$, defined at any point t_0 to be the largest exponent such that:

$$|X(t) - X(t_0)| \leq C|t - t_0|^{h(t_0)}, \text{ as } t \to t_0 \qquad (1)$$

where C is a constant. This definition holds for $0 \leq h \leq 1$, but it can be generalized to $h > 1$, as discussed in section 3.3 [see also *Muzy et al.*, 1994]. The Hölder exponent gives a local measure of the smoothness or degree of differentiability of the function $X(t)$: a value of $h(t_0) \geq 1$ indicates that the function is smooth at t_0, in the sense that it is at least once differentiable at the point t_0, whereas a function with $h(t_0) = 0$ is so rough that it is discontinuous at that point. Between these extremes, a value of $0 < h(t_0) < 1$ means that the function is continuous but not differentiable at t_0, with a higher h value (closer to 1) implying that the function is "smoother" or more regular, and a lower h value (closer to zero) implying that the function is "rougher" or more irregular.

[21] Having established a measure of local (point-wise) roughness in a signal, it is natural to ask what kind of $h(t_0)$ values are present in an observed time series, and how they are distributed. If we denote the set of all points in the function $X(t)$ with a particular value of Hölder exponent h as:

$$\Omega(h) = \{t_0 : h(t_0) = h\} \qquad (2)$$

then, in general, for a multifractal function these sets of points are interwoven fractal sets whose distribution can be characterized by the so-called singularity spectrum $D(h)$, defined as

$$D(h) = Dim_H(\Omega(h)) \qquad (3)$$

where Dim_H is the Hausdorff dimension of the fractal set [e.g., *Schroeder*, 1991]. In other words, the singularity spectrum $D(h)$ describes the relative frequency of occurrence of local abrupt fluctuations (singularities) with strength h. In a one-dimensional function like a time series, the value of h corresponding to the peak of the singularity spectrum indicates the most frequently occurring singularity or fluctuation strength. (Note that if $D(h)$ is symmetric, which is a good approximation for most signals, then this value characterizes the "average roughness" of the signal as it coincides with the arithmetic mean of the local singularities h.) The range of h over which $D(h) \geq 0$, or

the spread of the singularity spectrum, reflects the temporal heterogeneity of the local singularities; that is, it measures the degree of clustering in the abrupt local fluctuations of various strengths. Simply put, a signal with a wide $D(h)$ will have sparse regions where the strength of the local fluctuations is much greater than (or much less than) the mean fluctuation strength, and hence will display infrequent but exceptionally large "bursts" at small scales embedded within bursts of lesser strength; that is, the signal will be very "intermittent." On the other hand, a $D(h)$ spectrum which is just a spike, i.e., $D(h) = 1$ at $h = H$ and zero elsewhere, indicates a signal which exhibits one strength of singularity only, H also called the Hurst exponent, which is homogeneously distributed throughout the signal (in this case the signal has zero intermittency). It is noted that H, which is a local measure of variability, provides different information than the standard deviation of a signal, which is a global measure of variability; in other words two signals with the same standard deviation can have considerably different values of H [e.g., see *Turcotte*, 1997].

3.2. Multiscale Analysis

[22] While the spectrum of singularities $D(h)$ can be used to describe the "roughness" and "intermittency" of a signal, it can be difficult to estimate it directly from the data. An interesting mathematical result (the so-called multifractal formalism [*Parisi and Frisch*, 1985; *Muzy et al.*, 1994]) establishes that $D(h)$ relates to how the probability density function (pdf), or equivalently the statistical moments, of the signal fluctuations changes with scale. Let the fluctuation $S(t_0, a)$, at any time t_0 and scale a, be defined as

$$S(t_0, a) = X(t_0 + a) - X(t_0) \qquad (4)$$

and the statistical moments of the absolute values of these fluctuations by

$$M(q, a) = \langle |S(t_o, a)|^q \rangle \qquad (5)$$

where angle brackets denote expectation over time. For a process that exhibits statistical scale invariance, the statistical moments of the fluctuations behave as a power law function of scale:

$$M(q, a) \sim a^{\tau(q)} \qquad (6)$$

where $\tau(q)$ is the so-called spectrum of scaling exponents and is a function of the moment order q. Thus if the series exhibits scale invariance, the function $\tau(q)$ completely describes the manner in which the statistical moments of the pdf of fluctuations varies with scale.

[23] It is the scaling function $\tau(q)$ that can be used to retrieve the spectrum of singularities $D(h)$. The precise transform between these two representations is given by the Legendre transform [*Parisi and Frisch*, 1985; *Muzy et al.*, 1994]:

$$D(h) = \min_q [qh - \tau(q) + 1] \qquad (7)$$

In this way the spectrum of singularities describing the average roughness and intermittency of the signal can be

estimated through the scaling properties of the statistical moments of the signal fluctuations.

3.3. Generalized Fluctuations and the Wavelet Transform

[24] Although the fluctuations $S(t_0, a)$ of a time series can be computed by directly taking the first-order increments, as in equation (4), calculating the statistical moments in this way (which gives rise to the so-called structure function approach) has some limitations. First, these fluctuations can be corrupted by small-scale noise (since observations are used directly without local smoothing); in addition, they do not remove higher-order nonstationarities (it is easy to show that the first-order increments remove only constant level trends); and finally, they cannot estimate singularity strengths $h > 1$. To overcome these limitations, the continuous wavelet transform can be used to define generalized fluctuations in the time series [e.g., see *Arneodo et al.*, 1995; *Jaffard*, 1997; *Venugopal et al.*, 2006a; *Lashermes and Foufoula-Georgiou*, 2007]. In this framework we redefine the (generalized) fluctuations $S(t_0, a)$ to be

$$S(t_0, a) = \int_{-\infty}^{\infty} \psi_{a,t_0}(t) X(t) dt \quad (8)$$

where $\psi_{a,t_0}(t)$ is a "differencing function," as for example, the first derivative of a Gaussian function. In particular ψ_{a,t_0} is a wavelet resulting from shifting and scaling a mother wavelet $\psi(t)$, such that,

$$\psi_{a,t_0}(t) = \frac{1}{a} \psi\left(\frac{t - t_0}{a}\right) \quad (9)$$

where t_0 is the location and a is the scale parameter. For the continuous wavelet transform to be invertible, the mother wavelet must satisfy the invertibility condition $\int_{-\infty}^{\infty} t\psi(t) dt = 0$ i.e., it must have a zero mean (which makes it a kind of local differencing function; e.g., see *Mallat* [1998] or *Kumar and Foufoula-Georgiou* [1997]). A commonly used mother wavelet is the family of Gaussian wavelets defined as the Nth-order derivatives of a Gaussian function $g_0(t)$, i.e., $g_N(t) = (d^N/dt^N) g_0(t)$, modulus a proper multiplicative factor to ensure correct normalization. Defining the fluctuations $S(t_0, a)$ using the first-order derivative of the Gaussian function can be seen as computing first-order increments of the series after the series has been locally smoothed with a Gaussian kernel or, equivalently, as computing first-order increments and then performing a smoothing (weighted averaging). (This can be easily deduced from the convolution theorem [see also *Lashermes et al.*, 2007].) Similarly, defining multiresolution coefficients using $g_N(t)$ can be considered as smoothing the series with a moving Gaussian window, followed by Nth-order differencing (the standard deviation of the Gaussian function determines the "scale" at which the smoothing and thus differencing is done [see *Lashermes and Foufoula-Georgiou*, 2007]). The smoothing operation removes the noise and the higher-order differencing removes nonstationarities from the signal, rendering the wavelet-based

generalized fluctuations appropriate for characterization of statistical scaling [e.g., see *Muzy et al.*, 1994].

[25] One property that should be considered when choosing an appropriate mother wavelet for defining the mutiresolution coefficients is the number of vanishing moments. Note that the mother wavelet is said to have N vanishing moments if

$$\int_{-\infty}^{\infty} t^k \psi_o(t) dt = 0$$

for $0 \le k < N$. The Gaussian wavelet $g_N(t)$, defined above as the Nth derivative of the Gaussian, can be easily shown to have N vanishing moments. Defining multiresolution coefficients with a mother wavelet which has N vanishing moments can be shown to remove from the series an additive polynomial trend of degree less than N [e.g., see *Kumar and Foufoula-Georgiou*, 1997]. Therefore, the wavelet-based multiscale analysis proposed here renders the fluctuation series stationary if one chooses a wavelet with more vanishing moments than the degree of non-stationarity in the data. In practice, the degree of nonstationarity of the data series is not known in advance, so one applies the wavelet transform $g_N(t)$ with increasing values of N until the results of the analysis do not vary with N: this will imply that the order has been chosen large enough to remove any nonstationarities. The correct selection of multiresolution coefficients is important for a meaningful multifractal analysis as has been recently demonstrated by *Lashermes and Foufoula-Georgiou* [2007]. For example, using standard fluctuations (first-order differences) to analyze a nonstationary signal will result in a spurious estimate of $H = 1$ misleading one to assume that the signal is smooth and differentiable.

[26] In this study, the fluctuations, $S(t_0, a)$, of the bed load sediment and bed elevation series at various scales were computed using the wavelet transform (equation (8)) with the wavelet $g_3(t)$, since this was the lowest-order wavelet able to remove all nonstationarities from the sediment transport series (a lower-order wavelet g_2 proved sufficient for the bed elevation series but the use of the higher-order wavelet g_3 does not alter the results; this is discussed in more detail in section 4). The moments $M(q, a)$ were then estimated using equation (5), and the scaling exponents $\tau(q)$ computed from the log-log linear relationships (equation (6)) over the scaling range. This in turn allowed the calculation of the singularity spectrum $D(h)$ via equation (7).

3.4. Scale Dependence of the pdf of the Fluctuations

[27] The scaling exponents $\tau(q)$ are not only of interest for calculating the singularity spectrum $D(h)$, but also for describing how the pdf of the fluctuations depends on scale. As discussed in section 3.2, the statistical moments $M(q, a)$ in equation (5) describe how the fluctuations of a process change with scale and, for a scale-invariant process, this change is captured in the $\tau(q)$ curve. In the case of simple scaling, the scaling exponent function is linear in moment order, i.e., $\tau(q) = qH$ for some constant H (called the Hurst exponent), which can be shown to imply that the pdf of the fluctuations at scale a, $P_a(S) \equiv P(S(t, a))$, is related to the

pdf at another scale a by [e.g., see *Arneodo et al.*, 1997; *Venugopal et al.*, 2006a]

$$P_{a'}(S) = \left(\frac{a}{a'}\right)^{-H} P_a \left(\left(\frac{a}{a'}\right)^{-H} S\right) \qquad (10)$$

Note that the normalizing factor $(a/a')^{-H}$ is a deterministic kernel that depends on H and the ratio of scales (not each scale individually). As this type of statistical scaling behavior is controlled by a single parameter only, it is referred to as monoscaling. Note that equation (7) implies that in the monoscaling case $D(h) = \delta(h - H)$, i.e., the only Hölder exponent with dimension greater than zero is $h = H$, and the function is completely uniform in its roughness, i.e., not intermittent, at small scales.

[28] In the more general case of multiscaling, the scale invariance relation (equation (6)) still holds, but $\tau(q)$ is not linear but a concave function of the moment order q. In this case, the pdf of the fluctuations does not maintain its shape between two different scales but changes continuously via convolution with a kernel that depends on the ratio of scales [*Arneodo et al.*, 1999b; *Venugopal et al.*, 2006a]. The generalization of equation (10) for multifractals is obtained [*Castaing et al.*, 1990] by considering that H is not a constant but has a probability density function $\rho(h)$. In this case, expression (10) becomes

$$P_{a'}(S) = \int_{-\infty}^{\infty} \rho(h) \left(\frac{a}{a'}\right)^{-h} P_a \left(\left(\frac{a}{a'}\right)^{-h} S\right) dh \ \ \text{for } a' < a \quad (11)$$

In general, the pdf of the fluctuations is expected to widen and have fatter tails as the scale decreases. In turbulence, for example, the above transformation renormalizes the almost Gaussian pdf of turbulent velocity fluctuations at very large scales to a thick-tailed pdf at small scales. It is noted that the probability density involved in the renormalization of the pdf's is related to the spectrum of singularities $D(h)$, $\rho(h) \propto a^{-D(h)}$, and reflects the presence of Hölder exponents of various strengths which are inhomogeneously distributed throughout the signal (see *Frisch* [1995] and also *Venugopal et al.* [2006a] for a discussion of the equivalency of the geometrical and statistical interpretations). The pdf rescaling of (11) can be expressed in a convolution form as

$$P_{a'}(S) = \int_{-\infty}^{\infty} G_{aa'}(u) e^{-u} P_a(e^{-u}S) \, du \ \ \text{for } a' < a \quad (12)$$

where $u = h \ln(a/a')$ and $G_{aa'}(u) = \rho[u/\ln(a/a')]/\ln(a/a')$. This implies that the pdf at scale a' can be expressed as a weighted sum of dilated pdf's at larger scales $a > a'$. The kernel $G_{aa'}(u)$ is called the propagator and can be estimated from the data (see *Castaing et al.* [1990] for the theory and *Venugopal et al.* [2006a] for an application to high-resolution temporal rainfall series). Once the propagator is known, a known pdf at any scale can be used to derive the pdf at any smaller scale via equation (12).

[29] To gain better insight into how the $\tau(q)$ (or $D(h)$) curve controls the pdf change over scales, let us consider the coefficient of variation, C_v, which is the ratio of the standard deviation to the mean, $C_v = \sigma/\mu$. For a monoscaling process, this ratio would be constant with scale, as both the mean and standard deviation are rescaled equally, as shown by equation (6). In a multiscaling situation, however, the increasing width of the pdf leads to C_v increasing with decreasing scale. The precise behavior of C_v with scale can be seen by noting that $C_v^2 + 1 = M(2, a)/M(1, a)^2$, so that for a multiscaling process, equation (6) implies $(C_v^2 + 1) \sim a^{\tau(2)-2\tau(1)}$. In other words, $\tau(2) - 2\tau(1)$ characterizes the (second order) relative stretching of pdf's across scales, and its magnitude is also a measure of deviation from monoscaling. Similar relationships can be worked out for higher-moment ratios. As we will see for the sediment transport series, C_v significantly depends on scale, attesting to the presence of multiscaling.

3.5. Parameterizing the Scaling Properties and Singularity Spectrum

[30] While knowing the $\tau(q)$ (or $D(h)$) curve completely characterizes the scale dependence of the pdf's of fluctuations, for practical purposes it is often desirable to parameterize these curves concisely. Assuming an analytic form of the $\tau(q)$ curve, the simplest parameterization for multiscaling is to extend the linear model of $\tau(q)$ used for monoscaling to a quadratic model, that is,

$$\tau(q) = c_0 + c_1 q - \frac{c_2}{2} q^2 \qquad (13)$$

In this parameterization, the constant $c_0 = \tau(0)$ is the scaling exponent of the zeroth-order moment, which will be equal to zero if the support of the field under analysis fills the space, as we see for both sediment flux and bed elevation. This leaves two parameters to describe the (multi)scaling: the parameters c_1 and c_2 control the scaling of all the moments and the change in shape of the pdf with changing scale. The two parameters c_1 and c_2 in (13) can be estimated by fitting a quadratic function to the empirical $\tau(q)$ curve, or via a more robust methodology called the cumulant analysis (see *Delour et al.* [2001] and *Venugopal et al.* [2006a] for an application to rainfall series).

[31] For such a quadratic $\tau(q)$, it can be shown from equation (7) [e.g., *Venugopal et al.*, 2006a] that the spectrum of singularities is also quadratic, with

$$D(h) = 1 - \frac{1}{2c_2}(h - c_1)^2 \qquad (14)$$

This shows that the most frequently occurring value of the Hölder exponent (peak of the $D(h)$ curve), and hence the mean roughness/smoothness of the function, is given by the parameter c_1 (note that $D(h) = 1$ and $D(h)$ in (14) is symmetric around c_1). Alternatively, c_2 provides a measure of the spread of the $D(h)$ curve and hence prescribes the degree of intermittency. For this reason, c_2 is referred to as the "intermittency coefficient." The limiting case of $c_2 = 0$, that is the case of a monofractal, leads to a delta function $D(h) = \delta(h - c_1)$, and hence gives a single Hölder exponent $H = c_1$ (the same exponent H as in equation (10)). This means there is no intermittency: the function will have the same degree of local roughness (irregularity) everywhere. For a multifractal ($c_2 > 0$), however, a range of local

Table 2. Multifractal Parameters Estimated for Low and High Flows Using Different Gaussian Wavelets[a]

Shields Stress	Pan	Scaling Range (min)	Wavelet	c_1	c_2
		$Q = 4300$ L/s			
0.085	2	1.2 – 10	g2	0.57	0.12
	2	1.2 – 10	g3	0.56	0.14
	2	1.2 – 10	g4	0.54	0.12
	3	1.2 – 10	g2	0.52	0.11
	3	1.2 – 10	g3	0.49	0.13
	3	1.2 – 10	g4	0.48	0.13
	4	1 – 8	g2	0.49	0.10
	4	1 – 8	g3	0.47	0.10
	4	1 – 8	g4	0.45	0.10
		$Q = 5500$ L/s			
0.196	2	1 – 10	g2	1.04	0.09
	2	1 – 10	g3	1.07	0.09
	2	1 – 10	g4	1.09	0.10
	3	1 – 10	g2	1.04	0.11
	3	1 – 10	g3	1.07	0.10
	3	1 – 10	g4	1.09	0.11
	4	1 – 10	g2	1.09	0.11
	4	1 – 10	g3	1.12	0.11
	4	1 – 10	g4	1.14	0.11

[a]See text for definitions.

fluctuation strengths will be inhomogeneously distributed throughout the signal, with the minimum and maximum Hölder exponents given by $h_{\mathrm{min/max}} = c_1 \mp \sqrt{2c_2}$ (where the $D(h)$ curve crosses below 0). So with increasing c_2 there is a wider range of local fluctuation strengths present in the signal, and hence a greater degree of intermittency.

4. Results

4.1. Sediment Transport Scaling

[32] Bed load sediment transport fluctuations were analyzed using the multifractal formalism. Fluctuations were computed by applying a differencing filter on the accumulated sediment series $S_c(t)$, i.e., equation (8) with the generic function $X(t)$ replaced now by $S_c(t)$ and using as differencing filters wavelets of increasing order $g_N(t)$, where $N = 2, 3,$ and 4. It is noted that by using the third derivative of the Gaussian, $g_3(t)$, on the accumulated sediment series gives fluctuations that represent second-order increments of the bed load transport rates; that is, they capture the local rate of change in the sediment transport rates. This filtering guarantees removal of linear trends in the rate of sediment transport series, which, if present, can influence the results. Indeed such rate changes were found present during the 20 h duration of our data collection [see *Fienberg et al.*, 2008, Figure 3] and thus the $g_3(t)$ was adopted for our analysis. However, it is noted that the use of lower-order wavelets does not significantly change the estimates of the parameters as can be seen from the detailed Table 2. Having defined the fluctuations, the statistical moments $M(q, a)$ were then computed (equation (5)), and are shown as a function of scale in Figure 5, for pan 3 (see Figure 1). Similar results were obtained for the other pans, except for pans 1 and 5 which suffered from wall effects and showed no good scaling range. Three different regimes can be distinguished for both the low and high discharge: a small-scale regime (scales below 1 min) which is judged to be noise dominated (see section 2.1); a log-log linear

scaling regime in the temporal range of approximately 1 to 10 min; and then a short transitional regime before a leveling off of the moments is reached. Here we focus on the longer scaling regime between 1 min and 10 min marked by the dashed lines in Figure 5. The scaling exponents of the various moment orders, $\tau(q)$, were estimated using linear regression within this scaling range and are shown for both discharges in Figure 5 (bottom). It can be seen that both curves deviate from linear behavior and hence depart from simple scaling and instead demonstrate multiscaling. The parameters c_1 and c_2 found by fitting the quadratic model (equation (13)) to these curves are presented in Table 3, along with a summary of the scaling range and parameters for the other pans for which uninterrupted data were available. It is noted that the quadratic fit is very good and the fitted curves are indistinguishable from the measured points.

[33] This scaling of the moments reflects the scaling of the pdf of sediment fluctuations. Figure 6 shows the pdf's of the sediment transport rates (defined as accumulations over an interval divided by the length of that interval) for 2-min and 10-min intervals for both high and low discharge. It can be seen that for both flow conditions, the very skewed and fat-tailed pdf at 2 min changes to a much more symmetrical pdf at 10 min, although in the case of the low flow, there is still some skewness present even at the larger sampling time. It is recalled that the parameters c_1 and c_2 control this pdf change over scales through the rescaling kernel (equation (12)). An easy way to observe the relative narrowing of the pdf with increasing scale is via the coefficient of variation C_v computed from the data, which is plotted in Figure 7 as a function of scale. The decreasing values of C_v with increasing scale show that the width (spread) of the pdf changes with scale in a different manner compared to the mean (it reduces more quickly), in agreement with earlier observations by *Kuhnle and Southard* [1988], and hence reinforces the conclusion that sediment transport fluctuations exhibit multiscaling. A monoscaling function would have constant C_v as mean and standard deviation would rescale similarly (see equation (6)).

[34] Concentrating on the first-order ($q = 1$) statistical moment, which is the mean sediment accumulation in an interval Δt (scale a in the previous notation), we note that it scales as $\Delta t^{\tau(1)}$ where $\tau(1) = c_1 - c_2/2$ from equation (13). Using the values of c_1 and c_2 (Table 3) for low flows, it implies that within the scaling range of 1 and 10 min the mean amount of accumulated sediment ($\langle S(t, \Delta t)\rangle$) increases as approximately $\sqrt{\Delta t}$. If one doubles the sampling interval, for example, the amount of sediment accumulated does not double but increases only by a factor of about 1.41. When considering the mean sediment transport rate, ($\langle S(t, \Delta t)/\Delta t\rangle$), the above results imply that it scales as $(\Delta t)^{-0.5}$ or that the bed load transport rate decreases with increasing sampling interval Δt. In other words, doubling the sampling interval results in a transport rate that is approximately 0.7 ($= 1/\sqrt{2}$) times smaller.

[35] For high flow rates, the estimated value of $\tau(1)$ is approximately 1.1 (using the values of c_1 and c_2 from Table 3 in equation (13)) implying that within the scaling range of 1 and 10 min, the mean amount of accumulated sediment increases as approximately $(\Delta t)^{1.1}$. In this case, doubling the sampling interval increases accumulated sediment by a
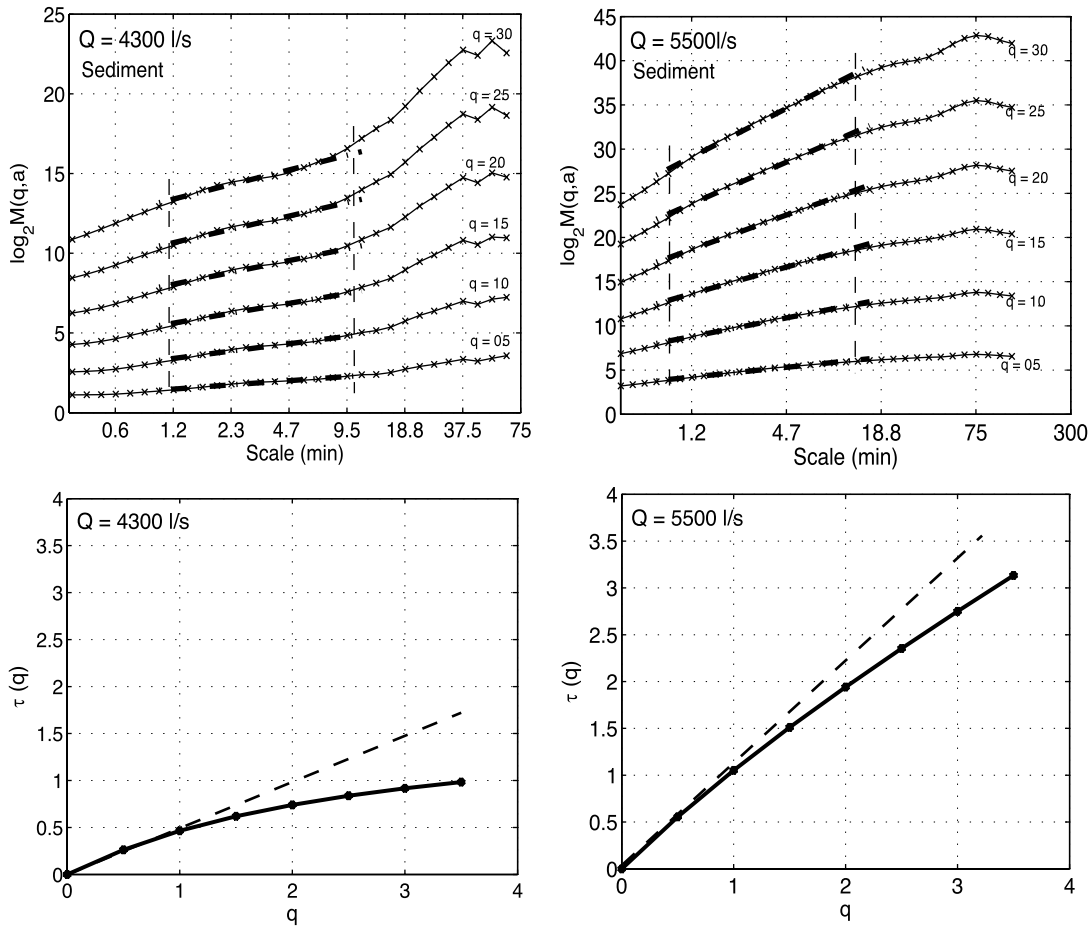
Figure 5. (top) Statistical moments of the fluctuations of the sediment transport series as a function of scale and (bottom) the scaling exponents $\tau(q)$ estimated from the log-log linear regressions within the scaling regions. Notice the deviation of $\tau(q)$ from the linear line establishing the presence of multifractality. (left) For low-transport conditions and (right) for high-transport conditions.

factor of about 2.1. Considering the mean sediment transport rate, one sees that in the high-flow conditions the rate does not remain constant with sampling interval (within the range of sampling interval of 1 to 10 min) but rather slightly increases by a factor of approximately 1.1 (= $2^{0.10}$).

[36] The above scaling applies only to the mean and is controlled by the value of ($c_1 - c_2/2$). As discussed in sections 3.2 and 3.4, our analysis allows one to quantify how higher-order statistical moments change with sampling interval in a similar way, for example the second moment about the origin changes as a power law on scale with an exponent $2(c_1 - c_2)$, etc., as dictated by equations (6) and (13).

[37] Turning to the singularity spectrum $D(h)$ which characterizes more directly the abrupt fluctuations of the sediment transport series, we recall that it can be computed from the scaling exponents $\tau(q)$ via the Legendre transform (equation (7)) or directly from equation (14) using the fitted parameters c_1 and c_2. Figure 8a shows the $D(h)$ spectrum for the sediment transport in pan 3, calculated from the quadratic model fit using the parameters in Table 3. It can be seen that at the low discharge, the sediment transport series is both rougher on the average and more intermittent

(lower c_1 and higher c_2, respectively). Conversely, the high-discharge case results in a much smoother and less intermittent sediment transport series (higher c_1 and lower c_2, respectively). As it can be seen from Figure 8a, for low flow rates, h_{min} is approximately zero, and h_{max} is slightly larger than 1. This implies that there are clustered regions in the sediment transport rate series where very high fluctuations are expected over very small intervals (a value of $h = 0$ corresponds to a discontinuous signal) while there are also

Table 3. Summary of Statistical Scaling Analysis Results for the Bed Load Sediment Series[a]

Pan	Scaling Range (min)	Shields Stress	$\tau(2) - 2\tau(1)$	c_1	c_2
		$Q = 4300$ L/s			
2	1.2–10		−0.20	0.56	0.14
3	1.2–10	0.085	−0.19	0.49	0.13
4	1–8		−0.15	0.47	0.10
		$Q = 5500$ L/s			
2	1–10		−0.13	1.07	0.09
3	1–10	0.196	−0.16	1.07	0.10
4	1–10		−0.15	1.12	0.11

[a]See text for definition of variables.
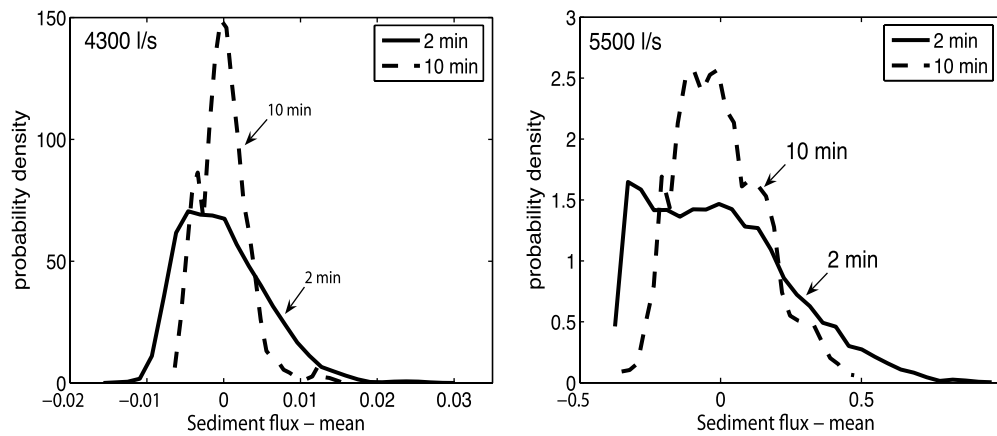
Figure 6. Probability distribution functions of the sediment transport rate (flux) for sampling intervals of 2 and 10 min for (left) low- and (right) high-discharge rates. The probability distributions have been shifted to zero mean for comparison.

regions that are very smooth (a value of $h = 1$ corresponds to a signal with continuous first derivative). For high flow rates the values of h_{min} and h_{max} are approximately 0.8 and 1.5, implying that the sediment transport series is very smooth overall but there are limited clustered regions where some abrupt fluctuations at small scales are encountered (signal slightly nondifferentiable as $h < 1$) while the majority of the series is very smooth. One would expect that these bursts in the sediment transport series are connected to high fluctuations in the bed elevation series which would allow to a lesser or larger degree a collective mobilization of gravel particles. In section 4.2 a multifractal analysis to characterize the roughness and intermittency of bed elevation fluctuations is presented.

4.2. Bed Elevation Scaling

[38] Spatial bed elevation fluctuations have been previously analyzed in terms of their scaling properties, and deviation from simple scaling has been reported [*Nikora and Walsh*, 2004]. Here the temporal fluctuations of bed elevation were analyzed with the wavelet-based multiscale framework, and scaling of the moments was documented within the range of scales from approximately 1 to 10 min (see Figure 9), which coincides with the scaling range observed in the sediment transport series and suggests a close link between the dynamics of the two series. Above the characteristic scale of 10 min, the moments leveled off and the statistical quantities became independent of time scale. The scaling exponents $\tau(q)$ for these moments are shown in Figure 9, for the high- and low-discharge experiments. As other authors have reported [e.g., see *Nikora and Walsh*, 2004], a deviation from simple scaling is observed for both discharge rates indicating the presence of temporal heterogeneity in the local roughness (what we have called "intermittency") in bed elevation fluctuations. The parameters c_1 and c_2 fitted to the $\tau(q)$ curves of the bed elevation fluctuation series are displayed in Table 4, and the corresponding singularity spectra $D(h)$ are presented in Figure 8b. Similar to the sediment transport fluctuations, we observe that bed elevation fluctuations are rougher on an average in the low-discharge case than in the high-discharge case ($c_1 = 0.57$ versus $c_1 = 0.68$), although to a lesser extent

than in the sediment series. However, considering the degree of intermittency in the bed elevation fluctuations, we see that it is higher at the high-transport case (a wider $D(h)$ spectrum and a larger c_2 value) with a coefficient of intermittency $c_2 = 0.13$, versus a narrower $D(h)$ and $c_2 = 0.06$ in the case of low transport. This is reverse from what is observed in the sediment transport fluctuations (see also Figure 8a) and calls for an explanation based on further experimentation and mechanistic modeling.

5. Discussion

[39] The simultaneous collection of bed load transport and bed elevation data in a field-scale channel is the major strength of the experimental setup used in this work. The large channel geometry, and high temporal resolution of the data, allowed robust statistical analysis over a wide range of temporal scales. Despite the more comprehensive data sets collected as part of the StreamLab06 experiments our analysis here is concentrated on two data sets at two different flow rates, as these are the only data currently
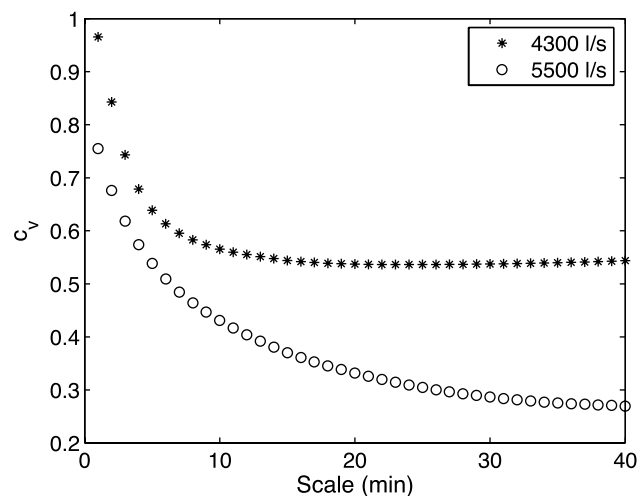
Figure 7. Coefficient of variation of the bed load sediment transport series.
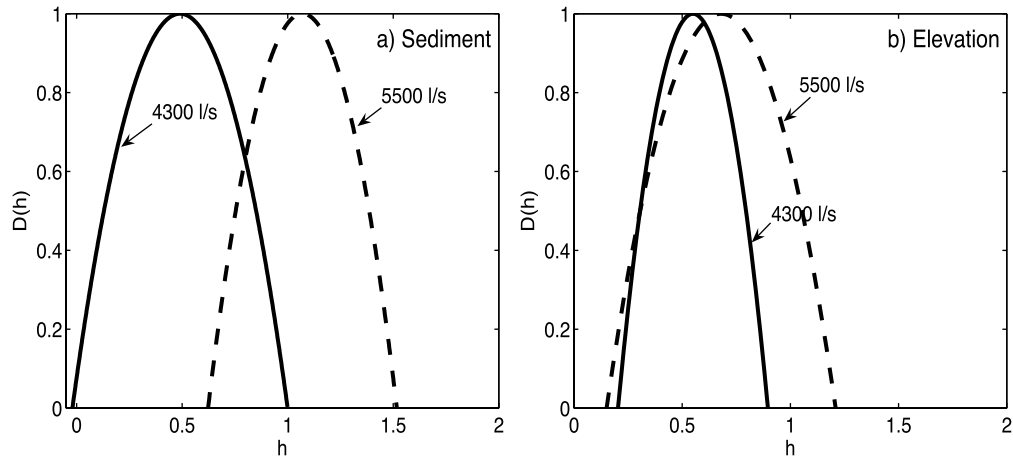
Figure 8. Fitted quadratic singularity spectra $D(h)$ obtained for (a) bed load sediment transport series and (b) bed elevation fluctuation series for the low- and high-discharge cases, respectively.
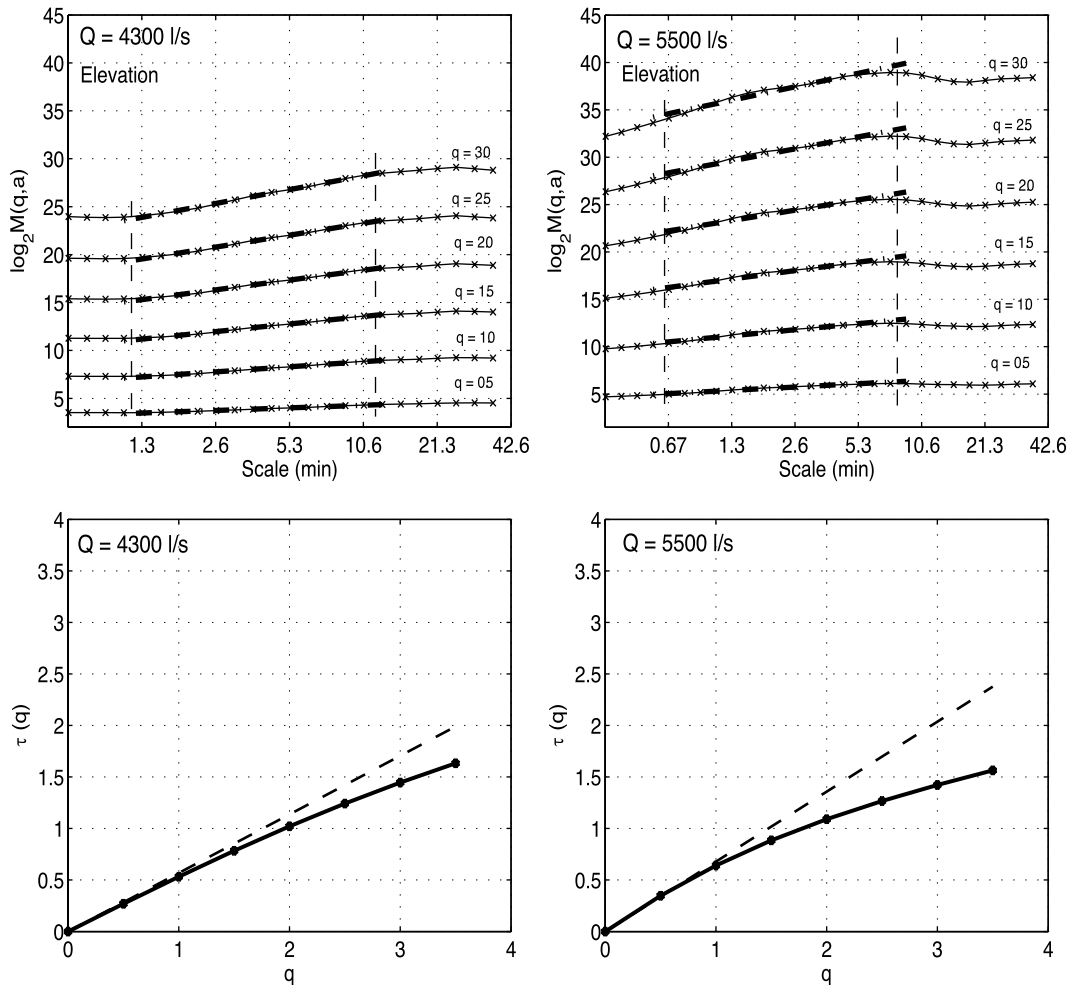
Figure 9. (top) Statistical moments of the fluctuations of the bed elevation time series as a function of scale and (bottom) the scaling exponents $\tau(q)$ estimated from the log-log linear regressions within the scaling regions. Notice the deviation of $\tau(q)$ from the linear line establishing the presence of multifractality. (left) For low-transport conditions and (right) for high-transport conditions.

Table 4. Summary of Statistical Scaling Analysis Results for the Bed Elevation Time Series[a]

| Probe	Scaling Range (min)	Shields Stress	$\tau(2) - 2\tau(1)$	c_1	c_2
		$Q = 4300$ L/s			
4	$1-10$	0.085	−0.04	0.57	0.06
5	$1-10$		−0.06	0.53	0.08
		$Q = 5500$ L/s			
2	$0.5-8$		−0.18	0.65	0.12
3	$0.5-8$	0.196	−0.19	0.68	0.14
4	$0.5-8$		−0.20	0.76	0.13

[a]See text for definition of variables.

available for analysis. The mixed grain size distribution of the feed material, while beneficial for mimicking a natural gravel stream, makes it more difficult to discern the influences of spatial grain size sorting [*Iseya and Ikeda*, 1987; *Kuhnle and Southard*, 1988; *Cudden and Hoey*, 2003; *Frey et al.*, 2003] from those of bed topography and collective grain motion [*Gomez et al.*, 1989; *Jerolmack and Mohrig*, 2005; *Ancey et al.*, 2008] on sediment transport fluctuations. Also, for this experiment we do not have any data regarding armoring of the streambed over the duration of the experiments, or the grain size distributions of individual sediment pulses. With these limitations in mind, in this section we place our experimental results and analysis in the context of laboratory and field studies of sediment transport fluctuations in uniform and mixed grain size channels.

[40] The multiscaling analysis demonstrates how the statistical moments of bed load transport rate depend on the time scale of observation. To illustrate, we first examine the behavior of the mean transport rate (the first moment). Estimating mean sediment transport rate is essential for measuring the material flux through a river, and for model input and/or calibration. For the low-discharge run ($\tau^*_b =$ 0.085), mean transport rate decreased with sampling interval, while at higher discharge ($\tau^*_b =$ 0.196), the trend reversed: mean transport rate slightly increased with sampling interval over a comparable time range. A similar trend was discovered by *Bunte and Abt* [2005], who studied the effect of sampling interval on bed load transport rates measured using Helley-Smith samplers deployed in a mixed gravel-cobble stream of a size comparable to our experiments. They found that in moderate to high flows (50% bankfull to almost bankfull conditions), 2 min sampling led to an average transport rate 2 to 5 times lower than that found with 10 min sampling. However, at lower flows (close to the incipient gravel motion), 2 min sampling overestimated the transport rates at 10 min sampling by a factor of almost 3. Although not directly comparable, the trends observed are qualitatively the same as our experiments (Figure 10). *Bunte and Abt* [2005] attribute the higher-discharge trend to the effect of large but infrequent transport events associated with the crests of bed forms: small sampling intervals underestimate mean transport because they are likely to miss these events. They suggest that the reversal in trend for the low-discharge observations is the result of sampling and computational difficulties, rather than a "real" effect. Our high-resolution experiments demonstrate that this trend reversal might in fact be real.

[41] It is stressed that it is difficult to quantitatively compare the field results to our laboratory experiments, due to differences in transport and lack of the detailed field

data. *Bunte and Abt* [2005] do not report Shields stress, but they report that their low-flow observations correspond to incipient sediment motion which is supported by our calculation of their critical Shields stress ($\tau^* = 0.047$) using their reported bankfull flow characteristics. Our low-flow experiment had a Shields stress almost twice the critical value, making it comparable in terms of stress to their moderate flow observations. Thus it seems that in both the study of Bunte and Abt and our study, suggest a reversal in trend, from decreasing to increasing mean transport rate with sampling interval, as bed stress increases. The fact that the reversal appears to occur for different stress values in the
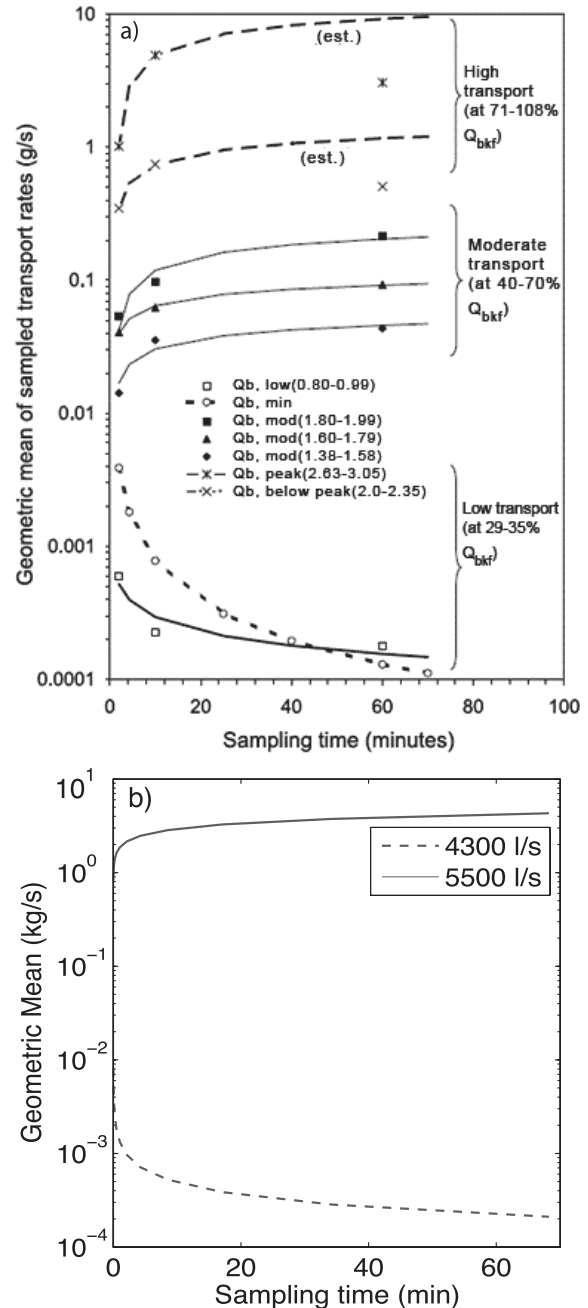
Figure 10. Geometric means at different sampling times from (a) field experiments (reproduced from *Bunte and Abt* [2005]) and (b) theoretical results from this study.

field and the laboratory may be the result of the multiple intricacies of sediment transport and grain size sorting of heterogeneous mixtures in turbulent flows. Clearly, experiments systematically document how the statistics of transport rate change with bed stress over a wide range of values would be helpful in illuminating this point.

[42] Several field and laboratory experiments have documented sediment transport fluctuations in mixed grain size sediments. *Iseya and Ikeda* [1987] found strong longitudinal grain size sorting in mixed gravel and sand experiments, which caused periodic fluctuations in transport rate due to changing local sediment supply. Such periodic pulses in gravel-sand mixtures have also been reported by *Kuhnle and Southard* [1988] and *Frey et al.* [2003]. These experiments cannot be directly compared to our results, however, because they had limited bed topography and/or antidunes, while our experimental channel allowed for the growth of large bed forms in subcritical flow. These studies suggest that the creation and destruction of sediment patches of different grain sizes [see also *Cudden and Hoey*, 2003] due to longitudinal grain size sorting within the channel likely contributed somewhat to the observed transport fluctuations in our experiments, but are not capable of explaining all of this variability.

[43] Sediment transport rates became smoother and less intermittent with increasing bed stress in our experiments, in agreement with previous observations. Near the threshold of motion, grains are in partial transport because local bed stress fluctuates above and below the threshold value. These turbulent fluctuations, along with grain-to-grain interactions at the bed, result in intermittent and collective motion of grains, leading to nonrandom transport rate fluctuations with heavy tails [*Ancey et al.*, 2008]. In a mixed grain size bed, size selective transport often occurs which may enhance this effect [*Kuhnle and Southard*, 1988]. The experiments of *Ancey et al.* [2008] demonstrate that such fluctuations can occur even in glass spheres of uniform size, with little or no bed topography. As bed stress is increased such that the local stress fluctuations are always above the critical value, all grains become entrained in the flow as the intermittent, collective motions of grains gives way to continuous transport [*Iseya and Ikeda*, 1987; *Kuhnle and Southard*, 1988; *Ancey et al.*, 2008; *Strom et al.*, 2004]. While this effect has been documented qualitatively by previous authors, our results quantify these changes in the statistics of sediment fluctuations with bed shear stress.

[44] Bed elevation also became smoother with increasing transport, meaning that the magnitude of high-frequency fluctuations at small scales was reduced overall. At low-flow conditions, topographic fluctuations were of the order of the grain scale (Figure 3), supporting the idea that grain-grain interactions (and perhaps longitudinal grain size sorting) dominated transport fluctuations as described above. With increasing bed stress, and presumably full mobility of all grains in transport based on Shields stress calculations, the bed organized into large-scale bed forms (Figure 4). Data indicate that higher-frequency (smaller-scale) topography, likely representing clusters of grains, became less prevalent at higher flows where bed topography was dominated by dune forms. Interestingly, although the bed became smoother overall from low to high discharge, intermittency increased. In other words, high small-scale

frequency fluctuations in bed topography became less prevalent overall, but also less uniformly distributed. This may be due to irregular clusters of grains superimposed on larger scale, more regular dune features. However, observations of grains on the bed were not made and so these ideas remain speculative at this stage. Our experiments highlight the need to simultaneously document bed topography, bed load transport rates and individual particle motions (e.g., as those of *Schmeeckle et al.* [2001], *Papanicolaou et al.* [2002], and *Ancey et al.* [2006]) in order to further our understanding of what contributes to transport fluctuations at the smallest to largest scales.

[45] The scaling ranges of both transport rates and bed elevation series are similar with a leveling off, or saturation, at approximately the same time scales, indicating that fluctuations in transport are intimately related to bed topography. While the nature of these dependencies is still unclear, a practical result may be obtained. The scale-dependent nature of transport (within 1 and 10 min in this study) means that measured rates at different time intervals are not directly comparable. In our experiments, both transport and bed elevation exhibit no time dependence when measured over intervals greater than 10 to 15 min. In other words, if we measure for a period of time that is larger than the time scale associated with the migration of the largest topographic feature, we can obtain mean values for bed topography and transport rate that have no time dependence [*Fienberg et al.*, 2008]. From a practical point of view, this is the mean transport rate one should try to obtain in the field. Measurements of bed topography from a river could be used to determine the upper scaling limit of fluctuations, which determines the time scale over which one should deploy a sampler to obtain a representative "mean" bed load transport value. As discussed by *Fienberg et al.* [2008], this approach is possible in flumes and small streams where the time scale is of the order of tens of minutes. Since the size of bed forms scales with river depth, however, this approach quickly becomes impractical as river size increases: deployment of bed load samplers for long durations can result in overfilling and clogging [e.g., *Bunte and Abt*, 2005], or integrating over changing flow conditions. In this case, determining the scale-dependent nature of transport rate becomes critical.

6. Conclusions

[46] In this paper we introduce a formalism, typically used in turbulence studies, to quantify two properties in sediment transport and concurrent bed elevation series: the "average roughness" of the series (depicting the average strength of local abrupt fluctuations in the signal) and the "intermittency" (depicting the temporal heterogeneity of fluctuations of different strength). In the bed load sediment transport rates, we documented the presence of a rougher and more intermittent behavior at low-transport conditions (dimensionless bed shear stress of about twice the critical value) transiting to a smoother and less intermittent behavior at high-transport conditions (dimensionless shear stress of about five times the critical value).

[47] Apart from simply quantifying roughness and intermittency of the sediment transport rates, the results of our analysis provide a framework for quantifying how the

probability distribution of sediment transport rates changes with sampling interval and thus have important practical implications. (It is interesting to note that the change of pdf with scale is parameterized in terms of the roughness and intermittency parameters which characterize the burstiness of the series.) Specifically, our analysis demonstrated that the statistics of bed load sediment transport rates depend strongly on scale (sampling interval) and this dependence varies with the discharge conditions. Our results agree with the field observations reported by *Bunte and Abt* [2005] for mean bed load rates and call for a more systematic study to precisely quantify this scale dependence in terms of grain size sorting and bed shear stress. It is noted that the theoretical framework we propose here offers the ability to go beyond the mean and compare the whole probability density function, including extreme values or quantiles, at different scales. This is important for example when the pdf of sediment transport rates has been estimated from data at one particular sampling interval and an extreme exceedance quantile (say, relevant to an ecological smaller-scale functional disturbance) needs to be estimated. Our methodology can bridge this gap in scales and also provide a framework with which comparison of sediment rates sampled with different instruments can be made.

[48] A problem of continuous interest in the literature is the relation of microscale (particle-scale) dynamics to the macroscale behavior of sediment transport [e.g., *Drake et al.*, 1988; *Papanicolaou et al.*, 2002; *Schmeeckle et al.*, 2001; *Schmeeckle and Nelson*, 2003; *Ancey et al.*, 2006, 2008]. Although not precisely quantified in this paper, it is worth noting that the multiscale statistical behavior of sediment transport rates (as quantified here via the signal roughness and intermittency) seems consistent with known particle-scale dynamics. For example, at low flows, a rougher but more temporally homogeneous (less intermittent) bed elevation series was documented, indicative of the dominance of high-frequency localized grain clusters; this bed microtopography apparently gave rise to sediment transport rates that are almost of equal roughness but are more inhomogeneous in time (more intermittent) (see Figure 8). This might be due to the collective motion of grains responding to local bed stress fluctuating above and below the critical value. It appears that as bed stress increased, grain patches became less prevalent and more irregular (roughness in bed elevations decreased but intermittency increased) as the bed organized into large-scale dunes, and bed load transport became smoother and more homogeneous in time as entrainment of all grains commenced. This speaks for the collective or cooperative behavior of particle movement that has different dynamics at low and high flows and depends on the presence or absence of self-formed structures on the bed [e.g., *Drake et al.*, 1988; *Ancey et al.*, 2008].

[49] We see our study as a first step in the direction of understanding the scale dependency of sediment transport rates over the continuum of flow discharge conditions and grain size distributions and relating the statistics of bed elevations to the statistics of bed load sediment transport. More controlled experiments have to be performed and analyzed with different particle sizes (from a single particle size to a broad particle size distribution and for gravel and sand beds) and a spectrum of discharge rates, to fully characterize the intermittency of bed load sediment trans-

port rates and how it relates to that of the bed elevation fluctuations, and (eventually) to particle size dynamics. Also, the documented statistical structure of sediment transport rates can be seen as providing an additional model diagnostic that mechanistic models should be able to reproduce, and as such, it is interesting to ask as to whether any known sediment transport model can reproduce the multiscaling characteristics reported in this study.

References

Aberle, J., and V. Nikora (2006), Statistical properties of armored gravel bed surfaces, *Water Resour. Res.*, *42*, W11414, doi:10.1029/2005WR004674.

Ancey, C., T. Böhm, M. Jodeau, and P. Frey (2006), Statistical description of sediment transport experiments, *Phys. Rev. E*, *74*(1), 011302, doi:10.1103/PhysRevE.74.011302.

Ancey, C., A. C. Davidson, T. Böhm, M. Jodeau, and P. Frey (2008), Entrainment and motion of coarse particles in a shallow water stream down a steep slope, *J. Fluid Mech.*, *595*, 83–114, doi:10.1017/S0022112007008774.

Arneodo, A., E. Bacry, and J. F. Muzy (1995), The thermodynamics of fractals revisited with wavelets, *Physica A*, *213*, 232–275, doi:10.1016/0378-4371(94)00163-N.

Arneodo, A., J. F. Muzy, and S. G. Roux (1997), Experimental analysis of self-similarity and random cascade processes: Application to fully developed turbulence data, *J. Phys. II*, *7*(2), 363–370, doi:10.1051/jp2:1997130.

Arneodo, A., N. Decoster, and S. G. Roux (1999a), Intermittency, lognormal statistics, and multifractal cascade process in high-resolution satellite images of cloud structure, *Phys. Rev. Lett.*, *83*(6), 1255–1258, doi:10.1103/PhysRevLett.83.1255.

Arneodo, A., S. Manneville, J. F. Muzy, and S. G. Roux (1999b), Revealing a lognormal cascading process in turbulent velocity statistics with wavelet analysis, *Philos. Trans. R. Soc., Ser. A*, *357*(1760), 2415–2438.

Bunte, K., and S. R. Abt (2005), Effect of sampling time on measured gravel bed load transport rates in a coarse-bedded stream, *Water Resour. Res.*, *41*, W11405, doi:10.1029/2004WR003880.

Castaing, B., Y. Gagne, and E. J. Hopfinger (1990), Velocity probability density-functions of high Reynolds-number turbulence, *Physica D*, *46*, 177–200, doi:10.1016/0167-2789(90)90035-N.

Cudden, J. R., and T. B. Hoey (2003), The causes of bedload pulses in a gravel channel: The implications of bedload grain-size distributions, *Earth Surf. Processes Landforms*, *28*, 1411–1428, doi:10.1002/esp.521.

Delour, J., J. Muzy, and A. Arneodo (2001), Intermittency of 1D velocity spatial profiles in turbulence: A magnitude cumulant analysis, *Eur. Phys. J. B*, *23*, 243–248, doi:10.1007/s100510170074.

Dinehart, R. L. (1992), Evolution of coarse gravel bed forms: Field measurements at flood stage, *Water Resour. Res.*, *28*(10), 2667–2689, doi:10.1029/92WR01357.

Drake, T., R. Shreve, W. Dietrich, P. Whiting, and L. Leopold (1988), Bedload transport of fine gravel observed by motion-picture photography, *J. Fluid Mech.*, *192*, 193–217, doi:10.1017/S0022112088001831.

Fienberg, K., A. Singh, D. Jerolmack, J. Marr, and E. Foufoula-Georgiou (2008), A theoretical framework for interpreting and quantifying the sampling time dependence of gravel bedload transport rates, paper presented at Bedload Research International Cooperative Meeting, Minneapolis, Minn., 11–14 April.

Foufoula-Georgiou, E., and V. Sapozhnikov (1998), Anisotropic scaling in braided rivers: An integrated theoretical framework and results from application to an experimental river, *Water Resour. Res.*, *34*(4), 863–867, doi:10.1029/98WR00216.

Frey, P., C. Ducottet, and J. Jay (2003), Fluctuations of bed load solid discharge and grain size distribution on steep slopes with image analysis, *Exp. Fluids*, *35*, 589–597, doi:10.1007/s00348-003-0707-9.

Frisch, U. (1995), *Turbulence: The Legacy of A. N. Kolmogorov*, Cambridge Univ. Press, New York.

Gangodagamage, C., E. Barnes, and E. Foufoula-Georgiou (2007), Scaling in river corridor widths depicts organization in valley morphology, *J. Geomorphol.*, *91*, 198–215, doi:10.1016/j.geomorph.2007.04.014.

Gomez, B., R. L. Naff, and D. W. Hubbell (1989), Temporal variation in bedload transport rates associated with the migration of bedforms, *Earth Surf. Processes Landforms*, *14*, 135–156, doi:10.1002/esp.3290140205.

Gupta, V., and E. Waymire (1996), Multiplicative cascades and spatial variability in rainfall, river networks, and floods, in *Reduction and Predictability of Natural Disasters*, *Proc. Vol. Santa Fe Inst. Stud. Sci. Complexity*, vol. 25, edited by J. B. Rundle, D. L. Turcotte, and W. Klein, Addison-Wesley, Boston, Mass.

Iseya, F., and H. Ikeda (1987), Pulsations in bedload transport rates induced by a longitudinal sediment sorting: A flume study using sand and gravel mixtures, *Geogr. Ann., Ser. A*, *69*, 15–27, doi:10.2307/521363.

Jaffard, S. (1997), Multifractal formalism for functions, *SIAM J. Math. Anal.*, *28*(4), 944–998, doi:10.1137/S0036141095282991.

Jerolmack, D. J., and D. Mohrig (2005), A unified model for subaqueous bed form dynamics, *Water Resour. Res.*, *41*, W12421, doi:10.1029/2005WR004329.

Jerolmack, D. J., and P. M. Sadler (2007), Transience and persistence in the depositional record of continental margins, *J. Geophys. Res.*, *112*, F03S13, doi:10.1029/2006JF000555.

Kuhnle, R. A., and J. B. Southard (1988), Bed load fluctuations in a gravel bed laboratory channel, *Water Resour. Res.*, *24*(2), 247–260, doi:10.1029/WR024i002p00247.

Kumar, P., and E. Foufoula-Georgiou (1997), Wavelet analysis for geophysical applications, *Rev. Geophys.*, *35*(4), 385–412, doi:10.1029/97RG00427.

Lashermes, B., and E. Foufoula-Georgiou (2007), Area and width functions of river networks: New results on multifractal properties, *Water Resour. Res.*, *43*, W09405, doi:10.1029/2006WR005329.

Lashermes, B., E. Foufoula-Georgiou, and W. E. Dietrich (2007), Channel network extraction from high resolution topography data using wavelets, *Geophys. Res. Lett.*, *34*, L23S04, doi:10.1029/2007GL031140.

Lovejoy, S., and D. Schertzer (1985), Generalized scale invariance and fractal models of rain, *Water Resour. Res.*, *21*(8), 1233–1250, doi:10.1029/WR021i008p01233.

Lovejoy, S., D. Schertzer, P. Silas, Y. Tessier, and D. Lavallée (1993), The unified scaling model of atmospheric dynamics and systematic analysis in cloud radiances, *Ann. Geophys.*, *11*, 119–127.

Mallat, S. (1998), *A Wavelet Tour in Signal Processing*, Academic, San Diego, Calif.

Marani, M., A. Rinaldo, R. Rigon, and I. Rodríguez-Iturbe (1994), Geomorphological width functions and the random cascade, *Geophys. Res. Lett.*, *21*, 2123–2126, doi:10.1029/94GL01933.

Meyer-Peter, E., and R. Müller (1948), Formulas for bed-load transport, paper presented at 2nd Congress, Int. Assoc. of Hydraul. Res., Stockholm.

Muzy, J. F., E. Bacry, and A. Arneodo (1994), The multifractal formalism revisited with wavelets, *Int. J. Bifurcat. Chaos*, *4*, 245–302, doi:10.1142/S0218127494000204.

Nikora, V., and D. M. Hicks (1997), Scaling relationships for sand wave development in unidirectional flows, *J. Hydraul. Eng.*, *123*, 1152–1156, doi:10.1061/(ASCE)0733-9429(1997)123:12(1152).

Nikora, V., and J. Walsh (2004), Water-worked gravel surfaces: High-order structure functions at the particle scale, *Water Resour. Res.*, *40*, W12601, doi:10.1029/2004WR003346.

Nikora, V., A. N. Sukhodolov, and P. M. Rowinski (1997), Statistical sand wave dynamics in one-directional water flows, *J. Fluid Mech.*, *351*, 17–39, doi:10.1017/S0022112097006708.

Nikora, V., H. Habersack, T. Huber, and I. McEwan (2002), On bed particle diffusion in gravel bed flows under weak bed load transport, *Water Resour. Res.*, *38*(6), 1081, doi:10.1029/2001WR000513.

Papanicolaou, A., P. Diplas, N. Evangelopoulos, and S. Fotopoulos (2002), Stochastic incipient motion criterion for spheres under various bed packing conditions, *J. Hydraul. Eng.*, *128*, 369–380, doi:10.1061/(ASCE)0733-9429(2002)128:4(369).

Parisi, G., and U. Frisch (1985), On the singularity structure of fully developed turbulence, in *Turbulence and Predictability in Geophysical Fluid Dynamics*, edited by M. Ghil et al., pp. 84–87, North-Holland, Amsterdam.

Rinaldo, A., I. Rodriguez-Iturbe, R. Rigon, E. Ijjasz-Vasquez, and R. Bras (1993), Self-organized fractal river networks, *Phys. Rev. Lett.*, *70*, 822–825, doi:10.1103/PhysRevLett.70.822.

Sadler, P. M. (1981), Sediment accumulation and the completeness of stratigraphic sections, *J. Geol.*, *89*, 569–584.

Sadler, P. M. (1999), The influence of hiatuses on sediment accumulation rates, *GeoRes. Forum*, *5*, 15–40.

Schmeeckle, M. W., and J. M. Nelson (2003), Direct numerical simulation of bedload transport using a local, dynamic boundary condition, *Sedimentology*, *50*(2), 279–301, doi:10.1046/j.1365-3091.2003.00555.x.

Schmeeckle, M. W., J. M. Nelson, J. Pitlick, and J. P. Bennett (2001), Interparticle collision of natural sediment grains in water, *Water Resour. Res.*, *37*(9), 2377–2391, doi:10.1029/2001WR000531.

Schroeder, M. (1991), *Fractals, Chaos, Power Laws: Minutes from an Infinite Paradise*, W. H. Freeman, New York.

Strom, K., A. N. Papanicolaou, N. Evangelopoulos, and M. Odeh (2004), Microforms in gravel bed rivers: Formation, disintegration, and effects on bedload transport, *J. Hydraul. Eng.*, *130*, 554–567, doi:10.1061/(ASCE)0733-9429(2004)130:6(554).

Sumer, B. M., L. H. C. Chua, N. S. Cheng, and J. Fredsoe (2003), Influence of turbulence on bed load sediment transport, *J. Hydraul. Eng.*, *129*, 585–596, doi:10.1061/(ASCE)0733-9429(2003)129:8(585).

Turcotte, D. L. (1997), *Fractals and Chaos in Geology and Geophysics*, 2nd ed., Cambridge Univ. Press, New York.

Venugopal, V., S. G. Roux, E. Foufoula-Georgiou, and A. Arneodo (2006a), Revisiting multifractality of high-resolution temporal rainfall using a wavelet-based formalism, *Water Resour. Res.*, *42*, W06D14, doi:10.1029/2005WR004489.

Venugopal, V., S. G. Roux, E. Foufoula-Georgiou, and A. Arneodo (2006b), Scaling behavior of high resolution temporal rainfall: New insights from a wavelet-based cumulant analysis, *Phys. Lett. A*, *348*, 335–345, doi:10.1016/j.physleta.2005.08.064.

Wilcock, P. R., C. H. Orr, and J. D. G. Marr (2008), The need for full-scale experiments in river science, *Eos Trans. AGU*, *89*(1), doi:10.1029/2008EO010003.

Yarnell, S. M., J. F. Mount, and E. W. Larsen (2006), The Influence of relative sediment supply on riverine habitat heterogeneity, *Geomorphology*, *80*, 310–324, doi:10.1016/j.geomorph.2006.03.005.

———————————

K. Fienberg, E. Foufoula-Georgiou, J. Marr, and A. Singh, St. Anthony Falls Laboratory, University of Minnesota-Twin Cities, 2 Third Avenue SE, Minneapolis, MN 55414, USA. (efi@umn.edu)

D. J. Jerolmack, Department of Earth and Environmental Science, University of Pennsylvania, Hayden Hall, 240 S. 33rd Street, Philadelphia, PA 19104, USA.

Nonlinearity and complexity in gravel bed dynamics

Arvind Singh · Stefano Lanzoni · Efi Foufoula-Georgiou

Abstract The dynamics of river bed evolution are known to be notoriously complex affected by near-bed turbulence, the collective motion of clusters of particles of different sizes, and the formation of bedforms and other large-scale features. In this paper, we present the results of a study aiming to quantify the inherent nonlinearity and complexity in gravel bed dynamics. The data analyzed are bed elevation fluctuations collected via submersible sonar transducers at 0.1 Hz frequency in two different settings of low and high discharge in a controlled laboratory experiment. We employed surrogate series analysis and the transportation distance metric in the phase-space to test for nonlinearity and the finite size Lyapunov exponent (FSLE) methodology to test for complexity. Our analysis documents linearity and underlying dynamics similar to that of deterministic diffusion for bed elevations at low discharge conditions. These dynamics transit to a pronounced nonlinearity and more complexity for high discharge, akin to that of a multiplicative cascading process used to characterize fully developed turbulence. Knowing the degree of nonlinearity and complexity in the temporal dynamics of bed elevation fluctuations can provide insight into model formulation and also into the feedbacks between near-bed turbulence, sediment transport and bedform development.

Keywords Nonlinearity · Complexity · Bedforms · Finite size Lyapunov exponent (FSLE) · Diffusion

1 Introduction

The evolution of alluvial river beds is the result of a number of often strongly nonlinear processes which give rise to the extraordinary large variety of patterns observed in nature. In gravel bed rivers, where the dominant form of sediment transport is bedload, both field observations (Drake et al. 1988) and laboratory experiments (Kirkbride 1993; Nelson et al. 1995) suggest that most of the transport occurs by the collective motion of clusters of particles mobilized by turbulent sweep events and outward interactions, while a relatively smaller contribution is associated with bursts (see also review of Best 1993). Clearly, the bed evolution is likely to be strongly affected by the intermittent process whereby coherent turbulent structures are randomly generated, grow and decay in the near-wall region.

Coherent structure dynamics, in turn, depend on the range of scales characterizing a given bed topography, and the flow variability at a given point contains both locally derived flow structures and structures inherited from upstream (Hardy et al. 2007). The bed evolution is further complicated by the formation of either free bedforms (e.g., Gomez et al. 1989), arising as a result of the instability of a cohesionless bed subject to a turbulent flow, or bedforms forced by geometrical constraints (e.g., channel curvature) (Seminara 1998). Finally, the heterogeneous character of the sediment leads to patterns associated with a spatial and

A. Singh (✉) · E. Foufoula-Georgiou
St. Anthony Falls Laboratory and National Center
for Earth-Surface Dynamics, Department of Civil Engineering,
University of Minnesota, 2 Third Avenue SE,
Minneapolis, MN, USA
e-mail: sing0336@umn.edu

E. Foufoula-Georgiou
e-mail: efi@umn.edu

S. Lanzoni
Dipartimento di Ingegneria Idraulica, Marittima, Ambientale e
Geotecnica, and International Center for Hydrology
''Dino Tonini'', Università di Padova, Padua, Italy
e-mail: lanzo@idra.unipd.it

temporal rearrangement of the grain size distribution of the sediments (Parker 1991) which are strongly related to the different mobility of particles having different diameter (Wilcock and McArdell 1993, 1997).

It then clearly appears that river bed evolution, even in the simplest case of a flat bed configuration, is an extremely complex phenomenon whose understanding needs the use of refined theoretical, experimental and data analysis techniques.

Several contributions have been so far devoted to the study of the spatial properties of water-worked gravel bed surfaces measured both in the laboratory and in the field (e.g., see Nikora and Walsh 2004, and references therein). In addition to conventional statistical parameters (i.e., standard deviation, skewness and kurtosis) of the bed elevation spatial distribution, second-order and higher-order structure functions have been proved particularly helpful for exploring the statistical properties and potential multiscaling behavior of bed elevations fields (Aberle and Nikora 2006). In a recent study, the multiscale statistical structure of the temporal evolution of bed elevation fluctuations at several locations on the evolving gravel bed under steady-state conditions has also been analyzed and the presence of a multiscaling behavior has been reported (Singh et al. 2008).

In the present contribution, a different type of analysis of temporal elevation series is performed aiming at quantifying the nonlinearity and complexity in gravel bed dynamics. It is noted that these dynamics are internally generated by the system itself rather than by an external stochastic forcing, since the discharge is kept constant and the system is under steady state conditions. To the best of our knowledge, the only other study that attempted a similar analysis is that of Gomez and Phillips (1999) who analyzed sediment transport rates (interestingly collected from a controlled laboratory experiment conducted in the same flume almost 20 years ago; see Hubbell et al. 1987). The overall goal of that study was to identify deterministic sources of uncertainty, or unexplained variation, in the time series of bedload transport rates by computing how much of the observed variability (quantified in terms of Kolmogorov entropy) was not explained by bedform migration effects. The assumption was made that the variability (entropy) due to bed migration would be fully captured by a Hamamori probability distribution. It is noted that the Hamamori distribution is derived from sediment movement over a purely geometrical self-similar bed morphology (Hamamori 1962) and does not account for the natural variability in bedform shapes and sizes. It is also restricted to sediment transport rates that are at most four times the mean rate—not the case in most observed series including the series analyzed in Gomez and Phillips (1999).

The purpose of the present study is to revisit the problem of quantifying the deterministic complexity in gravel bed dynamics with an assumption-free methodology and using more powerful techniques recently developed in the study of nonlinear systems (e.g., Aurell et al. 1997). The adopted methodologies have been proven to give a deep insight in other complex geophysical processes such as fluid turbulence (Aurell et al. 1996a; Boffetta et al. 2002), atmospheric boundary layer dynamics (Basu et al. 2002) and dispersive mixing in porous media (Kleinfelter et al. 2005), among others.

The paper is organized as follows. In Sect. 2 we briefly describe the bed elevation data collected in two laboratory experiments under low and high discharge conditions. Section 3 introduces the mathematical methodology used first to identify the presence or absence of inherent nonlinearity in time series and second the finite size Lyapunov exponent (FSLE) methodology to quantify the complexity and predictability of processes exhibiting many scales of motion. In Sect. 4, results of the analysis of the temporal sequences of bed elevation data series are presented. Finally, Sect. 5 presents concluding remarks and suggestions for future research.

2 Experimental data

The data examined in the present contribution were collected during a series of experiments conducted in the Main Channel facility at the St. Anthony Falls Laboratory, University of Minnesota. The channel is 2.74-m wide and has a maximum depth of 1.8 m. It is a partial-recirculating flume in that it has the ability to recirculate the sediment while the water flows through the flume without recirculation. Water for the channel was drawn directly from the Mississippi River, with a maximum discharge capacity of 8,000 l/s. The channel has a 55-m long test section and, in the experiments reported here, a poorly sorted gravel bed extended over the last 20 m of this test section. The gravel used in these experiments had a broad particle size distribution characterized by $d_{50} = 11.3$ mm, $d_{16} = 4.27$ mm and $d_{84} = 23.07$ mm. More details on this experimental setting can be found in Singh et al. (2008).

Measurements of bed elevation and sediment transport were taken at a range of discharges corresponding to different bed shear stresses. Here we focus our attention on the series of bed elevations collected under two different discharges: a low discharge case, with a discharge of 4,300 l/s, corresponding to a dimensionless bed stress of about twice the critical value (Shields stress = 0.085 using median diameter) and a high discharge, 5,500 l/s, corresponding to a Shields stress about five times the critical value (Shields stress = 0.196). For both bed stress

conditions, the flume was allowed to run long enough prior to data collection such that a dynamic equilibrium was achieved in transport and slope adjustment of the water surface and bed. Determination of the dynamic equilibrium state was made by checking that the 60-min average sediment flux was stabilized to an almost constant value during the flume run. The bed elevation was then recorded over a span of approximately 20 h for each experiment, by using submersible sonar transducers, with a frequency of 0.1 Hz and a vertical precision of ~ 1 mm. Figure 1 displays the time series of bed elevations measured at a location aligned with the main channel axis for both the low (Fig. 1a) and the high (Fig. 1c) discharge conditions over a period of 10 h during which the bed-elevation and sediment flux series were stationary. The low bed stress run (Fig. 1a) produced a nearly plane channel bed, with only limited topographic variations, i.e. without obvious large scale structures in the bed elevation (the standard deviation in the bed is 10.06 mm, compared to the initial d_{50} grain size of 11.3 mm). On the contrary, the higher stress run (Fig. 1c) generated substantial bed variability at large scale in the form of dunes, with intermediate to particle-scale fluctuations superimposed on these larger-scale features. In this study we focus on comparing these two runs in terms of the complexity of the underlying forming processes imprinted in the time series of bed elevation fluctuations. The analysis methodologies we employed are briefly described below.
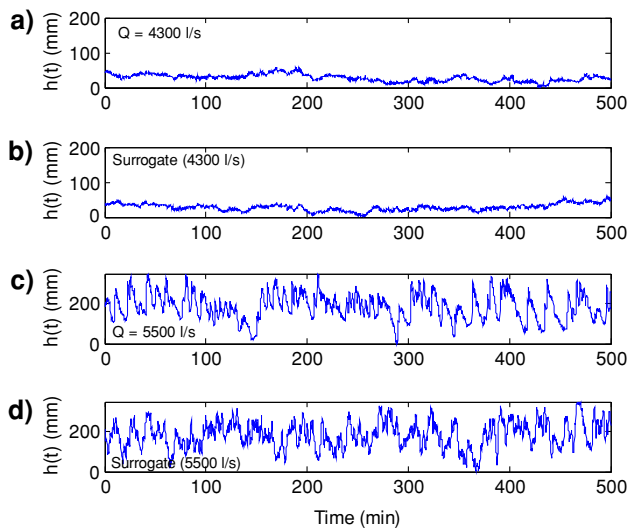
Fig. 1 Bed elevation time series for **a** low discharge (4,300 l/s; bed elevation mean is 27.38 mm and standard deviation 10.06 mm) and **c** high discharge (5,500 l/s; bed elevation mean is 185.51 mm and standard deviation 66.61 mm). Surrogate series for **b** low and **d** high discharge. Notice that although it is difficult to distinguish any difference between the original and the surrogate series, the surrogate series in high discharge has linear underlying dynamics while the original series is shown to be highly nonlinear (see Fig. 2)

3 Analysis methodologies

3.1 Test for nonlinearity

Nonlinearity is a necessary condition for deterministic chaos and thus methodologies for testing whether a time series has been generated by a linear or inherently nonlinear process have gained considerable attention in the literature. By inherent nonlinear process it is meant a process whose nonlinearity is not external, i.e., the result of a static nonlinear transformation applied on an otherwise linear underlying process, but it is weaved into its dynamics such as for example in a series arising as a result of a multiplicative cascade generator, a popular phenomenological model for turbulence (e.g., Frisch 1995). Detection of nonlinearity is not a trivial task and several methods are available, as for example based on "reversibility", information-theoretic approaches, singular value decomposition, and the use of "surrogates" (e.g., see a review in Basu and Foufoula-Georgiou 2002 and references therein). Here we adopt a surrogate-based methodology. Surrogate series maintain the probability density function (pdf) and correlation structure (and thus spectrum) of the original series but destroy any inherent nonlinearity since the process of generating the surrogates randomizes the phases in the Fourier space.

The method we used for surrogate series generation is the iterative amplitude adjusted Fourier transform (IAAFT) method of Schreiber and Schmitz (1996). This method is an improvement of the earlier amplitude adjusted Fourier transform (AAFT) method of Theiler et al. (1992), and iteratively adjusts both the pdf and linear correlation structure to minimize their deviation from the original series. The reader is referred to the original publications for details to supplement the brief exposition presented below.

The surrogate series $\{s_n\}$ is assumed to be generated by a process of the form

$$s_n = S(y_n), \quad y_n = \sum_{i=1}^{M} a_i y_{n-1} + \sum_{i=1}^{N} b_i \eta_{n-1}, \quad (1)$$

where S could be any invertible nonlinear function, $\{y_n\}$ is the underlying linear process, $\{a_n\}$ and $\{b_n\}$ are constants, and $\{\eta_n\}$ is Gaussian white noise. The steps involved in the generation of surrogate series are as follows:

1. Randomly shuffle the data points of the original series $\{x_n^o\}$ to destroy any correlation or nonlinear relationship, while keeping the pdf unchanged. The reshuffled series is the starting point for the iteration $\{s_n^{(o)}\}$.

2. Construct the discrete Fourier transform of the series at the ith iteration $\{s_n^{(i)}\}$, and adjust the amplitudes to recreate the power spectrum of the original data. Keep the phases unchanged. Perform inverse Fourier transform.

3. The pdf will no longer be correct. Transform the data to the correct pdf by rank ordering and replacing each value with the value in the original series $\{x_n^o\}$ with the same rank. This will result in an updated series $\left\{s_n^{(i+1)}\right\}$.

4. Repeat steps 2 and 3 until discrepancy in the power spectrum is below a threshold, or the sequence stops changing (reaches a fixed point). In this manner a surrogate data series can be generated with an identical pdf and optimally similar power spectrum to the original series.

Figure 1b and 1d shows two realizations of the surrogate series corresponding to the bed elevation series for low and high flow discharge. It is noted that in both cases it is difficult to distinguish visually any difference between the original series and their surrogates (compare Fig. 1a to 1b and 1c to 1d. It is reminded that the original and surrogate series share the same pdf and correlation structure or spectrum, but the surrogate series contain only linear correlation). However, as it will be demonstrated later, our methodologies depict important differences in the case of high discharge, emphasizing the presence of inherent nonlinearity in the bed forming process.

Once an ensemble of surrogate series is generated, a probabilistic metric of the "distance" between each one of those series to the original series $\{x_n^o\}$ and between multiple realizations of the surrogate series $\{s_n\} = \{x_n^i\}, i = 1, \ldots, N_s$ is formed. If the original series were linear, these two distance metrics would overlap as one would not be able to discriminate the original series from members of the ensemble of surrogates; however, if they do not overlap, nonlinearity in the original series can be inferred with confidence.

Following Basu and Foufoula-Georgiou (2002), we use the transportation distance functions $d_{oi} = d(x_n^o, x_n^i)$ and $d_{ij} = d(x_n^i, x_n^j), (i \neq j)$ to measure, respectively, the difference in the long term behavior between the original data set and the ith surrogate data set and the mutual distances between surrogates. The idea is to transform two given scalar time series (x, y) in vector time series (X, Y) by phase-space reconstruction using an embedding dimension (e) and an integer delay (τ), thus obtaining an e-dimensional embedding space $\mathcal{R}^e$ which captures the dynamics of the x and y systems' attractors (Moeckel and Murray 1997). The details of determining embedding dimension and delay can be found in Kennel et al. (1992), Hegger et al. (1999). In practice, a box in the reconstructed phase space, $\mathcal{R}^e$, containing both the X and Y vector time series is divided into a finite number $B_k, k = 1, \ldots, b$ of sub boxes, each characterized by the discretized probability measures p_k and q_k defined as

$$p_k = \sum_{l=1}^{b} \mu_{kl}, \quad q_k = \sum_{l=1}^{b} \mu_{kl}, \quad l = 1, \ldots, b \quad (2)$$

where $\mu_{kl} \geq 0$ defines the amount of "material" (information) shipped from box B_k to box B_l. These constraints ensure that the initial and final probability distributions are preserved and allow us to determine the set $M(p, q)$ [with $p = (p_1, \ldots, p_b)$ and $q = (q_1, \ldots, q_b)$] of all transportation plans. The transportation function is then obtained by minimizing (e.g., through the network simplex algorithm) the transportation cost

$$d(p, q) = \inf_{\mu \in M(p,q)} \sum_{k,l=1}^{b} \mu_{kl} \delta_{kl} \quad (3)$$

where δ_{kl} is the taxi cab metric (Moeckel and Murray 1997) normalized to the embedding dimension between the centres of B_k and B_l. If the pdf of the transportation distances d_{oi} between the original series and the surrogates is distinct from the pdf of the mutual distances d_{ij} between the surrogates, nonlinearity is inferred. Details of the methodology and examples of its application to known linear and nonlinear series, e.g., autoregressive series, Lorenz series, stochastic Van der Pol oscillator series, and the Santa Fe Institute competition series, can be found in Basu and Foufoula-Georgiou (2002).

3.2 Quantification of complexity

It is well known that many natural systems, although deterministic, are characterized by a limited degree of predictability owing to the presence of deterministic chaos which makes small errors in the initial conditions to grow exponentially fast with time (e.g., Lorenz 1969). In the traditional sense, predictability is assessed via computation of the maximum Lyapunov exponent which dictates that the predictability time is

$$T_p \approx \frac{1}{\lambda_{\max}} \ln \frac{\Delta}{\delta} \quad (4)$$

where $\lambda_{\max}$ is the leading (or maximum) Lyapunov exponent, measuring the average exponential rate of separation of nearby trajectories, δ is the size of the initial (strictly infinitesimal) perturbation, and Δ is the (still small) accepted error tolerance. The above formula holds only for infinitesimal perturbations, and, by construction, it cannot assess the predictability in systems with many scales of variability, such as turbulence which possesses a hierarchy of eddy turnover times. In those multiscale systems the predictability time T_p is determined by the nonlinear mechanism responsible for the error growth and it is not captured by $\lambda_{\max}$ which is governed by the linearized equations of motion, given the assumption of

small perturbations. To address these issues, Aurell et al. (1996b) proposed a generalization of the maximum Lyapunov exponent method. Specifically, they introduced the quantity $T_p(\delta, \Delta)$ which is the time it takes for a finite perturbation to grow from an initial size δ (in general not infinitesimal) to a tolerance level Δ. The so-called finite size Lyapounov exponent (FSLE) $\lambda(\delta, \Delta)$ is then the average of some function of this predictability time, such that if both δ and Δ are infinitesimally small one would recover the usual Lyapunov exponent:

$$\lambda(\delta, \Delta) = \left\langle \frac{1}{T_p(\delta, \Delta)} \right\rangle \ln\left(\frac{\Delta}{\delta}\right). \tag{5}$$

Various methodologies are available for computing finite-size Lyapunov exponent (see Aurell et al. 1997). In the present contribution we have adopted the method of Boffetta et al. (1998).

4 Results and discussion

4.1 Nonlinearity

The results of nonlinearity tests carried out on the two time series of bed elevations are reported in Fig. 2. For low discharge conditions (Fig. 2a), the pdf of the transportation distance between the original series and the surrogates overlaps the one obtained by considering multiple realizations of the surrogates. On the other hand, Fig. 2b shows that for the high discharge case the pdfs of the transportation distance between each surrogate series and the original time series and between multiple realizations of surrogates are completely different, suggesting that strong nonlinearities are inherent in the processes which shaped the bed morphodynamics. These nonlinearities are likely to be connected to the irregular and unsteady large-scale bedforms, mainly dunes, observed in this high flow experiment, promoting the formation of patterns of sorting and leading to a strong reworking of the sediment bed (Klaassen 1990; Blom et al. 2003).

To shed light into the above findings, we proceed with the following analysis guided by some recent findings in Singh et al. (2008). We synthetically generated two series with known underlying dynamics: a fractional Brownian motion (fBm) series and a multiplicative cascade series. The fBm series (with the Hurst exponent $H = 0.5$) is known to have linear underlying dynamics, arising from the integration of white noise. A multiplicative cascade series, on the other hand, arises from a nonlinear (multiplicative) mechanism of energy transfer from larger to smaller scales and thus possesses clearly nonlinear underlying dynamics. These latter dynamics cannot be rendered linear by any external transformation but rather are intrinsically embedded in all scales of variability of the process. In this work, we generated multiplicative cascade series using the random wavelet cascade (RWC) model (e.g., Arneodo et al. 1997) parameterized by two coefficients: c_1 and c_2. These two parameters dictate how the energy breaks down from larger to smaller scales, i.e., they characterize the probability distribution of the multiplicative weights of the cascade generator. Here we set $c_1 = 0.7$ and $c_2 = 0.1$ on the basis of the results recently obtained by Singh et al. (2008). This study employed a wavelet-based multifractal formalism and reported that the spectrum of scaling exponents of the same bed elevation fluctuation series analyzed here is well described by a quadratic model with c_1 and c_2 ranging in the intervals 0.53–0.76 and 0.06–0.14, respectively.

For visual comparison, Fig. 3 shows the fluctuations (computed as first order differences) of the original bed elevation series at low discharge (Fig 3a), the generated fBm series with $H = 0.5$ and the same standard deviation as the original series (Fig. 3b), the original bed elevation series at high discharge (Fig. 3c) and the generated RWC series (Fig. 3d) with $c_1 = 0.7$ and $c_2 = 0.1$ It is noted that there is much more "clustering" in the bed elevation series at high discharge than at low discharge which mathematically is depicted by the larger parameter c_2 (0.1 at high discharge vs. 0 at low discharge). More details of this multifractal analysis and interpretation of the parameters c_1 and c_2 can be found in Singh et al. (2008).
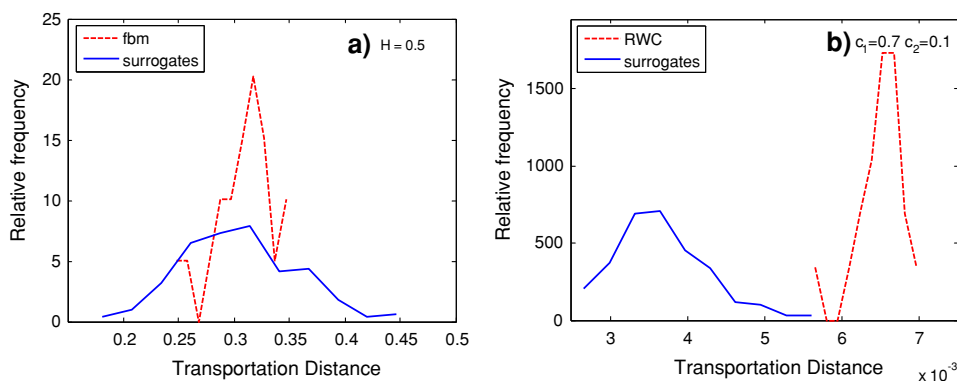

Fig. 2 Probability density function (pdf) of the transportation distances between the original series and the surrogates (*broken lines*), and among the surrogates (*solid lines*) for **a** low discharge, and **b** high discharge runs. Notice the linear underlying dynamics in the case of low discharge (overlapping pdfs) and the nonlinear dynamics in the case of high discharge (distinct pdfs)
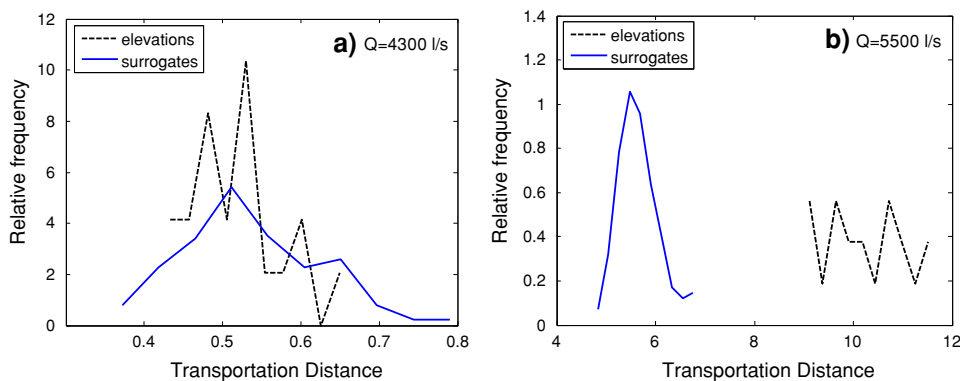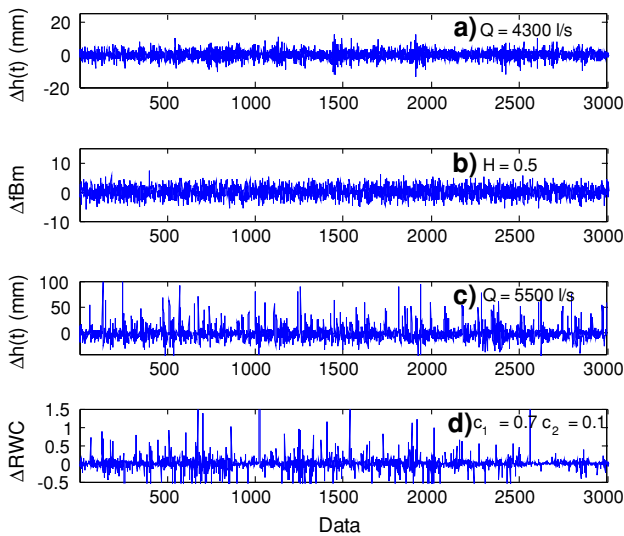
Fig. 3 Fluctuations (first order differences) of **a** measured bed elevation series for low discharge (4,300 l/s), **b** generated fBm series ($H = 0.5$), **c** measured bed elevation series for high discharge (5,500 l/s), and **d** generated random wavelet cascade (RWC) series with parameters $c_1 = 0.7$ and $c_2 = 0.1$

The nonlinearity test described in Sect. 3 was applied to these two generated series. As was expected, the results of the test shown in Fig. 4 correctly depict the inherent linearity of the fBm series and the strong nonlinearity of the RWC series. Comparison of Figs. 2 and 4 gives more confidence to conclude the presence of linear underlying dynamics in gravel bed formation at low discharge conditions which progressively evolve to strongly nonlinear dynamics at high flow conditions (i.e., when the bed shear stress is well above the critical value for incipient motion of sediments). The complexity analysis to follow will shed more light to those conclusions.

4.2 Complexity and predictability

As discussed before, bed elevation fluctuations are known to exhibit multiple scales of variability (e.g., see Nikora and Walsh 2004; Singh et al. 2008) and thus the FSLE approach is a more appropriate methodology for quantifying complexity, than is the standard maximum Lyapunov exponent analysis.

The delay time and embedding dimension adopted in the analysis of the bed elevation series for low and high discharge were chosen to be $d = 10$ and $e = 3$ following the mutual information and false nearest neighbor approaches, respectively (see Kantz and Schreiber 1997), and these algorithms were implemented using the TISEAN package (Hegger et al. 1999). Figure 5a displays the Lyapunov exponent for the two series as a function of the initial perturbation size $\delta = 1$ mm, while Fig. 5b shows the predictability time T_p (in seconds) for the same two series as a function of the prescribed tolerance level Δ ($\Delta = r\delta$, where r is the so-called threshold factor and is assumed to be as $\sqrt{2}$ in this work. (For more details about the threshold factor see Aurell et al. 1997.)

The following observations are worthwhile. First, from Fig. 5b it is observed that the high-discharge bed elevation series is less predictable (more complex) than the series at low-discharge. This is not surprising given the previous results which inferred a pronounced inherent nonlinearity in the high-discharge bed elevation series and simpler linear dynamics for the case of low discharge. It is also interesting to observe that for an initial error of $\delta = 1$ mm (measurement precision) the predictability time associated to a tolerance level of the order of the coarser sediment grain size ($\propto d_{84} = 23.07$ mm) is of the order of 2×10^2 and 4×10^3 seconds for high and low flow condition here examined, an information which can be used to assess the

Fig. 4 a Probability density function (pdf) of the transportation distances between the synthetically generated fractional Brownian motion series (fBm) with $H = 0.5$ and the surrogates (*broken lines*) and among the surrogates (*solid lines*); **b** same but for synthetically generated random wavelet cascade (RWC) series with $c_1 = 0.7$ and

$c_2 = 0.1$. The comparison clearly depicts the expected linearity of the fBm series (overlapping pdfs) and the inherent nonlinearity of the RWC series (distinct pdfs). Notice the similarity with the results of Fig. 2 which displays the same analysis for the original bed elevation series at low and high discharge conditions, respectively
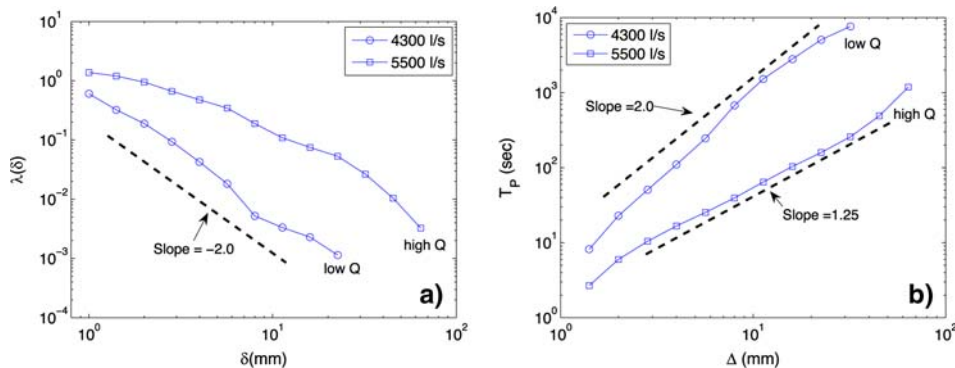
Fig. 5 a Finite size Lyapunov exponent (FSLE) $\lambda(\delta)$ as a function of perturbation δ for bed elevation at low discharge (*circle*) and high discharge (*square*). The line of slope -2 (deterministic diffusive behavior) is also shown; **b** Predictability time T_p, based on FSLE, as a function of prediction error tolerance Δ for bed elevation at low discharge (*circle*) and high discharge (*square*). The initial perturbation was specified to be $\delta = 1$ mm

performance of mechanistic models of sediment transport. Second, from Fig. 5a it is interesting to observe that for larger δ, the FSLE has a slope of -2.0, i.e., $\lambda(\delta) \propto \delta^{-2}$, a behavior consistent with that of deterministic diffusion (e.g., Aurell et al. 1997). To verify this assertion, we generated a series of equal length to the bed elevation series, using the 1D Lagrangian map
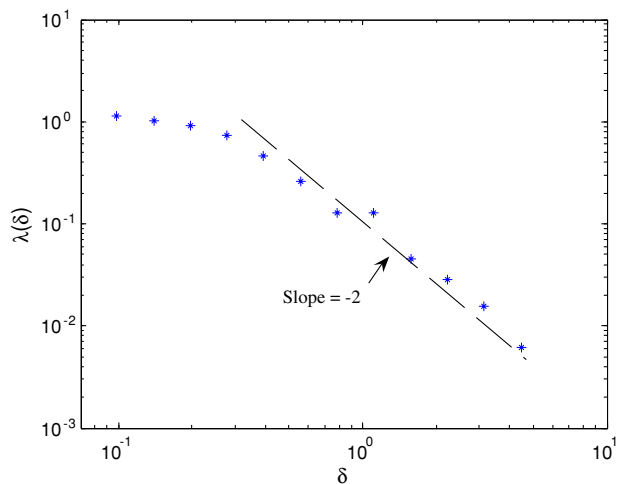
$$x_{n+1} = x_n + a\sin(2\pi x_n) \tag{6}$$

which is a well-known model for deterministic diffusion, and performed the FSLE on this series. Figure 6 shows the theoretically expected behavior of the size-dependent Lyapunov exponent for this series, that is, $\lambda(\delta) \propto$ const for small values of δ, while $\lambda(\delta) \propto \delta^{-2}$ for larger values of δ. The similarity of this behavior to that of Fig. 5a for the low-discharge bed elevation series is worth noting and calls for further exploration.

It is encouraging that for the low-discharge series the linearity inference (Fig. 2a), the similarity to a fBm with $H = 0.5$ (compare Figs. 3a, 3b and 4a to 2a), and the inference that the complexity of this series is similar to that of deterministic diffusion (compare Figs. 5a, 6), are all consistent with each other. It is also encouraging that for the high-discharge elevation series, the presence of strong nonlinearity (Fig. 2b), similar to that of a multiplicative cascade series (Fig. 4b) and the higher complexity (lower predictability) of this series (Fig. 5b), are consistent to each other and also consistent with the multifractal analysis results of this series in Singh et al. (2008). An interesting result is that the predictability time seems to follow a power law relationship with the tolerance level of prediction in both low and high discharge conditions, that is

$$T_p \sim \Delta^\beta \tag{7}$$

where β is approximately 2 for low discharge and 1.25 for high discharge (directly quantifying the lesser degree of

Fig. 6 FSLE for deterministic diffusion generated by the 1D Lagrangian map $x_{n+1} = x_n + a\sin(2\pi x_n)$, with $a = 0.8$, corresponding to a diffusion coefficient $D = 0.18$

predictability of bed elevation series at high discharge). This relationship can be of practical significance (sets the upper limit of prediction) and should also be reproducible by mechanistic models of sediment entrainment and transport.

5 Concluding remarks

The goal of this paper was to gain insight into the complexity of the processes governing the temporal evolution of gravel bed elevation by objectively analyzing data from a controlled experimental setting. Specifically, we analyzed bed elevation series under low and high discharge conditions (i.e., with a bed shear stress slightly higher or significantly higher than the critical value for incipient sediment motion) to quantify the presence of inherent

nonlinearity and the degree of complexity (the higher the complexity the lesser the degree of predictability of the series). We used the phase-space transportation distance metric to quantify the presence of nonlinearity in the series and the finite size Lyapounov exponent (FSLE) methodology to quantify complexity.

Overall, our results indicate that under higher discharge conditions, the presence of bedforms and substantial bed variability at all scales (from grain size to well-formed dunes) leads to bed elevation series whose nonlinearity and complexity are demonstrably more pronounced compared to the bed elevation series under low discharge. For low discharge conditions, in the substantial absence of bedforms, the bed elevation series was found statistically indistinguishable from a series with linear underlying dynamics and also exhibiting a behavior similar to that of deterministic diffusion. Conversely, for high discharge conditions, the temporal evolution of bed elevation was clearly nonlinear and, in fact, it showed a behavior similar to that of a multiplicative cascade process, which is extensively used to model turbulent velocity fluctuations. Given that bedforms are shaped by the near-bed turbulence which is expected to posses nonlinear and multi-scale structure for both low and high discharge, the differences found in the nonlinearity and complexity of bed elevation fluctuations in the two different discharges is interesting and requires further study. They highlight the nontrivial (and mostly unknown) two-way interactions between turbulent flow, sediment transport and bedforms and call for further experiments and analysis under a continuum of discharges and turbulence regimes.

We consider this study as a first step towards a more comprehensive study aimed to: (1) understand the complex multiscale dynamics of bed elevation and the resulting sediment transport series; (2) make inferences about the inherent predictability, or expected upper limit to prediction, by any mechanistic model of sediment transport; and (3) parameterize this complexity in terms of macroscopic flow and sediment properties (e.g., mean bed shear stress, grain size distribution) to provide useful information for physical model development.

References

Aberle J, Nikora V (2006) Statistical properties of armored gravel bed surfaces. Water Resour Res 42:W11414. doi:10.1029/2005WR004674

Arneodo A, Muzy JF, Roux SG (1997) Experimental analysis of self-similarity and random cascade processes: application to fully developed turbulence data. J Phys II 7:363–370

Aurell E, Boffetta G, Crisanti A, Paladin G, Vulpiani A (1996a) Growth of noninfinitesimal perturbations in turbulence. Phys Rev Lett 77:1262–1265

Aurell E, Boffetta G, Crisanti A, Paladin G, Vulpiani A (1996b) Predictability in systems with many characteristic times: the case of turbulence. Phys Rev E 53:2337–2349

Aurell E, Boffetta G, Crisanti A, Paladin G, Vulpiani A (1997) Predictability in the large: an extension of the concept of Lyapunov exponent. J Phys A Math Gen 30:1–26

Basu S, Foufoula-Georgiou E (2002) Detection of nonlinearity and chaoticity in time series using the transportation distance function. Phys Lett A 301:413–423

Basu S, Foufoula-Georgiou E, Porté-Agel F (2002) Predictabilty of atmospheric boundary-layer flow as function of scale. Geophys Res Lett 29:2038. doi:10.1029/2002GL015497

Best JL (1993) On the interactions between turbulent flow structure, sediment transport and bedform development: some considerations from recent experimental research. In: Clifford NJ, French JR, Hardisty J (eds) Turbulence: perspectives on flow and sediment transport. Wiley, NY

Blom A, Ribberink JS, de Vriend HJ (2003) Vertical sorting in bed forms: flume experiments with a natural and a trimodal sediment mixture. Water Resour Res 39:1025. doi:10.1029/2001WR001088

Boffetta G, Crisanti A, Paparella F, Provenzale A, Vulpiani A (1998) Slow and fast dynamics in coupled systems: a time series analysis view. Phys D 116:301–312

Boffetta G, Cencini M, Falconi M, Vulpiani A (2002) Predictability: a way to characterize complexity. Phys Rep 356:367–474

Drake TG, Shreve RL, Dietrich WE, Whiting PJ, Leopold LB (1988) Bedload transport of fine gravel observed by motion pictures. J Fluid Mech 192:193–217

Frisch U (1995) Turbulence: the legacy of A.N. Kolmogorov. Cambridge University Press, New York

Gomez B, Phillips JD (1999) Deterministic uncertainty in bed load transport. J Hydraul Eng 125:305–308

Gomez B, Naff RL, Hubbel DW (1989) Temporal variations in bedload transport rates associated with the migration of bedforms. Earth Surf Proc Land 14:135–156

Hamamori A (1962) A theoretical investigation on the fluctuation of bedload transport. Delft Hydraulics Lab. Rep R4. Delft Hydraulics Laboratory, Delft

Hardy RJ, Lane SR, Ferguson RI, Parsons DR (2007) Emergence of coherent flow structures over a gravel surface: a numerical experiment. Water Resour Res 43:W03422. doi:10.1029/2006WR004936

Hegger R, Kantz H, Schreiber T (1999) Practical implementation of nonlinear time series methods: the Tisean package. Chaos 9:413–435

Hubbell DW, HH Stevens, JV Skinner and JP Beverage (1987) Laboratory data on coarse-sediment transport for bedload-sampler calibrations, U.S. Geological Survey Water-Supply Paper 2299. U.S. Geological Survey, Washington DC

Kantz H, Schreiber T (1997) Nonlinear time series analysis. Cambridge University Press, Cambridge

Kennel MB, Brown R, Abarbanel HDI (1992) Determining embedding dimension for phase-space reconstruction using a geometrical construction. Phys Rev A 45:3403–3411

Kirkbride A (1993) Observations of the influence of bed roughness on turbulence structure in depth limited flows over gravel beds. In: Clifford NJ, French JR, Hardisty J (eds) Turbulence: perspectives on flow and sediment transport. Wiley, NY

Klaassen GJ (1990) Sediment transport in armoured rivers during floods-literature survey. Tech. Rep. Q790, Delft Hydraulics, Delft, The Netherlands

Kleinfelter N, Moroni M, Cushman JH (2005) Application of finite-size lyapunov exponent to particle tracking velocitmetry in fluid mechanics experiments. Phys Rev E 72:056306

Lorenz EN (1969) The predictability of a flow which possesses many scales of motion. Tellus 21:289–307

Moeckel R, Murray B (1997) Measuring the distance between time series. Phys D 102:187–194

Nelson JM, Shreve RL, McLean R, Drake TG (1995) Role of near-bed turbulence structure in bed load transport and bed form mechanics. Water Resour Res 31:2071–2086

Nikora V, Walsh J (2004) Water-worked gravel surfaces: high-order structure functions at the particle scale. Water Resour Res 40:W12601. doi:10.1029/2004WR003346

Parker G (1991) Some random notes on grain sorting. In: Proceedings of grain sorting seminar IAHR, pp 20–76

Schreiber T, Schmitz A (1996) Improved surrogate data for nonlinearity tests. Phys Rev Lett 77:635–638

Seminara G (1998) Stability and morphodynamics. Meccanica 33:59–99

Singh A, Fienberg K, Jerolmack DJ, Marr JG, Foufoula-Georgiou E (2008) Experimental evidence for statistical scaling and intermittency in sediment transport rates. J Geophys Res Earth (in press)

Theiler J, Eubank S, Longtin A, Galdrikian B, Farmer JD (1992) Testing for nonlinearity in time series: the method of surrogate data. Phys D 58:77–94

Wilcock PR, McArdell BW (1993) Surface-based fractional transport rates: mobilization thresholds and partial transport of a sand-gravel sediment. Water Resour Res 29:1297–1312

Wilcock PR, McArdell BW (1997) Partial transport of sand/gravel sediment. Water Resour Res 33:235–245

A nonlocal theory of sediment buffering and bedrock channel evolution

Colin P. Stark,[1] Efi Foufoula-Georgiou,[2] and Vamsi Ganti[2]

[1] Bedrock erosion in mountain river channels ultimately sets the erosion rate of the surrounding hillslopes and the rate of sediment supply to the channels. The supply of coarse bed sediment acts as a dampening effect on further erosion by depositing an alluvial cover that temporarily obscures the bedrock. For landscapes where the residence time of the alluvial bed cover is comparable to the timescale of bedrock incision, coarse sediment supply and transport generate a strong negative feedback on fluvial downcutting and the coupled process of hillslope-channel erosion is inherently self-buffering. Here we study a simple model of self-buffered bedrock channel erosion that incorporates the spreading of bed sediment cover downstream in a way that allows for a broad-tailed, power law probability distribution of transport velocities of bed sediment over the long-term. This leads us to consider a nonlocal transport law (fractional advection) parameterized by a scaling exponent $0 \leq \alpha < 1$ which collapses to local advection for $\alpha \rightarrow 1$. For strong sediment buffering, we find that nonlocality $1 - \alpha$ has a direct control on the power law scaling of channel slope S with upstream area A, giving $S \sim A^{-(1-\alpha)/2}$ at steady state. Empirical observations of slope-area scaling are consistent with $\alpha < 1$ and nonlocal transport. In general, the model predicts linear, logarithmic, or power law stream profiles depending on the extent of buffering, the degree of nonlocality, and the scaling of the bedrock erosion law. It also predicts, somewhat counterintuitively, that bed cover should thicken with distance x downstream slower than linearly as x^{α}, i.e., the more nonlocal the bed sediment spreading process ($\alpha \rightarrow 0$), the slower the bed cover increases downstream. We deduce that long-range, heterogeneous transport of coarse sediment in mixed bedrock-alluvial rivers may be a key element of landscape scaling and an important factor in landscape dynamics.

1. Introduction

[2] Mountain river channels with naked bedrock beds are rare [*Tinkler and Wohl*, 1998]. Most have an alluvial cover of coarse, bedload-grade sediments; this cover can be meters to tens of meters thick or more and can persist for thousands of years after deposition before the bedrock is exposed once again to erosion [*Turowski et al.*, 2008] (the more appropriate term for most "bedrock rivers" should be "mixed bedrock-alluvial rivers"). Nevertheless, most of the theoretical treatment of mountain river erosion has focused on true bedrock channels [*Dietrich et al.*, 2003; *Stock and Montgomery*, 1999; *Snyder et al.*, 2003; *Whipple and Tucker*, 1999; *Whipple*, 2004; *Tucker and Bras*, 2000; *Sklar and Dietrich*, 1998, 2001; *Stark*, 2006; *Wobus et al.*, 2006] and the role of alluvial bed cover in the buffering of channel

erosion has been sparsely studied [e.g., *Finnegan et al.*, 2007; *Sklar and Dietrich*, 2004, 2006].

[3] Alluvial bed cover develops through the coupled processes of hillslope erosion, channel incision and channel transport. Broadly speaking, hillslope erosion is slave to channel erosion (particularly on long timescales) with the average rate of catchment denudation essentially driven by the rate of downcutting in the channels. The greater the downcutting rate, the greater the flux of sediment into the channels, and therefore the greater the likely temporary storage of bedload-grade sediment along the channels.

[4] A continuum description of this kind understates the problem: on the short-term or storm event timescale, the patterns and rates of sediment supply and transport are strongly heterogeneous, and the transient nature of bed sediment storage is more pronounced. Mass-wasting events supplying coarse material to the channels often occur asynchronously to the high-stage flows capable of transporting such material [*Dadson*, 2004; *Gabet et al.*, 2008]; the volume of mass-wasted material may require hundreds to thousands or more flood events to completely flux the coarse sediment through the drainage network; the asynchroneity is exacerbated when

[1]Lamont-Doherty Earth Observatory, Columbia University, Palisades, New York, USA.
[2]St. Anthony Falls Laboratory, University of Minnesota, Minneapolis, Minnesota, USA.
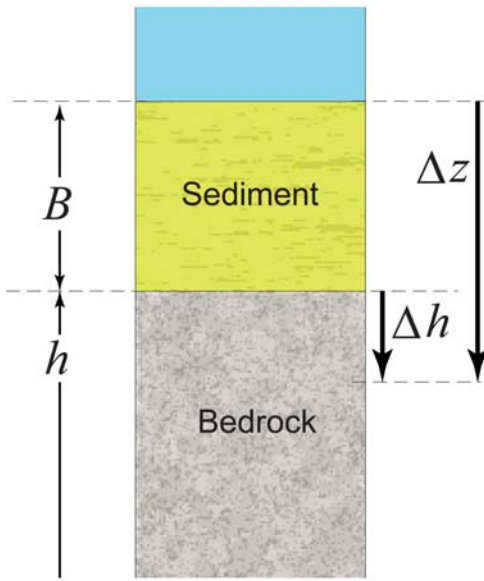
Figure 1. Schematic erosion of bed sediment cover and bedrock.

the mass-wasting events are triggered by earthquakes that deliver sediment independently of the storm events that generate the river flows capable of significant bed sediment transport [e.g., *Dadson et al.*, 2004; *Harp and Jibson*, 1996]; earthquake-driven mass wasting can saturate mountain river channels with coarse debris for very long periods of time, both by immediately generating landslides and debris flows and by priming the hillslopes for widespread failure during later heavy rainfall events [e.g., *Lin et al.*, 2003].

[5] Therefore, while bedrock incision in mountain rivers drives erosion of the surrounding hillslopes, it also impedes further incision by drawing coarse hillslope sediment onto the channel bed. This self-limiting, negative feedback process can be thought of as "sediment buffering." The purpose of this paper is to present a simple model for mountain river erosion that incorporates sediment buffering, i.e., a model to describe the evolution of a mixed bedrock-alluvial channel in which bed sediment cover may be the rate-limiting factor.

[6] The model addresses a second key issue in mountain rivers whose importance becomes clear when attempting to treat the heterogeneous transport of bed sediment through a catchment: the long-term motion of coarse sediment particles is not a spatially limited process that can be estimated by computing local bedload motions at each channel cross section. In reality, grains of bed sediment of variable mass are transported with a broad range of particle velocities over a wide range of distances by numerous flood discharges of varying magnitude [*Stark et al.*, 2000]. Although the composite, long-term probability distribution of transport distances is not yet known empirically, studies such as those of *Hassan and Church* [1991] and *Church and Hassan* [1992] have recorded semiheavy (exponential or gamma) probability density functions (pdfs) of particle transport distances after one or two floods, and on theoretical grounds it is reasonable to deduce that it is heavy tailed. Probability distributions with heavy, power law tails arise in nature for one of (at least) three reasons: (1) because the governing process is self-similar, (2) through the mixing of distributions

of constituent properties (Appendix A2), or (3) through summation of quantities with arbitary shape, broad-tailed distributions and convergence to a stable law pdf according to the Lévy limit theorem [*Lévy*, 1937; *Feller*, 1971]. All three phenomena are likely to pertain to the distributions of bed particle motions in mixed bedrock-alluvial rivers.

[7] The implication of a power-law tail is that the bed sediment acting to buffer bedrock erosion is spread from its hillslope supply points in a way that deviates from a simple advection process. Instead, the spreading process is probably strongly heterogenous, nonclassical, and best described using a fractional advection model [e.g., *Baeumer et al.*, 2001]. This heterogeneity needs to be incorporated in models of mixed bedrock-alluvial channel evolution, because its long-range properties will significantly affect the pattern of sediment distribution across the catchment and may ultimately determine the scaling relationships between channel gradient and upstream area.

2. Principles

[8] There are two key elements to the model: (1) the coupled process of bed sediment buffering and bedrock erosion and (2) the nonlocal spreading downstream of bed sediment. There are two key innovations that make the model tractable: (1) the conceit that the erosion of both sediment and bedrock can be treated in a consistent manner by writing the rates of both in terms of unit stream power and (2) the application of fractional calculus to the description of nonlocal advection of bed sediment.

[9] The governing equations are derived in detail in section 3 and are summarized here to stress the explicit coupling of the bed cover thickness and the temporal evolution of the channel profile. The rate of bedrock channel incision is given by

$$-\frac{\partial h}{\partial t} \sim \eta_{\text{rock}} \left(\frac{\Omega}{x} - \frac{B}{\eta_{\text{sed}}} \right), \tag{1}$$

where h is the elevation of channel bedrock profile (subject here to zero rock uplift rate), Ω is unit stream power, x is downstream distance (here implicitly giving channel width scale), t is time, $B(x, t)$ is the bed cover thickness, and η_{rock} and η_{sed} are bedrock and sediment erodibilities, respectively. The downstream spreading of coarse bed sediment is

$$x\frac{\partial B}{\partial t} \sim -v_0 \frac{\partial}{\partial x} \left(x^2 I_x^{1-\alpha} \left\{ \frac{B}{x} \right\} \right) - x\frac{\partial h}{\partial t} \tag{2}$$

where v_0 is a reference transport speed of bed sediment and $1 - \alpha$ is the degree of nonlocality of this transport (spreading) process, specifically, α is the exponent in the heavy-tailed probability distribution of transport velocities $p(v)$ that is encapsulated in the fractional integral $I_x^{1-\alpha}\{\cdot\}$.

3. Theory
3.1. Bed Cover Buffering

[10] Consider the time interval $\Delta\tau$ over which the bed sediment cover of thickness B is "eroded," the bedrock bed is exposed, and then the bedrock itself is eroded (Figure 1)
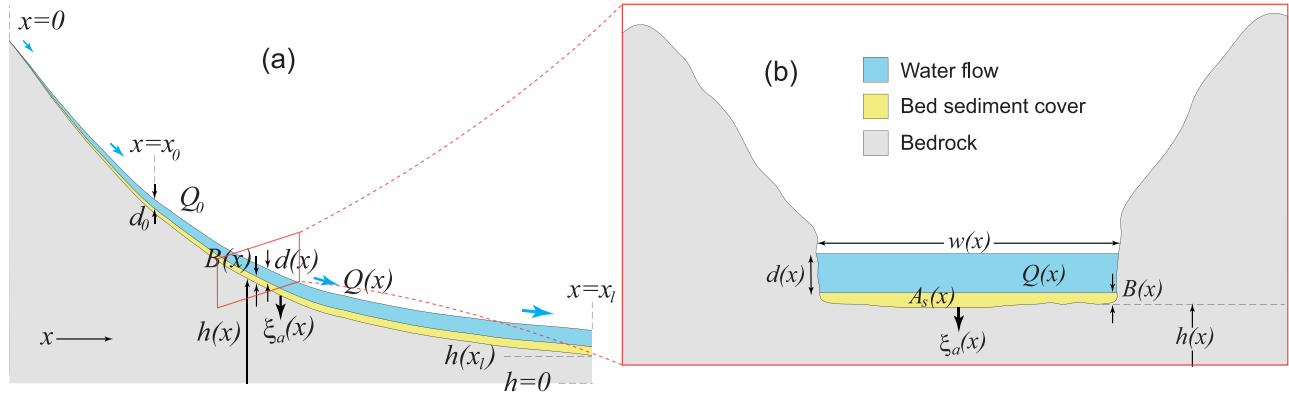
Figure 2. Model geometry shown in (a) downstream profile and (b) cross section.

by $-\Delta h \geq 0$ (h is measured positive upward); the net bedrock erosion during $\Delta \tau$ is therefore $\Delta z = B - \Delta h$. Define λ as the fraction of time spent in eroding sediment and ξ_{raw} as the raw (unscaled by material erodibilities) rate of erosion. The time spent eroding the bedrock is

$$(1 - \lambda)\Delta \tau = \frac{-\Delta h}{\eta_{\text{rock}} \xi_{\text{raw}}} \tag{3}$$

and the time spent "eroding" the sediment is

$$\lambda \Delta \tau = \frac{B}{\eta_{\text{sed}} \xi_{\text{raw}}}, \tag{4}$$

so that

$$\Delta \tau = \left(\frac{-\Delta h}{\eta_{\text{rock}}} + \frac{B}{\eta_{\text{sed}}} \right) \frac{1}{\xi_{\text{raw}}}, \tag{5}$$

where η_{rock} and η_{sed} are the respective erodibilities of rock and bed sediment. Rearranging, we obtain the actual bedrock erosion rate ξ_{a}

$$-\frac{\Delta h}{\Delta \tau} \rightarrow -\partial_t h = \xi_a = \eta_{\text{rock}} \xi_{\text{raw}} - \frac{\eta_{\text{rock}}}{\eta_{\text{sed}}} \frac{B}{\Delta \tau}. \tag{6}$$

If the bedrock is undergoing vertical motion, the frame of reference for h is moving and the rate of lowering of the profile $-\partial_t h$ must also include a term giving the rate of uplift (see below).

3.2. Dimensionless Bed Cover

[11] The cross-sectional area of the channel (Figure 2) taken up by bed sediment is

$$A_s(x, t) = wB(x, t) = wdC(x, t), \tag{7}$$

where w and d are the width and depth of the channel and B is the bed cover thickness, which can be expressed in terms of the dimensionless bed cover C as

$$B(x, t) = dC. \tag{8}$$

The parameter $C(x, t)$ is effectively the fraction of channel cross-sectional area occupied by bed sediment, so it can be thought of (loosely) as a sediment concentration in the flow at the channel cross section at a distance downstream x.

3.3. Nonlocal Bed Sediment Transport

[12] If grains of sediment pass through a channel cross-section x with a constant velocity (or random velocities following a probability distribution with a light tail), then $C(x, t)$ can be approximated by the number of particles in a thin strip of downstream width Δx. However, if the particle velocities follow a distribution with a heavy tail then the narrow strip Δx is too small to statistically capture particles that originate from far away transported at great speed. Thus one needs to enlarge the width of the strip to accommodate the heavy-tailed pdf of velocities.

[13] This is equivalent to saying that instead of considering a local flux $\phi(x)$ determined by the local particle concentration and velocities, one should consider a non-local, compound flux

$$\phi^*(x, t) = \int_0^x g(l)\phi(x - l, t)dl, \tag{9}$$

where the weighting function $g(l)$ should account for the likelihood of an incoming particle arriving from a distance l upstream of a location x. For a velocity distribution with a power law tail with exponent α (Appendix A2)
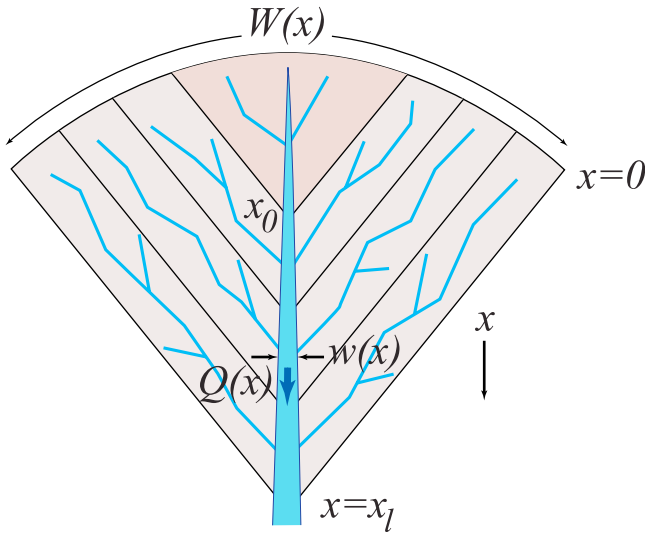
$$\mathbb{P}(V \geq v) \sim v^{-\alpha} \qquad 0 \leq \alpha < 1 \tag{10}$$

the weights take the form of a power law on lag

$$g(l) \sim l^{-\alpha} \tag{11}$$

and the nonlocal flux (volume per unit channel cross-sectional area per unit time) is equivalent (Appendix A1) to the fractionally integrated flux

$$\phi^*(x, t) = \frac{v_0}{x_0^{1-\alpha}} I_x^{1-\alpha}\{C(x, t)\}, \tag{12}$$

Figure 3. Nested catchment geometry used in model. The drainage network shown here is schematic.

where v_0 is a reference speed. It is worth noting that if we take the limit as $\alpha \to 1$ we recover the local flux $\phi(x, t)$ (simple advection). The corresponding sediment discharge (volume per unit time) through a channel cross section of mean flow width w and depth d at a distance x downstream is

$$Q_s(x, t) = wd\phi^*. \qquad (13)$$

[14] A heavy-tailed distribution of bed particle velocities (equation (10)) is used here to model (without distinction) both a power law pdf of velocities during a single flood and a power law pdf of particle transport distances over multiple floods and a long timescale. Such a heavy-tailed pdf is likely given the heterogeneous, composite nature of the stochastic process of sediment transport in mountain rivers, and given the ease with which heavy-tailed pdfs can arise through the mixing of lighter tailed pdfs (see Appendix A2 for an example of the mixing of exponential and gamma distributions of grain size and transport distance to give a composite particle velocity pdf with a power law tail).

3.4. Bedrock Erosion Model

[15] To make the linkage in a simple way between stream flow, stream power, bedrock erosion, raw bedrock channel incision, sediment-buffered channel incision and ultimately the channel slope-upstream-area relation, we assume here a linear model of channel bedrock erosion as a function of unit stream power per unit channel width w. The unit stream power at the characteristic flood discharge Q is

$$\Omega(Q) = \rho g Q |\partial_x h|, \qquad (14)$$

whose units are W/m or energy dissipated per unit time per unit distance downstream [*Rhoads*, 1987]. If bedrock erosion is linearly proportional to the rate of energy dissipation per unit area Ω/w, then the amount of vertical lowering during flood events of discharge Q, duration t_f and

annual frequency f, and reference bedrock erodibility γ (whose reciprocal has units of J/m^3), is

$$\xi_{\text{raw}} = f t_f \gamma \frac{\Omega}{w} = f t_f \gamma \rho g \frac{Q |\partial_x h|}{w}, \qquad (15)$$

which can be simplified by defining a flood effectiveness term

$$\mu = t_f \gamma \rho g, \qquad (16)$$

which has units of reciprocal velocity (seconds per meter). For downstream always-negative gradients the raw rate of erosion per year becomes

$$\xi_{\text{raw}} = f \mu \frac{Q}{w} (-\partial_x h). \qquad (17)$$

The sediment-buffered, actual rate of bedrock erosion, for bedrock with erodibility $\eta_r = \eta_{\text{rock}}$ and sediment cover with erodibility $\eta_s = \eta_{\text{sed}}$ comes from combining equation (6) with equation (17), and assuming $f = 1/\Delta\tau$,

$$\xi_a = f \eta_r \left(\mu \frac{Q}{w} (-\partial_x h) - \frac{1}{\eta_s} B \right). \qquad (18)$$

This is our first governing equation.

3.5. Sediment Supply

[16] Sediment supply from coupled erosion of the main channel, its tributaries and all surrounding hillslopes yields a total input of coarse sediment per unit downstream distance of

$$\varphi(x, t) = \chi \frac{dA_c}{dx} \xi_a = \chi W \xi_a, \qquad (19)$$

where $A_c(x)$ is the catchment area and $W(x)$ is an effective catchment width (Figure 3). The prefactor χ is the coarse fraction of eroded material that becomes bed sediment in our model; the remaining proportion of sediment is assumed to be suspended or wash load.

3.6. Mass Balance

[17] Conservation of nonlocal bed sediment flux (equation (13)) gives

$$\partial_t A_s = -\partial_x Q_s + \varphi = -\partial_x \{wd\phi^*\} + \chi W \xi_a, \qquad (20)$$

where $\partial_x \{\cdot\}$ is the divergence operator and A_s is the bed-sediment cross-sectional area (Figure 2b). This is our second governing equation.

[18] As a cross-check, lets see what would happen if there were no fractional advection and no source term

$$\partial_t \{x^2 C\} = -v_0 \partial_x \{x^2 C\}, \qquad (21)$$

which simplifies to

$$\mathcal{D}\{A_s\} = \partial_t A_s + v_0 \partial_x A_s = 0, \qquad (22)$$

which means that in the Lagrangian frame of the flow of sediment moving at speed v_0 downstream, the cross-sectional volume per unit distance downstream A_s is constant.

3.7. Rock Uplift Rate

[19] The vertical reference frame is set by the pattern of relative base level change ("uplift") $u(x, t)$ so that the absolute elevation of the river profile bedrock base is

$$\partial_t h = u(x, t) - \xi_a. \tag{23}$$

For the remainder of this paper we will assume a uniform and constant uplift rate $u(x, t) = u_0$ over the domain $0 \leq x \leq x_l$.

4. Implementation

[20] The model is implemented in an idealized catchment geometry with simple hydraulic geometry and scaling (Figures 2 and 3).

4.1. Hydraulic Geometry

[21] The characteristic flood discharge $Q(x)$ is assumed for simplicity to scale linearly with drainage area

$$Q(x) = Q_0 \left(\frac{x}{x_0}\right)^2. \tag{24}$$

Noninteger scaling (Hack's law) could be employed here if required. Uniformly constant downstream flow speed is assumed, along with a roughly rectangular channel cross section, an implicit Chézy formulation of steady open channel flow resistance and consequent hydraulic geometry, which means that the flow width (Figure 2b) scales as root discharge

$$w(Q(x)) = w_0 \sqrt{\frac{Q(x)}{Q_0}} = w_0 \sqrt{\frac{x^2}{x_0^2}} = \frac{w_0}{x_0} x \tag{25}$$

as does flow depth

$$d(Q(x)) = d_0 \sqrt{\frac{Q(x)}{Q_0}} = d_0 \sqrt{\frac{x^2}{x_0^2}} = \frac{d_0}{x_0} x. \tag{26}$$

The scaling of discharge per unit channel width is important

$$\frac{Q}{w} = \left(Q_0 \left(\frac{x}{x_0}\right)^2 \right) \Big/ \left(\frac{w_0}{x_0} x\right) = \left(\frac{Q_0}{w_0 x_0}\right) x \tag{27}$$

because it determines the scaling in the raw erosion rate calculation (equation (18)).

4.2. Catchment Geometry

[22] Catchment widening with downstream distance is the arc length for the "pie-shaped" drainage basin (Figure 3)

$$W(x) = \frac{W_0}{x_0} x. \tag{28}$$

The catchment area is the integral over x

$$A_c(x) = \frac{W_0}{2x_0} x^2. \tag{29}$$

4.3. Model Dynamics

[23] We can reduce the model equations (18) and (20) to a coupled pair of partial differential equations by incorporating the pattern of rock uplift, which in this treatment is assumed to be spatiotemporally uniform (equation (23)). The PDE pair is a closed form description of the evolution of the bedrock river profile over time and space.

[24] The constitutive equation, which describes bed-sediment buffered channel bedrock erosion ξ_a, is

$$u_0 - \partial_t h = f \eta_r x \left\{ \left(\frac{\mu Q_0}{w_0 x_0}\right) (-\partial_x h) - \left(\frac{d_0}{\eta_s x_0}\right) C \right\}. \tag{30}$$

The conservation equation, which describes the hillslope supply and downstream river channel spreading of bed sediment, is

$$x^2 \partial_t C = -v_0 \partial_x \left\{ \frac{1}{x_0^{1-\alpha}} x^2 I_x^{1-\alpha} C \right\} + \left(\frac{\chi W_0 x_0}{w_0 d_0}\right) x (u_0 - \partial_t h). \tag{31}$$

[25] The formulation and solution of such a coupled system of fractional advection and partial differential equations (with nonlinear terms) is wholly original. To date, the focus in the literature has been on fractional dispersion [e.g., *Benson*, 1998] and where nonlocal advection has been addressed [*Baeumer et al.*, 2001; *Zhang et al.*, 2007] it has taken a different form (Appendix A3).

5. Steady State Solution

[26] If we assume that the time scale of bedrock channel evolution is large compared to the equilibration timescale of the bed sediment, $t_h \gg t_c$, then C is effectively instantly equilibrated and therefore constant at the timescale of bedrock channel evolution. This implies that

$$\partial_t \{x^2 C\} = x^2 \partial_t C = 0. \tag{32}$$

Erosion rates balance the mass input everywhere at steady state, so that (equation (23))

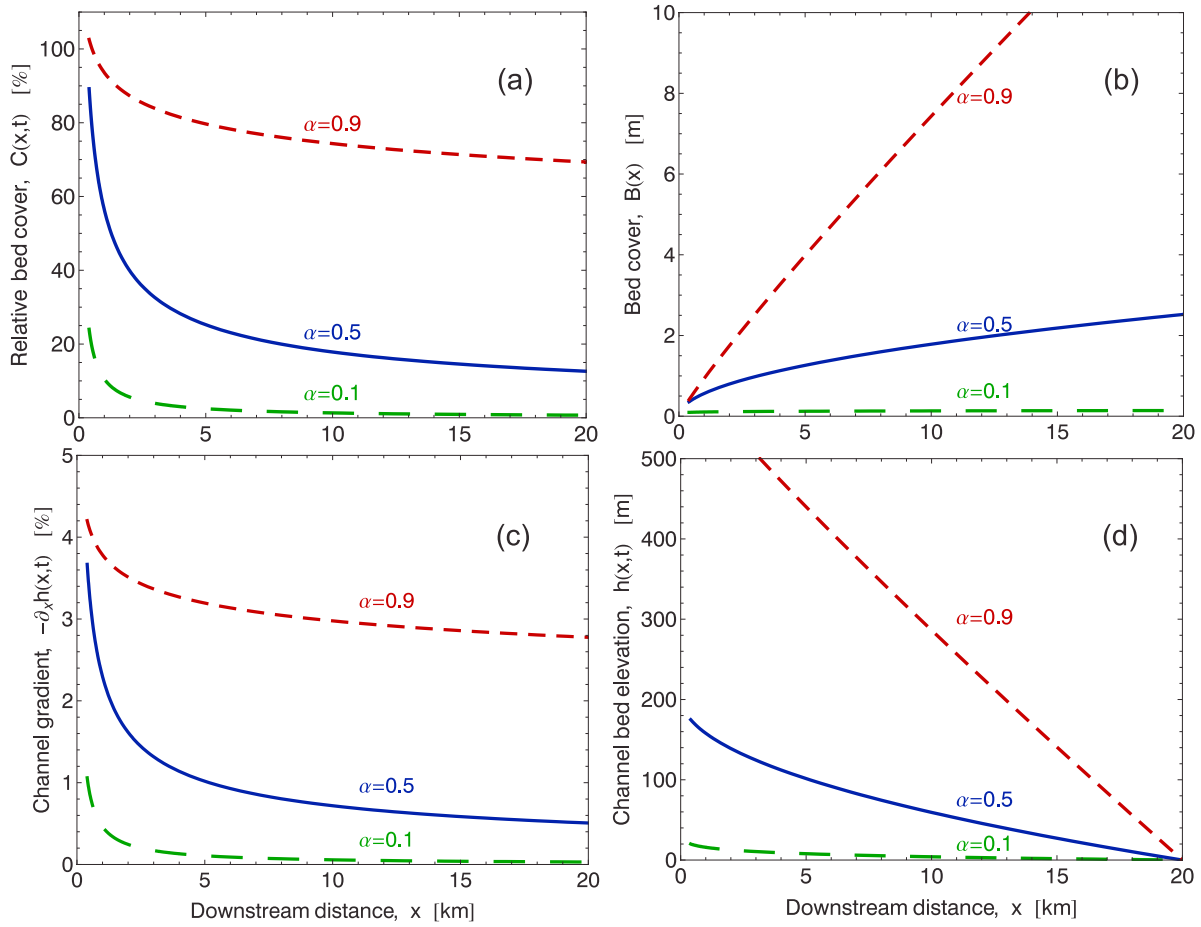$$\xi_a = u_0 \quad \Leftrightarrow \quad -\partial_t h = 0. \tag{33}$$

From equation (31) we have

$$\partial_x \left\{ \frac{1}{x_0^{1-\alpha}} x^2 I_x^{1-\alpha} C \right\} = \left(\frac{\chi W_0 x_0}{v_0 w_0 d_0}\right) u_0 x. \tag{34}$$

Integrating out gives

$$x^2 I_x^{1-\alpha} C = \left(\frac{\chi W_0 x_0^{2-\alpha}}{v_0 w_0 d_0}\right) u_0 \int_{x_{hc}}^{x} \zeta d\zeta. \tag{35}$$

Figure 4. Steady state solutions for (a) dimensionless bed sediment cover $C(x, t \to \infty)$, (b) bed sediment thickness $B(x, t \to \infty)$, (c) channel gradient $-\partial_x h(x, t \to \infty)$, and (d) channel bedrock bed elevation $h(x, t \to \infty)$ for three models with $\alpha = 0.1$ (long-dashed line), $\alpha = 1/2$ (solid line), and $\alpha = 0.9$ (short-dashed line).

The drainage divide $x = 0$ is the lower limit of the fractional integration $I_x^\alpha\{\cdot\}$ (see Appendix) and $x_{\rm hc}$ is the hillslope-channel transition length scale. The fractional differentation and integration operations here are associative and this equation can be rearranged to give

$$C(x, t \to \infty) = \left(\frac{\chi W_0 x_0^{2-\alpha}}{v_0 w_0 d_0}\right) u_0 \partial_x^{1-\alpha}\left\{\frac{x^2 - x_{\rm hc}^2}{2x^2}\right\}. \quad (36)$$

Since $0 \leq \alpha < 1$ this is a fractional derivative. For simplicity, we assume that the hillslope-channel transition length scale is $x_{\rm hc} \approx 0$ so that we have

$$C(x, t \to \infty) = \frac{1}{\Gamma(\alpha)} \left(\frac{\chi W_0 x_0}{2w_0 d_0}\right) \left(\frac{u_0}{v_0}\right) \left(\frac{x}{x_0}\right)^{\alpha-1}. \quad (37)$$

[27] This closed form result for the dimensionless bed cover is illustrated in Figure 4a for three values of α and the example set of model parameters given in section 8. In the limit as $\alpha \to 1$, fractional integration is turned off and we recover the result derived above for the nonfractional case with $x_{\rm hc} = 0$

$$C(x, t \to \infty) = \left(\frac{\chi W_0 x_0}{2w_0 d_0}\right) \left(\frac{u_0}{v_0}\right). \quad (38)$$

The bed sediment thickness for any α is derived by combining equations (8), (26) and (37)

$$B(x, t \to \infty) = \frac{1}{\Gamma(\alpha)} \left(\frac{\chi W_0 x_0}{2w_0}\right) \left(\frac{u_0}{v_0}\right) \left(\frac{x}{x_0}\right)^\alpha. \quad (39)$$

This result is illustrated in Figure 4b for three values of α and the example set of model parameters given in section 8.

5.1. Channel Slope

[28] Combining equations (30) and (33), we find the channel gradient at steady state can be written as

$$(-\partial_x h) = \left(\frac{w_0 x_0}{f \eta_{\rm r} \mu Q_0}\right) \frac{1}{x} \left\{u_0 + f\left(\frac{\eta_{\rm r}}{\eta_{\rm s}}\right) \left(\frac{d_0}{x_0}\right) x C\right\}. \quad (40)$$

Substitution of the dimensionless bed cover $C(x, t \to \infty)$ given by equation (37) gives

$$-\partial_x h(x, t \to \infty) = \left(\frac{w_0 x_0}{f \eta_{\rm r} \mu Q_0}\right) \frac{1}{x}$$

$$\times \left\{u_0 + f\left(\frac{\eta_{\rm r}}{\eta_{\rm s}}\right) \left(\frac{d_0}{x_0}\right) \frac{1}{\Gamma(\alpha)} \left(\frac{\chi W_0 x_0^2}{2w_0 d_0}\right) \left(\frac{u_0}{v_0}\right) \left(\frac{x}{x_0}\right)^\alpha\right\}, \quad (41)$$

which simplifies to

$$
-\partial_x h(x, t \to \infty) = \left(\frac{w_0 x_0}{\eta_r \mu Q_0}\right)\left(\frac{u_0}{v_0}\right)
$$
$$
\times \left\{\left(\frac{v_0 x^{-\alpha}}{f x_0^{1-\alpha}}\right) + \frac{1}{\Gamma(\alpha)}\left(\frac{\eta_r}{\eta_s}\right)\left(\frac{\chi W_0}{2 w_0}\right)\right\}\left(\frac{x}{x_0}\right)^{\alpha-1}. \tag{42}
$$

Several key aspects of model behavior can be gleaned from this equation. The two bracketed terms describe the respective importance of raw (left) versus buffered (right) bedrock erosion. If buffering is very weak, the right-hand bracketed term vanishes and the rate of channel bedrock incision is given simply by the raw rate of erosion (equation (15)); the channel slope has a hyperbolic decay that originates in the simple erosion law scaling:

$$
-\partial_x h(x, t \to \infty) \approx \left(\frac{w_0 u_0}{f \eta_r \mu Q_0}\right)\left(\frac{x}{x_0}\right)^{-1}. \tag{43}
$$

On the other hand, if buffering is strong, or if we simply examine the asymptotic limit for large x downstream, we find that channel slope is a power law decay

$$
-\partial_x h(x \to \infty, t \to \infty) \approx \frac{1}{\Gamma(\alpha)}\left(\frac{\chi W_0 x_0}{2 \eta_s \mu Q_0}\right)\left(\frac{u_0}{v_0}\right)\left(\frac{x}{x_0}\right)^{\alpha-1}, \tag{44}
$$

with exponent $\alpha - 1$ such that the decay is bounded between x^0 and x^{-1}. In other words, at the limiting values of α, we find the model predicts a constant gradient (and a linear river profile) for purely local bed sediment transport and $\alpha = 1$, whereas it predicts a hyperbolic decay in slope (and a logarithmic river profile) for extremal nonlocal transport ($\alpha = 0$) (see Figure 4c).

5.2. Channel Elevation

[29] For the case of negligible bed buffering, integration of equation (43) with $h(x_0) = h_0$ results in the river profile

$$
h(x, t \to \infty) \approx h_0 \left\{1 - \left(\frac{w_0 u_0}{f \eta_r \mu Q_0}\right) \log\left(\frac{x}{x_0}\right)\right\}. \tag{45}
$$

For the case of significant bed buffering, and/or for large x, integration of equation (44) results instead in the profile

$$
h(x, t \to \infty) \approx h_0 \left\{1 - \frac{1}{\Gamma(\alpha)}\left(\frac{\chi W_0 x_0}{2 \alpha \eta_s \mu Q_0}\right)\left(\frac{u_0}{v_0}\right)\left(\frac{x}{x_0}\right)^{\alpha}\right\}. \tag{46}
$$

This closed form result is illustrated in Figure 4d for three values of α and the example set of model parameters given in section 8.

5.3. Mass Balance

[30] The nonlocal sediment flux at steady state can be found by substituting the solution for dimensionless bed cover $C(x, t \to \infty)$ given by equation (37) into the fractional advection flux equation (12), which gives

$$
\phi^*(x, t \to \infty) = \frac{1}{\Gamma(\alpha)}\left(\frac{\chi W_0 x_0}{2 w_0 d_0}\right) u_0 I_x^{1-\alpha}\{x^{\alpha-1}\} \tag{47}
$$

and thus

$$
\phi^*(x, t \to \infty) = \left(\frac{\chi W_0 x_0}{2 w_0 d_0}\right) u_0. \tag{48}
$$

The sediment discharge is then

$$
Q_s(x, t \to \infty) = w d \phi^* = \left(\frac{w_0 d_0}{x_0^2}\right)\left(\frac{\chi W_0 x_0}{2 w_0 d_0}\right) u_0 x^2 \tag{49}
$$

and thus

$$
Q_s(x, t \to \infty) = \left(\frac{\chi W_0}{2 x_0}\right) u_0 x^2, \tag{50}
$$

which is consistent with simple mass balance, since this gives

$$
Q_s(x, t \to \infty) = \chi A_c u_0. \tag{51}
$$

Alternatively, we can integrate out the divergence in the second PDE,

$$
\partial_x Q_s = \varphi(x), \tag{52}
$$

so that using equation (19) yields

$$
Q_s(x, t \to \infty) = \left(\frac{\chi W_0}{x_0}\right) u_0 \int_0^x \zeta \, d\zeta, \tag{53}
$$

which gives the same result.

5.4. Slope-Area Scaling

[31] A key result of our model is the scaling of slope

$$
S = -\partial_x h, \tag{54}
$$

with area

$$
A = A_c = \frac{W_0}{2 x_0} x^2, \tag{55}
$$

which we find is

$$
S \sim A^{-(1-\alpha)/2}. \tag{56}
$$

In other words, the scaling exponent in the standard form of this equation

$$
S \sim A^{-\theta} \tag{57}
$$

is

$$
\theta = \frac{1-\alpha}{2}. \tag{58}
$$

[32] The implication is that if sediment buffering by fractional advection (in the simple scaling form presented here) were the only control on slope-area scaling, slopes would decrease no faster than $A^{-1/2}$

$$
0 \le \alpha < 1 \quad \Leftrightarrow \quad \frac{1}{2} \ge \theta > 0. \tag{59}
$$

Empirical studies of slope-area scaling [e.g., *Gupta and Waymire*, 1989; *Tarboton et al.*, 1989; *Sklar and Dietrich*, 1998; *Whipple*, 2004] typically find exponents around 1/2 or higher, which indicates that (1) advection is likely strongly nonlocal and (2) some of our model scaling simplifications, particularly in the treatment of hydraulic geometry, will need to be reexamined in future model developments to allow $\theta > 1/2$. Nevertheless, the main conclusion to draw is that our sediment buffering model offers an alternative explanation to the standard interpretation of slope-area power law scaling originating in a stream power law for bedrock erosion rate [e.g., *Montgomery*, 2001; *Whipple and Tucker*, 1999].

6. Time-Dependent Behavior

[33] The trick of assuming that C instantly adjusts to prevailing conditions on timescales $t_h \gg t_c$ can be extended to allow solution of the time-dependent behavior of bedrock channel evolution $h(x, t)$. In the conservation equation (31), the dimensionless sediment cover is effectively constant over time, so that the sediment cross-sectional area is also constant

$$\partial_t A_s = 0 \tag{60}$$

in equation (20). Thus the sediment discharge increases only over space (downstream) and not time by the sediment supply function

$$\partial_x Q_s = \varphi(x), \tag{61}$$

which expands, using equations (19), (23), and (28), into

$$\partial_x Q_s = \left(\frac{\chi W_0}{x_0}\right)(u_0 - \partial_t h)x. \tag{62}$$

In terms of the sediment flux, this equation can be written using equation (13) as

$$\partial_x\{wd\phi^*\} = \left(\frac{\chi W_0}{x_0}\right)(u_0 - \partial_t h)x, \tag{63}$$

which expands, using equations (25) and (26), to

$$\partial_x\left\{\frac{w_0 d_0}{x_0^2}x^2\phi^*\right\} = \left(\frac{\chi W_0}{x_0}\right)(u_0 - \partial_t h)x, \tag{64}$$

and then using equation (12) to

$$v_0\left(\frac{w_0 d_0}{x_0^{3-\alpha}}\right)\partial_x\{x^2 I_x^{1-\alpha}C\} = \left(\frac{\chi W_0}{x_0}\right)(u_0 - \partial_t h)x \tag{65}$$

or

$$v_0\partial_x\left\{\frac{1}{x_0^{1-\alpha}}x^2 I_x^{1-\alpha}C\right\} = \left(\frac{\chi W_0 x_0}{w_0 d_0}\right)(u_0 - \partial_t h)x. \tag{66}$$

Integrating out we obtain

$$\frac{v_0}{x_0^{1-\alpha}}x^2 I_x^{1-\alpha}C = \left(\frac{\chi W_0 x_0}{w_0 d_0}\right)\int_0^x (u_0 - \partial_t h)\zeta\mathrm{d}\zeta, \tag{67}$$

which is a useful form for numerical solution (section 7). It is always true that

$$C = \partial_x^{1-\alpha}\{I_x^{1-\alpha}C\}, \tag{68}$$

which allows rearrangement of equation (67) to give the dimensionless sediment cover in an explicit form

$$C(x, t \gg t_c) = \left(\frac{x_0^{1-\alpha}}{v_0}\right)\left(\frac{\chi W_0 x_0}{w_0 d_0}\right)\partial_x^{1-\alpha}\left\{\frac{1}{x^2}\int_0^x (u_0 - \partial_t h)\zeta\mathrm{d}\zeta\right\}. \tag{69}$$

This equation records how the (relative) bed cover comes about from the combined effects of upstream integration of sediment supply and the downstream spreading of this sediment by fractional advection.

7. Numerical Method

[34] An approximate solution for the evolution of $C(x, t)$ over time can be written in a way that avoids differentiation and provides sufficient stability to achieve numerical solution. This is achieved by integrating out equation (67)

$$\frac{1}{\Gamma(1-\alpha)}\left\{\int_0^x (x-\zeta)^{-\alpha}C(\zeta)\mathrm{d}\zeta\right\}$$
$$= -x^{-2}\left(\frac{x_0^{1-\alpha}}{v_0}\right)\left(\frac{\chi W_0 x_0}{w_0 d_0}\right)\int_0^x \zeta\Delta_t h(\zeta)\mathrm{d}\zeta, \tag{70}$$

where $\Delta_t h$ is the discretization of $\partial_t h$ with time step Δt. Using the Grünwald-Letnikov discrete approximation (equation (A6)) of the fractional integration in the left-hand side of this equation, we obtain the discrete form

$$\left(\frac{\Delta x}{x_0}\right)^{1-\alpha}\sum_{k=0}^{x/\Delta x}\frac{\Gamma(1-\alpha+k)}{k!\Gamma(1-\alpha)}C[x-k\Delta x]$$
$$= -x^{-2}\left(\frac{1}{v_0}\right)\left(\frac{\chi W_0 x_0}{w_0 d_0}\right)\sum_{k=0}^{n}k(\Delta x)^2\Delta_t h[k\Delta x]. \tag{71}$$

Discretization of equation (30) is more straightforward,

$$\Delta_t h(x, t) \approx f\frac{x}{x_0}\left\{\left(\frac{\eta_r \mu Q_0}{w_0}\right)\partial_x h + \left(\frac{\eta_r}{\eta_s}\right)d_0 C\right\}\Delta t. \tag{72}$$

Solution of the model is accomplished iteratively over a linear domain $0 \leq x \leq x_l$ divided into a series of n nodes at intervals Δx and thus located at distances $x_k = k\Delta x$ downstream. At each time step $t \to t + \Delta t$, a set of $2n$ simultaneous equations (a pair for each node $k \in [1, n]$ using equations (71) and (72)) is derived and solved to obtain successive values of dimensionless bed cover $\{C[k\Delta x, t]\}$ and bedrock elevation $\{h[k\Delta x, t]\}$. The number of terms in the equations for bed cover increases steadily across the domain (equation (71)), which makes solution an order n problem and computation very slow for large, finely resolved profiles. A more efficient means of solution is likely to be found in the future.

[35] The boundary conditions are: (1) zero sediment influx from the drainage divide (left boundary) at $x = 0$ and (2) the elevation beyond the solution domain is held at zero $h(x \geq x_l) = 0$. The initial conditions are: (1) the initial dimensionless bed cover is zero $C(x, 0) = 0$ and (2) the initial bed slope is small and constant across the domain, $-\partial_x h$ = const. Numerical solution of the successive simultaneous equations was achieved in a mixed symbolic and numerical fashion using Mathematica version 6.

8. Numerical Experiment

[36] We conducted several numerical experiments to verify the theoretical conclusions reached in sections 5 and 6, and to test the finite difference scheme derived in section 7. One of these experiments is presented here (Figures 5 and 6).

8.1. Uniform Block Uplift and Evolution to Steady State

[37] The intention of this experiment was to simulate the evolution of a mountain river channel in a moderately active tectonic and climatic environment. The following parameters were chosen:

$$\alpha = 1/2$$
$$x_0 = 1 \times 10^3 \text{ m}$$
$$Q_0 = 2 \text{ m}^3/\text{s}$$
$$w_0 = 10/\sqrt{5} \text{ m}$$
$$d_0 = 1/\sqrt{5} \text{ m}$$
$$\chi = 1/3$$
$$W_0 = 1 \times 10^3 \text{ m}$$
$$v_0 = 100 \text{ m/a}$$
$$u_0 = 1 \times 10^{-3} \text{ m/a}$$
$$f = 1 \times 10^{-2} \text{ years}^{-1}$$
$$\mu = 5000 \text{ s/m}$$
$$\eta_r = 0.1$$
$$\eta_s = 10$$
$$h_0 = 20 \text{ m}$$
$$x_l = 20 \times 10^3 \text{ m}$$
$$n = 100$$
$$\Delta x = x_l/n = 200 \text{ m}$$
$$\Delta t = 40 \times 10^3 \text{ years}$$

[38] These numbers define a model environment with the following properties. The catchment is $x_l = 20$ km long and $\frac{W_0}{x_0} x_l = 20$ km wide (equation (28)) with a downstream fault boundary (Figure 3), which slips at a rate $u(x_l, t) = u_0 = 1$ mm/a and which imposes a 1 mm/a rock uplift rate across the whole catchment. The erosion driven by this relative change in base level is mediated by the material properties μ, η_r and η_s, and by the frequency of characteristic discharge f, which is expressed as the number of such flood days per year; here $f = 10^{-2}$ years^{-1} or 1 day of 24-hour sustained discharge $Q(x_0) = Q_0$ about every 100 years. Sediment is supplied from the hillslopes and channels across the whole catchment at a rate set by the bedrock lowering rate along the main stream (Figures 2 and 3). The fraction of sediment transported as bedload is assumed to be a constant (across the catchment and downstream in the river) at $\chi = 1/3$.

[39] At the reference catchment scale $x = x_0 = 1$ km, the characteristic flood discharge is $Q_0 = 2$ cumecs, which is assumed to have a constant hydraulic geometry with flow width $w(x_0) = w_0 = 10/\sqrt{5}$ m and flow depth $d(x_0) = d_0 = 1/\sqrt{5}$ m for the anticipated bed slope and friction (more realistic hydraulic behavior would ultimately affect the scaling properties of the solutions, albeit weakly). The nested subcatchment width at this reference scale is $W_0 = 1$ km. The drainage area at $x = x_l$ is $A_c(x_l) = 200$ km^2 and the characteristic discharge from this area is $Q(x_l) = 400$ cumecs.

[40] The initial geometry of the landscape is a linear river bed profile (see Figures 6c and 6d) with a gradient of $-\partial_x h = 0.1\%$ and an initial elevation of $h_0 = 20$ m at the drainage divide ($x = 0$); the hillslopes and tributary channels are assumed to have already equilibrated with the mainstream geometry at $t = 0$.

[41] The time-space evolution was resolved over a uniform "grid" (vector) of $n = 100$ points with spacing $\Delta x = x_l/n = 200$ m and a time step of $\Delta t = 40$ ky. steady state was approximately achieved in about 750 ky.

8.2. Results

[42] The finite difference numerical solutions confirmed the theoretical predictions and demonstrated that the model is essentially a strongly overdamped, weakly oscillatory system that evolves stably to a steady state balance between rock uplift and mixed bedrock-alluvial channel erosion. Graphs of the model variables over x and t are shown in Figures 5 and 6. The numerical solutions (solid lines) converge to the closed form, steady state solutions (dashed lines) in all cases (see Figure 4 for comparison). These results are discussed in more detail in the next section.

9. Discussion and Conclusions

[43] We have formulated a model of bedrock river incision with sediment buffering that capitalizes on the following two innovations: (1) a single rate equation to describe both bed sediment cover removal and bedrock erosion in terms of work done on the bed and (2) treatment of the heterogeneous spreading of bed sediment using a fractional advection equation (which includes simple advection as a limiting case). Fractional advection was adopted to model the broad range of transport distances that bed sediment particles probably experience on the long-term, i.e., to deal with the combined effect of stochastic variability in grain size, bed armoring, transient depositional patterns, channel hydraulic geometry, flood discharge, and boundary shear stress, that likely generates a heavy-tailed probability distribution of particle motions (heavy-tailed pdfs of flood discharge are particularly extensively documented [e.g., *Dodov and Foufoula-Georgiou*, 2004; *Gupta et al.*, 1994; *Lague et al.*, 2005; *Molnar et al.*, 2006]). In such circumstances the classical notion of flux, and of advection and dispersion, does not work, because it assumes that local computation of the particle concentration gradient suffices
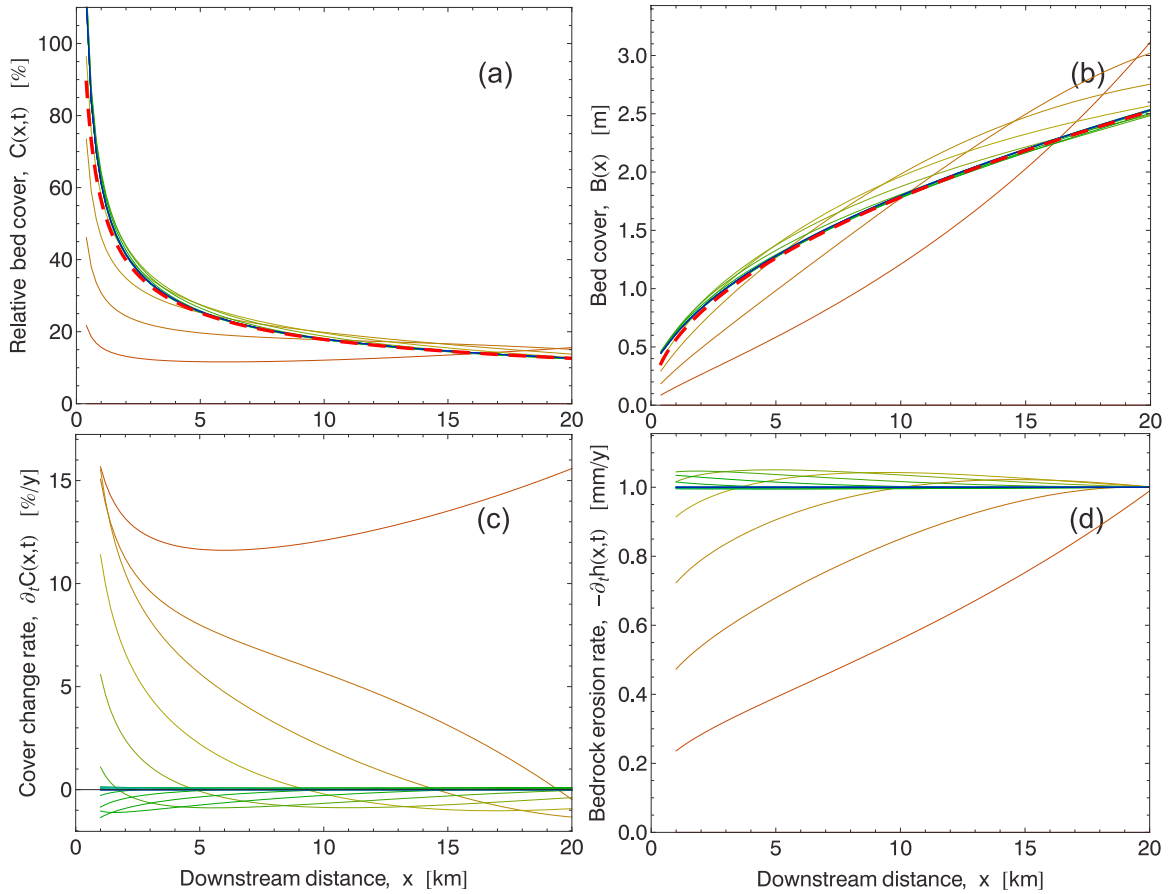
Figure 5. River profile evolution over time from an initial linear gradient to a steady state power law form obtained by numerical solution for (a) dimensionless bed cover $C(x, t)$, (b) bed cover thickness $B(x, t)$, (c) rate of change of dimensionless bed cover $\partial_t C(x, t)$, and (d) bedrock channel incision rate $-\partial_t h(x, t)$. Model parameters for this numerical simulation are given in section 8. Solid lines are numerical solutions at successive time steps; the dashed lines are the asymptotic, closed form solutions at steady state.

to estimate the numbers of particles passing by. No local computation can account for all the influxes of sediment from upstream if, on the same timescale, both short-range and long-range motions have nonvanishing probability. Instead, a nonlocal computation is needed to perform the distance-weighted sum of particle supply [*Benson*, 1998; *Cushman and Ginn*, 2000; *Berkowitz et al.*, 2002]. We have chosen fractional calculus to calculate this nonlocal flux, and we formulated a fractional advection equation that binds this nonlocal flux to the erosion of bedrock, to the buffering of the erosion rate by sediment cover, and to the hillslope-channel linked process of sediment supply.

[44] By assuming a simplified channel and catchment geometry, we have obtained closed form, steady state solutions of the two governing equations for sediment cover thickness, channel bed elevation and channel gradient as a function of downstream distance. These analytical solutions provide useful insights into the model behavior and its implications for bedrock rivers. For example, we find that if sediment buffering is very weak, a steady state logarithmic bedrock river profile is obtained (the log form originates in an assumption of simple scaling in the hydraulic geometry

and in the stream power model of bedrock incision); more general scaling forms would give a power law profile. If significant buffering of bed erosion is present, nonlocal advection of sediment results in a power law profile whose scaling exponent is set by the degree of fractional advection Lévy exponent α. These results are illustrated in Figure 4 where $\alpha = 0.9$ is close to local advection and $\alpha = 0.1$ signifies a high degree of nonlocal behavior.

[45] An important model result is that at steady state the nonlocal bed sediment flux (Figure 6a) reaches a constant value all along the river (equation (48)), which is equivalent to saying that the sediment discharge per unit channel cross-sectional area, Q_s/wd, reaches a constant. Since the flux is the distance-weighted summation of mobile bed sediment upstream calculated through the fractional integral of dimensionless bed sediment $I_x^{1-\alpha}\{C(x)\}$ (equation (12)), the variable $C(x)$ must decrease downstream as a power law $C(x) \sim x^{\alpha-1}$ (equation (37)). The nonintuitive consequence is that bed sediment cover thickens more slowly than linearly downstream as $B(x) \sim x^\alpha$, since $0 \leq \alpha < 1$.

[46] Perhaps the most important model result is that strong sediment buffering overwhelms the scaling effect
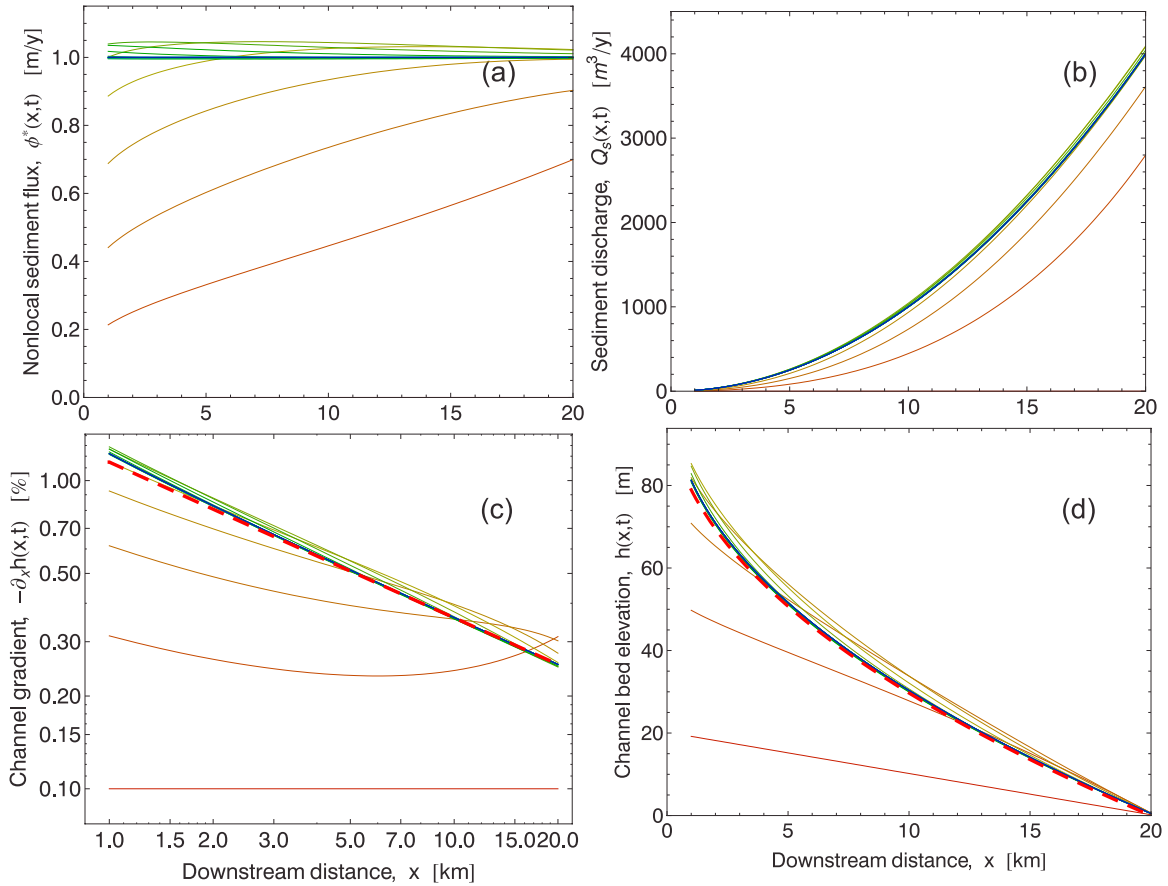
Figure 6. River profile evolution (continued from Figure 5) for (a) nonlocal bed sediment flux $\phi^*(x, t)$, (b) sediment discharge $Q_s(x, t)$, (c) bedrock channel gradient $-\partial_x h(x, t)$, and (d) bedrock channel elevation (river profile) $h(x, t)$. Solid lines are numerical solutions at successive time steps; the dashed lines are the asymptotic, closed form solutions at steady state.

of the underlying bedrock incision law [*Stark et al.*, 2000]. For heavy sediment cover, or simply at sufficient distance downstream, the asymptotic scaling of slope with upstream area is determined instead by the scaling of the fractional advection process, namely $S \sim A^{-(1-\alpha)/2}$. power law scaling of slope versus area is consistent with many empirical studies of topographic scaling [e.g., *Tarboton et al.*, 1989; *Sklar and Dietrich*, 1998; *Whipple*, 2004], for which $S \sim A^{-\theta}$ defines a "concavity index" [*Flint*, 1974] equal to $\theta = (1 - \alpha)/2$. Since typically observed values of this index are around $\theta \approx 1/2$, the empirical data are consistent with a strongly nonlocal process of sediment buffering for which $\alpha \to 0$. In fact, the simple model scaling assumptions used here (section 4) force an upper bound on our predicted concavity index of $\theta \leq 1/2$ since $\alpha \geq 0$ [*Lévy*, 1937; *Feller*, 1971; *Benson*, 1998]. However, a more general treatment of catchment and channel hydraulic scaling would relax this bound to permit higher values of $\theta > 1/2$ as observed in many analyses of digital elevation models. In any case, our model provides a radical alternative to the standard interpretation [e.g., *Montgomery*, 2001; *Whipple*, 2004] of this scaling that the concavity index is the ratio of the exponents in a stream power formulation of bedrock incision rate. A careful examination of slope-area scaling in the context of the pattern and duration of bed sediment

cover in mixed bedrock-alluvial rivers may provide a means of testing these alternative models.

[47] Finally, the temporal evolution of the proposed coupled system of governing equations provides insight into the dynamics of bedrock incision. Our one-dimensional results indicate that the bedrock sediment incision interplay results in a nonlinear but highly damped system which has well behaved steady state solutions. The transient effect of powerful perturbations on this model system, particularly when extended to two dimensions (a full network), is an issue that requires further study.

Appendix A

A1. Fractional Calculus

[48] Fractional integration of order q is defined as convolution with a power law "memory" kernel, which we write as

$$I_x^q \{f\} = \frac{1}{\Gamma(q)} \int_0^x \frac{f(\zeta)}{(x - \zeta)^{1-q}} d\zeta. \qquad (A1)$$

The lower limit of the integral at $x = 0$ defines (in this study) the drainage divide. Fractional differentation is derived from

this convolution: in its Riemann-Liouville form the fractional derivative operator of order q is

$$\partial_x^q \{f\} = \frac{1}{\Gamma(1-q)} \frac{d}{dx} \left\{ \int_0^x \frac{f(\zeta)}{(x-\zeta)^q} d\zeta \right\} \qquad (A2)$$

for $0 \leq q < 1$.

[49] Application of the fractional integral operator of order $1 - \alpha$ to a power function of order β gives

$$I_x^{1-\alpha} \{x^\beta\} = \frac{\Gamma(\beta+1)}{\Gamma(\beta-\alpha)} x^{\beta-\alpha+1} \qquad (A3)$$

and the fractional derivative of the same function is

$$\partial_x^{1-\alpha} \{x^\beta\} = \frac{\Gamma(\beta+1)}{\Gamma(\beta+\alpha)} x^{\beta+\alpha-1}, \qquad (A4)$$

and so the fractional derivative of order $1 - \alpha$ of a constant ($\beta = 0$) is

$$\partial_x^{1-\alpha} \{c\} = \frac{c}{\Gamma(\alpha)} x^{\alpha-1}. \qquad (A5)$$

[50] The idea of nonlocal transport of particles can be expressed as a hopping process where the hop length belongs to a heavy-tailed probability distribution: after many hops, the Lévy limit theorem [*Lévy*, 1937; *Feller*, 1971; *Stark et al.*, 2000] predicts that the pdf of transport distance will have a Lévy stable distribution whose tail decays as a power law. The motion of particles in an aggregate sense can be expressed as a convolution of the initial spread of particles with a power law kernel with the same scaling [e.g., *Cushman and Ginn* 2000]. Therefore the fractional integral equation (A1) is a macroscopic description of a nonlocal hopping process. Further details can be found in, for example, *Benson* [1998], *Benson et al.* [2000a, 2000b], *Feller* [1971], *Gorenflo and Mainardi* [1997, 1999, 1998b, 1998a], *Gorenflo* [1997], *Gorenflo et al.* [1999], *Mainardi et al.* [1998], *Lévy* [1937], *Mantegna* [1994], *Meerschaert et al.* [1999], *Miller and Ross* [1993], *Oldham and Spanier* [1974], *Podlubny* [1999], *Saichev and Zaslavsky* [1997], *Samko et al.* [1993], *Samorodnitsky and Taqqu* [1994]. If the power law tail is truncated, the formalism of continuous time random walks (CTRW) is more applicable [e.g., *Berkowitz et al.*, 2002; *Mantegna and Stanley*, 1994].

[51] The Grünwald-Letnikov discrete approximation of the fractional integral operator is [*Grünwald*, 1867; *Podlubny*, 1999]

$$I_x^\gamma \{f\} = \lim_{\Delta x \to 0} (\Delta x)^\gamma \sum_{k=0}^{x/\Delta x} \frac{\Gamma(\gamma+k)}{k! \Gamma(\gamma)} f(x - k\Delta x). \qquad (A6)$$

A2. Power Law Pdfs Via Mixing Distributions

[52] A common approach to treating distributions of empirical data is to assume the quantity in question belongs to a single pdf of parametric form, reducing the task to finding this form and inferring its parameters. In reality, physical data typically involve quantities derived from several "parent" quantities that are themselves distributed; even if the parent random variables belong to pdfs of classical form, the derived random variable likely will not. It is therefore safe to assume that most natural data are the result of the transformation and mixing of multiple random variables.

[53] Mixing can easily give rise to a power law pdf. For example, if one assumes that the distribution of sediment transport distances for a given grain size D is exponential then one can write

$$\mathbb{P}(X \geq x \mid D) = \exp(-x/\lambda_D). \qquad (A7)$$

The mean transport distance is the coefficient λ_D which we assume is inversely proportional to grain size [*Hassan and Church*, 1991],

$$\lambda_D = \kappa/D. \qquad (A8)$$

We further assume a gamma distribution of grain sizes

$$f(D \mid \alpha, D_{\mathrm{m}}) = \frac{\alpha^\alpha}{\Gamma(\alpha) D_{\mathrm{m}}^\alpha} D^{\alpha-1} \exp\left(-\alpha \frac{D}{D_{\mathrm{m}}}\right), \qquad (A9)$$

whose mean (not median) is D_{m} and whose shape parameter is $\alpha \geq 0$. Combining these equations we obtain the transport distance distribution of a grain of arbitrary (randomly selected) size

$$\mathbb{P}(X \geq x) = \left(1 + \left(\frac{D_{\mathrm{m}}}{\alpha\kappa}\right) x\right)^{-\alpha}, \qquad (A10)$$

which is a generalized Pareto distribution. For larger hop distances $x \gg \alpha\kappa/D_{\mathrm{m}}$ the transport probability decays as a power law. If the duration and intensity of transport events are single valued, the distribution of particle velocities will asymptotically be as given in equation (10). If event duration and intensity (bed shear stress) are stochastic variables, further mixing will occur and the power law tail will change shape further. Summation of multiple hops will drive the long-term distribution toward a Lévy stable law with $0 \leq \alpha \leq 2$.

A3. Connection to FADE Models

[54] The nonlocal flux equation (12) is a form of fractional advection that differs from the fractional advection-dispersion equations (FADE) tailored to treat contaminant transport problems in porous media [e.g., *Benson*, 1998; *Benson et al.*, 2000a, 2000b]. In such FADE models, a fractional derivative operator is used in the dispersion term only, i.e., such models describe fractional dispersion driven by classical advection. The sole published FADE model that considers nonlocality in both the advection and dispersion terms is that of *Baeumer et al.* [2001]. Their model considers the classical advection-dispersion equation to hold locally for each particle, but at rates that vary broadly as the particle samples (during the history of its motion) more

and more of the heterogeneities of the porous medium. This formulation leads *Baeumer et al.* [2001] to consider model time as a random variable ("operational time") and to extend the standard ADE to a combined fractional advection and fractional dispersion (FAFD) model through a stochastic operation known as subordination.

[55] The fractional advection component of the model presented here can be considered a special case of the FAFD model of *Baeumer et al.* [2001] in which, for the purpose of clarity, the dispersion term is set to zero. In the future, our model could be extended to include either classical or fractional dispersion, but the scaling effect on sediment buffering is likely to be very similar to that of the fractional advection already included in the model.

Notation

Model Variables

t	time (years).
x	distance downstream from divide (m).
$Q(x)$	characteristic discharge (m^3/s).
$w(x)$	flow width at characteristic discharge (m).
$d(x)$	flow depth at characteristic discharge (m).
$W(x)$	catchment width (m).
$A_c(x)$	catchment area (m^2).
$h(x, t)$	elevation of bedrock channel profile (m).
$\Omega(Q)$	unit stream power (W/m).
$\xi_a(x, t)$	sediment-buffered bedrock erosion rate (m/a).
$-\partial_t h(x, t)$	rate of bed lowering (m/a).
$-\partial_x h(x, t)$	downstream bed and energy slope (dimensionless).
$B(x, t)$	bed sediment cover thickness (m).
$C(x, t)$	relative bed cover (dimensionless).
$A_s(x)$	bed sediment cross-sectional area (m^2).
$\varphi(x, t)$	sediment supply by hillslope erosion (m^2/a).
$\phi^*(x, t)$	downstream bed sediment flux (m/a).
$Q_s(x)$	annual bed sediment discharge (m^3/a).
$u(x, t)$	uplift rate pattern (m/a).

Model Parameters

α	bed cover fractional advection exponent (dimensionless).
x_0	reference downstream distance (m).
Q_0	characteristic water discharge at x_0 (m^3/s).
w_0	channel flow width at x_0, Q_0 (m).
d_0	channel flow depth at x_0, Q_0 (m).
W_0	catchment width at x_0 (m).
χ	coarse (bed) fraction of sediment supply (dimensionless).
v_0	reference annual bedload speed (m/a).
u_0	uplift rate (regionally uniform) (m/a).
f	annual frequency of Q_0 flows (1/a).
ρ	density of water (kg/m^3).
g	acceleration due to gravity (m/s^2).
γ	reference erodibility (m^3/J).
t_f	duration of Q_0 flood event (s).
μ	flood effectiveness (s/m).
$\eta_r = \eta_{rock}$	bedrock erodibility (dimensionless).
$\eta_s = \eta_{sed}$	bed sediment erodibility (dimensionless).
h_0	initial bed elevation at divide $x = 0$ (m).

x_l	downstream limit distance (fault boundary) (m).
n	number of resolved points along profile (dimensionless).
Δx	point spacing along profile (m).
Δt	numerical solution time step (years).
θ	slope-area scaling exponent (dimensionless).

References

Baeumer, B., D. A. Benson, M. M. Meerschaert, and S. W. Wheatcraft (2001), Subordinated advection-dispersion equation for contaminant transport, *Water Resour. Res.*, *37*(6), 1543–1550.

Benson, D. A. (1998), The fractional advection-dispersion equation: Development and application, Ph.D. thesis, University of Nevada, Reno, Nev.

Benson, D. A., S. W. Wheatcraft, and M. M. Meerschaert (2000a), Application of a fractional advection-dispersion equation, *Water Resour. Res.*, *36*(6), 1403–1412.

Benson, D. A., S. W. Wheatcraft, and M. M. Meerschaert (2000b), The fractional-order governing equation of Lévy motion, *Water Resour. Res.*, *36*(6), 1413–1423.

Berkowitz, B., J. Klafter, R. Metzler, and H. Scher (2002), Physical pictures of transport in heterogeneous media: Advection-dispersion, random-walk, and fractional derivative formulations, *Water Resour. Res.*, *38*(10), 1191, doi:10.1029/2001WR001030.

Church, M., and M. A. Hassan (1992), Size and distance of travel of unconstrained clasts on a streambed, *Water Resour. Res.*, *28*(1), 299–303.

Cushman, J., and T. Ginn (2000), Fractional advection-dispersion equation: A classical mass balance with convolution-fickian flux, *Water Resour. Res.*, *36*(12), 3763–3766.

Dadson, S. J. (2004), Erosion of an active mountain belt, Ph.D. thesis, University of Cambridge, Cambridge, U. K.

Dadson, S. J., et al. (2004), Earthquake-triggered increase in sediment delivery from an active mountain belt, *Geology*, *32*(8), 733–736.

Dietrich, W. E., D. G. Bellugi, L. S. Sklar, J. D. Stock, A. M. Heimsath, and J. J. Roering (2003), Geomorphic transport laws for predicting landscape form and dynamics, in *Prediction in Geomorphology*, *Geophys. Monogr. Ser.*, vol. 135, edited by P. R. Wilcock and R. M. Iverson, pp. 103–132, AGU, Washington, D. C.

Dodov, B., and E. Foufoula-Georgiou (2004), Generalized hydraulic geometry: Derivation based on multiscaling formalism, *Water Resour. Res.*, *40*, W06302, doi:10.1029/2003WR002082.

Feller, W. (1971), *An Introduction to Probability Theory and Its Applications*, vol. 2, 2nd ed., Wiley, New York.

Finnegan, N. J., L. S. Sklar, and T. K. Fuller (2007), Interplay of sediment supply, river incision, and channel morphology revealed by the transient evolution of an experimental bedrock channel, *J. Geophys. Res.*, *112*, F03S11, doi:10.1029/2006JF000569.

Flint, J. J. (1974), Stream gradient as a function of order, magnitude, and discharge, *Water Resour. Res.*, *10*, 969–973.

Gabet, E. J., D. W. Burbank, B. Pratt-Sitaula, J. Putkonen, and B. Bookhagen (2008), Modern erosion rates in the High Himalayas of Nepal, *Earth Planet. Sci. Lett.*, *267*(3–4), 482–494.

Gorenflo, R. (1997), Fractional calculus: Some numerical methods, in *Fractals and Fractional Calculus in Continuum Mechanics*, edited by A. Carpinteri and F. Mainardi, pp. 277–290, Springer-Verlag, Wien, Germany.

Gorenflo, R., and F. Mainardi (1997), Fractional calculus: Integral and differential equations of fractional order, in *Fractals and Fractional Calculus in Continuum Mechanics*, edited by A. Carpinteri and F. Mainardi, pp. 223–276, Springer-Verlag, Wien, Germany.

Gorenflo, R., and F. Mainardi (1998a), Feller fractional diffusion and Lévy stable motions, paper presented at 5th Conference on Lévy processes: Theory and Applications, MaPhySto Cent., Dept. of Appl. Math. and Stat., Univ. of Aarhus, Copenhagen.

Gorenflo, R., and F. Mainardi (1998b), Random walk models for space-fractional diffusion processes, *Fractional Calculus Appl. Anal.*, *1*(2), 167–191.

Gorenflo, R., and F. Mainardi (1999), Approximation of Lévy-Feller diffusion by random walk, *J. Anal. Appl.*, *18*(2), 231–246.

Gorenflo, R., G. D. Fabritiis, and F. Mainardi (1999), Discrete random walk models for symmetric Lévy-Feller diffusion processes, *Physica A*, *269*, 79–89.

Grünwald, A. K. (1867), Uber "begrenzte" derivation und deren anwendung, *Z. Angew. Math. Phys.*, *12*, 441–480.

Gupta, V. K., and E. Waymire (1989), Statistical self-similarity in river networks parameterized by elevation, *Water Resour. Res.*, *25*(3), 463–476.

Gupta, V. K., O. J. Mesa, and D. Dawdy (1994), Multiscaling theory of floods: Regional quantile analysis, *Water Resour. Res.*, *30*, 3405–3421.

Harp, E. L., and R. W. Jibson (1996), Landslides triggered by the 1994 Northridge, California, earthquake, *Bull. Seismol. Soc. Am.*, *86*, S319–S332.

Hassan, M. A., and M. Church (1991), Distance of movement of coarse particles in gravel bed streams, *Water Resour. Res.*, *27*(4), 503–511.

Lague, D., N. Hovius, and P. Davy (2005), Discharge, discharge variability, and the bedrock channel profile, *J. Geophys. Res.*, *110*, F04006, doi:10.1029/2004JF000259.

Lévy, P. (1937), *Théorie de l'Addition des Variables Aléatoires*, Gauthier-Villars, Paris.

Lin, C. W., C. L. Shieh, B. D. Yuan, Y.-C. Shieh, S. H. Liu, and S. Y. Lee (2003), Impact of the Chi-Chi earthquake on the occurrence of landslides and debris flows: Example from the Chenyulan River watershed, *Eng. Geol.*, *71*, 49–61.

Mainardi, F., P. Paradisi, and R. Gorenflo (1998), Probability distributions generated by fractional diffusion equations, in *Econophysics*, edited by J. Kertèsz and I. Kondor, Kluwer, Dordrecht, Netherlands.

Mantegna, R. N. (1994), Fast, accurate algorithm for numerical simulations of Lévy stable stochastic processes, *Phys. Rev. E*, *49*, 4677–4683.

Mantegna, R. N., and H. E. Stanley (1994), Stochastic process with ultra-slow convergence to a Gaussian: The truncated Lévy flight, *Phys. Rev. Lett.*, *73*, 2946–2949.

Meerschaert, M. M., D. A. Benson, and B. Baeumer (1999), Multidimensional advection and fractional dispersion, *Phys. Rev. E*, *59*(5), 5026–5028.

Miller, K. S., and B. Ross (1993), *An Introduction to the Fractional Calculus and Fractional Differential Equations*, Wiley, New York.

Molnar, P., R. S. Anderson, G. Kier, and J. Rose (2006), Relationships among probability distributions of stream discharges in floods, climate, bed load transport, and river incision, *J. Geophys. Res.*, *111*, F02001, doi:10.1029/2005JF000310.

Montgomery, D. R. (2001), Slope distributions, threshold hillslopes, and steady-state topography, *Am. J. Sci.*, *301*, 423–454.

Oldham, K. B., and J. Spanier (1974), *The Fractional Calculus*, Academic, New York.

Podlubny, I. (1999), *Fractional Differential Equations*, vol. 198, Academic, San Diego.

Rhoads, B. (1987), Stream power terminology, *Prof. Geogr.*, *39*(2), 189–195.

Saichev, A. I., and G. M. Zaslavsky (1997), Fractional kinetic equations: Solutions and applications, *Chaos*, *7*(4), 753–764.

Samko, S. G., A. A. Kilbas, and O. I. Marichev (1993), *Fractional Integrals and Derivatives: Theory and Applications* (translated from Russian), Gordon and Breach, Zurich.

Samorodnitsky, G., and M. S. Taqqu (1994), *Stable Non-Gaussian Random Processes: Stochastic Models with Infinite Variance*, Chapman and Hall, London.

Sklar, L., and W. E. Dietrich (1998), River longitudinal profiles and bedrock incision models: Stream power and the influence of sediment supply, in *Rivers Over Rock: Fluvial Processes in Bedrock Channels, Geophys. Monogr. Ser.*, vol. 107, edited by K. J. Tinkler and E. E. Wohl, pp. 237–260, AGU, Washington, D. C.

Sklar, L., and W. E. Dietrich (2001), Sediment and rock strength controls on river incision into bedrock, *Geology*, *29*, 1087–1090, doi:10.1130/0091-7613(2001)029<1087:SARSCO>2.0.CO;2.

Sklar, L., and W. E. Dietrich (2004), A mechanistic model for river incision into bedrock by saltating bedload, *Water Resour. Res.*, *40*, W06301, doi:10.1029/2003WR002496.

Sklar, L., and W. E. Dietrich (2006), The role of sediment in controlling steady-state bedrock channel slope: Implications of the saltation-abrasion incision model, *Geomorphology*, *1–2*, 58–83.

Snyder, N. P., K. X. Whipple, G. E. Tucker, and D. M. Merritts (2003), Importance of a stochastic distribution of floods and erosion thresholds in the bedrock river incision problem, *J. Geophys. Res.*, *108*(B2), 2117, doi:10.1029/2001JB001655.

Stark, C. P. (2006), A self-regulating model of bedrock river channel geometry, *Geophys. Res. Lett.*, *32*, L04402, doi:10.1029/2005GL023193.

Stark, C. P., J. K. Weissel, and P. S. Dodds (2000), A Lévy diffusion model of sediment transport and landscape evolution, *EOS, Trans. AGU*, *81*(48), Fall Meet. Suppl., Abstract H12B-13.

Stock, J. D., and D. R. Montgomery (1999), Geologic constraints on bedrock river incision using the stream power law, *J. Geophys. Res.*, *104*(B3), 4893–4993.

Tarboton, D. G., R. L. Bras, and I. Rodriguez-Iturbe (1989), Scaling and elevation in river networks, *Water Resour. Res.*, *25*(9), 2037–2051.

Tinkler, K. J., and E. E. Wohl (Eds.) (1998), *Rivers Over Rock: Fluvial Processes in Bedrock Channels, Geophys. Monogr. Ser.*, vol. 107, AGU, Washington, D. C.

Tucker, G. E., and R. L. Bras (2000), A stochastic approach to modeling the role of rainfall variability in drainage basin evolution, *Water Resour. Res.*, *36*(7), 1953–1964.

Turowski, J. M., N. Hovius, A. Wilson, and M.-J. Horng (2008), Hydraulic geometry, river sediment and the definition of bedrock channels, *Geomorphology*, *99*(1–4), 26–38, doi:10.1016/j.geomorph.2007.10.001.

Whipple, K. X. (2004), Bedrock rivers and the geomorphology of active orogens, *Annu. Rev. Earth Planet. Sci.*, *32*, 151–185.

Whipple, K. X., and G. E. Tucker (1999), Dynamics of the stream-power river incision model: Implications for height limits of mountain ranges, landscape response timescales, and research needs, *J. Geophys. Res.*, *104*, 17,661–17,674.

Wobus, C. W., G. E. Tucker, and R. S. Anderson (2006), Self-formed bedrock channels, *Geophys. Res. Lett.*, *33*, L18408, doi:10.1029/2006GL027182, 1–6.

Zhang, Y., D. A. Benson, M. M. Meerschaert, and E. M. LaBolle (2007), Space-fractional advection-dispersion equations with variable parameters: Diverse formulas, numerical solutions, and application to the Macrodispersion Experiment site data, *Water Resour. Res.*, *43*, W05439, doi:10.1029/2006WR004912.

————————

E. Foufoula-Georgiou and V. Ganti, St. Anthony Falls Laboratory, University of Minnesota, 2 Third Avenue SE, Minneapolis, MN 55414, USA.

C. P. Stark, Lamont-Doherty Earth Observatory of Columbia University, 61 Route 9W, Palisades, NY 10964, USA. (cstark@ldeo.columbia.edu)

A Theoretical Framework for Interpreting and Quantifying the Sampling Time Dependence of Gravel Bedload Transport Rates

Kurt Fienberg[1], Arvind Singh[1], Efi Foufoula-Georgiou[1], Doug Jerolmack[1] and Jeffrey D.G. Marr[1]

[1]St. Anthony Falls Laboratory (SAFL) and National Center for Earth-surface Dynamics (NCED) University of Minnesota, Minneapolis, MN 55414

Abstract

Field studies have documented that the average bedload transport rate in gravel bed streams depends on the sampling time (or integration time) over which this average is computed. In this paper we use sediment transport data from a controlled laboratory experiment to document and quantify the dependence on sampling time not only of the mean but of the whole probability density function (pdf) of sediment transport rates in a gravel bed stream. We demonstrate that the higher moments (variance and skewness) scale differently than the mean and we provide a concise parameterization of this statistical scale-dependence. The results indicate that the mean sediment transport rate in moderate flows decreases with increasing sampling time, in agreement with results reported in field studies. The proposed methodology provides a framework within which to seek universal scaling relationships, compare results of different samplers, and also interpret extremes.

1. Introduction

In a recent study Bunte and Abt (2005) have provided an excellent account of the problem of sampling time dependence of gravel bedload transport rate and its importance for interpreting estimates from different samplers. They also provided a detailed quantification of this dependence for a range of flows in a gravel-bedded stream. Their results indicated that in moderate to high flows flows (50% bankfull to almost bankfull conditions) 2 min sampling led to an average transport rate 2 to 5 times lower than that found with 10 min sampling. However, at lower flows (close to the incipient gravel motion) 2 min sampling overestimated the transport rates at 10 min sampling by a factor of almost 3. The fact that bedload discharge measurements depend on both sampling time and mean flow rate was also shown by the field measurements at different time scales documented by Ergenzinger et al. (1994).In this study we restrict our analysis to the sampling time dependence in the low flow case, with results from a higher flow experiment to be presented by the authors in a follow-up work (Singh et al., 2008). The explanation of the sampling interval dependence at low flow has generally been that the instantaneous sediment transport rates exhibit rare but very high fluctuations (due to the irregular and stochastic nature of particle movement on the bed) and thus integrating over variable time intervals changes the chance of sampling these high fluctuations. Translating this to a statistical interpretation, at very small sampling intervals the chance of sampling very high fluctuations is small and thus the pdf of sediment transport rates is highly skewed (only a small number of very high values is present); as the sampling interval increases however, more of these high fluctuations are likely to be sampled. Although most studies have been concerned only with how the mean changes with the sampling interval, it is also of interest to study the whole pdf and quantify how the shape (or the higher order statistical moments) of this pdf change as the scale (sampling interval) changes. This is important as often it is not only the mean but the variability of the sediment transport rates, including extreme quantiles, that is important in many ecological studies, e.g., studies that incorporate the effect of bedload sediment on stream habitat.

The sampling-time dependence of bedload transport rates has important practical implications for bedload measurements in the field. Several researchers (e.g. Gomez et al. 1989, Kuhnle 1996, Wilcock 2001) have argued for sampling durations that are long enough to smooth out fluctuations and measure the "true mean" transport rate for a particular level of flow. But determining the time period that fits this criterion requires knowledge of the way in which the statistics of the transport rate vary with sampling interval. In addition, practical limitations can restrict sampling time to be less than this ideal: the sampling instrument used may have a limited capacity (such as a Helley-Smith type sampler), or variations in flow rate may mean that the system can not be considered stable over such a long period. In such situations, interpreting results and comparing measurements with different sampling times requires a quantitative understanding of the dependence of bedload transport on temporal scale.

The first objective of this study is to use the results of a controlled and well-instrumented experimental set-up, described in Section 2, to reproduce some of the effects of sampling interval that have been observed in the field. By continuously measuring the mass of transported gravel bedload through an experimental flume at high temporal resolution, and then averaging over different time intervals, it is possible to simulate sampling the transport rate over different time periods. The second objective is to develop a

1

theoretical framework for quantifying the variations in the statistical properties of bedload transport with changing sampling interval. This framework is outlined in section 3, and is focused on the ideas of scale-invariance, or the search for statistical quantities that remain the same with change of scale or can be transformed from one scale to another in a straightforward way. Of course, in this work the scale to which we refer is the temporal scale, i.e. the sampling time of the bedload transport. The results of applying this framework to the experimental data are presented in section 4, and the implications are discussed in section 5.

2. Data Used In This Study

2.1 Experimental set-up and data processing

In order to investigate the dependence of bedload sediment transport on sampling time, we examine experimental data from the Main Channel facility at the St. Anthony Falls Laboratory, University of Minnesota. These experiments were conducted as part of a larger-scale experimental program (called StreamLab06) supported by the National Center for Earth-surface Dynamics (NCED) at the University of Minnesota. The flume used in this study is 2.74 m wide and 55 m long, with a maximum depth of 1.8 m. Gravel with a median particle size (d_{50}) of 11.3 mm was placed in a 20m long mobile-bed section of the 55 m long channel. The grain size distribution for the bed material is shown in **Figure 1.** A constant discharge of water at 4300 liters per second was released into the flume. This was estimated to generate a dimensionless bed stress of about twice the critical value required to move the bedload sediment (Shields stress = 0.085 using median gravel diameter). At the downstream end of the test section was located a bedload trap, consisting of 5 weighing pans of equal size that spanned the width of the channel, as seen in **Figure 2**. Any bedload sediment transported to the end of the test-section of the channel would fall into the weigh pans, which automatically recorded the mass they contained every 1.1 seconds. Upon filling with a maximum of 20 kg the weigh pans would tip to release the sediment into the collection hopper located below and reset the weigh pan.

The flume is a partial-recirculating flume; it has the ability to recirculate gravel while water flows through the flume without recirculation. A large collection hopper located underneath the weigh pans serves to collect and store gravel dumped out of the weigh drums and also serves as the material source for the recirculation system. The rate of gravel removal out of this hopper and delivered to the upstream end of the flume via a large pump is set by adjusting the rotation speed of a large helix, which serves to push gravel laterally out of the hopper and into the recirculation line. In this way, the collection hopper and helix serve to buffer small fluctuations in sediment flux out of the flume and provide a more steady "feed-type" delivery of sediment to the upstream end. Because the physical size of the collection hopper is finite, the auger

speed (upstream feed rate) was adjusted to match the actual transport in the flume such that we would always observe storage of gravel in the hopper.
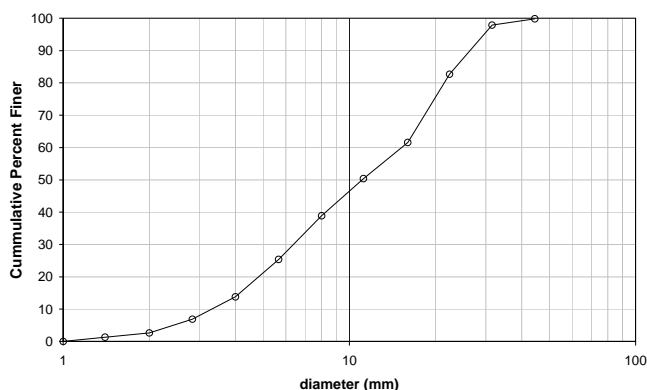
Figure 1 Grain Size Distribution of the bed surface.

Before any measurements were taken, the water supply in the flume was turned on to 4300 liters per second and was allowed to run 15 hr to develop a dynamic equilibrium in transport and slope adjustment of the water surface and bed. Determination of the dynamic equilibrium state was made by checking that the 60 min average flux was stabilized to an almost constant value during the flume run. The bedload transport data were then recorded continuously for approximately 16 hours through the rest of the experiment.

Figure 2. Weighing Pans located at the downstream end of the test channel. The experiment was conducted at the St. Anthony Falls Laboratory, National Center for Earth-surface Dynamics, University of Minnesota.

The raw sediment accumulation data was pre-processed prior to the analysis presented here. The pre-accumulation of sediment ($S_c(t)$) time series for each weigh pan over the duration of the experiment. An example of this series can be seen in Figure 3. A single tipping event requires the removal of no more than eight data points (~8.8 seconds) of the record. On average, a single weigh pan tipped every 1.5 hr. Overall, the data affected by the weigh pan tipping constitutes less than 0.15% of the total data record and is, thus, negligible. The sediment accumulation $S(t, \Delta t)$ measured over a sampling interval Δt is then simply

$$S(t, \Delta t) = S_c(t + \Delta t) - S_c(t). \qquad (1)$$
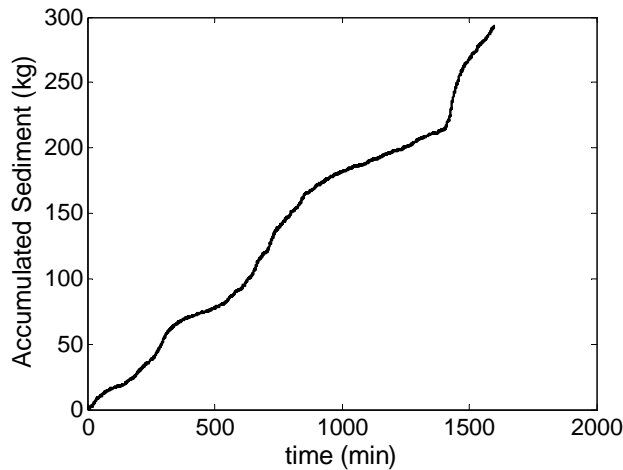
Figure 3 Time series of the total accumulated sediment $S_c(t)$

If the sampling interval Δt is taken to be very small, such as the original 1.1 sec resolution of the data series, one observes a large number of negative values of $S(t, \Delta t)$, as shown in **Figure 4a**. These negative values are clearly not physically plausible since by the experimental design (**Figure 2**) the sediment can only pass in one direction, down onto the weigh pans, and hence $S(t, \Delta t)$ should only be positive. Thus, these negative sediment accumulations are attributed to the mechanical noise produced by: the natural oscillation of the weigh pans after being hit by the falling gravel; the fluctuating water surface over the pan; and the vibration caused by the large gravel pump which was placed near to the weigh pans (for further discussion of the errors associated with weigh pans and possible processing techniques, see Laronne et al., 2003). This noise can be smoothed out by considering longer sampling

processing involves removal of weigh pan dumping events from the data and translating the data set into a continuous intervals Δt. It was found that the occurrence of negative values of $S(t, \Delta t)$, and hence the significance of the noise relative to the signal, was greatly reduced once the temporal scale Δt was increased to about 2 min. **Figure 4b** shows the time series $S(t, \Delta t)$ for $\Delta t = 2$ min. Hence to avoid noise distortion, we will mainly interpret results for temporal aggregation scales longer than 2 min.
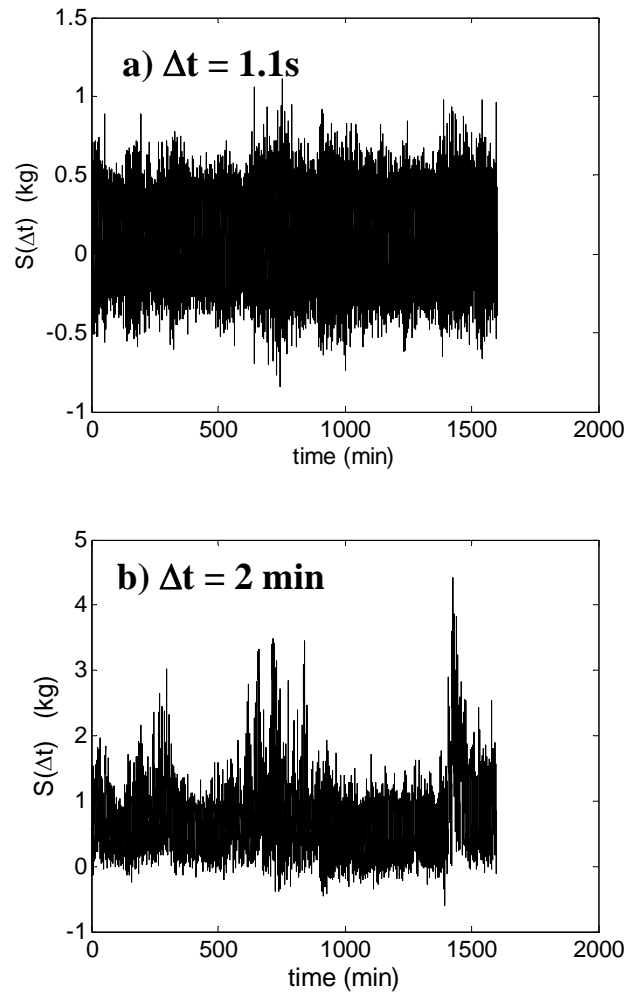
Figure 4. The time series of the sediment, $S(\Delta t)$, accumulated over sampling intervals Δt of: (a) 1.1 seconds and (b) 2 min.

2.2 Statistical distribution of the data.

To begin investigating the statistical properties of bedload transport and it's dependence on sampling interval, consider the sediment transport rate, given by $(S(t, \Delta t) / \Delta t)$. The pdfs of the sediment transport rate, calculated at sampling intervals of 2, 5, 10, and 15 min, are shown in **Figure 5**. At the smallest scale, $\Delta t = 2$ min, the probability distribution is wider, with a higher mean and standard deviation than at the longer sampling intervals. As the sampling interval increases, the mean decreases slightly and the standard deviation decreases more significantly, as the distributions become more tightly peaked at longer sampling time. Note that the pdf remains negatively skewed at the larger temporal scales. One measure of the shape of the probability distribution is the coefficient of variation, C_v, which is the ratio of the standard deviation to the mean,

$$C_v = \frac{\sigma}{\mu}.$$ For the sediment transport rate, C_v decreases with increasing temporal scale, as shown in **Figure 6**. So the width of the pdf, relative to the mean, diminishes with increasing sampling time.
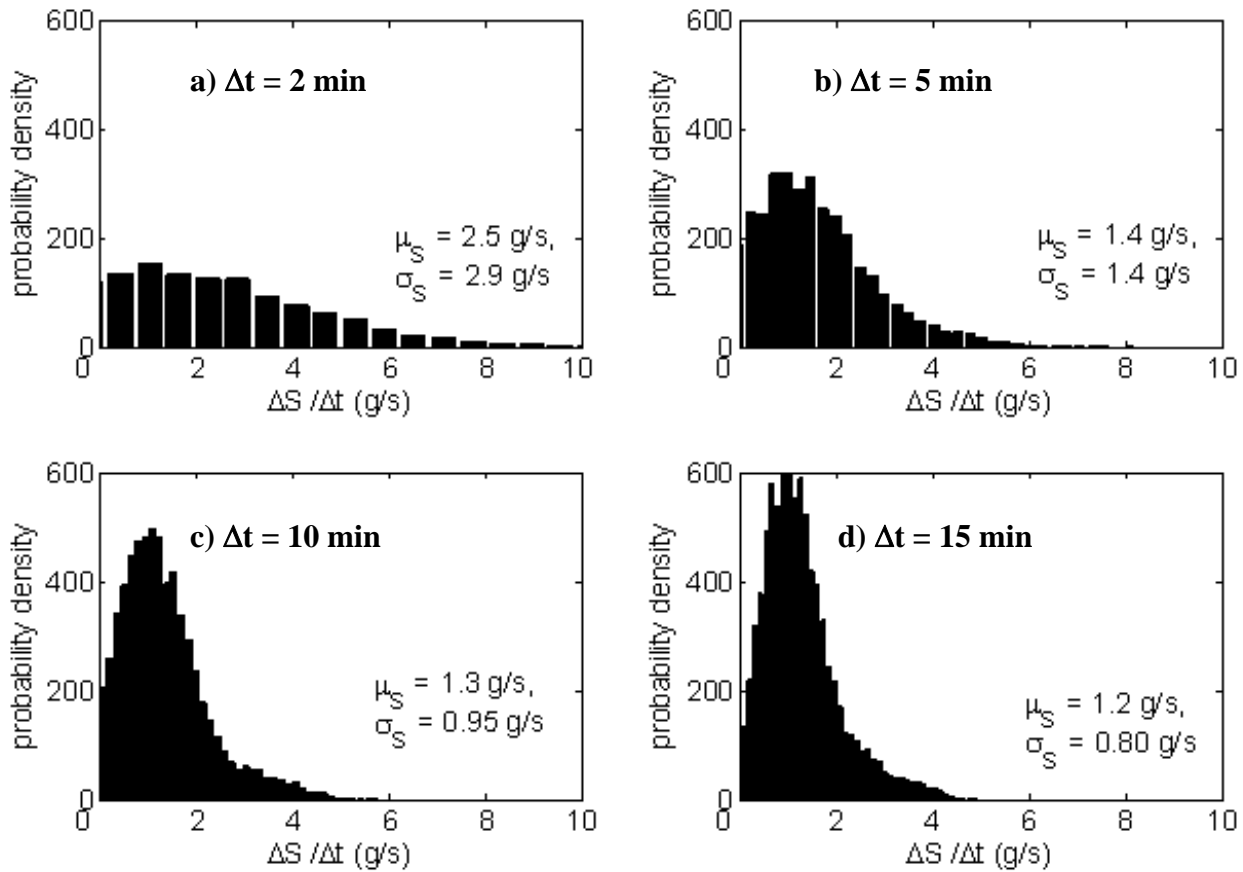
Figure 5. Probability density function of sediment transport rate for different sampling intervals (2, 5, 10, 15 min), with mean and standard deviation listed (units of g/s).
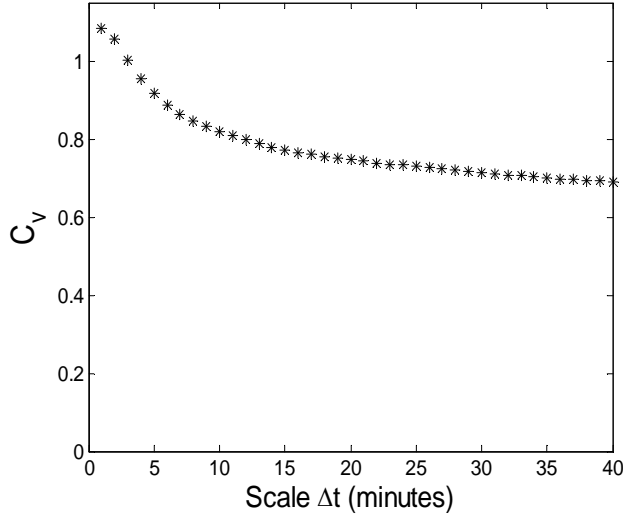
Figure 6. The coefficient of variation of sediment transport rate as a function of temporal scale Δt (sampling interval).

3. Framework of Analysis

If the sediment transport rate $(S(t, \Delta t) / \Delta t)$ was independent of the sampling interval, the mean of the accumulated sediment $S(t, \Delta t)$ would depend linearly on Δt; that is, in twice as large a sampling interval, on the average twice as much sediment would be accumulated,. In practice, however, it has been found that the mean of $S(t, \Delta t)$ depends on Δt in a way that has not yet been statistically characterized. The purpose of this paper is to explore whether this dependence falls under any scale invariance characterization, widely found in turbulence and other geophysical processes (e.g., see Parisi and Frisch 1985; Lovejoy et al., 1993; Gupta et al. 1994; Foufoula-Georgiou 1998; Sornette and Ouillon 2005; Venugopal et al. 2006, Lashermes and Foufoula-Georgiou, 2007).

Let us define the q-th statistical moment $< S(\Delta t)^q >$ as the expectation value of the q-th power of $S(t, \Delta t)$, which is estimated by

$$\left\langle S(\Delta t)^q \right\rangle = \frac{1}{N} \sum_{t=1}^{N} \left(S(t, \Delta t) \right)^q , \tag{2}$$

where N is the total number of data points available at the scale Δt. The 1st statistical moment is the mean and the 2nd statistical moment is a measure of the variability about the origin. Combined, the statistical moments $< S(\Delta t)^q >$ for all q completely capture the shape of the pdf. Statistical scaling, or scale invariance, requires that $< S(\Delta t)^q >$ is a power law function of the scale, that is

$$\left\langle S(\Delta t)^q \right\rangle \propto \left(\Delta t \right)^{\tau(q)} , \tag{3}$$

where $\tau(q)$ is the scaling exponent, which is independent of Δt and depends only on the order of the moment q. For a scale-invariant variable, the function $\tau(q)$ therefore completely determines how the pdf of the variable changes with scale. For example, the mean will vary as sampling

interval to the power of $\tau(1)$. The simplest form of scaling, known as simple scaling or monoscaling, is when the scaling exponents are a linear function of the moment order i.e. when $\tau(q) = Hq$. In this case the single parameter H characterizes how the whole pdf changes over scales, so that if $P(S(t, \Delta t))$ is the pdf of sediment transport at scale Δt, the pdf at a second scale $\Delta t'$ is given by (e.g., Kumar and Foufoula-Georgiou 1993)

$$P(S(t, \Delta t')) = \left(\frac{\Delta t}{\Delta t'} \right)^{-H} P\left(\left(\frac{\Delta t}{\Delta t'} \right)^{-H} S(t, \Delta t) \right) \tag{4}$$

That is, the pdf at sampling interval $\Delta t'$ is simply the original pdf normalized by a factor $\left(\frac{\Delta t}{\Delta t'} \right)^{-H}$.

If $\tau(q)$ is nonlinear, known as multiscaling, more than one parameter is required to define the behavior of the probability distribution change over scales. In fact, equation (4) takes on a more complicated form and involves a convolution of the pdf at the previous scales with a kernel that depends on the ratio of scales (e.g., Castaing and Dubrulle 1995; see also Venugopal et al. 2006). Concentrating on the second order moments, one can quantify the relative change in shape of the pdf with the coefficient of variation, C_v. Note that C_v is expressed in terms of the first and second moments as

$$C_v = \left[\frac{\left\langle S(\Delta t)^2 \right\rangle}{\left\langle S(\Delta t)^1 \right\rangle^2} - 1 \right]^{\frac{1}{2}} . \tag{5}$$

In the presence of scaling (equation 3) this results in

$$C_v{}^2 + 1 \propto \left(\Delta t \right)^{\tau(2) - 2\tau(1)} , \tag{6}$$

which, for the multiscaling case, indicates that the coefficient of variation changes across scales as a function of $\tau(2)-2\tau(1)$. On the contrary, for simple scaling $\tau(q)$ is linear and hence $\tau(2) = 2\tau(1)$, so that equation (6) means that C_v will be a constant across scales. The variation in the shape of the pdf with scale could also be quantified in more detail by higher order dimensionless moments, such as

$$\frac{< S(\Delta t)^4 >}{< S(\Delta t)^2 >^2} \text{ (e.g., Mahrt 1988).}$$

4. Results

To quantify the scale-dependence of bedload transport, this multiscale analysis methodology was applied to the experimental sediment transport series described in section 2. The statistical moments $< S(\Delta t)^q >$ are displayed as a function of Δt on a log-log plot in **Figure 7**. If the sediment transport series are scale invariant, we would expect to see a linear relationship in this figure, since the power law relationship between $< S(\Delta t)^q >$ and Δt expressed in equation (3) is linear on a log-log plot. Figure 7 indeed shows a linear relationship between the statistical moments and temporal scale over the range of approximately 1 min

5

to 15 min (indicated by the dashed lines on the figure), and hence implies a scale invariant regime within this range. At sampling times shorter than 1 min, the statistical moments do not decrease as would be implied by the scale invariant system, and in fact increase at short enough scales. This behavior of the statistics at short time-scales is interpreted as being dominated by the mechanical noise, discussed in section 2.1, which can be identified by the high frequency of occurrence of negative values in the sediment accumulation rate, which by experimental design should only be positive. At sampling times $\Delta t > 15$ min, the statistical moments also deviate from the log-log linear relationship, eventually leveling out to be relatively constant with sampling time. This is seen as reaching a critical scale, around 15-30 min, at which the largest fluctuations of the series are sampled regularly and above which the statistics of the flow are stable.
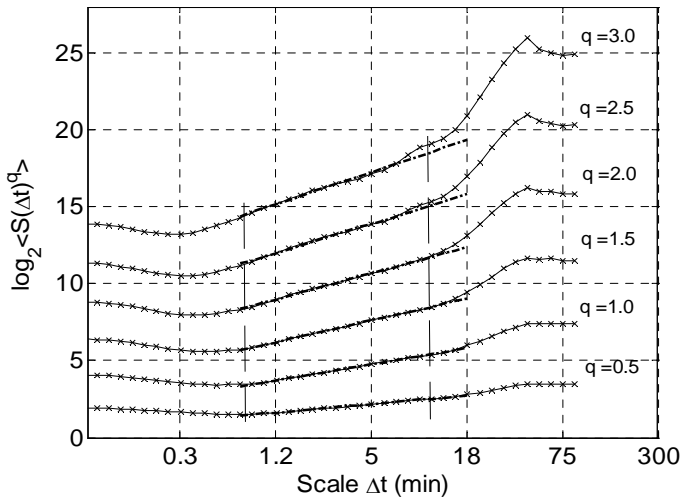
Figure 7 Statistical moments $\langle S(\Delta t)^q \rangle$ of the sediment flux as a function of temporal scale (sampling interval), for the range of moment orders q = 0.5, 1, 1.5, 2.0, 2.5, 3.0. The vertical dashed lines mark the limits of the scaling range.
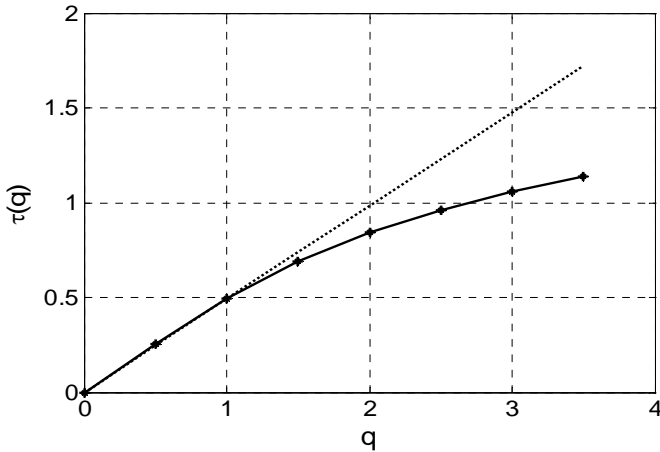
Figure 8 The scaling exponents $\tau(q)$ as a function of the moment order q (computed values from the sediment

transport series are shown as points for q=0 to 3 in increments of 0.5 and the solid line is the fitted quadratic approximation). Deviation from monofractality is depicted by the deviation from the straight line.

Within the scaling regime, it can be observed from **Figure 7** that the statistical moments have different slopes. Estimating these slopes by least squares fitting gives the scaling exponents $\tau(q)$ for all moment orders q, which are plotted in **Figure 8**. Concentrating on first order (q = 1) statistical moment, which is in fact the mean of $S(t, \Delta t)$, we see that $\tau(1) \approx 0.5$. This implies that within the scaling range the mean amount of sediment accumulated increases as approximately $\sqrt{\Delta t}$, so for example, if one doubles the sampling interval the amount of mean sediment accumulated does not double but only increases by a factor of about 1.41. When considering the mean sediment transport *rate*, $(S(t, \Delta t) / \Delta t)$, this implies that

$$\frac{S(t, \Delta t)}{\Delta t} \propto \frac{\sqrt{\Delta t}}{\Delta t} = \Delta t^{-0.5}, \qquad (7)$$

or that the bedload transport rate decreases with increasing sampling interval Δt. In other words, doubling the sampling interval results in a transport rate which is approximately $0.7 (=1/\sqrt{2})$ times smaller.

If one then considers the statistical moments of order q higher than 1, **Figure 8** indicates that their scaling exponents $\tau(q)$ do not increase as a linear power of q (the theoretical linear relationship is shown as a dashed line in the figure for comparison). So $\tau(2)$ is slightly less than twice $\tau(1)$, etc. Therefore, the simple scaling described by equation (4) does not hold, and a multiscaling framework is required. This is consistent with the fact that we saw in section 2.2 that C_v decreased with scale, corresponding to the pdf narrowing with increasing sampling time: using equation (6), a decreasing C_v implies that $\tau(2)$ is less that $2\tau(1)$.

Knowledge of the $\tau(q)$ curve allows the complete rescaling of the pdf with changing sampling interval. It is often convenient to parameterize $\tau(q)$ in order to describe the scaling properties of the data in a parsimonious way. Although several nonlinear parameterizations of $\tau(q)$ are possible, a typical parameterization results from assuming that $\tau(q)$ accepts a polynomial expansion of the form

$$\tau(q) = c_0 + c_1 q - \frac{c_2}{2} q^2 + \frac{c_3}{3!} q^3 + ..., \qquad (8)$$

with the constants c_i, i = 0, 1, 2, 3,... as the model parameters. In this work, due to the uncertainty in estimation of higher order moments from limited data, the polynomial is truncated at the second order i.e. it is assumed to be quadratic and all c_i are assumed to be zero for i > 2. This quadratic approximation, which is consistent with the so-called lognormal multiplicative cascade model (e.g., see Arneodo et al., 1998b), has been found adequate for modeling several geophysical processes including

6

atmospheric boundary layer flows (e.g., Basu et al. 2006) and high resolution temporal rainfall (Venugopal et al. 2006), among others. The constant $c_0 = \tau(0)$ is the scaling exponent of the zeroth-order moment, which will be equal to zero if the support fills the space, as is the case here. This leaves two parameters, c_1 and c_2, to describe the scaling, which can be obtained by fitting a second degree polynomial to the $\tau(q)$ curve. A least squares fitting was performed on the experimental data, and resulted in $c_1 \sqcup$ 0.56 and $c_2 \sqcup$ 0.05 (for comparison, for fully developed turbulence $c_1 \sqcup$ 1/3 and $c_2 \sqcup$ 0.025). The $\tau(q)$ curve fitted with this parameterization is shown as the solid curve in **Figure 8**, and can be seen to approximate very well the empirical curve. Assuming this model, the mean of the sediment accumulation is seen to scale as $\langle S(\Delta t) \rangle \propto (\Delta t)^{c_1 - c_2/2}$, which is dominated by the c_1 value, while the scaling of the coefficient of variation is given by $(C_v^2 + 1) \propto (\Delta t)^{-c_2}$. Hence, the parameter c_2 determines the widening of the pdf with decreasing scale. Scaling of higher order moments (and the whole pdf) can also be derived in terms of the two parameters c_1 and c_2 (e.g., see Venugopal et al., 2006 for an application to rainfall series).

5. Discussion and Conclusions

In this study the sampling-time dependence of the statistics of bedload transport has been examined, and the statistical moments have been found to change as power law functions of sampling time within a range of scales between 1 and 15 min. At temporal scales larger than around 30 min the statistics were observed to stabilize and become constant with sampling interval. This indicates that, at least for this system, the ideal way to measure bedload transport rates, to avoid any issues of scale-dependence, would be to use a sampling interval of 30 min or greater. While this would certainly be possible in a controlled laboratory experiment such as the one presented here, in field studies this approach may not be practical, since we expect that the critical sampling time will scale up with the dimension of the system, and so may require very long sampling times in large rivers. Such long sampling times may not be feasible if the bedload sampler has a finite capacity or if the flow conditions in the river change within this time. For this reason further research into the scale dependence of bedload transport is required, not only to determine the upper limit of variations with scale, but also to quantify the scale-dependence at shorter sampling times, in order to allow the correction of statistics in the cases when long sampling times are not feasible.

In this work we have outlined a framework to facilitate further investigation into sampling-time dependence, using the statistical moments of sediment transport to identify regimes of scale-invariance and scaling exponents $\tau(q)$ to quantify the changes in the probability distribution with scale. The quadratic parameterization of $\tau(q)$, equation (7), allows description of the continuum of scaling exponents with just two parameters. This should become increasingly useful in future studies as experiments are performed in a range of differing conditions and researchers attempt to identify how the scale-dependence of bedload transport varies with parameters such as flow rate and sediment size-distribution. In this study, under low flow conditions and with a gravel bed of median particle size of 11.3mm, c_1 was 0.56 and c_2 was estimated to be 0.05, indicating that the mean amount of sediment transported increased as approximately the square-root of sampling time. This means that the sediment transport *rate* decreased as the inverse of the square-root of sampling time (within the scaling range). However, there is no reason to expect this behavior to be universal for sediment transport. The flow rate and geometry in this experiment produced a moderate dimensionless shear stress of approximately twice the critical values for the median grain size. Preliminary analysis of data from an experiment with a higher flow rate, and hence higher bed-stress, indicate a reversal of this scaling behavior, with the mean sediment transport rate increasing with sampling interval through a similar scaling regime. These results will be presented in a further publication (Singh et al. 2008), along with analysis of the relationship between the modes of sediment transport and the features of the bed elevation, which may explain some of the characteristic scales of the sediment transport.

Another long-term goal for further research is to understand the cause of the observed scaling, and its connection to the particle-scale dynamics. We believe that the scaling we see is not completely driven by the near bed turbulence, for the reason that the two-point statistics of the sediment transport rates (not presented here) do not show long range dependence, which would be characteristic of the multiplicative mechanism of eddy energy transfer in turbulence (Arneodo et al. 1998a). Instead, there is no long-range correlation, implying a different mechanism giving rise to the observed scaling, which we suggest might be particle interactions and emergent collective behavior. Of course, the grain size pdf and the shear stress are both important factors that influence such particle-scale dynamics and thus would effect the statistics of the resulting sediment transport rates. Exactly what type of particle-scale dynamics describes the observed statistics remains an open question which we plan to investigate in the future.

References Cited

Arneodo, A., Bacry, E., Manneville, S., and Muzy, J.F, 1998a, Analysis of Random Cascades Using Space-Scale Correlation Functions, Phys. Rev. Lett., 80, 708 – 711.

Arneodo, A., Bacry, E., and Muzy, J.F., 1998b, Towards log-normal statistics in high Reynolds number turbulence, Eur. Phys. J. B, 1, 179-209.

Basu, S., Porté-agel, F., Foufoula-Georgiou, E., Vinuesa, J.F., and. Pahlow, M., 2006, Revisiting the Local Scaling Hypothesis in Stably Stratified Atmospheric Boundary-Layer Turbulence: an Integration of Field and Laboratory Measurements with Large-Eddy Simulations, Boundary-Layer Meteorol., 119, 473-500.

Bunte, K., and Abt, S.R., 2005, Effect of sampling time on measured gravel bedload transport rates in a coarse-bedded stream, Water Resources Research, Vol.41, W11405.

Castaing, B., and Dubrulle, B., 1995, Fully Developed Turbulence: A Unifying Point of View, J. Physique II, 5, 895-899.

Ergenzinger, P., de Jong, C., Reid, I., and Laronne. J.B. 1994. Short term temporal variations in bedload transport rates: Squaw Creek, Montana, USA and Nahal Yatir and Eshtemoa, Israel. p. 251-264 in Schmidt, C.H. and Ergenzinger, P. (eds.): Lecture Notes in earth Sciences, vol 52: Dynamics and Geomorphology of Mountain Rivers, Springer Verlag.

Foufoula-Georgiou, E., 1998, On scaling theories of space-time rainfall: some recent results and open problems, In Stochastic Methods in Hydrology: rain, landforms and floods, editors: Barndorff-Nielsen et al., World Scientific, Singapore.

Gomez, B.,. Naff, R.L., and Hubbell, D.W., 1989, Temporal variations in bedload transport rates associated with the migration of bedforms, Earth Surf. Processes Landforms, 14, 135-156.

Gupta, V.K., Mesa, O.J., and Dawdy, D., 1994, Multiscaling theory of floods: Regional quantile analysis, *Water Resour. Res*., 30(12), 3405-3421.

Kuhnle, R.A., 1996, Unsteady transport of sand and gravel mixtures, in Advances in Fluvial Dynamics and Stratigraphy, eds. P.A. Carling and M. Dawson, John Wiley, Hoboken, N.J., pp 183-201.

Kumar, P., and Foufoula-Georgiou, E., 1993, A new look at rainfall fluctuations and scaling properties of spatial rainfall, J. Applied Meteorology, 32 (2), 209-222.

Laronne, J.B., Alexandrov, Y.,Bergman. N., Cohen, H., Garcia, C., Habersack, H., Powell, M.P. and Reid, I., 2003. The continuous monitoring of bedload flux in various fluvial environments. p.134-145 in J. Bogen, T. Fergus and D.E. Walling (eds). Erosion and Sediment Transport Measurement in Rivers: Technological and Methodological Advances. Int'l Assoc. Hydrol. Sci. Publ. 283.

Lashermes, B., and E. Foufoula-Georgiou, 2007, Area and width functions of river networks: New results on multifractal properties, *Water Resour. Res.*, 43, W09405, doi:10.1029/2006WR005329.

Lovejoy, S., D. Schertzer, P. Silas, Y. Tessier, and D. Lavallée, 1993, The unified scaling model of atmospheric dynamics and systematic analysis in cloud radiances, *Ann. Geophys.*, 11, 119–127.

Mahrt, L., 1988, Intermittency of atmospheric turbulence, J. Atmos. Sci., 46, 79-95.

Parisi, G., and Frisch, U., 1985, On the singularity structure of fully developed turbulence, in Turbulence and Predictability in Geophysical Fluid Dynamics, edited by M. Ghil, R. Benzi and G Parisi, North -Holland, Amsterdam, 84.

Singh, A., K. Fienberg, D. Jerolmack, J. Marr, and E. Foufoula-Georgiou, 2008, Experimental evidence for statistical scaling and intermittency in sediment transport rates, *under preparation for submission to J. Geophys. Res. (Earth Surface))*.

Sornette, D., and G. Ouillon, 2005, Multifractal Scaling of Thermally Activated Rupture Processes, *Phys. Rev. Lett.*, 94, doi:10.1103/PhysRevLett.94.038501.

Venugopal V., Roux, S.G., Foufoula-Georgiou, E., and Arneodo, A., 2006, Revisiting multifractality of high-resolution temporal rainfall using a wavelet-based formalism, Water Resources Research, 42, W06D14, doi:10.1029/2005WR004489.

Wilcock, P.R., 2001, Toward a practical method of estimating sediment transport rates in gravel-bed rivers, Earth Surf. Processes Landforms, 26, 1395-1408.

Upscaling river biomass using dimensional analysis and hydrogeomorphic scaling

Elizabeth A. Barnes,[1,2] Mary E. Power,[3] Efi Foufoula-Georgiou,[1] Miki Hondzo,[1] and William E. Dietrich[4]

[1]   We propose a methodology for upscaling biomass in a river using a combination of dimensional analysis and hydro-geomorphologic scaling laws. We first demonstrate the use of dimensional analysis for determining local scaling relationships between *Nostoc* biomass and hydrologic and geomorphic variables. We then combine these relationships with hydraulic geometry and streamflow scaling in order to upscale biomass from point to reach-averaged quantities. The methodology is demonstrated through an illustrative example using an 18 year dataset of seasonal monitoring of biomass of a stream cyanobacterium (*Nostoc parmeloides*) in a northern California river. **Citation:** Barnes, E. A., M. E. Power, E. Foufoula-Georgiou, M. Hondzo, and W. E. Dietrich (2007), Upscaling river biomass using dimensional analysis and hydrogeomorphic scaling, *Geophys. Res. Lett.*, *34*, L24S26, doi:10.1029/2007GL031931.

1.   Introduction

[2]   Several studies have related stream periphyton biomass to local physico-chemical characteristics [e.g., *Lowe et al.*, 1986; *Mulholland et al.*, 2001; *Biggs and Gerbeaux*, 1993; *Biggs and Hickey*, 1994; *Biggs*, 1995] as well as to local hydrologic regimes and trophic interactions [e.g., *Power et al.*, 1996; *Wootton et al.*, 1996; *Power and Stewart*, 1987; *Clausen*, 1997]. Algae and cyanobacteria that make up the autotrophic component of periphyton are heterogeneously distributed down river networks, so it remains difficult to quantify their reach or basin-wide abundance, distribution and metabolism. Good estimates of the abundance of algae and cyanobacteria (the primary producers that often dominate periphyton) in rivers and streams are critical for management and restoration of watersheds and water supplies, as well as basic understanding of major energy sources for river food webs.

[3]   *Nostoc*, a genus of nitrogen-fixing cyanobacteria, is an important component of periphyton in temperate streams and rivers throughout the world [*Prosperi*, 1989; *Dodds et al.*, 1995]. Where abundant, it is likely a major source of biologically available nitrogen in ecosystems [*Dodds et al.*, 1995]. We demonstrate that a high percentage of the local variability in the height of epilithic *Nostoc parmeloides* (45% to 71%) can be explained by hydrologic and geomorphic variables, appropriately grouped via dimensional analysis. We also propose a methodology for combining these local relationships with stream geometry and streamflow scaling to estimate reach-average biomass and its uncertainty. Since these hydro-geomorphic variables can be readily extracted (or computed via hydraulics) from high resolution topography, e.g., LiDaR airborne laser altimetry, the proposed framework offers an attractive way of estimating and upscaling biomass even in regions for which limited biological sampling is available.

2.   Study System and Database

[4]   An 18 year data set includes measurements of *Nostoc* height and physical stream variables at three cross-stream transects located approximately one kilometer apart along the South Fork Eel River within the Angelo Coast Range Reserve in northern California (Figure 1). The South Fork Eel River experiences a Mediterranean hydrologic regime, with winter floods and summer drought. Further description of this site is given by *Power* [1990, 1992]. Colonies of *Nostoc parmeloides* Kutzing grow attached to bedrock, boulder, and cobble substrates on the river bed. Our index of biomass is 'height' measuring the diameter of a colony if it was spherical, or the major diameter of an ear-shaped, midge-infested colony.

[5]   Cross-stream transects were benchmarked at both ends with nails in trees or bedrock (nail to nail distance varied less than 1 cm over repeated surveys). At 0.5 m or 1.0 m intervals across the transect, water depth was measured, and surface velocity was estimated. The modal height of *Nostoc* colonies within an estimated 10×10 cm^2 area around each sampling point on the substrate was recorded (*Power* [1992] and *Power and Stewart* [1987] give further methodological details). *Nostoc* height and stream cross-sectional variables were measured 3 to 20 times each year from 1988–2005 during the growing season (April–August). Table 1 shows the different variables used in this study along with their definitions. It is noted that *Nostoc* biomass can be predicted from the height of the colony through empirical relationships (e.g., M. E. Power, unpublished data, 2006) but these relationships are not directly used in the present study.

[6]   Solar radiation (RAD) was measured at the ORLAND2.A weather station (operated by the University of California) approximately 80 miles from the transects. River discharge was measured at the USGS Branscomb gauge (USGS 11475500), a decommissioned USGS gauge that was reactivated in 1990 by Angelo Reserve researchers, and is located just south of transect

[1]St. Anthony Falls Laboratory, National Center for Earth-Surface Dynamics, University of Minnesota, Minneapolis, Minnesota, USA.
[2]Now at Department of Atmospheric Sciences, University of Washington, Seattle, Washington, USA.
[3]Department of Integrative Biology, University of California, Berkeley, California, USA.
[4]Department of Earth and Planetary Science, University of California, Berkeley, California, USA.
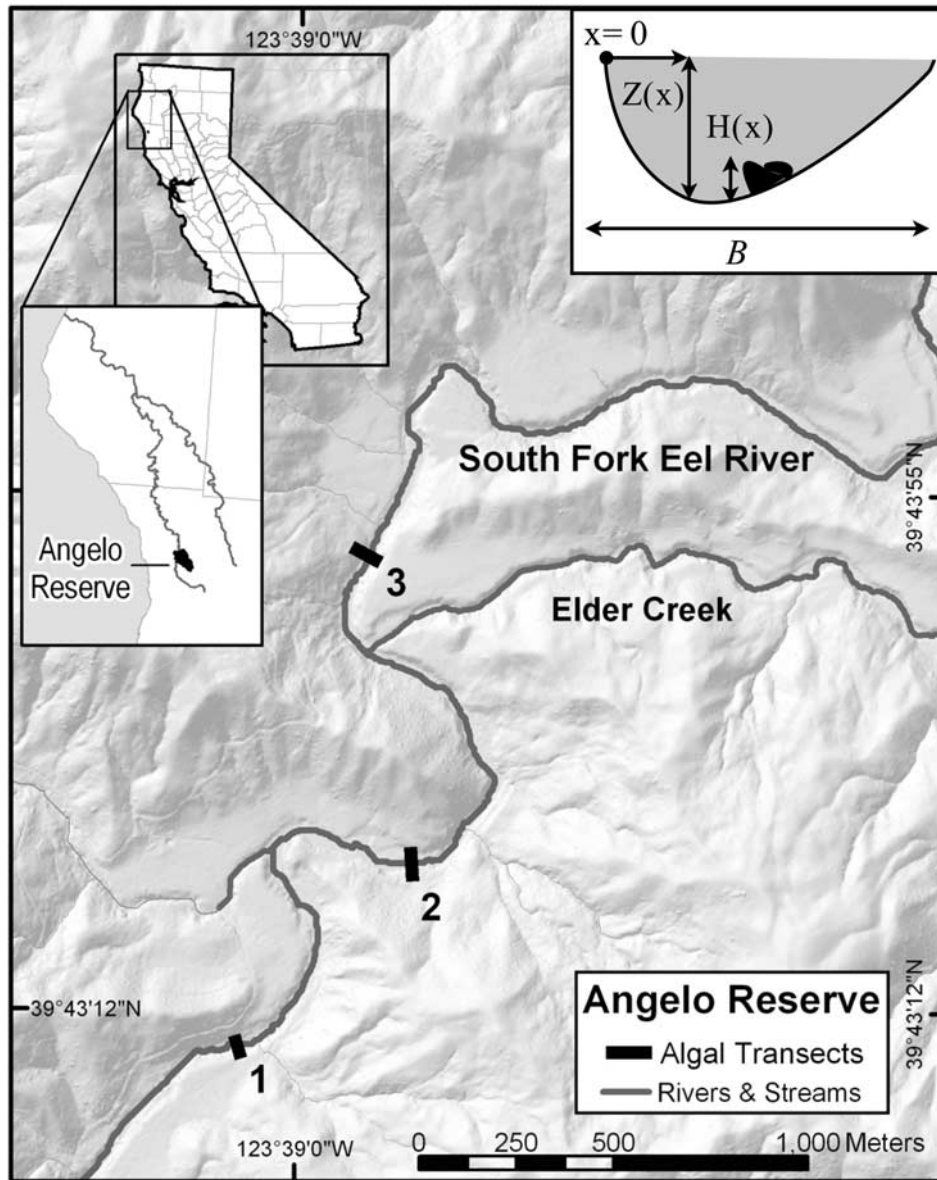
Figure 1. Three transects (1, 2, 3) in the South Fork Eel River, Mendocino County, CA. Transect 1 is the southern most (farthest upstream), while transect 3 is the northern most (farthest downstream) transect. The inset shows a cross-section with relevant variables.

1. Gaps in the hydrologic record from this station were filled with a scaling relationship between discharge at USGS Elder Creek gaugin station (USGS 11475560) 4 km away from the Branscomb gauge on a major tributary of the South Fork Eel.

3. Terminology and Framework of Analysis

[7] All variables considered in this study are referenced by a location along the river network (s), a location (x) across the considered transect (stream cross-section) and time (t) (see Figure 1). If we denote such a generic variable by $\xi(s, x, t)$, s can be an indexed variable representing the transects 1, 2, and 3; x varies between zero (at the left most position of the cross-section of the transect) and $B(t)$, where $B(t)$ represents the cross-section wetted channel width at time t.

[8] Given the limited data available to quantify environmental controls, a representative quantity for the whole transect is defined as the arithmetic average over all data across the transect. We denote the cross-sectional-averaged quantity with an overbar,

$$\overline{\xi}(s,t) = \frac{1}{B(t)} \int_0^{B(t)} \xi(s,x,t)dx. \quad (1)$$

We relate cross-sectional averaged *Nostoc* colony height, $\overline{H}(s, t)$, to groups of key geomorphic, hydrologic, and other environmental variables which can be observed or estimated. In general, at any transect

$$\overline{H}(s,t) = f_1\left[V_g\left(s^{\pm}, t^-\right), V_h\left(s^{\pm}, t^-\right), V_e\left(s^{\pm}, t^-\right)\right] \quad (2)$$

Table 1. Definitions of Variables

Variable	Dimensions	Units	Range[a]	Description
$\overline{H}(t)$	L	m	0.001–0.10 (0.005) [0.005]	transect-average *Nostoc* height at time t
$\overline{Z}(t)$	L	m	0.06–0.70 (0.28) [0.26]	transect-average water depth at time t
$\overline{U}(t)$	LT^{-1}	m/s	0.05–1.61 (0.45) [0.42]	transect-average velocity at time t
$B(t)$	L	m	3.00–27.0 (13.5) [8.31]	width of transect at time t
RAD	MT^{-3}	kg/s^3	186–715 (260) [303]	average solar radiation (past 45 days)
$\rho(t)$	ML^{-3}	kg/m^3	992–998 (996.33) [995.51]	water density ($\propto$ temp) at time t
$\overline{U}_{max}$	LT^{-1}	m/s	0.04–6.88 (1.32) [0.48]	transect-maximum velocity (past 45 days)

[a]Spring median in parentheses, summer median in brackets.

where f_1 is a function, V_g denotes a vector of geomorphic variables, V_h a vector of hydrologic variables, and V_e a vector of other environmental variables such as light, temperature and nutrient concentration. In the above relationship, $s^{\pm}$ denotes a location in the vicinity of location s (it would be mostly upstream although a dependence on an immediately downstream junction might be possible), and t^- denotes time t and previous times, e.g. dependence on maximum flow in the previous week or dependence on light not only during the specific day of measurement, but during a previous period of time. A dependence on a vector of biotic variables, $V_b(s^{\pm}, t^-)$, such as grazing could also be added in the above equation but it is not considered in this study.

[9] We assume the geomorphic vector V_g to be composed of B (channel width) and $\overline{Z}$ (channel-averaged depth) (Figure 1); the hydrologic vector V_f to be composed of Q (cross-section average flow) and Q_{max} (maximum flow over a pre-specified antecedent period), and the environmental vector V_e to be composed of RAD (daily radiation in W/m^2) and water density as a function of temperature (ρ). From this point on, the time dependence of each variable is implicitly assumed in each equation.

4. Dimensional Analysis

[10] The theory of dimensional analysis is elaborated in many textbooks [e.g., *Potter et al.*, 2002]. The purpose of the analysis is to formulate useful dimensionless groups of variables to describe a process and to establish a basis for similarity between the processes on different time and space scales [*Warnaars et al.*, 2007]. In this paper we use this technique to determine dimensionless groups that provide a basis for explaining *Nostoc* height at different years and transects. The variables chosen for our relationship and their dimensions are given in Table 1. Our generic scaling function takes the following form:

$$\overline{H} = f_2\left(\overline{Z}^a, B^b, \overline{U}^c, RAD^d, \overline{U}_{max}^e, \rho^h\right). \quad (3)$$

Although a multivariate regression that includes all variables in (3) is possible, the use of dimensional analysis has the advantage of reducing the number of independent variables and resulting in dimension-free parameters.

[11] Inserting the corresponding dimensions (Table 1) into (3), and combining equal dimensions, we obtain:

$$L = L^{a+b+c-3h+e}M^{d+h}T^{-c-3d-e} \quad (4)$$

where L is the dimension of length, M is the dimension of mass and T is the dimension of time. Solving for the above exponents, we derive the dimensionless model to be

$$\left(\frac{\overline{H}}{\overline{Z}}\right) = k\left(\frac{B}{\overline{Z}}\right)^{\alpha}\left(\frac{\overline{U}}{\overline{U}_{max}}\right)^{\beta}\left(\frac{RAD}{\rho\overline{U}^3}\right)^{\gamma}. \quad (5)$$

The first dimensionless group to the right of the equal sign represents an important geomorphic characteristic of the stream cross-section: width (B) to depth ($\overline{Z}$) ratio. As the width to depth ratio of the channel increases, light becomes more available to *Nostoc*, which, as a nitrogen-fixing autotroph, has a high demand for photosynthetically derived carbon energy. The next dimensionless group captures the cyanobacterium's dependence on moderate (numerator) and high (denominator) stream velocities. Under moderate flow velocities, *Nostoc*, like other attached stream autotrophs, benefits from increasing velocities (increasing flows increase delivery of nutrients and removal of waste products) up to a certain threshold, beyond which scouring, detachment and export occur [*Whitford and Schumacher*, 1964; *Hondzo and Wang*, 2002]. The final dimensionless group is the ratio between solar power (RAD) and stream power per unit stream bed area ($\rho\overline{U}^3$). The exponents α, β, γ and constant k must be determined by fitting (5) with our data.

5. Scaling of *Nostoc* Height

[12] During spring, *Nostoc* colonies re-establish following winter flood scour, and colonies grow, then senesce, during summer. We separated the analysis into two groups: biomass establishment in the spring (April–May) and growth accrual in the summer (June–August). We estimated the parameters of (5) using a weighted linear regression on the logs, with the best fit defined as the minimum sum of squares of the errors and weights inversely proportional to the number of measurements that season. Different time lags were investigated for the definition of $\overline{U}_{max}$ (see Table 1 for definition), and the highest R^2 was obtained for a time lag of 45 days.

[13] Comparing our data and the proposed scaling relationship (5), we found that the third dimensionless group ($RAD/\rho\overline{U}^3$) contributed an insignificant amount to explaining the variability of the data and it was eliminated from the model. Figure 2 shows the results for transects 1, 2 and 3 over the two seasons. Table 2 shows the results of six other scaling relationships for various seasons and transect combinations. It appears that transects 1 and 2 behave quite
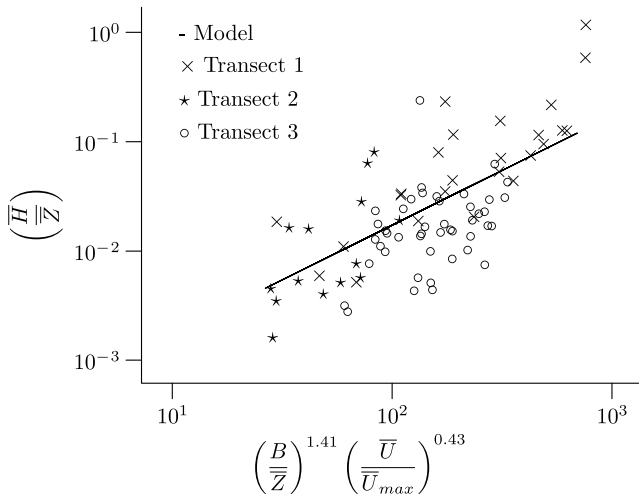
Figure 2. *Nostoc* height over three transects in the spring and summer (April–August) over the 18 years of record. Weighted least squares results in the scaling relationship $\left(\frac{\overline{H}}{\overline{Z}}\right) = 1.7 \times 10^{-4} \left(\frac{B}{\overline{Z}}\right)^{1.41} \left(\frac{\overline{U}}{\overline{U}_{\max}}\right)^{0.43}$ with an $R^2 = 0.45$.

similarly, for 71% of their variability over all seasons was accounted for. *Nostoc* height at transect 3 did not follow the trend depicted by transects 1 and 2, and there are two possible reasons for this. First, transect 3 is located downstream of a major tributary. Second, while transects 1 and 2 have similar valley geometries (symmetric with a slope of approximately 1:8) and thus receive comparable amounts of direct sunlight each day, the flat topography flanking the western shore of transect 3 increased its daily period of insolation. The RAD variable was not able to account for these differences as it was not transect specific and our results show that this radiation variability is not explainable via channel geometry alone (see Table 2 where a lower R^2 was found especially in the summer for transect 3).

6. A Framework for Upscaling Local Biomass

[14] Consider a hypothetical stream reach of 2 km length for which *Nostoc* height observations are available only at a few locations. How is one to estimate the *Nostoc* biomass along the entire stream from the available observations?

[15] Suppose that the *Nostoc* cross-sectional average colony height is scaled by the previously discussed local relationship (5):

$$\overline{H}(s) = k \cdot B(s)^{\alpha} \cdot \overline{Z}(s)^{1-\alpha} \cdot \left(\frac{\overline{U}(s)}{\overline{U}_{\max}(s)}\right)^{\beta} \tag{6}$$

The reach-averaged biomass over a stream reach of length Δs, $\langle \overline{H}(\Delta s)\rangle$, is defined as

$$\langle \overline{H}(\Delta s)\rangle = \frac{1}{\Delta s}\int_{s_0}^{s_0+\Delta s} \overline{H}(s)ds. \tag{7}$$

Due to the nonlinearity of (6), $\langle \overline{H}(\Delta s)\rangle$ cannot be estimated from (6) and (7) by substituting in the reach-averaged quantities $\langle B(s)\rangle$, $\langle \overline{Z}(s)\rangle$, etc. Instead, one must perform

integration of (7) by properly acknowledging how each of the variables varies along the stream.

[16] *Leopold and Maddock* [1953] demonstrated that $B(s)$, $\overline{Z}(s)$ and $\overline{U}(s)$ relate to streamflow $Q(s)$ at location s via the so-called hydraulic geometry (HG) relationships:

$$B(s) \propto Q(s)^{m_1} \tag{8}$$

$$\overline{Z}(s) \propto Q(s)^{m_2} \tag{9}$$

$$\overline{U}(s) \propto Q(s)^{m_3} \tag{10}$$

where $m_1 + m_2 + m_3 = 1$. These relationships apply to a specific location for varying flows (at-a-station HG) or at several locations along a stream for a flow of specific frequency (downstream HG). Since our interest is in integration along a stretch of the stream at a specific instant of time, the downstream HG is relevant for all quantities except for the maximum velocity $\overline{U}_{\max}(s)$ which is considered to result from an extreme flood (e.g., of a specified exceedance probability) at each location and thus (at-a-station HG), $\overline{U}_{\max}(s) \propto Q_{\max}(s)^{m'_3}$ needs to be employed. The exponents m_1, m_2, m_3 and m'_3 can be estimated locally (if high resolution topography data are available) or determined using regional relationships [e.g., see *Singh*, 2003]. Substituting these scaling relationships into (6), one obtains

$$\overline{H}(s) = k' \cdot Q(s)^{M_1} Q_{\max}(s)^{-M_2} \tag{11}$$

where $M_1 = m_1\alpha + m_2(1-\alpha) + m_3\beta$ and $M_2 = m'_3\beta$. By further introducing the known discharge-drainage area scaling relationships [e.g., see *Gupta and Dawdy*, 1995]

$$Q(s) \propto A(s)^{\theta_1} \tag{12}$$

$$Q_{\max}(s) \propto A(s)^{\theta_2} \tag{13}$$

where θ_1 and θ_2 are exponents dependent on flood frequency and watershed characteristics, we obtain

$$\overline{H}(s) = k'' \cdot A(s)^{p} \tag{14}$$

where $p = \theta_1 M_1 - \theta_2 M_2$. Equation (14) is an approximation of *Nostoc* height at a single transect as a function of

Table 2. Scaling Relationships With R^2 Values for Combinations of Transects and Seasons[a]

Transects and Seasons	α	β	k	R^2
T-1,2,3 spring & summer	1.41	0.43	1.7×10^{-4}	0.45
T-1,2 spring & summer	1.54	0.54	1.8×10^{-4}	0.71
T-3 spring & summer	0.90	0.47	6.9×10^{-4}	0.21
T-1,2 spring	1.70	0.69	0.6×10^{-4}	0.83
T-3 spring	0.14	0.40	172.8×10^{-4}	0.57
T-1,2 summer	1.79	0.62	0.8×10^{-4}	0.71
T-3 summer	0.61	0.52	18.0×10^{-4}	0.22

[a]Functions are of the form $\left(\frac{\overline{H}}{\overline{Z}}\right) = k\left(\frac{B}{\overline{Z}}\right)^{\alpha}\left(\frac{\overline{U}}{\overline{U}_{\max}}\right)^{\beta}$. The amount of variability accounted for by scaling is determined by the R^2 value, as defined by *Draper and Smith* [1981].

upstream drainage area $A(s)$ only, which is easy to extract from maps or digital elevation models. As such, it represents a derived "biological" scaling relationship akin to the hydrologic scaling relationships discussed above, which have found extensive use in hydrology (prediction in ungauged basins and regionalization).

[17] Equation 14 can be further explored for upscaling purposes by noting that $A(s)$ can be related to length $L(s)$ (from the watershed divide to location s) using a variant of Hack's law [e.g., *Rigon et al.*, 1996] for nested basins, $A(s) \propto L(s)^\delta$. Combining this with (14) and inserting it into (7), we obtain

$$\langle \overline{H}(\Delta s) \rangle = k^* \cdot \frac{[L^{m+1}(s_0 + \Delta s) - L^{m+1}(s_0)]}{(m+1)\Delta s}. \quad (15)$$

where $m = \delta(\theta_1 M_1 - \theta_2 M_2)$.

[18] The above relationship quantifies the dependence of reach-averaged biomass on reach length Δs, where the reach starts at an arbitrary location s_0. Assuming without loss of generality that $s_0 = 0$ (i.e. $L(s_0) = 0$ and $L(\Delta s) = \Delta s$), and considering two reaches of lengths Δs_1 and Δs_2, the above relationship results in

$$\frac{\langle \overline{H}(\Delta s_1) \rangle}{\langle \overline{H}(\Delta s_2) \rangle} = \left(\frac{\Delta s_1}{\Delta s_2} \right)^m \quad (16)$$

As an illustrative example, let $m_1 = 0.5$, $m_2 = 0.4$, $m_3 = 0.1$ and $m'_3 = 0.3$ (as defined by *Leopold and Maddock* [1953]; see also *Singh* [2003]), $\theta_1 = 1$ and $\theta_2 = 0.7$ [see *Gupta and Dawdy*, 1995, Table V], $\delta = 0.58$ (as extracted by us for the Eel River basin using LiDaR data), $\alpha = 1.41$ and $\beta = 0.43$ (spring and summer *Nostoc* in Table 1); then the final scaling exponent is $m = 0.3$. Thus, if $\Delta s_1 = 2$ km and $\Delta s_2 = 1$ km the above equation implies that *Nostoc* biomass per unit stream length scales by a factor of $2^{0.3} = 1.2$. In other words, starting from a given reference point and going downstream, a stream reach twice as long has total *Nostoc* biomass not twice, but 2.4 times larger. Of course, biomass cannot grow unbounded and a physically-imposed upper limit will constrain the range of applicability of the above scaling relationship. Determining this upper limit (empirically or mechanistically) is an issue that requires careful study.

[19] There is uncertainty associated with each HG and flow scaling exponent, and this uncertainty is separate from the errors associated with the dimensionless model's biomass predictions. To better understand the effects of HG related uncertainties, we performed first order analysis of variance [see *Benjamin and Cornell*, 1970] on (15) with respect to the HG exponents m_1, m_2, m_3, m'_3. Using the values given above, and letting $\Delta s = 1$ km, we find that a 5% uncertainty (standard deviation) in each scaling exponent leads to a 17% uncertainty in the reach-averaged biomass. Of course, as in any uncertainty analysis, it is expected that considering the uncertainty of all variables involved in the model will reduce the power of the predictive relationship.

7. Conclusions and Caveats

[20] We have demonstrated that cyanobacterial biomass scales with hydrologic and geomorphic local variables in a river network (5). Moreover, combining this scaling rela-

tionship with hydraulic geometry and other geomorphic and hydrologic scaling laws resulted in a simple nonlinear scaling relationship of transect-averaged biomass with upstream drainage area (14) and stream-averaged biomass with stream length (16). The proposed methodology, which can be further refined in its assumptions, e.g., to consider spatial inhomogeneity in the scaling of HG [see *Dodov and Foufoula-Georgiou*, 2004], can potentially be implemented across different drainage basins and abundances of biota. Being able to upscale local relationships aids in the understanding of the impacts of organisms on ecosystems (e.g. nitrogen loading to river ecosystems by *Nostoc*) as well as how populations are affected by landscape dynamics and heterogeneity. It also aids in efforts to improve (target) field sampling to develop mechanistically-based predictive models of biota at the reach or basin-wide scale by empirically determining the key controlling variables.

[21] In our upscaling example, the HG scaling exponents were assigned "mean regional" values for illustration purposes only. Values specific to each reach should be used to obtain more accurate estimates and thus increase the overall power of the predictive relationships, including uncertainty can be quantified within the proposed framework.

[22] The distribution and abundance of any species reflect not only whether the environment provides essential resources and tolerable conditions (Fundamental Niche), but also potentially limiting ecological interactions (Realized Niche) [*Hutchinson*, 1957]. *Nostoc* may be more predictable from physical features of its environment than more edible periphyton, because toxic secondary compounds and a tough, mucilaginous sheath deter grazing on this cyanobacterium [*Dodds et al.*, 1995]. Future field work in our system will estimate *Nostoc* biomass over larger areas of the river bed, and relate reach-level biomass to hydraulic scaling parameters and to per-area rates of biological activity (e.g., nitrogen fixation).

References

Benjamin, J. R., and C. Cornell (1970), *Probability, Statistics and Decision for Civil Engineers*, McGraw-Hill, New York.

Biggs, B. (1995), The contribution of disturbance, catchment geology and land use on the habitat template of periphyton in stream ecosystems, *Freshwater Biol.*, *33*, 419–438.

Biggs, B., and P. Gerbeaux (1993), Periphyton development in relation to macro-scale (geology) and micro-scale (velocity) limiters in two gravel-bed rivers, New Zealand, *N. Z. J. Mar. Freshwater Res.*, *27*, 39–53.

Biggs, B., and C. Hickey (1994), Periphyton responses to a hydraulic gradient in a regulated river in New Zealand, *Freshwater Biol.*, *32*, 49–59.

Clausen, B. B. (1997), Relationships between benthic biota and hydrological indices in New Zealand streams, *Freshwater Biol.*, *38*, 327–342.

Dodds, W., A. Gudder, and D. Mullenbauer (1995), The ecology of Nostoc, *J. Phycol.*, *31*, 2–18.

Dodov, B., and E. Foufoula-Georgiou (2004), Generalized hydraulic geometry: Derivation based on a multiscaling formalism, *Water Resour. Res.*, *40*, W06302, doi:10.1029/2003WR002082.

Draper, N., and H. Smith (1981), *Applied Regression Analysis*, 2nd ed., John Wiley, New York.

Gupta, V., and D. R. Dawdy (1995), Physical interpretations of regional variations in the scaling exponents of flood quantiles, *Hydrol. Processes*, *9*, 347–361.

Hondzo, M., and H. Wang (2002), Effects of turbulence on growth and metabolism of periphyton in a laboratory flume, *Water Resour. Res.*, *38*(12), 1277, doi:10.1029/2002WR001409.

Hutchinson, G. E. (1957), Concluding remarks, *Cold Spring Harbor Symp. Quant. Biol.*, *22*, 415–427.

Leopold, L., and T. J. Maddock (1953), The hydraulic geometry of stream channels and some physiographic implications, *U. S. Geol. Surv. Prof. Pap.*, *252*, 57 pp.

Lowe, R., S. Golladay, and J. Webster (1986), Periphyton response to nutrient manipulation in a clear-cut and forested watershed, *Bull. North Am. Benthol. Soc.*, *3*(2), 77.

Mulholland, P. J., et al. (2001), Inter-biome comparison of factors controlling stream metabolism, *Freshwater Biol.*, *46*, 1503–1517.

Potter, M., D. Wiggert, M. Hondzo, and T. Shih (2002), *Mechanics of Fluids*, 3rd ed., Brooks/Cole, Pacific Grove, Calif.

Power, M. E. (1990), Effects of fish in river food webs, *Science*, *250*, 811–814.

Power, M. (1992), Hydrologic and trophic controls of seasonal algal blooms in northern California rivers, *Arch. Hydrobiol.*, *125*, 385–410.

Power, M., and A. Stewart (1987), Disturbance and recovery of an algal assemblage following flooding in an Oklahoma (USA) stream, *Am. Midland Nat.*, *117*, 333–345.

Power, M., M. Parker, and J. Wootton (1996), Disturbance and food chain length in rivers, in *Food Webs: Integration of Patterns and Dynamics*, edited by G. A. Polis and K. O. Winemiller, pp. 286–297, Chapman and Hall, New York.

Prosperi, C. (1989), The life cycle of Nostoc cordubensis (Nostocaceae, Cyanophyta), *Phycologia*, *28*, 501–503.

Rigon, R., I. Rodriguez-Iturbe, A. Maritan, A. Giacometti, D. Tarboton, and A. Rinaldo (1996), On Hack's law, *Water Resour. Res.*, *32*, 3367–3374.

Singh, V. P. (2003), On the theories of hydraulic geometry, *Int. J. Sediment Res.*, *18*(3), 196–218.

Warnaars, T., M. Hondzo, and M. Power (2007), Abiotic controls on periphyton accrual and metabolism in streams: Scaling by dimensionless numbers, *Water Resour. Res.*, *43*, W08425, doi:10.1029/2006WR005002.

Whitford, L., and G. Schumacher (1964), Effect of a current respiration and mineral uptake in Spirogyra and Oedogonium, *Ecology*, *45*, 168–170.

Wootton, J., M. Parker, and M. Power (1996), Effects of disturbance on river food webs, *Science*, *273*, 1558–1560.

————————————

E. A. Barnes, Department of Atmospheric Sciences, University of Washington, 311 ATG Building, Box 351640, Seattle, WA 98195, USA. (eabarnes@atmos.washington.edu)

E. Foufoula-Georgiou and M. Hondzo, St. Anthony Falls Laboratory, National Center for Earth-Surface Dynamics, University of Minnesota, 2 Third Avenue SE, Minneapolis, MN 55414, USA.

W. E. Dietrich, Department of Earth and Planetary Science, University of California, Berkeley, 307 McCone Hall, Berkeley, CA 94720-4767, USA.

M. E. Power, Department of Integrative Biology, University of California, Berkeley, 4184 Valley Life Sciences Building, Berkeley, CA 94720-3140, USA.

Click Here for Full Article

Channel network extraction from high resolution topography using wavelets

Bruno Lashermes,[1] Efi Foufoula-Georgiou,[1] and William E. Dietrich[2]

[1]   The availability of high resolution topography from LIDAR offers new opportunities for objectively extracting the channels directly from a DEM using local topographic information, instead of inferring them indirectly based on global criteria, such as area or area-slope threshold relationships. Here we introduce the use of wavelet filtering to delineate threshold curvatures for defining valleys and threshold slope-direction-change for defining probable channeled portions of the valleys. This approach exploits the topographic signatures uniquely found in high resolution topography, and reveals the fuzzy topographic transition in which local weakly convergent areas lie at the transition between hillslopes and valleys. **Citation:** Lashermes, B., E. Foufoula-Georgiou, and W. E. Dietrich (2007), Channel network extraction from high resolution topography using wavelets, *Geophys. Res. Lett.*, *34*, L23S04, doi:10.1029/2007GL031140.

1.   Introduction

[2]   The automatic extraction of geomorphologic features from Digital Elevation Models (DEMs) has been a subject of considerable research over the past several decades. The two main challenges in channel network extraction algorithms from traditional DEMs have been: handling multiple direction flows [e.g., *Costa-Gabral and Burges*, 1994; *Tarboton*, 1997] and deciding where the channel begins [e.g., *Montgomery and Dietrich*, 1988, 1989, 1992; *Tarboton et al.*, 1991; *Montgomery and Foufoula-Georgiou*, 1993; *Giannoni et al.*, 2005; *Hancock and Evans*, 2006; *Lin et al.*, 2006]. Several criteria have been proposed for determining channel initiation from DEMs and these include a threshold on drainage area, a threshold on local slope, a combination of area and slope, and also a threshold on local curvature (e.g., see review by *Rodriguez-Iturbe and Rinaldo* [1997, chapter 1, and references therein], and *Heine et al.* [2004]). The resolution of the available DEMs and also the noise in the elevation data can considerably influence the accuracy, and thus interpretation, of the numerically computed local gradients and curvatures. In fact, "local" gradients and curvatures from typical 90 m or 30 m DEMs represent anything but local properties and in most landscapes these scales are already too large to be useful in detecting channel initiation [e.g., *Montgomery and Foufoula-Georgiou*, 1993]. It is also expected that the resolution-dependent estimates of local

gradients which are drivers of geomorphic transport laws [e.g., see *Dietrich et al.*, 2003] might result in resolution-dependent sediment fluxes (e.g., see *Stark and Stark* [2001] and a recent study by *Passalacqua et al.* [2006]).

[3]   High resolution (1 to 3 m data spacing) elevation data derived from airborne laser swath mapping (ALSM) now offer the opportunity to use direct topographic "signatures" of river incision and channel banks to map directly the channel network. In the uplands of tectonically active areas, the channel banks in steep small tributaries are typically cut against bedrock and lack sharp topographic boundaries relative to the hillslope. In this case, the primary topographic signature of active channel incision is the characteristic "V" shaped valleys (as compared to broadly curved valley axes). These channels rarely are plotted as "blue lines" on United States Geological Survey maps and are difficult to see in aerial photographs due to vegetation, yet they border most of the hillslopes, convey much of the sediment down to low gradient larger rivers, and constitute much of the total channel network [e.g., *Stock and Dietrich*, 2003]. Here we introduce the use of wavelet analysis to locally filter elevation data and to detect thresholds in topographic curvature and slope-direction change for defining valleys and probable channelized portions of the valley. We also propose that these topographic signatures may offer new metrics for model comparison with real landscapes.

2.   Computation of Local Gradients, Curvatures, and Slope-Direction Change at Multiple Scales Using Wavelets

[4]   We take advantage of the well-known property of the convolution product:

$$\frac{\partial}{\partial x}(h*g) = \frac{\partial h}{\partial x}*g = h*\frac{\partial g}{\partial x} \qquad (1)$$

which implies that smoothing a function h with a kernel g and then taking derivatives (left most term) is equivalent to taking derivatives of the function and smoothing these derivatives with the kernel g (middle term) or equivalent to smoothing the function h directly with the derivative of the kernel g (right most term). It is noted that computing first and second order derivatives from 1 m or 2 m elevation data using finite differences results in considerable noise and smoothing is usually required to reduce the noise. This is typically done by either first smoothing the topography and then computing derivatives [e.g., *Roering et al.*, 1999] or computing derivatives from the original high resolution topography and then smoothing these derivatives by averaging (e.g., *Tucker et al.* [2001], see also the review paper of *Schmidt et al.* [2003]). These methods correspond

---

[1]National Center for Earth-Surface Dynamics and St. Anthony Falls Laboratory, Department of Civil Engineering, University of Minnesota, Minneapolis, Minnesota, USA.
[2]Department of Earth and Planetary Science, University of California, Berkeley, California, USA.

to the left-most and middle terms of equation (1). Here we take advantage of the third term of the above equality which naturally introduces us to using wavelets for efficient computation of local slopes and curvatures of elevation surfaces. Specifically, the first and second derivatives of elevation heights $h(x, y)$ in the x direction (similar expressions hold for the y direction) can be written as:

$$\nabla_{x,\sigma} h(x,y) = \left(h * g^x_{1,\sigma,x,y} \right)(x,y) \qquad (2)$$

$$\nabla^2_{x,\sigma} h(x,y) = \left(h * g^x_{2,\sigma,x,y} \right)(x,y), \qquad (3)$$

where $g^x_{1,\sigma,x,y}$ and $g^x_{2,\sigma,x,y}$ are the first and second derivatives of a 2D Gaussian function of standard deviation σ and centered at location (x, y):

$$g_{0,\sigma,x,y}(u, v) = \frac{1}{2\pi\sigma^2} \exp\left[-\frac{(u-x)^2+(v-y)^2}{2\sigma^2} \right] \qquad (4)$$

The functions $g^x_{1,\sigma,x,y}$ and $g^x_{2,\sigma,x,y}$ are proper wavelets [e.g., *Mallat*, 1999] and $g^x_{2,\sigma,x,y}$ is the so-called Mexican hat wavelet popular in many geophysical applications [e.g., see *Foufoula-Georgiou and Kumar*, 1994]. Thus the gradients and curvatures defined by equations (2) and (3) are simply (apart from a normalization) the 2D continuous wavelet transforms (CWT) of the function $h(x, y)$ with two different wavelets. Defining the "scale" associated to a wavelet as the inverse of its band-pass frequency [e.g., *Mallat*, 1999; *Kumar and Foufoula-Georgiou*, 1997] it can be shown that the smoothing scale corresponding to $g^x_{1,\sigma,x,y}$ (gradients) is $a = \pi\sigma$ and to $g^x_{2,\sigma,x,y}$ (curvatures) $a = \sqrt{2}\pi\sigma$, while the scale of topography smoothing is $a = 4\sigma$, (see Table 1). For the rest of the paper, we adopt the notation of a for scale and compute the modulus of the steepest slope $m_a(x, y)$, its direction $\theta_a(x, y)$, and also the local curvature $\gamma_a(x, y)$ at scale a and at pixel (x, y) as:

$$m_a(x,y) = \sqrt{\left(\nabla h_{x,a}(x,y)\right)^2 + \left(\nabla h_{y,a}(x,y)\right)^2} \qquad (5)$$

$$\gamma_a(x,y) = \nabla^2_{x,a} h(x,y) + \nabla^2_{y,a} h(x,y) \qquad (6)$$

and

$$\theta_a(x,y) = \beta\pi + \arctan\left(\frac{\nabla_{y,a} h(x,y)}{\nabla_{x,a} h(x,y)} \right) \qquad (7)$$

where $\beta = 0$ if, $\nabla_{x,a} h(x, y) > 0$, $\beta = 1$ if $\nabla_{x,a} h(x, y) < 0$ and $\nabla_{y,a} h(x, y) > 0$ and $\beta = -1$ if $\nabla_{x,a} h(x, y) < 0$ and $\nabla_{y,a} h(x, y) < 0$.

[5] Channel incision in uplands topography leads to hillslopes on opposite sides that typically face each other obliquely, giving rise to "V" shaped topographic contour lines. We can use this signature to delineate the axis of valleys and the likely pathway of channels with limited floodplain area on their boundaries. We compute the derivative of the slope direction $\theta_a(x, y)$ as

$$d\theta_a = \sqrt{\left(d_x\theta_a\right)^2 + \left(d_y\theta_a\right)^2} \qquad (8)$$

where $d_x\theta_a = (\partial\theta_a/\partial x)dx$ and $d_y\theta_a = (\partial\theta_a/\partial y)dy$ are numerically estimated with finite differences. It is noted that the slope direction θ_a is defined modulo 2π and is counterclockwise oriented. θ_a ranges between $-\pi$ to $+\pi$ and takes the value 0 when the slope exactly "points to the East". So θ_a has an abrupt 2π variation when crossing the westward direction (this is not a continuous function) and the numerical derivative will exhibit a large value that is not due to a real direction change. To overcome this numerical issue, a direction θ'_a with a different zero origin ($\theta'_a = 0$ when the slope points to the North) is computed as well as its numerical derivative $d\theta'_a$. One then only needs to define the direction derivative as $\min(d\theta_a, d\theta'_a)$ in order to remove the spurious large values due to shifting between $-\pi$ and π values. The quantity $\min(d\theta_a, d\theta'_a)$ will be also referred to as $d\theta_a$ in the sequel.

[6] We propose here that from the wavelet-filtered elevation data we can use the probability density function (pdf) of curvature to detect a threshold below which well-defined valleys are absent. Furthermore, we suggest that a similar threshold exists in the pdf of the slope-direction change that delineates the transition from "U" shaped valleys to "V" shaped river canyons. These two analyses can be used to define valleys associated with channel incision, and, hence, the likely channel network.

3. Statistical Signatures of Geomorphic Transitions

[7] We use the ALSM data (∼2.6 m average bare earth data spacing, gridded to 1 m) acquired by NCALM for the South Fork Eel River in the coastal mountains of Northern California (available at data distribution archive http://www.ncalm.org/) to explore the use of our proposed methods. The site is a 2.8 km^2 mostly forested tributary that lies just north of the Angelo Coast Range Reserve, ∼3 km downstream from the junction of Ten Mile Creek and the South Fork Eel River. It receives about 1900 mm of strongly seasonal rainfall. The mainstem draining the watershed is steeper than 8% and all of its tributaries are steeper than 20%. These channels border hillslopes which are commonly pockmarked with amphitheater shaped topographic steps recording the deformation of the surface associated with extensive deep-seated landsliding. Some fine-scale topographic roughness is an artifact of dense impenetrable brush the tops of which are treated as bare earth, leading to an "acne" appearance of local areas. Based on channel slope [*Stock and Dietrich*, 2003] and field observations in similar terrain in the area, the channel network is cut by a combination of river incision and debris flow scour, perhaps tied to the periodic movement and release of sediment associated with movement of the large landslides (see also

Table 1. Smoothing Scales for Elevation, Gradients, and Curvatures Associated With the Gaussian Kernel of Standard Deviation σ From Which the Wavelets g_1 and g_2 Were Derived[a]

	Elevation, $g_{0,\sigma,x,y}^{x \text{ or } y}$	Gradients, $g_{1,\sigma,x,y}^{x \text{ or } y}$	Curvature, $g_{2,\sigma,x,y}^{x \text{ or } y}$
σ	$a = 4\sigma$	$a = 2\pi\sigma$	$a = \sqrt{2}\pi\sigma$
2 m	8 m	12.6 m	8.9 m
3 m	12 m	18.9 m	13.3 m
4 m	16 m	25.1 m	17.8 m
6 m	24 m	37.7 m	26.7 m
8m	32m	50.2m	35.5m
16m	64m	100.5m	71.1m

[a]See equations (2) to (4).

Gangodagamage et al. [2007] for a quantitative analysis of the roughness of valley morphology in the basin).

3.1. Multiscale Variability of Curvature and Interpretation

[8] The standard deviation of the probability density function (pdf) of local curvature computed for the study watershed at different scales is shown in Figure 1. An abrupt transition emerges at a scale of approximately 12 m (parameter of the analyzing wavelet is $\sigma = 3$ m; see Table 1). For scales smaller than 12 m, curvature variability rapidly increases with decreasing smoothing scale. This rapid increase in variability we attribute to the topographic roughness created by poor bare earth data in brushy areas, and to fine scale topographic complexity associated with the numerous landslide features. The progressive decrease in variability is to be expected with increasing smoothing scale, although the well defined power law was not anticipated. The slope of this relationship may prove useful in distinguishing landscapes with different degree of dissection.

3.2. Hillslope to Valley Transition

[9] Figure 2a shows the quantile-quantile plot (variable plotted against standard normal deviate of the same exceedance probability) of curvature,, γ_a for the study site analyzed at the scale $a = 26.7$ m (well above the roughness break shown in Figure 1). The deviation from a straight line indicates a deviation of the pdf from Gaussian. The positive γ_a's (relevant to channels) deviation from a normal pdf occurs at a standard normal quantile value z of approximately 1, and a curvature of about 0.02 m^2/m. Analysis at smoothing levels from $a = 17.8$ m to $a = 71.1$ m found the value of $z \simeq 1$ to be robust and scale-independent while, of course, the specific values of γ_a at which the transition occurs will depend on scale. This implies that the threshold value of γ_a at which a change in the shape of the pdf occurs is

$$\gamma_{a,th} = F_a^{-1}(0.84) \qquad (9)$$

corresponding to $F_a(\gamma_{a,th}) = \Phi(z = 1) = 0.84$, where Φ is the cumulative distribution of a standard normal deviate $z \sim N(0, 1)$ and F_a is the cumulative distribution of γ_a.

[10] We suggest that the deviation from the normal distribution records an approximate break in which higher curvature values delineate well organized valley axes and lower (but still positive) values record the disordered occurrence of localized convergent topography. Figure 2c shows the areas of high curvature for the threshold value of

the standard normal deviate (z) equal to 1. Lower values of z (and thus lower curvature) greatly increased the number of isolated patches. The network in this catchment is partly disrupted by deep-seated landsliding, and this contributes to the residual patchiness and discontinuous delineation of valleys with this threshold. This multiscaling analysis suggests that rather than expecting the hillslope-valley transition to be defined by the change in sign in curvature instead, some disorganized and perhaps nascent valleys not integrated with the watershed valley network are scattered across the hillslopes and a curvature threshold extracted from an abrupt transition in the statistical distribution of curvature better defines the valley system. Analysis at smoothing levels from $a = 17.8$m to $a = 71.1$m finds this threshold to be determined by a scale-independent parameter.

3.3. Valley to Channel Transition

[11] Figure 2b shows the quantile-quantile plot of the log of the change in slope direction, for the study site analyzed at the scale $a = 25.1$m (comparable to the 26.7 m smoothing scale reported for curvatures in Figure 2a; see Table 1). The deviation from normality occurs at the normal quantile $z_{\log_{d\theta a}} \simeq 1.5$. As in the curvature case (Figure 2a) we propose that the break from normality (thicker than Gaussian tail) is a topographic signature of process dominance change. In this case, we suggest that this break defines the transition from broadly curved, unincised valleys (often found to contain thick colluvial deposits) and valleys with active channel incision and sediment removal. This suggests that a value

$$d\theta_{a,th} = exp^{F_a^{-1}(0.93)} \qquad (10)$$

corresponding to $F_a(\log d\theta_{a,th}) = \Phi(z = 1.5) = 0.93$ could be indicative of valleys with active channels.

[12] Figure 2d shows the grid cells that lie above the slope-direction change threshold. As can be seen, the grid cells that satisfy this criterion define a more narrow skeleton mostly within the valleys of Figure 2c although there are also fewer continuous path lines compared to Figure 2c, possibly separating channeled from unchanneled valleys.
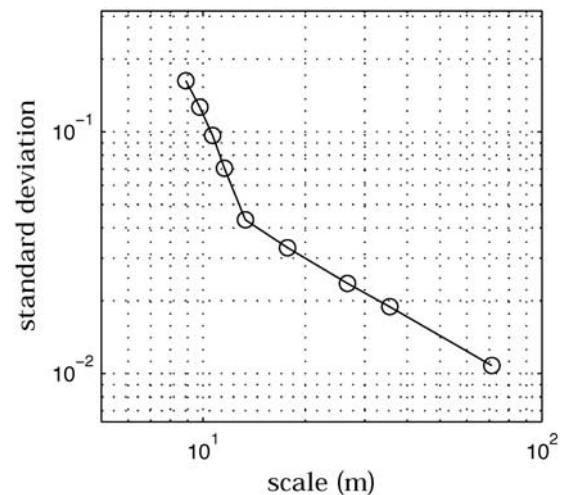
Figure 1. Scaling of the standard deviation of γ_a. The slope computed between the scales 13.3 m and 71.1 m is -0.82.
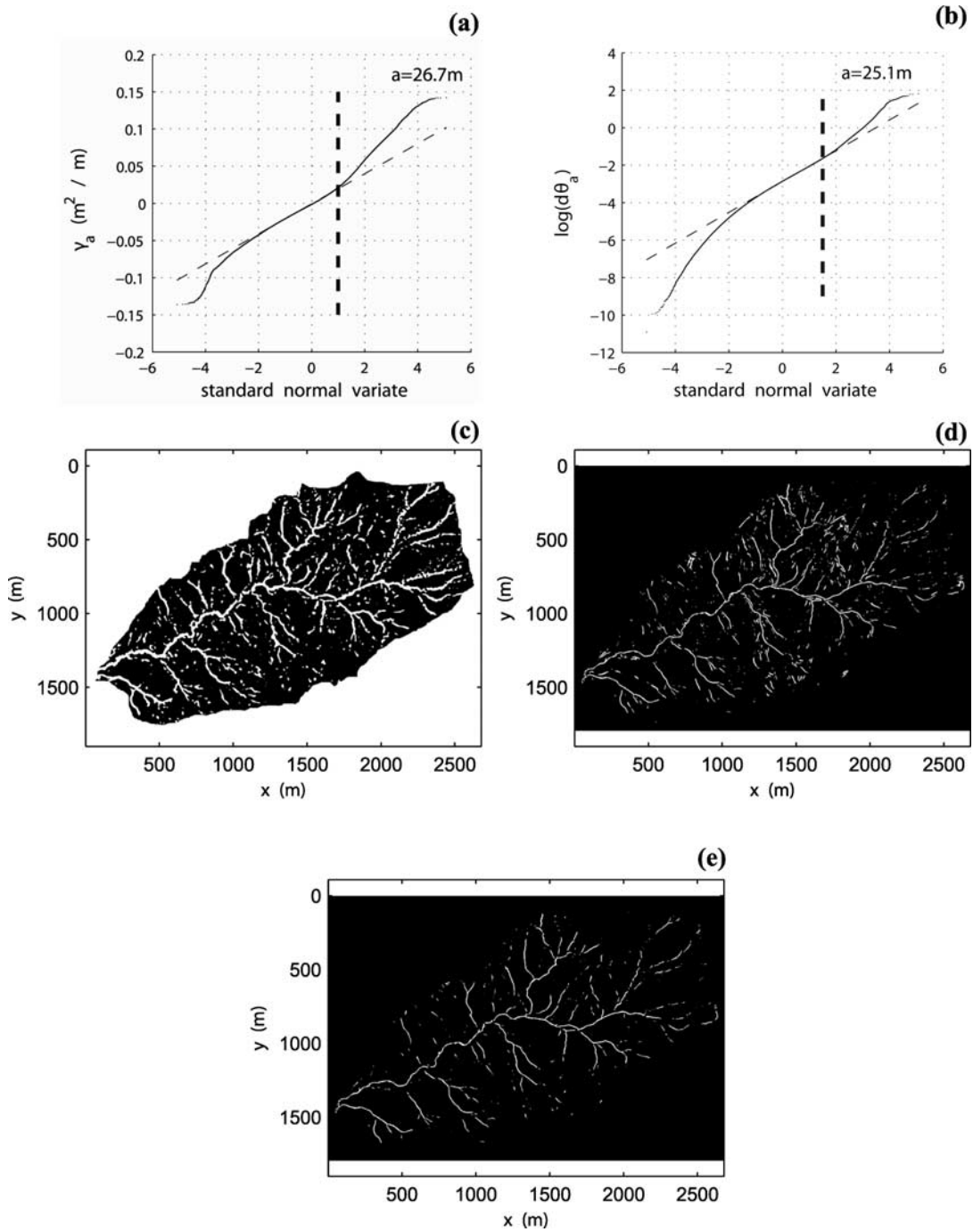
Figure 2. (a) Quantile-Quantile plot of local curvature γ_a defining the threshold curvature $\gamma_{a,th} \simeq 0.025$ for standard normal quantile z = 1. (b) Quantile-Quantile plot of $\log(d\theta_a)$, where $d\theta_a$ is the change in slope direction defining the threshold $d\theta_{a,th}$ for standard normal quantile z = 1.5. (c) The set of pixels S_1 for which $\gamma_a \geq \gamma_{a,th}$. (d) The set of pixels S_2 for which $d\theta_a \geq d\theta_{a,th}$. (e) The set of pixels that satisfy both constraints $S_1 \cap S_2$. The scale of analysis for curvatures is a = 26.7 m and for gradients a = 25.1 m (see Table 1).

By considering grid cells that satisfy both criteria of curvature and slope-direction-change threshold, a more continuous skeleton is obtained (see Figure 2e) indicating all cells most likely to be channelized.

3.4. Generating the Channel Network

[13] Starting from the likely channelized set of grids in Figure 2e, a fully connected channel network is obtained by an algorithm that connects the grid cells at which the derivative of the slope $\theta_a(x, y)$ is locally maximal. The procedure starts at the outlet and proceeds upstream linking all the $d\theta_a$ maxima along the mainstem. The extraction algorithm ends when either the derivative of the slope direction $d\theta_a$ or the curvature γ_a exceeds the thresholds $d\theta_{a,th}$ and $\gamma_{a,th}$ chosen according the statistics of $\log d\theta_a$ and γ_a (equations 9 and 10). A few other constraints were found necessary to avoid loops (which in some cases required manual intervention). The procedure is repeated for each
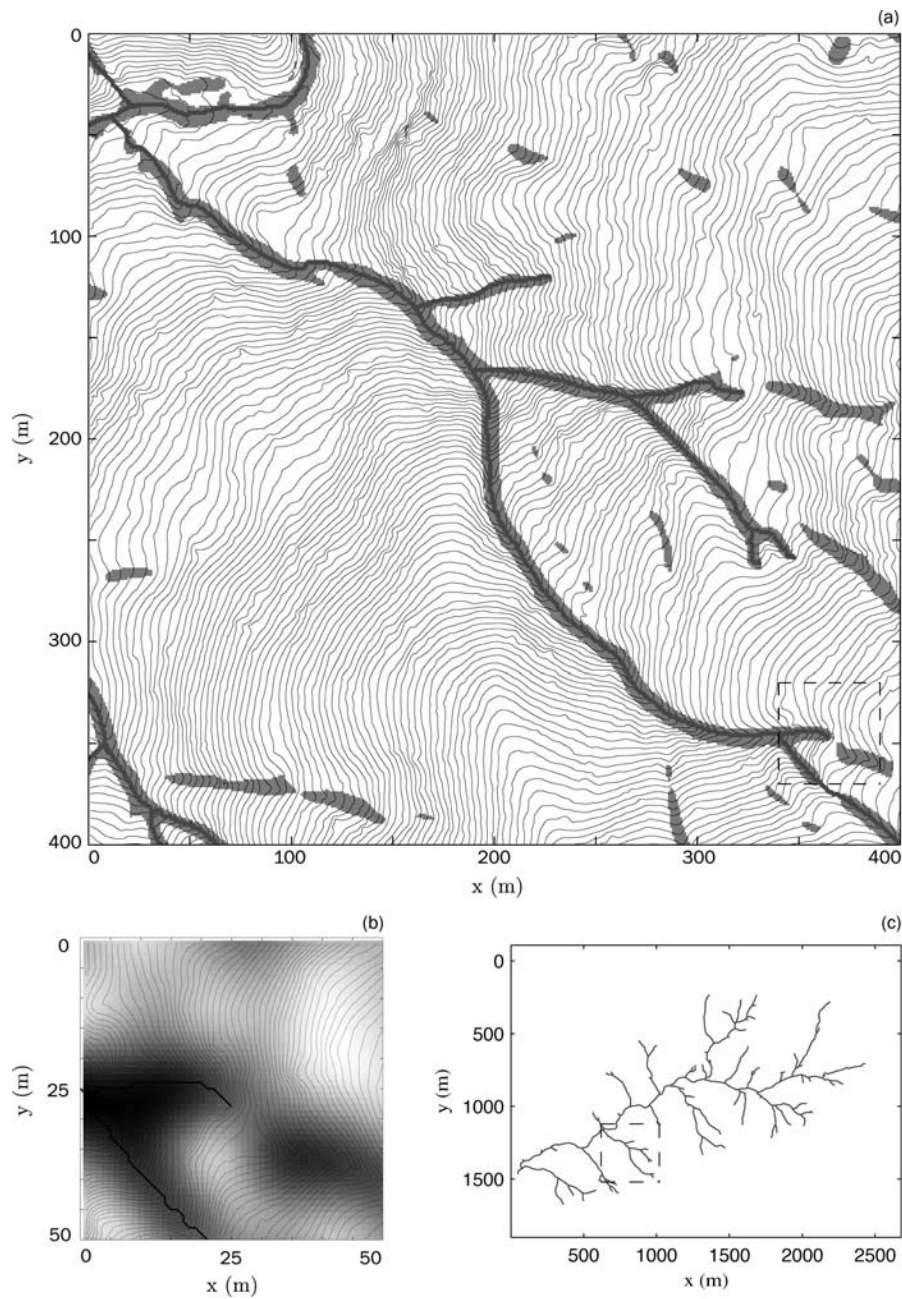
Figure 3. (a) A 400 m by 400 m area (see insert in Figure 3c) which through shading shows the set of pixels for which $\gamma_a \geq \gamma_{a,th}$ and $d\theta_a \geq d\theta_{a,th}$, and thus likely to be channelized, embedded in 2 m elevation contours. (b) A 50 m by 50 m box (see insert box in Figure 3a) showing in detail the extracted continuous channel network by tracing the centerline of the likely channelized areas shown in Figure 3a. Notice the disruption of the channel by a landslide which would be hard to identify with common methods of channel network extraction. The shading corresponds to curvature magnitude and 1m elevation contours are superimposed. (c) The continuous river network extracted for the whole river basin using the proposed methodology.

tributary junction. Junctions themselves often failed to meet one of the two criteria. However, we have resolved this issue by choosing the first point resolvable by the two thresholds and then by projecting towards the stream following the steepest gradient.

[14] The extracted river network for the study watershed is shown in Figure 3c. The insert box in Figure 3c (400 m by 400 m) is shown in detail in Figure 3a. The shaded areas in that Figure 3a are the grid cells that satisfy both threshold criteria (curvature and slope-direction-change) and thus are likely to be channelized. Note that the shaded area as it extends up into steep slopes is estimated to be highly discontinuous by this procedure. Many of the discontinuous patches are associated with the deep-seated landslide-induced steps in the topography. There is a complex interplay between landsliding and channel incision [e.g., *Kelsey*, 1978] that leaves channel traces in the topography well after movement has ceased. A smaller insert boxes (50 m by

50 m) is marked at the bottom right corner of Figure 3a, and is shown in detail in Figure 3b. In Figure 3b, the shading corresponds to curvature magnitude (darker shading for higher positive curvature) and the continuous river center-line as extracted by the proposed procedure is also shown. Figure 3b shows in detail the step-like topography associated with deep-seated landsliding and the disrupted channel network it creates. The channel head occurs on the face of a rotational block where the slope is only weakly convergent. A network drawn using just an area threshold would not have identified these discontinuities, and a method based on area and slope would generally infer incision where slopes are steep, but in the case shown in Figure 3b it would have incorrectly extended an inferred channel across topography that lacks the convergence and slope-change signature of channel incision. Hence, we propose that our procedure provides a more realistic, topographically-driven delineation of the likely channeled portions of the landscape.

4. Conclusions

[15] We proposed a wavelet-based filtering procedure that allows us to compute local curvature and slope-direction-change across scales and exploit their statistical structure for inferring physical transitions. Specifically, deviation of the positive tails of the pdfs of curvature and slope-direction-change from normality and log-normality, respectively, revealed two threshold values corresponding to approximately scale-invariant quantiles (16% exceedance quantile for curvatures and 7% for slope-direction-change). We interpret these breaks in the pdfs as arising from topographic signatures of process change and use the emerging threshold values to delineate valleys (from the curvature threshold) and channelized parts within those valleys (from the slope-direction-change threshold). We report a power law relationship of curvature variance with scale with a major break at a characteristic scale (of approximately 12 m) and two distinct scaling regimes: one at small scales reflecting roughness changes due to vegetation (and other) effects, and one at larger scales due to a progressive smoothing of the landscape variability by coarse graining. These new multiscale statistical relationships and the identified thresholds have been used to propose a methodology for objective extraction of channel networks in canyon upland rivers from high resolution LIDAR topography. They also offer new metrics which might be useful in refining and testing landscape evolution theories and in upscaling geomorphic transport laws.

References

Costa-Gabral, M. C., and S. J. Burges (1994), Digital elevation model networks (DEMON): A model flow over hillslopes for computation of contributing and dispersal areas, *Water Resour. Res.*, 30, 1681–1692.

Dietrich, W. E., D. Bellugi, A. M. Heimsath, J. J. Roering, L. Sklar, and J. D. Stock (2003), Geomorphic transport laws for predicting the form and evolution of landscapes, in *Prediction in Geomorphology*, Geophys. Monogr. Ser., vol. 135, edited by P. Wilcock and R. Iverson, pp. 103–132, AGU, Washington, D. C.

Foufoula-Georgiou, E., and P. Kumar (Eds.) (1994), *Wavelets in Geophysics*, 372 pp., Academic, New York.

Gangodagamage, C., E. Barnes, and E. Foufoula-Georgiou (2007), Scaling in river corridor widths depicts organization in valley morphology, *Geomorphology*, 91, 198–215.

Giannoni, F., G. Roth, and R. Rudari (2005), A procedure for drainage network identification from geomorphology and its application to the prediction of the hydrologic response, *Adv. Water Res.*, 28, 567–581.

Hancock, G. R., and K. G. Evans (2006), Channel head location and characteristics using digital elevation models, *Earth Surf. Processes Landform*, 31, 809–826.

Heine, R. A., C. L. Lant, and R. R. Sengupta (2004), Development and comparison of approaches for automated mapping of stream channel networks, *Ann. Assoc. Am. Geogr.*, 94(3), 477–490.

Kelsey, H. M. (1978), Earthflows in Franciscan melange, Van Duzen River basin, California, *Geology*, 6, 361–365.

Kumar, P., and E. Foufoula-Georgiou (1997), Wavelet analysis for geophysical applications, *Rev. Geophys.*, 35(4), 385–412.

Lin, W., W. Chou, C. Lin, P. Huang, and J. Tsai (2006), Automated suitable drainage network extraction from digital elevation models in Taiwan's upstream watersheds, *Hydrol. Processes*, 20, 289–306.

Mallat, S. (1999), *A Wavelet Tour of Signal Processing*, 2nd ed., Academic, San Diego, Calif.

Montgomery, D. R., and W. E. Dietrich (1988), Where do channels begin?, *Nature*, 336, 232–234.

Montgomery, D. R., and W. E. Dietrich (1989), Source areas, drainage density and channel initiation, *Water Resour. Res.*, 25, 1907–1918.

Montgomery, D. R., and W. E. Dietrich (1992), Channel initiation and the problem of landscape scale, *Science*, 255, 826–830.

Montgomery, D. R., and E. Foufoula-Georgiou (1993), Channel network source representation using digital elevation models, *Water Resour. Res.*, 29, 3925–3934.

Passalacqua, P., F. Porté-Agel, E. Foufoula-Georgiou, and C. Paola (2006), Application of dynamic subgrid-scale concepts from large-eddy simulation to modeling landscape evolution, *Water Resour. Res.*, 42, W06D11, doi:10.1029/2006WR004879.

Rodriguez-Iturbe, I., and A. Rinaldo (1997), *Fractal River Basins: Chance and Self-Organization*, Cambridge Univ. Press, New York.

Roering, J., J. Kirchner, and W. E. Dietrich (1999), Evidence for nonlinear, diffusive sediment transport on hillslopes and implications for landscape morphology, *Water Resour. Res.*, 35(3), 853–870.

Schmidt, J., I. S. Evans, and J. Brinkmann (2003), Comparison of polynomial models for land surface curvature calculation, *Int. J. Geogr. Inf. Sci.*, 17(8), 797–814.

Stark, C. P., and G. J. Stark (2001), A channelization model of landscape evolution, *Am. J. Sci.*, 301, 486–512.

Stock, J., and W. E. Dietrich (2003), Valley incision by debris flows: Evidence of a topographic signature, *Water Resour. Res.*, 39(4), 1089, doi:10.1029/2001WR001057.

Tarboton, D. R. (1997), A new method for the determination of flow directions and contributing areas in grid digital elevation models, *Water Resour. Res.*, 33, 309–319.

Tarboton, D. R., R. L. Bras, and I. Rodriguez-Iturbe (1991), On the extraction of channel networks from digital elevation data, *Hydrol. Processes*, 5, 81–100.

Tucker, G. E., F. Catani, R. L. Bras, and A. Rinaldo (2001), Statistical analysis of drainage density from digital terrain data, *Geomorphology*, 36, 187–202.

————————

W. E. Dietrich, Department of Earth and Planetary Science, University of California, Berkeley, McCone Hall, Berkeley, CA 94720, USA.

E. Foufoula-Georgiou and B. Lashermes, National Center for Earth-Surface Dynamics and St. Anthony Falls Laboratory, Department of Civil Engineering, University of Minnesota, 382 SAFL, 2 34th Avenue SE, Minneapolis, MN 55414, USA. (efi@umn.edu)

Area and width functions of river networks: New results on multifractal properties

Bruno Lashermes[1] and Efi Foufoula-Georgiou[1]

[1] This paper investigates the multiscale statistical structure of the area and width functions of simulated and real river networks via state-of-the-art wavelet-based multifractal (MF) formalisms. First, several intricacies in performing MF analysis of these signals are discussed, and a robust framework for accurate estimation of the MF spectrum is presented. Second, it considers the following three questions: (1) Does the topology of river networks leave a unique signature on the MF spectrum of area and width functions? (2) How different are the MF properties of commonly used simulated trees and those of real river networks? and (3) Are there differences between the MF properties of width and area functions, and what can these tell us about the topology of hillslope versus channelized drainage patterns in a river basin? The results indicate discrepancies between the statistical scaling of the area functions of real networks (found to be multifractal with a considerable spread of local singularities and the most prevailing singularity ranging from 0.4 to 0.8) and that of several commonly used stochastic self-similar networks (found to be monofractal with a single singularity exponent H in the range of 0.5–0.65). Moreover, differences are found between the MF properties of width and area functions of the same basin. These differences may be the result of distinctly different branching topologies in the hillslope versus channelized drainage paths and need to be further investigated.

1. Introduction

[2] The width function of a river network is a one-dimensional function which summarizes the two-dimensional branching structure of the river network. It represents the distribution of travel distances through the network and, under the assumption of constant flow velocity, the probability distribution of traveltimes. Thus its significance for understanding the hydrologic response of basins and the scaling characteristics of streamflow hydrographs is important. The link of hydrologic response and channel network topology via the width function has been recognized early on. For example, see *Kirkby* [1976], *Troutman and Karlinger* [1985], *Gupta et al.* [1986], and *Gupta and Mesa* [1988], who proposed a width function formulation of the geomorphologic unit hydrograph (GUH). These studies focused on the low-frequency component of the width function which exhibits a similarity to the shape of the instantaneous unit hydrograph. More recently, interest has been expressed in the high-frequency component of the width function and especially its multiscaling properties. This paper is a contribution in this direction.

[3] The width function $W(x)$ is defined as the number of channelized pixels at a flow distance $0 \leq x \leq L$ from the basin outlet, where L is the length of the longest channelized path in the network, i.e.,

$$W(x) = \#\{channelized\ M : x \leq l(M) \leq x + dx\}, \quad (1)$$

where $l(M)$ is the flow distance of pixel M from the outlet and dx is the scale of "coarsening." Typically the distance x is normalized by L (in which case the support of $W(x)$ is between 0 and 1) and $W(x)$ is normalized by the total number of pixels rendering it a density. For a given network topology, $W(x)$ can be viewed as a stochastic process indexed by the distance x.

[4] Another function of interest is the so-called area function $A(x)$ defined as the number of pixels, not necessarily channelized, at a flow distance x from the basin outlet:

$$A(x) = \#\{all\ M : x \leq l(M) \leq x + dx\}. \quad (2)$$

[5] It is noted that $A(x)$ does not require the extraction of the channel network from DEMs, a task that still faces the challenge of specifying the channel initiation processes [e.g., *Montgomery and Dietrich*, 1988; *Montgomery and Foufoula-Georgiou*, 1993], and reflects both the channelized and unchannelized (hillslope) parts of the basin.

[6] Several previous works have studied, analytically or via numerical simulation, the statistical scaling properties of $W(x)$ or $A(x)$ for tree topologies such as the Peano basin, Shreve's random topology model, and self-similar trees (SSTs) as well as real river networks [e.g., *Troutman and*

---

[1]St. Anthony Falls Laboratory and National Center for Earth-Surface Dynamics, Department of Civil Engineering, University of Minnesota–Twin Cities, Minneapolis, Minnesota, USA.
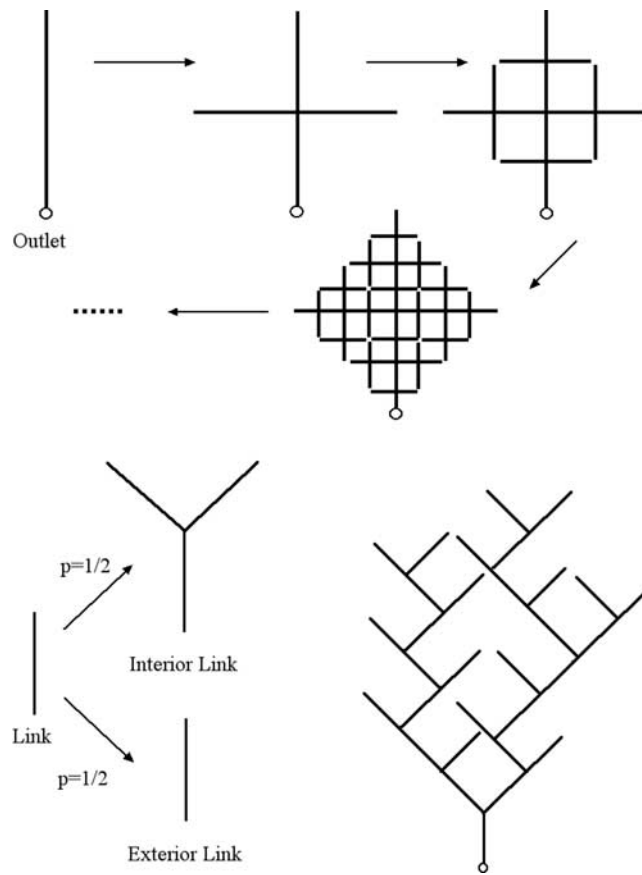
Figure 1.   (top) Peano's basin and (bottom) Shreve's random network construction schemes.

Karlinger, 1984, 1985; *Marani et al.*, 1991, 1994; *Rinaldo et al.*, 1993; *Veneziano et al.*, 1995; *Gupta and Waymire*, 1996; *Agnese et al.*, 1998; *Yang et al.*, 2001; *Richards-Pecou*, 2002]. Following earlier work of *Troutman and Karlinger* [1984], *Gupta et al.* [1986], and *Gupta and Mesa* [1988], recent studies have provided a renewed interest in using simulated river networks and corresponding width functions in efforts to understand, via hydrologic simulation or theoretical derivations, the physical origin of the scaling of floods as arising from the known scaling structure of rainfall and the known fractal properties of river networks [e.g., *Menabde et al.*, 2001; *Troutman and Over*, 2001].

[7]   Given the increasing importance of $W(x)$ and $A(x)$ in hydrogeomorphologic studies, the questions considered in this work are the following: (1) Does the topology of river networks leave a unique signature on the MF properties of the area and width functions? (2) How different are the MF properties of commonly used simulated trees and those of real river networks? and (3) Are there differences between the MF properties of width and area functions and what can these differences tell us about the topology of hillslope versus channelized drainage patterns in a river basin?

[8]   The ability to answer the above questions heavily relies on using the correct tools for MF analysis. *Veneziano et al.* [1995] pointed out some deficiencies in using the standard techniques of MF analysis for width functions, mainly addressing the nonstationary nature of these signals. In this paper, we present a robust framework for MF analysis of width and area functions which (1) offers accurate estimates of the MF spectrum without the need

to know apriori the intrinsic nature of the analyzed signal (i.e., measure versus function) and the form of nonstationarity (linear versus higher-order trends) and (2) offers a concise parameterization of multifractality (two parameters only) even for short signals for which high-order moments are unreliable. We use this framework to point out important differences between the MF properties of simulated and real river networks. Specifically, we show that the width function of real networks has a richer MF structure than reported before (i.e., high intermittency) which differs from the mostly monofractal structure of several commonly used simulated networks. We also point out that the MF properties of width and area functions are different, possibly reflecting the difference between the hillslope and channelized drainage patterns and begging further study.

[9]   This paper is structured as follows. Section 2 presents a review of theoretical branching trees commonly used in hydrology and describes models for their corresponding width and area functions. Section 3 presents a concise overview of MF formalisms which includes the commonly used box aggregation and structure function methods but goes beyond with the use of wavelet-based methodologies. It also presents the cumulant analysis method for accurate estimation of the singularity spectrum parameters especially for short signals as those available for geomorphologic analysis. Section 4 presents a robust framework for MF analysis of area and width functions and demonstrates that care must be exercised in selecting the proper multiresolution coefficients. Section 5 derives numerically the MF properties of the area function of stochastic self-similar
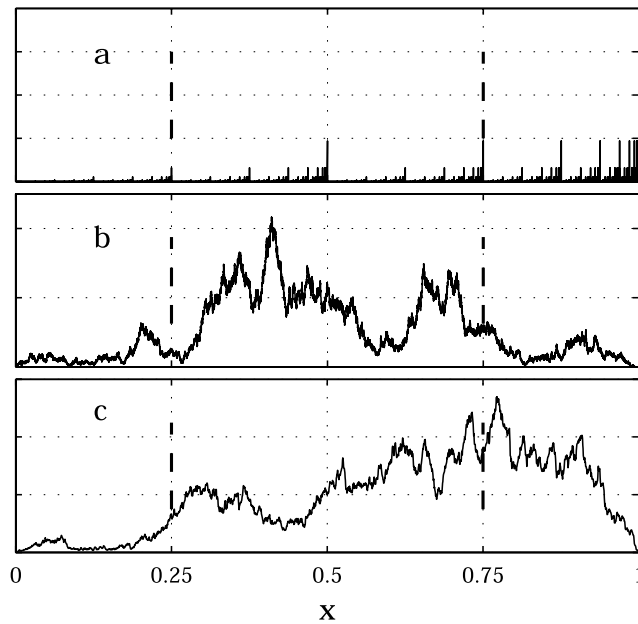
Figure 2. (a) Peano's basin, (b) Shreve's random network, and (c) stochastic self-similar model (with $(\alpha, \beta) = (1, 2)$) area functions. The corresponding order is $\omega = 18$ for Peano's basin and $\omega = 11$ for the stochastic self-similar model. The vertical dashed lines define the central half.

trees. Results from MF analysis are then presented and discussed for area and width functions of real river networks (section 6). Finally conclusions are given in section 7.

2. Models for Area and Width Functions of River Networks

2.1. Horton-Strahler Stream Ordering and Self-Similar Trees

[10] River network streams are usually classified according to the Horton-Strahler ordering scheme [*Horton*, 1945; *Strahler*, 1957]: the network is divided in links that connect either two tributary junctions (internal links) or a tributary junction and a channel source point (external links). (Note that for simplicity the definitions here are given for binary junctions but they can easily be extended to nonbinary ones.) Every external link is given order $\omega = 1$. One then applies a recursive algorithm to compute the order of every link: at every junction, two links of the same order ω give birth downstream to a link of order $\omega + 1$ while two links of order ω and ω' with $\omega \neq \omega'$ give birth downstream to a link of order $\max(\omega, \omega')$.

[11] Self-similar trees (SSTs) are topological descriptions of river networks first introduced by Tokunaga in 1966 and further studied by *Tokunaga* [1978] and *Peckham* [1995], among others. According to SSTs, every stream of order ω has two upstream tributaries of order $\omega - 1$ and several side tributaries of order ω' such that $1 \leq \omega' < \omega$. Let $T_{\omega,\omega'}$ denote the average number of tributaries of order ω' that branch into a stream of order ω. The assumption of self-similarity between streams (and associated drainage basins) of different orders [see, e.g., *Rodríguez-Iturbe and Rinaldo*, 1997] results in the constraint $T_{\omega,\omega'} = T_{\omega-\omega'} = T_k$ with $1 \leq k = \omega - \omega' \leq \omega - 1$. Tokunaga's trees [*Tokunaga*, 1978] are

trees for which the additional constraint holds $T_{k+1}/T_k = const$ which leads to a simple expression for T_k:

$$T_k = \alpha . \beta^{k-1}. \tag{3}$$

This class of trees has been used to describe real river networks. For instance, *Peckham* [1995] successfully characterized a real river network with values $\alpha = 1.2$ and $\beta = 2.4$.

[12] Under the assumption that links are of constant length, it can be shown [*Peckham*, 1995] that the fractal dimension of such trees is

$$D = \frac{\log_2\left[2 + \alpha + \beta + \sqrt{(2 + \alpha + \beta)^2 - 8\beta}\right] - 1}{\log_2 \beta}. \tag{4}$$

[13] This result is important since it defines a constraint on the choice of parameters α and β: one should choose these parameters such that $D < 2$ (non-space-filling network) or at most $D = 2$ (space-filling network). For instance $(\alpha, \beta) = (1, 2)$, which corresponds to Shreve's model to be discussed later, results in $D = 2$, i.e., a space-filling network.

2.2. Peano's Basin

[14] In a seminal work, *Peano* [1890] defined a fractal structure which has been widely used as a model of drainage networks, the so-called Peano's basin. Peano's basin defines a space-filling drainage network for which, as a result, the width and area functions coincide, i.e., $A(x) = W(x)$.

[15] Peano's basin is a specific case of the class of recursive replacement self-similar trees [see *Peckham*, 1995; *Gupta and Waymire*, 1996; *Mandelbrot and Viscek*, 1989] which is a subclass of the SSTs. The iterative building scheme of Peano's basin is illustrated in Figure 1. The tree at first step $\omega = 1$ consists of only one link of length 1. The tree at step ω is built from the tree at the previous order according to the following rule: each mother link of the network at step ω is replaced by four children links (whose lengths are the same and equal to half of the mother link), organized according to a cross pattern. The number of steps used for construction coincides with the largest stream order within the network and thus with the order of the network. This construction rule (which is purely deterministic) defines asymptotically a space-filling tree.

[16] The Peano's basin area function $A(x)$ can be easily derived and is shown to converge (when the number of iterations entering the Peano's basin construction tends to infinity) toward the Besicovitch's measure [e.g., *Marani et al.*, 1991]. First, note that the distance x takes values in $[0, 1]$ for every order ω. The area function at step ω ($A(\omega; x)$) is related to that at the previous step $\omega - 1$ through

$$A(\omega; x) = \begin{cases} \frac{1}{4}A(\omega - 1; 2x) & \text{if } 0 \leq x < \frac{1}{2} \\ \frac{3}{4}A(\omega - 1; 2x - 1) & \text{if } \frac{1}{2} \leq x \leq 1 \end{cases} \tag{5}$$

and thus does coincide with the definition of Besicovitch's measure (or binomial measure) with parameter $p = \frac{1}{4}$. This last is the archetype for a MF measure (equivalently called

distribution) and its singularity spectrum $D(h)$ (see appendix for definition) can be easily derived and expressed with the parameterized formulas [see, e.g., *Schroeder*, 1991]

$$D = -t \log_2 t - (1-t) \log_2 (1-t)$$
$$h = -t \log_2 p - (1-t) \log_2 (1-p)$$
(6)

with $0 < t < 1$ and $p = \frac{1}{4}$ for the specific case of Peano's basin.

[17] The Peano's basin model then predicts for the area function $A(x)$ a MF measure for which the singularity spectrum is known. The distribution $A(18; x)$ is plotted in Figure 2a and its MF analysis will be discussed in section 4.1.

2.3. Shreve's Random Topology Model

[18] *Shreve* [1966] introduced a stochastic model for river networks which provides also models for area and width functions. Shreve's model has been widely used to describe scaling properties of drainage networks and of their area and width functions [see, e.g., *Rodríguez-Iturbe and Rinaldo*, 1997; *Troutman and Karlinger*, 1984; *Agnese et al.*, 1998].

[19] Shreve's model is a binary branching tree defined through the very simple following construction rules. The main ingredient is the assumption that every link has equal probability to be either an exterior link (not connected to any other link upstream) or an interior link (connected to 2 links upstream). Construction of a realization of such a tree starts with one link. This link is then chosen with the same probability 0.5 to be an exterior link, and then the construction process ends, or an interior link and then 2 new children links are connected to it. The construction process recursively applies to each of the children links and so on until there are no more children links (i.e., all children links at previous steps have been chosen to be exterior links). The number of links of the Shreve's model is a random variable taking different values for every realization.

[20] The T_k coefficients can be computed for this model and are shown [see *Shreve*, 1966; *Tokunaga*, 1978; *Peckham*, 1995] to coincide with those of Tokunaga's SSTs: $T_k = \alpha . \beta^{k-1}$ with specific values $(\alpha, \beta) = (1, 2)$.

[21] Shreve's random topology model defines a space-filling network [*Peckham*, 1995] and thus area and width functions coincide as for the Peano's model. $A(x) = W(x)$ is a stochastic process for which realizations can be generated using the following algorithm. $A(x)$ is indexed with an integer argument and is initially set as $A(1) = 1$. Then $A(x + 1)$ is computed from $A(x)$ as $A(x + 1) = \sum_{k=1}^{A(x)} y(k)$ where the $y(k)$ are independent and identically distributed random variables that take the values 0 or 2 with equal probability (i.e., probability 1/2). The construction algorithm ends when $A(x) = 0$. A realization with 109,270 samples is plotted in Figure 2b.

[22] The MF properties of the area function of Shreve's model can be roughly understood as follows. The increments of $A(x)$ can be written as

$$A(x+1) - A(x) = \sum_{k=1}^{A(x)} z(k),$$
(7)

where $z(k) = y(k) - 1$ are independent and identically distributed random variables that take the values $\{-1; 1\}$

with equal probability. The central limit theorem [see, e.g., *Feller*, 1966] states that the normalized sum of i.i.d. random variables with zero mean and unit standard deviation (that are thus finite), i.e, $\frac{1}{\sqrt{N}} \sum_{k=1}^{N} z(k)$, does converge (in the limit $N \to +\infty$) toward a random variable distributed with a normal law of zero mean and unit standard deviation. One may hence approximate $\sum_{k=1}^{A(x)} z(k)$ by a random variable distributed with a normal law with zero mean and standard deviation $\sqrt{A(x)}$, if A(x) is "sufficiently" large. Then, the previous equation becomes

$$A(x + 1) - A(x) \simeq \sqrt{A(x)} n(x),$$
(8)

where $n(x)$ is a Gaussian random variable with zero mean and unit variance. This last equation is a discrete version of the stochastic differential equation:

$$dA(x) = \sqrt{A(x)} dB(x)$$
(9)

where $B(x)$ is the ordinary Brownian motion. The Feller diffusion process is solution of this equation and $A(x)$ may thus be interpreted as a discrete version of the Feller diffusion process [see, e.g., *Etheridge*, 2000]. This last is a process whose realizations are functions (and not measures). This property may be easily understood since $A(x)$ is defined from a (discrete) differential equation. Moreover, the MF properties of the Feller diffusion are known: this process is monofractal, with Hölder exponent: $H = 0.5$ (J. Beresticky, University of Provence, Marseille, private communication, 2006).

[23] This last interpretation is clearly confirmed by numerical analysis of realizations of the process $A(x)$, as it will be shown in section 4.1.

2.4. Stochastic Self-Similar Trees and Their Area and Width Functions

[24] The following recursive algorithm is proposed to generate the area and width functions of SSTs. Note that every link is assumed to have the same length, which defines the unit length (i.e., every link has length 1).

[25] 1. The coefficients T_k are chosen to correspond to those of Tokunaga's trees: $T_k = \alpha . \beta^{k-1}$.

[26] 2. Streams of order 1 possess only one link.

[27] 3. For every stream i of order ω, the number $X_k^{\omega,i}$ of side tributaries of order $\omega - k$ is chosen as the value taken by a random variable which is an integer and is distributed with a Poisson distribution with parameter $\lambda = T_k$. (Note that the mean of such a random variable is λ and its variance is also λ.) All the values $X_k^{\omega,i}$ are statistically independent; the choice of the $X_k^{\omega,i}$ then fixes the number of side tributaries of the stream i to $\sum_{k=1}^{\omega-1} X_k^{\omega,i}$ and hence its number of links to $C^{\omega,i} = 1 + \sum_{k=1}^{\omega-1} X_k^{\omega,i}$.

[28] 4. The locations of the junctions of every side tributary to the stream i are randomly and independently chosen, with a uniform distribution; that is, the probability of a given side tributary to link the stream i at the end of one of the $\sum_{k=1}^{\omega-1} X_k^{\omega,i}$ links is the same for every link and independent of the location of other side tributary junctions.

[29] 5. Two things are noted. First, a different choice for T_k coefficients than stated above can be used for the generation of area and width functions although this is not explored in this paper. Second, a specific choice of T_k does
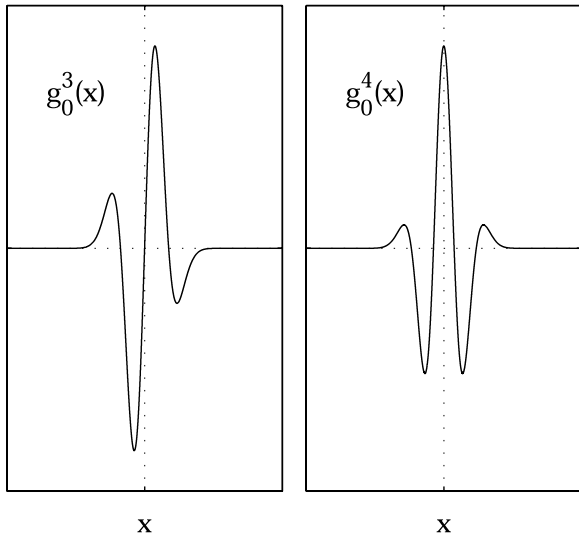
Figure 3. (left) Wavelets g_0^3 and (right) g_0^4 (arbitrary units).

not suffice in defining a unique model for width or area functions as will be demonstrated in section 5. This can be easily understood since the T_k are only the means of the distributions of the side tributaries and thus do not fully characterize them.

[30] 6. It is noted that the SSTs generated by the above algorithm form a specific case of the more general stochastic Tokunaga trees introduced by *Cui et al.* [1999]. The MF properties of the stochastic SSTs are not analytically derivable and will be studied via simulation in section 5.

3. Multifractal Analysis

3.1. Practical Multifractal Analysis

[31] MF formalisms aim to perform on actual data a MF analysis, i.e., estimate the singularity spectrum $D(h)$ (see Appendix A) from the statistics of the local fluctuations of the signal at different scales a and different locations x_0. Let us denote these fluctuations, also called multiresolution coefficients, $c(x_0, a)$, and define the partition functions $S(q, a)$ as estimates (by space averaging) of their qth statistical moments:

$$S(q,a) = \frac{1}{n(a)} \sum_{x_0} |c(x_0, a)|^q, \qquad (10)$$

where $n(a)$ is the number of coefficients $c(x_0, a)$ available at scale a. The scale invariance property of a signal results in power law behavior for the partition functions:

$$S(q,a) \sim a^{\tau(q)}, \qquad (11)$$

defining the usual spectrum of scaling exponents $\tau(q)$, indexed by moment order q. The MF formalism eventually states that the scaling exponents relate to the singularity spectrum through a Legendre transform:

$$D(h) = \begin{array}{ll} 1 + \min_q [qh - \tau(q)] & \text{for functions} \\ 1 + \min_q [qh - (q + \tau(q))] & \text{for measures.} \end{array} \qquad (12)$$

It is noted that the difference in the definitions of Legendre transform for functions and measures (see Appendix A for definition of a measure) is due to the common choice for normalization of the multiresolution coefficients (indeed, if one uses $a.c(x_0, a)$ instead of $c(x_0, a)$, the scaling exponents $\tau(q)$ are shifted to $q + \tau(q)$).

[32] Note that if the signal under analysis is monofractal then the scaling exponents vary linearly with respect to the moment order q, i.e., $\tau(q) = qH$. In contrast, if the singularity spectrum takes finite values on an interval $[h_{min}, h_{max}]$ with $h_{max} > h_{min}$, the scaling exponents $\tau(q)$ no longer define a linear but rather a nonlinear function.

3.2. Multiresolution Coefficients

[33] As discussed in the previous section one first needs to compute the multiresolution coefficients $c(x_0, a)$ in order to perform a MF analysis. There are several choices of multiresolution coefficients, that can be valid or not depending on the nature of the data under analysis, e.g., function or measure and the presence of nonstationarities. The correct selection of multiresolution coefficients is thus of first importance in order to perform a meaningful MF analysis.

3.2.1. Catalog of Multiresolution Coefficients

[34] The MF formalism was historically introduced with partition functions computed with first-order increments for functions (the so-called structure function method [*Parisi and Frisch*, 1985])

$$c(x_0, a) = \delta(x_0, a) = s(x_0 + a) - s(x_0) \qquad (13)$$

and box aggregation coefficients for measures [*Hasley et al.*, 1986]

$$c(x_0, a) = b(x_0, a) = \frac{1}{a} \int_{x_0 - a/2}^{x_0 + a/2} s(x)dx. \qquad (14)$$

Wavelet coefficients [*Mallat*, 1998] provide a more versatile and efficient choice for multiresolution coefficients and can be used for MF analysis of both functions and measures and for nonstationary signals [*Arneodo et al.*, 1995; *Jaffard*, 1997] (see also discussion below). Wavelet coefficients $w(x_0, a)$ are defined as the inner product between the data $s(x)$ and the wavelet $\psi_{x_0,a}(x)$, associated with location x_0 and scale a:

$$c(x_0, a) = w(x_0, a) = \int_{\mathbb{R}} \psi_{x_0,a}(x)s(x)dx, \qquad (15)$$

where $\psi_{x_0,a}(x)$ is a scale-dilated and time-shifted template of the mother wavelet $\psi_0(x)$:

$$\psi_{x_0,a}(x) = \frac{1}{a} \psi_0 \left(\frac{x - x_0}{a} \right). \qquad (16)$$

[35] A commonly used wavelet family is the Gaussian wavelets (which are continuous wavelets; that is, spatial location x_0 and scale a can take on any real value), defined as the N-order derivative of a Gaussian function, modulus a proper multiplicative factor to ensure correct normalization. The derivative of order N is denoted as $g_0^N(x)$. Wavelets $g_0^3(x)$ and $g_0^4(x)$ are plotted in Figure 3.

[36] An important feature of the mother wavelet ψ_0 for practical purposes is its number of vanishing moments: $N \geq 1$ such that $\int x^k \psi_0(x) dx = 0$ if $0 \leq k \leq N - 1$ and $\int x^N \psi_0(x) dx \neq 0$. The use of a wavelet with a given N allows the removal of an additive polynomial trend of degree less than N (which can cause a failure of MF analysis [see *Arneodo et al.*, 1995]). From a practical point of view, the number of vanishing moments has to be chosen sufficiently high such that robustness of the results is achieved; that is, there is no dependence on the chosen wavelet. The Gaussian wavelet $g_0^N(x)$ can be easily shown to have N vanishing moments.

3.2.2. Choice of Multiresolution Coefficients

[37] The previous section depicts several choices of multiresolution coefficients: increments or wavelet coefficients for MF analysis of functions (including functions with polynomial trends) and box aggregation coefficients or wavelet coefficients for MF analysis of measures. The ability of wavelet coefficients to be used for analysis of both functions and measures can be understood qualitatively since a wavelet gathers local average and differentiation patterns (cf. Figure 3): the wavelet coefficients are thus a common extension of both increments and box aggregation coefficients. This assertion will be quantitatively illustrated in section 4.1 via an example.

[38] It is important to point out that an erroneous choice, such as the use of increments for a measure or the use of box aggregation coefficients for a function, or use of increments of insufficient order for a nonstationary signal, leads to artifacts and thus to misleading conclusions: a correct MF analysis requires a correct choice of multiresolution coefficients. Since often one does not know before hand the exact nature of the analyzed signal, a robust MF analysis framework is proposed in this paper (see section 4) which can both identify the correct mathematical nature of a signal (measure, function, degree of nonstationarity) and correctly estimate its singularity spectrum.

3.2.3. Moments of Negative Order q

[39] From the Legendre transform relationship (equation (12)), it is seen that

$$q = dD(h)/dh, \tag{17}$$

and thus for estimating the decreasing (right) part of the $D(h)$ function, in order to gain access to the whole range of singularities from h_{min} to h_{max}, one needs to consider estimation of $\tau(q)$ for negative moments q. The MF formalism based on increments, or even on continuous wavelet transform (CWT) coefficients $c(x_0, a)$, suffers from the fact that it is not valid for estimation of $\tau(q)$ for $q < 0$. This is because the probability distribution of increments or CWT coefficients is centered at zero and thus negative moments diverge [see, e.g., *Venugopal et al.*, 2006b]. This drawback can be overcome by using the WTMM (Wavelet Transform Modulus Maxima) methodology which operates on the modula of the wavelet coefficients which are always positive [*Muzy et al.*, 1993, 1994; *Arneodo et al.*, 1995]. This methodology defines the WTMM coefficients, denoted as $m(x_0, a)$, which can be used to compute the partition functions and thus the scaling exponents and the singularity spectra of functions. The reader is referred to *Muzy et al.* [1993, 1994], *Arneodo et al.* [1995], or *Venugopal et al.*

[2006a, 2006b] for detailed presentation and illustration of this MF formalism. It is also noted that a new MF formalism, relying on a well-defined mathematical basis and based on the so-called wavelet leaders (defined from the discrete wavelet transform [*Mallat*, 1998]) has been recently introduced in order to overcome this difficulty [*Jaffard et al.*, 2005; *Lashermes*, 2005; B. Lashermes et al., Wavelet leaders based multifractal formalism: A comprehensive analysis of turbulent velocity, submitted to *European Physical Journal B*, 2007].

3.3. Multifractal Parameter Estimation With Cumulant Analysis

[40] The scaling exponent function $\tau(q)$ reflects the MF properties of the data under analysis since it is the Legendre transform of the singularity spectrum $D(h)$. As discussed above, estimation of $\tau(q)$ typically relies on computation of the partition function $S(q, a)$ for different order moments q (equation (10)) and estimation of the slopes of the log-log linear plots of $S(q, a)$ versus scale α. In order to depict the deviation of $\tau(q)$ from linearity (the hallmark of multifractality) one has to estimate moments of high-order (the literature reports moments up to order $q = 10$). This presents not only problems of statistical convergence for short signals but also problems of interpretation of high moments due to a degenerate linear behavior of $\tau(q)$, theoretically expected for $q > q_{max}$, where q_{max} depends on the inherent MF nature of the analyzed signal. Basically, the maximum interpretable q is determined by the largest Holder exponent h_{max} present in the signal; for $q > q_{max}$ a linear $\tau(q)$ curve is expected even for a true MF signal. The reader is referred to *Lashermes et al.* [2004] and also *Venugopal et al.* [2006a] for further details on these estimation problems.

[41] An alternative estimation methodology, called cumulant analysis method, which avoids the need to compute high-order moments and also leads to a concise MF parameterization, has recently been introduced in the literature [e.g., *Arneodo et al.*, 1998; *Malécot et al.*, 2000; *Delour et al.*, 2001] and has been used in geophysics for the analysis of high-resolution temporal rainfall [*Venugopal et al.*, 2006a, 2006b]. The reader is referred to these publications for details on the methodology.

[42] The cumulant analysis method, provides an estimation of the parameters c_p of the Taylor series expansion of $\tau(q)$ for $q \to 0$:

$$\tau(q) = \sum_{p \geq 1} (-1)^{p-1} \frac{c_p}{p!} q^p \tag{18}$$

by computing the statistical cumulants $C(p, a)$ of order p of the logarithm of the absolute value of the multiresolution coefficients $c(x_0, a)$ at a given scale a. Similarly to the partition functions (cf. equation (10)), the cumulants define a function of p and a which is furthermore linear with respect to $\ln a$ for MF functions. For instance, for $p = 1$ and 2,

$$C(1, a) = \frac{1}{n(a)} \sum_{x_0} \ln|c(x_0, a)| \simeq a_1 + c_1 \ln a \tag{19}$$

$$C(2, a) = \frac{1}{n(a)} \sum_{x_0} [\ln|c(x_0, a)| - C(1, a)]^2 \simeq a_2 - c_2 \ln a. \tag{20}$$
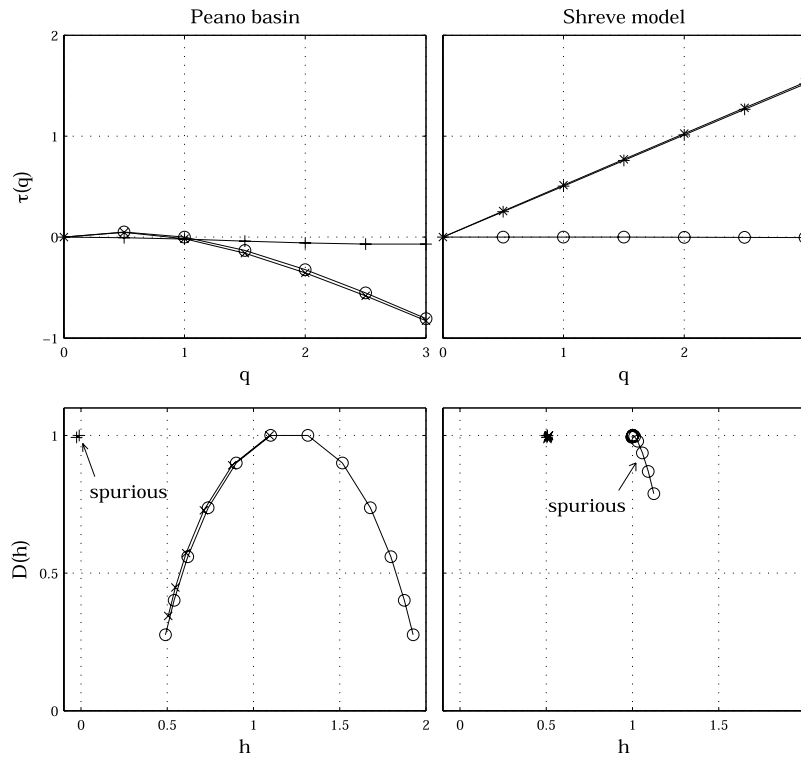
Figure 4. Measure or function? (top) Scaling exponents $\tau(q)$ and (bottom) predicted singularity spectra $D(h)$ computed with box aggregation (circles), increments (pluses), and wavelet coefficients (crosses) for (left) Peano's basin and (right) Shreve's model area function $A(x)$ (wavelet g_0^4). Scaling exponents are computed for negative q values for box aggregation coefficients in order to provide the right lobes of the singularity spectra; negative moments cannot be computed for increments or wavelet coefficients (see text for discussion).

Linear regressions of $C(p, a)$ versus $\ln a$ thus allow estimation of the c_p.

[43] If the process under analysis is monofractal then $c_1 = H \neq 0$ and $c_p = 0$ for $p > 1$. A nonzero value for c_2 explicitly establishes the multifractal (versus monofractal) nature of the data: c_1 is the most prevailing Hölder exponent value ($D(h)$ is maximum at $h = c_1$) and the parameter c_2 (also called the intermittency coefficient) relates to the spread of $D(h)$ around c_1. The quadratic approximation of the scaling exponent function

$$\tau(q) \simeq c_1 q - c_2 q^2/2, \qquad \text{when } q \to 0, \qquad (21)$$

which corresponds to a quadratic approximation of the singularity spectrum,

$$D(h) \simeq 1 - \frac{(h - c_1)^2}{2c_2}, \quad \text{when } h \to c_1 \qquad (22)$$

is a commonly used model of multifractality. This model has been shown to be both meaningful and a good approximation in turbulence (for which it corresponds to the so-called lognormal model).

[44] These tools will be applied in the sequel to characterize the MF properties of the width and area functions, using the CWT and the WTMM multiresolution coefficients. Since the WTMM coefficients allow the scaling exponent estimation both for $q < 0$ and $q > 0$, in contrast

to CWT coefficients which only allow estimation for $q > 0$, they are known to provide better estimators (faster statistical convergence for instance) at least for $p \geq 2$. The reader is referred to *Delour et al.* [2001] and *Venugopal et al.* [2006b] for further details of the methodology.

4. Potential Pitfalls and a Robust Methodology for Multifractal Analysis of Width and Area Functions

4.1. Discrimination Between Function and Measure: Peano's Versus Shreve's Models

[45] As was shown in section 2, different network topologies result in area and width functions that are distinctly different in terms of their mathematical nature. For example, the Peano basin area function is a mathematical measure (distribution) while that of Shreve's model is a mathematical function. Analyzing both signals with the same multiresolution coefficients for estimating their singularity spectra, e.g., using for both the first-order structure function approach or the box-counting approach, can lead to misleading interpretations. The purpose of this section is (1) to quantitatively demonstrate that erroneous results on MF characterization can be obtained by an innapropriate choice of the multiresolution coefficients and (2) to present a framework for MF analysis which does not require a priori knowledge of the mathematical nature of the signal, but
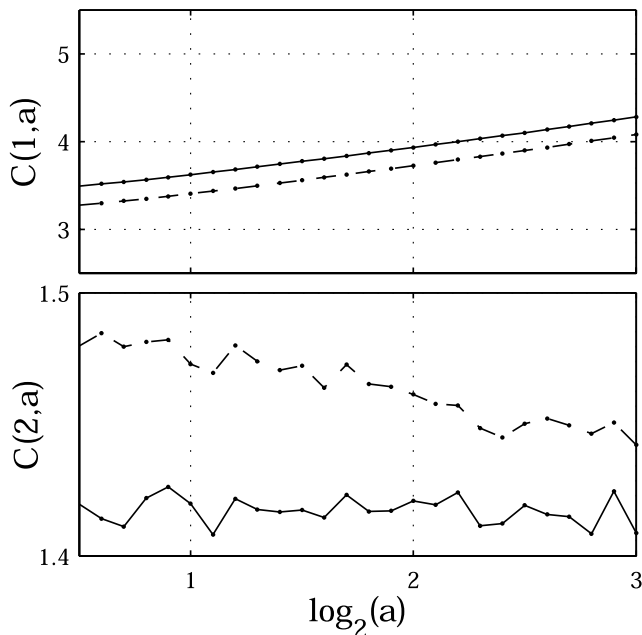
Figure 5. Effect of nonstationarity: average over $N = 100$ realizations of Shreve's model area function of (top) first and (bottom) second cumulants of the whole realization (dashed line) and the central half (solid line) computed with CWT coefficients (wavelet g_0^4).

rather the framework identifies the underlying structure and selects the appropriate multiresolution coefficients.

[46] Let us denote the scaling exponent function $\tau(q)$ defined with box aggregation, first-order increments and wavelet coefficients, respectively, as $\tau^b(q)$, $\tau^\delta(q)$ and $\tau^w(q)$. We will demonstrate below that when all of them are computed from a sampled signal (data set), if $\tau^b(q)$ and $\tau^w(q)$ coincide and depart from $\tau^\delta(q)$, then the data under analysis correspond to a measure, whereas if $\tau^\delta(q)$ and $\tau^w(q)$ coincide and depart from $\tau^b(q)$, then the data under analysis correspond to a function

$$\begin{aligned} \tau^\delta(q) \neq \tau^w(q) = \tau^b(q) &\longrightarrow \text{measure} \\ \tau^\delta(q) = \tau^w(q) \neq \tau^b(q) &\longrightarrow \text{function}. \end{aligned} \quad (23)$$

[47] Moreover, if the interest is not really in inferring the mathematical nature of the signal but in correctly estimating its MF spectrum, the above framework depicts the appropriate multiresolution coefficients and leads to a correct estimate of the MF spectrum.

[48] MF analysis of the Peano's and Shreve's models area functions (cf. section 2) are performed using box aggregation, increment and wavelet coefficients (the wavelet used is g_0^4) and the results are shown in Figure 4. Scaling exponents

with negative q values are computed with box aggregated coefficients only, thus yielding the right lobe of singularity spectrum, since negative moments are statistically meaningless for increment or wavelet coefficients. As theoretically expected, the Peano model results in a (multifractal) measure for $A(x)$ and one observes $\tau^\delta(q) \neq \tau^w(q) \simeq \tau^b(q)$, whereas the Shreve model results in a (monofractal) function for $A(x)$ and one observes $\tau^\delta(q) \simeq \tau^w(q) \neq \tau^b(q)$. These results clearly show how to characterize the intrinsic mathematical nature of the digital (sampled) data under analysis without apriori information about the signal.

[49] Figure 4 illustrates as well the fact that an erroneous choice of multiresolution coefficients leads to an incorrect estimate of the spectrum of singularities. For instance, performing MF analysis of the function $A(x)$ predicted by the Shreve's model using box aggregation coefficients (see Figure 4, right plots) leads to the erroneous conclusion that the singularity spectrum $D(h)$ (in the measure regularity sense) is reduced to one point with coordinates ($h = 1$, $D = 1$) with a decreasing right lobe. However, using first-order increment and wavelet coefficients gives results in perfect agreement with the expectation discussed in section 2, i.e., $\tau^\delta(q) \simeq \tau^w(q) \simeq 0.5q$ which is indeed the Legendre transform of the singularity spectrum of a monofractal process with $H = 0.5$. As will be discussed below such analyses, i.e., using box aggregation coefficients for real network width functions, are commonplace in the literature and have resulted in suggestions that real networks have area functions with $D(h) = 1$ at $h \simeq 1$.

4.2. Nonstationarity Property of Area and Width Functions

[50] The area and width functions by definition start and end at zero. Moreover, if the length of the longest flow path is L, few pixels or links are located close to the basin outlet (i.e., at flow distance $x \ll L$) or at distance close to L (i.e., at flow distance x such that $(L - x) \ll L$). These functions then exhibit a nonstationary behavior which one has to deal with before performing practical MF analysis. As discussed previously, the MF analysis indeed assumes a stationarity property for the local distribution of Hölder exponents: this last is expected to be everywhere the same, which allows to replace statistical averages by spatial averages for the estimation of moments defining the partition functions (cf. equation (10)). It is noted that although the wavelet-based MF formalism can automatically deal with nonstationary signals in terms of removing polynomial trends (since by using wavelets with N vanishing moments a polynomial of degree N is filtered out from the signal), the form of nonstationarity in the width and area functions is of a particular type arising from the fact that close to the outlet and the upper end of the river basin, the branching structure is not well developed yet and this is reflected in the

Table 1. Different Parameter Sets Investigated for Stochastic Self-Similar Model

(α, β)	(0.75, 1.894)	(1, 2)	(1.25, 2.095)	(1.5, 2.183)	(1.75, 2.266)	(1.5, 2.5)	(1, 3)
D	2	2	2	2	2	1.76	1.41
order	13	12	11	11	10	10	10
$\bar{n}$	3894	4160	3618	5817	3950	6435	14827
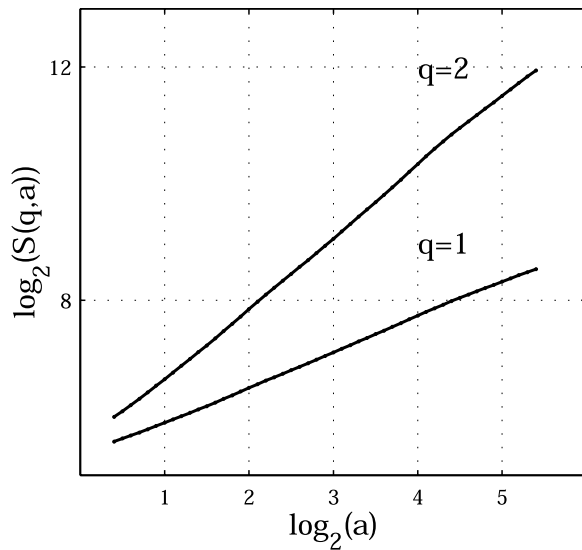
Figure 6. Stochastic self-similar model $((\alpha, \beta) = (1, 2))$ partition functions of order $q = 1, 2$ computed with CWT coefficients (wavelet g_0^4).

statistical nature of the width function fluctuations close to $x = 0$ and $x = L$.

[51] To assess the effectiveness of practical MF analysis to accurately estimate the MF spectra of the data under consideration, the analysis is performed both on the whole realization and on its central half only (i.e., if the realization has n samples, its central half is defined as the part between $n/4$ and $3n/4$) of the Shreve's model area function (cf. section 2.3). The results obtained with cumulant analysis are discussed below.

[52] Averages over 100 realizations (of length between 4096 and 8092 samples) of first and second-order cumulants (computed with CWT coefficients and wavelet g_0^4) for both the whole realization and the central part are plotted in Figure 5. All cumulants exhibit power law behavior and the cumulant exponents can hence be estimated. Estimation of the first-order cumulant exponent results in $c_1 \simeq 0.53 \pm 0.02$ for the whole realization and $c_1 \simeq 0.49 \pm 0.03$ for the central half, both statistically consistent with the expected value $c_1 = 0.5$. However, it is obvious that for the case when the whole realization is used, $C(2, a)$ has a significantly different than zero slope ($c_2 > 0$) while when the central half only is used, $C(2, a)$ is constant ($c_2 \simeq 0$). Interpreting these results through a MF lens would lead to conclude a multifractality for the whole realization and monofractality for its central half. MF analysis on the whole realization is then misleading since the function $A(x)$ is known to be monofractal with $H = 0.5$.

[53] We then conclude that the data fluctuations within the central part of the width and area functions may be assumed to be stationary and that MF formalisms may be meaningfully applied to the central half giving results that correctly reflect the properties of the underlying branching structure of the network [see also *Veneziano et al.*, 1995]. MF analysis of area and width functions of all networks (either synthetic or real) discussed in this paper is then performed on the central half for the remaining of this paper.

4.3. Analysis of Real Width and Area Functions: A Review of Other Efforts

[54] Several studies have considered MF analysis of width and area functions of real and simulated river networks [e.g., *Rinaldo et al.*, 1993; *Marani et al.*, 1994; *Veneziano et al.*, 1995; *Yang et al.*, 2001; *Richards-Pecou*, 2002] but some of the findings need to be reconsidered. First, several studies have reported that the area function of real river networks is a multifractal with $D(h) = 1$ at $h \simeq 1$ and a slowly falling right limb for $h > 1$ [e.g., see *Rodríguez-Iturbe and Rinaldo*, 1997, Figures 3.16, 3.17, 3.23; *Yang et al.*, 2001]. The same results have been reported for simulated optimal channel networks (OCNs) [e.g., see *Rodríguez-Iturbe and Rinaldo*, 1997, Figures 4.26, 42.7].

[55] These studies have used the box-counting method, which works fine for the Peano basin whose $A(x)$ is a measure, but is not appropriate for the Shreve model or for real networks for which the $A(x)$ is a function. It is worth noting that an estimate of $D(h)$ concentrated around $h = 1$ has prompted suggestions in the literature that the width function of real networks is close to that of the Peano basin for which the theoretical H is 1.207. This is an artifact of the analysis methodologies.

[56] A second problem is that inferences about the deviation from multifractality (nonlinear $\tau(q)$) have been based on very high order moments (e.g., from -10 up to 10) computed from short series. This can lead to spurious lobes of the singularity spectrum. Yet, since the left lobe is always found to decrease very rapidly allowing thus no discrimination (e.g., see the previously mentioned figures in the literature), the right lobe has been used for discriminating among modeled and real networks and also for assessing the effects of threshold area for channel initiation on the MF properties of width functions [e.g., see *Rodríguez-Iturbe and Rinaldo*, 1997, Figure 3.23; *Yang et al.*, 2001]. This
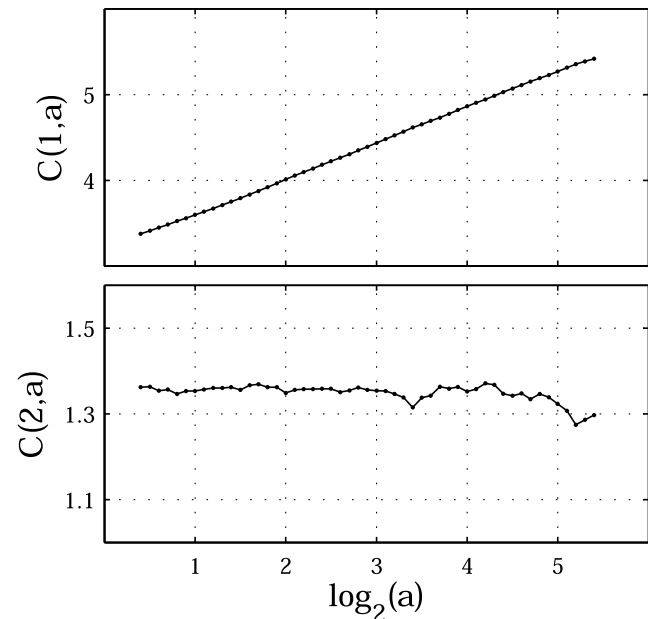
Figure 7. Stochastic self-similar model $((\alpha, \beta) = (1, 2))$ cumulants of order (top) $p = 1$ and (bottom) $p = 2$ computed with CWT coefficients (wavelet g_0^4).

Table 2. Mean of Cumulant Exponents for Area Functions of Stochastic Self-Similar Trees, Computed on the Central Half Portion With CWT and WTMM Coefficients Averaged Over $N = 100$ Realizations[a]

	(α, β)	(0.75, 1.894)	(1, 2)	(1.25, 2.095)	(1.5, 2.183)	(1.75, 2.266)
CWT	c_1	0.65 ± 0.01	0.62 ± 0.01	0.55 ± 0.01	0.55 ± 0.01	0.55 ± 0.01
	c_2	0.00 ± 0.01	0.01 ± 0.01	0.00 ± 0.01	0.01 ± 0.01	0.00 ± 0.01
	c_3	0.00 ± 0.04	0.01 ± 0.02	0.01 ± 0.02	0.00 ± 0.02	-0.01 ± 0.04
WTMM	c_1	0.64 ± 0.02	0.60 ± 0.01	0.56 ± 0.01	0.56 ± 0.01	0.54 ± 0.01
	c_2	0.01 ± 0.01	0.00 ± 0.01	0.00 ± 0.01	0.00 ± 0.01	0.01 ± 0.01
	c_3	0.02 ± 0.01	0.00 ± 0.01	0.01 ± 0.01	0.01 ± 0.01	0.01 ± 0.01

[a]The wavelet used is g_0^4. The given confidence intervals are $\pm 2\sigma / \sqrt{N}$, where σ is the estimated standard deviation. Note that all considered combinations of (α, β) parameters result in space-filling trees (see equation (4)).

right lobe however is all an artifact of the analysis methodology; it relies on negative statistical moments which, although statistically feasible to compute from box aggregation coefficients, have no meaning since the box aggregation coefficients are not appropriate for analyzing a MF function. The proposed framework (using WTMM coefficients and cumulant analysis) provides accurate estimates of the whole singularity spectrum and also a concise parameterization which does not require the computation of high-order moments.

5. Numerical Multifractal Characterization of Stochastic Self-Similar Trees

[57] The stochastic SSTs presented in section 2.4 do not receive analytical expressions for the MF properties of their area and width functions. Thus these properties are investigated through numerical analysis of a large number (100) of realizations with the same values for order ω and parameters α and β (cf. Table 1). Several values of the parameters (α, β) are investigated with practical MF analysis, corresponding both to space-filling or non-space-filling networks. Note that the network orders have been chosen so that the average number of samples, denoted as $\overline{n}$, is almost the same for every choice of parameters α and β.

[58] The first step is to check that both partition functions and cumulants do behave like power laws with respect to scale a. For (α, β) values corresponding to space-filling networks this is indeed true (cf. Figures 6 and 7 for (α, β) = (1, 2); similar power law behaviors are observed for other

parameter value choices) but no clear power law behavior is observed when the network is not space filling. The origin of the departing behavior from scaling is intriguing and requires further study in the future. Here, only (α, β) values such that $D = 2$ are considered, thus defining processes for which the practical MF analysis is fully consistent and results in reliable estimates of the scaling and cumulant exponents.

[59] MF analysis is performed on the central half of every realization, using both the CWT and WTMM methodology (the wavelet used is g_0^4). Table 2 presents the results obtained for the three first cumulant exponents. For every set of parameters (α, β), the results obtained from the numerical analysis, within confidence intervals (confidence interval is the common 95% confidence interval for the empirical average estimator on N samples of a Gaussian random variable: $\pm 2\frac{\sigma}{\sqrt{N}}$ where σ is the estimated standard deviation), show a monofractal behavior, characterized by the parameter c_1 only. Moreover, the estimated value of c_1 depends on the choice of (α, β) and ranges from 0.54 to 0.65, which are all larger than the one corresponding to Shreve's model area function (i.e., 0.5). Also, it is interesting to note that for (α, β) corresponding to space-filling SSTs, c_1 clearly decreases when α increases. In other words, when the "branching rate," that is, the number of tributaries of streams of a given order increases, the area function exhibits wilder fluctuations and becomes more and more irregular.

[60] Another interesting result concerns the values obtained for (α, β) = (1, 2): though the T_k coefficients of the
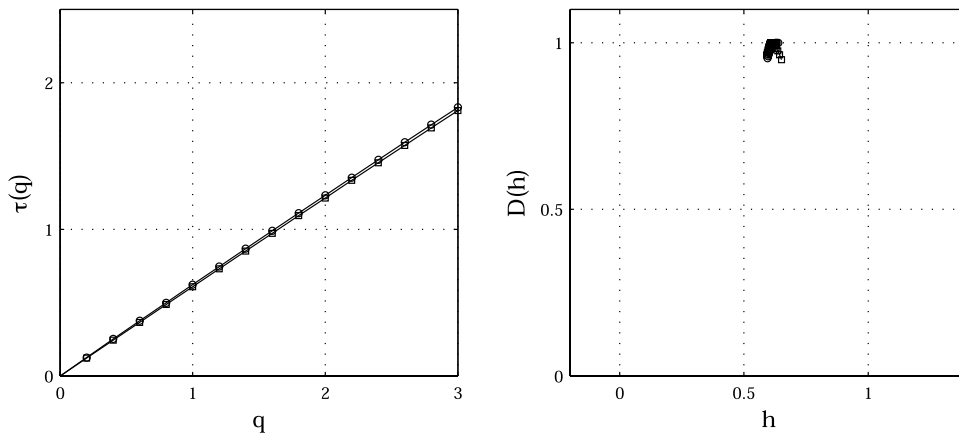
Figure 8. Stochastic self-similar model $((\alpha, \beta) = (1, 2))$ (left) scaling exponents $\tau(q)$ and (right) singularity spectrum $D(h)$ of area function $A(x)$ computed with CWT (circles) and WTMM (squares) coefficients (wavelet g_0^4).

Figure 9. Drainage basins and river networks for (top left) Walawe River (DEM resolution 90 m), Sri Lanka; (top right) South Fork Eel River (DEM resolution 1 m), California, United States; and (bottom) Noyo River (DEM resolution 10 m), California, United States.

underlying trees do coincide with those of the Shreve's model (cf. section 2.3), the related area functions clearly exhibit different regularity properties, i.e., with $H = 0.50$ for Shreve's model (see Figure 4, right) or $H = 0.60$ for SSTs (see Figure 8). This result supports the fact that knowledge of the coefficients T_k is not sufficient information to fully characterize a river network, since the T_k are only the means of the distributions of the number of side tributaries and do not account for higher-order statistical moments. A systematic analysis of the MF properties of the more general stochastic SSTs introduced by *Cui et al.* [1999], is an interesting topic for further study which however falls outside the scope of the present paper.

6. Multifractal Analysis of Real River Basin Area and Width Functions

6.1. Data Used for Analysis

[61] Analysis of area and width functions extracted from DEM of three real river basins (Figure 9) is performed in this paper. Walawe River is a river located in Sri Lanka and its drainage area is almost 2000 km^2. The area ($A(x)$) and width ($W(x)$) functions are extracted from DEM of spatial resolution 90 m × 90 m. The area function of the upper part of the South Fork Eel River basin, California, USA (corresponding drainage area of 154 km^2) is extracted from high-resolution 1 m × 1 m DEM (LIDAR technology) and 10 m × 10 m DEM (see *Gangodagamage et al.* [2007] for more details on this basin). Finally, the area and width function of the Noyo River basin, California, USA are

extracted from DEM of spatial resolution 10 m × 10 m (corresponding drainage area of 143 km^2 [see *Sklar et al.*, 2006, and references therein] for more details on this basin). All these basins are plotted in Figure 9.

[62] From a practical point of view, one important parameter when extracting the area and width functions from a DEM is the bin size dx: $\{A(dx; x)\} = \# \{all\ M: x \le l(M) \le x + dx\}$, where $l(M)$ denotes the flow distance of pixel M to the outlet. One should carefully select the value for dx: if dx is too close to the DEM spatial resolution, then the computed $A(x)$ or $W(x)$ will take only small integer values and thus will be polluted by high-digitization noise. This effect can be specifically important for $W(x)$ since the percentage of channelized pixels is very small. On the other hand, a large value for dx may mask, because of averaging, the MF signatures of the underlying network structure. The bin size dx is chosen sufficiently large so as not to affect the results presented in this paper. The number of samples is 2,513 for the Walawe River area and width functions, 3,962 for the South Fork Eel River area function and 1,948 for the Noyo River area and width functions. All area and width functions are plotted in Figure 10.

6.2. Multifractal Characteristics of Several River Basin Area Functions

[63] The singularity spectra of the area and width functions of the Walawe river basin have been computed using box aggregation, increment and wavelet coefficients (the wavelet used in this section is g_0^4).

[64] The results are plotted in Figure 11 in a similar way as for the synthetic data (see Figure 4). Both for area and
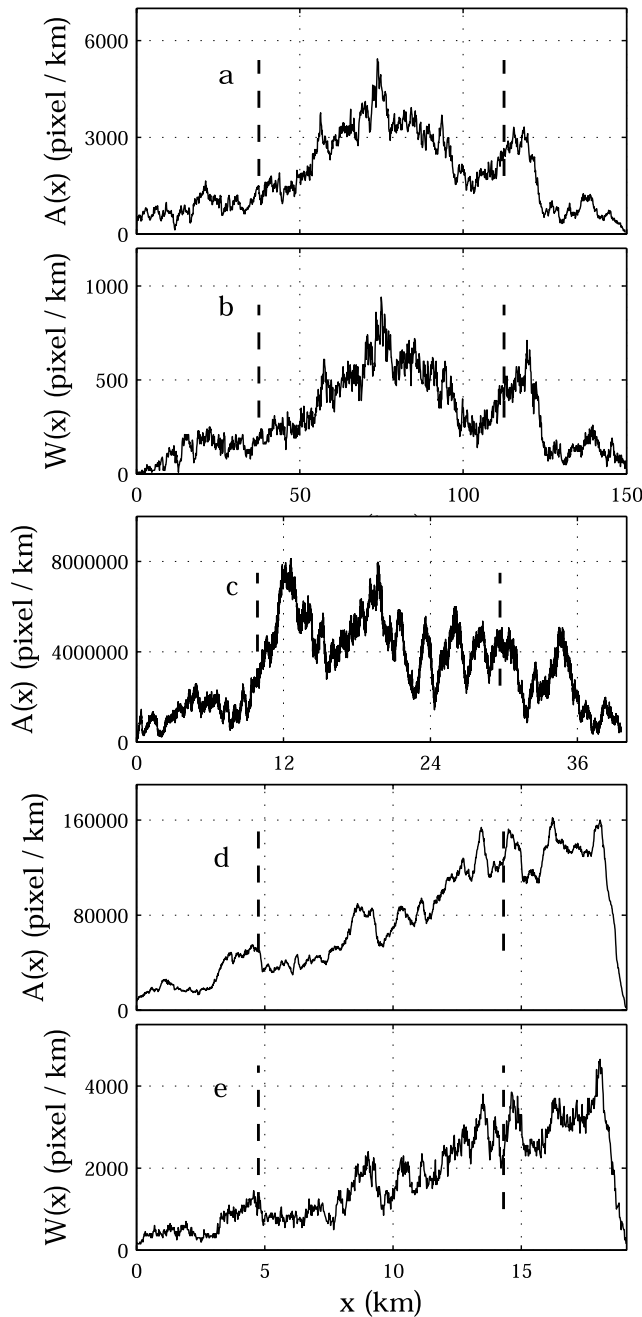
Figure 10. Area and width functions for Walawe River basin (a) area and (b) width functions, South Fork Eel River basin (c) area functions, and Noyo River basin (d) area and (e) width functions. The vertical dashed lines define the central half portion of the signal on which the MF analysis was performed.

width functions an agreement between the scaling exponents computed with increments and wavelet coefficients is found: $\tau^{\delta}(q) \simeq \tau^{w}(q)$, whereas the scaling exponents computed with box-aggregated coefficients $\tau^{b}(q)$ clearly depart from $\tau^{\delta}(q) \simeq \tau^{w}(q)$. We then conclude that both the area and width functions extracted from the Walawe River basin are by nature functions and not measures. The same result is obtained for the area function of the South Fork Eel River and Noyo River basins. Furthermore, as it is seen in

Figure 11 using box aggregation coefficients results in the wrong inference of MF properties close to those of Shreve's model as previously reported in the literature (cf. Figure 4), i.e., one point with coordinates ($h \simeq 1$, $D = 1$) with a decreasing right lobe, while using the increments or wavelet coefficients results in singularity spectrum centered at c_1 approximately 0.4 for $A(x)$ and 0.5 for $W(x)$.

[65] Figures 12 shows the log-log plots of the partition functions $S(q, a)$ versus a for $q = 1, 2$ computed using CWT and WTMM coefficients for the three different basins. The range of scales over which linear fits of the $\log_2(S(q, a))$ versus $\log_2(a)$ plots have been performed is shown in Table 3. On the basis of these fits, the $\tau(q)$ and (via the Legendre transform) $D(h)$ spectra were estimated and are shown for all three basins in Figure 13.

[66] Cumulant analysis for estimation of the parameters c_p has also been performed for all these basins using the CWT and WTMM coefficients. For illustration purposes, Figure 14 shows the cumulants $C(p, a)$ versus $\log a$ for $p = 1, 2$ for the Walawe basin; similar plots were found for the other basins. Using the range of scales reported in Table 3, the estimates of c_1 and c_2 were computed and are reported in Table 4. It is observed that the singularity spectra of the area functions of the three analyzed basins are clearly different as are the estimates of their c_1 and c_2 coefficients. More precisely, the singularity spectra of South Fork Eel River and Noyo River basins have their peak at $h = c_1 \simeq 0.8$ which is significantly larger than the value around which the peak of the singularity spectrum of the Walawe River basin is found: $h = c_1 \simeq 0.4$. It is moreover worth noting that the numerical analysis performed on both 1 m and 10 m resolution data sets (South Fork Eel River) yield the same results (cf. Table 4) supporting the fact that the observed difference in the value of c_1 is not an artifact due to the fine 1 m spatial resolution.

[67] The observed differences in the estimated values of the parameter c_1 means that the South Fork Eel River and Noyo River basins area functions exhibit more regular (in terms of singularity, i.e., larger c_1) local behavior than the Walawe River one. Eventually, all these area functions are MF functions, characterized by values of the parameter c_2 around 0.05 to 0.11. These values can be compared to the well known value of $c_2 \simeq 0.025$ for Eulerian turbulent velocity [e.g., *Frisch*, 1995] and values $c_2 \simeq 0.30$ for fine resolution (seconds) temporal rainfall [e.g., *Venugopal et al.*, 2006a].

[68] The robustness of the estimation methods used in this work enables us to confidently conclude that indeed there are significant differences in the singularity spectra of $A(x)$ of different basins. This is an encouraging result and points to the possibility that differences in the geomorphological processes controlling flow paths, both on the river network itself and on the hillslopes, might be reflected in the scaling properties of the area and width functions. A comprehensive analysis of a large number of basins needs to be undertaken to systematically study these connections.

6.3. Comparison Between Area and Width Functions

[69] In this section, the MF properties of the width and area functions of the Walawe River and Noyo river basins are compared. The scaling properties of the width function of the South Fork Eel River basin could not be reliably
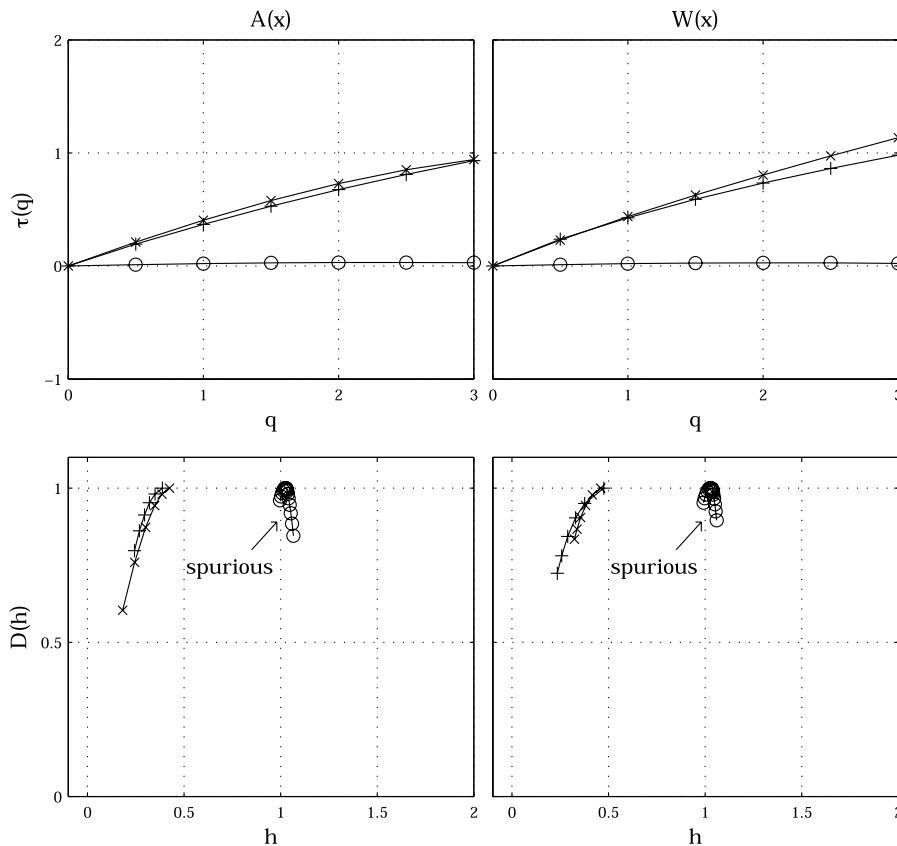
Figure 11. Walawe River (top) scaling exponents $\tau(q)$ and (bottom) predicted singularity spectra $D(h)$ computed with box-aggregation (circles), increments (pluses), and wavelet coefficients (crosses) for (left) area function $A(x)$ and (right) width function $W(x)$ (wavelet g_0^4). Scaling exponents are computed for negative q values for box aggregation coefficients in order to provide the right lobes of the singularity spectra; negative moments cannot be computed for increments and wavelet coefficients (see text for discussion).

analyzed because no sufficiently large scaling range was available for estimation.

[70] The scaling exponents $\tau(q)$ and the cumulant exponents c_p are computed from the CWT coefficients, using the wavelet g_0^4. The results are reported in Figure 15 and Table 5. It is first important to note that the width function $W(x)$ cannot be analyzed using the WTMM coefficients as the scale range within which a power law behavior is observed for the partition functions defined from the CWT coefficients is quite small, and it is known that use of WTMM coefficients results in an even smaller scaling range (a larger value of a_{min}), making it hard to estimate the scaling or cumulant exponents.

[71] Figure 15 shows that the computed scaling exponents $\tau(q)$ and then the estimated singularity spectra $D(h)$ vary appreciably. This difference is quantified with the cumulant exponent c_1 since this is actually the abscissa of the maximum value of $D(h)$: $c_1 \simeq 0.5$ for $W(x)$ and $c_1 \simeq 0.4$ for $A(x)$ for the Walawe River basin, and $c_1 \simeq 0.5$ for $W(x)$ and $c_1 \simeq 0.8$ for $A(x)$ for the Noyo River basin (see summary in Table 5). It is worth noting that while the MF properties for $W(x)$ are similar for these two basins, $A(x)$ was found much "rougher" for the Noyo River basin and "smoother" for the Walawe River basin. The apparent "smoothness" of the hillslope dissection for the Walawe

River basin may simply be the result of the 90 m DEM resolution which is not enough to resolve the drainage patterns at the hillslope scale. This needs further study by a systematic analysis of several basins at high resolution and also by theoretical constructs in which distinctly different branching structures are superimposed on the basic branching structure of the river network. However, it is worth noting that both $A(x)$ and $W(x)$ are found MF (as opposed to monofractal) functions as their singularity spectra are not reduced to one point and c_2 is significantly different than zero.

7. Concluding Remarks

[72] The problem of extracting geomorphologic features from landscapes which allow distinct characterization and can be used for discrimination or classification purposes, has been of continuous interest in hydrogeomorphologic research. It is therefore of interest to examine whether the width and area functions of real basins imbed in them distinct signatures of landscape dissection which could be used to differentiate between different network or drainage path topologies. These distinct geomorphological features would also be expected to result in distinct hydrological behavior.
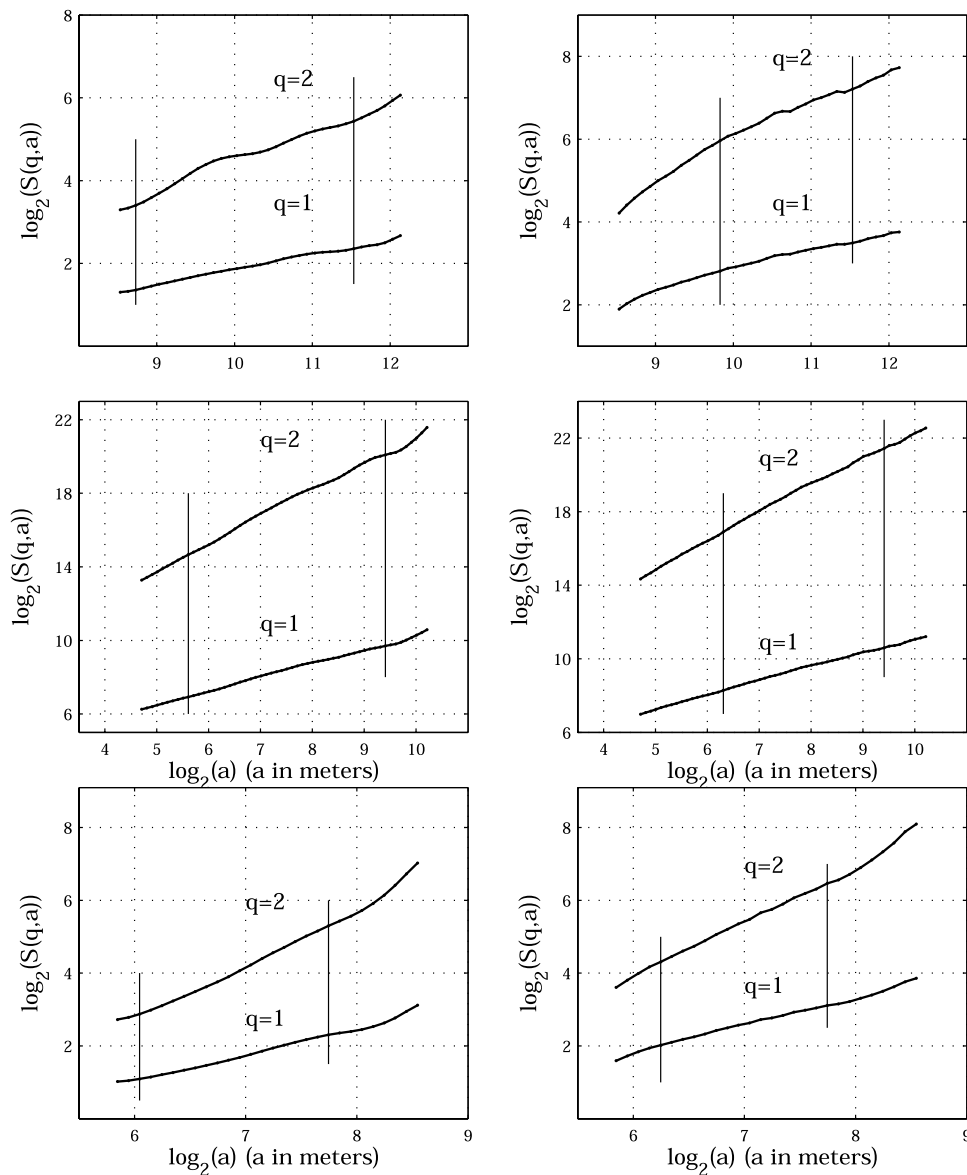
Figure 12. Partition functions of area functions $A(x)$: partition functions of order $q = 1, 2$ computed using (left) CWT and (right) WTMM coefficients for (top) the Walawe River basin, (middle) the South Fork Eel River basin, and (bottom) the Noyo River basin (wavelet g_0^4). Vertical lines denote the range of scales over which estimation of $\tau(q)$ is performed (see Table 3).

[73] In this paper we presented a robust framework for multifractal (MF) analysis of width and area functions of simulated and real river networks using wavelets. We pointed out the subtleties and potential pitfalls of such analyses, and introduced a new methodology, called cumulant analysis, for accurate and concise parameterization of multifractality using mainly two parameters, c_1 and c_2: c_1 is the most frequently occuring singularity, and c_2, the so-called intermittency coefficient, depicts the degree of deviation from monofractality and characterizes the degree of spatial heterogeneity of fluctuations. It is noted that for a monofractal, $c_1 = H$ and that a higher (lower) value of c_1 implies a "rougher" ("smoother") signal.

[74] The results obtained in this work establish some trends but also highlight the need for further research along three main directions.

Table 3. Scale Ranges Used for Log-Log Linear Regressions of the Partition Functions[a]

	Function	Method	a_{min}, m	a_{max}, m
Walawe River	$A(x)$	CWT	425	2960
		WTMM	911	2960
	$W(x)$	CWT	2400	5920
South Fork Eel R. (1 DEM)	$A(x)$	CWT	49	552
		WTMM	79	552
South Fork Eel R. (10 DEM)	$A(x)$	CWT	64	837
		WTMM	112	837
Noyo River	$A(x)$	CWT	66	429
		WTMM	76	429
	$W(x)$	CWT	132	697

[a]See Figure 12. Note that the same wavelet (g_0^4) has been used for all the analyses.
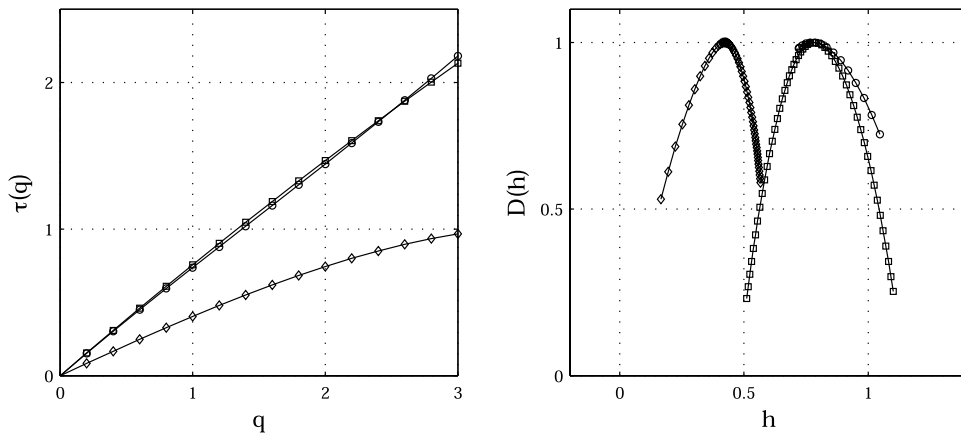
Figure 13. Area functions: (left) scaling exponents $\tau(q)$ and (right) singularity spectra $D(h)$ of Walawe River basin (diamonds), South Fork Eel River basin (squares), and the Noyo River basin (circles) area functions $A(x)$ (wavelet g_0^4).

7.1. Simulated Versus Real River Networks

[75] Our results established differences between the multiscale statistical structure of area functions $A(x)$ of real networks (found to be multifractal, as opposed to monofractal, with c_1 between 0.4 to 0.8 and a considerable intermittency) and that of a large class of commonly used space-filling SSTs (found to be monofractal with H between 0.5 to 0.65). We also pointed out that previous studies that have inferred multifractality in real river networks with c_1 close to 1.0 suffer from artifacts of the analysis methodology. Given the increased use of simulated river networks in understanding the interplay between space-time precipitation variability and river network topology on the emergent scaling of floods, the proposed robust MF analysis framework offers opportunity to study several new and relevant questions that have emerged from our analysis.

[76] 1. Do simulated self-similar trees (SSTs) which are not space-filling exhibit scaling in their width functions? Preliminary evidence in this paper suggests that scaling might not be present in these trees (see section 5) but this needs to be further investigated. This question is relevant as real river networks are not always space filling.

[77] 2. What class of SSTs exhibits multifractality in their width functions $W(x)$ similar to that exhibited by real river networks? One possible class is the extended class of stochastic SSTs proposed by *Cui et al.* [1999], which considers an additional source of spatial variability by randomizing the mean λ of the Poisson distribution of the number of side tributaries (see section 2.4). The MF properties of this extended class of models have not been studied yet, to the best of our knowledge. It is conjectured that this class might lead to width functions with multifractal (as opposed to monofractal) singularity spectra as those found in real networks and that this extra source of "randomness" might be a necessary condition for multifractality. This problem requires further study.

[78] 3. Do the MF parameters of $W(x)$ relate to any specific topological properties of the branching trees? In this study we found that for space-filling SSTs, a decreasing c_1 (rougher $W(x)$) corresponded to an increasing branching rate (see section 5). This implies that a "smoother" $W(x)$ might be expected for a branching network that has a smaller branching rate. Does this relation hold for other
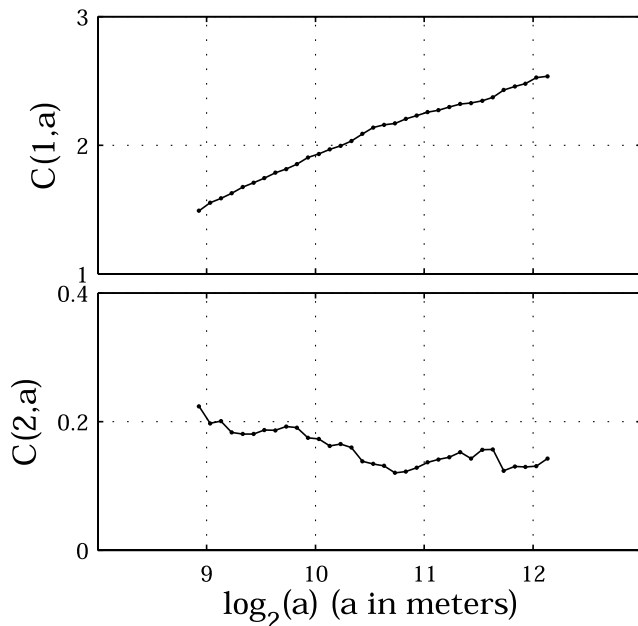
Figure 14. Walawe River cumulants of order $p = 1, 2$ of the area function $A(x)$ computed with WTMM coefficients (wavelet g_0^4).

Table 4. MF Characteristics of $A(x)$ for Several Basins[a]

| | | Walawe River | South Fork Eel River | | Noyo River |
			1 DEM	10 DEM	
CWT	c_1	0.37	0.78	0.80	0.77
	c_2	0.06	0.05	0.05	0.11
WTMM	c_1	0.42	0.78	0.77	0.78
	c_2	0.03	0.06	0.04	0.10

[a]Cumulant exponents are computed with CWT and WTMM coefficients (wavelet g_0^4).
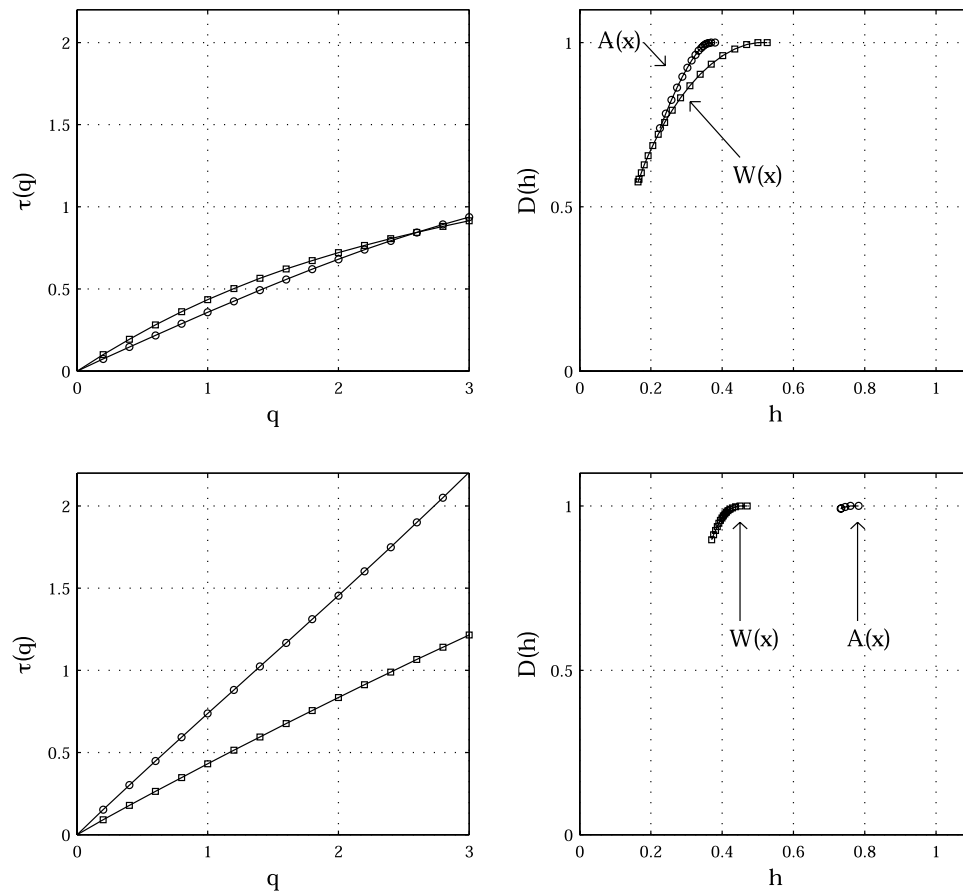
Figure 15. Area function versus width function: (left) scaling exponents $\tau(q)$ and (right) singularity spectra $D(h)$ of area $A(x)$ (circles) and width $W(x)$ (squares) functions computed with CWT coefficients (wavelet g_0^4) for (top) Walawe River basin and (bottom) Noyo River basin.

non-space-filling simulated trees and does it hold for real river networks?

7.2. Area $A(x)$ Versus Width $W(x)$ Function

[79] Our analysis suggests that the area function A(x) of different real networks possesses distinctly different MF properties, whose meaning needs to be carefully interpreted. For the three basins analyzed, the larger Walawe basin was found to have $A(x)$ with $c_1 \simeq 0.4$ and $c_2 \simeq 0.03$ which are distinctly different from those of the much smaller, steeper and still tectonically active California basins ($c_1 \simeq 0.8$ and $c_2 \simeq 0.05$ to 0.10). To rule out the possibility that the unusually large value of $c_1 = 0.8$ is the result of the 1m DEM resolution, the results were confirmed with area functions extracted from DEMs of 1m and 10m DEMs. Our analysis also indicates that the $A(x)$ and $W(x)$ functions of the same basin posses distinctly different MF properties depicting the different drainage topologies of the main river network and the hillslope drainage paths. For example, for the Noyo River basin, we found $c_1 \simeq 0.8$ for $A(x)$ versus $c_1 \simeq 0.5$ for $W(x)$, while for the Walawe basin $c_1 \simeq 0.4$ for $A(x)$ versus $c_1 \simeq 0.5$ for $W(x)$.

[80] However, several questions remain unanswered, such as the following.

[81] 1. What is the effect of DEM resolution and the channel initiation criterion for river network extraction (critical threshold area versus a slope-area threshold) on

the MF properties of $W(x)$? Notice that these questions have been studied before in the literature but with limited MF analysis methodologies as discussed in 4.3 and have to be repeated with the proposed more robust methodology.

[82] 2. When the DEM resolution is small enough (1m to 10 m DEMs) and is able to resolve hillslope flow paths, does in general $A(x)$ emerge as "less rough" than W(x) as was suggested by the two very high resolution basins we analyzed? Note that when the DEM resolution is low, we found that the MF properties of $A(x)$ and $W(x)$ were approximately the same (and in fact $A(x)$ was slightly "rougher" than $W(x)$), but this might be due to the inability of 90 m DEMs to resolve hillslope flow paths and thus to "see" the hillslope drainage patterns.

[83] 3. Can the MF properties of $W(x)$ and $A(x)$ be classified according to basin size as suggested by

Table 5. Comparison Between $A(x)$ and $W(x)$[a]

		Walawe River	Noyo River
$A(x)$	c_1	0.37	0.77
	c_2	0.06	0.11
$W(x)$	c_1	0.51	0.46
	c_2	0.13	0.10

[a]Cumulant exponents are computed with CWT coefficients (wavelet g_0^4) for the Walawe River basin and the Noyo River basin.

Richards-Pecou [2002]? While our results do not contradict this hypothesis, we believe that factors other than basin size are at work. Although it is possible that large-scale forcing due to boundary constraints spill over to all other smaller scales of landscape dissection, basin slope, drainage density, geology, etc. might play a role in the MF properties of river networks. A comprehensive analysis using the proposed methodology would provide insight into this problem.

[84] 4. How do two different branching topologies, say one corresponding to the river network at larger scales and another corresponding to the hillslope path topology at smaller scales, mix to give rise to the MF properties of $A(x)$? Can this problem be studied theoretically via constructed multiscale mixed-topology networks?

[85] 5. Do the MF properties of $A(x)$, mostly dominated by the hillslope flow paths, relate to the MF properties of the River Corridor Widths (RCW) introduced by *Gangodagamage et al.* [2007] to directly depict the hillslope topography roughness?

7.3. Hydrologic Implications

[86] Finally, one wonders whether the multiscaling property of area and width functions, apart from a geometrical interpretation related to flow path topology, can be given any hydrological significance. Recently, *Richards-Pecou* [2002] suggested that the multiscaling structure of the area function (actually the author refers to the width function but analyzes the area function) might associate to the scaling structure of at-site flood peaks and can thus serve for regionalization purposes. Specifically, the conjecture was made that the one parameter of the universal multifractals (the Levy-stable α parameter) might relate to the heaviness of the tails of the distributions of floods (see also *Dodov and Foufoula-Georgiou* [2005] for fitted Levy-stable pdfs to maximum annual floods). This is a plausible hypothesis, but one has to be careful with the chosen parameterization of multifractality; in our study we chose a nonparametric class of models as opposed to the universal multifractals used by *Richards-Pecou* [2002] and thus no direct comparison can be made.

[87] Some preliminary ideas on a different hydrologic interpretation of the MF structure of $W(x)$ are offered in this paper. Recalling that $W(x)$ denotes the number of channels intersected by a contour of equal length x to the outlet, $|W(x + \delta x) - W(x)|$ can be interpreted as the net number of channels within a strip of flow distance δx to the outlet. First, the presence of multifractality (c_2 different than zero) implies a strong dependence of the statistics of $|W(x + \delta x) - W(x)|$ on the size of the strip (scale) δx and especially a coefficient of variation of this pdf which increases as the scale δx decreases. That is, there is a disproportionally larger net change in the number of channels (or drainage pathways) expected to appear or disappear in the network at smaller distances apart than at larger distances apart (the larger the value of c_2 the larger this dependence on scale is). On the basis of the above argument, it is clear that the values of c_1 and c_2 are directly related to the scale-dependent probability distribution of the number of in-phase hillslope hydrographs joining the network within a strip of size δx from the outlet, thus expected to affect the properties of the overall hydrograph at the outlet. It is suggested that this scale dependence of $W(x)$ should be further explored toward a scale-dependent convolution framework for routing and toward alternative explanations of geomorphologic dispersion using higher-order moments of river network topology.

Appendix A: Singularity Spectrum

[88] A MF function $f(x)$ is described as a collection of local singularities, i.e., $|x - x_0|^{h(x_0)}$ whose strength is characterized by the Hölder exponent. The Hölder exponent $h(x_0)$ is properly defined as follows (these definitions actually hold for $h < 1$ but easily extent to $h \geq 1$):

$$h(x_0) = \text{Sup}\{\alpha : f \in C^\alpha(x_0)\}, \qquad (A1)$$

where

$$f \in C^\alpha(x_0) \text{ if } |f(x) - f(x_0)| \leq A|x - x_0|^\alpha \qquad (A2)$$

for $|x - x_0| \leq \epsilon$. The Hölder exponent can be interpreted as follows: the closer $h(x_0)$ is to 0, the more irregular the function is at point x_0. In contrast, larger values for $h(x_0)$ are related to a smoother (more regular) behavior at x_0. For a MF function, the Hölder exponents are spatially distributed on interwoven fractal subsets

$$S(h) = \{x_0 : h(x_0) = h\}, \qquad (A3)$$

where $S(h)$ is the collection of points with Hölder exponent h. An efficient framework to characterize MF functions with a hierarchical classification of the subsets $E(h)$ is by using the Hausdorff dimension of these subsets [see, e.g., *Schroeder*, 1991]:

$$D(h) = \text{Dim}_\text{H} S(h). \qquad (A4)$$

[89] The function $D(h)$ is called the singularity spectrum of the function $f(x)$ and its estimation is the goal of MF analysis.

[90] Monofractal functions are an important subclass of MF functions for which the Hölder exponent takes everywhere the same value H and then the singularity spectrum reduces to a single point: $D(h) = 1$ if $h = H$ and $D(h) = -\infty$ if $h \neq H$ (by convention, $D(\phi) = -\infty$ if ϕ denotes the empty set). A well known example of monofractal process is the ordinary Brownian motion, for which $H = 0.5$. MF functions have a $D(h)$ curve which spans a range of Hölder exponents from h_min to h_max. The MF formalism [*Parisi and Frisch*, 1985] relates $D(h)$ to the spectrum of scaling exponents $\tau(q)$ describing how the statistical moments of fluctuations change with scale.

[91] A similar description can be made for positive measures (or distributions) $\mu(x)$ which are mathematical objects defined through their integral over any interval of $\mathbb{R}$: $x \to \int_0^x \mu(u) du$ defines an increasing function which may not posses any derivative. A measure is also described as a collection of singularities: $\int_{x_0-r/2}^{x_0+r/2} \mu(u) du \sim r^{h(x_0)}$ with Hölder exponent $h(x_0)$ defined as

$$h(x_0) = \text{Sup}\{\alpha : \mu \in C^\alpha(x_0)\}, \qquad (A5)$$

where

$$\mu \in C^\alpha(x_0) \text{ if } \int_{x_0-r/2}^{x_0+r/2} \mu(u)du \le Ar^\alpha \qquad (A6)$$

for $r \le \epsilon$. Except for the Hölder exponent definition and the Legendre transform definition (see equation (12)), the MF framework for measures is the same as the one for functions.

References

Agnese, C., A. Criminisi, and F. D'Asaro (1998), Scale invariance properties of the peak of the width function in topologically random networks, *Water Resour. Res.*, 34, 1571–1583.

Arneodo, A., E. Bacry, and J. Muzy (1995), The thermodynamics of fractals revisited with wavelets, *Physica A*, 213, 232–275.

Arneodo, A., S. Manneville, and J. Muzy (1998), Towards log-normal statistics in high Reynolds number turbulence, *Eur. Phys. J. B*, 1, 129.

Cui, G., B. Williams, and G. Kuczera (1999), A stochastic Tokunaga model for stream networks, *Water Resour. Res.*, 35, 3139–3147.

Delour, J., J. Muzy, and A. Arneodo (2001), Intermittency of 1d velocity spatial profiles in turbulence: A magnitude cumulant analysis, *Eur. Phys. J. B*, 23, 243–248.

Dodov, B., and E. Foufoula-Georgiou (2005), Fluvial processes and streamflow variability: Interplay in the scale-frequency continuum and implications for scaling, *Water Resour. Res.*, 41, W05005, doi:10.1029/2004WR003408.

Etheridge, A. (2000), *An Introduction to Superprocesses*, Am. Math. Soc., Providence, R. I.

Feller, W. (1966), *An Introduction to Probability Theory and Its Applications*, vol. 2, John Wiley, Hoboken, N. J.

Frisch, U. (1995), *Turbulence: The Legacy of A. N. Kolmogorov*, Cambridge Univ. Press, New York.

Gangodagamage, C., E. Barnes, and E. Foufoula-Georgiou (2007), Scaling in river corridor widths depicts organization in valley morphology, *Geomorphology*, 43, doi:10.1016/j.geomorph.2007.04.414.

Gupta, V. K., and O. Mesa (1988), Runoff generation and hydrologic response via channel network geomorphology—Recent progress and open problems, *J. Hydrol.*, 102, 3–28.

Gupta, V., and E. Waymire (1996), Multiplicative cascades and spatial variability in rainfall, river networks, and floods, in *Reduction and Predictability of Natural Disasters*, edited by J. B. Rundle, D. L. Turcotte, and W. Klein, Santa Fe Inst. Stud. Sci. Complexity, vol. 25, Addison-Wesley, Boston, Mass.

Gupta, V. K., E. Waymire, and I. Rodriguez-Iturbe (1986), On scales, gravity, and network structure in basin runoff, in *Scale Problems in Hydrology*, edited by V. K. Gupta, I. Rodriguez-Iturbe, and E. F. Wood, pp. 159–184, D. Reidel, Hingham, Mass.

Hasley, T., M. Jensen, L. Kadanoff, I. Procaccia, and B. Shraiman (1986), Fractal measures and their singularities: The characterization of strange sets, *Phys. Rev. A*, 33, 413–423.

Horton, R. (1945), Erosional development of streams and their drainage basins: Hydrophysical approach to quantitative geomorphology, *Geol. Soc. Am. Bull.*, 56, 275–370.

Jaffard, S. (1997), Multifractal formalism for functions, *SIAM J. Math. Anal.*, 28(4), 944–998.

Jaffard, S., B. Lashermes, and P. Abry (2005), Wavelet leaders in multifractal analysis, paper presented at 4th International Conference on Wavelet Analysis and Its Applications, Univ. of Macao, Macao, China.

Kirkby, M. (1976), Tests of random model and its application to basin hydrology, *Earth Surf. Processes Landforms*, 1, 197–212.

Lashermes, B. (2005), Practical multifractal analysis: Wavelet leaders and critical orders. Applications to fully developed turbulence. Finite Reynolds number effects, Ph.D. thesis, Ecole Normale Super. de Lyon, Lyon, France.

Lashermes, B., P. Abry, and P. Chainais (2004), New insights into the estimation of scaling exponents, *Int. J. Wavelets Multiresolut. Inf. Process.*, 2(4), 497–523.

Malécot, Y., C. Auriault, H. Kahalerras, Y. Gagne, O. Chanal, B. Chabaud, and B. Castaing (2000), A statistical estimator of turbulence intermittency in physical and numerical experiments, *Eur. Phys. J. B*, 16, 549–561.

Mallat, S. (1998), *A Wavelet Tour of Signal Processing*, Academic, San Diego, Calif.

Mandelbrot, B., and T. Viscek (1989), Directed recursive models for fractal growth, *J. Phys. A Math. Gen.*, 22, L377–L383.

Marani, M., R. Rigon, and A. Arneodo (1991), A note on fractal channel networks, *Water Resour. Res.*, 27, 3041–3049.

Marani, M., A. Rinaldo, R. Rigon, and I. Rodríguez-Iturbe (1994), Geomorphological width functions and the random cascade, *Geophys. Res. Lett.*, 21, 2123–2126.

Menabde, M., S. Veitzer, V. Gupta, and M. Sivapalan (2001), Test of peak flow scaling in simulated self-similar river networks, *Adv. Water Resour.*, 24, 991–999.

Montgomery, D., and W. Dietrich (1988), Where do channels begins?, *Nature*, 336, 232–234.

Montgomery, D., and E. Foufoula-Georgiou (1993), Channel networks representation using digital elevation models, *Water Resour. Res.*, 29, 1925–1934.

Muzy, J., E. Bacry, and A. Arneodo (1993), Multifractal formalism for fractal signals: The structure-function approach versus the wavelet-transform modulus-maxima method, *Phys. Rev. E*, 47, 875–884.

Muzy, J., E. Bacry, and A. Arneodo (1994), The multifractal formalism revisited with wavelets, *Int. J. Bifurcation Chaos*, 4, 245–302.

Parisi, G., and U. Frisch (1985), On the singularity structure of fully developed turbulence, in *Turbulence and Predictability in Geophysical Fluid Dynamics*, Proc. Int. Summer Sch. Phys. Enrico Fermi, vol. 88, edited by M. Ghil, R. Benzi, and G. Parisi, pp. 84–88, Elsevier, New York.

Peano, G. (1890), Sur une courbe qui remplit toute une aire plane, *Mat. Ann.*, 36, 157–160.

Peckham, S. (1995), New results for self-similar trees with applications to river networks, *Water Resour. Res.*, 31, 1023–1029.

Richards-Pecou, B. (2002), Scale invariance analysis of channel network width function and possible implications for flood behavior, *Hydrol. Sci. J.*, 47(3), 387–404.

Rinaldo, A., I. Rodríguez-Iturbe, R. Rigon, E. Ijjasz-Vasquez, and R. Bras (1993), Self-organized fractal river networks, *Phys. Rev. Lett.*, 70, 822–825.

Rodríguez-Iturbe, I., and A. Rinaldo (1997), *Fractal River Basins. Chance and Self-Organization*, Cambridge Univ. Press, New York.

Schroeder, M. (1991), *Fractals, Chaos, Power Laws. Minutes from an Infinite Paradise*, W. H. Freeman, New York.

Shreve, R. (1966), Statistical laws of streams numbers, *J. Geol.*, 74, 17–37.

Sklar, L. S., W. E. Dietrich, E. Foufoula-Georgiou, B. Lashermes, and D. Bellugi (2006), Do gravel bed river size distributions record channel network structure?, *Water Resour. Res.*, 42, W06D18, doi:10.1029/2006WR005035.

Strahler, A. (1957), Quantitative analysis of watershed geomorphology, *Eos Trans. AGU*, 38, 913.

Tokunaga, E. (1978), Consideration on the composition of drainage networks and their evolution, *Geogr. Rep. 13*, Tokyo Metrop. Univ., Tokyo.

Troutman, B., and M. Karlinger (1984), On the expected width function for topologically random channel networks, *J. Appl. Probab.*, 21, 836–849.

Troutman, B., and M. Karlinger (1985), Unit hydrograph approximations assuming linear flow through topologically random channel networks, *Water Resour. Res.*, 21, 743–754.

Troutman, B., and T. Over (2001), River flow mass exponents with fractal channel networks and rainfall, *Adv. Water Resour.*, 24, 967–989.

Veneziano, D., E. Glenn, and R. Bras (1995), Multifractal analysis: Pitfalls of standard procedures and alternatives, *Phys. Rev. E*, 52, 1387–1398.

Venugopal, V., S. Roux, E. Foufoula-Georgiou, and A. Arneodo (2006a), Scaling behavior of high resolution temporal rainfall: New insights from a wavelet-based cumulant analysis, *Phys. Lett. A*, *348*, 335–345.

Venugopal, V., S. G. Roux, E. Foufoula-Georgiou, and A. Arneodo (2006b), Revisiting multifractality of high-resolution temporal rainfall using a wavelet-based formalism, *Water Resour. Res.*, *42*, W06D14, doi:10.1029/2005WR004489.

Yang, D., S. Herath, and K. Musiake (2001), Spatial resolution rensitivity of catchment geomorpholic properties and the effect on hydrological simulation, *Hydrol. Processes*, *15*, 2085–2099.

————————————————

E. Foufoula-Georgiou and B. Lashermes, St. Anthony Falls Laboratory and National Center for Earth-Surface Dynamics, Dept. of Civil Engineering, University of Minnesota–Twin Cities, 23rd Ave SE, Minneapolis, MN 55414, USA. (efi@umn.edu)

Scaling in river corridor widths depicts organization in valley morphology

Chandana Gangodagamage, Elizabeth Barnes, Efi Foufoula-Georgiou [*]

St. Anthony Falls Laboratory and National Center for Earth-Surface Dynamics, Department of Civil Engineering, University of Minnesota, Minneapolis, USA

Abstract

Landscapes have been shown to exhibit numerous scaling laws from Horton's laws to more sophisticated scaling in topography heights, river network topology and power laws in several geomorphic attributes. In this paper, we propose a different way of examining landscape organization by introducing the "river corridor width" (lateral distance from the centerline of the river to the left and right valley walls at a fixed height above the water surface) as one moves downstream. We establish that the river corridor width series, extracted from 1 m LIDAR topography of a mountainous river, exhibit a rich multiscale statistical structure (anomalous scaling) which varies distinctly across physical boundaries, e.g., bedrock versus alluvial valleys. We postulate that such an analysis, in conjunction with field observations and physical modeling, has the potential to quantitatively relate mechanistic laws of valley formation to the statistical signature that underlying processes leave on the landscape. Such relations can be useful in guiding field work (by identifying physically distinct regimes from statistically distinct regimes) and advancing process understanding and hypothesis testing.
© 2007 Elsevier B.V. All rights reserved.

Keywords: River corridor widths; Valley morphology; Hillslope processes; Landscape organization; Multiscaling; Multifractals

1. Introduction

"Why are scaling laws of such distinguished importance? The answer is that scaling laws never appear by accident. They always manifest a property of the phenomenon of basic importance ...This behavior should be discovered, if it exists, and its absence should also be recognized." — Barenblatt (2003).

A piece of landscape can be analyzed in several ways. One way is to analyze the statistical properties of the topography heights $z(x,y)$ and related attributes, such as, local gradients and curvatures. Another way is to extract the channelized paths of the topography and study the topological structure of the ordered river network. The former method examines the vertical structure of the topography, while the latter studies the planar dissection of the topography. Here, we introduce a different approach for examining landscapes focusing on the "river corridor width" (RCW) as one moves along the river. The river corridor width is extracted by "flooding" the river at a certain height D_0 above the water surface and recording the left and right distance to the valley walls measured from the centerline of the river and orthogonal to this centerline (see Fig. 1). We denote this function by $V_L(x; D_0)$ and $V_R(x; D_0)$, where L and R stand for the left and right side, respectively, looking downstream, x is the

[*] Corresponding author. Tel.: +1 612 626 0369; fax: +1 612 624 4398.
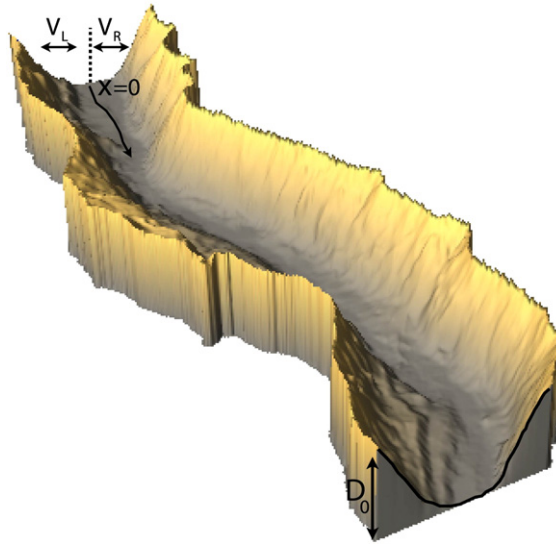*E-mail address:* efi@umn.edu (E. Foufoula-Georgiou).

Fig. 1. River corridor width at depth D_0 above the water surface to the left and right of the river centerline, $V_L(x; D_0)$ and $V_R(x; D_0)$, respectively, where x is the distance measured along the river from the basin outlet $x=0$.

distance measured along the river from the basin outlet $x=0$, and D_0 is the depth above the water level.

This particular definition of "river corridor width" is different from the definition of "valley width" used in other studies. For example, Montgomery (2002) defined valley width as the total ridgetop-to-ridgetop width of valley-spanning cross-sections orthogonal to the valley centerline. Montgomery's study aimed to understand how valley morphometry scales with drainage area in glaciated versus unglaciated valleys for the purpose of arriving at a process-based classification of valley morphology. Thus, valley widths were extracted in his study from several cross-sections throughout the basin and were selected to avoid the influence of tributary valleys. In our study, we follow the valley as we move downstream the mainstream and record the river corridor width to the left and right side of the river centerline as we "flood" the valley to different heights D_0 (see Fig. 1). The scope of our analysis is not to extract regional scaling characteristics but instead to quantify the detailed statistical structure of the valley morphology as one follows the river downstream with the eventual goal of relating this statistical structure to the processes responsible for valley formation. The river corridor width series is extracted from high resolution airborne altimetry (LIDAR) topography data at cross-sections 1 m apart as we move downstream along the river and, thus, depicts landscape organization down to the meter scale.

The small-scale fluctuations of the river corridor width series are interpreted to have resulted from the complex, and often interacting, processes forming valleys, including hillslope transport, mass wasting, terraces, debris flows,

landsliding and the interactions with the streams. The question we pose is whether the river corridor width series exhibit any distinct statistical scaling properties, and in particular any form or statistical organization across a range of scales, i.e., scale invariance or self-similarity. The methodology of analysis heavily borrows from current state-of-the-art methodologies for analyzing turbulent velocity fluctuations. We demonstrate how spectral analysis provides a limited, or partial, characterization of the multiscale structure of the river corridor width series. The use of a rigorous multifractal analysis unravels a rich scaling structure and, in particular, a deviation from scale invariance and presence of strong intermittency, the so-called anomalous scaling. These findings are revealing and call for further analysis of the statistical signature that valley forming processes leave on the landscapes in diverse geomorphic environments and also along tributaries of nested sub-basins. It is postulated that distinct statistical signatures identified from high resolution topography can be further explored towards (a) discriminating among different valley morphologies, (b) suggesting the nature of the underlying mechanisms responsible for valley formation, and (c) guide field work and data collection efforts for the purpose of advancing modeling and hypothesis testing.

2. Study area and extraction of river corridor width series

The South Fork Eel River basin is located in northern California and has a drainage area of 351 km^2 (see Fig. 2). Its relief is approximately 500 m. The mainstream of the
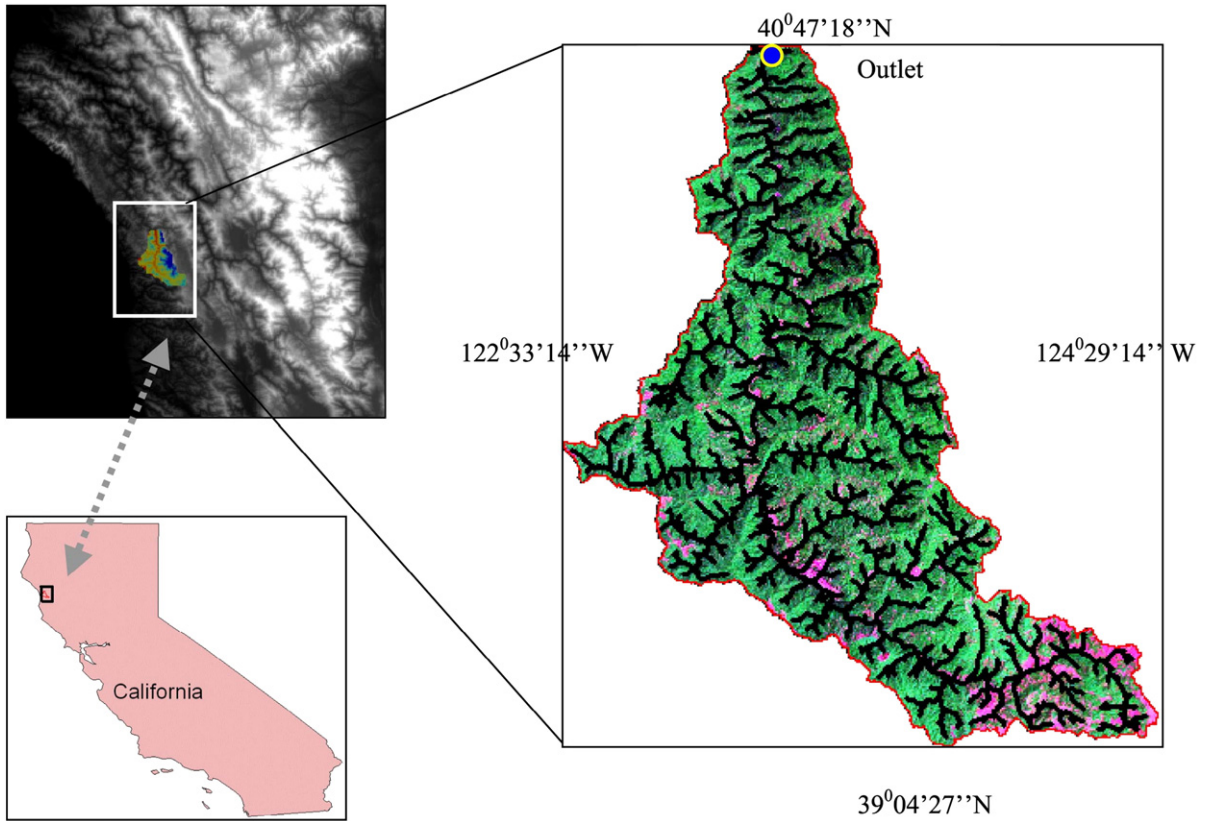
Fig. 2. Location of the South Fork Eel River basin (351 km^2) in California. The panel on the right shows the stream network superimposed on Landsat GeoCover (Bands 7, 4, 2) image of the basin.

Fig. 3. Longitudinal profile along the main channel of the South Fork Eel River basin. The main channel is divided into eight segments (see discussion in text and Table 1) whose respective along-channel slopes (in degrees) and distances from the outlet (in km) are shown above.

Table 1
Segments along the mainstream of the Eel River ($x=0$ denotes the outlet of the basin, see Fig. 1) and the scaling properties of their right and left river corridor width (RCW) series

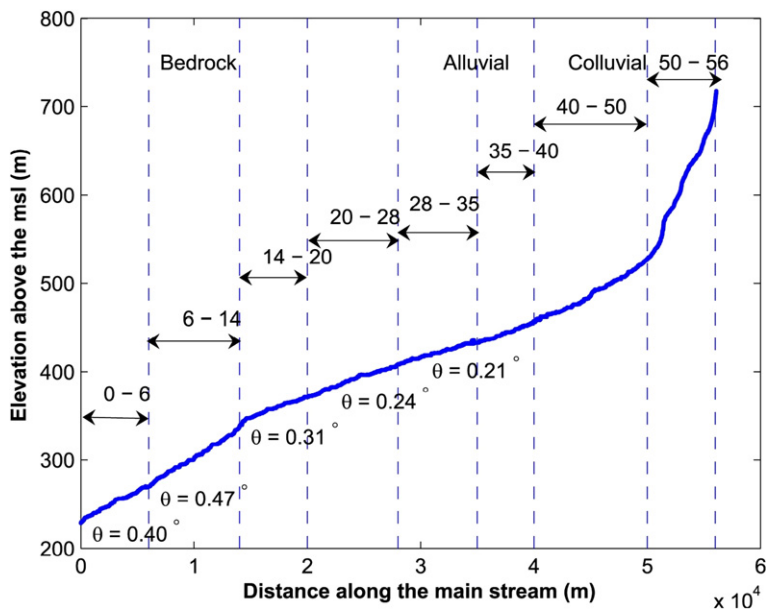| Distance from outlet (km)	Along stream slope (°)	Side of the corridor (Left/Right)	Spectral slope	Scaling range (m)	Scaling range (octaves)	Holder exponent $\langle H \rangle$	(h_{min}, h_{max})	c_1	c_2
$0<x<6$	0.40	Right	1.27	5.0–36.8	2.5–5.2	0.45	$(-0.1, 1.18)$	0.45	0.07
		Left	1.36	9.2–64	3.0–6.0	0.47	$(0.02, 1.02)$	0.50	?
									0.0
$6<x<14$	0.47	Right	1.63	9.2–56	3.2–5.8	0.51	$(0, 1.30)$	0.51	?
									0.0
		Left	1.45	8.6–56	3.1–5.8	0.49	$(0.1, 1.22)$	0.48	0.02
$14<x<20$	0.31	Right	1.18	8.0–56.0	3.0–5.8	0.29	$(-0.1, 1.20)$	0.32	0.13
		Left	1.19	9.8–36.8	3.3–5.2	0.39	$(0.0, 1.07)$	0.41	0.25
$20<x<28$	0.24	Right	1.21	8.0–64	3.0–6.0	0.58	$(0.1, 1.10)$	0.59	0.05
		Left	1.28	16.0–128	4.0–7.0	0.22	$(-0.1, 0.60)$	0.23	0.17
$28<x<35$	0.21	Right	1.41	8.0–128	3.0–7.0	0.81	$(0.0, 2.00)$	1.00	0.38
		Left	1.43	8.0–128	3.0–7.0	0.76	$(0.0, 1.60)$	0.77	0.10

The reported Hölder exponent $\langle H \rangle$ is estimated from the CWT multifractal analysis, the (h_{min}, h_{max}) from the WTMM multifractal analysis, and c_1, c_2 from the cumulant analysis. Notice the pronounced multifractality ($c_2 \neq 0$) of the RCW series for some segments (e.g. both left and right sides of 14–20 km and left side only of the 20–28 km segment.) Also note the different values of $\langle H \rangle$ (and c_1) suggesting a smoother RCW series for the 0–14 km steep-sloped, bedrock stretch and a much rougher RCW series for the milder-sloped, alluvial 14–28 km stretch.

basin has a length of approximately 56 km and fairly steep along-the-channel slopes (see Fig. 3 and Table 1). We have subdivided this channel reach into eight smaller sub-reaches according to slope and other morphologic characteristics, such as the presence of tributaries. These eight segments were then analyzed separately. The idea was to avoid mixing different physical regimes at the expense of classifying the reaches in more detail than necessary. The presence of similar statistical properties could then be used to group reaches into fewer categories (and this was indeed the case from our analysis). Following Montgomery (2002), valleys have been classified as bedrock, alluvial and colluvial (see Fig. 3). For vegetation and other

geomorphological characteristics of this region, the reader is referred to Power (1992) and Seidl and Dietrich (1992).

For this watershed, 1 m topography data from airborne altimetry (LIDAR) is available from which we extracted the cross-sections of the ridgetop-to-ridgetop valleys perpendicular to the river centerline every 1 m along the mainstream. Then, at specified depths D_0 above the water level, the distances from the centerline of the river to the left and right valley walls were recorded. The analysis was performed at depth $D_0=5$ m and $D_0=10$ m for the whole river. In this paper we report the analysis of the $D_0=5$ m river corridor widths for the very steep 35 km stretch from the outlet to the divide. The 20 km stretch close to the
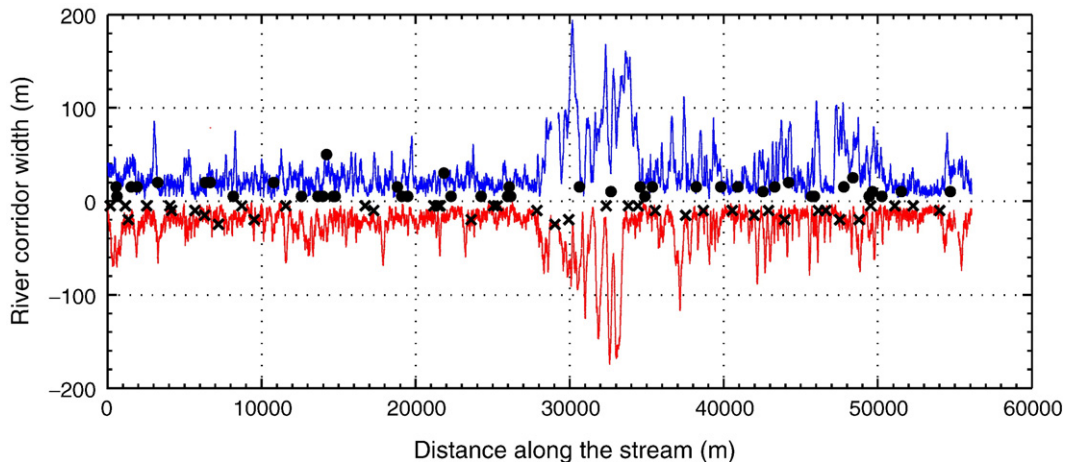

Fig. 4. River corridor widths for the mainstream of the South Fork Eel River (56 km in length) extracted at a depth $D_0=5$ m: top ($+Y$) is at the right side and bottom ($-Y$) is at the left side of the river as we travel downstream. Dots (●) and crosses (×) indicate the location of tributaries joining the mainstream at the right and left sides respectively. (See text for more details.)

divide did not show a clear scaling signature and requires further analysis.

Fig. 4 displays the left and right river corridor width (RCW) series for the whole 56 km mainstream and also indicates the location of the tributary junctions. To provide an indication of the "significance" of each tributary, we have positioned the marks at a vertical distance proportional to the drainage area of each tributary. Specifically, the 89 tributaries have been grouped into 10 categories based on the contributing drainage areas. These groups are then scaled such that the smallest contributing area of 1 km^2 corresponds to (is plotted at) a RCW of 5 m, and the

largest area of 152 km^2 corresponds to a RCW of 50 m (See Fig. 4).

Fig. 5 shows a magnification of the river corridor width series for the 0–6 km river stretch and the detailed topography and location of this stretch within the whole basin. It also associates selected values in the river corridor width with the locations on the topographic map. Finally, Fig. 6 shows the river corridor width series for the 20–28 km alluvial stretch. As will be discussed later, this stretch exhibits a rich multiscale structure in its RCW series and a pronounced asymmetry between the left and right sides. This asymmetry (not visually
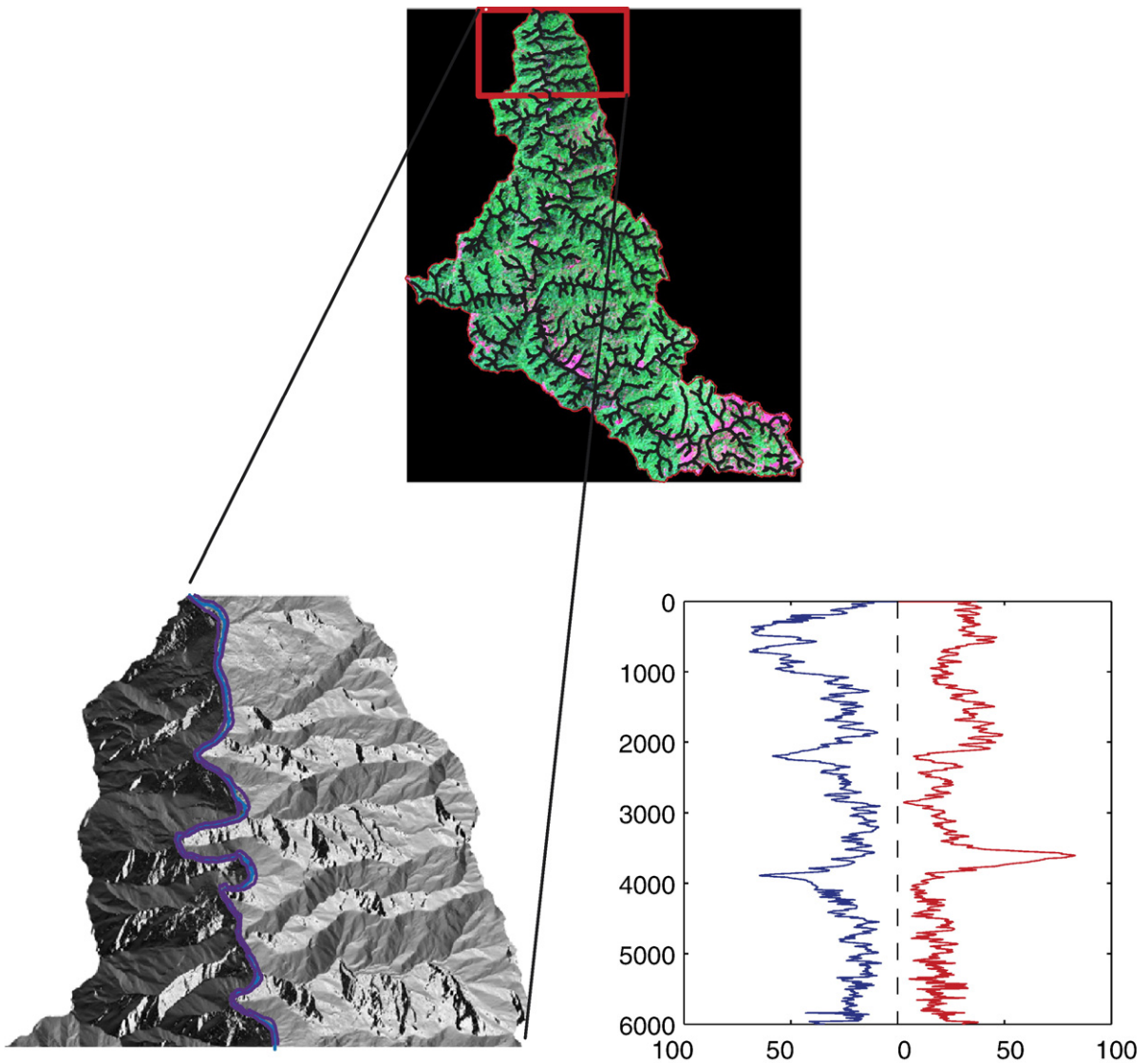

Fig. 5. The 0–6 km bedrock stretch of the South Fork Eel River basin. Selected values of river corridor width are associated with their locations on the topographic map.
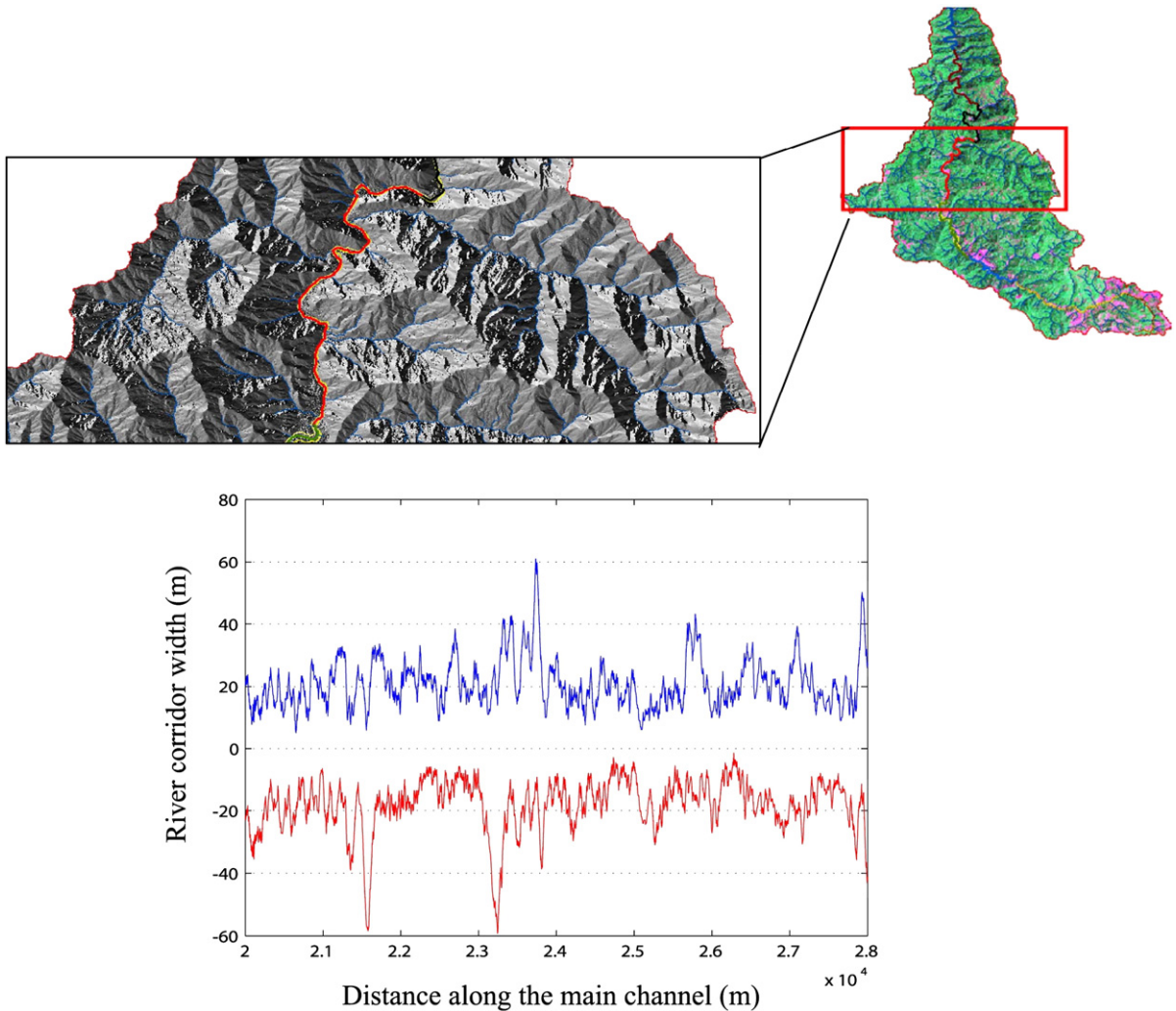
Fig. 6. The 20–28 km stretch of the South Fork Eel River basin main channel (top panel). The bottom panel shows the right (top series) and left (bottom series) river corridor widths extracted from this 8 km stretch at depth $D_0 = 5$ m. This stretch exhibits a high asymmetry in the statistical scaling properties of its left and right valley geometries; although not apparent visually, the right side is much "smoother" than the left side (see Table 1 and discussion in text). This suggests different valley forming processes in each side of the mainstream, with much more localized processes in the left side.

apparent from Fig. 6, but clearly depicted by the multiscale analysis) can been seen as suggesting different valley-forming processes for each side.

3. Fourier analysis of river corridor width series

A commonly used tool to explore the energy distribution of a signal across frequencies (or scales) is the power spectrum. The power spectra of the left and right RCW series of the five segments analyzed are shown in Fig. 7. First, we observe the presence of a log–log linearity over a significant range of scales with an abrupt break of scaling at a scale of approximately 10 m except

for the 0–6 km stretch which does not exhibit a pronounced scaling break. For scales smaller than approximately 10 m (wavenumber larger than 10^{-1} m^{-1}) a significant increase of energy (variability) is present. This is interpreted as the result of noise in the LIDAR data that shows up as concentrated energy at characteristic scales of the order of 5–10 m (the so-called "acne" in the bare soil LIDAR extracted topography.) This scale of 10 m, below which the LIDAR data are not globally interpretable (although locally they do depict smaller than 10 m variability), represents the "effective resolution" of these topography data and has also been documented from a break in the
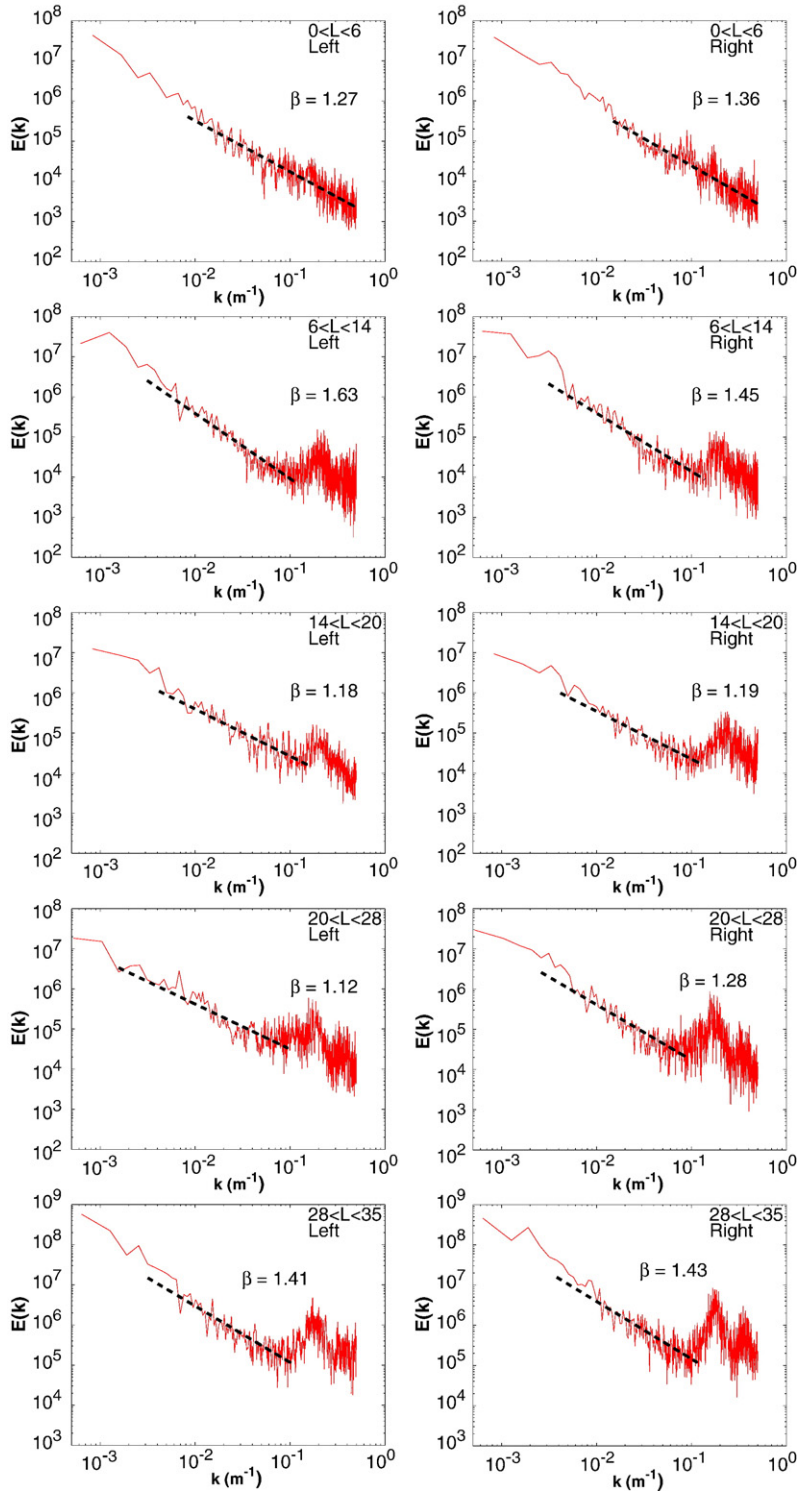
Fig. 7. Power spectra of the river corridor widths (at 5 m above water level) for the five segments along the mainstream of the South Fork Eel River basin. The dotted black lines give the power law fits, $E(k) = k^{-\beta}$. The horizontal axis represents frequency k, in m^{-1}.

multiscale statistical properties of basin-wide curvature pdfs at approximately the same scale (Lashermes and Foufoula-Georgiou, 2007).

It is well known that the presence of large-scale features with sharp edges in a process can be misinterpreted in the usual Fourier spectrum as energy

coming from distinct small-scale features, because the Fourier analysis cannot distinguish between the two. Thus, we do not know from Fig. 7 whether the log–log linearity in the spectrum within the scaling range is the result of uniformly distributed high-energy fluctuations over the whole support of the signal or a richer preferential and localized energy distribution. The former is the hallmark of scale-invariance, implying a spatially homogeneous distribution of abruptly high values within the support of the signal (arising from a homogenous energy transferring mechanism), while the latter is indicative of a break-down of scale invariance, implying a localized intermittent distribution of abruptly large values within the signal (probably arising from a spatially inhomogeneous energy transferring mechanism). In turbulence, the realization that the statistical moments of turbulent velocity fluctuations grow faster as the scale becomes smaller, prompted the replacement of the global Fourier-based analysis of Kolmogorov (K41 theory, Kolmogorov, 1941) with the local multi-fractal formalism analysis of Parisi and Frisch (1985).

The multifractal formalism aims to characterize the very abrupt local fluctuations in the signal using the so-called multifractal (MF) spectrum. The MF spectrum, or spectrum of singularities $D(h)$, describes the "richness" of the local irregularities of a function, i.e., abrupt local fluctuations, in terms of local singularities characterized via the so-called Hölder exponent h (see Parisi and Frisch, 1985). If singularities are of the same strength throughout the support of the signal (i.e., homogeneously distributed), $D(h)$ receives the value of 1 at a single value of $h=H$ which coincides with the well-known Hurst exponent. If the singularities of various strengths are non-homogeneously spread in the signal (in what turns out to be interwoven fractal sets), however, $D(h)$ is a density function which quantifies the range of the strength of these singularities (h_{min} to h_{max}) and the degree of their presence in the signal. In other words, the set of points that exhibit singularity of order h_1 forms a fractal set of dimension $D(h_1)$ and is interwoven with the set of points that exhibit singularity of order h_2, which forms a fractal set of dimension $D(h_2)$, etc. In the next section, an overview of the multifractal analysis methodologies is presented followed by the results of analysis of the river corridor width series.

4. Multifractal analysis: methodology overview

4.1. Preliminaries

A typical goal of multiscale analysis of a signal $f(x)$ is to characterize how the statistical properties (or the whole pdf) of the signal changes with the "scale" at which the signal is examined. For that, the statistical moments of the fluctuations of the signal $\delta(x,a)=f(x+a)-f(x)$, at scale (separation distance) a are computed, and the change with scale a is examined. log–log linearity between the statistical moments of order q and scale implies the presence of scaling and the slopes of these lines $\tau(q)$ for different order moments q characterize the nature of scaling. A linear $\tau(q)$ vs. q relationship, i.e., $\tau(q)=q \cdot H$, where H is the Hurst or scaling exponent, implies simple scaling whereas a nonlinear relationship implies a deviation from simple scaling, or multiscaling. In the first case, the single exponent H can be used to obtain the whole pdf at one scale from the pdf at any other scale, while in the second case more than one scaling exponents are needed to renormalize the pdfs across scales (i.e., the tails of the pdfs scale differently than the body). Often, only the second order statistical moment ($q=2$) is checked (second-order structure function or variogram) in which case the single estimated exponent H can be used to renormalize the pdfs only up to second order statistics.

It is instructive to place the above statistical interpretation of mono-or multi-scaling (i.e., looking at how the pdfs renormalize across scales) in the context of an equivalent geometrical interpretation (i.e., what does the scaling really mean about the nature and frequency of very extreme fluctuations in the signal). The multifractal formalism of Parisi and Frisch (1985) connects the statistical and geometrical interpretations intuitively and mathematically, as will be discussed in the next section. Specifically, abrupt fluctuations in the signal (geometrically characterized by the local regularity of the function or the so-called Hölder exponent defined later) occur uniformly or homogeneously throughout the signal in the case of a mono-fractal, while they occur heterogeneously or intermittently in the case of a multifractal. The two imply different mechanisms for how the energy is distributed across scales, i.e., a uniform cascading of energy across scales in the first case, versus a spatially heterogeneous energy cascading in the second case deriving from the presence of intermingled very active and dormant regions of energy transfer.

The processes creating the valley geometry are multiple in nature including hillslope sediment transport, landsliding, mass wasting, tributary influences, etc. and one expects that this can lead to a complex statistical structure of the RCW series. Whether the RCW series exhibit any statistical organization (mono-or multi-scaling) and how this organization is to be statistically and geometrically interpreted, is the scope of this paper. Emphasis is placed on higher order moments which can characterize the local behavior of

abrupt fluctuations as this is considered significant for interpreting the nature of the underlying valley forming processes.

In the rest of this section the mathematical details of the multiscale analysis methodologies we employ are presented. The reader is referred to Venugopal et al. (2006a,b) and the references therein for a more detailed exposition.

4.2. Multifractal formalism

The local singularity of a function $f(x)$ at a point x_0 is characterized by the so-called Hölder exponent $h(x_0)$, defined as the largest exponent such that

$$|f(x) - f(x_0)| \sim C|x - x_0|^{h(x_0)} \tag{1}$$

in the neighborhood of x_0, i.e. for $|x - x_0| \leq \varepsilon$. A small (large) value of $h(x_0)$ signifies a rough (smooth) behavior of the function $f(x)$ at x_0. The above definition holds for $0 \leq h \leq 1$ but extension to singularities $h > 1$ (i.e., singularities in the higher-order derivatives of the function) can easily be achieved by filtering out a polynomial of degree higher than one, which is equivalent to working with higher-order increments of the signal. As will be seen later, this filtering can be formally achieved via a wavelet-based formalism (e.g. see Muzy et al., 1991, 1993; or Venugopal et al., 2006a,b).

The singularity spectrum $D(h)$ is defined as

$$D(h) = d_h\{x_0 : h(x_0) = h\} \tag{2}$$

that is, $D(h)$ is the Hausdorff dimension d_h of the set of points x_0 which have Hölder exponent $h(x_0) = h$. Estimating $D(h)$ is the goal of multifractal analysis and the so-called multifractal formalism (e.g. Parisi and Frisch, 1985) allows estimation of $D(h)$ from the statistics of local fluctuations of the signal at different scales a and different locations x_0, denoted by $\delta(x_0, a)$. One way of determining these fluctuations is via standard first order differences, i.e.,

$$\delta(x_0, a) \equiv f(x_0 + a) - f(x_0). \tag{3}$$

Let us denote the structure functions $S(q,a)$ of the signal as the qth statistical moments of the fluctuations of the signal:

$$S(q, a) = <|\delta(x_0, a)|^q> \tag{4}$$

where $<\cdot>$ stands for expectation (via spatial averaging). For a multifractal signal

$$S(q, a) \sim a^{\tau(q)} \tag{5}$$

which defines the $\tau(q)$ curve, or spectrum of scaling exponents, indexed by moment order q. The multifractal formalism states that $\tau(q)$ relates to $D(h)$ through a Legendre transform:

$$D(h) = \min_q [qh - \tau(q) + 1]. \tag{6}$$

If the signal under analysis is monofractal, then $\tau(q)$ is linear with respect to the moment order, i.e., $\tau(q) = q \cdot H$ and $D(h)$ receives a single value equal to 1 at the specific value of $h = H$. In contrast, if the singularity spectrum takes on finite values in an interval $[h_{min}, h_{max}]$, the scaling exponents $\tau(q)$ define a nonlinear function of q (multifractal signal). The nonlinearity of $\tau(q)$ implies a scale dependence of the dimensionless moments. For example, for a monofractal process it can easily be shown from (5) that the coefficient of variation, $CV = (M_2(a)/M_1^2(a) - 1)^{1/2}$, of the process is independent of scale a, while this is not the case for a multifractal process. The same applies to other dimensionless structure functions such as the coefficients of skewness and kurtosis, $M_3(a)/M_1(a)^{3/2}$ and $M_4(a)/M_2(a)^2$ respectively, where $M_q(a)$ is used to denote $S(q,a)$ (see Mahrt, 1989).

It is understood that an increase of the dimensionless structure functions with decreasing scale is an indication of strong intermittency, i.e., occasional large gradients which enhance the higher order moments at small scales (break-down of scale invariance). This empirical observation, documented from long series of wind-tunnel turbulence data, is what lead to the development of the multifractal formalism in turbulence (e.g. Parisi and Frisch, 1985) and shed new light into how energy is cascaded in a turbulent field, typically very intensely in localized regions and less so in other (dormant) regions. As it will be seen in the next section, the river corridor widths are also found to exhibit such a multifractal behavior (break of scale-invariance), suggesting a rich local structure of energy dissipation in the valley-forming processes.

4.3. Wavelet-based MF formalism

While one could confine themselves to using structure functions in (4) as computed from the standard first order differences of the signal as defined in (3), it is often advantageous to use "generalized differences" defined via wavelet filtering. One advantage is that wavelets allow the analysis of non-stationary signals. By choosing an appropriate wavelet (i.e., wavelets with a high number of vanishing moments), polynomial trends of increasing order can be filtered out from the

signal and accurately characterize the local behavior of a function without danger of having this behavior masked by the large-scale trends (e.g. Jaffard, 1989; Mallat and Hwang, 1992). Another advantage of wavelets is their natural ability to depict sharp edges or discontinuities from a signal (e.g. Muzy et al., 1994; Mallat, 1998) and, thus, better characterize the statistical nature of singularities. In addition, as we explain below, a wavelet-based multifractal formalism allows one to work with the maxima of the wavelet coefficients (the so-called wavelet transform modula maxima; WTMM) and, thus, extend the structure function analysis to negative moments q (which are necessary for computation of the right limb of the $D(h)$ spectrum.) Such an extension also allows access to the whole spectrum of singularities, including $h > 1$ which is not possible by using the standard definition of fluctuations (3).

A wavelet-based multifractal formalism uses as fluctuations

$$\delta(x_0, a) = c(x_0, a) = \int_R \psi_{x_a,a}(x) f(x) \mathrm{d}x \tag{7}$$

where $\psi_{x_a,a}(x)$ is a scale-dilated and shifted version of the mother wavelet $\psi_0(x)$, i.e.,

$$\psi_{x_a,a}(x) = \frac{1}{|a|} \psi_0 \left(\frac{x - x_0}{a} \right). \tag{8}$$

The so-defined $S(q,a)$ in (4) is called the partition function or generalized structure function. The use of a wavelet with N vanishing moments, i.e., $\int x^K \psi_x(x) \mathrm{d}x = 0$, for $(0 \leq K \leq N-1)$ and $\int x^N \psi_0(x) \mathrm{d}x \neq 0$, allows for the removal of a degree–N polynomial trend (see Mallat, 1998). This is important if first order differences do not completely remove trends in the data, for then the standard multifractal analysis will fail.

A standard wavelet, and the one used in this analysis, is the first and second order derivative of a Gaussian function, i.e.,

$$g^{(N)}(x) = \frac{d^{(N)}}{\mathrm{dx}^{(N)}} \left(e^{\frac{-x^2}{2}} \right) \tag{9}$$

which has been extensively used as a smooth generalization of N-th order increments to study the behavior of fractal functions (e.g. Muzy et al., 1994; Arneodo et al., 1995).

From the Legendre transform (6), in the case of a continuously differentiable $\tau(q)$, it follows that

$$q = \frac{\mathrm{d}D(h)}{\mathrm{d}h}. \tag{10}$$

Thus, the right limb of $D(h)$, where $(dD(h)/dh < 0)$, can only be estimated from the negative moments ($q < 0$) of the fluctuations. Computing negative moments of pdfs that have mass concentrated at zero (such as the pdfs of fluctuations), however, leads to divergence. To be able to take negative moments and estimate the complete singularity spectrum, Muzy et al. (1991, 1994) proposed to use the wavelet transform modulus maxima (WTMM) method, i.e., concentrate on the lines formed by following the maxima of the wavelet coefficients across scales and, thus, following the same singularity from the lowest scale to higher and higher scales. For details on this estimation, the reader is referred to the original publications (Muzy et al., 1991, 1993; Arneodo et al., 1998; and also Venugopal et al., 2006a,b).

4.4. Cumulant analysis

Cumulant analysis presents an efficient method of estimating the multifractal nature of a process and quantifying it in terms of a small number of parameters (e.g. Arneodo et al., 1998; and Delour et al., 2001). This method relies on a Taylor series expansion of $\tau(q)$, leading to

$$\tau(q) = \sum_{p \geq 1} (-1)^{p-1} \frac{c_p}{p!} q^p, q \rightarrow 0. \tag{11}$$

From the above equation one observes that a non-zero value of c_2 (also called the intermittency coefficient) implies deviation from monofractality and explicitly characterizes the richness of the spatial inhomogeneity of very high fluctuations. In fact, the value of c_2 formally relates to the change of the variance of the Hölder exponents (strength of singularities) with scale, (e.g. see Venugopal et al., 2006a,b, Appendix B and references therein) and, thus, characterizes the second order statistics of the singularities. Indeed, a quadratic approximation of $\tau(q)$

$$\tau(q) \cong c_1 q - c_2 \frac{q^2}{2}, q \rightarrow 0 \tag{12}$$

which corresponds to a quadratic approximation of $D(h)$

$$D(h) \cong 1 - \frac{(h - c_1)^2}{2c_2}, h \rightarrow c_1 \tag{13}$$

is a commonly used model of multifractality (the so-called log–normal model in turbulence).

The coefficients c_p can be estimated from the statistical cumulants $C(p,a)$ of order p of the logarithms of the absolute value of the wavelet coefficients $|c(x_0,a)|$ at a given scale, a, (Eq. (7)), or from the logs of the

WTMM coefficients. For details see Delour et al. (2001) and Venugopal et al. (2006a,b). For instance, for $p = 1, 2$

$$C(1, a) = \frac{a}{n(a)} \sum_{x_0} \ln|c(x_0, a)| \cong a_1 + c_1 \ln(a) \qquad (14)$$

$$C(2, a) = \frac{a}{n(a)} \sum_{x_0} [\ln|c(x_0, a)| - C(1, a)]^2 \cong a_2 \\ - c_2 \ln(a). \qquad (15)$$

Thus, linear regression of $C(p, a)$ versus In (a) allows for an easy estimation of c_p and only two linear regressions (giving estimates of c_1 and c_2) characterize the multifractality up to a quadratic approximation of the $\tau(q)$ function.

In the next section, the continuous wavelet-based multifractal analysis, the WTMM analysis, and the cumulant analysis are applied to the RCW series for a detailed characterization of the series' multifractal structure. It is emphasized that one of the goals of this study is to be able to depict the signature that mechanistic processes leave on the valleys, and thus accuracy and high discriminatory power of the multifractal characterization methodologies is a necessity.

5. Multifractal analysis: results

The river corridor widths of the five different segments from 0 to 35 km (see Fig. 3) have been analyzed using the multifractal formalism. It was found that the coefficient of variation (which characterizes the first two moments only) for these series shows a dependence on scale (see Fig. 8)
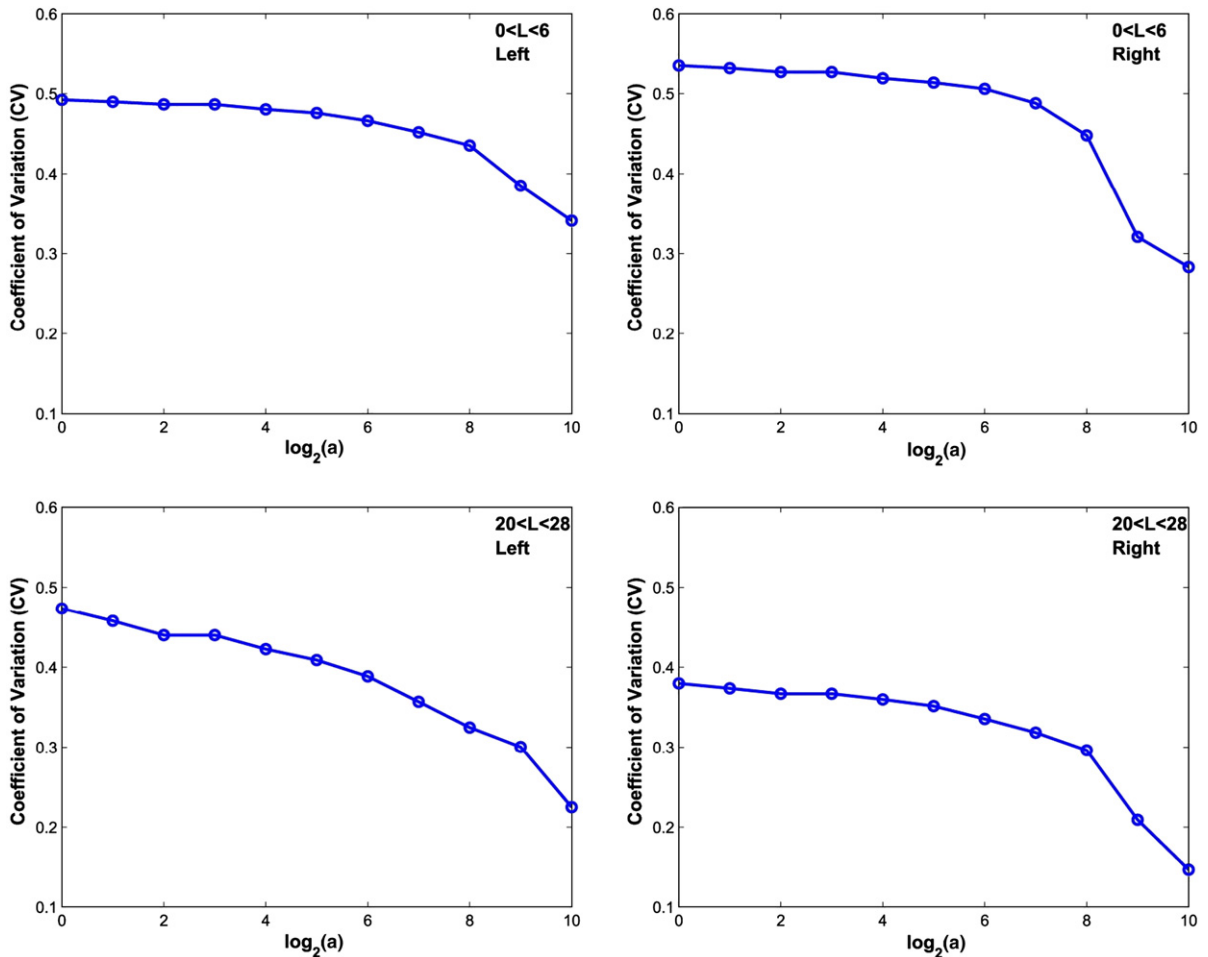

Fig. 8. Coefficient of variation of the river corridor widths as a function of scale for the two segments (0–6 km and 20–28 km) along the mainstream of the South Fork Eel River. The dependence on scale implies deviation from monoscaling. Similar plots were found for all other segments.

and, as expected, an increase as the scale decreases. This is an indication of deviation from monofractality and prompts analysis of higher order moments via the proposed wavelet-based multifractal formalism.

The top panels of Fig. 9 show the partition functions for $q=0$ to 3 (computed in intervals of $q=0.1$, but displayed in intervals of 0.5) for the right and left side river corridor widths of the first ($x=0–6$ km) segment of the South Fork Eel River. The analysis was performed using the continuous wavelet transform (CWT) with wavelet $g^{(2)}$ and $g^{(3)}$ i.e., the second and third order derivative of the Gaussian, (Eq. (9)). As can be seen, log–log linearity can be assumed between a range of scales as marked in Fig. 9. This range of scales corresponds to approximately 5 m to 40 m for the right side valley and 9 m to 64 m for the left side valley (see Table 1). Fitting straight lines to all moments and computing the slopes results in the $\tau(q)$ curves (middle

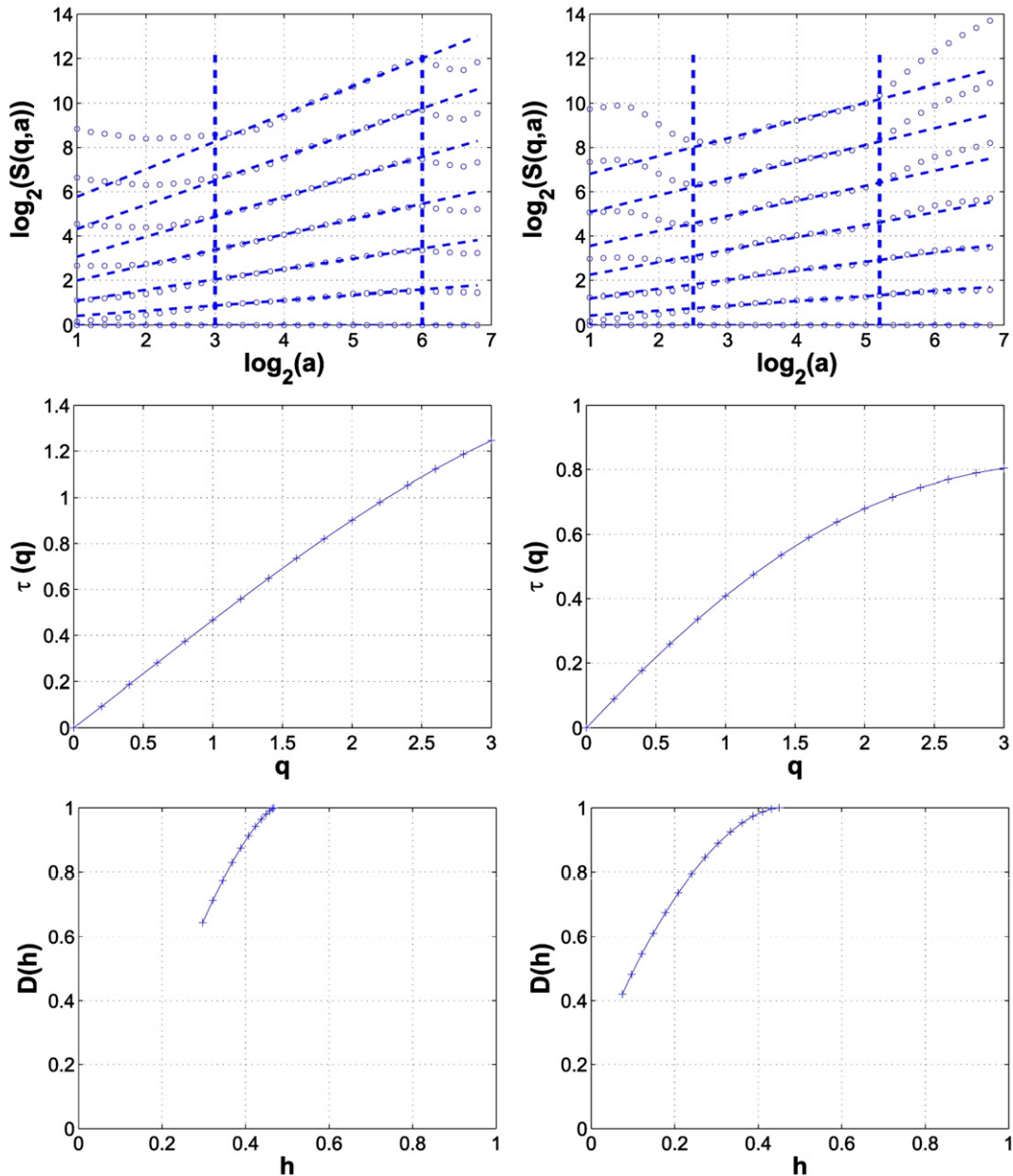Fig. 9. River reach of 0–6 km, partition functions of order $q=0.0$ to 3.0 using CWT (top), scaling exponent spectrum (middle) and singularity spectrum (bottom) for the left and right river corridor width series at depth $D_0=5$ m. The scaling range of the left corridor (3.2 to 6.0 octaves) and the right corridor (2.5 to 5.2 octaves) is indicated by the dashed vertical lines (see Table 1 for the scaling range in meters).

panels of Fig. 9), and via the Legendre transform results in the $D(h)$ curves (bottom panels of Fig. 9). The nonlinearity of the $\tau(q)$ curves is noted, as was expected from the coefficient of variation dependence on scale, signifying again a deviation from monofractality and, thus, the presence of singularities of various strengths, as quantified in the $D(h)$ spectra. Similar analysis has been performed for all other series. For example, see Fig. 10 for the segment of 20–28 km. A summary of the

scaling ranges for each river reach and the estimates of the most prevailing Hölder exponent $<H>$ (the value of h corresponding to the max value of $D(h)$) is given in Table 1.

As was discussed in the previous section, using continuous wavelet transforms does not allow characterization of the right part of the spectrum of singularities. To estimate the full $D(h)$ curve, the WTMM-based multifractal analysis was also applied to these series
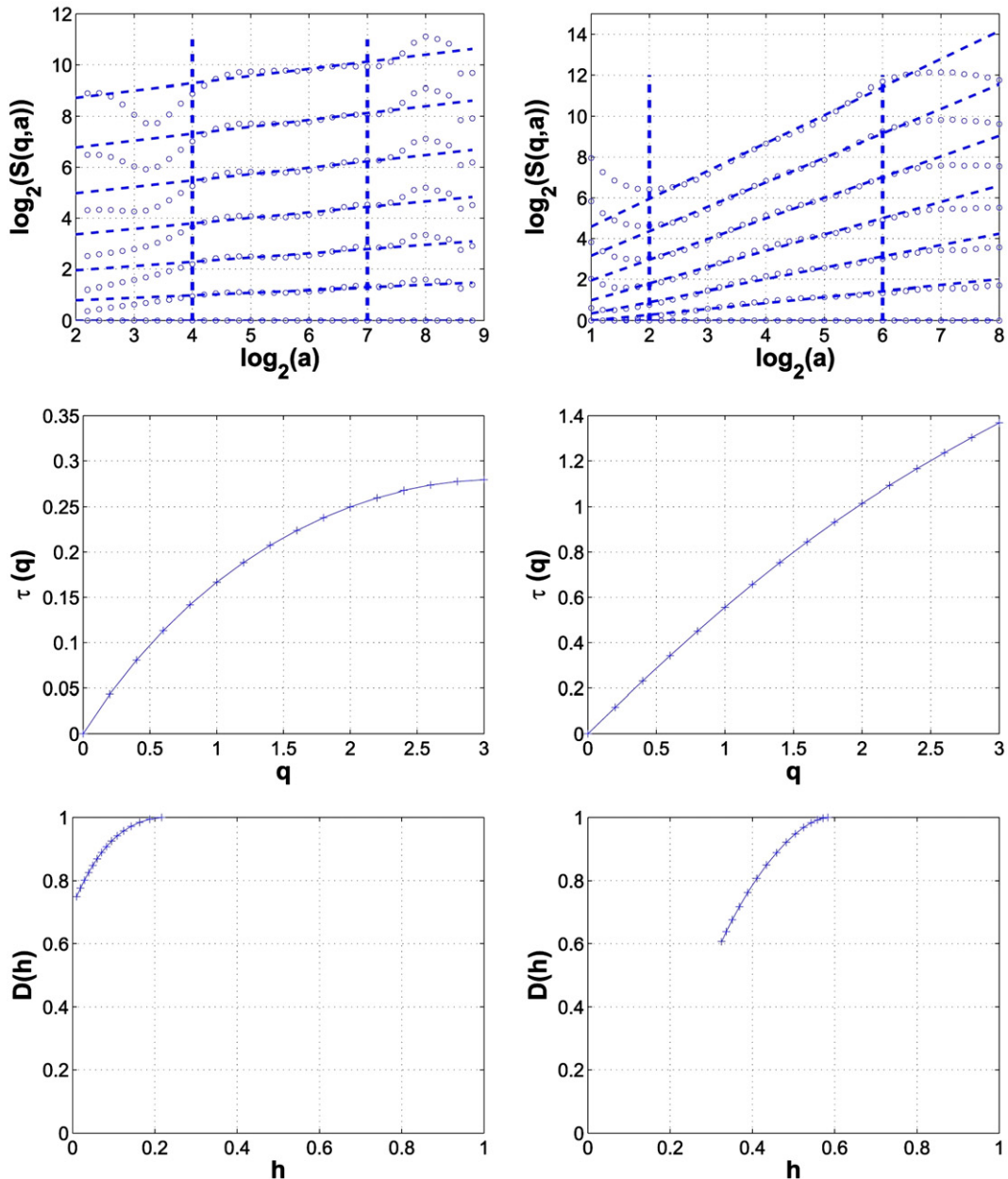
Fig. 10. Same as Fig. 9 but for the 20–28 km river reach. See Table 1 for scaling range.

which allows estimation of the statistical moments for negative order q. Fig. 11 shows the analysis for the 0–6 km river stretch. The top panels display the partition function for $q=-3$ to $+3$ (in increments of 0.5) and the fitted log–log linear lines within the scaling range previously reported. The middle panel shows the $\tau(q)$ curves and the bottom panels the complete $D(h)$ curve. On the same figures, we have superimposed the estimated $\tau(q)$ and $D(h)$ curves from the CWT analysis.

Some small differences in the estimation of the left part of $D(h)$ curve between the CWT and WTMM methods is noted, but also the ability of WTMM to provide an estimate of the right part of $D(h)$ is appreciated. The WTMM analysis was repeated for all series and the values of h_{min} and h_{max} (depicting the width of the spectrum of singularities) are summarized in Table 1. It is noted that for several sites, h_{max} was found to be greater than one. This emphasizes the need to adopt a wavelet-

Fig. 11. River reach of 0–6 km, partition functions of order $q=-3.0$ to 3.0 using WTMM (top), scaling exponent spectrum $\tau(q)$ (middle) and singularity spectrum $D(h)$ (bottom) for the left and right river corridor width series at depth $D_0=5$ m using CWT (+) and WTMM (O).

based multifractal analysis, as the standard structure function analysis based on first order increments cannot resolve singularities of order greater than one.
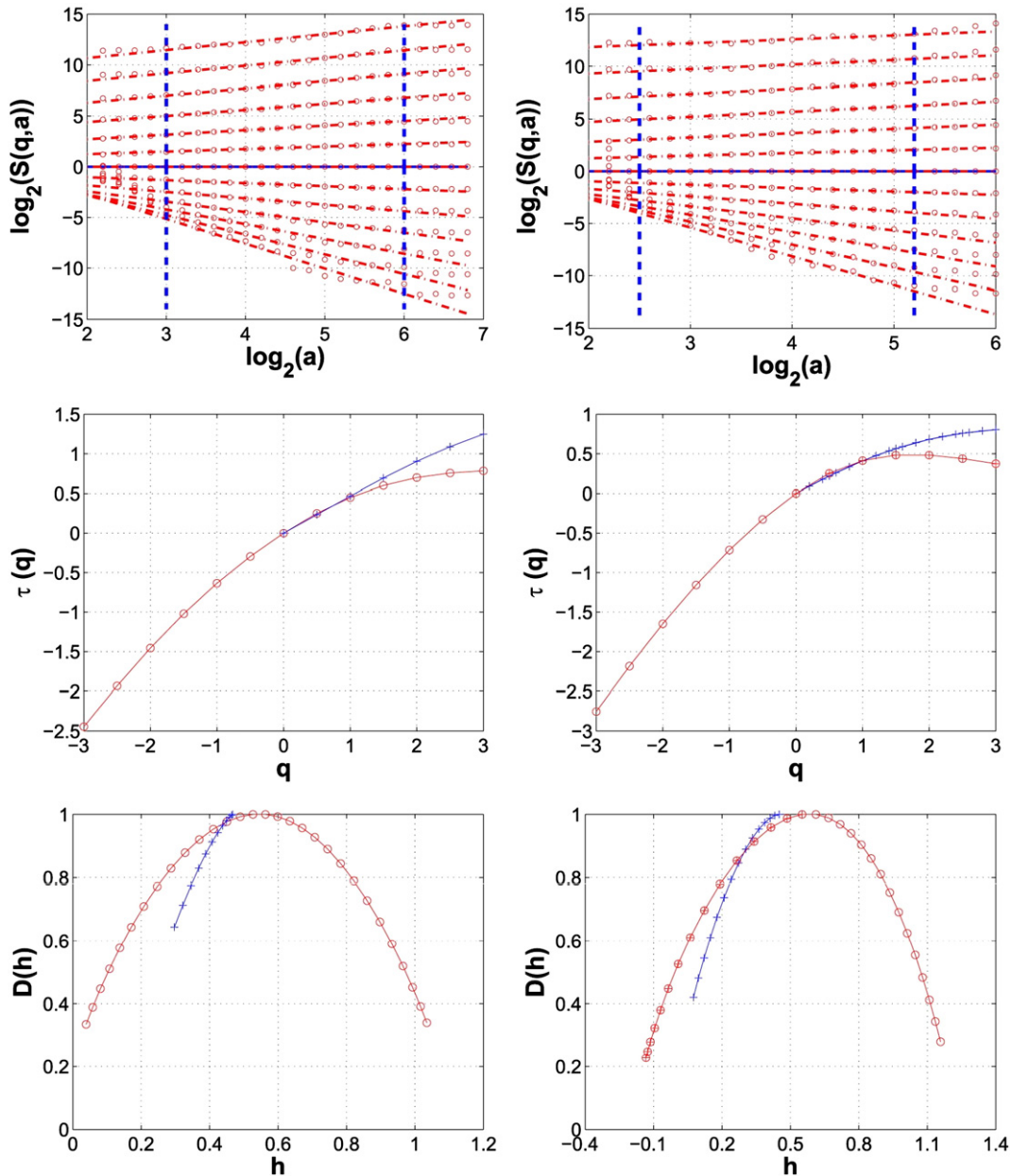
Having established the presence of multifractality, the next step in the analysis is to explicitly estimate the c_1 and c_2 coefficients using the cumulant analysis method. It is expected that c_1 will be very close to the value of $\langle H \rangle$ estimated from the CWT partition function method, but the particular interest is to estimate c_2 which concisely characterizes the intermittency of each series.

Fig. 12 shows the first two cumulants for the right and left river corridor width series of segment 0–6 km. As expected, a log–log linear relationship in $C(1, a)$ vs. ln (a) yields an estimate of c_1 very close to the estimate of $\langle H \rangle$ obtained from the partition function approach (see Table 1). The $C(2, a)$ vs. ln (a) plots show a non-zero slope for the right valley (consistent with the wide spectrum of singularities displayed in the bottom right panels of Figs. 9 and 11) and an almost zero slope for the left valley (consistent with the more narrow spectrum of singularities for this series) as seen in Figs. 9 and 11

bottom left panels. Similar analysis was performed for all other series and the estimates of c_1 and c_2 are summarized in Table 1.

It is instructive to display in Fig. 13 the cumulant analysis of the right and left river corridor width series of the segment 20–28 km for which a significant left-to-right asymmetry was noted from the Hölder exponent $\langle H \rangle$ (see Table 1). Specifically, the left side valley was found to have much "rougher" fluctuations (smaller $\langle H \rangle$) that the right side valley (larger $\langle H \rangle$). It is pleasing to see that the cumulant analysis is able to further quantify this asymmetry (see values of c_1 in Table 1) and also depict an asymmetry in intermittency. Specifically, the left side RCW series shows a much more intermittent structure (larger c_2 value) and indicates the presence of more complex or interacting mechanisms forming this side of the valley. From the 20–28 km river segment, shown in Fig. 6, it is noted that from the RCW series themselves, one cannot visually depict the significant statistical differences we were able to establish using the proposed methodologies, although by close inspection of the high resolution topography,
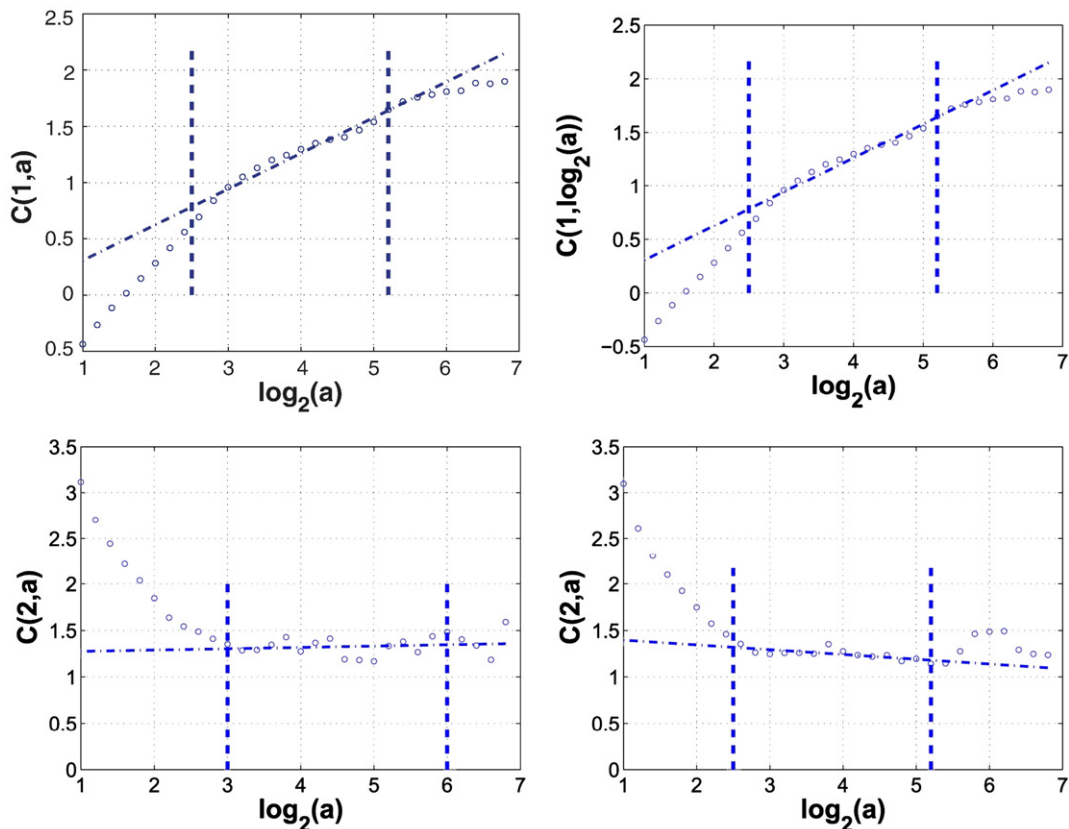

Fig. 12. Cumulant analysis of the left and right river corridor width series of reach 0–6 m, to estimate parameters c_1 and c_2 in Table 1.
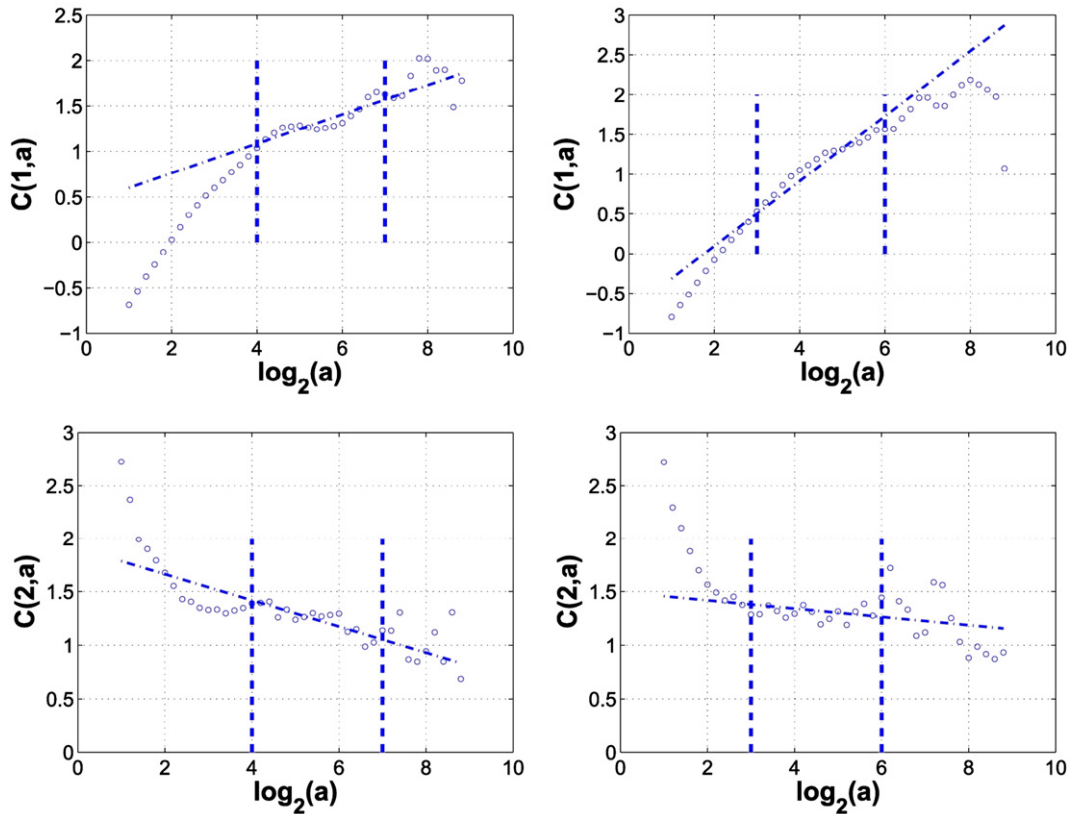
Fig. 13. Same as Fig. 12 for the river reach of 20–28 km.

one can notice a higher degree of dissection in the left-side valley. Also, it is noted that spectral analysis of the left and right corridor widths for this segment (Fig. 7) was not able to depict the subtle differences depicted by MF analysis.

6. Discussion and conclusions

The goal of this work was to examine the multiscale statistical properties of the river corridor width (RCW) series along the mainstream of a 35 km mountainous channel reach with the goal of assessing whether the valley forming processes imprint on this series any particular statistical organization.

Some clear results have emerged from this analysis. First, river corridor width fluctuations exhibit a rich multiscale statistical structure and a deviation from scale-invariance or monoscaling. Second, as one goes further away from the outlet of the basin to less steep, alluvial valleys, the statistical "roughness" of the RCW series increases (smaller c_1 or $\langle H \rangle$ values) and also the degree of multifractality, or intermittency, increases (larger c_2 values) (see Table 1). Third, for the particular

basin analyzed, a significant left-right asymmetry exists in the statistical structure of valley geometry: the left side is consistently rougher and more intermittent implying that different physical mechanisms shaped the valley at the left and right sides of the mainstream. This difference does not seem to be directly related to the number of tributaries joining the main river, as an equal number of tributaries is present on both sides of the river stretch (see Fig. 4). Rather, other mechanisms of sediment transport, landsliding, etc., seem to be the underlying cause. As we go further up to even steeper along-river slopes, no scaling is present at all, at least not in a significant range of scales, and further careful analysis needs to be undertaken.

Our analysis objectively depicted two statistically distinct regimes with transitions at around 14 km and also 28 to 35 km (see Fig. 14). An interesting question is whether these statistically distinct regimes are the result of physically distinct valley-forming processes. Another interesting question is whether the documented statistical structure of river corridor widths, which is seen as an emergent property of the physical system, can be faithfully reproduced by numerical models of landscape
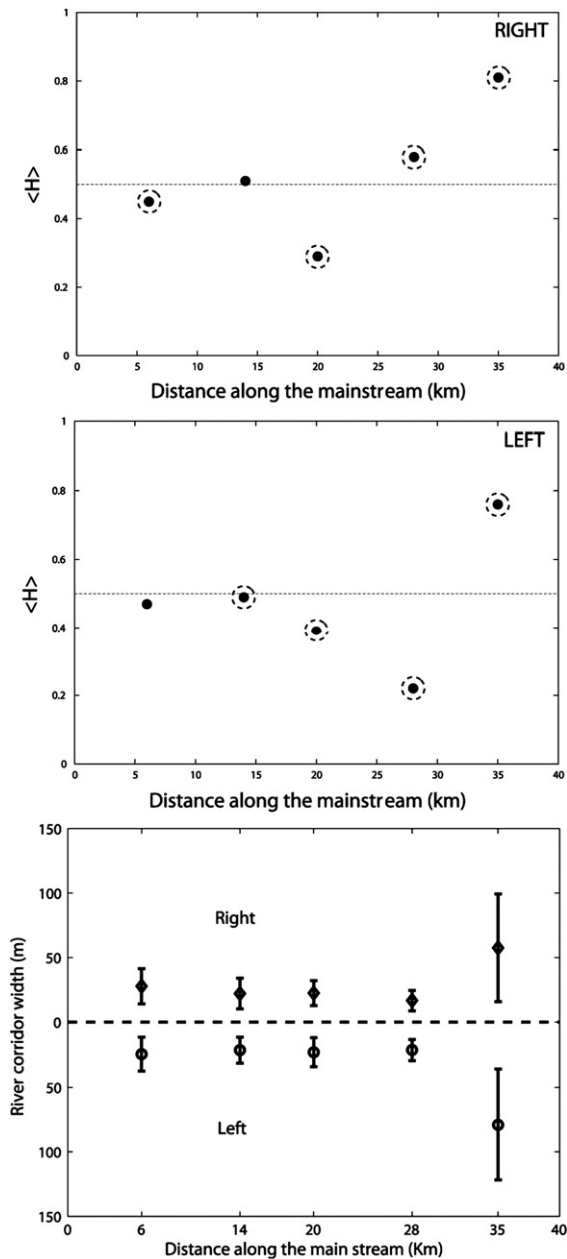
Fig. 14. Hurst exponents for the right side (top) and left side (middle) RCW series (at $D_0=5$ m). Larger values of $\langle H \rangle$ indicate "smoother" signals. Points with circles around them indicate reaches with a significant deviation from monoscaling (large c_2 values (see Table 1). The bottom panel shows the mean of the RCW series ± 1 standard deviation for each of the five segments. Note that the dramatic increase of the variance for the 28–35 km segment comes from large-scale features (see Fig. 4) and not from very abrupt high frequency (small scale) fluctuations, as this segment exhibits a very smooth fractal structure (see the large $\langle H \rangle$ in top two panels).

evolution at the hillslope scale (e.g., see Roering et al., 1999). Both of these questions are the subject of future investigations.

References

Arneodo, A., Bacry, E., Muzy, J., 1995. The thermodynamics of fractals revisited with wavelets. Physics A 213, 232–275.

Arneodo, A., Bacry, E., Jaffard, S., Muzy, J., 1998. Singularity spectrum of multifractal functions involving oscillating singularities. J. Fourier Anal. Appl. 4, 159–174.

Barenblatt, G.I., 2003. Scaling. Cambridge University Press, Cambridge. 186 pp.

Delour, J., Muzy, J., Arneodo, A., 2001. Intermittency of 1d velocity spatial profiles in turbulence: a magnitude cumulant analysis. Eur. Phys. J., B Cond. Matter Phys. 23, 243–248.

Jaffard, S., 1989. Exposants de Hölder en des points donnés et coefficients d'ondelettes. C. R. Acad. Sci., Ser. 1 Math. 308, 79–81.

Kolmogorov, A.N., 1941. The local structure of turbulence in incompressible viscous fluid for very large Reynolds number. Dokl. Akad. Nauk SSSR 30, 299–303.

Lashermes, B., Foufoula-Georgiou, E., 2007. Area and width functions in river networks: new results on multifractal properties. Water Resour. Res. 43. doi:10.1029/2006 WR005329.

Mahrt, L., 1989. Intermittency of atmospheric turbulence. J. Atmos. Sci. 46, 79–95.

Mallat, S., 1998. A Wavelet Tour of Signal Processing. Academic Press, San Diego, CA.

Mallat, S., Hwang, W.L., 1992. Singularity detection and processing with wavelets. IEEE Trans. Inf. Theory 38, 617–643.

Montgomery, D., 2002. Valley formation by fluvial and glacial erosion. Geology 30 (11), 1047–1050.

Muzy, J., Bacry, E., Arneodo, A., 1991. Wavelets and multifractal formalism for singular signals: application to turbulence data. Phys. Rev. Lett. 67, 3515–3518.

Muzy, J., Bacry, E., Arneodo, A., 1993. Multifractal formalism for fractal signals: the structure-function approach versus the wavelet-transform modulus-maxima method. Phys. Rev., E Stat. Phys. Plasmas Fluids Relat. Interdiscip. Topics 47, 875–884.

Muzy, J., Bacry, E., Arneodo, A., 1994. The multifractal formalism revisited with wavelets. Int. J. Bifurc. Chaos Appl. Sci. Eng. 4, 245–302.

Parisi, G., Frisch, U., 1985. On the singularity structure of fully developed turbulence. In: Frisch, U. (Ed.), Proc. Int. Summer school Phys. Enrico Fermi, North Holland.

Power, M., 1992. Hydrologic and trophic controls of seasonal algal blooms in northern California rivers. Arch. Hydrobiol. 125, 385–410.

Roering, J., Kirchner, J., Dietrich, W.E., 1999. Evidence for nonlinear, diffusive sediment transport on hillslopes and implications for landscape morphology. Water Resour. Res. 35 (3), 853–870. doi:10.1029/1998WR900090.

Seidl, M., Dietrich, W., 1992. The problem of channel erosion into bedrock. Catena 23 (Supplement).

Venugopal, V., Roux, S., Foufoula-Georgiou, E., Arneodo, A., 2006a. Revisiting multifractality of high-resolution temporal rainfall using a wavelet-based formalism. Water Resour. Res. 42 (6), W06D14. doi:10.1029/2005WR004489.

Venugopal, V., Roux, S.G., Foufoula-Georgiou, E., Arneodo, A., 2006b. Scaling behavior of high resolution temporal rainfall: new insights from a wavelet-based cumulant analysis. Phys. Lett., A 348, 335–345.

Application of dynamic subgrid-scale concepts from large-eddy simulation to modeling landscape evolution

Paola Passalacqua,[1,2,3] Fernando Porté-Agel,[1,2,3] Efi Foufoula-Georgiou,[1,2,3] and Chris Paola[1,2,4]

[1] Landscapes share important similarities with turbulence: both systems exhibit scale invariance (self-similarity) over a wide range of scales, and their behavior can be described using comparable dynamic equations. In particular, modified versions of the Kardar-Parisi-Zhang (KPZ) equation (a low-dimensional analog to the Navier-Stokes equations) have been shown to capture important features of landscape evolution. This suggests that modeling techniques developed for turbulence may also be adapted to landscape simulations. Using a "toy" landscape evolution model based on a modified 2-D KPZ equation, we find that the simulated landscape evolution shows a clear dependence on grid resolution. In particular, mean longitudinal profiles of elevation at steady state and bulk erosion rates both have an undesirable dependence on grid resolution because the erosion rate increases with resolution as increasingly small channels are resolved. We propose a new subgrid-scale parameterization to account for the scale dependence of the sediment fluxes. Our approach is inspired by the dynamic procedure used in large-eddy simulation of turbulent flows. The erosion coefficient, assumed exactly known at the finest resolution, is multiplied by a scale dependence coefficient, which is computed dynamically at different time steps on the basis of the dynamics of the resolved scales. This is achieved by taking advantage of the self-similarity that characterizes landscapes over a wide range of scales. The simulated landscapes obtained with the new model show very little dependence on grid resolution.

1. Introduction

[2] The fascinating self organized spatial patterns of natural landscapes have long attracted the attention of researchers. The most obvious and widespread of these patterns are the tributary channel networks generally characteristic of erosional landscapes. Building on earlier landscape models such as those of *Culling* [1960, 1963], which used a diffusion model of slope erosion, the 1990s saw a renaissance of landscape modeling [e.g., *Willgoose et al.*, 1991a, 1991b; *Chase*, 1992; *Rinaldo et al.*, 1992; *Howard*, 1994; *Rodriguez-Iturbe et al.*, 1994; *Rodriguez-Iturbe and Rinaldo*, 1997; *Smith et al.*, 1997a, 1997b; *Tucker et al.*, 2001]. In general, these models have focused on reproducing "whole-system" properties of the landscape such as fractal dimensions, network topology, and spatial statistics (e.g., slope distributions, slope-area relations). Landscape evolution models have also been coupled to tectonic models

to simulate the evolution of mountain belts on long timescales [*Kooi and Beaumont*, 1994; *Tucker and Slingerland*, 1994; *Koons*, 1995]. Comprehensive reviews on landscape evolution modeling approaches are given on *Dietrich et al.* [2003], *Peckham* [2003], and *Willgoose* [2005].

[3] A fundamental problem arises in numerical modeling of systems whose dynamics spans a wide range of scales: selection of a computational grid (usually dictated by the size of the domain over which a solution is sought and the smallest grid that can be afforded computationally) leaves out scales whose dynamics are not explicitly resolved. Yet, it is known that even if the interest is not in resolving the smallest scales, their effect on the dynamics of the larger scales (due to nonlinearities) is considerable. Thus ignoring the subgrid scales compromises the accuracy of the solution at the resolved scales and also makes the numerical simulation resolution-dependent. This problem presents itself in numerical modeling of many natural processes which exhibit multiscale variability, including flow and transport in porous media, atmospheric modeling from cloud resolving models to mesoscale to global circulation models, land-atmosphere interactions, atmospheric turbulence and, foremost, modeling of turbulent flows. Several methodologies have been proposed to address this problem and these include derivation of "effective" parameters in coarse grained equations [e.g., *Bear*, 1988; *Bou-Zeid et al.*, 2004], statistical downscaling [e.g., *Harris and Foufoula-*

---

[1]St. Anthony Falls Laboratory, Minneapolis, Minnesota, USA.
[2]National Center for Earth-Surface Dynamics (NCED), Minneapolis, Minnesota, USA.
[3]Department of Civil Engineering, University of Minnesota–Twin Cities, Minneapolis, Minnesota, USA.
[4]Department of Geology and Geophysics, University of Minnesota–Twin Cities, Minneapolis, Minnesota, USA.

Georgiou, 2001], and analytical derivation of closure terms [e.g., *Meneveau and Katz*, 2000; *Sagaut*, 2002], among others.

[4] The field in which subgrid-scale parameterizations have been the most advanced is that of turbulence, where direct numerical simulation (DNS), i.e., numerical solution of the Navier-Stokes equations using a resolution as small as the dissipation (Kolmogorov) scale, is only feasible for relatively low Reynolds number flows. A technique that has become popular to simulate higher Reynolds number turbulent flows is large-eddy simulation (LES), which consists of solving the spatially filtered Navier-Stokes equations, using a spatial filter of size equal to or slightly larger than the grid size. This filtering operation applied to the nonlinear advection terms leads to the so-called subgrid-scale fluxes, which represent the effect of the subgrid scales on the evolution of the resolved scales and need to be parameterized. As a result, LES explicitly resolves all scales of motion (eddies) larger than the grid scale, while the subgrid-scale fluxes are parameterized using a subgrid-scale model. Comprehensive reviews on LES and subgrid-scale modeling are given by *Meneveau and Katz* [2000], *Pope* [2000, 2004], and *Geurts* [2004]. A particularly interesting development in subgrid-scale modeling of turbulent flows is the so-called dynamic modeling approach [*Germano et al.*, 1991; *Moin et al.*, 1991; *Porté-Agel et al.*, 2000; *Porté-Agel*, 2004]. It takes advantage of the scale similarity of turbulence to optimize the value of the subgrid model coefficient(s) based on the dynamics of the resolved scales, thus not requiring any parameter tuning.

[5] In the case of landscape evolution, it is well known that landscapes present multiscale self-similar properties through a wide range of scales, from the system scale (typically $10^2 - 10^4$ km) down to the spacing of the smallest channels, which is typically on the order of $10-100$ m and below which diffusion processes dominate. As in high Reynolds number turbulence, numerical solution of the entire range of scales is usually impractical. Instead, landscape models are run at relatively coarse resolution, i.e., one solves the so-called coarse-grained transport equations (Figure 1). However, the accuracy of this methodology is unknown since channels smaller than the grid size are not taken into account. This suggests the possibility that the calculated erosion rates and landscape evolution are likely affected by the grid resolution. This was pointed out by *Stark and Stark* [2001] who developed a subgrid-scale parameterization based on a parameterization measure called channelization. *Rodriguez-Iturbe and Rinaldo* [1997] have shown the effect of "coarse graining" a specific landscape on the scaling relationships of elevation.

[6] Landscapes share important similarities with turbulence: both systems exhibit scale invariance (self-similarity) over a wide range of scales and their behavior can be described using comparable dynamic equations. This similarity can be seen, for example, in the behavior of power spectra: Turbulence velocity spectra exhibit a well-known $-5/3$ slope in the inertial subrange [*Kolmogorov*, 1961], representing the energy cascade from large scales to small scales. In the case of landscapes, power spectra of linear transects in topography also exhibit a log-log scaling range with slope of -2. Another parallel between the two systems is the existence of a lower limit on the size of the turbulent

structures (eddies): the Kolmogorov scale, the scale at which viscous effects dominate and the effective Reynolds number approaches unity. In landscapes, the analogous fine scale would be the spacing of the smallest channels, determined by the scale at which (diffusive) hillslope processes dominate [e.g., *Dietrich et al.*, 2003]. This analogy between the viscous length scale of turbulence and the hillslope scale in landscapes has also been discussed by others [e.g., *Peckham*, 1995]. Moreover, turbulence has been used as a metaphor for other complex systems such as earthquakes [*Kagan*, 1992] and stream braiding [*Paola*, 1996; *Paola et al.*, 1999].

[7] The purpose of this paper is to explore concepts of LES in the context of landscape evolution modeling. Using a minimum complexity model, used previously by several authors for landscape simulation [e.g., *Sornette and Zhang*, 1993; *Somfai and Sander*, 1997; *Banavar et al.*, 2001], we demonstrate its scale dependence and propose a dynamic subgrid-scale model to take into account the effect of subgrid-scale processes in a landscape evolution model.

[8] It is important to point out that the goal of this study is not to strictly apply the LES technique, as developed for turbulent flows, to landscape evolution simulations. There are some limitations to the direct extension of the LES technique to landscapes. Typical governing equations for landscape evolution, even though often similar in form to the Navier-Stokes equations (including nonlinear terms that generate fluctuations as well as diffusion terms), are not as well established for the description of the system at all scales. For example, the nonlinear erosion flux term is already a parameterization containing tuning coefficient(s). This makes it challenging to formally define the subgrid-scale erosion fluxes and to develop subgrid-scale models for them. Instead, our approach here consists of developing a tuning-free dynamic procedure, inspired from the dynamic modeling approach used in LES, to "optimize" the value of the erosion coefficient (in the nonlinear erosion flux term) using the scale dependence of the coefficient quantified from the smallest resolved scales in the simulations.

2. Landscape Evolution Modeling and Effect of Grid Resolution

2.1. KPZ Model

[9] As discussed above, a number of different models have been proposed for landscape evolution. Here we use a modified version of the Kardar-Parisi-Zhang (KPZ) equation, originally used in the context of growth of atomic interfaces by ion deposition [*Kardar et al.*, 1986]. The KPZ equation as applied to modeling the evolution of land surface elevation *h* reads [*Sornette and Zhang*, 1993; *Somfai and Sander*, 1997; *Banavar et al.*, 2001]:

$$\frac{\partial h(\vec{x}, t)}{\partial t} = D\nabla^2 h + C|\nabla h|^2 + \eta(\vec{x}, t) \qquad (1)$$

The right hand side of equation (1) includes, from left to right, a diffusion term, where *D* is the diffusion coefficient, a nonlinear term, where C is a constant and ∇h is the slope, and a white noise term.

[10] It is important to note that, with a simple transformation of variables, the KPZ equation without noise
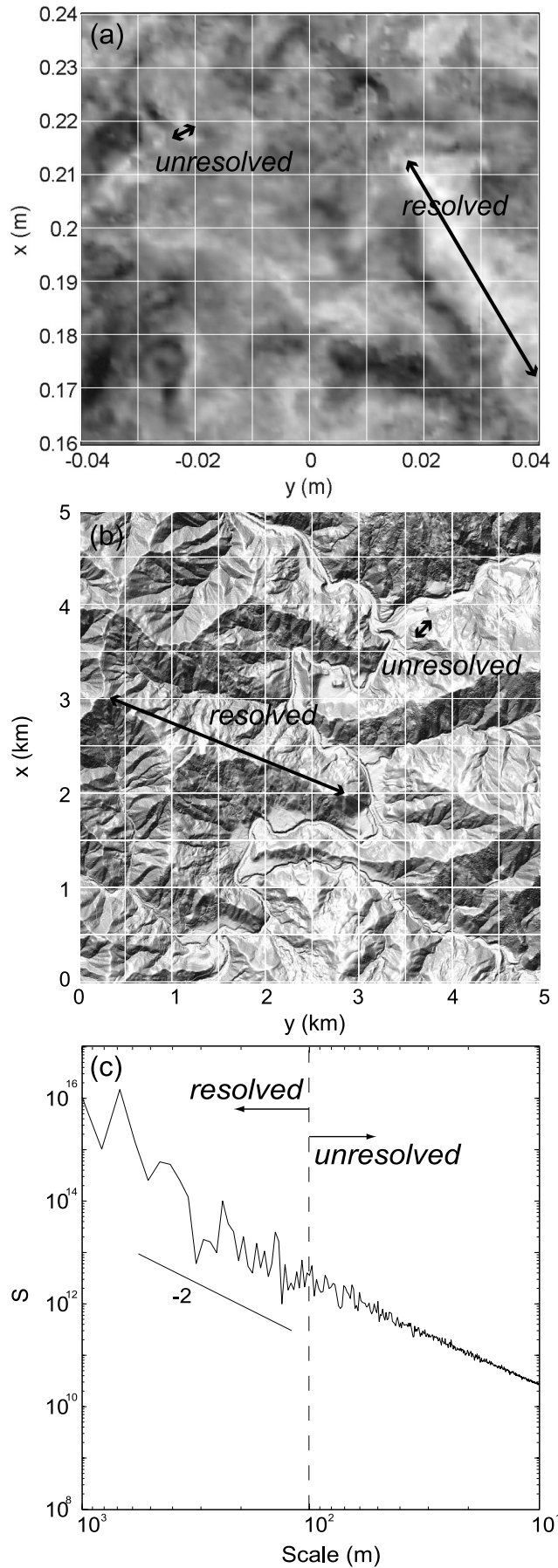
becomes the Burgers equation, a low-dimensional analog to the Navier-Stokes equations governing fluid flow and turbulence.

[11] The initial application of the KPZ equation to landscape evolution [*Sornette and Zhang*, 1993] shows the importance of the nonlinear terms in the evolution of surface topography and the associated drainage network. At a coarse grained scale, the effect of diffusion is often neglected [*Somfai and Sander*, 1997; *Banavar et al.*, 2001] since this mechanism is effective mainly at the small (subgrid) scales. Neglecting also the noise term, (1) has only the non linear term on the right hand side. Furthermore, taking into account that the evolution of the landscape is coupled with the water flux q acting on the surface, the constant C in front of the nonlinear term in (1) can be written as an erosion coefficient α times the water flux q [*Somfai and Sander*, 1997; *Banavar et al.*, 2001]. The governing equation then becomes:

$$\frac{\partial h}{\partial t} = -\alpha \cdot q \cdot |\nabla h|^2. \tag{2}$$

Under the assumption of uniform rainfall acting on the surface, the water flux at a given point is proportional to the area draining at that location. We have chosen a fairly simple landscape evolution model, best suited for bedrock landscape evolution modeling, which does not allow both erosion and deposition to occur. This choice has been motivated by the fact that a simple type of equation would maximize clarity in deriving the subgrid model. This work will be extended in the future to more comprehensive landscape evolution models.

[12] Notice that (2) is a special case of the general governing equation, widely used in landscape modeling [e.g., *Rodriguez-Iturbe and Rinaldo*, 1997]:

$$\frac{\partial h}{\partial t} = -\alpha \cdot A^m \cdot |\nabla h|^n, \tag{3}$$

with $\frac{m}{n} \approx 0.5$.

[13] The nature of the steady state reached by the system depends on the external conditions applied in the problem. If the boundary condition at the output is a fixed elevation, with constant rock uplift, the steady state is reached when the erosion rate balances the rock uplift rate over the whole system [*Hack*, 1960; *Adams*, 1980; *Howard*, 1994; *Somfai and Sander*, 1997; *Willett and Brandon*, 2002]. If the uplift

Figure 1. Schematic of the separation between resolved and subgrid scales in turbulence (Figure 1a) and landscapes (Figures 1b and 1c). (a) Gray scale rendering of the vertical velocity component measured in a turbulent boundary layer at the St. Anthony Falls Laboratory wind tunnel. (b) Bare-earth LIDAR shaded-relief image (1-m resolution) of a portion of the Angelo Coast Range Reserve, northern California, grid spacing of 500 m. (c) Fourier spectrum of the topography shown in Figure 1b, showing a −2 power law dependence of spectral power on wave number. Separation between resolved and unresolved scales is 100 m. In both turbulence and landscapes, only structures with length scales larger than the grid size are explicitly resolved.
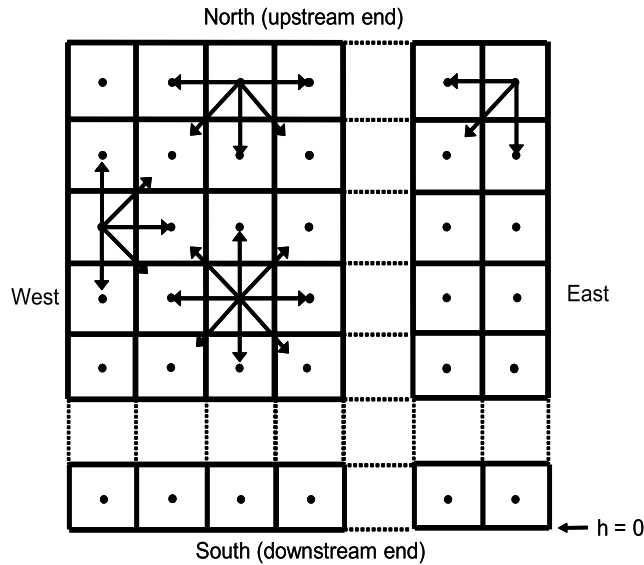
Figure 2. Boundary conditions and allowed flow directions. The output of the system is located at the downstream end of the field where the elevation is kept fixed at zero. At the upstream end the boundary condition is an infinite wall, so that no flow exits upstream of the field. At the east and west boundaries, the flow directions are likewise restricted to those inside the field. Thus the only allowed output is at the downstream end of the field.

rate is zero, the system reaches a steady state when there is no remaining material to erode [*Inaoka and Takayasu*, 1993].

[14] The river networks obtained with the modified KPZ equation have been shown to satisfy scaling laws characteristic of natural landscapes: the slope-area law, the power law of distribution of drainage area, and Horton's laws for branching ratio and length ratio [*Somfai and Sander*, 1997]. In addition to these laws, the simulations also yield realistic profiles for the average elevation along the mainstream direction [*Banavar et al.*, 2001].

2.2. Numerical Implementation

[15] The initial field is a sloping surface with a small noise, obtained using the following expression [*Somfai and Sander*, 1997]:

$$h(x, y, t = 0) = s_0 \cdot (y + dy \cdot rand(x, y)), \qquad (4)$$

where h is the elevation, s_0 represents the initial slope, y is the north-south coordinate, dy is the grid constant and *rand* is a uniform random number in the range [0,1]. This initial configuration prevents the formation of lakes.

[16] We study the evolution of the system at three different resolutions: the same field is divided into 256×256 grid cells, 128×128 grid cells and 64×64 grid cells. We focus initially on the simplest case (uniform rainfall, no groundwater, uniform and structureless substrate, no redeposition), applying the simplified erosion model discussed earlier (equation (2)) with the addition of a constant uplift u:

$$\frac{\partial h}{\partial t} = u - \alpha \cdot q \cdot |\nabla h|^2, \qquad (5)$$

Equation (5) represents an erosional model for an incisional process where the erosion rate depends linearly on water flux and nonlinearly on slope.

[17] Water is routed using the steepest descent rule. In every site the elevation is compared with the one of the eight surrounding neighbors and the water is assumed to follow the steepest path. Recently, *Pelletier* [2004] has shown that computing the slope using a multiple-direction algorithm eliminates an undesirable consequence of the steepest descent rule: evolution to a frozen steady state of the river network in which erosion exactly balances uplift at each point [*Hasbargen and Paola*, 2000, 2003]. Once the flow direction is computed in every site, the slope and the water flux can be computed and used to update the elevation via (5). Because of the assumption of a uniform rainfall and no loss of water, the water flux is given by the drainage area times the unit rainfall.

[18] The boundary conditions are: an infinite wall at the upstream end of the field (north boundary); an output boundary at fixed height equal zero located at the downstream end of the field (south boundary); on the lateral sides (east and west boundaries) the flow is forced to drain into the system. This condition could be easily changed to periodic boundary conditions [*Somfai and Sander*, 1997; *Banavar et al.*, 2001]. A sketch of the computational domain with the applied boundary conditions is shown in Figure 2.

[19] The simulations with the three resolutions are run independently until the systems reach steady state. The steady state is reached when the erosion rate is in equilibrium with the uplift. The simulated evolution of the landscape shows two different timescales: a freezing time, at which the river network reaches its final configuration but the elevation continues adjusting, and a relaxation time at which the system reaches its equilibrium profile and the surface stops evolving [*Sinclair and Ball*, 1996; *Banavar et al.*, 2001]. The time needed to freeze the system is usually smaller than the time needed to reach the final profile. It should be noted that a freezing time, and a corresponding frozen configuration of the system, can be defined as we have done only because the model allows for an (unrealistic) static steady state. Revised definitions would be needed for the more realistic dynamic-steady-state condition.

[20] The freezing time of the system is obtained by computing at every time step the number of unstable sites. An unstable site is defined as a point in the system where the flow direction changes in one time step [*Inaoka and Takayasu*, 1993]. When the number of unstable sites remains equal to zero for a sufficiently large number of time steps, the river network is considered at its final configuration. Before reaching the equilibrium profile, the number of unstable sites remains zero, while the topography continues adjusting. The relaxation time instead is given by the time at which the topography also reaches a static steady state.

2.3. Effect of Grid Resolution

[21] We analyze the results of the numerical simulations using 256×256, 128×128 and 64×64 grid cells in terms of several statistics. The systems obtained at steady state with resolutions 256×256, 128×128 and 64×64 are
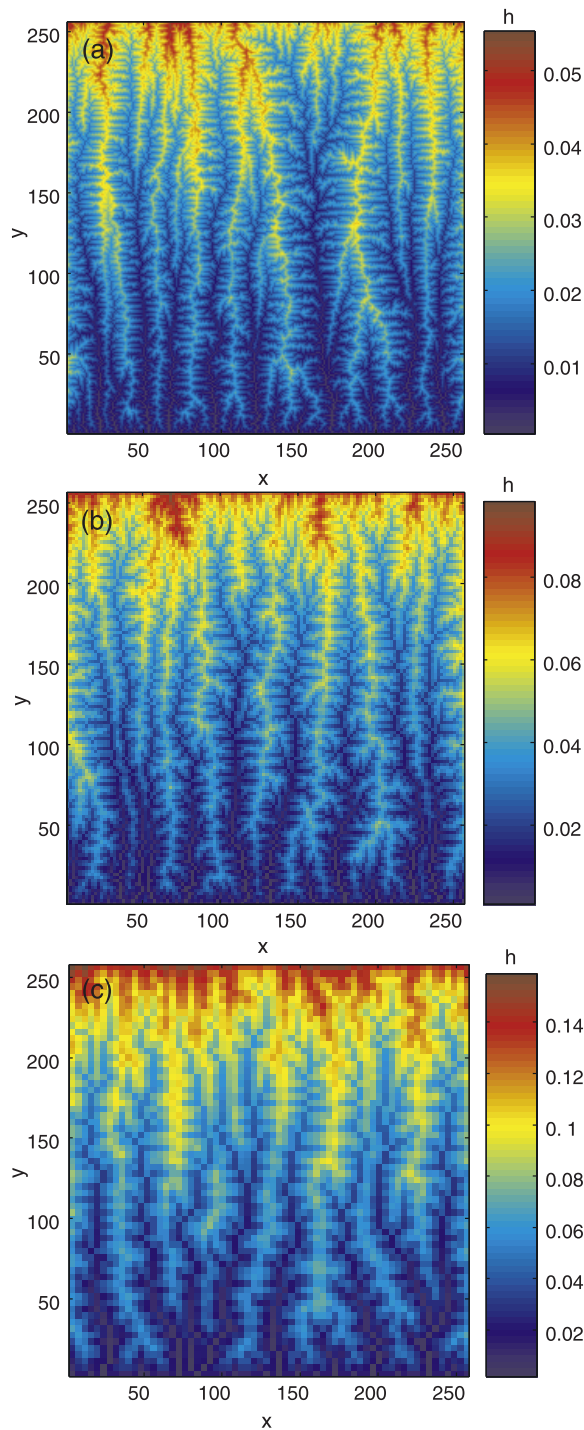
Figure 3. Elevation fields obtained for three grid resolutions at steady state using equation (5): (a) 256 × 256, (b) 128 × 128, and (c) 64 × 64.

shown in Figure 3. The corresponding river networks were extracted with River Tools (http://www.rivix.com/) and are shown in Figure 4 (channels of Strahler order greater than 2 only). The modified KPZ model produces channel networks with the expected loss of detail as the resolution is decreased.

[22] The power spectral density (spectrum) provides an estimate of the distribution of elevation variance across scales. Figure 5 shows a comparison of spectra from trans-ects across the upstream part of the domain for the three resolutions. Except at the largest scales, there is a wide range of scales for which the spectra obtained at all resolutions show a slope of approximately −2, which is in good agreement with observations from linear transects in topography [*Vening Meinesz*, 1951; *Mandelbrot*, 1975; *Sayles and Thomas*, 1978; *Newman and Turcotte*, 1990]. However, the total variance in elevation observed at the three resolutions does depend on scale.

[23] Mean longitudinal profiles obtained at steady state with the three resolutions are shown in Figure 6a. The results indicate that the basin topography required to produce a balance between erosion and rock uplift in the simulation is strongly scale dependent. In particular, both slope and curvature increase with decreasing resolution, which is not realistic. This behavior can be attributed to the fact that erosion due to subgrid-scale channel networks (occurring at scales smaller than the grid scale) is not accounted for in the simulations. Since the subgrid-scale erosion flux is expected to be relatively larger in the case of coarser resolutions, landscapes simulated at those resolutions experience less efficient erosion than the ones obtained at higher resolutions.

[24] Strong scale dependence is also shown by the volume of material eroded per time step. As Figure 6b shows, the higher the resolution, the higher the volume of eroded material per time step. This is consistent with the observed behavior of the mean longitudinal profiles. The area under the curves, which gives the total amount of material eroded until steady state is reached, increases with resolution. The rate of erosion gives also an idea of the timescale dependence of the erosion process at the three resolutions: the higher the resolution, the higher the rate of erosion and the faster the process. The lowest resolution needs more time to reach the steady state.

3. A Dynamic Subgrid-Scale Model

3.1. Derivation of the Dynamic Subgrid-Scale Model

[25] The resolution dependence of the results obtained in the previous section using (5) highlights the need to account for the fact that erosion rates depend on the grid size used in the simulations. In this section, we develop a procedure to account for the scale dependence of the erosion coefficient α in (5). The methodology is based in part on the so-called dynamic modeling approach used in LES of turbulent flows [*Germano et al.*, 1991; *Moin et al.*, 1991; *Meneveau et al.*, 1996]. In the context of landscapes, we parameterize the effect of the subgrid-scale erosion rates by calculating a modified erosion coefficient α using information contained in the resolved elevation field and assuming scaling in the elevation statistics.

[26] For the purpose of developing the technique, one needs to know the exact value of the erosion coefficient at some reference scale. For simplicity, without loss of generality, here we consider the highest resolution simulated (256 × 256) as the exact solution, and the value of the erosion coefficient at this scale is assumed to be exactly known. However, the same approach can be extended to other reference scales for which erosion coefficients could be determined. The grid size corresponding to resolution 256 × 256 is taken as $\Delta/2$.
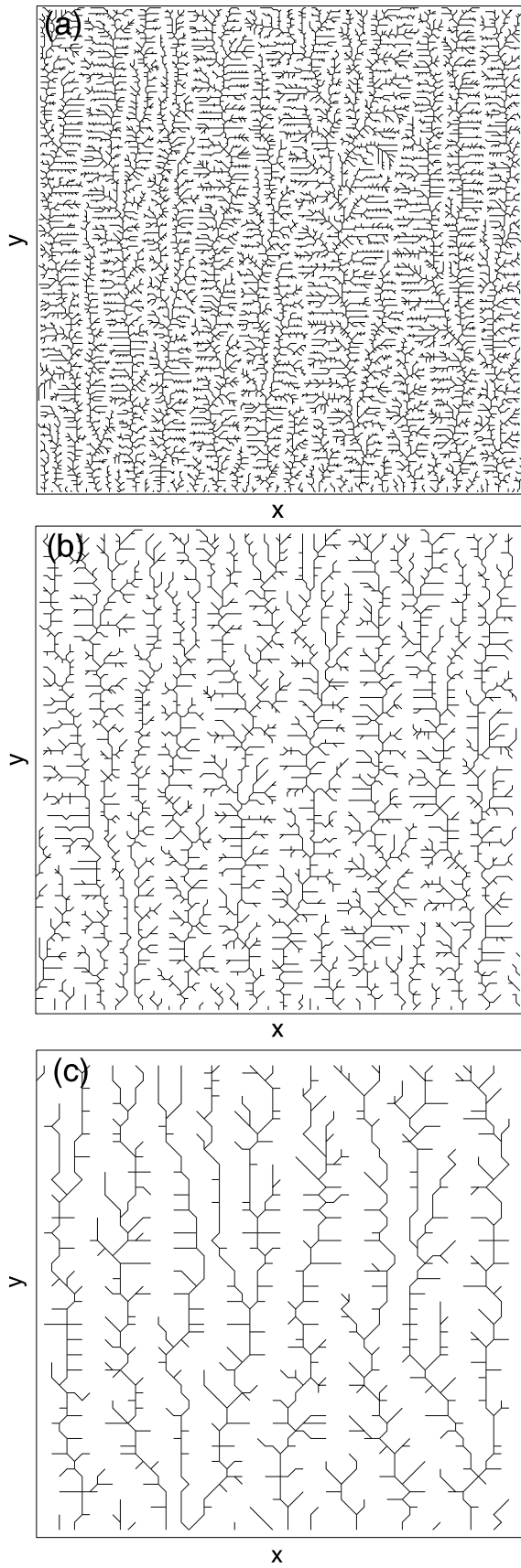
Figure 4. River network extracted from elevation fields for three grid resolutions at steady state. Only channels of Strahler order greater than 2 are shown: (a) 256 × 256, (b) 128 × 128, and (c) 64 × 64.

[27] At coarser resolutions the model is now written in a filtered form, as it is done in LES. At resolution 128x128 (resolution Δ), (5) becomes

$$\frac{\partial \tilde{h}}{\partial t} = u - \alpha_\Delta \cdot \tilde{q} \cdot \left| \nabla \tilde{h} \right|^2,\qquad(6)$$

where the tilde indicates quantities spatially filtered (with an implicit filter imposed by the grid size) at scale Δ. At resolution 64 × 64 (resolution 2Δ) equation (5) becomes

$$\frac{\partial \bar{\bar{h}}}{\partial t} = u - \alpha_{2\Delta} \cdot \bar{\bar{q}} \cdot \left| \nabla \bar{\bar{h}} \right|^2,\qquad(7)$$

where the overbar denotes spatial filtering at scale 2Δ.

[28] Modeling erosion without explicitly accounting for scale effects on the erosion coefficient, as we did in the previous section, implicitly amounts to assuming that

$$\alpha_{2\Delta} = \alpha_\Delta = \alpha_{\Delta/2} = \alpha_0,\qquad(8)$$

where α_0 is the erosion coefficient, which we assume is known and independent on resolution. The simulation results from section 2 indicate instead that α depends on the scale Δ. Our goal, then, is to account for this, dynamically computing α at each time step as the simulation progresses. To do that, one has to make some assumptions about the dependence of α on Δ. As a first approximation, we assume that the ratio between the erosion coefficients at scales Δ and $\Delta/2$ is the same as the ratio between scales 2Δ and Δ, i.e., we assume a constant value for the scale dependence ratio β, defined as

$$\beta = \frac{\alpha_\Delta}{\alpha_{\Delta/2}} \approx \frac{\alpha_{2\Delta}}{\alpha_\Delta} \approx \frac{\alpha_{4\Delta}}{\alpha_{2\Delta}}.\qquad(9)$$

Note that this is a much weaker assumption than the original one that the erosion coefficient α does not depend on scale. The erosion coefficients at scales Δ (resolution
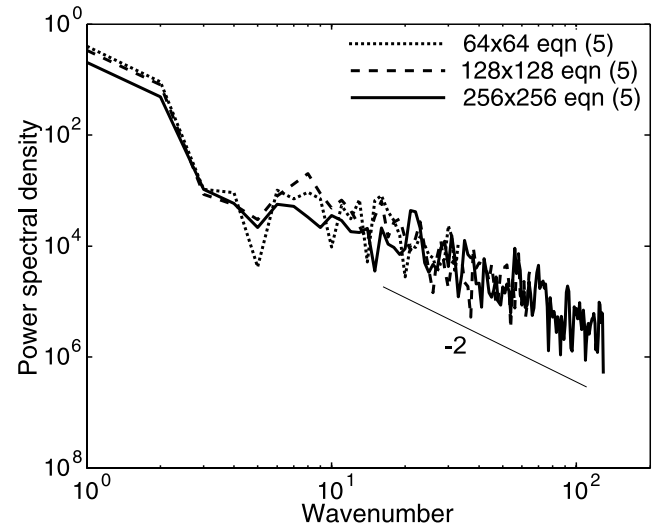
Figure 5. Elevation power spectra at the three resolutions averaged during the simulations. The spectral slope is not affected by the grid resolution and is near −2, consistent with observed spectra from natural topography.
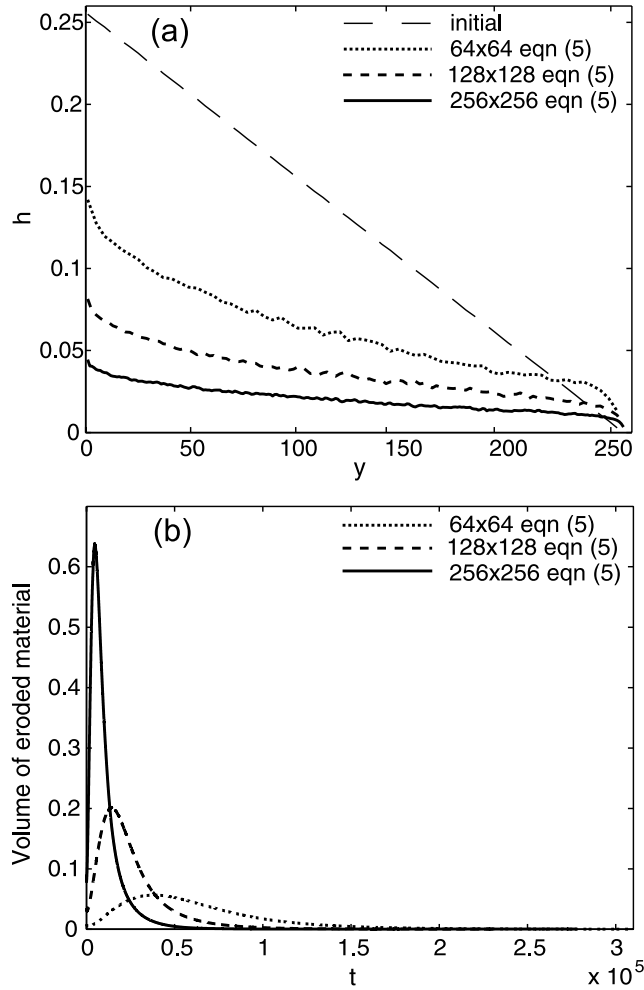
Figure 6. Dependence on grid resolution of model results using equation (5). (a) Mean longitudinal profiles obtained at steady state. (b) Volumes of eroded material per time step during the simulations. Both steady state profile and eroded volumes show strong scale dependence.

128×128) and 2Δ (resolution 64×64) can be expressed as a function of the erosion coefficient at the finest scale ($\Delta/2$) as follows:

$$\alpha_\Delta = \beta \cdot \alpha_{\Delta/2}$$
$$\alpha_{2\Delta} = \beta \cdot \alpha_\Delta = \beta^2 \cdot \alpha_{\Delta/2} \qquad (10)$$

Note that we assume the coefficient at the smallest scale equal to the known value, i.e., $\alpha_{\Delta/2} = \alpha_0$.

[29] On the basis of the expression for the scale dependence coefficient given by (9), β must be computed at scale Δ based only on information at the available scale Δ and larger, since during the simulation the behavior at finer scales is not known. Thus in our case, to compute β dynamically, we use information at scales Δ and 2Δ, together with the assumption that β is constant. The variables corresponding to scale 2Δ can easily be computed by spatially filtering the simulated field (implicitly filtered at scale Δ) using a two-dimensional filter of size 2Δ. As mentioned above, that operation is denoted by an overbar.

[30] On the basis of these ideas, we derive the new model with subgrid-scale parameterization in detail for simulations at resolution Δ. Applying the model at scales Δ and 2Δ leads to (6) and (7), given above. Spatially filtering (6) using a filter of size 2Δ (operation denoted by an overbar) and then averaging equations (6) and (7) over the entire field (operation denoted by $\langle \ \rangle$) yields

$$\left\langle \frac{\partial \bar{\bar{h}}}{\partial t} \right\rangle = \left\langle u - \alpha_\Delta \cdot \overline{\tilde{q} \cdot \left|\nabla \tilde{h}\right|^2} \right\rangle \qquad (11)$$

$$\left\langle \frac{\partial \bar{\bar{h}}}{\partial t} \right\rangle = \left\langle u - \alpha_{2\Delta} \cdot \bar{\tilde{q}} \cdot \left|\nabla \bar{\tilde{h}}\right|^2 \right\rangle \qquad (12)$$

[31] Combining (11) and (12) leads to an expression for the ratio between the effective erosion coefficients at scales 2Δ and Δ:

$$\frac{\alpha_{2\Delta}}{\alpha_\Delta} = \frac{\overline{\left\langle \tilde{q} \cdot \left|\nabla \tilde{h}\right|^2 \right\rangle}}{\left\langle \bar{\tilde{q}} \cdot \left|\nabla \bar{\tilde{h}}\right|^2 \right\rangle} \qquad (13)$$

The right hand side of (13) can be explicitly calculated using information contained in the simulated elevation field.

[32] Taking advantage of the scale similarity assumption in (9), (13) can be used to define the scale dependence coefficient β:

$$\beta = \frac{\alpha_\Delta}{\alpha_{\Delta/2}} \approx \frac{\alpha_{2\Delta}}{\alpha_\Delta} = \frac{\overline{\left\langle \tilde{q} \cdot \left|\nabla \tilde{h}\right|^2 \right\rangle}}{\left\langle \bar{\tilde{q}} \cdot \left|\nabla \bar{\tilde{h}}\right|^2 \right\rangle} \qquad (14)$$

Following the above procedure and using (14), we compute β dynamically at every time step, thus not requiring any a priori calibration or tuning. It is important to point out that the averaging operation ($\langle \ \rangle$) is needed to avoid unrealistic local fluctuations of β that would be obtained without averaging.

[33] The same approach can be followed to compute the coefficient β to be used in the simulations at other resolutions. For example, in the case of a grid of size 2Δ, the information at scale 4Δ would be used, and the expression for the scale dependence coefficient β would become

$$\beta = \frac{\alpha_{2\Delta}}{\alpha_\Delta} \approx \frac{\alpha_{4\Delta}}{\alpha_{2\Delta}} = \frac{\widehat{\left\langle \bar{q} \cdot \left|\nabla \bar{h}\right|^2 \right\rangle}}{\left\langle \hat{\bar{q}} \cdot \left|\nabla \hat{\bar{h}}\right|^2 \right\rangle}, \qquad (15)$$

where the hat denotes a filtering operation using a two-dimensional filter of size 4Δ over the simulated variables, obtained at a grid resolution of 2Δ. Just as for scale Δ, β is computed dynamically at every time step following (15), and again does not require calibration or tuning.

[34] The new value of β is used to define the erosion coefficient $\alpha\Delta$ at the corresponding grid scale Δ in terms of
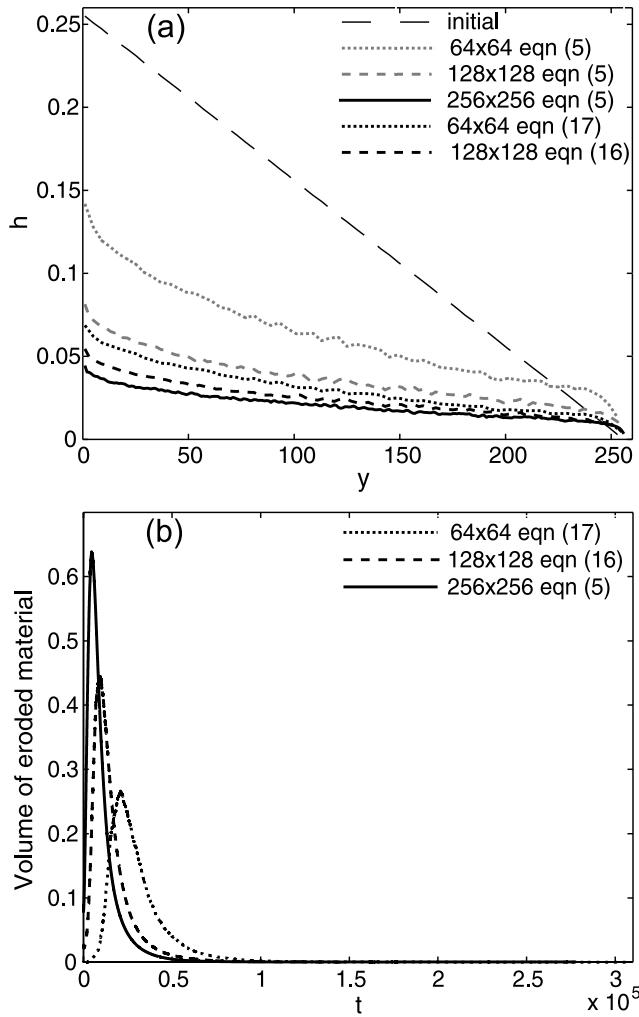
Figure 7. Comparison of results from the original model (equation (5)) and the dynamic subgrid model (equations (16) and (17)). (a) Mean longitudinal profiles obtained at steady state. The results obtained with the subgrid-scale parameterization show a relatively weak dependence on grid resolution. (b) Volumes of eroded material per time step obtained at steady state. The results obtained with the subgrid-scale parameterization again show a relatively weak dependence on grid resolution.

the erosion coefficient at scale $\Delta/2$, which we assume is exactly known, according to (10). Thus the model at scale Δ is now given by

$$\frac{\partial \tilde{h}}{\partial t} = u - \beta \cdot \alpha_{\Delta/2} \cdot \tilde{q} \cdot \left| \nabla \tilde{h} \right|^2 \qquad (16)$$

Furthermore, the model at scale 2Δ can be written as

$$\frac{\partial \bar{\tilde{h}}}{\partial t} = u - \beta^2 \cdot \alpha_{\Delta/2} \cdot \bar{\tilde{q}} \cdot \left| \nabla \bar{\tilde{h}} \right|^2 \qquad (17)$$

[35] To test the efficacy of the proposed dynamic subgrid-scale scheme, we redo the simulations at the three resolutions, using (5) at resolution 256×256, (16) at resolution 128×128 and (17) at resolution 64×64. Initial and boundary conditions are the same as used in the previous section. At every time step, the slope and the water flux are

computed at each location from the simulated field. Then the field is filtered at a resolution double the grid size and slope and water flux are computed from the filtered field at each location. With these quantities the scale dependence coefficient β is computed from equation (14) (or (15) at 64×64) and the field is then updated using equation (16) (or (17) at 64×64).

3.2. Results and Discussion

[36] The elevation fields and the extracted river networks are qualitatively similar to the ones obtained in the previous section using equation (5) at all resolutions. However, the erosion rate is clearly affected by the new formulation of the model at the lower resolutions. The mean longitudinal profiles obtained at steady state for the simulations with dynamic subgrid-scale modeling are shown in Figure 7a. The profiles at resolution 128×128 and 64×64 obtained with the new model are close to the profile at 256×256, indicating that the dynamic subgrid-scale method accounts for most of the scale dependence. The same behavior is found in the volume of eroded material per time step, shown in Figure 7b: the new model with dynamic subgrid-scale parameterization yields much more consistent erosion rates across the different grid resolutions than the simulations using a constant erosion coefficient.

[37] We stress that in this first stage of our investigation, we have used the simplest plausible scheme for dynamic subgrid-scale modeling. Despite this, the method seems able to eliminate much of the dependence of erosional landscape dynamics on grid resolution. The dynamic procedure is now modified to allow for scale dependence of the coefficient β. A similar dynamic, tuning-free approach has recently been developed in the context of subgrid-scale models for LES of turbulent flows [*Porté-Agel et al.*, 2000; *Porté-Agel*, 2004; *Stoll and Porté-Agel*, 2006.].

4. A Scale-Dependent Dynamic Subgrid-Scale Model

4.1. Derivation of the Scale-Dependent Dynamic Subgrid-Scale Model

[38] The dynamic procedure is now modified to allow for scale dependence of the coefficient β. This requires the use of an additional test filtering operation (e.g., at scale four times the grid scale), from which the scale dependence of β can be determined dynamically. The scale dependence coefficient β is now allowed to change with scale, and therefore

$$\beta_\Delta \neq \beta_{2\Delta} \neq \beta_{4\Delta}. \qquad (18)$$

[39] At this point, an assumption has to be made about the functional form of the scale dependence of β. Assuming a simple power law dependence of β with scale [*Porté-Agel et al.*, 2000], we can write

$$\frac{\beta_\Delta}{\beta_{2\Delta}} \approx \frac{\beta_{2\Delta}}{\beta_{4\Delta}} \approx \frac{\beta_{4\Delta}}{\beta_{8\Delta}}. \qquad (19)$$

Note that this is a much weaker assumption than the previous one of β constant across scales. Using equation (19), the
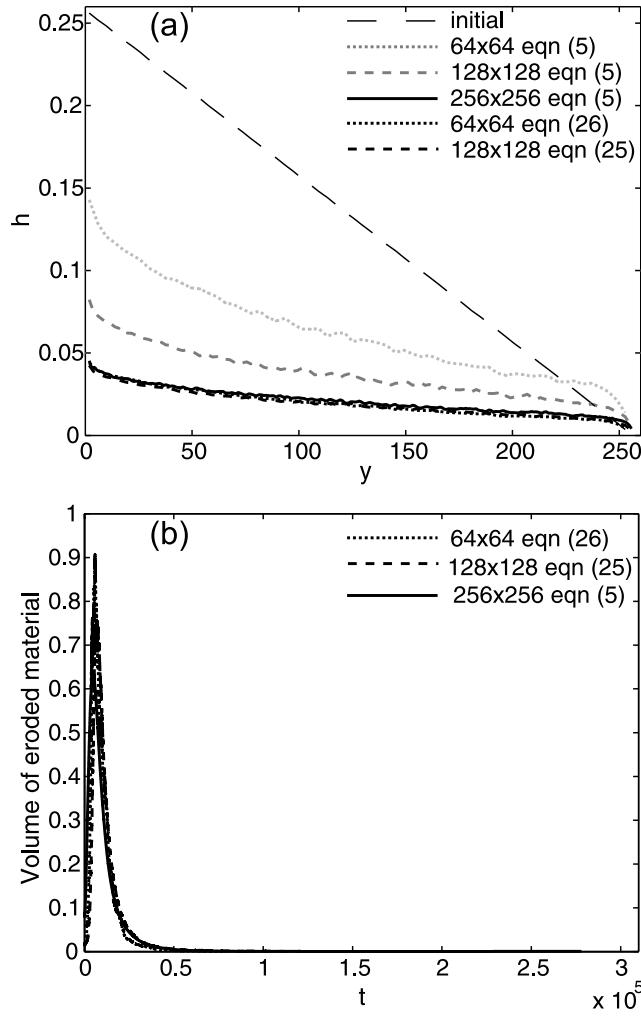
Figure 8. Comparison of the results from the original model (equation (5)) and the new scale-dependent dynamic subgrid model (equations (25) and (26)). (a) Mean longitudinal profiles obtained at steady state. The profiles obtained with the subgrid-scale parameterization are almost indistinguishable. (b) Volumes of eroded material per time step obtained at steady state. The results obtained with the subgrid-scale parameterization again show very little dependence on grid resolution and time.

scale dependence coefficient at scale Δ, β_Δ, can be expressed as

$$\beta_\Delta \approx \beta_{2\Delta} \cdot \frac{\beta_{2\Delta}}{\beta_{4\Delta}} = \frac{\beta_{2\Delta}^2}{\beta_{4\Delta}}, \tag{20}$$

where $\beta_{2\Delta}$ and $\beta_{4\Delta}$, recalling (14) and (15), can be computed dynamically from the resolved elevation field as

$$\beta_{2\Delta} = \frac{\alpha_{2\Delta}}{\alpha_\Delta} = \frac{\left\langle \widetilde{\tilde{q} \cdot \left| \nabla \tilde{h} \right|^2} \right\rangle}{\left\langle \bar{\tilde{q}} \cdot \left| \nabla \bar{\tilde{h}} \right|^2 \right\rangle}$$

$$\tag{21}$$

$$\beta_{4\Delta} = \frac{\alpha_{4\Delta}}{\alpha_{2\Delta}} = \frac{\left\langle \widehat{\bar{q} \cdot \left| \nabla \bar{h} \right|^2} \right\rangle}{\left\langle \hat{\bar{q}} \cdot \left| \nabla \hat{\bar{h}} \right|^2 \right\rangle},$$

The same procedure can be applied at scale 2Δ to express the unknown parameters β_Δ and $\beta_{2\Delta}$ as a function of $\beta_{4\Delta}$ and $\beta_{8\Delta}$ as

$$\beta_{2\Delta} \approx \beta_{4\Delta} \cdot \frac{\beta_{4\Delta}}{\beta_{8\Delta}},$$

$$\beta_\Delta \approx \beta_{2\Delta} \cdot \frac{\beta_{2\Delta}}{\beta_{4\Delta}} = \left(\beta_{4\Delta} \cdot \frac{\beta_{4\Delta}}{\beta_{8\Delta}} \right)^2 \cdot \frac{1}{\beta_{4\Delta}} = \frac{\beta_{4\Delta}^3}{\beta_{8\Delta}^2}, \text{ and} \tag{22}$$

$$\beta_{2\Delta} \cdot \beta_\Delta \approx \frac{\beta_{4\Delta}^5}{\beta_{8\Delta}^3}$$

Note that $\beta_{4\Delta}$ can be obtained from the resolved elevation field using equation (21), and $\beta_{8\Delta}$ can also be computed dynamically using the identity

$$\beta_{8\Delta} = \frac{\alpha_{8\Delta}}{\alpha_{4\Delta}} = \frac{\left\langle \widehat{\hat{q} \cdot \left| \nabla \hat{h} \right|^2} \right\rangle}{\left\langle \hat{\hat{q}} \cdot \left| \nabla \hat{\hat{h}} \right|^2 \right\rangle}, \tag{23}$$

where the curved overbar denotes a filtering operation using a two-dimensional filter of size 8Δ over the simulated variables, obtained at a grid resolution of 2Δ.

[40] With the new definitions of β_Δ and $\beta_{2\Delta}$, α_Δ and $\alpha_{2\Delta}$ become

$$\alpha_\Delta = \beta_\Delta \cdot \alpha_{\Delta/2} = \frac{\beta_{2\Delta}^2}{\beta_{4\Delta}} \cdot \alpha_{\Delta/2}$$

$$\tag{24}$$

$$\alpha_{2\Delta} = \beta_{2\Delta} \cdot \beta_\Delta \cdot \alpha_{\Delta/2} = \frac{\beta_{4\Delta}^5}{\beta_{8\Delta}^3} \cdot \alpha_{\Delta/2}$$

and equations (16) and (17) become

$$\frac{\partial \tilde{h}}{\partial t} = u - \frac{\beta_{2\Delta}^2}{\beta_{4\Delta}} \cdot \alpha_{\Delta/2} \cdot \tilde{q} \cdot \left| \nabla \tilde{h} \right|^2 \tag{25}$$

$$\frac{\partial \bar{\tilde{h}}}{\partial t} = u - \frac{\beta_{4\Delta}^5}{\beta_{8\Delta}^3} \cdot \alpha_{\Delta/2} \cdot \bar{\tilde{q}} \cdot \left| \nabla \bar{\tilde{h}} \right|^2 \tag{26}$$

To test the proposed scale-dependent dynamic subgrid-scale scheme, we perform the same simulations using equation (5) at resolution 256×256, and equations (25) and (26) at resolutions 128×128 and 64×64, respectively.

[41] Initial and boundary conditions are the same used in the previous sections. At every time step, the slope and the water flux are computed at each location from the simulated field. Then the field is filtered at a resolution two and four times the grid size and slope and water flux are computed from the filtered field at each location. The scale dependence coefficients β corresponding to scales twice and four times the grid scale are computed dynamically using equations (21) for the 128×128 resolution, or equations (21) and (23) for the 64×64 resolution. These values are then used in equations (25) and (26) to obtain the time evolution of the simulated elevation field. The simulations are run until steady state is reached.

4.2. Results and Discussion

[42] Similar to the case of the dynamic model presented in Section 3, the elevation fields and river networks obtained with the scale-dependent dynamic model are

quantitatively similar to the ones obtained without subgrid-scale model. However, the mean longitudinal profile obtained at steady state and the volume of eroded material per time step show an additional improvement compared to the scale-invariant dynamic model. As shown in Figures 8a and 8b, the simulation results obtained with the three resolutions are very similar, which highlights the ability of the new model to systematically (and without parameter tuning) account for the scale dependence of the erosion coefficient. Moreover, the previously observed time dependence of the results is substantially reduced (Figure 8b), indicating that the new model is also able to minimize the effects of resolution on the time evolution of the simulated landscapes.

[43] Note that there are a number of ways in which the scale-dependent dynamic approach could be improved. For example, the coefficient β could be computed locally using alternative averaging methods, such as the Lagrangian dynamic procedure introduced by *Meneveau et al.* [1996]. High-resolution digital elevation data could also be used to test some of the assumptions made in the dynamic models (e.g., power law scaling of the coefficients) and provide guidance for further improvements, as done in a priori experimental studies of turbulent flows [e.g., *Meneveau and Katz*, 2000].

5. Conclusions

[44] 1. Landscapes simulated using a modified 2-D KPZ equation show a systematic dependence on grid resolution: increasing resolution allows for increased channel density, and thus erosion rates and mean longitudinal profiles of elevation at steady state have an undesirable dependence on grid resolution.

[45] 2. A new subgrid-scale parameterization, inspired by the scale-dependent dynamic modeling approach used in turbulence simulations, is able to correct most of this scale dependence. The erosion coefficient, assumed exactly known at the finest resolution, is multiplied by a scale dependence coefficient, which is computed dynamically as a function of time based on the landscape dynamics at the resolved scales. The scheme takes advantage of the self-similarity that characterizes landscapes over a wide range of scales and produces landscapes that show very little dependence on grid resolution.

[46] There is no reason the proposed approach could not be applied to other landscape evolution models. The applicability of the LES-inspired approach to modeling erosional landscapes suggests that the technique may be generalizable to other systems as well. The basic requirement is that the system be self-similar over a sufficiently wide range of length scales to justify the estimation of the effect of subgrid processes by comparison of the model behavior over scales coarser than the resolved scale. Possible candidates in morphodynamics include braided rivers [*Sapozhnikov and Foufoula-Georgiou*, 1996, 1997], distributary channel networks, and bed forms.

References

Adams, J. (1980), Contemporary uplift and erosion of Southern Alps, New Zealand: Summary, *Geol. Soc. Am. Bull.*, *91*, 2–4.

Banavar, J., F. Colaiori, A. Flammini, A. Maritan, and S. Rinaldo (2001), Scaling, optimality and landscape evolution, *J. Stat. Phys.*, *104*, 1–49.

Bear, I. (1988), *Dynamics of Fluids in Porous Media*, 784 pp., Dover, Mineola, N. Y.

Bou-Zeid, E., C. Meneveau, and M. B. Parlange (2004), Large-eddy simulation of neutral atmospheric boundary layer flow over heterogeneous surfaces: Blending height and effective surface roughness, *Water Resour. Res.*, *40*, W02505, doi:10.1029/2003WR002475.

Chase, C. G. (1992), Fluvial landsculpting and the fractal dimension of topography, *Geomorphology*, *5*, 39–57.

Culling, W. E. H. (1960), Analytical theory of erosion, *J. Geol.*, *68*, 336–344.

Culling, W. E. H. (1963), Soil creep and the development of hillside slopes, *J. Geol.*, *71*, 127–161.

Dietrich, W. E., D. Bellugi, A. M. Heimsath, J. J. Roering, L. Sklar, and J. D. Stock (2003), Geomorphic transport laws for predicting landscape form and dynamics, in *Prediction in Geomorphology*, Geophys. Monogr. Ser., vol. 136 edited by P. Wilcock and R. Iverson, pp. 103-132, AGU, Washington, D. C.

Germano, M., U. Piomelli, P. Moin, and W. H. Cabot (1991), A dynamic subgrid-scale eddy viscosity model, *Phys. Fluids*, *3*, 1760–1765.

Geurts, B. J. (2004), *Elements of Direct and Large Eddy Simulations*, 388 pp., R. T. Edwards, Flourtown, Pa.

Hack, J. T. (1960), Interpretation of erosional topography in humid temperate regions, *Am. J. Sci.*, *258A*, 80–97.

Harris, D., and E. Foufoula-Georgiou (2001), Subgrid variability and stochastic downscaling of modeled clouds: Effects on radiative transfer computations for rainfall retrieval, *J. Geophys. Res.*, *106*, 10,349–10,362.

Hasbargen, L. E., and C. Paola (2000), Landscape instability in an experimental drainage basin, *Geology*, *28*, 1067–1070.

Hasbargen, L., and C. Paola (2003), How predictable is local erosion rate in erosional landscapes?, in *Prediction in Geomorphology*, Geophys. Monogr. Ser., vol. *136* edited by P. R. Wilcock and R. M. Iverson, pp. 231–240, AGU, Washington, D. C.

Howard, A. D. (1994), A detachment-limited model of drainage basin evolution, *Water Resour. Res.*, *30*, 2261–2285.

Inaoka, H., and H. Takayasu (1993), Water erosion as a fractal growth process, *Phys. Rev. E*, *47*, 899–910.

Kagan, Y. Y. (1992), Seismicity: The turbulence of solids, *Nonlinear Sci. Today*, *2*, 123–134.

Kardar, M., G. Parisi, and Y.-C. Zhang (1986), Dynamic scaling of growing interfaces, *Phys. Rev. Lett.*, *56*, 889–892.

Kolmogorov, A. (1961), Dissipation of energy in the locally isotropic turbulence, in *Turbulence: Classic Papers on Statistical Theory*, edited by S. K. Friedlander and L. Topper, pp. 151–155, Wiley-Interscience, Hoboken, N. J.

Kooi, H., and C. Beaumont (1994), Escarpment evolution on high-elevation rifted margins: Insights derived from a surface-processes model that combines diffusion, advection, and reaction, *J. Geophys. Res.*, *99*, 12,191–12,209.

Koons, P. O. (1995), Modelling the topographic evolution of collisional mountain belts, *Annu. Rev. Earth Planet. Sci.*, *23*, 375–408.

Mandelbrot, B. (1975), Stochastic models for the Earth's relief, the shape and the fractal dimension of coastlines, and the number-area rule for islands, *Proc. Natl. Acad. Sci. U.S.A.*, *72*, 3825–3828.

Meneveau, C., and J. Katz (2000), Scale invariance and turbulence models for large-eddy simulation, *Annu. Rev. Fluid Mech.*, *32*, 1–32.

Meneveau, C., T. S. Lund, and W. H. Cabot (1996), A Lagrangian dynamic subgrid-scale model of turbulence, *J. Fluid Mech.*, *319*, 353–385.

Moin, P., K. D. Squires, and S. Lee (1991), A dynamic subgrid-scale model for compressible turbulence and scalar transport, *Phys. Fluids*, *3*, 2746–2757.

Newman, W. I., and D. L. Turcotte (1990), Cascade model for fluvial geomorphology, *Geophys. J. Int.*, *100*, 433–439.

Paola, C. (1996), Incoherent structure: Turbulence as a metaphor for stream braiding, in *Coherent Flow Structures in Open Channels*, edited by P. J. Ashworth et al., pp. 705–723, John Wiley, Hoboken, N. J.

Paola, C., G. Parker, D. C. Mohrig, and K. X. Whipple (1999), The influence of transport fluctuations on spatially averaged topography on a sandy, braided fluvial fan, in *Numerical Experiments in Stratigraphy: Recent Advances in Stratigraphic and Sedimentologic Computer Simulations*, edited by J. Harbaugh et al., *Spec. Publ. SEPM Soc. Sediment. Geol.*, *62*, 211–218.

Peckham, S. D. (1995), Self-similarity in the three-dimensional geometry and dynamics of large river basins, Ph.D. thesis, Univ. of Colo., Boulder.

Peckham, S. D. (2003), Fluvial landscape models and catchment-scale sediment transport, *Global Planet. Change*, *39*, 31–51.

Pelletier, J. D. (2004), Persistent drainage migration in a numerical land-form evolution model, *Geophys. Res. Lett.*, 31, L20501, doi:10.1029/2004GL020802.

Pope, S. B. (2000), *Turbulent Flows*, 771 pp., Cambridge Univ. Press, New York.

Pope, S. B. (2004), Ten questions concerning the large-eddy simulation of turbulent flows, *New J. Phys.*, 6, 35.

Porté-Agel, F. (2004), A scale-dependent dynamic model for scalar transport in the atmospheric boundary layer, *Boundary Layer Meteorol.*, 112, 81–105.

Porté-Agel, F., C. Meneveau, and M. B. Parlange (2000), A scale-dependent dynamic model for large-eddy simulation: Application to a neutral atmospheric boundary layer, *J. Fluid Mech.*, 415, 261–284.

Rinaldo, A., I. Rodriguez-Iturbe, R. Rigon, R. L. Bras, E. Ijjasz-Vasquez, and A. Marani (1992), Minimum energy and fractal structures of drainage networks, *Water Resour. Res.*, 28, 2183–2195.

Rodriguez-Iturbe, I., and A. Rinaldo (1997), *Fractal River Basins*, 539 pp., Cambridge Univ. Press, New York.

Rodriguez-Iturbe, I., M. Marani, R. Rigon, and A. Rinaldo (1994), Self-organized river basin landscapes: Fractal and multifractal characteristics, *Water Resour. Res.*, 30, 3531–3539.

Sagaut, P. (2002), *Large Eddy Simulation for Incompressible Flows: An Introduction*, 426 pp., Springer, New York.

Sapozhnikov, V. B., and E. Foufoula-Georgiou (1996), Self-affinity in braided rivers, *Water Resour. Res.*, 32, 1429–1439.

Sapozhnikov, V. B., and E. Foufoula-Georgiou (1997), Experimental evidence of dynamic scaling and indications of self-organized criticality in braided rivers, *Water Resour. Res.*, 33, 1983–1991.

Sayles, R. S., and T. R. Thomas (1978), Surface topography as a non-stationary random process, *Nature*, 271, 431–434.

Sinclair, K., and R. C. Ball (1996), Mechanism for global optimization of river networks from local erosion rules, *Phys. Rev. Lett.*, 76, 3360–3363.

Smith, T. R., G. E. Merchant, and B. Birnir (1997a), Towards an elementary theory of drainage basin evolution: I. The theoretical basis, *Comput. Geosci.*, 23(8), 811–822.

Smith, T. R., G. E. Merchant, and B. Birnir (1997b), Towards an elementary theory of drainage basin evolution: II. A computational evaluation, *Comput. Geosci.*, 23(8), 823–849.

Somfai, E., and L. M. Sander (1997), Scaling and river networks—A Landau theory for erosion, *Phys. Rev. E*, 56, R5–R8.

Sornette, D., and Y.-C. Zhang (1993), Non linear Langevin model of geomorphic erosion processes, *Geophys. J. Int.*, 113, 382–386.

Stark, C. P., and G. J. Stark (2001), A channelization model of landscape evolution, *Am. J. Sci.*, 301, 486–512.

Stoll, R., and F. Porté-Agel (2006), Dynamic subgrid-scale models for momentum and scalar fluxes in large-eddy simulations of atmospheric boundary layers over heterogeneous terrain, *Water Resour. Res.*, 42, W01409, doi:10.1029/2005WR003989.

Tucker, G. E., and R. L. Slingerland (1994), Erosional dynamics, flexural isostasy, and long-lived escarpments: A numerical modeling study, *J. Geophys. Res.*, 99, 12,229–12,243.

Tucker, G. E., S. T. Lancaster, N. M. Gasparini, and R. L. Bras (2001), The channel-hillslope integrated landscape development (CHILD) model, in *Landscape Erosion and Evolution Modeling*, edited by R. S. Harmon and W. W. Doe III, pp. 349–388, Springer, New York.

Vening Meinesz, F. A. (1951), A remarkable feature of the Earth's topography, *Proc. K. Ned. Akad. Wet. Ser. B. Palaeontol. Geol Phys. Chem. Anthropol.*, 54, 212–228.

Willett, S. D., and M. T. Brandon (2002), On steady states in mountain belts, *Geology*, 30, 175–178.

Willgoose, G. (2005), Mathematical modeling of whole landscape evolution, *Annu. Rev. Earth Planet. Sci.*, 33, 443–459.

Willgoose, G., R. L. Bras, and I. Rodriguez-Iturbe (1991a), A coupled channel network growth and hillslope evolution model: 2. Nondimensionalization and applications, *Water Resour. Res.*, 27, 1685–1696.

Willgoose, G., R. L. Bras, and I. Rodriguez-Iturbe (1991b), A coupled channel network growth and hillslope evolution model: 1. Theory, *Water Resour. Res.*, 27, 1671–1684.

————————————

E. Foufoula-Georgiou, C. Paola, F. Porté-Agel, and P. Passalacqua, St. Anthony Falls Laboratory, 2 Third Avenue SE, Minneapolis, MN 55414, USA. (cpaola@umn.edu)

Do gravel bed river size distributions record channel network structure?

Leonard S. Sklar,[1] William E. Dietrich,[2] Efi Foufoula-Georgiou,[3] Bruno Lashermes,[3] and Dino Bellugi[2]

[1] Bed load sediment particles supplied to channels by hillslopes are reduced in size by abrasion during downstream transport. The branching structure of the channel network creates a distribution of downstream travel distances to a given reach of river and thus may strongly influence the grain size distribution of the long-term bed load flux through that reach. Here we investigate this hypothesis, using mass conservation and the Sternberg exponential decay equation for particle abrasion, to predict bed material variability at multiple scales for both natural and artificial drainage networks. We assume that over a sufficiently long timescale, no net deposition occurs and that grains less than 2 mm are swept away in suspension. We find that abrasion during fluvial transport has a surprisingly small effect on the bed load sediment grain size distribution, for the simple case of spatially uniform supply of poorly sorted hillslope sediments. This occurs because at any point in the channel network, local resupply offsets the size reduction of material transported from upstream. Thus river bed material may essentially mirror the coarse component of the size distribution of hillslope sediment supply. Furthermore, there is a predictable distance downstream at which the bed load grain size distribution reaches a steady state. In the absence of net deposition due to selective transport, large-scale variability in bed material, such as downstream fining, must then be due primarily to spatial gradients in hillslope sediment production and transport characteristics. A second key finding is that average bed load flux will tend to stabilize at a constant value, independent of upstream drainage area, once the rate of silt production by bed load abrasion per unit travel distance is equal to the rate of coarse sediment supply per unit channel length (q). Bed load flux equilibrates over a distance that scales with the inverse of the fining coefficient in the abrasion rate law (α) and can be approximated simply as $q/3\alpha$. Thus the efficiency of particle abrasion sets a fundamental length scale, shorter for weaker rocks and longer for harder rocks, which controls the expression in the river bed of variability in sediment supply. We explore the role of the abrasion length scale in modulating the influence of sediment supply variability in a number of channel network contexts, including individual tributary junctions, a sequence of tributary inputs along a main stem channel, and variable basin shapes and network architecture as expressed by the width function. These findings highlight the need for both data and theory that can be used to predict the grain size distributions supplied to channels by hillslopes.

1. Introduction

[2] The self-organized pattern of a river network creates a hierarchical structure of channel pathways down which runoff and the sediment waste from hillslopes travels. Much has been written about the fractal characteristics of river networks [e.g., *Rodriguez-Iturbe and Rinaldo*, 1997], of the incoming precipitation that drives landscape erosion and channel incision [e.g., *Venugopal et al.*, 2006], and of the resulting runoff characteristics that record the integral of precipitation and runoff paths [e.g., *Gupta et al.*, 1996; *Menabde and Sivapalan*, 2001; *Dodov and Foufoula-Georgiou*, 2005; *Troutman and Over*, 2001]. There are other possible scaling relationships associated with the introduction and passage of sediment down through the networks. Sediment entering rivers is typically very poorly sorted and arrives episodically both spatially and through

[1]Department of Geosciences, San Francisco State University, San Francisco, California, USA.
[2]Department of Earth and Planetary Science, University of California, Berkeley, California, USA.
[3]St. Anthony Falls Laboratory and Department of Civil Engineering, University of Minnesota–Twin Cities, Minneapolis, Minnesota, USA.

Noyo Basin, CA
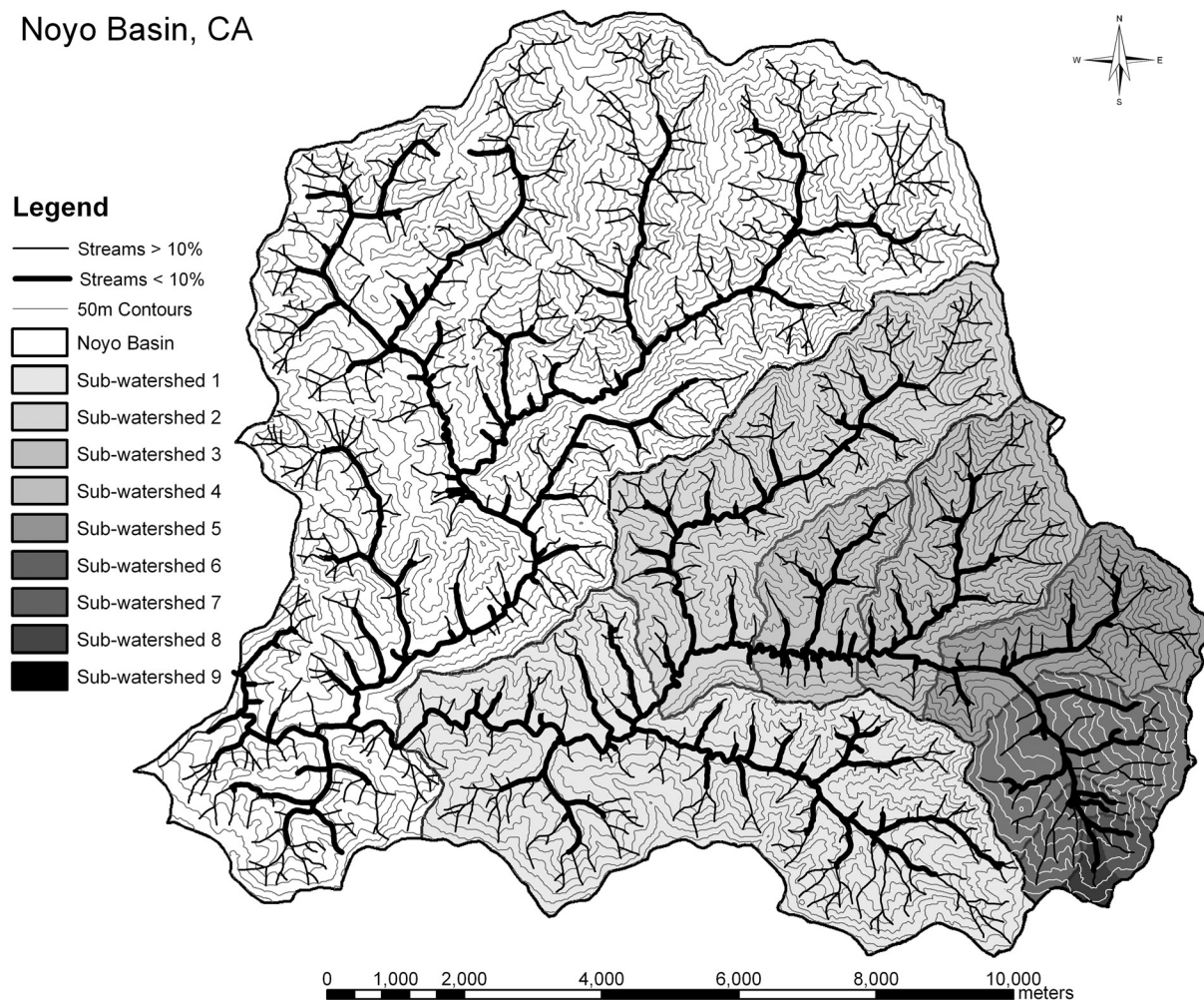
Figure 1. Map of the Upper Noyo River Basin, Mendocino County, northern California. Outlet located at 39°26′N, 123°45′W.

time along channels. These sediment pulses are swept by runoff events, sorted hydraulically, and their particles are broken and abraded during transport. Along any channel path, tributaries introduce local infusions of sediment that mix with channels from other sources [e.g., *Rice and Church*, 1998; *Jacobson and Gran*, 1999]. Might the channel network structure and the dynamic, unsorted additions of sediment lead to scale-invariant patterns of bed load sediment grain size and flux along the channel?

[3] If we look at this from the perspective of examining gravel at a specific location on the riverbed, other questions emerge. Each particle on a gravel bed of a river has a distinct travel history from its source. Some originate at the farthest portions of the contributing watershed, and others only a short distance from a point of observation. Most of the grains are not the size they were when they entered the stream. Commonly, particles e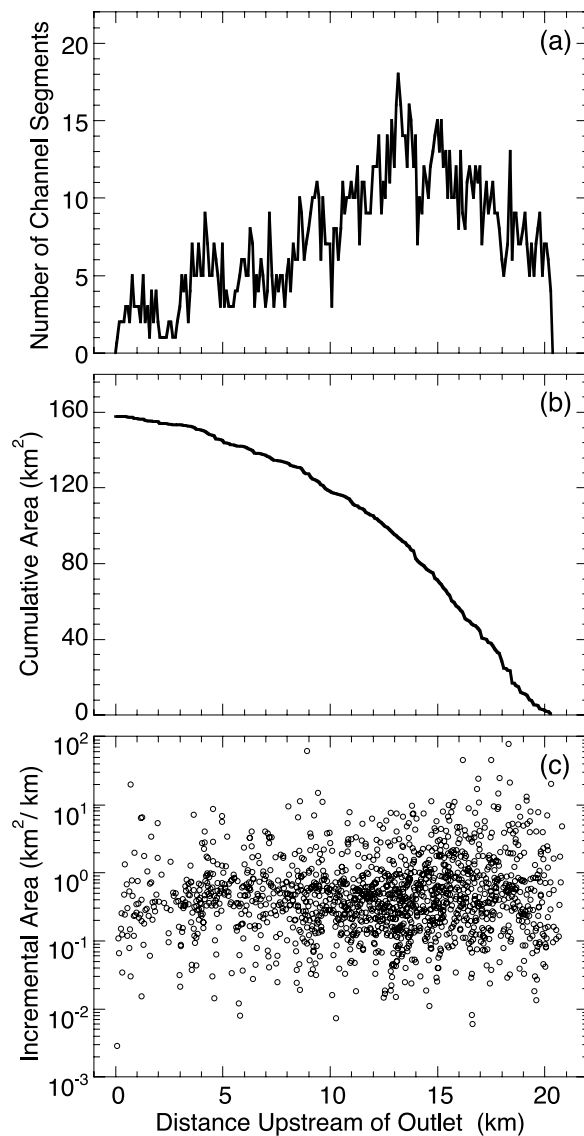ntering a stream are derived from the chemical, biotic and mechanical breakdown of bedrock, and this derivation not only imparts a size distribution to the incoming sediment, it also weakens the particles such that subsequent bed load transport downstream causes wear and fragmentation, sometimes quite rapidly. Even relatively unweathered bedrock fragments will be pounded and reduced in size. These downstream

fining particles follow the channel network and merge with particles arriving through different channel branches and other parts of the landscape. These branches may access steeper slopes shedding coarser sediment of the same bedrock, or cut into harder bedrock with more durable particles [e.g., *Pizzuto*, 1995]. Does this mingling of sediment with different transport paths and different bedrock sources create a distinct size distribution of bed sediment? Is there a signature of the channel network structure and its bedrock heterogeneity in the size distribution of the sediment?

[4] This seems a reasonable hypothesis in that the channel network structure imposes a travel distribution function to any point along the channel. For example, in Figure 1 the channel network of a catchment is shown, and the corresponding width function is plotted in Figure 2a. The width function gives the number of channel segments along the channel network at a specified distance from the mouth [e.g., *Rodriguez-Iturbe and Rinaldo*, 1997]. Along each interval of distance from the mouth, there is a contributing drainage area, which sets the scale for the amount of sediment entering the channel. For example, in Figures 2b and 2c, the cumulative drainage area and incremental area per unit length entering each channel segment are plotted as

Figure 2. Noyo River channel network characteristics: (a) Width function (distribution of channel segments at specified distance from downstream outlet), (b) cumulative area function, and (c) incremental drainage area per channel segment length.

sizes entering a channel network is or how that should vary throughout a watershed. Some have argued that fragmentation of bedrock should produce fractal scaling of particle numbers with grain size [e.g., *Turcotte*, 1997; *Perfect*, 1997] and there have been studies of the finer fraction of some soils that suggest multifractal scaling of grain sizes [e.g., *Bittelli et al.*, 1999]. Whether fractal or not, certainly soils, screes and glacial deposits have a wide range of particle sizes [e.g., *Matsuoka and Sakai*, 1999; *Posadas et al.*, 2001; *Hooke and Iverson*, 1995].

[6] A common observation is that the gravel clasts making up the beds of rivers are typically derived from the harder bedrock lithologies underlying the watershed, even when the harder rock types compose a relatively small proportion of the landscape [e.g., *Hack*, 1957; *Brush*, 1961; *Dietrich and Dunne*, 1978; *Parker*, 1991b; *Pizzuto*, 1995]. The network travel distribution function (the width function) operates, then, on materials with differing resistance to breakdown and differing starting grain size distributions which may occur systematically in parts of the basin, or scattered throughout. The network structure leads to injections of sediment into main stem reaches from tributaries of widely differing sizes (Figure 2c) that may deliver sediment of greatly differing durability. Under what conditions do these injections perturb the sediment mass and size distribution of the bed of the main stem [e.g., *Rice and Church*, 1998; *Rice*, 1998] and propagate downstream?

[7] Studies of changes in gravel bed size distributions along channels have focused on the tendency for downstream fining [e.g., *Knighton*, 1980, *Rice and Church*, 1998; *Heller et al.*, 2001; *Gomez et al.*, 2001; *Surian*, 2002; *Moussavi-Harami et al.*, 2004, *Malarz*, 2005]. Field measurements of median grain sizes of the bed surface are typically plotted as a function of distance along a longitudinal profile, and downstream decreases are attributed to either selective sorting or particle size reduction due to abrasion or some combination of these processes. In cases of net deposition along the channel, selective sorting has been shown to be an effective agent of downstream fining [e.g., *Paola et al.*, 1992; *Ferguson et al.*, 1996; *Gomez et al.*, 2001]. Where no net deposition occurs (in rivers actively cutting through bedrock for example) abrasion is held responsible for downstream fining [e.g., *Kodama*, 1994a]. Abrasion of particles appears to follow Sternberg's law

$$D = D_0 e^{-\alpha x} \qquad (1)$$

where the initial grain size D_0 wears down to D at distance x from the origin at a rate given by α (1/m) (see reviews by *Parker* [1991a], *Kodama* [1994a, 1994b], *Gomez et al.* [2001], *Lewin and Brewer* [2002], and *Malarz* [2005]). Particles are presumed to wear by shedding silt and clay size mass, rather than by splitting, although splitting could be important in some rock types [*Kodama*, 1994b]. Tumbling experiments support the form of equation (1) and α has been experimentally estimated [e.g., *Kuenen*, 1956; *Adams*, 1978; *Kodama*, 1994b; *Lewin and Brewer*, 2002]. Translation of tumbling experiments to the field setting can be controversial because of the large differences in particle collision dynamics and the absence of weathering in tumbling mills. Alternatively, plots of median or maximum

a function of distance from the mouth. The sum over all upstream distances of the product of the local erosion rate times the local contributing area and the total number of points at that distance from the mouth (i.e., the width function, Figure 2a), gives the total influx of sediment to the channel at the specified distance. If particle breakdown depends on travel distance, then one would expect bigger particles to be derived locally, and finer particles from farther away, and depending on how tributaries come in, the grain size distribution may be tipped toward the coarse or fine fraction.

[5] Watersheds rarely drain homogeneous bedrock, and probably rarely receive grain size distributions that are identical throughout the basin even if the bedrock is relatively uniform. At present, there are essentially no data or theory to tell us what the distribution function of grain

grain size against distance downstream have been used to parameterize α and D_0 [e.g., *Moussavi-Harami et al.*, 2004; *Malarz*, 2005], but interpretation of such plots requires demonstrating that net storage of sediment is not occurring.

[8] It is reasonable to propose that over a sufficiently long timescale, in upland catchments with active channel incision into bedrock, there is no net storage of sediment in the channel. All sediment entering the channel is either flushed through the system as wash and suspended bed material load, or travels as bed load and abrades to finer particles. The long-term average bed load size distribution at any point on the reach will represent some balance of sediment introduction and abrasion, and it is the size distribution of this load we wish to relate to the channel network and travel paths. For any reach of river the best short-term estimate of that size distribution is probably the spatially averaged subsurface grain size [e.g., *Parker and Klingeman*, 1982; *Parker*, 1990], rather than the size found just at the surface, which is influenced by vertical sorting.

[9] To address the questions posed here, we theoretically derive the effects of grain size input functions and abrasion rates on downstream changes in grain size for simple single-channel basins and for basins with branching networks. As described above, the grain size distribution modeled is the long-term bed load size that passes through a particular reach, not necessarily the surface grain size found on bars. We discover that the abrasion coefficient α sets fundamental length scales in the system beyond which, surprisingly, grain size distributions and total bed load flux become independent of travel distance. Bed load flux becomes independent of drainage basin size, and proportional to the ratio of hillslope erosion rate per unit channel length divided by the abrasion coefficient, α. Furthermore, the theory predicts that if the size distribution of input sediment is relatively broad, abrasion has very little effect on the size distribution of resulting bed load flux. The only way significant downstream fining occurs in this case is if the size distribution of the sediment supplied by the hillslopes decreases downstream. The channel network structure introduces perturbations in bed load flux along the main stem of a watershed, but only influences the size distribution if the tributaries introduce coarser sediment (derived from coarser sediment inputs). Depending on the durability of this coarser sediment, the effect may quickly damp out downstream. Hence, in a watershed with uniform bedrock and small spatial variation in grain size sediment input, abrasion causes little change in bed load grain sizes and instead the size closely reflects the input size distribution. Our findings highlight the need for theory and observations on the grain size distribution of sediment shed to channels.

2. Theoretical Framework

2.1. Assumptions

[10] We make several key assumptions in developing the theory presented below. First, we assume that all sediment delivered by hillslopes to the channel network is either actively transported downstream and out of the watershed as bed load or as suspended load, or, in the case of very large, essentially immobile boulders, are abraded and weathered in place. Hence there is no net deposition of sediment. This is consistent with a tectonically active landscape, where channels and valley floors have only a thin veneer of sediment over bedrock, and is consistent with a relatively long timescale of analysis that averages over shorter-term fluctuations in sediment supply and sediment transport capacity which produce episodes of sediment accumulation in storage reservoirs such as fans and floodplains. As discussed in more detail below, the assumption of no net deposition implies no net selective transport of finer grain sizes because coarse grains would otherwise continuously accumulate over time. Another corollary of the assumption of no net deposition is the assumption that all segments of the channel network receive lateral inputs of sediment from adjacent hillslopes, without interception by intervening storage elements such as floodplains, and that bed load sediment transport is continuous across all tributary junctions.

[11] A second key set of assumptions concerns the simple Sternberg exponential model for particle size reduction with downstream transport (equation (1)). We assume that the Sternberg relation is valid not just for the bulk bed load mass but for individual sediment particles as well, and that the abrasion efficiency parameter α depends only on lithology and is independent of local transport conditions and constant for all grain sizes. There are potentially important physical mechanisms that are thus either lumped into the single model parameter α or are neglected entirely, including abrasion in place of bed surface grains [e.g., *Schumm and Stevens*, 1973], weathering rind formation during floodplain storage [e.g., *Heller et al.*, 2001], rapid initial wear of freshly input hillslope sediments [e.g., *Adams*, 1979] and particle splitting, which may be important in particular lithologies [e.g., *Kodama*, 1994a, 1994b].

[12] Another important assumption is that there is a minimum grain size $D_{\min}$ below which particles travel in suspension and do not contribute to the bed load mass flux or bed load grain size distribution. In all calculations reported here we set $D_{\min} = 2$ mm. We treat the transition from bed load to suspended transport as abrupt, and assume that once in suspension, fine-grained sediments are rapidly transported downstream and out of the watershed. We thus ignore abrasion during suspended transport and the potential contribution of sand to the bed load grain size and mass flux [e.g., *Wilcock et al.*, 2001]. Finally, we assume that sediment production by channel incision into bedrock can be ignored because it makes a negligible contribution to the total bed load supply.

2.2. Analytical Development

[13] In this section, we derive the probability distribution (pdf) of bed load grain diameter D, in terms of both size and mass, given the probability distribution of the entering sediment diameter D_e and the spatially variable load of sediment $q(L)$ to the river. We start with the simplest case of constant (uniform) size of entering sediment and a spatially uniform lateral load and progress to the most complex case of spatially variable probability distribution of entering sediment and spatially variable lateral load.

2.2.1. Uniform Load $q(L) = q$, Constant D_e

[14] The lateral uniform load (mass per unit stream length per unit time) is $q = N_e k D_e^3$ where N_e is the number of grains

entering the stream, D_e is the constant size of the grains and $k = \rho_s \pi / 6$ where ρ_s is the density of the sediment. Following Sternberg's law $D(L) = D_e \cdot e^{-\alpha L}$, a grain of initial diameter D_e will reach a diameter $D_{\min}$ and go to suspension after a distance L_D^* given by

$$L_D^* = \frac{1}{\alpha} \cdot \ln\left(\frac{D_e}{D_{\min}}\right) \tag{2}$$

For any distance $L \geq L_D^*$ along the river, the bed load grain size distribution will be at steady state and will be independent of L, while for all distances $L < L_D^*$ a dependence on distance L is expected. It can be shown (see Appendix A) that for a uniform unit load of q, the pdfs of the bed load sediment diameter by grain $f_b^g(D)$ and by mass $f_b^m(D)$ take the following forms. For $L \geq L_D^*$ and $D_{\min} \leq D \leq D_e$

$$f_b^g(D) = \frac{1}{\alpha L_D^* D} = \frac{1}{D} \cdot \frac{1}{\ln\left(\frac{D_e}{D_{\min}}\right)} \tag{3}$$

$$f_b^m(D) = \frac{3}{D_e^3 - D_{\min}^3} \cdot D^2 \tag{4}$$

and for $L < L_D^*$ and $D_e e^{-\alpha L} \leq D \leq D_e$

$$f_b^g(D) = \frac{1}{\alpha L D} \tag{5}$$

$$f_b^m(D) = \frac{3}{D_e^3 (1 - e^{-3\alpha L})} \cdot D^2 \tag{6}$$

For values of D outside the specified intervals, the pdfs are zero. The mass flux of bed load sediment M at distance L downstream can be shown to be (see Appendix B), for $L < L_D^*$

$$M(L) = \frac{q}{3\alpha} \left(1 - e^{-3\alpha L}\right) \tag{7}$$

and $L \geq L_D^*$

$$M(L) = M_{ss} = \frac{q}{3\alpha} \left[1 - \left(\frac{D_{\min}}{D_e}\right)^3\right] \tag{8}$$

where M_{ss} stands for the steady state mass flux, and L_D^* is given by equation (2).

[15] Importantly, this means that beyond the distance L_D^* the bed load flux is constant and no longer increases with drainage area, as discussed at length in section 3 below. Note that 95% of the mass flux is achieved at the distance $L_{M,0.95}^*$ at which

$$1 - \exp\left[-3\alpha L_{M,0.95}^*\right] = 0.95 \tag{9}$$

which results in

$$L_{M,0.95}^* \cong 1/\alpha \tag{10}$$

An example illustrating these theoretical results is presented below in section 2.3.

2.2.2. Uniform Load $q(L) = q$, pdf of Entering Sediment $f_e^g(D_e)$

[16] Let the entering sediment have a probability distribution by grain, and correspondingly by mass, denoted by $f_e^g(D_e)$, and $f_e^m(D_e)$ respectively. First, we note that $f_e^g(D_e)$ and $f_e^m(D_e)$ relate to each other. One might specify $f_e^g(D_e)$ as lognormal, and derive the pdf of $f_e^m(D_e)$ by acknowledging that mass $= k \cdot D_e^3$, where $k = \pi \cdot \frac{\rho_s}{6}$. We can write that

$$f_e^m(D_e) = \frac{D_e^3 \cdot f_e^g(D_e)}{\int\limits_{D_{\min}}^{\infty} D_e^3 \cdot f_e^g(D_e) dD_e} \tag{11}$$

i.e., the pdf by number of grains is multiplied by the mass of the grain and normalized by the total mass to render it a pdf by mass.

[17] Having an unbounded probability distribution of grain sizes implies that very large particles (theoretically of infinite size) are possible albeit with a very small probability. Thus defining a length L_D^* at which a steady state by grain size is reached is not as straightforward as when the entering sediment is of constant size. In this case, an upper maximum size $D_{\max}$ must be externally imposed based on either deterministic or probabilistic reasoning. In the deterministic case, the value of $D_{\max}$ may be prespecified based on physical considerations, e.g., rare particles larger than $D_{\max}$ are too large to be transported with the flow and do not contribute to the bed load. This $D_{\max}$ value implies a probability of nonexceedance $p = F_e^m(D_{\max})$, where $F_e^m(D_e)$ is the cumulative probability by mass, at which the pdf of the entering sediment will have to be truncated. In the probabilistic case, a probability of nonexceedance p may be prespecified (say, 95%) and the corresponding value of $D_{\max,p}$ (quantile) can be computed as $D_{\max,p} \equiv F_e^{m^{-1}}(p)$. In both cases, the truncated pdf (below by $D_{\min}$ and above by $D_{\max,p}$) of the entering sediment has to be used in the calculations. On the basis of this size $D_{\max,p}$ an equivalent distance $L_{D,p}^*$ to steady state bed load pdf by mass can be defined as

$$L_{D,p}^* = \frac{1}{\alpha} \cdot \ln\left(\frac{D_{\max,p}}{D_{\min}}\right) \tag{12}$$

It can be shown that the bed load sediment pdfs are given as for $L \geq L_{D,p}^*$ and $D_{\min} \leq D \leq D_{\max,p}$

$$f_b^g(D) = \frac{1}{D} \cdot \frac{\int_D^{D_{\max,p}} f_e^g(D_e) dD_e}{\int_{D_{\min}}^{D_{\max,p}} f_e^g(D_e) \ln\left(\frac{D_e}{D_{\min}}\right) dD_e} \tag{13}$$

and for $L < L_{D,p}^*$ and $D_{\min} \leq D \leq D_{\max,p}$

$$f_b^g(D) = \frac{1}{D} \cdot \int_{\min(D, D_{\max}(L))}^{\max(D_{\max}(L), e^{\alpha L} D)} f_e^g(D_e) dD_e / K \tag{14}$$

where

$$K = \int_{D_{\min}}^{D_{\max}(L)} f_e^g(D_e) \ln\left(\frac{D_e}{D_{\min}}\right) dD_e + \alpha L \int_{D_{\max}(L)}^{D_{\max,p}} f_e^g(D_e) dD_e$$

$$D_{\max(L)} \equiv D_{\min} \cdot e^{\alpha L}$$

[18] From the pdf of the bed load sediment by grain, one can derive the pdf of the bed load sediment by mass using equation (11) so these equations are not displayed here. Finally, the mass flux of bed load sediment as a function of distance downstream can now be derived. This involves a trivial extension of equations (7) and (8), i.e., for $L < L_{D,p}^*$

$$M(L) = \frac{q}{3\alpha}\left(1 - e^{-3\alpha L}\right) \quad (15)$$

where now

$$q = N_e k \int_{D_{\min}}^{D_{\max,p}} D_e^3 f_e^g(D_e) dD_e$$

and for $L \geq L_{D,p}^*$ the steady state mass flux becomes

$$M_{ss} = \frac{q}{3\alpha} \cdot \left[1 - D_{\min}^3 \Big/ \int_{D_{\min}}^{D\max,p} D_e^3 f_e^g(D_e) dD_e\right] \quad (16)$$

Because the second term in brackets will generally be very small, the steady state mass flux M_{ss} can be approximated as $q/3\alpha$, providing a simple estimate for long-term bed load downstream of $L_{D,p}^*$. Assuming a lognormal pdf of the entering sediment by number of grains (which we will use in the example applications below), it can be shown that the steady state mass becomes

$$M_{ss} = \frac{N_e k}{3\alpha} \cdot \exp\left[3\mu_{\ln D_e} + \frac{9}{2}\sigma_{\ln D_e}^2\right] \quad (17)$$

where $\mu_{\ln D_e}$ and $\sigma_{\ln D_e}$ are the mean and standard deviation of the lognormal distribution. We note that, as before, 95% of the steady state mass is reached at distance $L_M^* = 1/\alpha$ which does not depend on the pdf of the entering sediment but only on the abrasion coefficient. An example illustrating these theoretical results is presented in section 2.3.

2.2.3. Nonuniform Load $q(L)$, D_e = Constant

[19] In the previous two cases, we treated the lateral load of entering sediment per unit stream length per unit time as uniform. Now, we consider the case of a spatially variable load, i.e., load that depends on the distance L downstream. Such a case is motivated by the need to consider spatial variations in hillslope sediment supply due to differing erosion rates, or variations in the fraction of the sediment supply in the bed load size range due to differences in hillslope soil or bedrock properties.

[20] Let $q(L)$ denote the load rate per unit stream length and unit time as a function of distance L. It can be shown

that the bed load sediment pdf by grain is given, for $L \geq L_D^*$ and $D_{\min} \leq D \leq D_e$, by

$$f_b^g(D) = \frac{1}{\alpha D} \cdot \frac{q\left(L - \frac{1}{\alpha} \cdot \ln\left(\frac{D_e}{D}\right)\right)}{\displaystyle\int_{L-L_D^*}^{L} q(x) dx} \quad (18)$$

and for $L < L_D^*$ and $D_e e^{-\alpha L} \leq D \leq D_e$

$$f_b^g(D) = \frac{1}{\alpha D} \cdot \frac{q\left(L - \frac{1}{\alpha} \cdot \ln\left(\frac{D_e}{D}\right)\right)}{\displaystyle\int_{0}^{L} q(x) dx} \quad (19)$$

The pdfs by mass can be easily derived from the above pdfs and equation (11). An example illustrating the above result is presented in section 3.3 where the load function $q(L)$ is patterned after the width function of a river network.

2.2.4. Nonuniform Load $q(L)$, pdf of Entering Sediment $f_e^g(D_e)$

[21] In a similar manner as before, we can derive the following expression for the bed load pdf by grain size for $L \geq L_{D,p}^*$ and $D_{\min} \leq D \leq D_{\max,p}$

$$f_b^g(D) = \frac{1}{\alpha D} \cdot \int_{D}^{D_{\max,p}} q\left(L - \frac{1}{\alpha} \cdot \ln\left(\frac{D_e}{D}\right)\right) f_e^g(D_e) dD_e / K \quad (20)$$

where

$$K = \int_{D_{\min}}^{D_{\max,p}} f_e^g(D_e) \left(\int_{L-\frac{1}{\alpha}\ln\left(\frac{D_e}{D}\right)}^{L} q(x) dx\right) dD_e$$

For $L < L_{D,p}^*$ the equation becomes too complex to display here.

2.2.5. Nonuniform Load $q(L)$, pdf of D_e Varying Downstream

[22] This is the most general case and allows for the parameters of the pdf of the entering sediment to depend on the distance downstream. This might occur when hillslope sediment supply changes systematically downstream or tributaries enter the main stem and contribute sediment with distinct grain size distributions reflecting differing upstream lithologies, hillslope processes or erosion rates. The equations become cumbersome to write but not conceptually difficult to extend from those of the previous cases.

2.3. Application to a River Reach

[23] We illustrate the above theoretical results with an example application that considers a river reach having a uniform lateral load rate of entering sediment. We set $D_{\min} = 2$ mm, and the abrasion coefficient $\alpha = 0.0002$ m^{-1}. In the first case we consider a constant entering size $D_e = 500$ mm. Note that for this case, the distance L_D^* required to wear the sediment down to the suspension size and the distance at which steady state mass flux (at the 95% level) is achieved are $L_D^* = 27.6$ km and $L_M^* \simeq 5$ km (computed by equations (2) and (10), respectively).

[24] Figure 3a shows the pdf of bed load sediment by grain $f_b^g(\ln D)$ for various distances L downstream with a
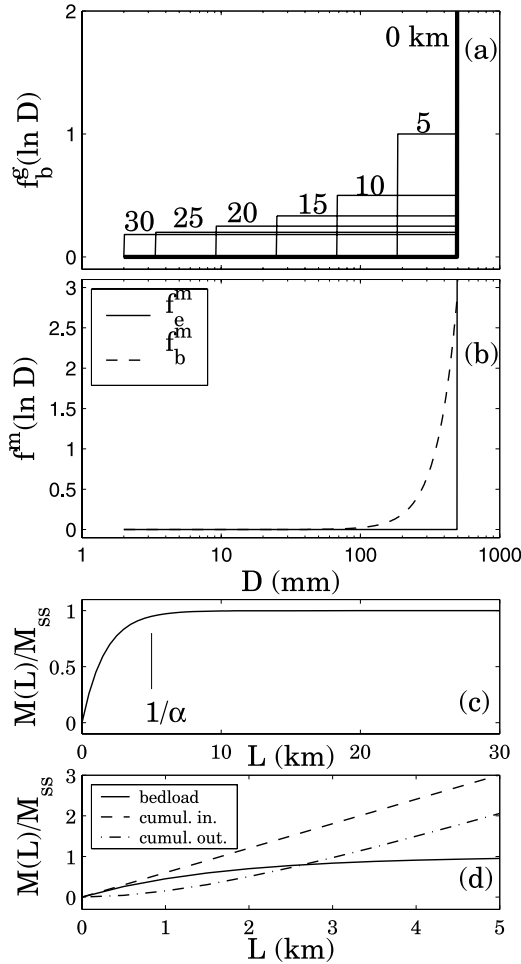
Figure 3. Entering sediment of constant grain size ($D_e =$ 500 mm) and constant lateral load rate: (a) evolution of the pdf of bed load grain diameter, with frequency in terms of number of grains, for 5 km increments of downstream distance L. Note the steady state pdf (for $L = 30$ km) with an equal number of grains in each size (above $D_{min} = 2$ mm). (b) Steady state pdf of bed load grain diameter, with frequency in terms of mass, achieved at distance $L_D^* \simeq 27.6$ km. (c) Bed load mass flux as a function of distance downstream, normalized by the steady state mass flux M_{ss}. (d) Normalized bed load sediment flux, cumulative input flux to the bed load from entering sediment, and cumulative output flux from bed load to suspended load, as a function of downstream distance (note that only the first 5 km are displayed before steady state is reached).

constant size of entering sediments $D_e = 500$ mm (from $L = 0$ km to $L = 30 > 27.6$ km at which the steady state pdf is achieved). Note that since the pdf of D is $\dfrac{1}{\alpha L_D^* D}$ (equation 5), the pdf of $\ln D$ which is given by

$$f(\ln D) = D \cdot f(D) \qquad (21)$$

becomes a uniform pdf equal to $1/\alpha L$. The area under each pdf in Figure 3a is equal to 1 as the range of D over which each pdf is defined is αL. For example, for $L = 10$ km, $\alpha L = 2.0$, and the corresponding value on the probability axis is 0.5, such that the area under the pdf is 1.0.

[25] Figure 3b shows the pdf by mass of the entering and bed load sediment. Note that in Figure 3b we again plot the pdf of ln D (i.e., f_b^m (ln D) versus ln D) because a lognormal pdf in D_e (which will be considered in the next section) would plot as Gaussian or normal curve. Using the transformation of equation 11, the pdf by mass, which goes as $1/D^2$, becomes a pdf that decays as $1/D$, as displayed in Figure 3b.

[26] Figure 3c shows the mass flux as a function of distance L downstream $M(L)$, normalized by the steady state mass flux M_{ss}, and illustrates how $M(L)$ reaches approximate steady state at $L = 1/\alpha$. Figure 3d shows the normalized mass flux as a function of downstream distance together with the cumulative sediment flux input and output, focusing in the upstream 5 km of the river reach. As the bed load flux $M(L)$ approaches steady state, the rate of suspended load (silt and sand) production begins to match the rate of sediment input; the difference between the cumulative input and output curves is a constant equal to the bed load flux. Figure 4 shows the mass flux as a function of distance downstream for different values of the abrasion coefficient α and illustrates how rock durability, as parameterized by α, controls the magnitude of steady state bed load flux and the distance required to reach steady state (equations (7) and (10)). For Figure 4 we used an erosion rate E of 0.1 mm/year, a contributing area per unit length a of 0.5 km^2/km and a density of the entering sediment of $\rho_s = 2500$ kg/m^3 and computed the load rate $q = E\,a\,\rho_s$.

[27] We now consider a second example application to contrast the cases of constant grain size of entering sediment as analyzed above with the case of a probability distribution of entering sediment which can be narrow (sorted sediment) or wide (unsorted sediment). The practical use of this example will be to quantitatively assess the effect of the pdf of the sediment entering from the hillslopes to the bed load grain size distribution found downstream. We assume a
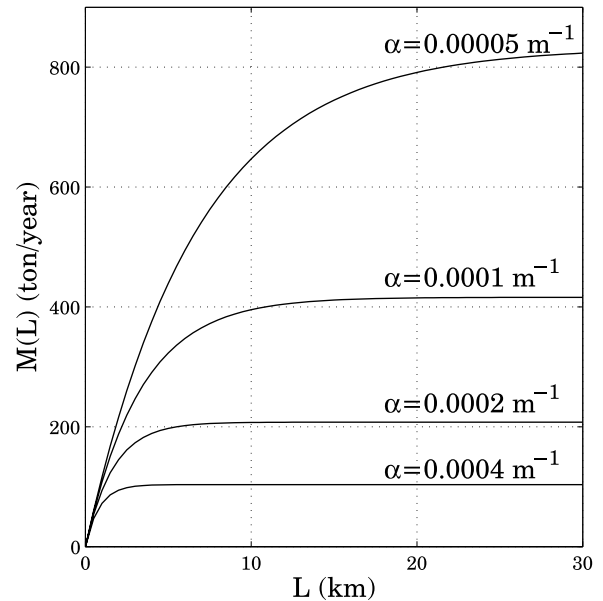
Figure 4. Mass flux $M(L)$ as a function of distance downstream L for different values of the abrasion coefficient α. See text for explanation of the other parameters used for this computation.

Table 1. Comparison of the Statistical Moments of the Entering and Bed Load Grain Size Distributions for Constant Size and Three Lognormal pdfs of Entering Sediment by Mass[a]

pdf	Constant Size	LN1	LN2	LN3
$\mu_e^m = \mu_{\ln D}^m$	6.21	5.34	4.46	3.20
$\mu_b^m = \mu_{\ln D}^m$	5.88	5.01	4.14	3.00
$D_{50,e}$	500 mm	211 mm	89 mm	23 mm
$D_{50,b}$		150 mm	65 mm	18 mm
$\sigma_e^m = \sigma_{\ln D_e}^m$	0	0.45	0.90	1.39
$\sigma_b^m = \sigma_{\ln D}^m$	3.333	0.56	0.95	1.34
$S_e^m = S_{\ln D_e}^m$	0	−0.34	−0.33	+0.17
$S_b^m = S_{\ln D}^m$	−2.0	−0.59	−0.33	+0.24
$K_e^m = K_{\ln D_e}^m$	0	2.8	2.8	2.1
$K_b^m = K_{\ln D}^m$	9.0	3.6	2.8	2.1

[a]Subscript e indicates entering, and subscript b indicates bed load. Note that for all pdfs the value of $D_{\max} = 500$ mm (ln 500 = 6.21), which corresponds to the 5% exceedance quantile.

lognormal distribution for the entering sediment by grain. We remind the reader that a lognormal pdf is specified by its two parameters $\mu_{\ln D_e}$ and $\sigma_{\ln D_e}$,

$$f_e^g(D_e) = \frac{1}{\sqrt{2\pi}\sigma_{\ln D_e} \cdot D_e} \cdot \exp\left[-\frac{(\ln D_e - \mu_{\ln D_e})^2}{2\sigma_{\ln D_e}^2}\right] \quad (22)$$

and that the statistics of D_e are given as

$$\mu_{D_e} = e^{\mu_{\ln D_e}} + \frac{\sigma_{\ln D_e}^2}{2}$$
$$\sigma_{D_e} = \mu_{D_e} \cdot \left(e^{\sigma_{\ln D_e}^2} - 1\right)^{\frac{1}{2}} \quad (23)$$

where $e^{\mu_{\ln D_e}}$ is the geometric mean and also the median of D_e. It can be shown that if $f_e^g(D_e)$ is lognormal then $f_e^m(D_e)$ is also lognormal with parameters

$$\mu_{\ln D_e}^m = \mu_{\ln D_e} + 3\sigma_{\ln D_e}^2$$
$$\sigma_{\ln D_e}^m = \sigma_{\ln D_e} \qquad .$$

It follows that the D_{50} by mass parameter typically reported relates to the parameters of the grain size distribution of the entering sediment by

$$D_{50} = \exp\left(\mu_{\ln D_e} + 3\sigma_{\ln De}^2\right).$$

[28] There are several ways by which one can specify the lognormal distribution parameters such that the results can be contrasted with those obtained for the constant size D_e of entering sediment presented in the previous section. A simple way to specify the lognormal pdf of the entering sediment would be to set $\mu_{\ln D_e} = \ln 500$ which would imply a geometric mean of grain size equal to 500 mm, which was the constant $D_e = D_{\max}$ value used in the previous example. The variance $\sigma_{\ln D_e}$ could be changed to mimic a narrow or wide pdf of grain size. Such a specification would result in 95% quantiles which would vary widely and would be hard to compare the results to those obtained using the maximum size $D_{\max} = 500$ mm of the previous case. Since the maximum size of D_e sets the "length scale" of the system,

in terms of the distance downstream at which steady state pdf of bed load sediment is achieved, we propose that a more meaningful comparison would result if the lognormal pdfs were specified such that the corresponding systems have comparable length scales to each other and to the system of constant grain size. Thus we consider lognormal pdfs such that their upper 5% quantile is reached at $D_{\max} = 500$ mm and by specifying $\sigma_{\ln D_e}^m = 0.1, 0.5,$ and 1.0 we derive the corresponding values of $\mu_{\ln D_e}$. The parameters of the lognormal pdfs are given in Table 1 and the pdfs are displayed in Figure 5.

[29] For the three different lognormal pdfs of entering sediment by mass, we compute the steady state bed load pdfs by mass and these are shown in Figure 6. As the distribution of the entering sediment widens (less sorted sediment entering from the hillslopes), the steady state pdf of the bed load approaches a shape that is close to the shape of the pdf of the entering sediment and is not very sensitive to further changes in the variance of the entering sediment pdf. To quantify this further, we have computed (via numerical evaluation) the moments of the derived pdfs (i.e., mean $\mu_b^m \equiv \mu_{b,\ln D}^m$, standard deviation $\sigma_b^m \equiv \sigma_{b,\ln D}^m$, coefficient of skewness $S_b^m \equiv S_{b,\ln D}^m$ and coefficient of kurtosis $K_b^m \equiv K_{b,\ln D}^m$). These are shown in Table 1 together with the same parameters of the entering sediment pdfs by mass. Note that the reported μ_e^m and σ_e^m are not exactly the specified parameters of the entering sediment LN pdf but rather the numerically computed moments of the resulting truncated pdfs. For example, for LN1 the specified parameter $\sigma_{\ln D_e}^m$ was 0.1 but the computed standard deviation $\sigma_e^m = \sigma_{\ln D_e}^m$ shown in Table 1 was 0.09. Figure 7 shows the ratio of the means of the entering to bed load sediment, the ratio of the standard deviations and coefficients of skewness and kurtosis of the bed load sediment pdf by mass, all for ln D. We observe that as the variance of the entering sediment pdf increases the coefficient of skewness of the bed load sediment approaches zero and the coefficient of kurtosis approaches 3, implying an approach to a normal distribution for ln D, or lognormal
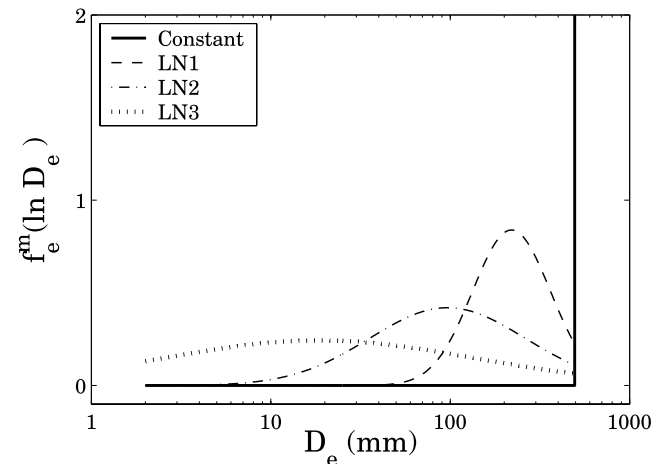
Figure 5. Specification of three lognormal pdfs of entering sediment by mass such that for all pdfs the probability of exceeding $D_e = 500$ mm is 5%. The parameters of the lognormal pdfs are shown in Table 1 (see text for explanation).
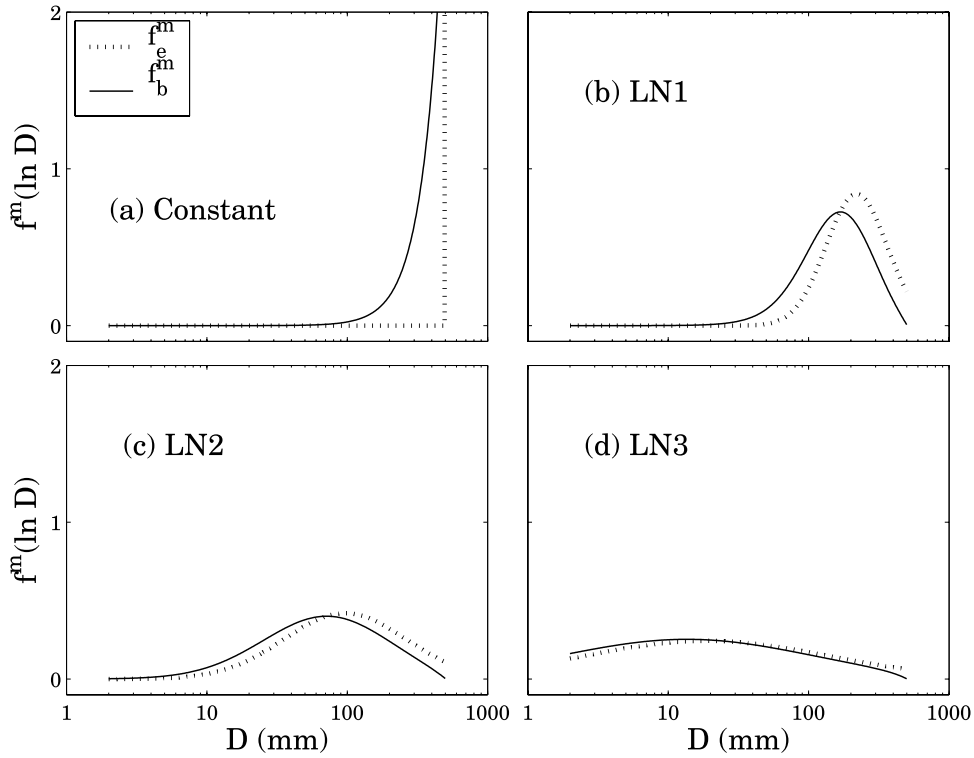
Figure 6. Comparison of pdfs of entering sediment by mass $f_e^m(\ln D_e)$ (dashed lines) to those of the steady state pdfs by mass of the bed load $f_b^m (\ln D)$ (solid lines) for (a) the constant size D_e and (b−d) the three pdfs of Table 1 (narrow to very wide).

distribution for the bed load sediment. We conclude that the wider the pdf of the entering sediment, the closer the bed load sediment pdf by mass is to that of the entering sediment. Although little is known about the pdfs of sediments delivered to channels by hillslopes, it is reasonable to assume that the most common case is a very wide (unsorted) distribution.

3. Application to Channel Networks

[30] Several important and previously unrecognized insights emerge from the theoretical results of the preceding section. First, for the case of input sediment grain size distributions that are spatially uniform and poorly sorted, the effect of abrasion during downstream transport on the bed material grain size distribution may be so small as to be undetectable in the field. Because of continuous downstream resupply of the input size distribution, the bed material should essentially mirror what the channel is receiving from adjacent hillslopes. This implies that, in the absence of net deposition due to selective transport, measurable spatial variations in bed material size distributions result primarily from spatial variations in the size of sediments entering the channel network.

[31] A second key result that emerges from the theory is that the downstream trend in the long-term average bed load flux does not scale in a simple way with the upstream contributing drainage area. Rather, the bed load mass grows only until the rate of silt production by abrasion matches the rate of coarse sediment input, at which point the bed load flux becomes constant and independent of drainage area. Importantly, for a given abrasion rate coefficient (α), the

steady state bed load mass is achieved relatively rapidly (equation (10)), compared to the distance required for the bed material grain size distribution to reach steady state (equation (2)). As illustrated in detail below, this implies that spatial variations in bed load flux created by the branching structure of drainage networks will not depend simply on the pattern of accumulation of drainage area at tributary junctions, but will depend instead on the upstream travel distances of discrete sediment travel pathways, relative to the distances at which mass L_M^* and sediment grain size L_D^* reach steady state.

[32] In this section we use the theory to investigate the potential sources of variation in bed material grain size distributions through channel networks. To simulate spatial variation in input sediment sizes and rates of abrasion, we focus on the effect of lithologic heterogeneity, assuming that rock properties will strongly influence the size distribution of hillslope sediments and the rate of particle breakdown in the channel. Although the size of input sediments should also depend on the rates and styles of hillslope sediment production and transport, for simplicity we assume a spatially uniform landscape erosion rate in all of the following calculations. Thus the sediment loading rate $q(L)$ can be written as

$$q(L) = \rho_s E \, a(L) \qquad (24)$$

where ρ_s is the density of both bedrock and bed load sediment (kg/m^3), E is erosion rate (m/yr), and $a(L)$ is the incremental addition of drainage area per unit channel length (m). Note that $a(L)$ can be spatially variable, reflecting in part the channel network structure.
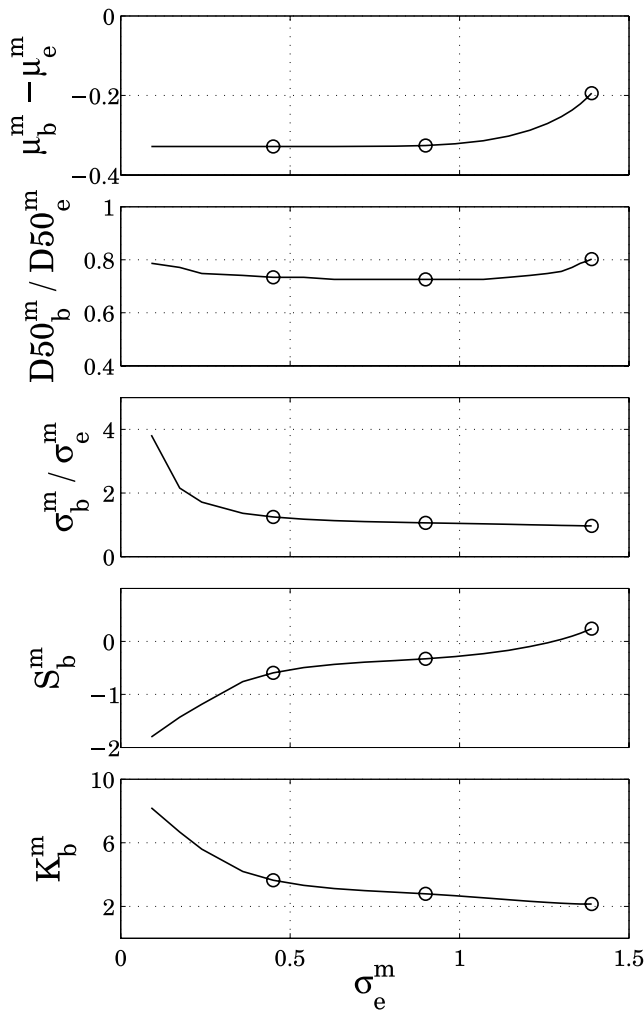
Figure 7. Moments of the bed load pdf as a function of the variance of the entering sediment pdf: (a) difference in mean size of entering μ_e^m and bed load μ_b^m sediment, (b) ratio of geometric mean diameter of bed load to entering sediment, (c) ratio of standard deviations of bed load and entering sediment σ_b^m/σ_e^m, (d) coefficient of skewness of bed load sediment, and (e) coefficient of kurtosis of bed load sediment. Circles indicate values for the three lognormal distributions, LN1, LN2, and LN3, of Figures 5 and 6 and Table 1.

[33] A simple example application of the theory relates to the common observation that river bed sediments are often enriched in the more durable lithologies that outcrop within the upstream drainage area. For an illustrative case where a single geologic unit is composed of two rock types of differing durability (e.g., interbedded sandstones and mudstones), we can predict the mass fraction in the bed material of the more durable rock type as a function of its mass fraction in the input sediment and the ratio of the abrasion coefficients of the two rock types, as shown in Figure 8. For this calculation we assume that the downstream travel distance L exceeds the length L_M^* required to reach the steady state mass M_{ss}, which is set by the inverse of the abrasion coefficient for the more durable rock (i.e., $1/\alpha_h$).

Note that equations (7) or (15) could be used for the slightly more complex case where $L < 1/\alpha_h$.

[34] Figure 8 shows that as the durability of the two rock types diverges, the relative enhancement in the hard rock fraction on the bed is approximately proportional to the ratio of abrasion coefficients (α_w/α_h). As the hard rock becomes the dominant component of the bed material, with larger values of α_w/α_h, the sensitivity of the bed composition to the durability contrast declines. For very large differences in abradability, the hard fraction dominates irrespective of its mass fraction in the hillslope source material. Implicit in this calculation is the assumption that abrasion coefficients for the two rocks are independent. We expect, however, that the abradability of weak rocks should be enhanced by the presence of more durable rocks in the bed load sediment mixture; at present no experimental data are available to constrain this relationship.

[35] In the remainder of this section, we further explore the influence of particle abrasion and travel distance on bed material grain size distributions by considering downstream fining, variations in bed load mass and particle size across tributary junctions, and the effect of differing drainage basin shapes as represented by the width function.

3.1. Downstream Fining

[36] For more than a century, a downstream reduction in bed material grain size has been reported in studies of river networks in a diverse set of landscapes [e.g., *Gilbert*, 1877; *Hack*, 1957; *Brush*, 1961; *Kodama*, 1994a; *Gomez et al.*, 2001]. Recently, debate has centered on the question of whether selective transport or particle abrasion is the dominant control in rates of downstream fining [e.g., *Parker*, 1991a, 1991b; *Kodama*, 1994a, 1994b]. In depositional environments selective transport has been shown to be responsible for very rapid fining over short distances [e.g., *Paola et al.*, 1992; *Ferguson et al.*, 1996]. Many workers have assumed that where selective transport cannot
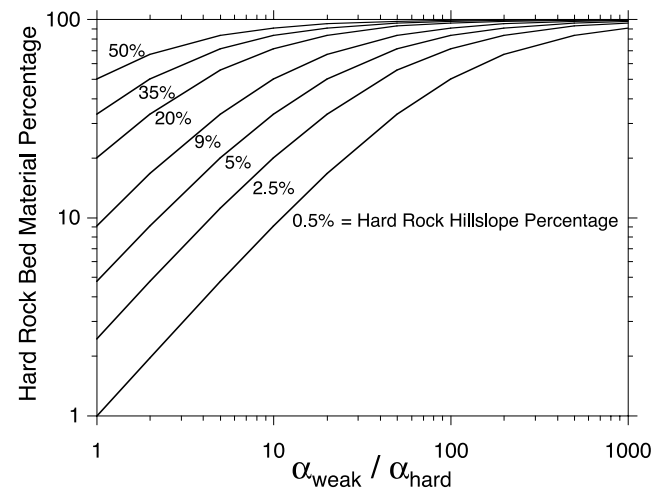
Figure 8. Variation in percentage by mass of hard rock, in a bed load sediment mixture of both weak and hard bedrock source material, as a function of the ratio of abrasion coefficients for the weak and hard rock types (α_w/α_h), for $L > 1/\alpha_h$. Curves shown are for various mass percentages of the hard rock in the coarse sediment entering the channel network.
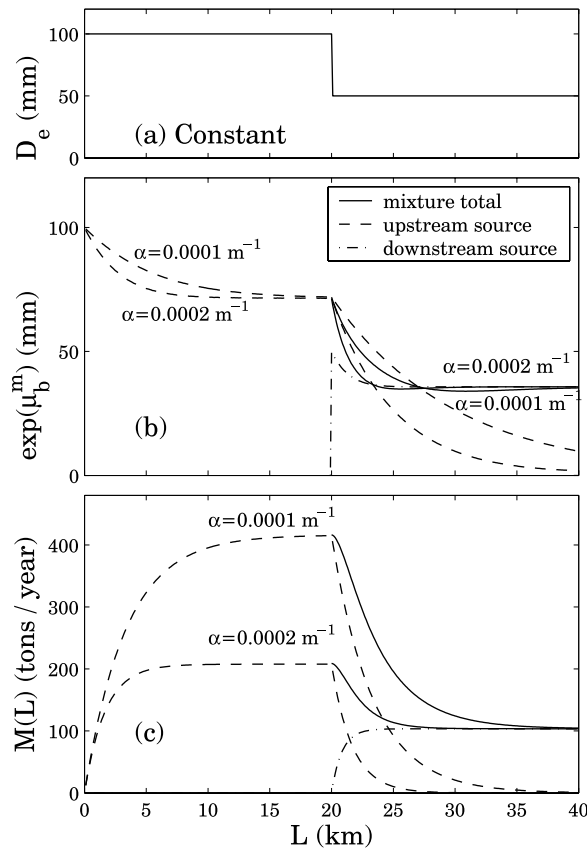
Figure 9. Downstream fining example. Variation with downstream distance L of (a) entering sediment uniform grain size, (b) geometric mean diameter of the bed load, and (c) the bed load mass flux. Results are shown for two different abrasion coefficients ($\alpha = 0.0001$/m and $\alpha = 0.0002$/m) for the upstream coarse sediment ($D_e = 100$ mm); for downstream source sediment ($D_e = 50$ mm), $\alpha = 0.0004$/m. Also shown are the grain size and mass flux for the bed load mixture downstream of the lithologic contact at $L = 20$ km.

fully explain observed fining rates, then abrasion must be responsible for the balance of the size reduction [e.g., *Rice*, 1998; *Gomez et al.*, 2001; *Moussavi-Harami et al.*, 2004]. As shown by the theoretical results presented above in section 2, however, abrasion can only be effective in reducing bed material size when there is a downstream change in the grain size distribution supplied by hillslopes to the channel network.

[37] We can consider two kinds of downstream changes in input grain size distribution, gradual and abrupt. Gradual fining of the coarse sediment supply is probably common in actively incising landscapes for a number of reasons. The highest ridges that make up the watershed divide furthest from the drainage basin outlet are likely to have the steepest average hillslope gradients. To the extent that geologic materials and structure influence channel network architecture, the more distal portions of the watershed are also more likely to be underlain by more durable bedrock. In transient landscapes, where erosion rates are not spatially uniform, it may often be the case that higher erosion rates occur on steeper slopes in low-order subbasins. In large watersheds,

gradients in temperature and precipitation may result in a greater role at higher elevations for mechanical (versus chemical) weathering processes in producing transportable regolith. Each of the these factors may correlate with a coarser hillslope sediment size distribution. Moreover, hillslope sediment production and transport processes likely to supply coarse material to the drainage network, such as debris flow generating landslides, are also more likely to deliver sediment to the steeper channels further from the outlet. Abrupt changes in input grain sizes can occur where channels cross lithologic contacts, and at tributary junctions where channels draining different lithologic units, or landscapes of differing erosional characteristics, combine to form a new bed load mixture.

[38] Here we explore two downstream fining scenarios, each of which is driven by an abrupt change in the grain size distribution of the supplied sediments. We focus on abrupt supply transitions because for the case of a gradual downstream reduction in the input grain size, the change in bed material size distribution should closely track the changing input; bed load fining rate is specified precisely by the input fining rate as long as the characteristic scale over which D_e varies is greater than L_D^*. The close coupling of the bed load and input distributions will also occur when the fining of the supply coincides with a gradual change in mass input rate $q(L)$.

3.1.1. Fining in a Simple Channel

[39] In the first example, we consider a simple main stem channel without major tributary inputs, where the channel receives a spatially uniform rate of sediment mass input (i.e., $q(L)$ is constant). This is perhaps equivalent to a narrow bedrock canyon where sediment is supplied predominantly from the canyon side slopes. As depicted in Figure 9a, we simulate the crossing of a lithologic contact at the midpoint of a 40 km long channel by imposing an abrupt reduction in the input size of a uniform grain size (D_e), from 100 mm to 50 mm. The coarser sediment supplied upstream is also assumed to be more durable than the finer downstream supply, hence it has a lower value of the abrasion coefficient α.

[40] Figure 9b shows the downstream change in the geometric mean of the bed load size distribution, for both the upstream- and downstream-supplied sediments, and for the total bed load mixture below the contact. Upstream of the contact the mean grain size declines initially and then stabilizes, due to the evolution of the bed load pdf away from the entering sediment pdf of a single grain size spike (as in Figure 3b and Table 1). Results for two values of upstream sediment α are shown; the evolution of the bed load distribution is more rapid for the less durable case ($\alpha = 0.002$/m) than for the case of more durable rock ($\alpha = 0.001$/m). For both values of upstream α, the bed load pdf reaches steady state before the lithologic contact at $L = 20$ km. Immediately downstream of the contact the supply shifts to the less durable ($\alpha = 0.004$/m), finer-grained sediment, and the mean grain size of the bed load mixture (labeled "total") declines rapidly until it stabilizes at a value equal to the mean of the steady state bed load pdf determined by the input size distribution.

[41] The fining downstream of the contact occurs for three reasons. First, abrasion of the coarse material supplied from upstream is no longer balanced by resupply of coarse
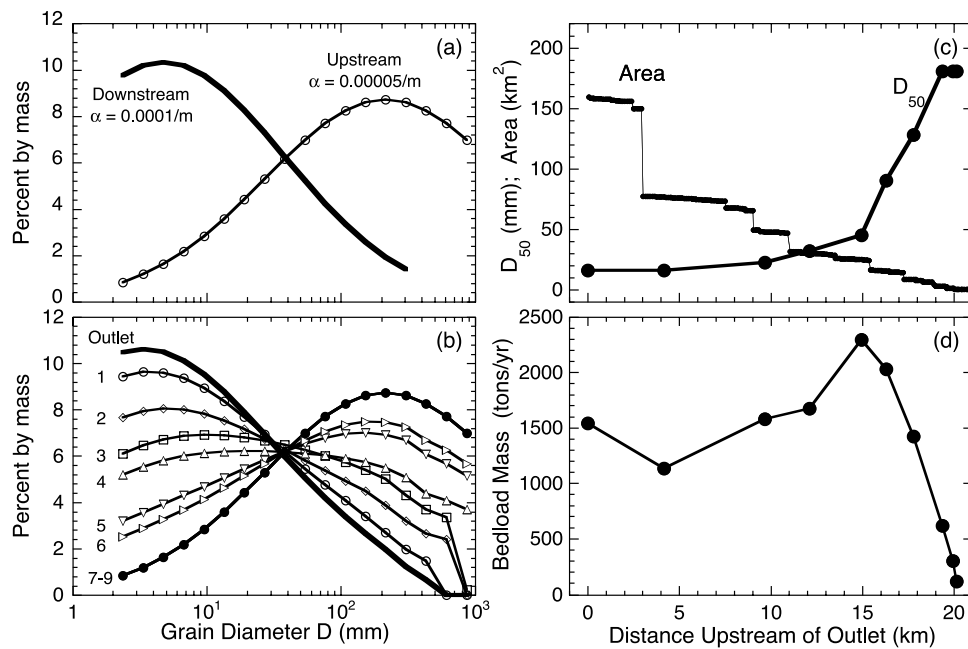
Figure 10. Simulated downstream fining in the Noyo river basin. (a) Entering size distributions for the more durable ($\alpha = 0.00005$/m) upstream ($x > 19$ km) sediment and less durable ($\alpha = 0.0001$/m) downstream sediment. (b) Bed load sediment size distributions for nine nested subbasins and the outlet (locations shown in Figure 1). (c) Variation in median grain size and drainage area with distance upstream of the outlet along the main stem. (d) Predicted annual bed load mass flux with distance upstream of the outlet along the main stem.

material, and the particles of the upstream lithology that cross the contact are progressively reduced in size until all have been converted to silt and sand and swept away in suspension (Figure 9c). Second, the mean size of the newly introduced finer material also declines as its pdf evolves from the initial spike input to the steady state bed load pdf (Figure 3b). Third, the mean of the resulting bed load mixture is an average of the upstream- and downstream-derived materials (both of which are declining), weighted by the relative mass of each component of the mixture. As shown in Figure 9c, the mass of the upstream component of the mixture drops off rapidly below the contact, while the mass of the downstream component climbs to its steady state value. The rate of mass loss of the coarse fraction, and thus the rate of fining of the bed load sediment mixture, is more rapid when the upstream sediment is less durable, as expected.

[42] This example illustrates how the efficiency of abrasion, as parameterized by α, controls the rate of fining downstream of an abrupt change in the input size distribution. The abrasion coefficient controls both the steady state mass of the coarse material as it arrives at the lithologic contact, and the rate of size reduction with distance. Also, because we assumed that the finer sediments are less durable, the downstream sediment mass equilibrates to a lower mass, thus reducing the mass component of the finer sediments in the bed load mixture and lengthening the distance over which the fining occurs.

3.1.2. Fining Along a Channel Network Mainstem

[43] We next consider downstream fining due to an abrupt reduction in the mean of the size distribution of entering sediment, in the setting of a real channel network,

the upper Noyo River in Mendocino County, California (Figures 1, 2a, 2b, and 2c). In contrast to the previous example, we specify two very poorly sorted entering sediment size distributions (Figure 10a), both derived from log normal distributions but with the coarse tail of the coarser upstream distribution severely truncated (resulting in negative skew) and the fine tail of the finer downstream distribution severely truncated (resulting in positive skew). We assign $\alpha = 0.0001$/m to the finer distribution and $\alpha = 0.00005$/m to the coarser distribution. The lithologic contact is assumed to cross the watershed such that the more durable coarse sediment is supplied to all channel segments that are greater than 19 km upstream of the downstreammost point in the network (the "outlet"). Note that the modeled input grain size distributions are not based on field measurements, but rather are selected to illustrate how downstream fining might occur in a channel network.

[44] The upper Noyo River channel network and watershed topography are derived from overlaying the USGS blue line DLG onto a 10m DEM and extending the channel network by using a 40,000 m^2 channel initiation threshold. The tips of the channel network used here have been pruned to exclude channels steeper than 10%, because of the presumed dominance of debris flow sediment transport and valley incision in the steeper headwater channels [e.g., *Stock and Dietrich*, 2003; *Dietrich et al.*, 2003].

[45] For the outlet and for each of nine points midway between major tributary junctions along the main stem, we use a numerical routine to calculate the resulting grain size distribution and mass of the bed load. For each point of

analysis we calculate the width function and the coinciding incremental area function (Figures 2a and 2c show these functions for the outlet). The sediment loading for each upstream distance is obtained by summing the mass input of each incremental area (equation (24)), assuming a uniform erosion rate E of 0.1 mm/yr, and a rock density ρ_s of 2500 kg/m^3. From the mass loading and the appropriate grain size pdf by mass, we calculate the number of input particles in each size class. Finally, for each travel distance, the grain size reduction due to abrasion is calculated and the grain size distribution is obtained by summing over all upstream distances.

[46] Figure 10b shows the bed material grain size distributions for each of the nine nested subbasins and for the outlet. The downstream evolution of the median grain sizes is shown in Figure 10c, along with the downstream accumulation of drainage along the main stem. Where the channel is upstream of the shift in supply ($x > 19$ km, subbasins 7, 8 and 9), the bed load pdf is indistinguishable from the entering sediment. Downstream of the shift to the finer supply, the median grain size declines rapidly (Figure 10c), reflecting the gradual shift in the grain size distribution of the bed load mixture from the coarse to the finer supply. The bed load pdf at the outlet is not identical to the steady state bed load pdf that corresponds to the finer entering sediment distribution, however, for two reasons. First, $L_D^* \sim 52$ km for that distribution, so the fine supply component of the bed load is still evolving. Second, there is also a significant fraction of the bed load particles at the outlet which are derived from the coarse supply delivered in the distal portions of the watershed because $L_D^* \sim 125$ km for the coarser upstream distribution of entering sediment. All the coarse supply particles initially larger than about 5 mm are thus still part of the bed load mixture at the outlet, but their size has been greatly reduced by abrasion. As a result, the mean of the outlet distribution is somewhat smaller than the mean of the fine-grained supply, but the outlet distribution also has a slightly thicker tail in the coarse size classes.

[47] The downstream evolution of the bed load flux $M(x)$ is shown in Figure 10d. Mass increases rapidly and continuously in the upstream portion of the main stem profile (15 km < x < 20 km), with no apparent effect from crossing the supply discontinuity at 19 km. Below $x =$ 15 km, however, the bed load flux drops to about half the peak value, reflecting the increased efficiency of abrasion (greater α) of the less durable downstream supply and the reduced rate of area accumulation downstream of the peak in the width function (Figures 2a and 2b).

3.2. Tributary Junctions

[48] The branching structure of channel networks should most strongly influence bed material grain size distributions at tributary junctions, where abrupt changes in the characteristics of sediment supply to the main stem channel are possible. Tributary junctions are commonly observed to be sites of infusions of coarse material, particularly where debris flows arriving from steep tributary channels are halted by high angle junctions with the main stem [e.g., *Howard and Dolan*, 1981; *Montgomery et al.*, 2003]. Where lateral sediment supply from adjacent hillslopes is intercepted by wide valley bottoms, pronounced downstream

fining between tributary junctions has been observed [*Rice and Church*, 1998; *Rice*, 1998, 1999], although selective transport may be the dominant influence if there is net deposition [e.g., *Ferguson et al.*, 1996; *Hoey and Bluck*, 1999]. Here we consider how particle abrasion and spatial variability in sediment supply can affect the magnitude of perturbation of the main stem bed material at tributary junctions, for the case of no net deposition over geomorphic timescales.

3.2.1. Individual Tributary Junctions

[49] If the two streams are transporting the same bed load size distribution, composed of rocks of equal durability (i.e., same α), there will be no change in the main stem grain size distribution downstream, only a change in bed load mass flux. Where the size distributions of the bed load in each stream are not the same, the resulting change in main stem grain size (ΔD) will scale with the magnitude of the change in bed load mass flux in the main stem (ΔM) after the addition of the tributary input. Figures 11a and 11b show schematic diagrams of changes in bed load mass flux and median grain size across a tributary junction. For this simple example, the main stem contribution of bed load flux (M_m) is assumed to come from the upstream supply of sediment from the valley side slopes, and is shown as constant in Figure 11 although we might expect it to change over the scale of the diagram due to variations in the local side slope supply rate. We first consider changes in only the bed load mass flux, and then changes in grain size.

[50] Because particle abrasion converts a significant fraction of the bed load material supplied upstream to silt, the fractional change in bed load mass immediately downstream of the junction ($\Delta M/M_m$) will not scale simply with relative drainage area, but rather should depend on the upstream lengths of the two channels (L_{trib} and L_{ms}). For the case of spatially uniform erosion rate in both the tributary and upstream main stem watersheds (i.e., uniform side slope supply for all channels), we can identify three classes of tributary junctions, scaled by the ratio of the upstream lengths of the two channels (L_{trib} and L_{ms}) to the mass equilibration length $1/\alpha$. The simplest case is where both channels have reached steady state bed load mass flux (i.e., $L_{trib} > 1/\alpha$; $L_{ms} > 1/\alpha$) and the flux doubles immediately downstream of the junction ($\Delta M/M_m \sim 1$). Where only the main stem mass has equilibrated ($L_{trib} < 1/\alpha$; $L_{ms} > 1/\alpha$), the fractional change in mass $\Delta M/M_m \approx 1 - e^{-\alpha L_{trib}}$ and where both stream lengths are less than $1/\alpha$, the fractional mass change $\Delta M/M_m \approx (1 - e^{-\alpha L_{trib}})/(1 - e^{-\alpha L_{ms}})$. As shown in Figure 11a, the mass perturbation will decay exponentially downstream, because the sediment resupply from side slope erosion is only sufficient to sustain the original main stem bed load flux M_m. The length scale for the decay of the mass is simply $1/\alpha$, the distance over which 95% of the tributary mass will have been abraded to silt.

[51] Where tributaries transport a coarser size distribution than the main stem, the mean size distribution of the sediment mixture immediately downstream will be approximately equal to the average of the two distributions, weighted by their relative mass contribution. For lognormal pdfs of bed load sediments we can use a simple mixing relation to calculate the change in mean grain size ($\Delta D = D_{mix} - D_m$) as a function of the mean grain sizes of
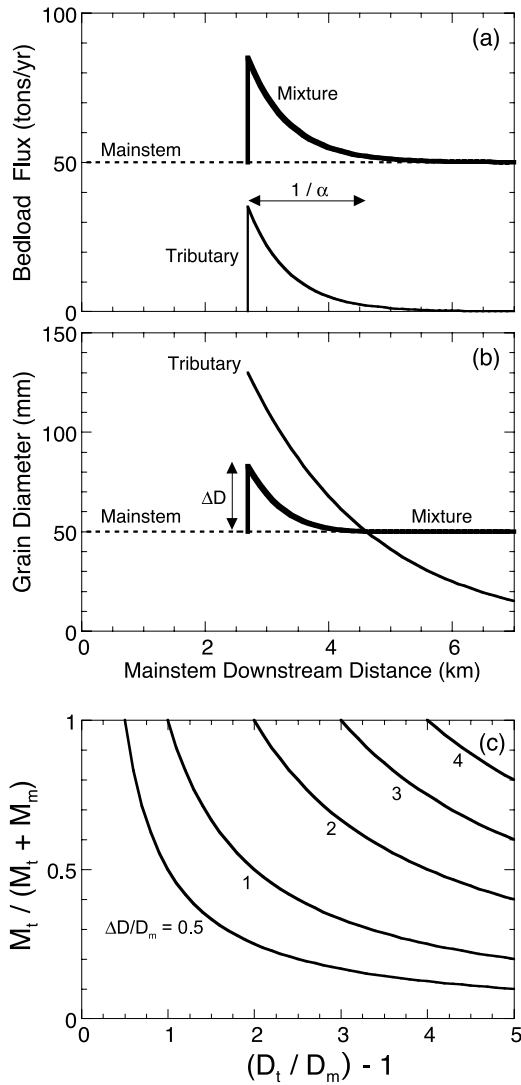
Figure 11. Perturbations to main stem bed load flux and mean grain size at individual tributary junctions. (a) Variation in bed load mass flux with downstream distance of the main stem sediments supplied from upstream and the valley side slopes M_m, the sediments supplied by the tributary M_t, and the resulting sediment mixture M_{mix}. (b) Variation in mean grain size with downstream distance of the tributary D_t and mainstream D_m sediments and the resulting sediment mixture D_{mix}. (c) Contours of constant relative grain size perturbation $\Delta D/D_m$ as a function of the mass fraction of tributary sediments $M_t/(M_t + M_m)$ and ratio $(D_t/D_m) - 1$ at the tributary junction.

the main stem (D_m) and tributary (D_t) and the bed load mass of the two streams, M_m and M_t respectively, as

$$\frac{\Delta D}{D_m} = \left(\frac{M_t}{M_t + M_m}\right)\left(\frac{D_t}{D_m} - 1\right) \quad (25)$$

Note the constraint that $0 \leq [M_t/(M_t + M_m)] \leq 1$.

[52] Figure 11c shows solutions of equation (25) as contours of constant ($\Delta D/D_m$), for the relative grain size range of $1 < D_t/D_m < 5$, and for all possible mass ratios. Small perturbations in grain size (e.g., $\Delta D/D_m = 0.5$) occur

when the tributary mass contribution is small but the grain size difference is large, or when the grain size difference is small but the tributary mass is large. For large grain size changes (e.g., $\Delta D/D_m = 4$) both the mass contribution and the grain size difference must be large. The distance over which the grain size perturbation decays $L_{\Delta D}^*$ will scale with the travel distance required to abrade the coarser tributary sediments down to the size of the main stem inputs from upstream

$$L_{\Delta D}^* = \frac{1}{\alpha} \ln\left(\frac{D_t}{D_m}\right) \quad (26)$$

These results are consistent with the field observations and qualitative arguments of *Knighton* [1980].

3.2.2. Multiple Tributary Junctions

[53] If the spacing between tributary junctions is small relative to the tributary mass decay length scale $1/\alpha$ then the effects on the main stem of an individual tributary sediment injection will be superposed on the partially decayed legacy of upstream tributary junctions. Conversely, if $1/\alpha$ is much smaller than the distance between tributary junctions, then the bed load sediments of large segments of the main stem channel will reflect only the local valley side slope supply, with no hint of disruptions due to upstream tributary junctions. Here we explore the range of potential bed load mass flux variability along the main stem of the Noyo River, by varying the rock durability parameter α over three orders of magnitude.

[54] For this calculation we selected the 26 tributaries entering the Noyo River main stem along its ~20 km course that have a contributing area greater than 0.38 km^2. Every junction is associated with a main stem channel length segment. (Each channel segment arc has a unique length, the average is ~100 m.) For the remaining nontributary channel segments we then used the length-weighted average incremental drainage area addition ($a = 0.68$ km^2/km), and equation (24), to calculate an average valley side slope loading rate (q_{vss}) of 0.17 tons/yr km, and assumed that this value applies to the main stem and each tributary above its confluence with the main stem. For each tributary we measured the upstream maximum travel distance within the subnetwork to obtain L_{trib} and calculated the bed load mass flux of the tributary M_t and the main stem M_m just upstream of the confluence using a simplified form of equation (15)

$$M(L) = \frac{q_{vss}}{3\alpha}\left(1 - e^{-3\alpha L}\right) \quad (27)$$

For $L = 1/\alpha$ the bed load flux approaches the steady state value $M_{ss} \approx q_{vss}/3\alpha$.

[55] Figure 12 shows a dramatic difference in the predicted pattern of bed load flux variation along the main stem, due to the combination of tributary and main stem valley side slope inputs, as we vary α from 0.01/m (very weak rocks) to 0.00001/m (very hard rocks). When the bed load sediments break down very rapidly ($\alpha = 0.01$/m; Figure 12a), the bed load flux of both the tributary and the main stem is at the steady state side slope supply value M_{ss}, and the main stem flux doubles at each tributary junction. The doubling is short-lived, however, as the perturbation to the main stem bed load flux decays very rapidly. For this end-member case of very weak rocks, the bed load flux at any point along the main stem channel is
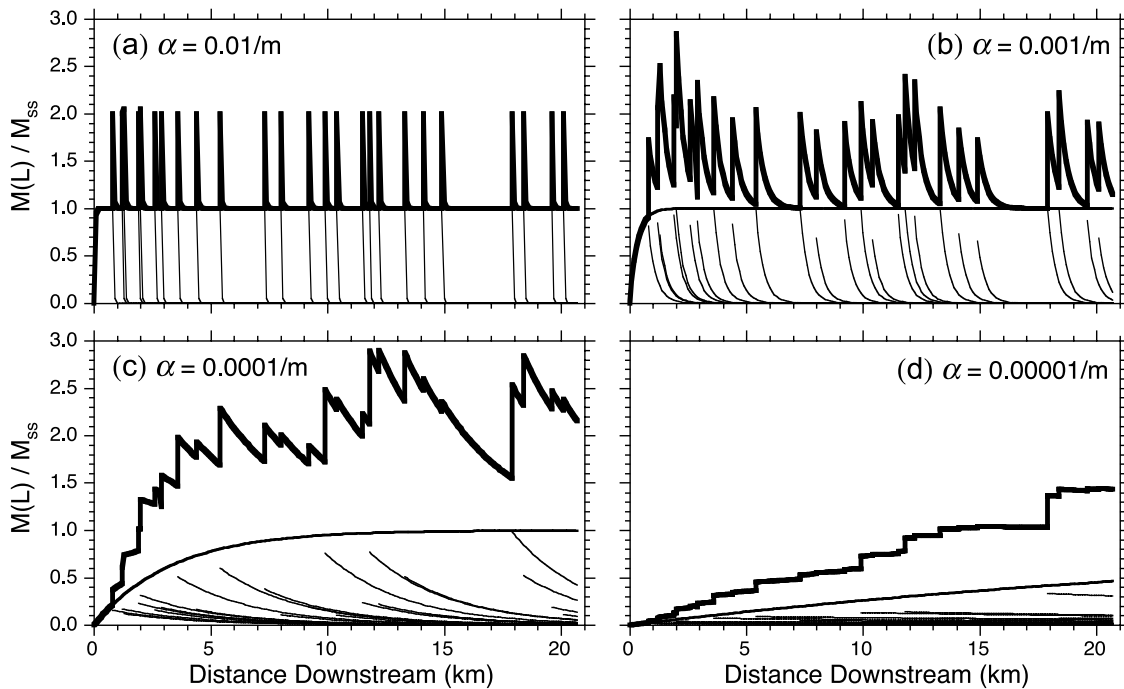
Figure 12. Variation in bed load mass flux along the Noyo River main stem due to tributary sediment inputs for various values of the abrasion coefficient α. Mass flux $M(L)$ is normalized by the steady state mass flux M_{ss} for uniform side slope input $q(L) = 170$ ton yr^{-1} km^{-1}. Thickest line shows total mass flux M_{mix}, which is a sum of the tributary bed load M_t (thinnest lines, lower portion of each panel) and the main stem bed load due to valley side slope supply M_m (medium thick line, which asymptotes to M_{ss}).

essentially independent of both the drainage area of any individual tributary basin and the spacing between tributary junctions.

[56] Differences among tributary junctions begin to emerge when we consider moderately weak rocks ($\alpha = 0.001$/m; Figure 12b). The perturbation decay length scale $1/\alpha$ is an order of magnitude longer than in the previous case, longer than the spacing between most adjacent confluences. Only two gaps between junctions (at $L_m \sim 7$ and 17 km) are large enough for the mass flux to drop back to the steady state value M_{ss}. Some of the smaller tributary basins have $L_{trib} < 1/\alpha$ and thus contribute less than M_{ss} to the bed load mixture, however, even the smallest subbasins have reached $\sim$70% of the steady state flux. As a result, there is some minor variability in the size of the main stem flux perturbation, mostly due to the occurrence of some closely spaced confluences, where the tributary mass superposition is significant.

[57] Increasing rock durability by another order of magnitude ($\alpha = 0.0001$/m; Figure 12c) fundamentally alters the pattern. For these moderately hard sediments, the tributary decay distance $1/\alpha$ is greater than all interjunction distances, and much greater than most, so that tributary superposition elevates the average main stem flux to roughly double M_{ss}. Pronounced differences emerge in the magnitude of mass perturbations caused by tributaries of differing sizes. Large tributaries, particularly those entering downstream of a long unbranched length (e.g., $L_m \sim 18$ km), cause the largest change in bed load flux, while small tributaries (e.g., $L_m \sim 8$ km) result in very small changes in flux, but do have the effect of resetting the decay and prolonging the spatial duration of elevated bed load mass.

[58] For the end-member case of very hard rock ($\alpha = 0.00001$/m; Figure 12d), the decay distance $1/\alpha$ is much longer than the entire modeled profile length so that bed load mass flux, due to both tributary and valley side slope supply, increases steadily, roughly in proportion to the increase in upstream drainage area. Individual confluences result in step function increases in bed load, with no portions of the profile showing downstream decline in flux. At the downstream end of the 20km profile, bed load mass due to valley side slope supply has grown to about half of the steady state side slope flux M_{ss} of 6000 ton/yr. Because of abrasion, however, the total mass flux is only 20% of the total upstream coarse sediment supply for this 160 km^2 basin.

3.3. Width Function

[59] We now consider how the branching structure of channel networks, as represented by the width function, might influence bed material grain size distributions and bed load mass flux at any single point within the network. The width function (Figure 2a) is the distribution of travel distances to a downstream point, and its low-frequency component broadly reflects the shape of the drainage basin [e.g., *Rinaldo et al.*, 1995], and at finer scales reflects the internal branching structure of the network [e.g., *Troutman and Karlinger*, 1984; *Rinaldo et al.*, 1993]. Because size reduction by abrasion is a simple function of travel distance, it is reasonable to expect that basins with differing width functions will have different bed material characteristics. Moreover, because the width function is a function of length, its characteristic scales of variability in the low-frequency component (depicting the shape of the basin) and its high-frequency components (depicting the fractality of
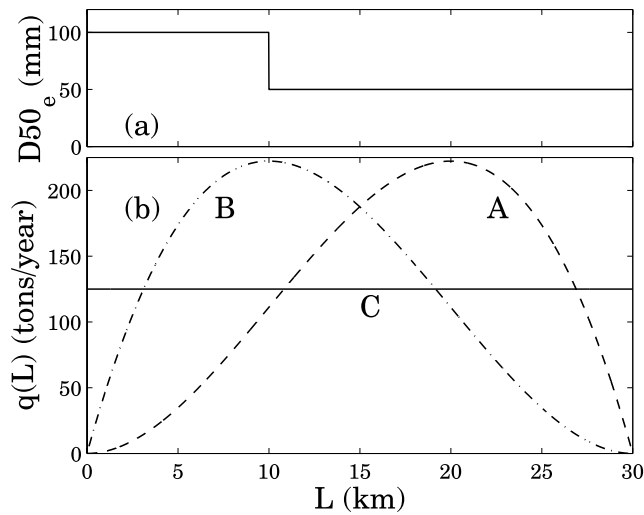
Figure 13. Variable entering sediment size and load rates for numerical experiments with the width function. (a) Entering grain size used only in experiment of Figure 16 showing abrupt downstream fining of supply at L = 10 km. (b) Three different load rate functions (A, B, and C), where functions A and B mimic the lateral load that would enter the main stem in two different basins of width functions having shapes similar to A and B and C is equivalent to a constant width basin. The outlet of the basin is at distance L = 30 km.

the branching structure), relative to the fundamental abrasion length scale $1/\alpha$, will influence both the grain size pdf and mass of bed load sediment at the outlet of the basin. Note that if the erosion rate E and the incremental drainage area per unit channel length a are uniform across the basin, the width function would be equivalent to the incremental sediment loading function $q(L)$.

[60] Here we report the results of three numerical experiments in which we compare three different loading functions (equivalent to width function shapes), shown in Figure 13b. Note that the basin outlet is located at L = 30 km, so that the upstream is on the left of Figure 13 and the downstream on the right, the reverse of the conventional representation of the width function. The basin that corresponds to width function "A" would have a large fraction of the drainage area located close to the outlet. The most common basin shape, which narrows toward the outlet and only has a small area fraction close to the outlet, would correspond to "B." Width function "C" is equivalent to a long, narrow basin without significant branching structure.

3.3.1. Effect of Variance of the Entering Sediment pdf

[61] In the first experiment we varied the spread of the distribution of entering sediment to see how the basin shape would affect the resulting pdf of bed load sediment at the outlet. We used the same four pdfs of entering sediment, one of constant size and the other three lognormal, as in Figure 6 and Table 1. Figure 14 shows the steady state bed load sediment pdfs of the four entering sediment pdfs, for each of the three width functions. Two clear patterns are apparent.

[62] First, there is a systematic difference in the extent to which the bed load pdfs are different from the entering pdfs,
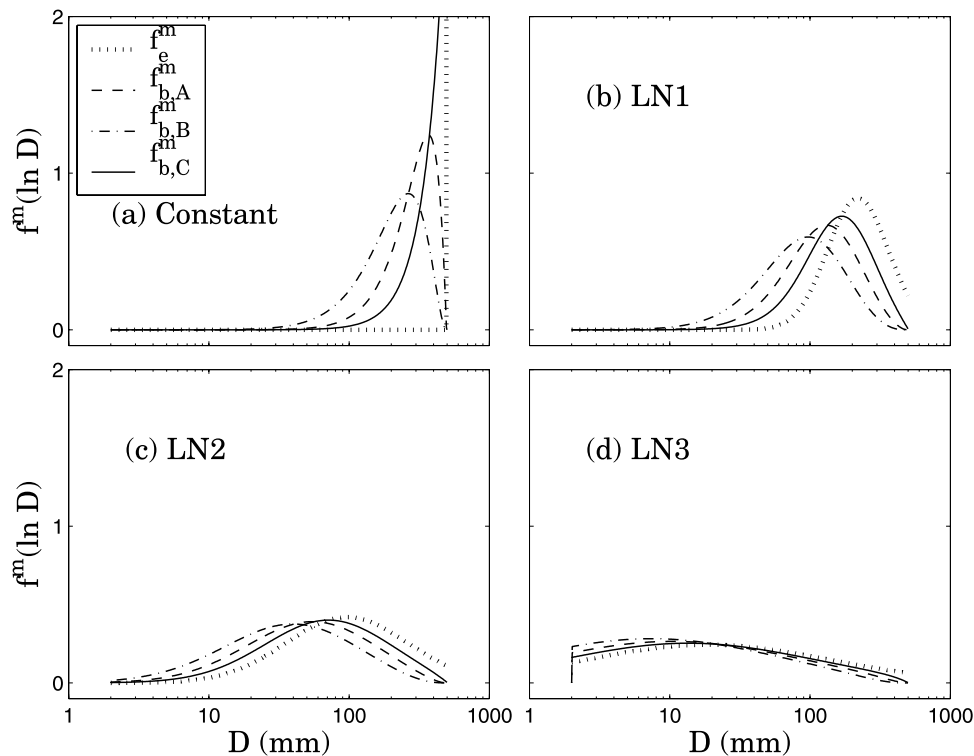
Figure 14. Comparison of the pdfs of entering and steady state bed load diameter by mass for the three different load functions A, B, and C given in Figure 13 for four input pdfs of varying width (Table 1): (a) a constant size of entering sediment D_e = 500 mm, (b) LN1, (c) LN2, and (d) LN3.
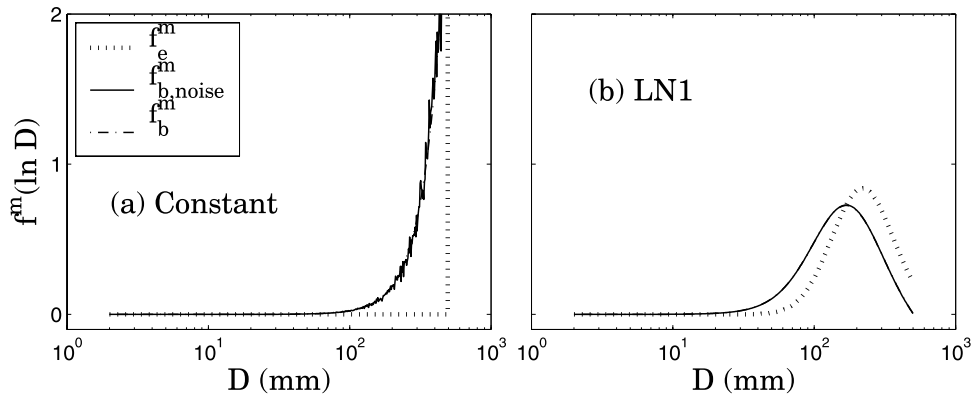
Figure 15. Comparison of pdfs of entering sediment diameter by mass $f_e^{\ m}(\ln D_e)$ (dashed lines) to those of the steady state pdfs by mass of the bed load $f_b^{\ m}(\ln D)$ (solid lines) for (a) the constant size and (b) the narrow width pdf LN1 for a constant load function with 10% Gaussian noise. Note how the fluctuations in the load are dissipated when there is even modest width to the pdf of the entering sediment.

which is most apparent for the case of a single uniform entering grain size (Figure 14a). Width function C is the least modified, B is the most modified, and A is intermediate. This pattern can be explained by considering the area under the loading curves in Figure 13 and recognizing that for this example the travel distance required to convert the coarsest entering grains to sand ($L^* = 27.6$ km) is the same order of magnitude as the length of the simulated basins. The loading nearest the outlet ($L \sim 30$ km) will have the greatest influence on the bed load pdf, particularly for the pdf by mass because of the cubic dependence of mass on grain diameter. Width function 'C' has the largest near-outlet loading and thus produces a bed load pdf that most closely resembles the entering sediment pdf, while B has very little loading over the nearest 5 km to the outlet so much more of its sediments have been reduced in size by abrasion.

[63] Second, as the variance of the entering sediment pdf increases, the effect of the differing width functions decreases. For the distribution with the largest variance, LN3 (Figure 14d), there is almost no difference between the width functions A, B and C, implying a very weak dependence of the bed load sediment pdf on the basin shape and the branching structure of the river network. Width function C is equivalent to the analytical result discussed above for a constant load q (Figure 6). The effect of the asymmetrical loading is to allow abrasion to modify the entering pdf slightly more extensively, by suppressing the resupply of the fresh entering pdf near the outlet. This near-outlet resupply reduction is greater for the case of B than A, thus the B bed load pdfs are somewhat finer than the others, even for the largest variance (Figure 14d). Overall, however, it can be said that for highly unsorted sediment entering from the hillslopes, the structure of the river network does not leave its imprint on the bed load sediment size downstream.

3.3.2. High-Frequency Variability in Sediment Supply and Travel Distances

[64] For the problem under consideration, i.e., bed material grain size distribution and bed load mass flux, the fractality of the river network enters into the picture in two distinct but related ways. First, the sediment supply to the main stem can be considered proportional to the incremental drainage area per unit channel length, which is known to exhibit high-frequency variability (e.g.,

Figure 2c). Second, the travel distances to the outlet, which control the size reduction by abrasion, are also known to exhibit high-frequency variability and are imprinted in the high-frequency fluctuations of the width function, which have been extensively studied in the literature [e.g., *Rinaldo et al.*, 1993].

[65] These two sources of high-frequency variability are bound to influence the bed load size distribution but it is not obvious how. Here we have performed a numerical experiment in which a channel reach of 30 km receives a lateral load with high-frequency fluctuations mimicking those of the incremental area per unit channel length of Figure 2c. This load function $q(L)$ is created by superimposing Gaussian white noise on a constant load q, and the standard deviation of the noise is set as 10% of the constant load.

[66] Figure 15 shows the steady state bed load pdfs by mass for the case of constant entering sediment load (solid lines) and load with high-frequency fluctuations superimposed (dashed lines) and for two pdfs of entering sediment (constant size and narrow-width lognormal). We observe that only in the case of a single input sediment size do the high-frequency fluctuations in the load get propagated to the pdf of the bed load sediment. In all other cases, the high-frequency variability of the input sediment is effectively eliminated even by the most modest variance of input sediment (LN1 in Figure 15b). Fluctuations of long memory or long-range dependence and power law distributions can be easily tested and will be the subject of subsequent research.

3.3.3. Effect of the Abrasion Length Scale $1/\alpha$

[67] As previous examples have illustrated clearly, the rock durability parameter α sets the length scale for the downstream propagation of signals created by spatial variability in the rate and grain size of sediments supplied to the channel network. Here we investigate how this fundamental length scale modulates the influence of the upstream basin shape on the bed load sediments passing the outlet. For this experiment we use the simple pdf of a single entering grain size, and impose an abrupt shift 20 km upstream of the outlet (Figure 13a), from $D_e = 100$ mm upstream to $D_e = 50$ mm downstream; rock durability is assumed equal for both entering sizes. To simulate the range of possible outcomes for rocks ranging in strength from
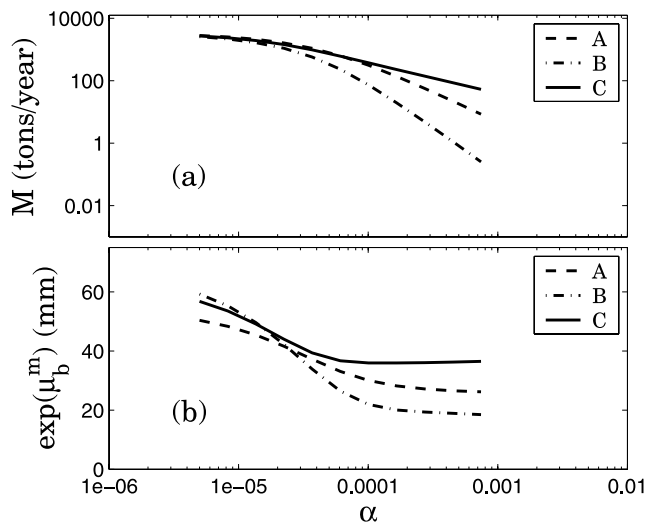
Figure 16. (a) Mass flux and (b) geometric means of the bed load sediment for the load functions A, B, and C of Figure 13 as a function of the abrasion coefficient α.

very hard to very weak we vary α through almost three orders of magnitude.

[68] Figure 16a shows the variation in bed load mass flux for the three basin shapes (A, B, and C, Figure 13) over the range of rock durability. For the hardest rocks ($\alpha \approx 0.00001$/m), there is no significant difference between the three width functions, abrasion is so inefficient that the mass flux scales simply with the area under the width function curves (Figure 13), which is the same for each basin shape. As rock durability declines (greater values of α) the bed load mass flux out of each basin is reduced, due to the increased mass transfer from bed load to suspended load by abrasion upstream of the outlet. The reduction in bed load flux with increasing α is most pronounced for basin B, and least for basin C because of the increased importance of the sediment input rate from the portion of the basin located close to the outlet. For the weakest rocks simulated ($\alpha = 0.001$/m), the length scale for mass equilibration with the local supply rate is approximately 1% of the basin length; virtually all gravel and coarser material supplied to the channel network by hillslopes is ground to silt before passing the outlet point. The modeled step function fining in entering sediment grain size at 20 km from the outlet does not significantly affect the bed load mass reaching the outlet, even when the rocks are very durable (low values of α).

[69] The effect of varying rock durability on the mean grain size of the bed load grain size distributions at the outlet is shown in Figure 16b, for the three width function shapes. When the rocks are very resistant to abrasion ($\alpha \approx 5 \times 10^{-6}$/m), all three width function shapes deliver a relatively coarse mean grain size to the outlet, because the coarser 100mm particles supplied from upstream retain significant mass at the outlet despite their long travel distance. The mean delivered by width function shape A is less coarse than the means for the other two shapes because A has about half as much area under the loading curve upstream of the shift in input sizes as the other two width functions. As rock durability decreases (α increases), the mean grain size for all width functions becomes smaller

because the downstream finer supply begins to dominate. For the weakest rocks the mean grain size is no longer a mix of the coarse and fine supplies because all the coarse grains are ground to silt before reaching the outlet. Instead, for this example, the variation between width functions in the mean grain size depends on the rate of change of the loading nearest the outlet. Width function C has a uniform load and thus delivers the steady state bed load size distribution that evolves from the single size input of 50 mm. Width functions A and B deliver finer sediments to the outlet than 'C' because the load rates are declining, particularly for B, such that the resupply near the outlet does not fully offset the size reduction of the sediments supplied just upstream.

[70] This example illustrates that the basin shape and branching structure can influence grain size distributions at a downstream point in the network, but the effect of variable width function shape is strongly modulated by the efficiency of particle abrasion.

4. Discussion

[71] Contrary to our initial expectations, channel network structure alone does not appear to meaningfully influence bed material grain size distributions. Rather, basin shape and the internal branching pattern can either amplify or dampen the effects of spatial variability in the size of sediments delivered to channels by hillslopes. In the absence of strong spatial variations in input sizes, rock durability or erosion rate, downstream abrasion and continuous replenishment of coarse sediment supply combine to drive the channel system to a steady state bed load flux and size distribution independent of network structure. As illustrated above, the influence on bed load variability of channel network properties such as the width function and the spacing between tributary junctions depends on the fundamental length scale imposed by particle abrasion. Sediments derived from weak rocks wear to silt over such a short distance that the evidence of the upstream network structure is effectively destroyed. The most abrasion-resistant rocks require such long distances to wear significantly that differences in travel path to a point don't result in strong differences in grain size. It is for sediments of intermediate rock durability that we expect the greatest variability in bed load mass, because fluctuations in valley side slope supply (Figure 2c), tributary junction spacing (Figure 12c), and basin width are most likely to occur at length scales that allow for significant wear but not complete destruction of sediments supplied from upstream.

[72] Our results offer a new perspective on the debate over the cause of downstream fining. As *Rice* [1999] and *Heller et al.* [2001] have previously suggested, abrasion alone will not cause fining when there is active resupply from local sources, which there must be over a sufficiently long timescale. Thus observed patterns of fining in actively incising terrain may be due to a combination of relatively short-term ($\sim 1-10$ ka) selective transport of finer bed load material and net deposition of coarser grains, and a systematic landscape-scale gradient in the size distribution of sediments delivered by hillslope processes. This second scenario has been previously suggested by *Pizzuto* [1995] in modeling the pattern of fining first reported by *Brush* [1961] in an Appalachian watershed with strong lithologic contrasts.

[73] The tendency for bed load mass flux to approach a steady state value has important implications for understanding the influence of sediment supply on river incision and landscape evolution. From our analysis and simulations, a picture emerges of the mobile bed load mass as a silt factory, which efficiently adjusts its productivity to match the rate of coarse sediment input. Contrary to the common assumption that bed load mass flux increases steadily with increasing drainage area, our results suggest that bed load mass equilibrates with hillslope supply over a length scale of $1/\alpha$, after which it becomes independent of drainage area. For spatially uniform sediment inputs, the fraction of the total load that travels in suspension should then increase downstream while the bed load fraction is reduced. Discharge obviously does scale with drainage area [e.g., *Leopold and Maddock*, 1953; *Gupta et al.*, 1996], so that we might expect the ratio of bed load sediment supply to transport capacity to decrease downstream, resulting in greater exposure of bedrock in the channel bed [*Sklar and Dietrich*, 1998, 2004] and perhaps a less rapid growth in the bedrock channel width with downstream distance [e.g., *Montgomery and Gran*, 2001; *Whipple*, 2004]. If the slope of bedrock rivers depends on the bed load sediment supply relative to transport capacity [*Sklar and Dietrich*, 2006], then tributary junctions where $L_{trib} < 1/\alpha < L_m$ might form convexities in the main stem profile, even in the absence of grain size variations [*Sklar and Dietrich*, 1998]. This would occur because the marginal increase in main stem load downstream of the junction is greater than the increase in discharge, requiring a steeper slope than upstream of the junction to maintain partial exposure of bedrock and active bed incision. In the extreme case, hanging valleys could result where tributaries with high bed load sediment loads relative to available discharge cannot incise rapidly enough to keep up with main stem channels that have abundant discharge but only limited bed load flux. Because bedrock lithology and rainfall are generally heterogeneous at length scales equal to or less than the abrasion length scale $1/\alpha$, feedbacks between hillslope sediment supply, bed load composition, and bedrock incision may be important in driving dynamic evolution of the drainage network structure itself.

[74] We can also use our results to speculate about the influence of rock durability on the timescale of adjustment of bed material to shifts in sediment supply. Temporal variations in the size distribution or rate of sediment supply might be caused at longer timescales by changes in hillslope sediment production processes brought on by changes in climate [e.g., *Inman and Jenkins*, 1999] or erosion rate [e.g., *Peizhen et al.*, 2001] or exhumation of different lithologies [e.g., *Clapp et al.*, 2000], and at shorter timescales by shifts in land use [e.g., *Doyle and Shields*, 2000] or simply the temporal variability in sediment delivery inherent in magnitude-frequency relations of different hillslope sediment production and transport processes (e.g., landsliding versus soil creep). The timescale of bed response τ should scale with the ratio of the abrasion length scale L_D^* to the average sediment velocity u_s

$$\tau \approx \frac{L_D^*}{u_s} = \frac{\ln(D_{\max}/D_{\min})}{\alpha u_s} \qquad (28)$$

Annual downstream transport distances for gravel- and cobble-sized grains are of order 100m [e.g., *Hassan et al.*, 1991] so, for example, if $D_{\max} = 100$ mm, $\alpha = 0.0002$/m, and $L_D^* \sim 20$ km, then approximately $\tau = 200$ years are required for the evidence (in the bed load) of the prechange sediment supply to be destroyed. For harder, coarser rocks (e.g., $D_{\max} = 500$ mm, $\alpha = 0.00005$/m, $L_D^* \sim 100$ km), $\tau = 1000$ years, while for weaker rocks producing a finer grained supply (e.g., $D_{\max} = 50$ mm, $\alpha = 0.005$/m, $L_D^* \sim 0.6$ km) τ might be less than a decade. This back of the envelope calculation suggests that the composition of active river bed sediments adjusts quite rapidly to temporal changes in sediment supply characteristics, and that significant supply from long-term storage reservoirs in floodplains, terraces and fans is required for a previous sediment supply regime to maintain its influence over contemporary bed materials.

[75] The predicted tendency for the mass flux to reach a steady state $M_{ss} = q/3\alpha$ after a distance L_D^* downstream of the most distant channel head may provide a simple method for estimating long-term average bed load in a field setting. This would require estimating the average hillslope sediment production rate, the fraction of the hillslope sediment supply coarse enough to move initially as bed load, and a representative value for the abrasion coefficient α. The local topography and channel network structure can then be used to determine the incremental area per unit channel length and the location of L_D^*. Estimates of M_{ss} might be useful in a wide variety of practical and theoretical contexts, from predicting the gravel fraction of reservoir sediment deposits [e.g., *Willis and Griggs*, 2003] to interpreting longitudinal profile concavity [e.g., *Sklar and Dietrich*, 2006].

[76] Caution in sampling bed load material sediments ($D \gg 2$ mm) for cosmogenic radionuclide estimates of watershed-scale erosion rates [e.g., *Reusser et al.*, 2004; *Wolkowinsky and Granger*, 2004] is also suggested by our results. The more efficient the abrasion process (greater α), the less the bed material will reflect watershed-wide sediment supply conditions. For the weakest rocks, only the most local sources will be represented in a sample of bed load material. Even for the hardest rocks, for sufficiently large basins abrasion will tend to destroy the signal carried by coarse sediments entering in the distal portions of the watershed. Although not considered here, suspended material is also subjected to abrasion during transport, so that samples of sand may also be biased toward the local supply.

[77] Two major priorities for further research are suggested by this work. First, the overarching question of what controls the grain size distribution of sediments supplied by hillslopes to the channel network encompasses a rich set of questions about the roles of, and feedbacks between, bedrock lithology, climate, erosion rate, and hillslope sediment production and transport processes, and represents a broad frontier in process geomorphology. Second, and more narrowly important, we need an improved basis for quantifying the rate of abrasion of bed load sediments in rivers. The Sternberg abrasion coefficient α sets the scale for bed material evolution, yet this model parameter remains somewhat of a black box. Improved models for grain size reduction that account for splitting as well as abrasion may also change the predicted extent and pattern of grain

size evolution with downstream transport. Methods are needed both for translating experimental measurements of size reduction and calibrations of α to specific field contexts, and for distinguishing in the field the particle size reduction due to abrasion from other sources of spatial variability in bed material grain size.

5. Conclusion

[78] We began this study with the thought experiment of standing next to a gravel river bed in actively incising terrain, looking upstream, and asking how the distribution of fluvial travel distances and transport pathways imposed by the drainage network structure should affect the size distribution and flux rates of the bed material at this point. We conclude that we need to look farther upstream, out of the channel and up to the hillslope source of sediments, to understand the spatial trends and variability in bed load size distributions. The processes of particle size reduction by abrasion during transport, and resupply of the entering sediment by local sources, combine to drive the bed load transport system toward two related equilibria: a steady state grain size distribution that differs little from the hillslope supply, and a steady state mass flux that abrades bed load mass to silt at the rate of resupply of coarse sediment. The efficiency of abrasion, parameterized by α, the exponent in the exponential abrasion rate law, sets the fundamental length scale for bed material adjustment to spatial and temporal changes in sediment supply characteristics, whether those changes are due to emergent properties of the channel network structure such as tributary junction spacing, or locally contingent factors introduced by lithologic contacts or changes in land use. Rock durability, the dominant factor in abrasion efficiency, then controls where and how spatial variation in sediment supply is expressed in the bed load size distribution and mass flux across the landscape. This work highlights the need to greatly improve our understanding of what controls the size distribution of sediments produced and delivered to channel networks by hillslopes.

Appendix A: Derivation of $f_b^g(D)$

A1. Constant D_e

[79] We use a derived distribution approach by which the pdf of a transformed random variable $Y = g(X)$ is easily seen to be given in terms of the pdf of X, $f_X(x)$, as

$$f_Y(y) = f_X(x)/|g'(x)| \tag{A1}$$

where $g'(x)$ is the derivative of $g(x)$. The relevant transformation here is Sternberg's law which transforms a distance, and thus lateral load over that distance, to a grain size D by

$$D(x) = D_e e^{-\alpha x} \tag{A2}$$

We note from (A2) that $dD/dx = -\alpha D$ and thus for a uniform lateral load of constant rate q (kg km^{-1} yr^{-1}) we can write that

$$f_b^g(D) = \frac{1}{L} \left/ \left| \frac{dD}{dx} \right| \right. = \frac{1}{\alpha DL} \tag{A3}$$

A2. The pdf of Entering Sediment $f_e^g(D_e)$

[80] The last formula (A3) can be generalized to the case for which the entering sediment is distributed according to a probability distribution by grain $f_e^g(D_e)$.

[81] Let us first assume that the length of the channel L is such that

$$L > L_{D,p}^* = \frac{1}{\alpha} \cdot \ln\left(\frac{D_{\max,p}}{D_{\min}}\right) \tag{A4}$$

i.e., the bed load distribution has reached its steady state. The entering sediments with size in the range $[D_e, D_e + dD_e]$ result in the following number of grains at distance L:

$$q \cdot f_e^g(D_e)dD_e \times L_{D_e}^* = q \frac{1}{\alpha} \cdot \ln\left(\frac{D_e}{D_{\min}}\right) f_e^g(D_e)dD_e \tag{A5}$$

since the corresponding "active" part of the channel ranges from the distance $L - L_{D_e}^*$ down to the distance L. The total number of grains is given by

$$\int_{D_{\min}}^{D_{\max,p}} q \frac{1}{\alpha} \cdot \ln\left(\frac{D_e}{D_{\min}}\right) f_e^g(D_e)dD_e \tag{A6}$$

and the relative weight of the entering sediments with size in $[D_e, D_e + dD_e]$ is then

$$p(D_e) = \frac{\ln\left(\frac{D_e}{D_{\min}}\right) f_e^g(D_e)dD_e}{\displaystyle\int_{D_{\min}}^{D_{\max,p}} \ln\left(\frac{D_e}{D_{\min}}\right) f_e^g(D_e)dD_e} \tag{A7}$$

[82] These bed load grains, (abraded from input sediments with size $[D_e, D_e + dD_e]$) are distributed with the following conditional pdf:

$$f_b^g(D|D_e) = \frac{1}{D \ln(D_e/D_{\min})} \tag{A8}$$

and thus the pdf of the bed load sediment is given by

$$f_b^g(D) = \int_{D_{\min}}^{D_{\max,p}} f_b^g(D|D_e)p(D_e)dD_e \tag{A9}$$

Simple calculations eventually lead to

$$f_b^g(D) = \frac{1}{D} \cdot \frac{\displaystyle\int_D^{D_{\max,p}} f_e^g(D_e)dD_e}{\displaystyle\int_{D_{\min}}^{D_{\max,p}} f_e^g(D_e) \ln\left(\frac{D_e}{D_{\min}}\right) dD_e} \tag{A10}$$

for $D_{\min} \leq D \leq D_{\max,p}$. The computation of the bed load sediment pdf in the nonsteady state case is similar and results in equation (14) in the text.

Appendix B: Derivation of $M(L)$

[83] The incremental mass change $dM(L)$ in a length of stream dL is given as

$$dM(L) = qdL - 3\alpha M(L)dL \qquad (B1)$$

where the first term in the right hand side is the entering mass over a distance dL and the second term is the lost mass by abrasion. This second term is derived by noting that each grain of size D_e entering at $L = 0$ becomes $D_i = D_e e^{-\alpha L}$ at distance L, and its mass $M_i = D_e^3 e^{-3\alpha L}$; thus the mass lost to abrasion for this grain is $dM_{a,i}(L) = M_i e^{-3\alpha L}$ and the total mass lost to abrasion from all grains $M_a(L) = \sum dM_{a,i}(L) = M(L)e^{-3\alpha L}$ yielding the total mass lost due to abrasion $dM_a(L) = -3\alpha M(L)dL$. From (B1), we solve for $M(L)$ assuming initial condition $M(0) = 0$ to get

$$M(L) = \frac{q}{3\alpha}\left(1 - e^{-3\alpha L}\right), \qquad L < L_D^* \qquad (B2)$$

[84] In the case of $L \geq L_D^*$, there do exist grains of initial size D_e that have been abraded to the size $D_{\min}$ and that are since washed out by the stream. At distance L, there are $N_e dL = q/kD_e^3 \, dL$ such grains, since all grains with size $D_{\min}$ at distance L have entered the stream at the same (upstream) distance $L - L_D^*$. The corresponding lost mass is $N_e k D_{\min}^3 \, dL = q\left(\dfrac{D_{\min}}{D_e}\right)^3 dL$. Equation (B1) then becomes

$$dM(L) = qdL - 3\alpha M(L)dL - q\left(\frac{D_e}{D_{\min}}\right)^3 dL \qquad (B3)$$

whose solution is, since $M(L_D^*)$ is analytically known through (B2)

$$M(L) = \frac{q}{3\alpha}\left[1 - \left(\frac{D_{\min}}{D_e}\right)^3\right], \qquad L \geq L_D^* \qquad (B4)$$

Note that for $L \geq L_D^*$ the bed load mass flux does not depend on L.

Notation

a	incremental drainage area per unit channel length $(\text{km}^2 \, \text{km}^{-1})$.
D	bed load grain diameter (mm).
D_e	diameter of entering sediment (mm).
$D_{\max}$	maximum bed load grain diameter; $D > D_{\max}$ is immobile (mm).
$D_{\max(L)}$	grain diameter that will wear to $D_{\min}$ after traveling a distance L (mm).
$D_{\max,p}$	maximum grain diameter having probability of nonexceedance p (mm).
$D_{\min}$	minimum bed load grain diameter; $D < D_{\min}$ travels in suspension (mm).
E	erosion rate (mm yr^{-1}).
$f_b^g(D)$	pdf of bed load grain diameter, frequency by number of grains.
$f_b^m(D)$	pdf of bed load grain diameter, frequency by mass.
$f_e^g(D_e)$	pdf of entering sediment diameter, frequency by number of grains.
$f_e^m(D_e)$	pdf of entering sediment diameter, frequency by mass.

$F_e^m(D_e)$	cumulative distribution of entering sediment diameter, by mass.
k	grain mass coefficient (kg m^{-3}).
L	downstream travel distance along channel (m or km).
L_D^*	travel distance to reach steady state bed load size distribution (m or km).
$L_{D,p}^*$	distance to steady state size distribution, entering pdf truncated at p.
L_M^*	travel distance to reach steady state bed load mass flux (m or km).
$L_{M,0.95}^*$	travel distance to reach 95% of steady state bed load mass flux (m or km).
$M(L)$	bed load sediment mass flux (kg yr^{-1}).
M_{ss}	steady state bed load mass flux (kg yr^{-1}).
N_e	Number of entering grains per unit distance (m^{-1}).
p	probability of nonexceedance.
q	uniform sediment load entering river laterally $(\text{kg m}^{-1} \, \text{yr}^{-1})$.
$q(L)$	spatially variable lateral sediment load $(\text{kg m}^{-1} \, \text{yr}^{-1})$.
u_s	annual average bed load particle velocity (m yr^{-1}).
α	abrasion coefficient (m^{-1}).
α_h	abrasion coefficient of hard rock (m^{-1}).
α_w	abrasion coefficient of weak rock (m^{-1}).
ΔD	change in mean main stem grain size across tributary junction (mm).
ΔM	change in main stem bed load mass flux across tributary junction (kg yr^{-1}).
ρ_s	sediment density (kg m^{-3}).
τ	timescale of bed response to changes in sediment supply.

References

Adams, J. (1978), Data for New Zealand pebble abrasion studies, *N. Z. J. Sci.*, *21*, 607–610.

Adams, J. (1979), Wear of unsound pebbles in river headwaters, *Science*, *203*, 171.

Bittelli, M., G. S. Campbell, and M. Flury (1999), Characterization of particle-size distribution in soils with a fragmentation model, *Soil Sci. Soc. Am. J.*, *63*, 782–788.

Brush, L. M. (1961), Drainage basins, channels, and flow characteristics of selected streams in central Pennsylvania, *U.S. Geol. Surv. Prof. Pap.*, *282-F*, 175 pp., U.S. Gov. Print. Off., Washington, D. C.

Clapp, E. M., P. R. Bierman, A. P. Schick, J. Lekach, Y. Enzel, and M. Caffee (2000), Sediment yield exceeds sediment production in arid region drainage basins, *Geology*, *28*, 995–998.

Dietrich, W. E., and T. Dunne (1978), Sediment budget for a small catchment in mountainous terrain, *Z. Geomorphol. Suppl.*, *29*, 191–206.

Dietrich, W. E., D. Bellugi, L. S. Sklar, J. D. Stock, A. M. Heimsath, and J. J. Roering (2003), Geomorphic transport laws for predicting landscape form and dynamics, in *Prediction in Geomorphology*, *Geophys. Monogr. Ser.*, vol. 135, edited by P. Wilcock and R. Iverson, pp. 103–132, AGU, Washington, D. C.

Dodov, B., and E. Foufoula-Georgiou (2005), Fluvial processes and streamflow variability: Interplay in the scale-frequency continuum and implications for scaling, *Water Resour. Res.*, *41*, W05005, doi:10.1029/2004WR003408.

Doyle, M. W., and F. D. Shields Jr. (2000), Incorporation of bed texture into a channel evolution model, *Geomorphology*, *34*, 291–309.

Ferguson, R. I., T. Hoey, S. Wathen, and A. Werritty (1996), Field evidence for rapid downstream fining of river gravels through selective transport, *Geology*, *24*, 179–182.

Gilbert, G. K. (1877), *Report on the Geology of the Henry Mountains: Geographical and Geological Survey of the Rocky Mountain Region*, 160 pp., Gov. Print. Off., Washington D. C.

Gomez, V., B. J. Rosser, D. H. Peacock, D. M. Hicks, and J. A. Palmer (2001), Downstream fining in a rapidly aggrading gravel bed river, *Water Resour. Res.*, *37*, 1813–1823.

Gupta, V. K., S. L. Castro, and T. M. Over (1996), On scaling exponents of spatial peak flows from rainfall and river network geometry, *J. Hydrol.*, *187*, 81–104.

Hack, J. T. (1957), Studies of longitudinal stream profiles in Virginia and Maryland, *U.S. Geol. Surv. Prof. Pap.*, *294-B*, 97 pp.

Hassan, M. A., M. Church, and A. P. Schick (1991), Distance of movement of coarse particles in gravel bed streams, *Water Resour. Res.*, *27*, 503–511.

Heller, P. L., P. E. Beland, N. F. Humphrey, S. K. Konrad, R. M. Lynds, M. E. McMilan, K. E. Valentine, Y. A. Widman, and D. J. Furbish (2001), Paradox of downstream fining and weathering-rind formation in the lower Hoh River, Olympic Peninsula, Washington, *Geology*, *29*, 971–974.

Hoey, T. B., and B. J. Bluck (1999), Identifying the controls over downstream fining of river gravels, *J. Sediment. Res., Sect. A*, *69*, 40–50.

Hooke, R. L., and N. R. Iverson (1995), Grain-size distribution in deforming subglacial tills: Role of grain fracture, *Geology*, *23*, 57–60.

Howard, A., and R. Dolan (1981), Geomorphology of the Colorado River in the Grand Canyon, *J. Geol.*, *89*, 269–299.

Inman, D. L., and S. A. Jenkins (1999), Climate change and the episodicity of sediment flux of small California rivers, *J. Geol.*, *107*, 251–270, doi:10.1086/314346.

Jacobson, R. B., and K. B. Gran (1999), Gravel sediment routing from widespread, low-intensity landscape disturbance, Current River Basin, Missouri, *Earth Surf. Processes Landforms*, *24*, 897–917.

Knighton, A. D. (1980), Longitudinal changes in size and sorting of streambed material in four English rivers, *Geol. Soc. Am. Bull.*, *91*, 55–62.

Kodama, Y. (1994a), Downstream changes in the lithology and grain-size of fluvial gravels, the Watarase River, Japan: Evidence of the role of downstream fining, *J. Sediment. Res., Sect. A*, *64*, 76–85.

Kodama, Y. (1994b), Experimental study of abrasion and its role in producing downstream fining in gravel-bed rivers, *J. Sediment. Res., Sect. A*, *64*, 76–85.

Kuenen, P. H. (1956), Experimental abrasion of pebbles 2. Rolling by current, *J. Geol.*, *64*, 336–368.

Leopold, L. B., and T. Maddock (1953), The hydraulic geometry of stream channels and some physiographic implications, *U.S. Geol. Surv. Prof. Pap.*, *252*, 56 pp.

Lewin, J., and P. A. Brewer (2002), Laboratory simulation of clast abrasion, *Earth Surf. Processes Landforms*, *27*, 145–164.

Malarz, R. (2005), Effects of flood abrasion of the Carpathian alluvial gravels, *Catena*, *64*, 1–26.

Matsuoka, N., and H. Sakai (1999), Rockfall activity from an alpine cliff during thawing periods, *Geomorphology*, *28*, 309–328.

Menabde, M., and M. Sivapalan (2001), Linking space-time variability of rainfall and runoff fields on a river network: A dynamic approach, *Adv. Water Res.*, *24*, 1001–1014.

Montgomery, D. R., and K. B. Gran (2001), Downstream variations in the width of bedrock channels, *Water Resour. Res.*, *37*, 1841–1846.

Montgomery, D. R., T. M. Massong, and S. C. S. Hawley (2003), Influence of debris flows and log jams on the location of pools and alluvial channel reaches, Oregon Coast Range, *Geol. Soc. Am. Bull.*, *115*, 78–88.

Moussavi-Harami, R., A. Mahboubi, and M. Khanehbad (2004), Analysis of controls on downstream fining along three gravel-bed rivers in the Band-e-Golestan drainage basin NE Iran, *Geomorphology*, *61*, 143–153.

Paola, C., G. Parker, R. Seal, S. K. Sinha, J. B. Southard, and P. R. Wilcock (1992), Downstream fining by selective deposition in a laboratory flume, *Science*, *258*, 1757–1760.

Parker, G., and P. C. Klingeman (1982), On why gravel bed streams are paved, *Water Resour. Res.*, *18*, 1409–1423.

Parker, G. (1990), Surface-based relation for bedload transport in gravel rivers, *J. Hydraul. Eng.*, *28*(4), 417–436.

Parker, G. (1991a), Selective sorting and abrasion of river gravel, I. Theory, *J. Hydraul. Eng.*, *117*, 131–149.

Parker, G. (1991b), Selective sorting and abrasion of river gravel, II. Applications, *J. Hydraul. Eng.*, *117*, 150–171.

Peizhen, Z., P. Molnar, and W. R. Downs (2001), Increased sedimentation rates and grain sizes 2–4 Myr ago due to the influence of climate change on erosion rates, *Nature*, *410*, 891–897, doi:10.1038/35073504.

Perfect, E. (1997), Fractal models for the fragmentation of rocks and soils: A review, *Eng. Geol.*, *48*, 185–198.

Pizzuto, J. E. (1995), Downstream fining in a network of gravel-bedded rivers, *Water Resour. Res.*, *31*, 753–759.

Posadas, A., D. Gimenez, M. Bittelli, C. M. P. Vaz, and M. Flury (2001), Multifractal characterization of soil particle-size distributions, *Soil Sci. Soc. Am. J.*, *65*, 1361–1367.

Reusser, L. J., P. R. Bierman, M. J. Pavich, E. Zen, J. Larsen, and R. Finkel (2004), Rapid late Pleistocene incision of Atlantic passive-margin river gorges, *Science*, *305*, 499–502.

Rice, S. (1998), Which tributaries disrupt downstream fining along gravel-bed rivers?, *Geomorphology*, *22*, 39–56.

Rice, S. (1999), The nature and controls on downstream fining within sedimentary links, *J. Sediment. Res., Sect. A*, *69*, 32–39.

Rice, S., and M. Church (1998), Grain size along two gravel-bed rivers: Statistical variation, spatial pattern and sedimentary links, *Earth Surf. Processes Landforms*, *23*, 345–363.

Rinaldo, A., I. Rodriguez-Itube, R. Rigon, E. Ijjasz-Vasquez, and R. L. Bras (1993), Self-organized fractal river networks, *Phys. Rev. Lett.*, *70*, 822–826.

Rinaldo, A., G. Vogel, R. Rigon, and I. Rodriguez-Iturbe (1995), Can one gauge the shape of a basin?, *Water Resour. Res.*, *31*, 1119–1127.

Rodriguez-Iturbe, I., and A. Rinaldo (1997), *Fractal River Basins: Chance and Self-Organization*, Cambridge Univ. Press, New York.

Schumm, S. A., and M. A. Stevens (1973), Abrasion in place: A mechanism for rounding and size reduction of coarse sediments in rivers, *Geology*, *1*, 37–40.

Sklar, L. S., and W. E. Dietrich (1998), River longitudinal profiles and bedrock incision models: Stream power and the influence of sediment supply, in *Rivers Over Rock: Fluvial Processes in Bedrock Channels*, *Geophys. Monogr. Ser.*, vol. 107, edited by K. J. Tinkler and E. E. Wohl, pp. 237–260, AGU, Washington, D. C.

Sklar, L. S., and W. E. Dietrich (2004), A mechanistic model for river incision into bedrock by saltating bedload, *Water Resour. Res.*, *40*, W06301, doi:10.1029/2003WR002496.

Sklar, L. S., and W. E. Dietrich (2006), The role of sediment in controlling bedrock channel slope: Implications of the saltation-abrasion incision model, *Geomorphology*, doi:10.1016/j.geomorph.2005.08.019, in press.

Stock, J. D., and W. E. Dietrich (2003), Valley incision by debris flows: Evidence of a topographic signature, *Water Resour. Res.*, *39*(4), 1089, doi:10.1029/2001WR001057.

Surian, N. (2002), Downstream variation in grain size along an Alpine river: Analysis of controls and processes, *Geomorphology*, *43*, 137–149.

Troutman, B. M., and M. R. Karlinger (1984), On the expected width function for topological random channel networks, *J. Appl. Probab.*, *22*, 836–849.

Troutman, B. M., and T. M. Over (2001), River flow mass exponents with fractal channel networks and rainfall, *Adv. Water Resour.*, *24*, 967–989.

Turcotte, D. L. (1997), *Fractals and Chaos in Geology and Geophysics*, 2nd ed., Cambridge Univ. Press, New York.

Venugopal, V., S. G. Roux, E. Foufoula-Georgiou, and A. Arneodo (2006), Revisiting multifractality of high-resolution temporal rainfall using a wavelet-based formalism, *Water Resour. Res.*, *42*, W06D14, doi:10.1029/2005WR004489.

Whipple, K. X. (2004), Bedrock rivers and the geomorphology of active orogens, *Annu. Rev. Earth Planet. Sci.*, *32*, 151–185.

Wilcock, P. R., S. T. Kenworthy, and J. C. Crowe (2001), Experimental study of the transport of mixed sand and gravel, *Water Resour. Res.*, *37*, 3349–3358.

Willis, C. M., and G. B. Griggs (2003), Reductions in fluvial sediment discharge by coastal dams in California and implications for beach sustainability, *J. Geol.*, *111*, 167–182, doi:10.1086/345922.

Wolkowinsky, A. J., and D. E. Granger (2004), Early Pleistocene incision of the San Juan River, Utah, dated with ^{26}Al and ^{10}Be, *Geology*, *32*, 749–752, doi:10.1130/G20541.1.

————————————

D. Bellugi and W. E. Dietrich, Department of Earth and Planetary Science, University of California, Berkeley, CA 94720, USA.

E. Foufoula-Georgiou and B. Lashermes, St. Anthony Falls Laboratory, 2 Third Avenue SE, Minneapolis, MN 55414, USA.

L. S. Sklar, Department of Geosciences, San Francisco State University, 1600 Holloway Avenue, San Francisco, CA 94132, USA. (leonard@sfsu.edu)

Toward a unified science of the Earth's surface: Opportunities for synthesis among hydrology, geomorphology, geochemistry, and ecology

Chris Paola,[1] Efi Foufoula-Georgiou,[2] William E. Dietrich,[3] Miki Hondzo,[2] David Mohrig,[4] Gary Parker,[5] Mary E. Power,[6] Ignacio Rodriguez-Iturbe,[7] Vaughan Voller,[2] and Peter Wilcock[8]

[1]   The Earth's surface is shaped by the interaction of tectonics, water, sediment, solutes, and biota over a wide range of spatial and temporal scales and across diverse environments. Development of a predictive science of Earth surface dynamics integrates many disciplines and approaches, including hydrology, geomorphology, ocean and atmospheric science, sedimentary and structural geology, geochemistry, and ecology. This paper discusses challenges, opportunities, and a few example problems that can serve as pathways toward this integration.

1.   Earth Surface Dynamics as an Integrator

[2]   Understanding the dynamics of the Earth's surface, from tectonic processes to microbial weathering, is one of the great integrating challenges of modern science. The emerging field of "morphodynamics," the study of the properties and evolution of surface morphology, is at the center of this challenge. Because the Earth's surface spans an enormous range of environments, spatial scales, and timescales, a fully realized science of Earth surface dynamics serves as a natural integrator of many disciplines and approaches, including hydrology, geomorphology, ocean and atmospheric science, geology and ecology. Unfortunately, the level of interaction among these fields to date has been nowhere near adequate to the task.

[3]   This short paper is a call for the scientific community to work together toward this grand goal: developing a unified surface process science that would integrate insight from all of the above fields to provide a comprehensive and predictive understanding of the dynamics of our planet's surface. Integrated Earth surface dynamics is at the core of

environmental science; after all, the Earth's surface is "the environment" for most life and human activity. Hydrology is clearly central to the effort, and not only because of the role of terrestrial surface and groundwater in creating surface morphology. A quantitative style is deeply ingrained in hydrology, hence it has much to offer in accelerating the infusion into Earth surface dynamics of quantitative methods for dealing with complex natural systems.

[4]   In this paper we focus on channels and channel networks as a starting point in the development of a unified approach to surface process science. Most of the continental surface is drained by channels, which can be seen as the arterial system of the landscape, which control, to a large extent, the spatial and temporal patterns of physical, chemical, and biotic processes. Channel networks illustrate a fascinating aspect of morphodynamics: the occurrence of similar patterns across a wide range of environments and scales. Tributary networks are the most prominent example but the list of recurring structures includes distributary networks; braided networks; bed forms; channel bends, bars, and scour pits; splays and lobes; and clinoforms (e.g., deltas, continental margins). These spatial patterns are not restricted to the terrestrial landscape but, with remarkable similarity of form, structure submarine landscapes as well.

[5]   The similarity of channel networks across environments and scales has been known for some time, but the last 20 years have seen a revolution in the range and power of quantitative tools to explore and measure spatial structure and similarity [*Rodriguez-Iturbe and Rinaldo*, 1997]. This has been accompanied by a dramatic increase in the quality and quantity of topographic data on which to apply them, and by major advances in the theory of fundamental channel structures [*Federici and Seminara*, 2003; *Parker and Izumi*, 2000; *Seminara and Tubino*, 1989, 2001; *Sun et al.*, 1996; *Sun and Parker*, 2005]. The importance of these recurring, self-formed patterns is not restricted to the physical landscape. By structuring the landscape and localizing the flow of water, sediment, and nutrients, channels and channel

[1]Department of Geology and Geophysics and St. Anthony Falls Laboratory, University of Minnesota Twin Cities, Minneapolis, Minnesota, USA.

[2]Department of Civil Engineering and St. Anthony Falls Laboratory, University of Minnesota Twin Cities, Minneapolis, Minnesota, USA.

[3]Department of Earth and Planetary Science, University of California, Berkeley, California, USA.

[4]Department of Earth, Atmospheric, and Planetary Science, Massachusetts Institute of Technology, Cambridge, Massachusetts, USA.

[5]Department of Civil Engineering, University of Illinois, Urbana, Illinois, USA.

[6]Department of Integrative Biology, University of California, Berkeley, California, USA.

[7]Department of Civil and Environmental Engineering, Princeton University, Princeton, New Jersey, USA.

[8]Department of Geography and Environmental Engineering, Johns Hopkins University, Baltimore, Maryland, USA.

networks play a major role in controlling spatial patterns and dynamics of biota and geochemical processes. The combination of ubiquity, similarity, and strong control on topography and material fluxes makes channel networks and related spatial forms a natural organizing template for environmental observation, modeling, and prediction. Channels and channel networks provide a common spatial framework for interpreting a broad range of local environmental observations, for transferring results from one system and scale to another (including from laboratory to nature), and, by understanding how the channel structure mediates organization in local physical, ecological, and geochemical variables (e.g., vegetation and fluxes of sediment and nutrients), for environmental modeling and prediction.

[6] Channel networks have been traditionally seen by hydrologists as relatively static boundary conditions. Water is routed through them to predict the hydrologic response of a basin to a given precipitation input. Less emphasis has been placed on the evolution of the channel geometry and the coevolution of the channel and its floodplain, which determine nutrient and sediment delivery downstream as well as the variability of extreme floods, which are influenced by overbank storage and release of water. In terms of physical processes, we can divide the surface realm into three broad timescales, corresponding to shortest scale on which important variability occurs: a "water" timescale of minutes to hours; a "sediment" timescale of hours to centuries, and a "tectonic" timescale of centuries and up. The static view of channel systems breaks down as we move from the "water" to the "sediment" scale because the channel geometry is essentially controlled by the sediment flux, including storage, at a given time. Thus the connection between hydrology and surface dynamics must strengthen as hydrologists tackle longer-term forecasting problems, or problems where changes in land use or climate could lead to major changes in sediment yield and hence channel properties and conveyance.

2. Motivation for Integrated Earth Surface Science: Three Examples

[7] There are many ways in which a unified approach to Earth surface dynamics would benefit science and society. Major application areas include environmental forecasting, river and landscape restoration and management, assessing location, size, and geometry of subsurface fluid conduits and reservoirs, hazard assessment and reduction, and quantifying cycling and storage of carbon and other major geochemical actors. Here we provide three examples that illustrate the need for combined research in hydrology, ecology, geochemistry, and geomorphology:

2.1. Generalized Environmental Forecasting: Beyond Climate

[8] It is now becoming possible to forecast the effect of, for instance, a doubling of atmospheric carbon dioxide level on rainfall and temperature in a given area [*Bonan et al.*, 2002; *Stainforth et al.*, 2005; *Intergovernmental Panel on Climate Change*, 2001]. How would such climatic changes affect streamflow and the spatial and temporal patterns of sediment and solute flux through the channel network? This question is difficult to answer for a static channel network and all the more difficult when dynamic interactions between network fluxes and geometry are considered. Chang-

ing rainfall, for example, would directly affect rates of sediment and solute creation and delivery to streams in ways that cannot at present be predicted with confidence. Sediment flux and caliber strongly influence channel dimensions and so would be expected to affect flood statistics and habitat. In addition, the rainfall changes could also change the distribution of biota from microbes to trees and burrowing animals on hillslopes and floodplains. These organisms are directly involved in mediating sediment production and delivery, so changes in the ecosystem could significantly affect sediment flow as well as channel morphology (through, for instance, bank stabilization). The point is that at present, considering the whole physical-biological-chemical system of a watershed, we cannot predict even qualitatively how it will respond to climate and land use changes.

2.2. Stream Restoration

[9] An increasing public interest in the environmental, recreational, and esthetic values of rivers has led to increased recognition of the impact of human actions and the desire to return rivers to a more natural, attractive, and resilient state. This has created a substantial demand for restoration or rehabilitation of impaired streams, creating a booming but mostly small-scale industry known generically as "stream restoration" [*Wohl et al.*, 2005]. Projects in the United States alone number in the tens of thousands, with associated costs measured in billions of dollars per year [*Bernhardt et al.*, 2005]. Restoration efforts range from local projects on short reaches of small streams to multibillion dollar projects such as restoration of the Everglades and the Mississippi Delta.

[10] The scientific basis for stream restoration is weak, the success of existing projects not well known, and the connection between research and practice is poorly developed. Current stream restoration practice is based on analogy; a template is sought in a nearby or idealized channel that the designer judges to be suitable. However, if a disturbed stream is adjusting to changes in essential controlling factors, a template for analog-based design is unlikely to exist [*Wilcock*, 1997]. What is needed instead is a testable, predictive framework linking cause and effect. Such a framework must be based on a quantitative, transdisciplinary understanding of the physical, chemical, and biological dimensions of disturbance and recovery in streams, accounting for natural and human-induced variability.

[11] A major challenge facing a predictive restoration science is placing the restoration project in a watershed context. The most obvious and persistent cause of physical failure is ignoring, or inadequately predicting, the supply of water and sediment from the watershed. Current best practice is generally based on a narrative watershed history identifying the timing and location of major watershed disturbances, including anthropogenic changes. Predictive restoration science requires transforming this history to a quantitative basis and integrating historical records with landscape-scale predictive modeling.

2.3. Surface to Subsurface

[12] The interaction of surface water and groundwater is a major research issue in hydrology. An analogous problem in surface dynamics is the relation between surface dynamics in active depositional systems and subsurface stratigraphy.

Depositional subsurface architecture in turn controls the spatial heterogeneity of permeability and porosity, and hence the flow of subsurface fluids like water and hydrocarbons. Major challenges include: understanding surface dynamics in depositional systems, including biotic influences; understanding how surface processes interact with external drivers like sea level, sediment supply, climate, and subsidence; and understanding how surface dynamics in time and space is transformed into three-dimensional subsurface structure. Modern high-resolution seismic imaging methods [*Davies and Posamentier*, 2005] provide subsurface data analogous to LIDAR topography data, except that the subsurface data are three-dimensional and provide a record of temporal evolution. Learning to exploit these records will transform sedimentary geology, and what it can tell us about both surface dynamics and subsurface structure, just as high-resolution topographic data have transformed geomorphology. The data are costly to obtain and are mostly privately held, so building new partnerships between academia and industry will be critical to advancing this field. However, the effort will be worthwhile: in addition to improved prediction of subsurface heterogeneity, quantitatively coupling surface to subsurface can help provide long-term flux records needed for sustainable restoration and landscape management.

3. Four Problems for Integrative Research

[13] Next we pose four problems in integrated Earth surface science that lie at the interface of hydrology, geomorphology, geochemistry, and ecology. These problems, structured around channel networks, represent opportunities for major advances during the coming decade: (1) understanding channel networks across environments and scales to learn from similarities and dissimilarities, (2) relating channel morphology and network geometry to the spatial organization and scaling of floods, sediment fluxes, riparian vegetation, and river food webs, (3) developing new mathematical techniques for modeling and prediction, and (4) exploring the role of new observational techniques and laboratory studies in advancing surface process research.

3.1. Channel Networks Across Environments and Scales: Tributary Networks, Deltas, Braided Rivers, and Submarine Channels

[14] Channels organize themselves into networks of various forms that recur across many environments and frequently show self-similarity. Some central questions are: How does the overall (macroscale) pattern arise from small-scale local interactions? What can be learned from the similarities and dissimilarities of those patterns across diverse environments e.g., subaerial and submarine, depositional and erosional? Can organizational principles of channels and channel networks be unified and their physical causes understood for the purposes of improved modeling and prediction? Considerable progress has been made over the years in regard to the scaling signatures of river basins in the upper portion of the river system where most of the water and sediment are produced [*Rodriguez-Iturbe and Rinaldo*, 1997]. The progress made in understanding the network structure in the erosional uplands stands in contrast with the fact that we are just beginning to understand the

distributary structure that characterizes depositional deltas and fans [*Syvitski*, 2005; *Sun et al.*, 2002]. Yet deltas and fans, though globally much smaller in area, are critical sediment sinks and so determine rates and patterns of delivery of sediment, organic matter, nutrients, and pollutants to the sea. They are also storehouses of hydrocarbons, home to a sizable fraction of the world's population, and as recent events make abundantly clear, a crucial buffer between ocean storms and urban and industrial centers.

[15] Another type of channel organization is that of braided channel systems [*Sambrook Smith et al.*, 2006]; these in effect have a topology intermediate between tributary (junction dominated) and distributary (division dominated) such that both junction types occur about equally often. These are highly complex dynamic systems characterized by intensive but spatially localized erosion, sediment transport and deposition and frequent channel shifting. They have been found to exhibit a statistical scale invariance in their morphology and dynamics which is of similar form in diverse flow regimes, slopes, types of bed material and braid plain widths, indicating the presence of universal features in the underlying mechanisms responsible for the formation of their spatial structure [*Foufoula-Georgiou and Sapozhnikov*, 2001; *Murray and Paola*, 1994; *Sapozhnikov and Foufoula-Georgiou*, 1997] We still need to improve our understanding of the hydraulic geometry of braid channels (e.g., depth-width relationships, velocities at junctions, speed of lateral channel shifts), how these channels interact with vegetation [*Bennett and Simon*, 2004], and how they dictate the spatial distribution and storage of hydrocarbons and other substances in the subsurface [*Lunt et al.*, 2004a, 2004b].

[16] The submarine landscape is veined with channel systems that appear to be analogous in many ways to their subaerial equivalents. Analogous morphologies include tributary systems [*Mitchell*, 2004], lobes, bed forms, and meandering channels [*Abreu et al.*, 2003; *Das et al.*, 2004; *Imran et al.*, 1999]. Submarine channel systems are formed largely by turbidity currents: density underflows driven by the weight of suspended sediment. At present, work on developing the analogy between subaerial and submarine channel systems is in a period of rapid growth, fueled in large part by intense interest in deep-water hydrocarbon reservoirs. Since each realm (subaerial, submarine) amplifies certain aspects of the fundamental channel dynamics relative to the other, we gain a clearer picture of channel dynamics by studying them together.

3.2. Effect of Network Topology and Channel-Floodplain Morphology on the Scaling of Floods, Sediment and Nutrient Fluxes, and Ecosystem Dynamics

[17] Scaling of floods has been the subject of considerable research in hydrology starting with the simple normalization methods, e.g., the index flood method, to the recent statistical multiscaling theories [*Gupta et al.*, 1994]. A key question concerns the variation of flood intensity and frequency with the drainage area of the basin (scale). Analysis of observations from several regions has supported the inference that floods exhibit a multiscaling structure (i.e., the statistical moments scale as power laws with drainage area with an exponent that depends nonlinearly on the order of the moment) with a scaling break at a characteristic scale. Although such an approach yields a concise statistical model which can be useful for regional

flood quantile estimation of design events, a number of open questions remain: For example, what is the physical origin of the observed scaling and what determines the scale of the break? What is the relative role of space-time precipitation variability versus geomorphologic controls, e.g., systematic variability of hydraulic geometry with scale and dynamic channel-floodplain interactions, in determining the scaling of floods and streamflow hydrographs [*Dodov and Foufoula-Georgiou*, 2004, 2005; *Menadbe and Sivapalan*, 2001]? Bringing sediment into the picture, what controls the size distribution of sediments produced and delivered to channel networks by hillslopes? How are the size distribution and flux rates of bed material affected by the drainage network struture? And how does bedload sediment flux relative to available discharge drive the dynamic evolution of the drainage network structure itself?

[18] Recent research has shed new light on how the spatial structure of ecosystems interacts with the spatial structure of the landscape [*Caylor et al.*, 2004, 2005; *Porporato et al.*, 2004; *Porporato and Rodriguez-Iturbe*, 2002]. Channel networks provide an organizing template for the ecohydrological and biogeochemical interactions that determine the vegetation patterns and ecosystem dynamics in a river basin. Important questions remain to be answered: What are the feedbacks between flow regime and dynamics of riparian vegetation? What is the relative role of large-scale determinants of vegetation patterns, e.g., optimal response to water stress, and smaller-scale controls mediated by the network structure? What is the relative role of space-time rainfall variability versus channel network topology in determining the spatial patterns and dynamics of vegetation? How does the physical structure of the landscape influence habitat quality and diversity, and how does it control sources and flows of organisms and limiting nutrients [*Power et al.*, 1995, 2005]? In turn, how do organisms shape the landscape through microbial weathering, the stirring and diffusion of soil, flow baffling and the stabilization of bars, banks and floodplains [*Dietrich and Perron*, 2006]? What are the coupled dynamics of hillslope-floodplain-stream interactions and what is their role in biogeochemical cycling [*Green et al.*, 2006]?

3.3. Modeling Tools: Coping With Self-Organization and Variability Across Scales

3.3.1. Hierarchical Modeling, Upscaling, or Direct Simulation?

[19] Channel networks span a wide range of length and timescales. Identifying the scales at which each of these processes operate, i.e., the scales at which they exhibit most of their variability and the major interactions will determine what classes of numerical models would be most pertinent for modeling and prediction. Important questions to be explored include: (1) Can the concepts of homogenization and upgridding, widely used in porous media flows, be adapted for land surface process modeling? (2) Can the concept of large-eddy simulation (LES), widely used in the atmospheric sciences, be adapted to earth surface process sciences to enhance the range of spatial scales over which prediction of earth surface processes can be made? (3) How can we apply often nonlinear slope-dependent flux laws [*Dietrich et al.*, 2003] to fractal landscape surfaces? (4) Is direct simulation, i.e., mechanistic modeling based on

small-scale processes, computationally feasible and conceptually valid in light of the complexity of earth surface systems and the spontaneous emergence of organization at larger scales [*Werner*, 1999]?

3.3.2. Data Assimilation and Ensemble Prediction in Earth Surface Dynamics

[20] Data assimilation and probabilistic prediction are now recognized to be essential elements of any numerical modeling system of complex natural phenomena. The goal of data assimilation is to produce a regular, physically consistent representation of a system from a heterogeneous collection of in situ and remote sensing observations that sample the system imperfectly and irregularly in space and time. Can naturally occurring similar spatial structure such as that provided by channel networks be used to improve both positioning of local environmental sensors and assimilation and interpolation of locally sensed data?

[21] Probabilistic prediction acknowledges that there is uncertainty in our understanding of the physical system and therefore in the equations and/or parameters that we use to describe it as well as in the initial conditions of the system. Therefore a single deterministic prediction of a future state of the system is not adequate and a suite of such predictions (ensemble prediction) which account for all uncertainties is needed. The areas of data assimilation and ensemble prediction have been extensively explored in the oceanic and atmospheric sciences and more recently in the hydrologic sciences. How can these methods be best adapted to Earth surface science?

3.3.3. Coupling Across Scales, Nonlinear Dynamics, and Predictability

[22] Channel systems, and landscapes in general, are formed by nonlinear processes that interact with each other over a wide range of scales. Prediction of a future state of the system knowing its initial conditions is a fundamental problem with important applications in geomorphologic restoration and planning. It is known that in many natural systems, small perturbations can lead to larger-scale disturbances (even under constant forcing) altering the evolution of the system and reducing its predictability from an initial known state. Models based on the equations of motion show limitations in predicting future states of geomorphologic systems [*Werner*, 1999]. It is important to analyze the intrinsic predictability of attributes of these systems, such as flow, sediment flux, channel geometry and shifts, and to understand how system predictability varies as a function of scale, adapting techniques from other fields [*Basu et al.*, 2002]. Theoretical advances in the physics and dynamics of coupled systems have considerably advanced over the past few years but much remains to be done to apply these advances to the highly nonlinear, highly interactive space-time evolution of Earth surface systems.

3.3.4. Self Organization, Pattern Formation, and Moving Boundaries

[23] Channels and channel networks represent the most spatially significant instance of spontaneous pattern formation and self-organization on Earth. In many cases the evolution of these patterns requires tracking evolving boundaries between specific transport domains, for instance, the boundary between gravel-dominated and sand-dominated

sediment transport, a shoreline, or an ecological boundary. These are termed "moving boundary" problems because the front must be found and tracked as part of the problem's solution [*Paola and Voller*, 2005; *Swenson et al.*, 2000; *Voller et al.*, 2006]. The development of numerical techniques for tracking moving boundaries, starting with methods developed for, for instance, solid-liquid fronts, is a major research frontier in surface dynamics.

3.4. Role of New Observational Techniques

[24] Geosciences is witnessing an era of rapid development of new sensor technology and observational techniques that are poised to revolutionize our understanding, and thus predictive modeling capabilities, of Earth surface dynamics. High-resolution topography (e.g., 1 m topography data from LIDAR) and wireless sensor technology with embedded networked sampling (e.g., concurrent and adaptive sampling over large spatial coverage and short time intervals; and particle-tracking techniques) provide an opportunity to bridge the gap between the small scales at which biogeochemical processes occur and the larger scales at which organizing patterns are observed. Wireless technology, smart sensors with controlled activation capabilities, e.g., during extreme floods or high temperatures, small sensors that can be attached to moving gravel ("talking stones") [*McNamara and Borden*, 2004], isotopes for dating, radar imaging, etc. can all work synergistically to sample processes at scales ranging from a few mm and seconds to planetary length and time scales. However, despite the extreme spatial and temporal variability and the large range of scales of interacting processes, one cannot sample everywhere and all the time. Thus the challenge exists to use even rudimentary knowledge of the underlying variability, of cause-effect relationships, and of possible scaling relationships to optimize sampling network design. To that effect, detailed knowledge of topography is expected to play a significant role.

[25] The newly available high-resolution LIDAR topographic data [*Carter et al.*, 2001] provide the opportunity to explicitly resolve channel and floodplain morphology, stream corridor geometry (including geomorphologic disturbances at confluences), and vegetation characteristics throughout the basin. Having such high-resolution channel morphology continuously available along stream reaches and over the whole watershed offers the potential of understanding cause-effect relationship between channel attributes and biological and geochemical processes. Such relationships can guide efficient design of environmental observatories and also guide efforts to upscale local processes, e.g., algal production [*Hondzo and Wang*, 2002], denitrification potential, etc., to stream reach averages, and ultimately to indices characterizing the state of the whole watershed [*Boyer et al.*, 2006]. However, existing methods for extracting channel networks from 90 m or 30 m DEMs do not perform well when applied to the extraction of topographic features from 1 m LIDAR data. New "geomorphologically informed" image processing techniques are needed to take advantage of the rich information provided by these sensors, including the automatic mapping of service roads and skid trails created during logging that are large contributors of sediment to the streams.

3.5. Role of Laboratory Studies

[26] The complexity and tendency toward spontaneous pattern formation of channels and channel networks make them inviting targets for study under controlled conditions in a laboratory setting (flume or outdoors facility) where individual and interactive effects of primary drivers can be teased apart. Experiments yield improved process understanding and provide the basis for testing hypotheses rigorously. Laboratory study is a useful complement to field studies for processes that are too slow, infrequent, inaccessible, and/or violent to permit direct observation in the field. This includes a wide range of important natural processes, so we expect experimentation to play a major role in Earth surface science for some time to come. Laboratory study has been especially fruitful for the study of self-organization, where the ability of the experimental system to develop patterns on its own is important. Self organized natural patterns that are fractal (a small part of the spatial pattern shows statistical similarity to the whole pattern) are especially appropriate for laboratory study even where formal conditions for dynamic similitude cannot be satisfied. A newer area for experimental study is physical-biological interactions, for example the contest between vegetation and physical processes that strongly influences the form and kinematics of river channels [*Gran and Paola*, 2001; *Tal et al.*, 2004]. In addition, we see bright prospects for experiments combining physical, geochemical and microbial processes, but as far as we know very little work has been done in this area.

4. Conclusion

[27] Prediction of the evolution of the Earth's surface is at the heart of environmental science: the surface is the environment in which most life and human activity take place. At present, we do not have the tools needed to reliably model and predict the interwoven physical, biological, geochemical, and human dynamics that shape the Earth's surface. Developing these tools will require integrating a broad range of fields including Earth sciences, hydrology, ecology, geochemistry, social sciences, physics, and mathematics. Earth surface dynamics should be an attractive area for young researchers with quantitative skills and a taste for interdisciplinary work.

References

Abreu, V., M. Sullivan, C. Pirmez, and D. Mohrig (2003), Lateral accretion packages (LAPs): An important reservoir element in deep water sinuous channels, *Mar. Pet. Geol.*, *20*, 631–648.

Basu, S., E. Foufoula-Georgiou, and F. Porte-Agel (2002), Predictibility of atmospheric boundary-layer flows as a function of scale, *Geophys. Res. Lett.*, *29*(21), 2038, doi:10.1029/2002GL015497.

Bennett, S. J., and A. Simon (Eds.) (2004), *Riparian Vegetation and Fluvial Geomorphology*, *Water Sci. Appl. Ser.*, vol. 8, 290 pp., AGU, Washington, D. C.

Bernhardt, E. S., et al. (2005), Synthesizing U.S. river restoration efforts, *Science*, *308*, 636–637.

Bonan, G. B., K. W. Oleson, M. Vertenstein, S. Levis, X. Zeng, Y. Dai, R. E. Dickinson, and Z.-L. Yang (2002), The land surface climatology of the

Community Land Model coupled to the NCAR Community Climate Model, *J. Clim.*, 15, 3123–3149.

Boyer, E. W., R. W. Howarth, J. N. Galloway, F. J. Dentener, P. A. Green, and C. J. Vörösmarty (2006), Riverine nitrogen export from the continents to the coasts, *Global Biogeochem. Cycles*, GB1S91, doi:10.1029/2005GB002537.

Carter, W., R. Shrestha, G. Tuell, D. Bloomquist, and M. Sartori (2001), Airborne laser swath mapping shines new light on Earth's topography, *Eos Trans. AGU*, 82, 549–550, 555.

Caylor, K. K., T. M. Scanlon, and I. Rodriguez-Iturbe (2004), Feasible optimality of vegetation patterns in river basins, *Geophys. Res. Lett.*, 31, L13502, doi:10.1029/2004GL020260.

Caylor, K. K., S. Manfreda, and I. Rodriguez-Iturbe (2005), On the coupled geomorphological and ecohydrological organization of river basins, *Adv. Water Resour.*, 28, 69–86.

Das, H. S., J. Imran, C. Pirmez, and D. Mohrig (2004), Numerical modeling of flow and bed evolution in meandering submarine channels, *J. Geophys. Res.*, 109, C10009, doi:10.1029/2002JC001518.

Davies, R. J., and H. W. Posamentier (2005), Geologic processes in sedimentary basins inferred from three-dimensional seismic imaging, *GSA Today*, 15, 4–9.

Dietrich, E. W., and W. T. Perron (2006), The search for a topographic signature of life, *Nature*, 439, 411–418.

Dietrich, W. E., D. Bellugi, A. Heimsath, J. J. Roering, L. Sklar, and J. D. Stock (2003), Geomorphic transport laws for predicting landscape form and dynamics, in *Prediction in Geomorphology*, *Geophys. Monogr. Ser.*, vol. 135, edited by P. Wilcock and R. Iverson, pp. 103–132, AGU, Washington, D. C.

Dodov, B., and E. Foufoula-Georgiou (2004), Generalized hydraulic geometry: Insights based on fluvial instability analysis and a physical model, *Water Resour. Res.*, 40, W12201, doi:10.1029/2004WR003196.

Dodov, B., and E. Foufoula-Georgiou (2005), Fluvial processes and streamflow variability: Interplay in the scale frequency continuum and implications for scaling, *Water Resour. Res.*, 41, W05005, doi:10.1029/2004WR003408.

Federici, B., and G. Seminara (2003), On the convective nature of bar instability, *J. Fluid Mech.*, 487, 125–145.

Foufoula-Georgiou, E., and V. B. Sapozhnikov (2001), Scale invariances in the morphology and evolution of braided rivers, *Math. Geol.*, 33, 273–291.

Gran, K., and C. Paola (2001), Riparian vegetation controls on braided stream dynamics, *Water Resour. Res.*, 37, 3275–3283.

Green, E. G., W. E. Dietrich, and J. F. Banfield (2006), Quantification of chemical weathering rates across an actively eroding hillslope, *Earth Planet. Sci. Lett.*, in press.

Gupta, V. K., O. J. Mesa, and D. Dawdy (1994), Multiscaling theory of flood peaks: Regional quantile analysis, *Water Resour. Res.*, 30, 3405–3421.

Hondzo, M., and H. Wang (2002), Effects of turbulence on growth and metabolism of periphyton in a laboratory flume, *Water Resour. Res.*, 38(12), 1277, doi:10.1029/2002WR001409.

Imran, J., G. Parker, and C. Pirmez (1999), A nonlinear model of flow in meandering submarine and subaerial channels, *J. Fluid Mech.*, 400, 295–331.

Intergovernmental Panel on Climate Change (2001), *Climate Change 2001: Synthesis Report*, edited by R. T. Watson and the Core Writing Team, 184 pp., Cambridge Univ. Press, New York.

Lunt, I. A., J. S. Bridge, and R. S. Tye (2004a), Development of a 3-D depositional model of braided river gravels and sands to improve aquifer characterization, in *Aquifer Characterization*, edited by J. S. Bridge and D. Hyndman, pp. 139–169, Soc. for Sediment. Geol., Tulsa, Okla.

Lunt, I. A., J. S. Bridge, and R. S. Tye (2004b), A quantitative, three-dimensional depositional model of gravelly braided rivers, *Sedimentology*, 51, 377–414.

McNamara, J. P., and C. Borden (2004), Observations on the movement of coarse gravel using implanted motion-sensing radio transmitters, *Hydrol. Processes*, 18, 1871–1884.

Menadbe, M., and M. Sivapalan (2001), Linking space-time variability of rainfall and runoff fields on a river networks: A dynamic approach, *Adv. Water Resour.*, 24, 1001–1014.

Mitchell, N. C. (2004), Form of submarine erosion from confluences in Atlantic USA continental slope canyons, *Am. J. Sci.*, 304, 590–611.

Murray, A. B., and C. Paola (1994), A cellular model of braided rivers, *Nature*, 371, 54–57.

Paola, C., and V. R. Voller (2005), A generalized Exner equation for sediment mass balance, *J. Geophys. Res.*, 110, F04014, doi:10.1029/2004JF000274.

Parker, G., and N. Izumi (2000), Purely erosional cyclic and solitary steps created by flow over a cohesive bed, *J. Fluid Mech.*, 419, 203–238.

Porporato, A., and I. Rodriguez-Iturbe (2002), Ecohydrology: A challenging multidisciplinary research perspective, *J. Hydrol. Sci.*, 47, 811–821.

Porporato, A., E. Daly, and I. Rodriguez-Iturbe (2004), Soil water balance and ecosystem response to climate change, *Am. Nat.*, 164, 625–632.

Power, M. E., A. Sun, G. Parker, W. E. Dietrich, and J. T. Wootton (1995), Hydraulic food-chain models, *BioScience*, 45, 159–167.

Power, M. E., N. Brozovic, C. Bode, and D. Zilberman (2005), Spatially explicit tools for understanding and sustaining inland water ecosystems, *Frontiers Ecol. Environ.*, 3, 47–55.

Rodriguez-Iturbe, I., and A. Rinaldo (1997), *Fractal River Basins*, 539 pp., Cambridge Univ. Press, New York.

Sambrook Smith, G., J. Best, C. Bristow, and G. Petts (Eds.) (2006), *Braided Rivers*, 368 pp., Blackwell, Malden Mass.

Sapozhnikov, V. B., and E. Foufoula-Georgiou (1997), Experimental evidence of dynamic scaling and indications of self-organized criticality in braided rivers, *Water Res. Res.*, 33, 1983–1991.

Seminara, G., and M. Tubino (1989), Alternate bars and meandering: Free, forced and mixed interactions, in *River Meandering*, *Water Resour. Monogr. Ser.*, vol. 12, edited by S. Ikeda and G. Parker, pp. 267–320, AGU, Washington, D. C.

Seminara, G., and M. Tubino (2001), Sand bars in tidal channels. Part 1. Free bars, *J. Fluid Mech.*, 440, 49–74.

Stainforth, D. A., et al. (2005), Uncertainty in predictions of the climate response to rising levels of greenhouse gases, *Nature*, 433, 403–406.

Sun, T., and G. Parker (2005), Transportational cyclic steps created by flow over an erodible bed. Part 2. Theory and numerical simulation, *J. Hydraul. Eng.*, 43, 502–514.

Sun, T., P. Meakin, T. Jøssang, and P. Meakin (1996), A simulation model for meandering rivers, *Water Resour. Res.*, 32, 2937–2954.

Sun, T., C. Paola, G. Parker, and P. Meakin (2002), Fluvial fan deltas: Linking channel processes with large-scale morphodynamics, *Water Resour. Res.*, 38(8), 1151, doi:10.1029/2001WR000284.

Swenson, J. B., V. R. Voller, C. Paola, G. Parker, and J. G. Marr (2000), Fluvio-deltaic sedimentation: A generalized Stefan problem, *Eur. J. Appl. Math.*, 11, 433–452.

Syvitski, J. P. M. (2005), The morphodynamics of deltas and their distributary channels, in *River, Coastal, and Estuarine Morphodynamics*, pp. 143–150, Springer, New York.

Tal, M., K. Gran, A. B. Murray, C. Paola, and D. M. Hicks (2004), Riparian vegetation as a primary control on channel characteristics in multi-thread rivers, in *Riparian Vegetation and Fluvial Geomorphology*, *Water Sci. Appl. Ser.*, vol. 8, edited by S. J. Bennett and A. Simon, pp. 43–58, AGU, Washington, D. C.

Voller, V. R., J. B. Swenson, W. Kim, and C. Paola (2006), A fixed grid method for moving boundary problems on the Earth's surface, *Int. J. Heat Fluid Flow*, in press.

Werner, B. T. (1999), Complexity in natural landform patterns, *Science*, 284, 102–104.

Wilcock, P. R. (1997), Friction between science and practice: The case of river restoration, *Eos Trans. AGU*, 78, 454.

Wohl, E., P. L. Angermeier, B. Bledsoe, G. M. Kondolf, L. MacDonnell, D. M. Merritt, M. A. Palmer, N. L. Poff, and D. Tarboton (2005), River restoration, *Water Resour. Res.*, 41, W10301, doi:10.1029/2005WR003985.

———————————

W. E. Dietrich, Department of Earth and Planetary Science, University of California, Berkeley, CA 94720, USA.

E. Foufoula-Georgiou, M. Hondzo, C. Paola, and V. Voller, St. Anthony Falls Laboratory, University of Minnesota Twin Cities, Minneapolis, 2 Third Avenue SE, MN 55414, USA. (cpaola@umn.edu)

D. Mohrig, Department of Earth, Atmospheric, and Planetary Science, Massachusetts Institute of Technology, Cambridge, MA 02139, USA.

G. Parker, Department of Civil Engineering, University of Illinois, Urbana, IL 61801, USA.

M. E. Power, Department of Integrative Biology, University of California, Berkeley, CA 94720, USA.

I. Rodriguez-Iturbe, Department of Civil and Environmental Engineering, Princeton University, Princeton, NJ 08544, USA.

P. Wilcock, Department of Geography and Environmental Engineering, Johns Hopkins University, Baltimore, MD 21218, USA.